STUDIES ON THE ROLE OF HVOF COATINGS IN IMPROVING RESISTANCE TO HOT CORROSION AND EROSION

A THESIS

Submitted in partial fulfilment of the
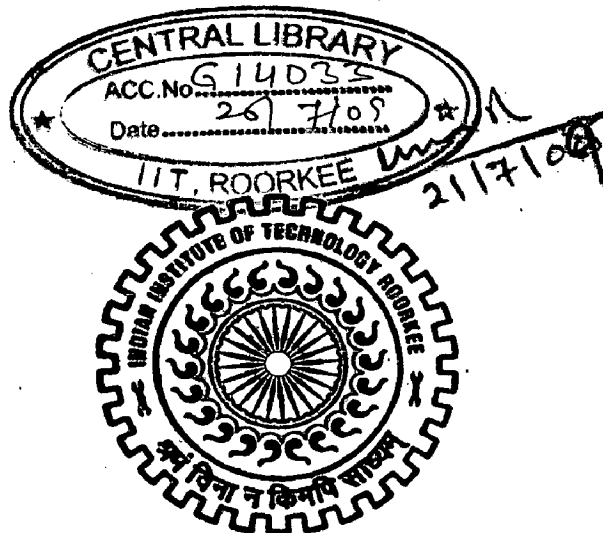*requirements for the award of the degree*
of

DOCTOR OF PHILOSOPHY

in

METALLURGICAL AND MATERIALS ENGINEERING

By

RAMESH M R

DEPARTMENT OF METALLURGICAL AND MATERIALS ENGINEERING
INDIAN INSTITUTE OF TECHNOLOGY ROORKEE
ROORKEE-247 667 (INDIA)
FEBRUARY, 2008

INDIAN INSTITUTE OF TECHNOLOGY ROORKEE
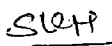# ROORKEE

CANDIDATE'S DECLARATION

I hereby certify that the work which is being presented in the thesis entitled **STUDIES ON THE ROLE OF HVOF COATINGS IN IMPROVING RESISTANCE TO HOT CORROSION AND EROSION** in partial fulfilment of the requirements for the award of the degree of Doctor of Philosophy and submitted in the Department of Metallurgical and Materials Engineering, Indian Institute of Technology Roorkee, Roorkee is an authentic record of my own work carried out during a period from July 2003 to February 2008 under the supervision of Dr.Satya Prakash, and Dr.S.K.Nath, Professors, Metallurgical and Materials Engineering, Indian Institute of Technology Roorkee, Roorkee.

The matter presented in this thesis has not been submitted by me for the award of any other degree of this or any other Institute.

(RAMESH M R)

This is to certify that the above statement made by the candidate is correct to the best of our knowledge.

(S.K.Nath)
Supervisor

(Satya Prakash)
Supervisor

Date: 21/3/08

The Ph. D. Viva-Voce Examination of **Mr. Ramesh M R** , Research Scholar, has been held on

....

Signature of Supervisors   Signature of External Examiner

i

ABSTRACT

The operating conditions in power station boilers are conducive to fireside corrosion and erosion, both in the furnace wall and in the super heater and reheater areas, and these effects cause tube wall thinning and premature failure. In the coal fired boiler, corrosion is occurs in several fashions due to combustion products which change their state of matter and become salts as a result of the high temperature. Combustion of coal generates very corrosive media particularly near the superheater tubes, forming highly aggressive ash deposits that contain alkali metals of sodium and potassium, and sulphur. This phenomenon can also be seen in the gas side of power station boilers when the fuel is a residual oil. Ashes formed due to the combustion of such fuels have a high concentration of compounds formed by vanadium, sodium and sulphur, mainly as Na_2SO_4–V_2O_5 complex and sodium–vanadates mixtures. Some mixtures of these compounds have low melting points 550°C. These compounds easily liquify at the operating temperatures of boilers and cause accelerated corrosion. Erosion is even more localized in its effect, and results from impact of particulates, such as coal ash, dolomite and unburned carbon particles on the surface of heated boiler tubes. High temperature oxidation and erosion are recognized as being one of the main causes of downtime in these installations. Maintenance costs for replacing failed tubes in these installations are also very high.

The materials used in these installations are fabricated from low-alloy carbon steels with chromium and molybdenum as the primary alloy additions. Although chromium is expected to impart corrosion resistance to high-temperature alloys through the formation of a passive oxide layer on the alloy surface, its concentration in boiler tube alloys in not sufficient to form a protective external scale.

Present materials being capable of resisting erosive and corrosive environments are highly alloyed, and thus expensive. In search for cost-effective solutions for Erosion –Corrosion problems, various coatings like thermal sprayed coatings have become attractive. The high-velocity oxy-fuel (HVOF) processes belong to the family of thermal spraying techniques, and are widely used in many industries to protect the components against erosion, corrosion and wear. This process has been shown to produce coatings with better density, coating cohesive strength and bond strength than many thermal spray processes. The possibilities of applying the HVOF process to a much wider range of materials are now being addressed. The role of the coating, in this case, is to provide a metal surface composition that will react with the environment to produce the most

protective scale possible, combining corrosion-erosion resistance with long term stability and resistance to cracking or spallation under mechanical and thermal stresses induced during operation of the component.

HVOF spraying has been carried out using a HIPOJET 2100 equipment (M/S Metallizing Equipment Co.Pvt.Ltd, Jodhpur, India), which utilises the supersonic jet generated by the combustion of liquid petroleum gas and oxygen mixture. The complex formulations containing Ni, Al, Cr, Si, Mo, WC, Co and boron have been used to develop combined corrosion and erosion resistant coatings. Four types of commercially available feed stock powders namely NiCrAl, NiAlCrFeMo, NiCrFeSiB and WC-Co/NiCrFeSiB were HVOF sprayed on three kinds of boiler tube steels designated as ASTM-SA210-Grade A1, ASTM-SA213-T11 and ASTM-SA213-T22. Differences in chemical compositions of coatings and substrate alloys can lead to inter-diffusion across the coating substrate interface, which can modify the oxidation and hot corrosion resistance of the coatings. Under the given spray parameters, seemingly dense laminar structured coating with thickness in the desired range of 260-295 μm and porosity less than 2 % has been achieved. All the coatings have retained the phases observed in starting powder, containing nickel rich FCC structure as a principal phase and has not undergone significant phase transformation. Oxidation, decomposition and decarburization of the coating powder are not serious due to higher particle speed and chosen parameters during HVOF spraying.

Understanding the behavior of these coated steels at elevated temperature in various environments has become an object of scientific investigation. Thermo cyclic oxidation studies are performed in static air as well as in molten salt (Na_2SO_4-60%V_2O_5) environment at 900°C for 50 cycles. The cumulative weight gain for all the HVOF coated GrA1, T11, and T22 steels are significantly lower than that of uncoated steels subjected to oxidation and molten salt hot corrosion. Based on the thermogravimetric data, the relative oxidation and hot corrosion resistance of the various coating under study can be arranged in the following sequence:

In Static air: NiCrFeSiB > WC-Co/NiCrFeSiB > NiCrAl > NiAlCrFeMo

In molten salt: NiCrFeSiB > NiCrAl > NiAlCrFeMo > WC-Co/NiCrFeSiB

The superior performance of NiCrFeSiB coating can be attributed to continuous protective oxide scale of amorphous glassy SiO_2 and Cr_2O_3 formed on the surface. The SiO_2 scale found to be passive in acidic molten $NaVO_3$ melt and hence all the NiCrFeSiB coated steel showed slow oxidation kinetics which indicated that the reaction rate is diffusion limited. The oxidation resistance of NiCrAl coatings can be ascribed to the thermodynamically stable phase of α-Al_2O_3 and Cr_2O_3 formed on the outermost surface. The preferential oxidation of Al and Cr along the nickel rich splat boundary blocks the

transport of oxygen into the coating through pores and voids, thereby making the oxidation rate to reach steady state. Because of accelerated oxidation induced by the molten salt, which act as catalyst and oxygen carrier, metastable θ-Al_2O_3 has formed in the initial cycles of studies and shows polymorphic transformation.

The oxides and spinels of Si, Cr and Co formed on surface during the oxidation of WC-Co/NiCrFeSiB coatings stabilized the formation of volatile tungsten oxide. While in molten salt environment, preferential oxidation of W and Cr during the initial stage impedes the formation of continuous layer of SiO_2. Tungsten oxide decreases the oxide ion activity of the molten salt environment to cause acidic fluxing of the active elements in the coating. The massive, loosely held needle microstructure of the oxides formed on the surface leads to least hot corrosion resistance of the WC-Co/NiCrFeSiB coatings in molten salt environment.

Comparatively lower oxidation resistance of NiAlCrFeMo coated steels may be attributed, to some extent, to severe internal oxidation along the splat boundary due to higher porosity content. In molten salt, the formation of nickel and chromium molybdates, which are liquid at 900°C, resulted in highly friable and porous scale. The corrosion rate reduces once the available Mo at the surface has been consumed. With the progress of oxidation, protective oxides of Ni, Cr and Al are formed at the subscale level.

Iron oxide protrusions are observed on the corroded surface of all the coated T22 steels except NiCrFeSiB coated steels. These protrusions lead to higher weight gains and rapid growth of inhomogeneous oxides. The probable cause of oozing out of iron oxide might be attributed to the presence of molybdenum in the T22 steel substrate. In general, coated GrA1 steels showed lower weight gain in comparison to coated T11 and T22 steels.

Solid particle erosion studies have been carried out as per ASTM G76 standard at 30° and 90° impact angles to provide the maximum erosion condition for both ductile and brittle materials under silica sand erodent. Relative erosion resistance of the various coating under study can be arranged in the following sequence:

WC-Co/NiCrFeSiB > NiCrFeSiB > NiCrAl > NiAlCrFeMo

The better erosion resistance of NiCrFeSiB coatings may be ascribed to its higher ductility and homogeneous microstructure. The erosion resistance of NiCrFeSiB coatings found to be increased by adding refractory WC-Co particles. The morphology of the eroded surface of WC-Co/NiCrFeSiB coatings point out craters, groove formation in binder matrix, lips and platelet formation, and carbide particle pull out as the prevailing erosion mechanism which signifies composite ductile and brittle modes of material removal. The principal erosion mechanism in NiCrAl coating is by severe plastic deformation even though fracture of some Ni-rich splats is observed. Higher erosion

losses observed for NiAlCrFeMo coatings might be attributed to relatively higher porosity of the coatings. Indentations, craters, and lips observed on the surface indicate the ductile erosion behavior of the coatings.

Substrate GrA1 steel exhibit lower steady state volume erosion rate in comparison to all the HVOF coatings under similar test conditions. The higher hardness ratio between silica erodent particle and substrate steel might have caused the penetration of silica particles in to the surface which bestow some shielding effect against impacting particles leading to lower wear loss.

The HVOF coated and uncoated samples were exposed to actual service conditions of the boiler for 1000 hours. The samples were tested in super heater zone of the coal fired boiler at Guru Gobind Singh Super Thermal Plant, Ropar, India. The flue gas temperature in this region is about 778±20°C. The erosion-corrosion behavior of all the HVOF sprayed coatings is promising in comparison to substrate boiler steels. Analogous to the observations in laboratory conditions, NiCrFeSiB coatings showed minimum thickness loss as well as lower weight gain in comparison to other coatings under study. The superior performance of these coating can be attributed to the thin and continuous oxide scale of SiO_2 and Cr_2O_3 formed on the surface. The weight gains for WC-Co/NiCrFeSiB coated steels are almost equivalent to that of NiCrFeSiB coated steels. Both these coatings got oxidized only at the uppermost surface to for thin protective oxide scale and rest of the coatings remain unoxidised. Low porosity content and rapid growth of protective oxides during the initial cycles leads to enhanced hot corrosion resistance of these coatings.

The better performance of NiCrAl coatings can be credited to thin protective oxide scale of α-Al_2O_3 and Cr_2O_3 formed on the surface as well as preferential oxidation of Al and Cr along the nickel rich splat boundary. Relatively lower erosion-corrosion resistance offered by NiAlCrFeMo coatings might be associated with higher porosity content in the coating. The entire cross section of the coating has been partially oxidized along the splat boundary.

The coatings under study have been found to be successful in protecting the given substrate boiler steels tested in laboratory as well as in actual coal fired boiler environment. NiCrFeSi coating shows superior performance among the coatings used in the present study. In addition to applications in superheater zone of coal fired boilers, these coatings can be applied to other applications like fluidized bed combustors, industrial waste incinerators, internal combustion engines, gas turbine, steam turbines etc.

ACKNOWLEDGEMENTS

CONTENTS

LIST OF TABLES

ABBREVIATIONS

HVOF	High Velocity Oxy-Fuel
BSEI	Back Scattered Electron Image
EDAX	Energy Dispersive X-ray Analysis
EPMA	Electron Probe Micro Analyser
SEM	Scanning Electron Microscopy
XRD	X-ray Diffraction
K_p	Parabolic Rate Constant
mpy	Mils per year
Hv	Vickers Hardness
m.p.	Melting Point
hr	Hour
.min	Minute
Bal	Balance
Fcc	Face-Centered Cubic
LPG	Liquefied Petroleum Gas
Wt%	Weight Percentage

CHAPTER 1
INTRODUCTION

The behaviour of material at elevated temperature is becoming of increasing technological importance, yet it is a problem man has to face and solve from the very beginning of his existence. It is important to understand the nature of all types of environmental degradation of metals and alloys as vividly as possible so that preventive measures against metal loss and failures can be economically devised to ensure safety and reliability in the use of metallic components. Corrosion of metals had received maximum attention of engineers and researchers in the field of environmental degradation of metals (Chatterjee et al, 2001).The materials used for high temperature applications are subjected to high temperature corrosion and wear under corrosive industrial environment. Hot corrosion was first recognised as a serious problem in 1940s in connection with the degradation of fireside boiler tubes in coal-fired steam generating plants. Since then the problem has been observed in boilers, internal combustion engines, gas turbines, fluidized bed combustion and industrial waste incinerators (Khanna and Jha, 1998).

Power plants are one of the major industries suffering from severe corrosion and erosion problems resulting in the substantial losses. For instance, steam temperature of boilers is limited by corrosion and creep resistance of boiler components, which affects the thermal efficiency of the boilers. Consequently, the thermal efficiency decreases and, hence the electricity production is reduced (Uusitalo et al, 2003). According to a survey (Metals Handbook,1975) conducted over a period of 12 years, encompassing 413 investigations, overheating was listed as the cause of 201 failures or 48.7% of those investigated. Fatigue and corrosion fatigue were listed as the next most common causes of failure accounting for a total of 89 failures or 21.5%. Corrosion, stress corrosion and hydrogen embitterment caused a total of 68 failures or 16.5%. In a case study of a coal fired boiler of a power plant in north western region of India, Prakash et al (2001) have reported that out of 89 failures occurring in one year duration, 50 failures were found to be due to hot corrosion and erosion by ash. Moreover fly ash content of the Indian coal is very high and causes severe erosion-corrosion of the materials in the power plants. High temperature oxidation and erosion of heat exchanger tubes and other structural materials in coal-fired boilers are recognized as being the main cause of downtime at power-generating plants, which could account for 50–75% of their total arrest time. Maintenance costs for replacing broken tubes in the some installations are also very high, and can be estimated at up to 54 % of the total production costs (Hidalgo et al, 2001A).

Some of the examples of surface damage in the power generation components as suggested by Stringer (1998) include:

1) Accelerated high-temperature fire-side corrosion associated with the presence of molten alkali-containing salts of super heater and reheater tubing in fossil fuel-fired boilers.

2) Accelerated medium-temperature fire-side corrosion, associated with the presence of a low oxygen activity environment and sulfur, of water-wall tubes in coal-fired boilers; and of gas-cooler tubes in coal gasifiers.

3) Accelerated high-temperature corrosion of gas turbine vanes and blades: normally associated with alkali salt deposits. Type I at higher temperatures; Type II at lower temperatures.

4) Steam-side oxidation of tubing, piping, and valves in fossil fuel-fired boilers.

5) Wastage (erosion or abrasive wear, sometimes coupled with corrosion) of fireside components in fluidized bed combustors, both bubbling and circulating.

6) Fireside erosion in coal-fired boilers; fly ash erosion and soot-blower erosion.

7) Erosion of combustion turbine components in dusty environments; e.g. expander turbines in pressurized fluidized bed combustors.

8) Erosion of combustion turbine first stage vanes and blades by carbon shed by improperly operating combustors, or by material collected by, and shed by, the compressor.

High-temperature corrosion varies widely, depending on the kind and grade of fuel and the operational conditions of the boilers, many studies are aimed to understand the corrosion mechanism of a particular system and to solve the practical problem for it. One of the most severe types of high temperature corrosion is ash deposit corrosion. This ash deposit corrosion can be divided as coal ash deposit corrosion and oil ash deposit corrosion depending on the fuel used for the boilers. Both types of ash deposit corrosion are due to fluxing action of the salt deposit. The use of different coals under a variety of combustion conditions, ranging from widely varying combustion gas chemistry to widely varying nucleation, growth and condensation of particulates, can have a direct effect on material degradation in these systems. Contaminants such as alkali, chlorine, and sulfur vaporize during gasification and combustion and eventually condense on metal surfaces, removing the protective layer from those surfaces by chemical reactions, fluxing, or fracturing. While the oil ash corrosion is induced mainly by action of the low melting vanadium oxides (Seong et al. 2000 and Natesan, 1993).

The presence of particulates such as coal ash and unburnt carbon in a rapidly moving gaseous stream can result in the mechanical removal of material or fire side oxide from

components. At elevated temperatures the process is complicated by the simultaneous effects of oxidation or the more aggressive corrosive environment. The impacting fly ash particles can deposit or embed themselves on the test surface in quite significant quantities and chemical reactions of erodent particles and oxide scales can develop on the eroding surface, so that the erosion rate is also dependent on the oxidation kinetics and erodent particle reactivity (Hidalgo et al 2001A and Warren, 1992). It is generally believed that the most erosive species in the fly ash are quartz, which is a crystalline form of SiO_2 and mullite. More than one quarter of all the boiler tube failures worldwide are caused by fly ash erosion. In the United States it has been estimated that about 28% of all failures in water wall tubes and 22% of those in superheater and reheater tubes are caused by fly ash erosion, making it the second largest cause of availability loss in fossil-fuel power plants (Stultz et al 1992).

The present materials used in these installations are fabricated from low-alloy carbon steels with chromium and molybdenum as the primary alloy additions. Although chromium is expected to impart corrosion resistance to high-temperature alloys through the formation of a passive oxide layer on the alloy surface, its concentration in boiler tube alloys is not sufficient to form a protective external scale. None of the alloys currently in use are completely resistant to corrosion. (Bluni et al 1996 and Harb et al 1990).

In view of the quantum of loss due to combined corrosion and erosion, it become imperative for an engineer to develop better defense against such degradation by exploring newer material system for the industrial service conditions. Strong corrosion and erosion resistance is required for high temperature materials, in addition to excellent mechanical properties such as high temperature strength, good creep resistance and microstructure stability. However, these requirements some times cannot be achieved simultaneously by alloy development alone. An alternate approach, where mechanical strength is accomplished by alloy development and corrosion or erosion resistance by surface coating is now generally acceptable practice in fossil fuel energy processes. Coatings will only be used, therefore, when resistance to environmental degradation cannot be combined with the necessary properties for the component to perform its function, or where the resulting alloy or its fabrication become so expensive that a coated system is economically preferable. Coatings can add value to products up to 10 times the cost of the coating (Matthews et al 1998 and Stringer 1987A).

Generally speaking, coatings can be regarded as materials with greater resistance to the significant surface degradation process. In the case of corrosion, the coating itself has a greater resistance to the corrosive environment. In the case of erosion or wear, the coating is resistant to this aspect. Surface engineering plays an important role in the operation of

all high temperature plants, whether for power generation, chemical processing or component heat treatment (Nicholls, 2000). The specific difficulties in the protection of metallic components at very high temperatures derive from the extreme reactivity of the environment and the very high mobility of the metallic species, leading to rapid diffusion and thus to instability of the protective layer. The role of the coating, in this case, is to provide a metal surface composition that will react with the environment to produce the most protective scale possible, combining corrosion resistance with long term stability and resistance to cracking or spallation under mechanical and thermal stresses induced during operation of the component (Gurrappa, 2003). A combination of the development of materials specifically designed for erosion-corrosion resistance and the appropriate technique for the application of these materials, as a coating would be the optimum solution.

Among the coating techniques, the thermal spray coatings are especially interesting for their cost/performance ratio. Unique alloys and microstructures can be obtained with thermal spraying. It is a process with almost no limitation of materials and with the ability to deposit coatings with thicknesses ranging from several micrometers to tenths of millimeters. Additionally, it is suitable for a great variety of shapes and sizes and has the advantage of maintaining the substrate temperature relatively low (Rodriguez et al. 2003).

Particle degradation and open porosity were two important factors that affect corrosion and erosion resistance. HVOF processing did not degrade significantly the composition of the consumable and produced coatings with low porosity, low oxide content, high sulfidation resistance, and high resistance to sulfur penetration. In contrast, APS processing caused significant degradation to the consumable and created coatings with a significant quantity of alloy depleted regions, high oxide content and high porosity (Luer et al., 2000).

Recent advances in modern coating technology resulted into several novel coating compositions according to the requirements. In the particular case where combined corrosion and erosion resistance at elevated temperature is required, the application of Ni-based coatings received widespread use. Nickel-based coatings with alloying elements of chromium, silicon, molybdenum and other minor elements have been tried. Also the combination of Ni-alloy with WC-Co has been evaluated for its performance in erosion-corrosion environment. The present investigation aims to study the corrosion and erosion behavior of these coatings in various environments.

CHAPTER 2
LITERATURE REVIEW

This chapter contains a comprehensive review of the literature with a special reference to oxidation, hot corrosion and erosion studies. HVOF spray process has been described in detail. The problem has been formulated after critical analysis of the literature towards the end of this chapter.

2.1   HIGH TEMPERATURE OXIDATION

It has long been established that most metals and alloys would react with oxygen to oxidize to some extent in gaseous atmosphere. Oxides are generally more thermodynamically stable than reaction products from other species (like N and S) which may be present in the environment. It is therefore common for oxides to form at the gas-metal interface (Pettit, 1977). Considering the total chemical equation for the reaction between a metal and oxygen gas to form the metal oxide,

$$aM + \frac{b}{2}O_2 \rightarrow M_aO_b$$
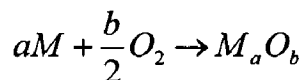
Oxidation of metals may seem to be among the simplest chemical reactions. However, according to Kofstad (1966), the reaction path and oxidation behaviour of a metal may depend on a variety of factors, and reaction mechanisms as a result may prove to be complex. The initial step in the metal-oxygen reaction involves the adsorption of gas on the metal surface. As the reaction proceeds, oxygen may dissolve in the metal, resulting in the formation of oxide on the surface either as a film or as separate oxide nuclei. Both the adsorption and the initial oxide formation are functions of surface orientation, crystal defects at the surface, surface preparation and impurities in both the metal and the gas. Thermodynamically, an oxide is likely to form on a metal surface when the oxygen potential in the environment is greater than the oxygen partial pressure in the equilibrium with the oxide.

When the oxidation process involves an alloy instead of a pure metal, many factors described for the oxidation of pure metals may be applied to the oxidation of the alloy. However, for alloys oxidation is generally much more complex as a result of some, or all, of the following (Kofstad 1966, Kbaschewshki, 1967, and Birks et al., 1983)

1. The elements of the alloy will have different affinities for oxygen reflected by the different free energies of formation of the oxides.

2. Ternary and higher oxides may be formed.

3. A degree of solid solubility between the oxides may exist.

4. The various metal ions will have different mobility in the oxide phases.

5. The various metals will have different diffusivities in the alloy.

6. Dissolution of oxygen into the alloy may result in sub-surface precipitation of oxides of one or more alloying elements (internal oxidation).

As the equilibrium partial pressure of oxygen for oxides is generally very small, initially all the elements on the surface of the alloy will form their respective oxides. However, as time goes on, the formation of the oxides on the surface of an alloy depends upon the individual activities of the elements and their relative affinities for oxygen (Li 1997).

Further, the requirement of a protective oxide scale is to have a slow growth rate. Oxidation reactions of protective oxide generally follow a parabolic rate equation given by:

$$x^2 = K_p t$$

Where x is the scale thickness in dimensions of length, t is the time and K_p the parabolic-growth rate constant in dimensions of length^2/time. However minor deviations from the parabolic behaviour are often observed (Doychak, 1995).

2.2   HOT CORROSION

Hot corrosion may be defined as an accelerated corrosion, resulting from the presence of salt contaminants such as Na_2SO_4, $NaCl$, and V_2O_5 that combine to form molten deposits, which will damage the protective surface oxides In hot corrosion, metals and alloys are subjected to degradation at much higher rates than in gaseous oxidation, with a porous non-protective oxide scale formed at their surface and sulphides permeating into the substrate. The behaviour of the metallic alloy is then dependent not only upon their oxidation resistance but also upon the reaction of oxide products with the molten salt deposits (Khajavi et al. 2004, Sidhu et al. 2003A and Lambert et al. 1991).

Corrosion damage from molten salts can occur in a wide variety of materials and by different mechanisms. It has been pointed out that although many studies have been performed, quantitative data for materials selection and performance prediction are rarely

available (Koger, 1987). Some factors that can make molten salts extremely corrosive include the following (Roberge, 2000):

1) By acting as fluxes, molten salts destabilize protective oxide layers (on a microscopic scale).

2) High temperatures are typically involved.

3) Molten salts are generally good solvents, preventing the precipitation of protective surface deposits.

4) Direct chemical reaction between the containment material and the salt.

5) The presence of noble metal ions in the molten salt, more noble than the containment material itself.

2.2.1   High Temperature (Type I) Hot Corrosion (HTHC)

High temperature (Type I) hot corrosion (HTHC) is nominally observed in the temperature range of about 825-950^{0}C when the condensed salt film is clearly liquid. The typical microstructure for HTHC shows the formation of sulphides and a corresponding depletion of the reactive component in the alloy substrate. The external corrosion products frequently comprise oxide precipitates dispersed in the salt film (Rapp and Zhang, 1994). The dominant salt in HTHC is Na_2SO_4 due to its high thermodynamic stability. The macroscopic appearance of HTHC is characterised in many cases by severe peeling of the metal and by significant colour changes (greenish tone, resulting from the formation of NiO) in the area of the accelerated attack (Eliaz et al, 2002).

2.2.2   Low Temperature (Type II) Hot Corrosion (LTHC)

Low temperature (Type II) hot corrosion (LTHC) occurs well below the melting point of pure Na_2SO_4. The reaction product morphology for this type of corrosion can be characterised by a non-uniform attack in the form of pits, with only little sulphide formation close to the alloy/scale interface and little depletion of Cr or Al in the alloy substrate (Rapp and Zhang, 1994). This form of corrosion is observed mainly within the temperature range 650-800^{0}C (Nicholls, 2000). The formation of low melting point eutectics causes typical LTHC pitting for instance the formation of Na_2SO_4-$NiSO_4$ eutectics for nickel-based superalloys. Wright (1987) suggested that a high partial pressure of SO_3 in the gaseous phase is required in the LTHC reactions to occur, in contrary to HTHC.

2.2.3 Hot Corrosion Degradation Sequence

All corrosion resistant alloys degrade in two stages namely, initiation and a propagation stage. The initiation of hot corrosion is often attributed to failure of the protective oxide layer and repair of oxide layer by itself. Once repair of the oxide is no longer possible, the propagation phase results in the rapid consumption of the alloy (Nicholls, 2000). Simons et al. (1955) first suggested the two-stage degradation; triggering phase and autocatalytic destruction. According to Pettit and Meier (1985), it is a fact that all corrosion resistant alloys degrade via these two stages and, it is the result of using selective oxidation to develop oxidation or corrosion resistance. They further elaborated that the conditions causing hot corrosion therefore do nothing more than shortening the time for which the alloys can form protective oxides via selective oxidation.

During the initiation stage of hot corrosion, alloys are being degraded at rates similar to those that would have prevailed in the absence of the deposits. Elements in the alloy are oxidised and electrons are transferred from metallic atoms to the reducible substances in the deposit. Consequently, the reaction product barrier that forms beneath the deposit on the alloy surface usually exhibits primarily those features resulting from the gas–alloy reaction (Pettit and Giggins, 1987).

In some cases of hot corrosion an increasing amount of sulphide particles become evident in the alloy beneath the protective reaction product barrier. In other small holes become evident in the protective reaction product barrier where the molten deposit begins to penetrate it. Eventually the protective barrier formed via selective oxidation is rendered ineffective, and the hot corrosion process enters into the propagation stage. Obviously in attempting to develop resistance to hot corrosion one should strive to have the superalloys remain in the initiation stage as long as possible. Initiation stage is important to the life of the alloy. Numerous factors affect the time at which the hot corrosion process moves from the initiation stage into the propagation stage as shown in Fig. 2.1. These factors also play the dominant role in determining the type of reaction product that is formed in the propagation stage. (Pettit and Meier, 1985).

The propagation stage of the hot corrosion sequence is the stage for which the alloy must be removed from service since this stage always has much higher corrosion rates than that in the initiation stage. The nonprotective corrosion products are formed during propogation stage and often results in catastrophic corrosion rates.

8

HOT CORROSION CHRONOLOGY

Initiation Stage

Salt deposit

Reaction product barrier

Alloy

Important factors

❖ Alloy composition
❖ Fabrication condition
❖ Gas composition & velocity
❖ Salt composition
❖ Salt deposition rate
❖ Condition of salt
❖ Temperature
❖ Temperature cycles
❖ Erosion
❖ Specimen geometry

Propagation Stage

Lesser protective
reaction product

Alloy
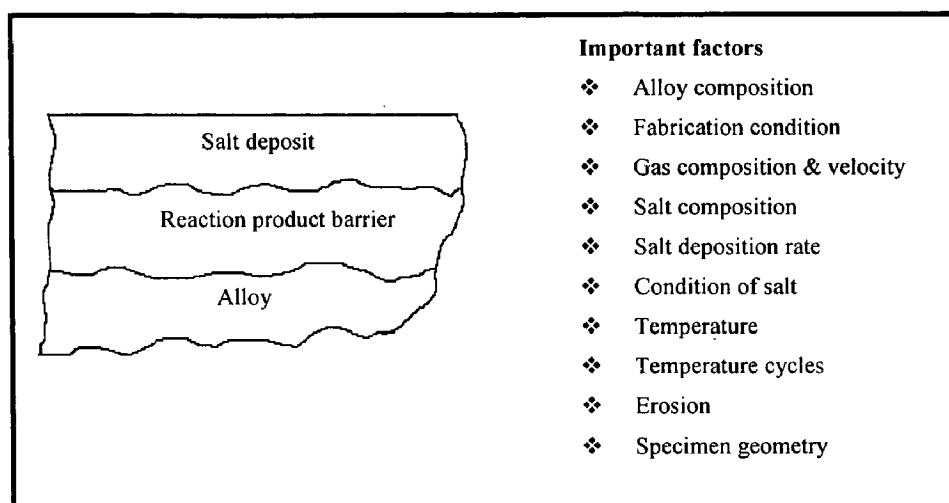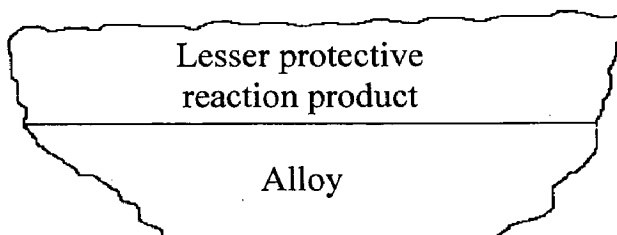
Fig. 2.1 Schematic diagram to illustrate the conditions that develop during the initiation and the propagation of hot corrosion attack, and to identify the factors that determine the time at which the transition from the initiation to the propagation stage occurs (Pettit and Meier, 1985).

2.2.4 Hot Corrosion Mechanisms.

Several mechanisms have been proposed for explaining the rapid degradation of alloys during the propagation stage of hot corrosion.

2.2.4.1 Sulfidation-Oxidation

Simons et al (1955) were among the first to study the chemical reaction between the salt and the metal or scale. They examined the oxidation of alloys involving Na_2SO_4 and found protective scale was ineffective and sulfide was observed at the oxidation front. They concluded the hot corrosion process is triggered by the initial reduction of the salt through an unspecified reducing agent R.

$$Na_2SO_4 + 3R = Na_2O + 3RO + S$$

$$M + S = MS$$
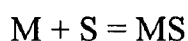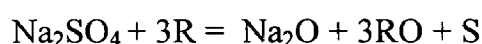
Where M is some metallic component in the alloy. The above reactions thus produced metallic sulfides that could then react with more Na_2SO_4 to liberate sulfur.

$$Na_2SO_4 + 3 MS = 4S + 3MO + Na_2O$$

$$4M + 4S = 4MS$$
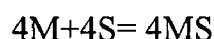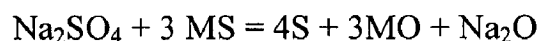
The above equation indicates autocatalytic destruction.

Seybolt (1968, 1970) extended the theory and reported that the triggering of the reaction could be accomplished by the reaction of the salt with the scale to form mixed oxides with sodium (e.g. Na_2CrO_4) and cause breakdown of the protective scale. The sulfur released by the above reaction result in depleting the substrate containing Cr to form CrS_x precipitates and oxidation rate was accelerated because of the chromium depletion.

Earlier works were focused on the effects of sulphur, as sulphides were often found in the microstructures of failure components. But it proved difficult to develop a coherent description of the process on this basis alone. It was not until about 1969 that the logical mechanisms which recognize the acid-base properties of molten Na_2SO_4 began to emerge (Bornstein and DeCrescente, 1969; Cutler, 1971; Goebel et al., 1973).

2.2.4.2 Salt Fluxing Reactions

The processes by which the reaction product barrier becomes non-protective due to the formation of species that are soluble in the liquid deposit have been referred to as basic or acidic fluxing reactions.

Bornstein and DeCrescente (1969) first explain the propagation stage of hot corrosion based on fluxing reactions. The removal of sulfur and its reaction with chromium promotes the formation of Na_2O. Further they suggest that hot corrosion associated with sulfidation is due to the reaction between Na_2O and the substrate.

According to Goebel and Petit (1970A and 1970B), the protection efficiency of the surface oxide layer might be lost as a result of fluxing of this layer in the molten salt. This fluxing may be either due to combination of oxides with O^{2-} to form anions (basic fluxing) or by decomposition of the oxides into the corresponding cations and O^{2-} (acidic fluxing). They suggested that low oxygen activity in the Na_2SO_4 caused the sulfur activity to increase so that sulfur diffused into the alloy and formed sulfides. Removal of sulfur and oxygen from Na_2SO_4 caused the oxide ion activity of Na_2SO_4 to increase such that the protective oxide layer was destroyed due to a basic fluxing reaction.

$$SO_4^{2-} = 1/2 \ S_2 + 3/2 \ O_2 + O^{2-}$$

$$MO \text{ (protective scale)} + O^{2-} = MO_2^{2-}$$
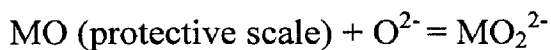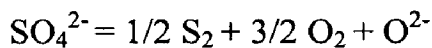
Further this degradation was not self-sustaining since the reaction ended when the conditions for the formation of sulfides were no longer favorable.

As compared to basic fluxing, acidic fluxing causes more severe oxidation. The acidic fluxing takes place when the O^{2-} activity in the molten salt is markedly lowered. In contrast to basic fluxing the acidic fluxing can be self-sustaining because the displacement of the salt from the stoichiometry does not become progressively more difficult as the reaction proceeds (Stringer, 1987B). In general the hot corrosion of superalloys with high contents of aluminium and chromium is often reported to occur according to the basic fluxing mechanism, whereas the hot corrosion of alloys with high contents of tungsten, molybdenum and vanadium has been reported to follow the acidic fluxing mechanism.

Goebel et al. (1973) proposed that protective oxide scales can also be destroyed by acidic fluxing due to presence of refractory elements in the alloy.

$$MO \text{ (protective scale)} = M^{2+} + O^{2-}$$
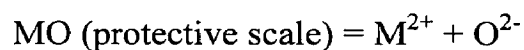
This type of reaction is self-sustaining.

11

2.2.4.3 Rapp-Gotto Criterion

The next step in the development of fluxing model was taken by Rapp and Goto (1981). They have proposed that protective scales on alloy could be made non-protective when the solubility gradients of the protective oxides in the molten deposit were negative since continuous dissolution and reprecipitation of oxide is then possible. Their mechanism permits fluxing to be either basic or acidic, within the need for a source or sink for O^{2-} ions which means that attack may continue without the additional supply of the deposit. They suggested that the electrochemical reduction reaction should generally be expected to create a condition of local high basicity, because reduction reactions may generate oxide ions as reaction products. However, the basicity produced by the electrochemical reduction cannot be understood well. Also, specific examples of this type of the mechanism were not given. Shores (1983) has examined the Rapp-Goto precipitation criteria for a variety of conditions and remarked that basic fluxing reactions are not always self sustaining.

2.2.4.4 Salt component induced hot corrosion

Another important characteristic of hot corrosion is the reduction of oxygen activity over the alloys by the deposit. This occurs because elements are present in the alloys that have high affinities for oxygen. If the salt is Na_2SO_4 the reaction is sulfidation or if the salt is NaCl, the reaction is chlorination. The effect of vanadium on hot corrosion has also been studied by different researchers. Bornstein et al (1973) and Goebel et al (1973) opined that a self-sustained acidic dissolution of the protective Cr_2O_3 or Al_2O_3 scales could take place when the salt film contains vanadium, because V_2O_5 is a strong acidic oxide. Further, Zhang and Rapp (1987) believed that every oxide should form an acidic solute with much higher solubility in the presence of vanadate, which should contribute to the more accelerated attack of oxides by mixed sulphate-vanadate melts than by a pure sulphate melt.

2.2.5 Vanadate - Induced Hot Corrosion

The phase stability diagram for the Na-V-S-O system at 900°C reported by Hwang and Rapp (1989) has been shown in Fig. 2.2. The dashed lines present the isoactivity lines for the vanadate species in the salt solution. They determined the dependence of the equilibrium concentrations of various vanadate solutes in the sodium

sulphate-vanadate solutions on the melt basicity by considering following equilibrium reactions:

$$Na_2SO_4 \rightarrow Na_2O + SO_3$$

$$Na_3VO_4 \rightarrow Na_2O + NaVO_3$$

$$2NaVO_3 \rightarrow Na_2O + V_2O_5$$
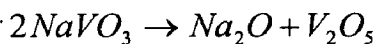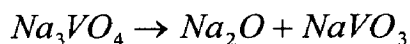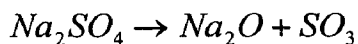
The equilibrium concentration of each vanadium compound varies continuously with melt basicity. Na_3VO_4 is the dominant component in the melt at basicity less than 8.2 and V_2O_5 is dominant at basicity greater than 16.3. For basicities between 8.2 and 16.3, $NaVO_3$ is the most important vanadium solute.

Based on the available thermodynamic data, Na_2SO_4 can react with V_2O_5 to increase the acidity of melt through the formation of vanadates $NaVO_3$ (m.p.$\approx$ 610°C) as a result of following reaction at 900°C (Kolta et al, 1972)

$$Na_2SO_4 + V_2O_5 \rightarrow 2NaVO_3\,(l) + SO_2 + \tfrac{1}{2}\,O_2$$
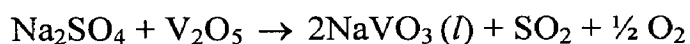
Vanadium and sodium are common impurities in low-grade petroleum fuels. Molten sulphate-vanadate deposits resulting from the condensation of combustion products of such fuels are extremely corrosive to high temperature materials in the combustion systems. Thermodynamic calculations for the equilibrium concentrations of Na_3VO_4, $NaVO_3$ and V_2O_5 in a mixed sodium sulphate-vanadate solution containing 30 mol% vanadate as a function of melt basicity have been reported by Hwang and Rapp (1989). They suggested that vanadate ions greatly increase the acidic solubility of all metal oxides compared to that in pure Na_2SO_4.

According to Otero et al (1987) Na_2SO_4-60%V_2O_5 deposit was detected on a number of components in actual service which were operated at high temperature and were in contact with high-temperature gases from combustion of dirty fuels, containing certain amounts of impurities, i.e. Na, V, and S etc. The presence of sulphur and its oxidised compounds were reported to favour the formation of isolated lobes with radial morphology having great permeability to facilitate the access of oxygen which further led to reduction in the protector character of scale. The presence of vanadium and its oxidised products was observed to generate compounds with aciculate morphology, identified to look like alkaline vanadate complexes. These aciculate shapes further contribute to reduce the protective character of the scale. The equilibrium diagram for varying composition of
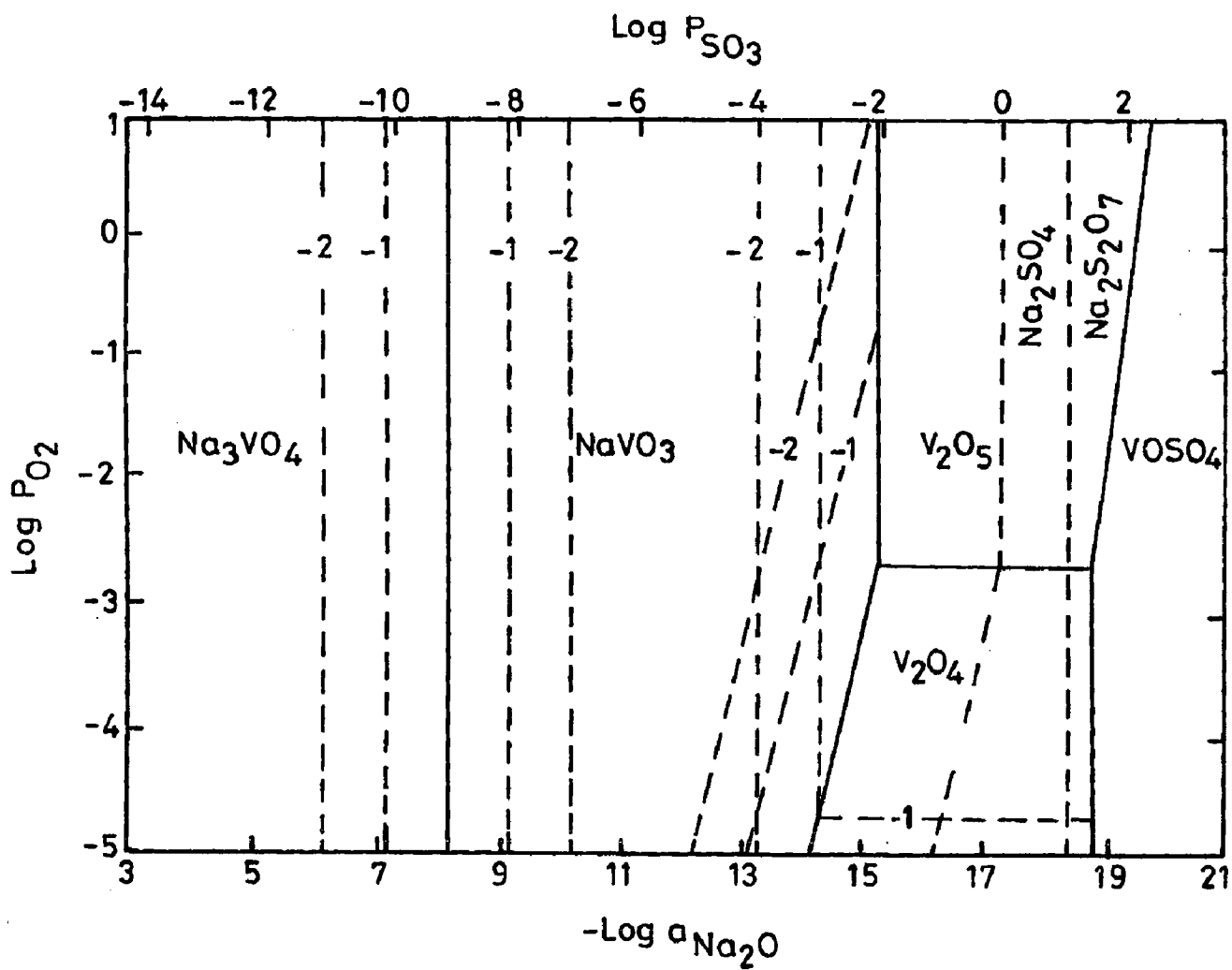
Fig. 2.2 Phase stability diagram for Na-V-S-O system at 900 ^{0}C (Hwang and Rapp, 1989).

Na$_2$SO$_4$ is shown in Fig. 2.3 and the mixture of Na$_2$SO$_4$-60%V$_2$O$_5$ is seen to be the lowest eutectic temperature.

Kofstad (1988) proposed that during combustion, the vanadium contaminants are oxidized to the higher valence vanadium oxides (V$_2$O$_4$ and V$_2$O$_5$) and sodium vanadates are formed by the reaction of vanadium oxides and sodium salts, e.g. Na$_2$SO$_4$. Accordingly the composition of the vanadates may be presented in a simplified form as (Na$_2$O)$_x$V$_2$O$_5$, but the detailed compositions of the individual vanadates may be more complex as part of the vanadium may be in the +IV state. The solid compounds comprise (Na$_2$O)$_x$V$_2$O$_4$(V$_2$O$_5$)$_{12-x}$ (often termed β bronze), (Na$_2$O)$_5$(V$_2$O$_4$)$_x$(V$_2$O$_5$)$_{12-x}$ (K bronze), NaVO$_3$ (sodium metavanadate), Na$_4$V$_2$O$_7$ (sodium pyrovanadate) and Na$_3$VO$_4$ (sodium orthovanadate). A notable feature of the vanadates is that they have relatively low melting points, which extend from 535^{0}C upwards. Furthermore, metal oxides dissolved in the vanadates may suppress the melting points and eutectic temperatures even further.

Tiwari and Prakash (1996 and 1997) and Tiwari (1997) have reported hot corrosion studies on some industrial superalloys in temperature range 700-900^{0}C in the environments comprising of pure Na$_2$SO$_4$, Na$_2$SO$_4$-15%V$_2$O$_5$ and Na$_2$SO$_4$-60%V$_2$O$_5$. Corrosion rates were observed to very high in the environment having Na$_2$SO$_4$-60%V$_2$O$_5$ composition. The extremely corrosive nature of this composition was attributed to its low melting point i.e. 500^{0}C. Tiwari et al (1997) further revealed that in Na$_2$SO$_4$-60%V$_2$O$_5$ melt, the degradation was due to the cracking of the protective scale under the influence of the fluxing action of the melt for both Fe-base alloy Superfer 800H and Co- base alloy Superco 605.

Sidhu and Prakash (2006A) studied the performance of plasma sprayed NiCrAlY, NiCr, Stellite-6 and Ni$_3$Al coatings in Na$_2$SO$_4$-60%V$_2$O$_5$ environment at 900°C under cyclic conditions. They reported comparatively lesser corrosion resistance offered by Ni$_3$Al coatings due to the internal sulphidation. Penetrated sulphur reacts with the reactive elements of the base metal to form sulphides with in the metal, which eventually convert into oxides due to advancing scale-metal interface.

Bornstein et al (1973) investigated the relationship between vanadium oxide and Na$_2$SO$_4$ accelerated oxidation for nickel-base superalloy B-1900 and seven binary nickel-base alloys. It was established that the corrosion attack commenced by dissolution of the normally protective oxide scale into the fused salt. The dissolution was suggested to occur by a reaction between oxide ions present in melt and the oxide scale. They further opined

that the sulphidation attack can be inhibited by decreasing the oxide ion content of the fused salt.

Sidky and Hocking (1987) investigated the mechanisms of hot corrosion by molten sulphate-vanadate deposits for Ni-10Cr, Ni-30Cr, Ni-20Cr-3Al, Ni-21Cr-0.3Si, Ni-20Cr-5V alloys and IN738 superalloy. Corrosion in rich VO_3^- melts was aggressive due to the fluxing action of the salt, which takes place along internally sulphidised areas.

Oxidation and hot corrosion in sulphate, chloride and vanadate environment of a cast nickel base superalloy have been reported by Deb et al (1996). It was proposed that the presence of vanadate in conjunction with sulphate and chloride provided additional fluxing action, which destroyed the integrity of the alloy and weakened its mechanical properties.

Singh et al. (2005A) investigated the corrosion behaviour of a nickel-base superalloy in Na_2SO_4-60%V_2O_5 environment at 900 °C under cyclic conditions for 50 cycles of one hour each. They revealed that superalloy Superni 601 showed intense spalling of the scale and the weight gain, including the spalled scale, was enormous during hot corrosion studies in the given aggressive environment. They revealed that $NaVO_3$ formed due to the reaction of Na_2SO_4-60%V_2O_5 acts as a catalyst and also serves as an oxygen carrier to the metal.

Singh (2003) studied the effect of V_2O_5 on the sulphate ion reduction and its influence on the hot corrosion of metal in the sulphates melt. The author reported that addition of V_2O_5 in the melt increases the hot corrosion of nickel extensively. According to Tafel plots measurement, corrosion or oxidation rate of nickel increases more than two orders of magnitude higher in the presence of 3% V_2O_5 in (Li, Na, K)$_2$ SO$_4$ melt at 550 °C.

2.2 EROSION WEAR

Erosive wear is caused in the solid bodies by the action of sliding or impact of solids, liquids, gases or a combination of these (Ramesh et al. 1991). Erosion can be divided in to three basic types: Solid particle erosion, liquid impact erosion and cavitation erosion. Cavitation erosion is the loss of material due to the repeated formation and collapse of bubbles in a liquid. Liquid impact erosion is the damage by water droplets. Solid particle erosion involves the impact of solid particles on a solid surface.

Solid particle erosion is an important material degradation mechanism encountered in a number of engineering systems such as thermal power plants, aircraft gas
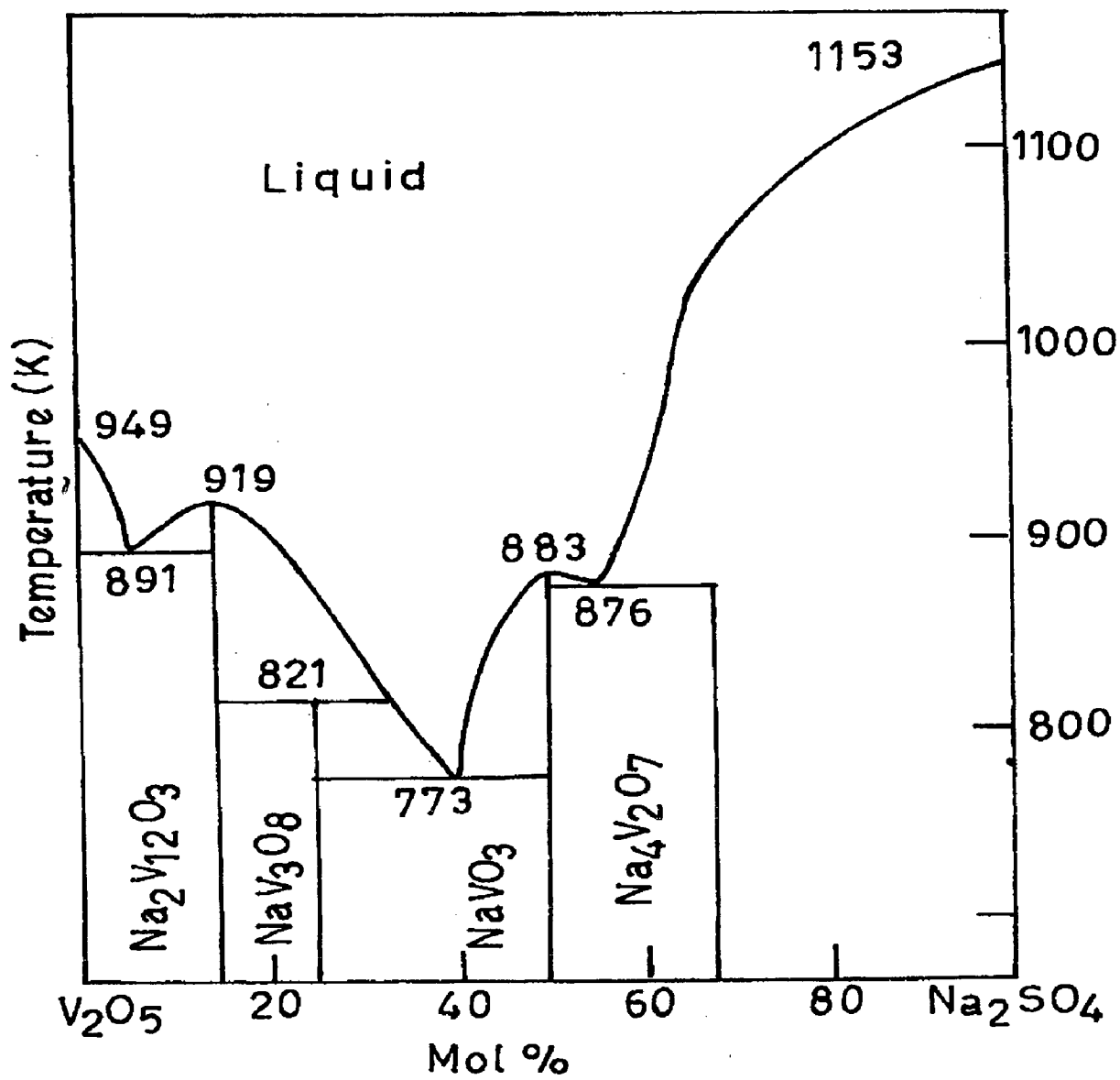
Fig. 2.3 Phase Diagram for Na_2SO_4-V_2O_5 System (Otero et al, 1987).

turbine engines, pneumatic bulk transport systems, coal liquefaction/gasification plants and ore or coal slurry pipe lines. At the same time, the erosion process has been used to advantage in number of situations like sand blasting of castings, shot peening of rotating components, cutting of hard and brittle materials by abrasive jets and rock drilling (Sundararajan 1995 and 1997).

Manifestations of solid particle erosion in service usually include thinning of components, a macroscopic scooping appearance following the gas/particle flow field, surface roughening, lack of the directional grooving characteristic of abrasion and in some but not all cases, the formation of ripple patterns on metals. Solid particle erosion can occur in a gaseous or liquid medium containing solid particles. In both the cases, particles can be accelerated or decelerated and their directions of motion can be changed by the fluid (Davis 2001).

Power station boiler-walls and other utility parts of coal-fired plants are subjected to frequent degradation by erosion–corrosion problems relevant to the reliability and economics of these installations. The environment of the furnaces is characterised by high-temperature conditions together with aggressive atmospheres, leading to corrosive deposits adhered to the walls and to erosion processes due to the ash particles (Fagoaga et al., 1998).

In erosion, several forces of different origins may act on a particle in contact with a solid surface. These are shown in Fig.2.4. Neighboring particles may exert contact forces, and a flowing fluid, if present, will cause drag. Under some conditions, gravity may be important. However, the dominant force on an erosive particle, which is mainly responsible for decelerating it from its initial impact velocity, is usually the contact force exerted by the surface. Erosion of metals usually involves plastic flow, whereas more brittle materials may wear predominantly either by flow or by fracture depending on the impact conditions (Hutchings 1992).

2.3.1 Factors Affecting Erosion

It is well understood that the erosion rates are affected by various factors (Davis 2001, Kosel 1992, Levy 1995, Sundararajan 1984, and Tilly 1973). These factors can be broadly classified into three types: impingement variables describing the particle flow, particle variables, and material variables. The primary impingement variables are particle velocity, angle of incidence, flux (particle concentration) and target temperature. Particle

variables include particle shape, size, hardness, and friability (ease of fracture). Material variables include all the material properties, such as hardness, work hardening behavior, and microstructure.

2.3.2 Erosion Mechanisms

Several mechanisms have been proposed for the material removal by solid particle impact for different alloys. Finnie (1958 and 1960) suggested a process involving cutting or micromachining as in metal cutting or grinding. According to him the impacting particle penetrates the target by a small amount, translates along the surface removing material ahead of it in a machining mode and finally leaves the surface. His analysis of the cutting action of a single particle launched against a ductile target was the first model of solid particle erosion capable of predicting material removal rate. He could solve for the trajectory of the particle in closed form as it cuts the surface, and thus predict material removal rates. This theory formed the foundation for later rigid-plastic models, which removed the restriction of particle rotation during impact. Finnie's model (1958 and 1960) predicts well angle dependence for less than 45°.

Bitter (1963 A, B) and Neilson and Gilchrist (1968) have further modified this micromachining mechanism model, primarily to account for erosion at large impingement angle. They have all tended to use the equation of motion of the particle translating along the surface of the specimen as a starting point for developing an analytical model. Bitter (1963 A ,B) has reported that erosion occurs by two types wear, one type, "deformation wear", caused by repeated deformation during collisions, eventually resulting in breaking loose pieces of the material. The other type," cutting wear", caused by the cutting action of the free-moving particles and it is similar to Finnie's model at low angle of impingement

Tilly (1969) reported that erosion to be a two-stage process: the initial stage being the formation of raised lips, and the second stage being the removal of these lips by the radial flow of the fragments resulting from the comminution of adjacent particle. Sheldon and Kanhere (1972) argued that, the metal removed flows around the sides of the impacting particle until it is strained sufficiently to break off.

Hutchings (1974 and 1979) have identified the two different regimes of deformation, referred to as ploughing and cutting. Studies of the impact of single particles on to metals at 30° impact angle show three type of impact damage, as illustrated in Fig 2.5.According to them rounded particles deform the surface by ploughing, displacing material to the side and
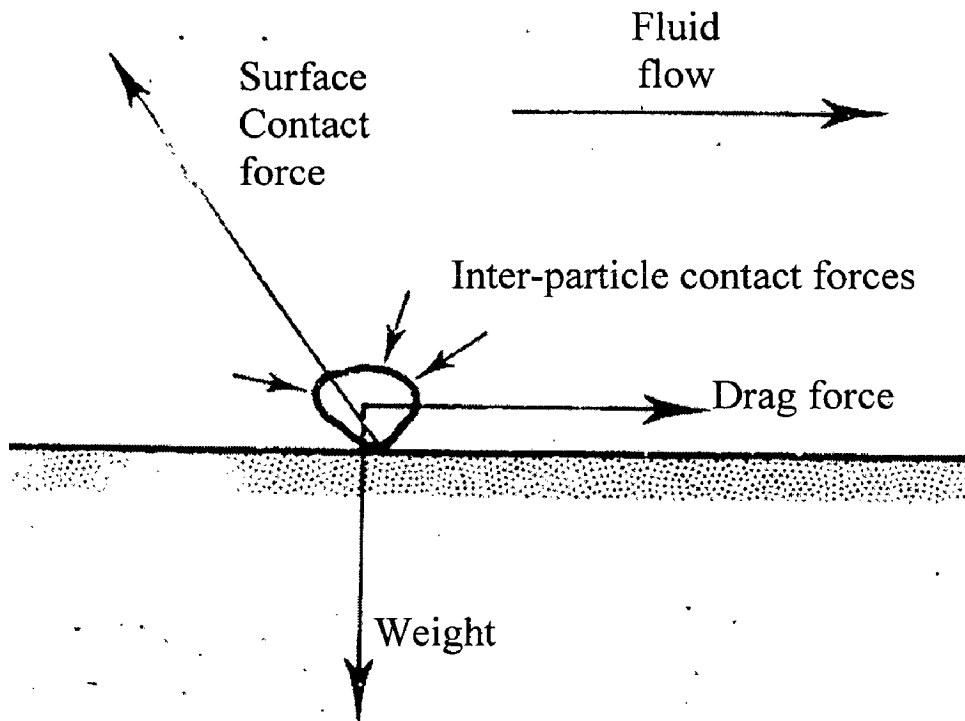
Fig. 2.4   Diagram showing the forces which can act on a particle in contact with a solid surface (Hutchings 1992)
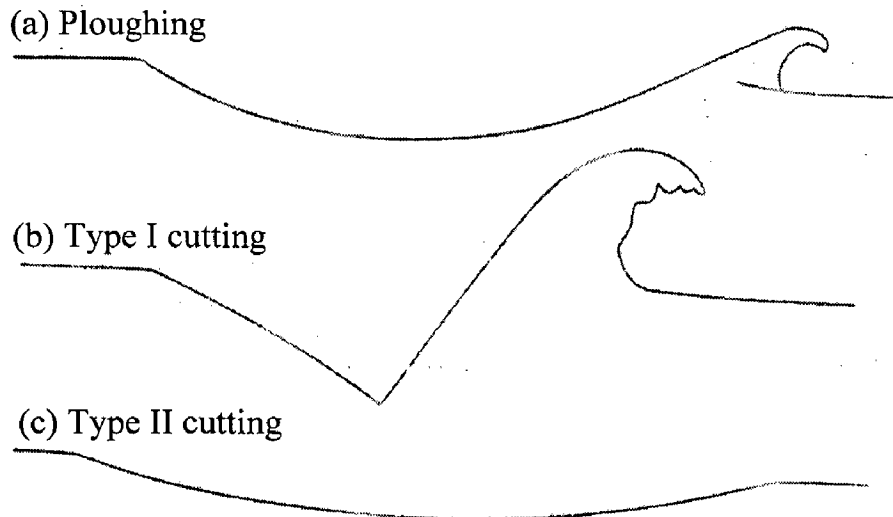
Fig. 2.5   Section through impact sites formed by hard particles on a ductile metal, showing typical shapes. (a) Ploughing deformation by a sphere (b) type I cutting by an angular particle, rotating forwards during impact: (c) type II cutting by an angular particle, rotating backwards during impact (Hutchings, 1979).

in front of the particle. Further impacts on neighbouring areas lead to the detachment of heavily-strained material from the rim of the crater or from the terminal lip. The deformation caused by an angular particle depends on the orientation of the particles as it strikes the surface, and on whether the particle rolls forwards or backwards during contact. He proposed that in the mode which has been termed type I cutting, the particle rolls forward, indenting the surface and raising material into a prominent lip, which is vulnerable to removal by subsequent nearby impacts. If the particle rolls backward, a true machining action can occur, in which the sharp corner of the abrasive grain cuts a chip from the surface. The type II cutting occurs over only in a narrow range of particles geometries and impact orientations. Ploughing tends to occur at large negative rake angles; i.e. when the angle between the surface and the leading edge of the particle is small. Whereas at large positive rake angle cutting deformation occurs.

Smeitzer et al. (1970) based on observations of the damage caused by individual impact events, suggested two erosion mechanisms for material removal of ductile metals. The first mechanism considers erosion due to localized melting of the target material followed by splattering of the molten material. The second mechanism considers the erosion by particles achieving bonding to the target material. Dislodging of these particles by subsequent impacts thereby, removes a small amount of target material adhering to the bonded particles.

Bellman and Levy (1981) and levy (1984 & 1986A) reported that the erosion of ductile materials can be described in terms of three distinct phases, that which occur sequentially in the steady state condition. In the initial phase, an impacting particle forms a crater, and material is extruded or displaced from the crater to form a raised lip or mound. In the second phase the displaced metal is deformed by subsequent impacts; this may lead to lateral displacement of the material which is part of the surface, and can be accompanied by some ductile fracture in heavily strained regions. Finally, after a relatively few impacts, the displaced material becomes so severely strained that it is detached from the surface by ductile fracture. In the steady erosion, all three phases occur simultaneously at different locations over the surface. This erosion mechanism is identified as "platelet mechanism". Soderberg et al (1981) have tested about 50 metals and alloys and further have classified them with respect to erosion mechanism. Their result indicates that almost all the metals and alloys lose material by formation of lip or platelet and their subsequent fracture.

Sundararajan (1991) developed a model valid for all impact angles based on the assumption that the localization of plastic flow underneath the impacting particle is

responsible for lip formation and hence erosion. He reported that it is capable of rationalizing the important experimental observations related to erosion, namely the effects of material properties, impact velocity and angle and particle shape.

Solid particle erosion damage of brittle materials has been investigated by Sheldon and Finnie (1966) who studied the erosive regime, usually referred to as hertzian fracture, where the contact between the particle and the body is exclusively elastic. In their analysis they considered dynamic forces between the surface and the particle and this resulted in a prediction of the volume removed for a material with specific properties. They also concluded that the fracture at the surface is a function of the volume of material constrained in the primary erosion zone in relation to the surface and volume flows.

The principal erosion mechanism in the brittle materials is mainly due to brittle fracture often accompanied by a small amount of plastic flow (Zambelli and Levy 1981 and, Levy 1983A). During the initial stage, network of fine cracks are created which make it possible for the impacting erodent particles to remove small chips of the brittle materials.

Wensink and Elwenspoek (2002) reported that the brittle erosion deals with material removal due to crack formation as illustrated in Fig. 2.6. When a brittle material is impacted by a hard sharp particle, the contact area is plastically deformed due to the high compressive and shear stresses and a radial crack is formed. After the impact, the plastic deformation leads to large tensile stresses that result in lateral cracks causing the material removal.

2.2 CORROSION-EROSION OF SUPERHEATERS

Superheaters are a series of tubes placed with in the flue gas path of the boiler, whose purpose is to heat the boiler steam beyond saturated conditions. The supersaturated steam is then delivered to a turbine for electric power generation in thermal power plants, to run plant and machineries in a process and manufacturing industry. Figure 2.7 illustrates a typical boiler

Fire side corrosion and erosion of metallic structural materials at elevated temperature in complex multicomponent gas environments that include particulates are potential problems in many fossil energy systems, especially those using coal as a feedstock (Natesan 1993). The combustion products of pulverized coal for the purposes of generating heat in a thermal power station are: coarse ash, fly ash, as well as the accompanying flue gases. The coarse ash or boiler bottom ash consists of 10-20% of the total ash load and the fly ash consists of 80-90% of the total ash load. As suggested by the
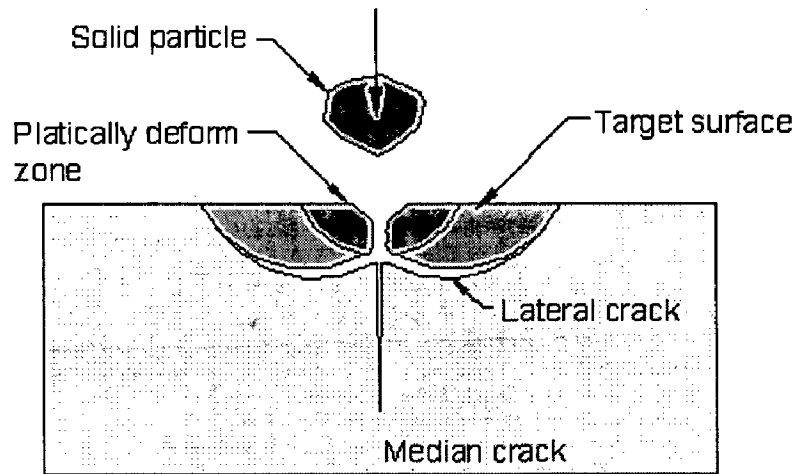
Fig. 2.6 Simplified schematic drawing of crack formation from a single particle impact.(Wensink and Elwenspoek, 2002)
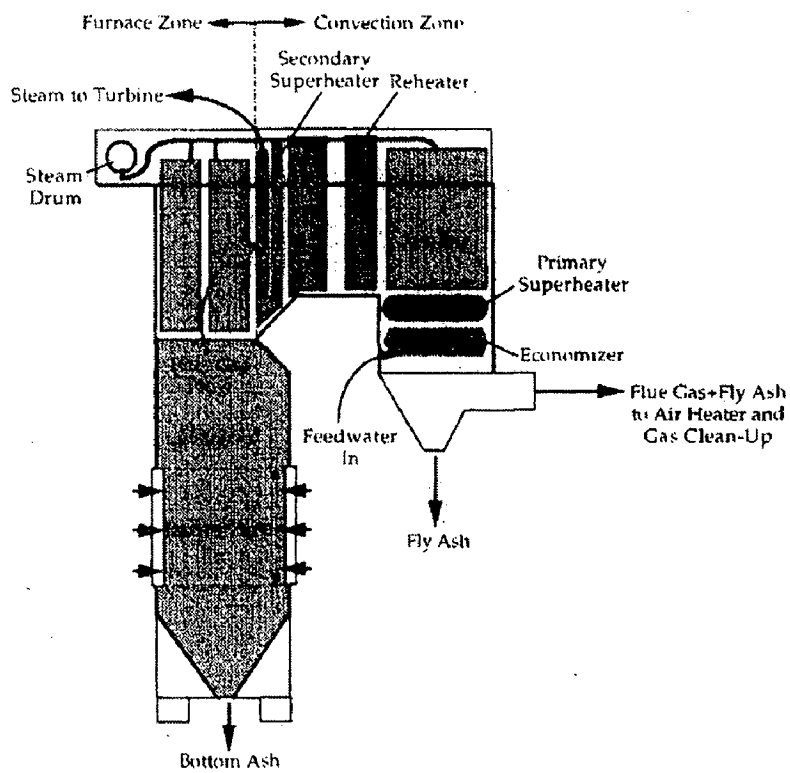
Fig. 2.7 Layout of a typical pulverized coal-fired boiler (Stringer John, 1995)

term "boiler bottom ash", the coarse ash drops out of the bottom of the boiler under the influence of gravity after combustion, whilst the fly ash entrained in the flue gas is ducted out. The nature of the fly ash is such that at high temperature it will form deposits on the boiler tubes in its path. The buildup of ash deposits in the convective pass may also be detrimental from a corrosion aspect. However, when passing through the latter stages of the boiler where the temperatures are substantially lower, the fly ash displays rebound as opposed to captive behaviour. This causes localized erosive wear that can lead to unscheduled and costly boiler tube failures (Suckling and Allen 1995).

There are several factors which motivate continued research on superheater corrosion. First, high temperature corrosion is one of the most important factors which limits the maximum steam temperature, and thus the efficiency of industrial boilers. Also, alloys used to combat corrosion are expensive and often depend on strategic elements. In addition, corrosion may become increasingly important as a result of the need to burn a wider range of coals or the need to change operating conditions to meet stricter environmental standards. A fundamental mechanistic understanding of superheater corrosion may provide a wider range of solution methods which are more economical than the present control strategies (Harb 1990).

The condensed thick layer of ash deposits on superheaters and reheaters leading to three kinds of problems: (a) reduced heat transfer of the tube, (b) plugging of gas passages in severe cases and (c) providing the environment in which complex sulphates are formed causing metal wastages. These sintered ash deposits formed on boiler tubes and superheater tubes are usually of layered structure, because the main constituents of ash, such as silicates and sulphates, are immiscible. The layered structure is further enhanced by high porosity of sintered matrix and the temperature gradient of the ash material (Srivastava 1997).

The corrosion steps start with the formation of Na_2O and K_2O in the flame, and the reaction with SO_3 to form sodium or potassium sulfate (Na_2SO_4 or K_2SO_4) in the ash deposit. Iron oxide, alkali sulfate and sulfur trioxide, react to form the trisulfates on the cooler tube surface. These alkali-iron trisulphates are molten at the operating temperature of the boiler due to their low melting temperature and can flux the scale or react with metallic iron resulting in the formation of massive amount of FeS in the corroded areas

(French 1983, Srivastava et al. 1997, Weulersse-Mouturat et al. 2004 and Harb et al.1990).

Oil ash cause corrosion of superheater and reheater due to low-melting ash deposits. Also, as with coal combustion products, back-end corrosion due to acid dew point corrosion is a possibility. The primary culprit in ash corrosion is vanadium, which comes from minerals in the soil and from the creatures that decomposed to form oil. Vanadium released in combustion forms several oxides, V_2O_3, V_2O_4, and V_2O_5. These combine with alkali salts to form low-melting compounds that accumulate on tube surfaces. The following equation illustrates a typical reaction:

$$Na_2SO_4 + V_2O_5 = 2NaVO_3 + SO_3$$
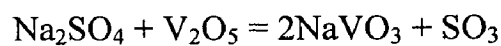
The melting point of $NaVO_3$ is 629°C. The low-melting sodium vanadium compounds are directly corrosive to steel. The corrosion rate accelerates with increasing metal temperature (Buecker 2002).

Fly ash erosion is a significant boiler tube failure concern. More than one quarter of all the boiler tube failures worldwide are caused by fly ash erosion. Fly ash erosion accelerates tube wastage by direct material removal and by removal of fireside oxide which increases the fireside oxidation rate. The free oxygen content in power plant boiler atmosphere is sufficient to account for a combined erosion-corrosion process, consisting of an oxidizing gas at elevated temperature carrying erosive fly ashes which impact against metallic surfaces. The process is complicated by the simultaneous effects of oxidation or the more aggressive corrosive environments. Hence the erosion rate is also dependent on the oxidation kinetics and erodent particle reactivity. The temperature at which the fly ash entrained in the flue gas strikes the tubes varies between 500C at the economizer, and 1200C at the superheater tubes. The higher the temperature of the flyash, the more the erosion propensity of the ash depends on the corrosion resistance of the alloy it is striking, i.e. the more susceptible the alloy is to forming an oxide layer, the more susceptible the tube will be loosing the oxide scale by brittle failure (Hidalgo et al 2001A, Stringer 1987A, and Suckling 1995).

Corrosion from the firing of coal or oil is essentially related to specific impurities in the fuels, which can lead to the formation of nonprotective scales or can disrupt normally protective oxide scales. The relevant impurities in coal are sulfur (about 0.5 to 5.2% in United States coals), sodium (0.01 to 0.7%), potassium (0.2 to 0.7%), and chlorine

(0.01 to 0.28%). In oil, the important impurities are sodium, which from United States refineries may range up to 300 ppm by weight; vanadium (up to 150 ppm by weight); and sulphur (0.6 to 3.6%). During combustion, these impurities can be melted or vaporized and will deposit upon contact with surfaces at temperatures lower than the condensation temperatures of the specific species. This provides a mechanism for the accumulation of deposits of fly ash on cooled surfaces downstream of the burners (Reid 1971, Raask 1985). In oil-fired boilers; superheater and reheater tube corrosion rates of as much as 0.75 mm/yr (30 mils/yr) have been observed in field measurements (ASM Handbook1992).

Unacceptable levels of surface degradation of metal containment walls and heat exchanger tubing by a combined erosion-corrosion (E-C) mechanism have been experienced in some boilers, particularly fluidized bed combustors by Levy (1993). They observed that extent of such degradation varied considerably, both between different boilers and within the same boiler operating on different feedstocks. The E-C mechanism that primarily occurred was a single one that has integrated both chemical and mechanical behaviour of the base metal and the boiler particles. According to them continuous, dynamic surface layer forms that consist of a mechanical mixture of particles from the boiler gases and oxide scale growing from the base metal. It was constantly being refurbished and removed at a rate that resulted in an essentially constant thickness of the deposit/scale layer during steady state operation of the boiler. Thereby indicated that the loss of sound metal is related to the rate of oxidation of metal.

Hoop and Allen (1999) have reported that in the year 1996 for example, there were a total of 23 fly ash erosion related boiler tube failures resulting in a total load loss of some 610,000 MW h in the power generation industry in South Africa.

Boilers and other steam power plant equipments are subjected to a wide variety of failures involving one or more of several mechanisms. Overheating is reported to be the main cause of failure in steam generators. A survey compiled by one laboratory over a period of 12 years, encompassing 413 investigations, listed overheating as the cause in 201 failures or 48.7% of those investigated. Fatigue and corrosion fatigue were listed as the next most common causes of failure accounting for 89 failures or 21.5%. Corrosion, stress corrosion and hydrogen embrittlement caused a total of 68 failures or 16.5%. Defective or improper material has been cited as the cause of most of the remaining failures (13.3%). Although "defective material" is often blamed for a failure but this survey indicates that

statistically it is one of the least likely cause of failure in power plant equipments (Metals Handbook, 1975).

Shortages of natural gas and petroleum-based fuels have prompted the investigation of various methods of increased utilization of coal. These methods include the direct combustion of coal in unique boilers as well as the conversion of coal to liquid and gaseous fuels. The conversion processes present problems of corrosion and erosion in various plant components. The combustion, of coal derived fuels, particularly liquid fuels, may well present corrosion and erosion fouling problems of much greater magnitude than have hitherto been experienced. Currently, boilers use ferritic alloys such as 2¼ Cr-I Mo or 9 Cr-1 Mo in applications up to about 426 °F metal temperatures and austenitic stainless steels to about 704 °F. These selections are based primarily on mechanical property considerations although the more highly alloyed austenitics show substantial corrosion resistance. Where greater resistance to sulfide corrosion is required, coatings have been employed (Frankel 1977).

2.5   PROTECTIVE COATINGS

Energy systems present a wide range of situations where components must survive in aggressive high temperature environments. Degradation processes include oxidation, mixed oxidant attack, deposit-induced degradation and molten salt attack, all potentially complicated by erosion. Combating these problems involves a number of approaches, one of which is the use of protective coatings. Increasingly greater demand imposed on materials makes it more difficult or, at the current stage of development, even impossible to combine the different properties required in one single material. Therefore, a composite system of a base material providing the necessary mechanical strength with a protective surface layer different in structure and/or chemical composition and supplied by a surface treatment can be an optimum choice in combining material properties. Coatings provide a way of extending the limits of use of materials at the upper end of their performance capabilities, by allowing the mechanical properties of the substrate materials to be maintained while protecting them against wear or corrosion (Sidky and Hocking, 1999, Stringer 1987, and Stroosnijder et al, 1994).

Warren (1992) reported that coatings have been applied to boiler tubes in UK power stations since the early 1980s. Most of the early trials were small, and designed to

evaluate procedures and materials for erosion and corrosion protection. Early considerations led to selection of plasma spraying for coating deposition. The use of coatings has been explored as a possible means of corrosion control. The use of coatings was reviewed by Raask (1985) who indicated that additional work is needed to develop corrosion resistant coatings with adequate life times. An advantage of coatings is that they are relatively cheap and they can be applied in-situ.

Hidalgo (2001A) reported that erosive, high-temperature wear of heat exchanger tubes and other structural materials in coal-fired boilers has become a key material issue in the design and operation of thermal power plants and is recognized as being one of the main causes of downtime in these installations. According to them maintenance costs for replacing broken tubes in these installations are also very high. They opinioned that use of thin wear and oxidation resistant coatings with good thermal conductivities, such as flame, plasma-sprayed or hypersonic velocity oxygen fuel (HVOF) nickel based or cermet (carbide–metal) alloys can be used to cope with these problems. Wang and Luer (1994) reported the recent use of coatings to protect the heat exchanger tubes of fluidized bed combustor from E-C problems and Hocking (1993) also suggested the use of corrosion resistant alloys as coatings to protect substrate alloys having good mechanical properties.

Sidhu and Prakash (2006B&C, 2005A) and Sidhu et al. (2006D) studied the performance of various thermal sprayed coatings in actual industrial environment of coal fired boiler for 1000 hours and reported better erosion-corrosion resistance of coatings with respect to boiler tube steels and nickel based superalloys.

Studies in Japan and Soviet Union with exposure periods up to 6500 hours have demonstrated the resistance of chromium diffusion coatings in field applications. Spray coatings of 50%Cr and 50%Ni have also been applied with success to local areas of superheater tubes and have survived 20,000 hours with only minimal attack. Therefore, coatings can be effective in controlling corrosion (Paul 1991).

Nicholls (2000) reported that the desire for higher operating temperature, improved performance, extended component lives, and cleaner and more fuel-efficient power plant/processes places severe demands on the structural materials used to construct such a high-temperature plant. As a result, many components operating at high temperature within such plants are coated or surface treated.

2.6 COATING TECHNIQUES

There are many coating deposition techniques available, and choosing the best process depends on the functional requirements, adaptability of the coating material to the technique intended, level of adhesion required, (size, shape, and metallurgy of the substrate), and availability and cost of the equipment. In general, widely used techniques to obtain coatings on boiler tubes are weld overlay, diffusion coatings, thermal spraying and laser cladding. The most important drawbacks of diffusion coatings are that they are thin and cannot be produced on-site or repaired. In comparison with diffusion coatings thermal sprayed coatings do not require such a high temperature of the base metal that would impair the mechanical or microstructural properties or bend treated tubes. In the case of weld overlay, there is increasing concern that repeated weld overlay application to the same tube area may result in embrittlement of the old overlay and lead to cracks that could propagate into the overlayed tube. Because of aforementioned shortcomings in diffusion and weld overlay coatings, attention is increasingly being focused on thermal sprayed coatings (Uusitalo 2002A & 2003, Rogers 1995, Solomon 1998).

2.6.1 Thermal Spray Process

Coating technologies have advanced a lot during the last decades. Thermal spraying is one of the most versatile processes of deposition of coating materials to enhance the wear and corrosion performances. It is a technique that produces a wide range of coatings for diverse applications. They are line-of-sight processes in which powder is heated to near or above its melting point and accelerated. The powder is directed at a substrate (surface to be coated) and on impact, forms a coating consisting of many layers of overlapping thin lamellar particles or splats. Almost any material that can be melted without decomposing can be used to form the coating and with the ability to deposit coatings with thicknesses ranging from several micrometers to tens of millimeters. The substrate, for most applications, is not heated above 150°C, so its metallurgical properties remain unchanged. The bond between a sprayed coating and the substrate is primarily mechanical (Bunshah 1994).

Thermal spraying uses two principal energy sources, chemical energy of the combusting gases that power the flame spray torches (e.g. HVOF spraying), and electric currents providing energy for the plasmatons (e.g. Atmospheric Plasma spraying).Generally, these coatings appear to be chosen on the basis of their good high

temperature oxidation resistance and are mainly alloys containing high quantities of nickel and/or chromium. Whilst it has been reported that uniformly deposited and coherent metallic coatings can provide erosion protection, only a few systematic experimentations have been undertaken to quantify the erosion performance of these materials (Miguel 2003 and Hoop et al. 1999).

Thermal spray coatings are especially interesting for their cost/performance ratio. Unique alloys and microstructures can be obtained with thermal spraying which are not possible with a wrought material. This includes continuously graded composites and corrosion resistant amorphous phases. Thermal spray coatings additionally offer the possibility of on-site application and repair of components, given a sufficient accessibility for the sprayer and his equipment.However, thermal spraying in the workshop is preferred, whenever possible, to achieve optimum results. (Heath et al., 1997).

Advanced thermal spray coatings which have been used in industries from many years for high temperature corrosion erosion protection are enlisted below:

1. Flame spraying with a powder or wire

2. Plasma spraying

3. High Velocity Oxy-fuel (HVOF) spraying

4. Detonation Gun

The properties of the coatings and its service performance depend essentially on the thermal spray process selected. Table 2.1 shows the characteristics of the WC-Co coatings sprayed by different thermal spray techniques (Sobolev 2004).

Meadowcroft (1987), Tani et al. (1998), and Wang (1997) reported that Conventional coating processes such as flame spraying were tested unsuccessfully in earlier years, but recent advances and ready availability of plasma spraying or HVOF equipments, including portable systems, has prompted an examination of these processes in the last few years. HVOF spraying is a competitive method for producing high quality coatings. HVOF coatings are homogeneous and dense coatings compared to the other thermal sprayed coatings (Moskowitz 1993 and Uusitalo et al., 2002B). The possibilities of applying the HVOF process to a much wider range of materials are now being addressed and there are several reports in the literature relating to the spraying of Ni and

other metallic alloys for corrosion resistant applications where dense, micro structurally homogeneous coatings are essential (Edris et.al.1997 and Li 2004).

2.6.2 HVOF Spray Process

The latest technology that completes the current family of thermal spray techniques is the high velocity oxy fuel process. This thermal spray technology uses the kinetic energy and the output of a supersonic flow of burned gases, to soften and to propel the spray powder, producing dense, very low porosity, good inter-particle cohesion and well-bonded coatings.

This process has been shown to produce coatings with better density, coating cohesive strength and bond strength than any thermal spray processes. Although a variety of high velocity combustion spray devices have been developed, most have in common a combustion chamber with ports leading to a nozzle, shown schematically in Fig. 2.8. The HVOF deposition process involves the combustion of oxygen and a fuel gas such as propylene, hydrogen or kerosene, under high pressure within a cooled confined combustion chamber. The products of combustion are then discharged through a cooled nozzle at high velocities. Powders to be deposited are fed into the combustion area by a carrier gas, where they are heated and carried by the gases exiting from the nozzle. Molten or partially molten droplets arrive at the substrate, flatten and solidify on impact. Coating thicknesses are normally in the range of 100 to 300 μm. Depending upon the injection pressures of the fuel gases, jet velocities exiting the nozzles are in the order of 1700 m s^{-1}, i.e. supersonic. High velocity combustion spray is a line-of-sight process hence it should be expected that the properties of the coatings will vary with the angle of deposition. In addition, stand-off may be in important parameter, a distance which is too short allows too little time for heating and acceleration of the powder particles or overheating of the substrate, while a stand-off which is too long may allow the powder particle velocities to diminish and their temperature to drop too far. The actual powder temperature and velocity distributions are strongly a function of the design of the high velocity combustion spray device as well as the operating parameters, morphology, and composition. (Mohanty et al. 1996 and Bunshah 1994).

Particle degradation and open porosity were two important factors that affect corrosion resistance. HVOF processing did not degrade significantly the composition of the consumable and produced coatings with low porosity, low oxide content, high

31

Deposition Technique	Heat Source	Propellant	Typical Temperature (°C)	Typical Particle Velocity (m s^{-1})	Average Spray Rate (kg h^{-1})	Coating Porosity (% by Volume)	Relative Bond Strength
Flame Spraying	Oxyacetylene/ Oxyhydrogen	Air	3000	30–120	2–6	10–20	Fair
Plasma Spraying	Plasma Arc	Inert Gas	16000	120–600	4–9	2–5	Very Good to Excellent
Low Pressure Plasma Spraying	Plasma Arc	Inert Gas	16000	Up to 900	-	< 5	Excellent
Detonation Gun Spraying	Oxygen/ Acetylene/ Nitrogen Gas Detonation	Detonation Shock Waves	4500	800	0.5	0.1–1	Excellent
High Velocity Oxyfuel (HVOF)	Fuel Gases	Combustion Jet	3000	800	2–4	0.1–2	Excellent

Table 2.1 Comparison of the characteristics for various thermal spraying (Sobolev 2004)
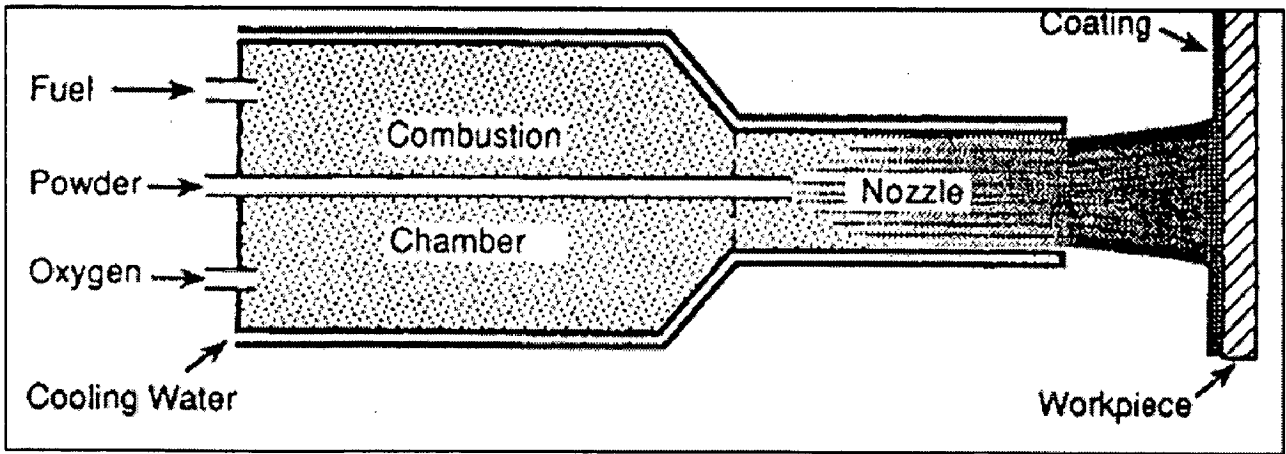
Fig.2.8   Schematic representation of high velocity oxy fuel spray process (Bunshah 1994)

sulfidation resistance, and high resistance to sulfur penetration. In contrast, APS processing caused significant degradation to the consumable and created coatings with a significant quantity of alloy depleted regions, high oxide content and high porosity. As a result, sulfur attack alloy-depleted regions with in the spalts and permeated through porous splat boundaries to the coating-subtrate interface (Luer et al., 2000).

Major advantages of the HVOF process includes

1) Due to higher kinetic energy of the particles impacting, HVOF coatings are homogeneous and dense coatings compare to the other thermal sprayed coatings. The gas velocities of 700m/s are typical with this process.

2) Due to particles shorter residence time in the flame (Lower powder temperature), degradation of the powder during spraying is less.

3) Bond strength as high as 90MPa and inter-particle cohesion are greater than any of the other processes.

4) Low porosity (<1%) and low oxide content (<1-2%), increase corrosion and wear resistance of the coating.

5) Since the particles are heated to moderate temperature, it is preferably used for coating material that tends to decompose at higher temperature.

6) Large size components can be easily coated with this technique.

7) It offers the possibility of on-site application and repair of components.

2.6.2 COATING FORMATION AND BONDING MECHANISM

The state of the particle as it exits the combustion zone has an effect on the final microstructure of the coating. The kinetics of droplet flattening depends upon the droplet size and the impact velocity. Initially, just after impact, inertial effects dominate, the viscous flow effect becomes more important as the droplet spreads, and the influence of the surface energy could become a significant factor towards the end of the spreading process (Pawlowski 1995 and Sobolev 2004). During the rapid solidification of the spray particles there is a close contact between particles and the substrate surface. This leads to bonding effects due to mechanical interlocking, adhesion, diffusion, chemical reactions, and sometimes partial fusion of the contact surfaces. These bonding effects permit the formation of a continuous coating layer as illustrated in Fig. 2.9. Mechanical interlocking

is the main mechanism of thermal spray coating adhesion/ adherence, if the substrate temperature is kept within the above mentioned range. The bond between impacting particles and the substrate surface is established to a high degree through the arriving droplets liquid flowing and solidifying around the substrate asperities/ roughness. Usually these asperities are formed by mechanical means such as abrasive blasting, grit blasting, or rough turning, which also activate and clean the surfaces prior to coating.

The quenching stresses within the spray particles increase the interlocking effects. In Fig. 2.10, the possible bonding interactions are illustrated. The adhesive bonding mechanisms are effective at microcontact areas between particles and/or substrate. These forces correspond to the atomic attractive forces within crystalline solid matter, since the particles approach one another as close as atomic levels. Depending on the type of atomic bonding, on the one hand Vander Waals forces (physisorption) and on the other hand an exchange of valence electrons (chemisorption) may take place.

Between spray particles, as well as between spray particles and the substrate, melting and diffusion within micro dimensions may occur due to the interface temperature being somewhat higher than the melting point of the substrate, despite the high cooling rates (Bunshah 2001).

2.7 PRINCIPAL COATING TYPES

The major criteria for the development of an optimized coating are that the coating should form thermodynamically stable protective phases on its surface by the reaction with the process environment. The "classical" protective phases will be Al_2O_3, Cr_2O_3 and SiO_2 as well as some of the spinels. These protective phases should be slow growing in order to keep coating reservoir depletion rates by the surface reaction on a low level. Again the above-mentioned phases play a key role in high temperature corrosion protection (Schütze et al. 2006).

Uusitalo et al. (2002B) and Warren (1992) also suggest that coatings for combined erosion-corrosion protection, complex formulations containing Ni, Al, Cr, Mo, Si, borides and other minor elements may also be used. Nickel-based materials are more resistant than iron-based materials. Chromium is considered as the most beneficial alloying element for sulfidation resistant steels. Aluminum and silicon are also reported to increase sulfidation resistance of steels. Depending on the partial pressures of oxygen and sulfur, oxide
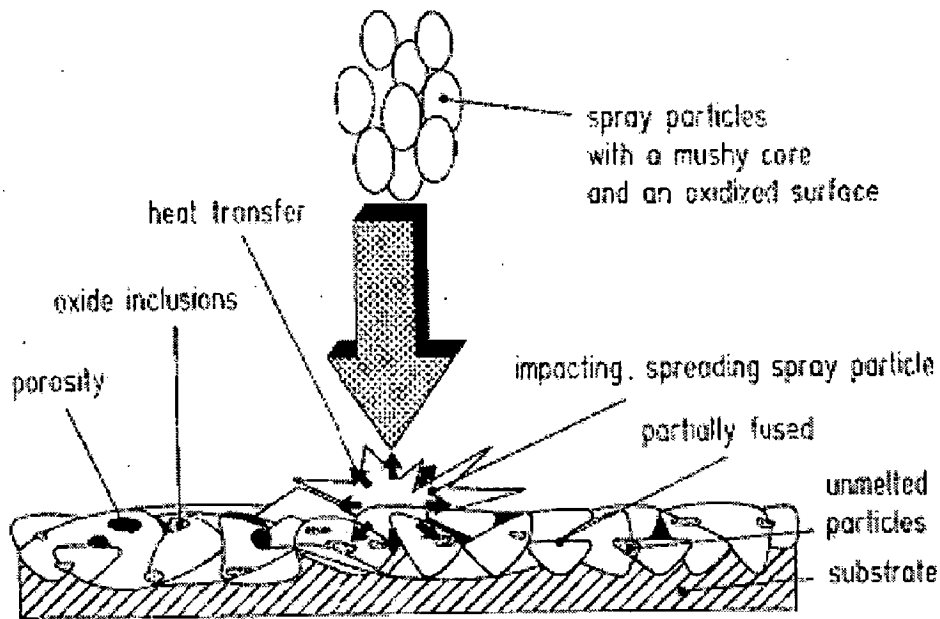
Fig.2.9   Schematic of a typical structure of sprayed coating (Bunshah 2001).

| Particle in flight | Impact | Heat transfer to substrate | Solidification and shrinkage of splat |

COATING FORMATION

| Mechanical Interaction | Local Welding |

BONDING MECHANISMS
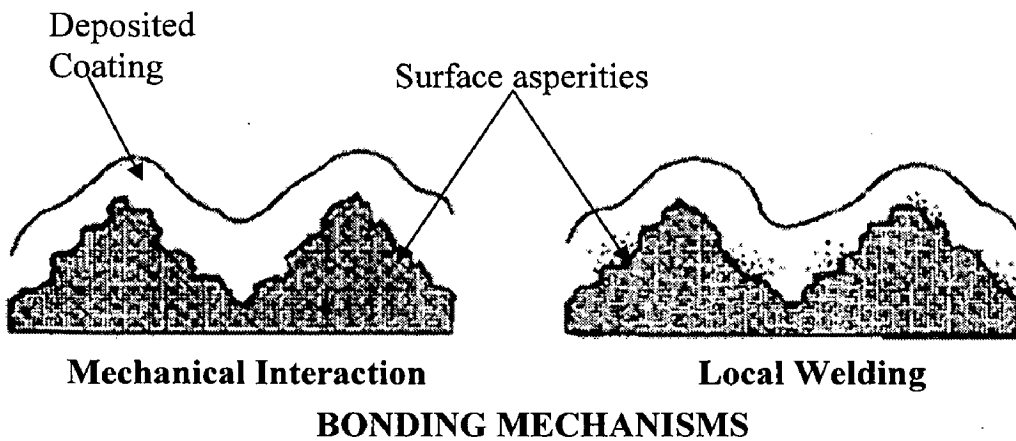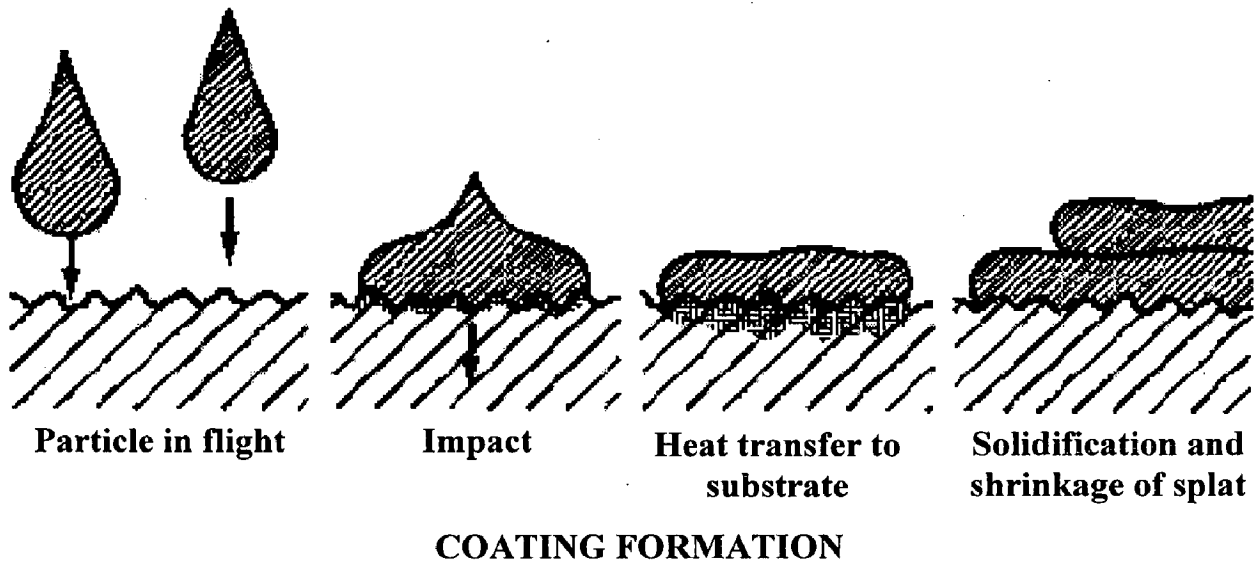
Fig.2.10   Bonding interactions with in a spray coating (Bunshah 2001).

formers, like chromium and silicon, may form oxides also in reducing combustion atmospheres, whereas iron and nickel form mainly sulfides. Cobalt, aluminum and some other minor additives are reported to increase sulfidation resistance on nickel-based alloys. An addition of molybdenum has also a positive effect on corrosion resistance of alloys in chlorine-containing environments (Lai 1990, Chou 1986, Strafford 1989, Levi 2001, Agarwal 1995, Zahs et al. 2000, Kawahara et al. 1999 and Norton 1999).

Coatings resistant to high-temperature oxidation most frequently rely on the formation of a dense, adherent Al_2O_3 (alumina) layer at the interface between the coating and the environment. This means that the coating itself must have enough aluminum for alumina to be the preferred oxide, and to provide an adequate reservoir to reform the protective oxide if it is removed. Alumina is relatively soluble in molten alkali salts; and in some circumstances where a molten salt is a component of the corrosive environment a coating which will form a dense adherent Cr_2O_3 (chromia) layer is preferable (John Stringer, 1998). Nickel-based coatings with high chromium content have been applied to boilers to improve the corrosion resistance of the boiler components. Additional alloying of coatings with silicon, molybdenum and other minor elements may also be used. Besides Ni-based coatings, also intermetallic Fe_3Al coatings have been reported to perform well in combustion environments (Kawahara, 1997).

Many coatings contain aluminum, chromium or silicon. As with high-temperature structural alloy design, iron-, nickel-, or cobalt-based alloys containing concentrations of aluminum in excess of about 10 wt. % or chromium in excess of 16 wt. % will, in an oxidizing atmosphere, eventually form scales in which alumina and/or chromia predominate. When aluminium and chromium are present in combination, much lower levels of aluminium are required (typically 5 wt. %) to establish a protective alumina scale. It should be noted that many intermetallic compounds require high aluminum and chromium contents to form stable alumina and/or chromia scales (Nicholls, 2000).

Ni based coatings are used in applications when wear resistance combined with oxidation or hot corrosion resistance is required. The largely employed Ni based powder belongs to the Ni-B-Si system with the addition of other alloying elements. Boron decreases the melting point of Ni and gives the alloy self-fluxing properties which are very useful for powder welding. This self fluxing is intensified by further addition of Si. Chromium addition in the alloy promoted the oxidation and corrosion resistance at

elevated temperatures and increases the hardness of the coating by the formation of hard phases. Carbon produces hard carbides with elevated hardness that promotes the wear resistance of the coating. Hence special attention has been paid in Ni based self fluxing alloy as they provide greater stability at high temperatures (Miguel 2003 and Hurricks 1972).

Wang et al., 1996 and Kulu et al., 2002 reported that the wear resistance of self fluxing alloys (NiCrFeSiB) coatings can be greatly increased by adding refractory carbides such as WC, VC, WC-Co, TiC, $B_{13}C_2$ and CrC to the metallic matrix. WC-Co coatings are often used in applications that require abrasive wear resistance. In order to combine the satisfactory corrosion resistance of NiCr alloys with the high abrasive wear resistance of WC–Co, thermally sprayed coatings were produced by mixing both components. The resulting structure is also termed as "double cemented". Better corrosion performance was found to be dependent on the resulting microstructure of the coating (Godoy 2003 and 2004, Kulu et al., 2002 and, Shipway et al. 2002).

Berger et al. (1998) observed linear oxidation behaviour at 500°C for WC, but he inferred that when WC is mixed with a metallic matrix, its oxidation behaviour is highly dependent on the matrix alloy. The presence of the refractory metal strengthener is quite necessary for the mechanical properties.

Kim et al. (2003) observed that the coating of 35% WC with NiCrBSiC shows the best quality in terms of hardness and porosity. The increase of the WC content from 0 to 35% increases the coating hardness. There is a toughening effect and general hardness increase without significant brittleness increase. Further increase of the WC content makes the hardness decrease. This is due to a sharp increase of the porosity and pore size that generates high stress concentration.

Ni based coatings are used in applications when wear resistance combined with oxidation or hot corrosion resistance is required. Dense and small-grained nickel-based coatings with high chromium content and additional minor alloying elements performed well. It is obvious that the chromium content has a positive effect on erosion resistance of Ni-based coatings. Modifications of HVOF Ni.50Cr coatings are used in boilers for corrosion protection. Alloying with Mo and B seemed to stabilize the structure. Nickel-chromium alloys have been used as coatings to deal with oxidation environments at high

temperature. When nickel is alloyed with chromium, this element oxidises to Cr_2O_3 at rates which could make it suitable for use up to about 1200°C, although in practice use is limited to temperatures below about 800°C(Goward,1986).

Hidalgo et al.(2001A) suggest that the use of nickel–chromium coatings may be regarded as a sound practice when taking into account the good results, which have been shown in all the simulative tests along with the economic advantage of these coated materials in relation to the totally stainless steel pieces. They reported that the promising results described in their study have to be confirmed by means of field testing inside real power plant boilers. They also reported that use of flame-sprayed, may be disregarded as a result of the formation of internal thermal cracks when submitted to high temperature cycles.

Schütze et al.(2006) suggest that coatings based on the formula Me_1Me_2CrAlX with Me_1, $Me_2 = Ni$, Co, Fe and $X = Ce$, Hf, La, Y, etc. if they are applied as overlay coatings can act as a reservoir phase for the formation of protective and slow growing Al-based oxide scales by reaction with the operation environment, thus providing an environmental barrier against the ingress of more aggressive species down to the metal to be protected and slowing down metal consumption rates by the oxidation process itself.

2.8   Formulation of problem

Components in energy-production systems required to operate at high temperatures may suffer a variety of degradation processes as a consequence of complex multicomponent gas environment. These include oxidation, mixed oxidant attack, molten-salt-induced attack and erosion. The development of wear and high temperature oxidation protection systems in industrial boilers is a very important topic from both engineering and an economic perspective.

In the laboratory at Metallurgical and Materials Engg, IIT Roorkee, ongoing research to develop inhibitors and thermal spray coatings to over come environmental degradations such as oxidation, hot corrosion and erosion in various industrial applications is under progress. Use of inhibitors like MgO, CeO2, CaO, MnO2, etc. have already been investigated and decrease in the extent of hot corrosion in the most aggressive environment of Na_2SO_4-60%V_2O_5 at 900°C has been achieved. However, the major problem being envisaged is the application of these inhibitors to hot metal surface. In this regard, use of the thermal sprayed protective coatings has been identified as a potential area and the present investigation has been carried out in this context.

Present materials being capable of resisting erosive and corrosive environments are the alloys having large concentration of alloying elements and thus expensive. The use of coatings is often justified because of difficulties associated with mechanical properties, workability and high material price of highly alloyed materials. The use of appropriate thin wear and corrosion resistant coatings with good thermal conductivities, offers an avenue to minimize material degradation and to extend component life. Particle degradation and open porosity were two important factors that affect corrosion ad erosion resistance. HVOF thermal spray technology uses the kinetic energy and the output of a supersonic flow of burned gases, to soften and to propel the spray powder, producing dense, very low porosity, good inter-particle cohesion and well-bonded coatings. Due to particles shorter residence time in the flame (Lower powder temperature), degradation of the powder during spraying is less.

The possibilities of applying the HVOF process to a much wider range of materials are now being addressed and there are several reports in the literature relating to the spraying of Ni and other metallic alloys for corrosion-erosion resistant applications where dense, microstructurally homogeneous coatings are essential. Nickel-based coatings with high chromium content have been reported to perform well in oxidizing biofuel combustion environments. Additional alloying with Aluminum, silicon, molybdenum and other minor elements has been tried in the present investigation. These alloying elements help in improving resistance to erosion. The coatings with tungsten carbide-cobalt incorporated in Ni-alloy matrix, uniquely combining the wear resistance of WC-Co and high temperature corrosion resistance of Ni-alloy has been evaluated.

Four types of commercially available feed stock powders namely NiCrAl, NiAlCrFeMo, NiCrFeSiB and WC-Co/NiCrFeSiB were HVOF sprayed on three kinds of boiler tube steels designated as ASTM-SA210-Grade A1, ASTM-SA213-T11 and ASTM-SA213-T22. Differences in chemical compositions of coatings and substrate alloys can lead to inter-diffusion across the coating substrate interface, which can modify the oxidation and hot corrosion resistance of the coatings. The microstructure and several properties have been characterized to evaluate their potential as high temperature corrosion and erosion resistant coatings for application in power plant boilers.

Understanding the corrosion and erosion behavior of these coated steels in various laboratory simulated environments and also contrasted by means of field testing inside real power plant boilers has become an object of scientific investigation. Thermo cyclic oxidation studies were performed in static air as well as in molten salt (Na_2SO_4-60%V_2O_5) environment at 900°C for 50 cycles. Each cycle of experiment consisted of 1 hour heating followed by 20 min of cooling at room temperature. The reaction rate and kinetics has

been studied by means of thermogravimetry. The aim of cyclic loading is to create severe conditions for testing and repeated under similar test conditions for reproducibility. As learnt from the literature that the oxidizing time of 50 hours is considered adequate to allow for steady-state oxidation. The temperature of study was intentionally kept high (900°C) as this will take into consideration the overheating effects in case of boilers, which has been identified as the major cause of failure (Metals Handbook, 1975). Moreover, at 900°C, the rate of high temperature hot corrosion (HTHC) has been reported to be the severest, Fig.2.1 (National Materials Advisory Board, 1996). Experiments have been conducted in a silicon tube furnace, which provides a means to control conditions such as temperature and environment more precisely. Saunders et al 1984 reported that both burners rig tests and test in tube furnace are capable of reproducing the corrosion observed in service.

Sodium and vanadium appears to be the primary culprit in causing deposit formation on the surface of heat exchangers of thermal power plant and hence the salt mixture Na_2SO_4-60%V_2O_5 constitutes eutectics with a low melting point of 550°C are used in the present study. So far as the testing in air environment is concerned, the study could also provide useful information regarding the adhesion of the coatings and the spalling tendency of their oxide scales (Burman and Ericsson, 1983), apart from air oxidation behaviour of the coatings.

The solid particle erosion experiments have been carried out using air-jet erosion test rig as per ASTM-G76 standard at room temperature. Solid particle erosion studies has been carried out at 30° and 90° to provide the maximum erosion condition for both ductile and brittle materials. Given the fact that quartz as the main constituent of fly ash, silica sand has been used as erodent material. Volumetric steady state erosion rates for different coatings and substrate steel are evaluated.

The results obtained in laboratory simulated environments have been contrasted by means of field testing inside real power plant boilers. In the actual boiler environment of Guru Gobind Singh Super Thermal Plant, Ropar, India, the samples were inserted into the superheater zone of the coal fired boiler with the help of stainless steel wires. The flue gas temperature in this region is about 778±20°C. The experiments are conducted for 10 cycles, each cycle consisted of 100 hours exposure followed by cooling at ambient conditions. The extent of erosion-corrosion has been monitored by measuring the thickness loss and weight change of the samples.

Identification and structural investigation of the reaction products of the corroded samples are made by means of XRD, SEM/EDAX and EPMA techniques.

CHAPTER 3
EXPERIMENTAL
EQUIPMENTS AND PROCEDURES

This chapter contains description of the experimental equipments used and the procedures employed for deposition and characterizations of the coatings, oxidation, hot corrosion and erosion studies and analyses of the corrosion products.

3.1 SUBSTRATE MATERIALS

Low carbon steel ASTM-SA210 grade A1 (GrA1) and chrome moly steel ASTM-SA213-T11 and ASTM-SA213-T22, which are used as material for water wall, super heater and reheater tubes in some coal fired thermal power plants in northern part of India has been used as a substrate in the study. The actual chemical composition for the substrate steels determined by spectroscopy is given in Table 3.1. The specimens with approximate dimensions of 20mm × 15mm × 5mm and 30mm × 30mm × 5mm were cut from the tubes for corrosion and erosion studies respectively. Samples are polished with SiC papers down to 180 grit.

Table 3.1 Chemical composition (Wt %) for various steels.

Type of Steel	ASTM code	Composition	C	Mn	Si	S	P	Cr	Mo	Fe
GrA1	SA210-Grade A1	Nominal	0.27	0.93	0.1	0.058	0.048	-	-	Bal.
		Actual	0.2471	0.5649	0.2314	0.0049	0.0104	-	-	Bal.
T-11	SA213-T-11	Nominal	0.15	0.3-0.6	0.5-1	0.03	0.03	1-1.5	0.44-0.65	Bal.
		Actual	0.1361	0.5102	0.4852	0.0073	0.0159	1.1067	0.5204	Bal.
T-22	SA213-T-22	Nominal	0.15	0.3-0.6	0.5	0.03	0.03	1.9-2.6	0.87-1.13	Bal.
		Actual	0.1420	0.5281	0.4311	0.0089	0.0182	2.5529	1.1007	Bal.

3.2 COATING POWDERS

Four types of commercially available feedstock materials in the form of powder have been used to spray to deposit coatings using HVOF process on three different types of

substrate steels. The chemical composition, particle size and shape of all the powders have been reported in Table 3.2.

Table 3.2 Chemical Composition, particle size and shape of the coating powders

Coating powder	Chemical Composition (wt %)	Shape	Particle size
NiCrAl (MEC-1047)	Ni - 17.92Cr - 6.66Al	Spherical	30 -110 μm
NiAlCrFeMo (MEC-1044)	Ni - 8Al - 8.86Cr - 6.24Fe - 4.52Mo	Irregular	30-110 μm
NiCrFeSiB (MEC-1260A)	Ni - 14.5Cr - 4.3Fe - 4.3Si - 3B - 0.6C	Spherical	-45 + 15 μm
WC-Co / NiCrFeSiB 35/65 (MEC-1031C)	29.2W - 4.2Co - 9.4Cr - 47.6Ni – 1.9B - 2.8Si - 2.8Fe - 2C	Spherical	-45 + 15 μm

3.3 DEPOSITION OF THE COATINGS

HVOF spraying has been carried out using a HIPOJET 2100 equipment (M/S Metallizing Equipment Co.Pvt.Ltd, Jodhpur, India), which utilize the supersonic jet generated by the combustion of liquid petroleum gas and oxygen mixture. HIPOJET 2100 system is shown in Fig.3.1. The spraying parameters employed during HVOF deposition are listed in Table 3.3. All the process parameters, including the spray distance were kept constant throughout coating process. Substrate steels were grit-blasted with Al_2O_3(Grit 45) before HVOF spraying to develop better adhesion between the substrate and the coating.

3.4 HIGH TEMPERATURE OXIDATION AND HOT CORROSION STUDIES

3.4.1 Experimental Setup

Oxidation and hot corrosion studies were conducted at 900°C in a laboratory silicon carbide tube furnace, Digitech, India make. The furnace was calibrated to an accuracy of ±5°C using Platinum/Platinum-13% Rhodium thermocouple fitted with a temperature indicator of Electromek (Model-1551 P), India. The uncoated as well as the coated specimens were polished down to 1μm alumina wheel cloth polishing to obtain
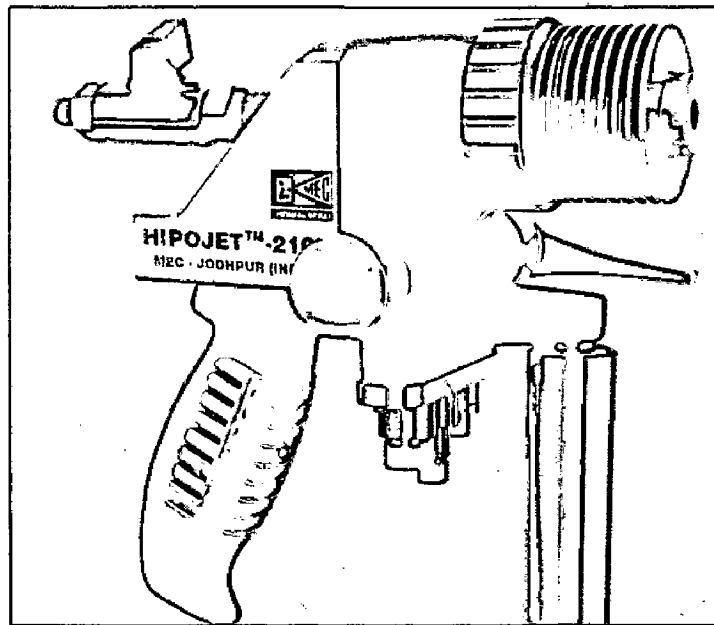
Fig.3.1   HVOF system hipojet 2100 used in the current research

Oxygen flow rate	250 SLPM
Fuel (LPG) flow rate	60 SLPM
Air-flow rate	700 SLPM
Spray distance	200 mm
Powder feed rate ■ NiCrAl powder ■ NiAlCrFeMo powder ■ NiCrFeSiB powder ■ WC-Co/NiCrFeSiB powder	 38 gm/min 38 gm/min 28 gm/min 26 gm/min
Fuel pressure	6 kg/cm^2
Oxygen pressure	9 kg/cm^2
Air pressure	6 kg/cm^2

SLPM: Standard liters per minute.

Table 3.3   Spray parameters employed for HVOF spray process

similar condition of reaction before being subjected to corrosion run. Physical dimensions of the specimens were then recorded carefully with Sylvac digital vernier caliper (Swiss make, resolution 0.01), to evaluate their surface areas. Subsequently, the specimens were washed properly with acetone and dried in hot air to remove any moisture. During experimentation the prepared specimens were kept in an alumina boat and the weight of boat and specimen was measured. The alumina boats used for the studies were pre heated at a constant temperature of 1200°C for 10 h, so that their weight would remain constant during the course of high temperature cyclic oxidation/corrosion study. The boat containing the specimen was inserted into hot zone of the furnace set at a temperature of 900°C. Holding time in the furnace was one hour in still air after which the boat with specimen was taken out and cooled at the ambient temperature for 20 minutes. Following this, weight of the boat along with specimen was measured and this constituted one cycle of the oxidation study. Any spalled scale in the boat was also taken into consideration for the weight change measurements. Electronic Balance Model CB-120 (Contech, Mumbai, India) with a sensitivity of 10^{-3} g was used to conduct the thermogravimetric studies. The weight change values were measured at the end of each cycle with the aim to understand the kinetics of corrosion. Visual observations were made after the end of each cycle with respect to colour, luster or any other physical aspect of the oxide scales being formed. All oxidation and hot corrosion studies were cyclic in this work and were carried out for 50 cycles. The reproducibility in the experiments was established by repeating the experiments for some samples.

3.4.2 Oxidation Studies in Air

The oxidation tests at 900°C were performed on uncoated and HVOF coated steels in laboratory furnace up to 50 cycles as discussed in section 3.4.1.

3.4.3 Hot Corrosion Studies in Molten Salt (Na_2SO_4-60%V_2O_5)

3.4.3.1 Molten Salt Coating

The uncoated as well as coated specimens were prepared for the hot corrosion studies as discussed in section 3.4.1. The specimens were then heated in an oven up to 250°C, which helps in uniform application of salt mixture. The salt mixture of Na_2SO_4-60%V_2O_5 dissolved in distilled water was coated on the warm polished samples with the help of camel hair brush. The amount of the salt coating varies from 3.0 -5.0 mg/cm^2. The

44

salt coated specimens as well as the alumina boats were then dried in the oven for 3-4 hours at 100°C and weighed before being exposed to hot corrosion tests.

3.4.3.2 Hot Corrosion Studies

The uncoated as well as coated specimens after application of salt coating were subjected to hot corrosion in the silicon carbide tube furnace at 900°C for 50 cycles as discussed in section 3.4.1.

3.5 EROSION-CORROSION STUDIES IN ACTUAL INDUSTRIAL ENVIRONMENT

The coatings and alloy samples were exposed to actual service conditions of the coal fired boiler for 1000 hours. The samples were tested in super heater region of I[st]-stage boiler of Guru Gobind Singh Super Thermal Plant, Ropar, India. This zone was selected for the present study as many failures due to erosion-corrosion have been reported to occur in this power plant. The flue gas temperature in this region is about 778±20°C and volumetric flow of flue gas was around 250 m³/s. A hole of diameter 2mm was drilled in all the samples to hang them in the boiler for experimentation. The uncoated as well as coated specimens were polished down to 1μm alumina on a wheel cloth polishing machine to obtain similar conditions on all the samples before being subjected to boiler environment. The physical dimensions of the specimens were measured with a vernier caliper to evaluate their surface areas. To evaluate the thickness loss during experimentations, the thickness of each specimen was measured using Sylvac micrometer screw gauge. The samples were hanged in this region with the help of stainless steel wire through soot blower dummy points which is at the height of 45.47m from the base of the boiler. The SEM/EDAX analysis of the fly ash is shown in Fig 3.2. The samples were exposed to combustion gases for 10 cycles each of 100 hours duration and followed by one hour cooling at ambient conditions. After the end of each cycle the specimens were visually observed for any change in the surface texture and weight change of the samples were measured subsequently. The thickness change in the samples was measured at the end of study.
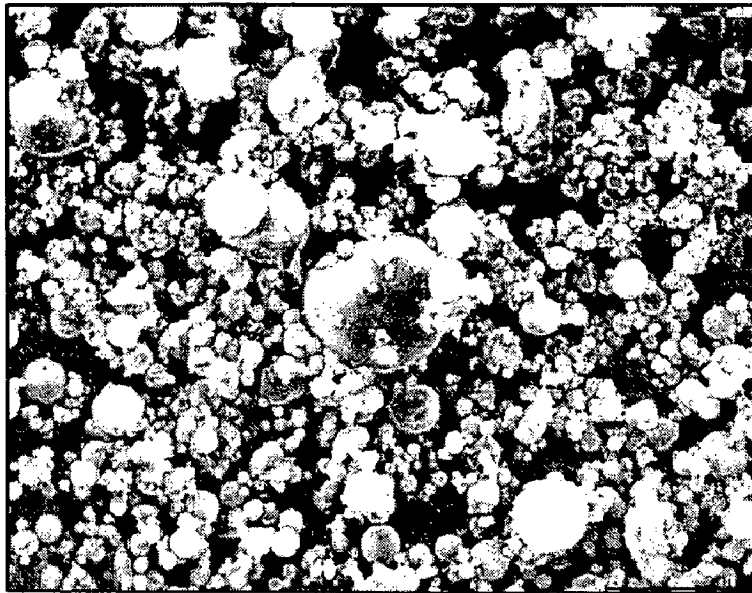
(a)
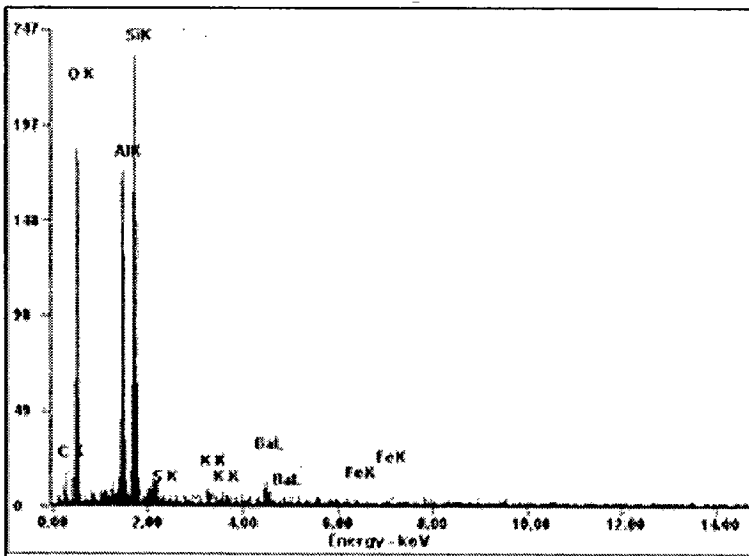
Element	Wt%	At%
CK	05.58	09.72
OK	41.03	53.70
AlK	18.80	14.59
SiK	25.47	18.99
SK	00.44	00.29
KK	01.49	00.80
FeK	03.70	01.39
Matrix	Correction	ZAF

(b)

Fig. 3.2   Analysis of fly ash (a) SEM morphology (b) EDAX compositional analysis

3.5 SOLID PARTICLE EROSION TESTS

3.6.1 Experimental Setup

Room temperature erosion test was carried out using air jet erosion test rig (Fig3.3) as per ASTM G76-02 standard at the Defence Metallurgical Research Laboratory, Hyderabad, India. The rig consisted, of an air compressor, and particle feeder, an air particle mixing and accelerating chambers. Dry compressed air was mixed with the particles, which were fed at a constant rate from a conveyor belt type feeder in the mixing chamber and then accelerated by passing the mixture through a tungsten carbide converging nozzle of 4.5mm diameter. These accelerated particles impacted the specimen, which could be held at various angles with respect to the impacting particles using an adjustable sample holder. The feed rate of the particles could be controlled by monitoring the distance between the particle feeding hopper and the belt drive carrying the particles to the mixing chamber. The impact velocities of the particles could be varied by varying the pressure of the compressed air. The velocity of the eroding particles was determined using a well known rotating double-disc method as described by Ruff and Ives (1975).

3.6.2 Erosion Studies

The erosion studies were performed on uncoated as well as coated samples for the purpose of comparison. The erosion test conditions utilized in the present study are listed in Table 3.3. The sample was first cleaned in acetone using an ultrasonic cleaner, dried and then weighed using an electronic balance having a resolution of 0.01 mg. The sample was then fixed to the sample holder of the erosion rig and eroded with silica sand (Fig.3.4) at the predetermined particle feed rate, impact velocity and impact angle for a period of about 5 min. The sample was then removed, cleaned in acetone and dried and weighed to determine the weight loss. This weight loss normalised by the mass of the silica particles causing the weight loss (i.e., testing time x particle feed rate) was then computed as the dimensionless incremental erosion rate. The above procedure was repeated till the incremental erosion rate attained a constant value independent of the mass of the erodent particles or, equivalently, of testing time. This constant value of the incremental erosion rate was defined as the steady-state erosion rate. The incremental erosion rate was converted into volume wear rate to take into account the different densities of the coating material and the substrate.

Table 3.4   Erosion conditions

Erodent material	Silica sand (Angular)
Erodent size (μm)	125-180
Particle velocity (m/s)	40
Erodent feed rate (gm/min)	5
Impact angle (°)	30 and 90
Test temperature	Room Temperature
Test time (min)	Cycles of 5 minutes
Sample Size (mm)	30 x 30 x 5
Nozzle diameter (mm)	4.5
Stand off distance (mm)	10

3.7   CHARACTERISATION OF COATINGS, ANALYSIS OF CORROSION AND EROSION PRODUCTS

3.7.1 Preparation of Samples for Cross Sectional Analysis

Samples were cut along their cross-sections with diamond cutter (Buehler's Precision Diamond Saw, Model ISOMET 1000, USA make). Thereafter, the cut sections were hot mounted in Buehler's transoptic powder (20-3400-080) and polished down to 1000 grit using SiC emery papers. Final polishing was carried out using cloth polishing wheel machine with 1 μm lavigated alumina powder suspension.

3.7.2 Measurement of As-Sprayed Coating Thickness

The thickness of the as-sprayed coatings was continuously monitored during the process of HVOF spraying with the help of Minitest-2000 thin film thickness gauge (Elektro-Physik Koln Company, Germany, precision ±1 μm). Further, to verify the thickness of the deposited coatings, back scattered images were obtained along the cross section. A Scanning Electron Microscope (LEO 435VP) with an attached Robinson Back Scattered Detector (RBSD) was used to obtain the back scattered electron images (BSEI).

3.7.3 Optical Microscopy, Porosity and Density Measurement

Zeiss Axiovert 200 MAT inverted optical microscope, interfaced with image analyzing software Zeiss Axiovision Release 4.1(Carl Zeiss Ltd., Germany) was used to obtain optical image along the cross-section of as-sprayed coatings and to determine the porosity
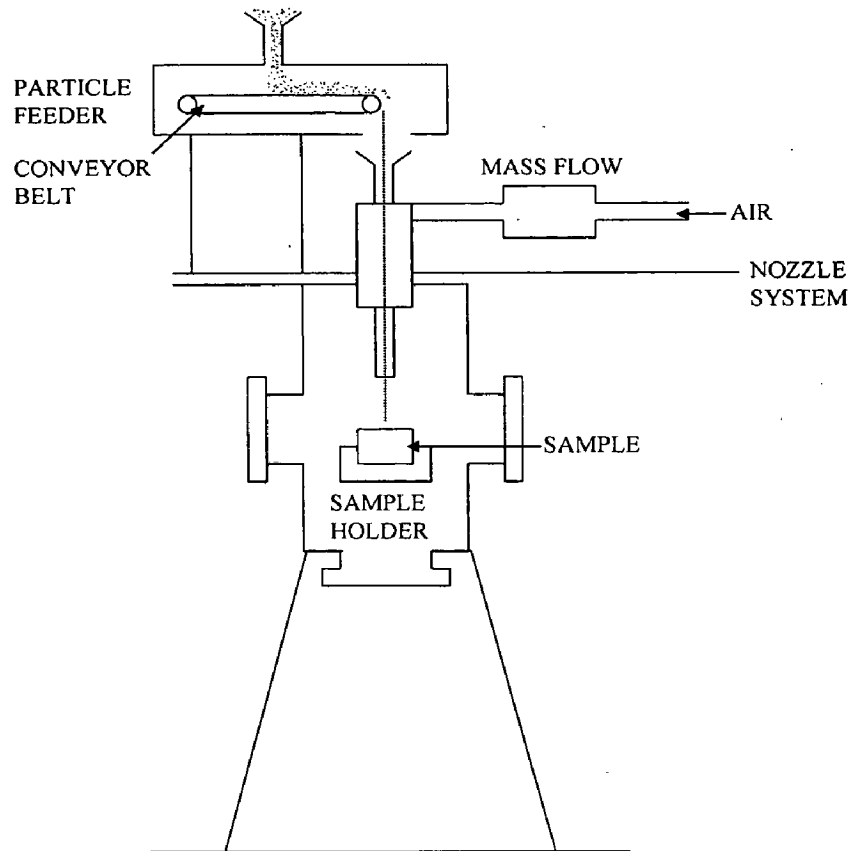
Fig. 3.3   Schematic view of an Air Jet Erosion Test Rig
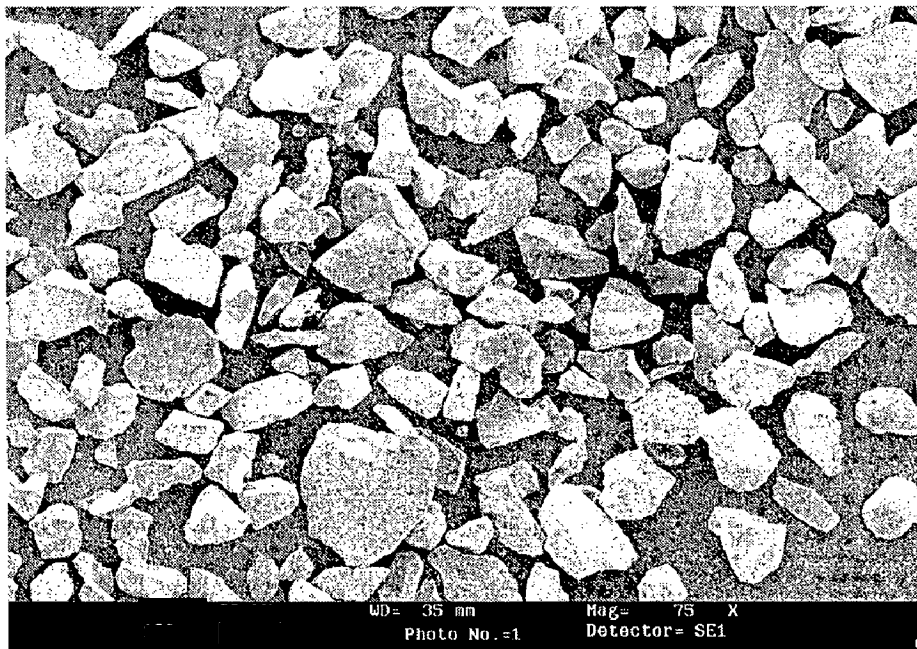
Fig. 3.4   Scanning electron micrograph of the silica sand particles

content. Twenty fields of view were taken per sample at 250X magnification. The densities of the coatings have been measured by the method of water immersion in accordance with standard ASTM test method designation C-135-96.

3.7.4 Microhardness Measurement

Vickers micro hardness measurements(Leitz Wetzlar hardness tester, Germany) using 300 gram load were performed in order to assess the as-sprayed coating hardness and substrate plastic strain hardening promoted by the high velocity projection. Hardness values were calculated from the relation $Hv = 189030 \times F/d^2$ (where F is load in Newton and d is length of the indentation diagonal in micrometer). Microhardness profile of all the coatings as a function of distance from the coating-substrate interface are shown in figure 4.4 and 4.5.
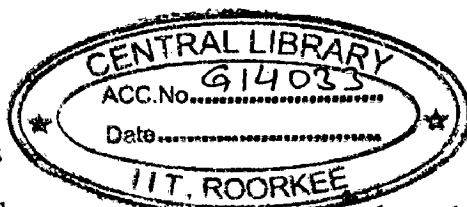
3.7.5 Surface Roughness

Surface roughness of the as-sprayed coatings and eroded zone was recorded with WYKO NT1100 Optical Profilometer (USA) using Veeco Vision 32 software. Also 3-Dimensional surface topography illustrating the surface roughness profiles of the eroded zone was taken.

3.7.6 X-Ray Diffraction (XRD) Analysis

X-ray diffraction patterns were obtained for feed stock powders, as-sprayed coatings and corrosion products. Diffraction patterns were obtained by Bruker AXS D-8 Advance Diffractometer (Germany) with CuK_α radiation and nickel filter at 20 mA under a voltage of 35 kV. The specimens were scanned with a scanning speed of 1 Kcps in 2θ range of 10 to 110° and the intensities were recorded at a chart speed of 1 cm/min with 1°/min as Goniometer speed. The relative intensities of all the peaks have been calculated by assuming height of the most prominent peak as 100%. The diffractometer being interfaced with Bruker DIFFRAC^{plus} X-Ray diffraction software provides'd' values directly on the diffraction pattern. These'd' values were then used for identification of various phases with the help of inorganic ASTM X-Ray diffraction data cards.

50

3.7.7 Scanning Electron Microscopy (SEM) and Energy Dispersive X-Ray (EDAX) Analysis

Surface morphology of the coating powder, as-sprayed coatings, eroded surface and corrosion products were studies using scanning electron microscopy. Back scattered images were taken along the cross-section of the polished samples. The elemental compositions of different phases observed on the surface as well as along the cross-section have been obtained using energy dispersive X-ray analysis. SEM/EDAX analysis was performed using Field Emission Scanning Electron Microscope (FEI, Quanta 200F, Czech Republic) with EDAX Genesis software attachment, JEOL scanning microscope (JSM-840A and JSM-5800) with LinkISIS(UK) EDAX attachment, and Scanning Electron Microscope (LEO 435VP, UK).

3.7.8 Electron Probe Micro Analyser (EPMA)

Qualitative elemental X-ray mapping images along the cross-section of the as-sprayed and corroded coatings were taken, which indicates the distribution chemistry of the various elements in the scanned area. The EPMA analysis was carried out using a Cameca SX100, 3 Wavelength Dispersive Spectrometer, made in France.

CHAPTER 4

CHARACTERISATION OF COATINGS

This chapter describes substrate steels used in the present study and the characterization of various coatings applied on them. Further, the microstructures and physical properties like porosity and micro-hardness of as-sprayed coatings have been reported and discussed with respect to the existing literature. The combined techniques of X-ray diffraction, optical microscopy, scanning electron microscopy, and electron probe micro analysis are used to characterize the deposited coatings. The results are discussed at the end of this chapter.

4.1 MICROSTRUCTURES OF SUBSTRATE STEELS

The optical microstructures of the substrate steels are shown in Fig. 4.1. The microstructures for Grade A1 steel (Fig 4.1.a) are found as ferrite and pearlite. The ferrite appears white in colour, and the boundaries between the ferrite grains of different orientations appear as dark lines. The pearlite appears uniformly black as the interlamellar spacing of the pearlite is too fine to be resolved by a light microscope. The microstructures of the T11 and T22 steels (Figs. 4.1b and 4.1c) consist of polygonal ferrite (white constituent) and bainite (dark constituent).

4.2 MORPHOLOGY OF COATING POWDERS

The morphology of the coating powders have been evaluated using the scanning electron microscopy which is shown in Fig.4.2. It is found from this figure that the NiAlCrFeMo powder particles have irregular shapes, whereas the NiCrAl, NiCrFeSiB, and WC-Co/NiCrFeSiB powder particles have spherical morphology. The particle size distribution of the powder as determined by the image analysis of the secondary electron micrographs are found to be consistent with the nominal size distribution as provided by the manufacturer.

4.3 VISUAL EXAMINATION AND ROUGHNESS OF COATINGS

The optical macrographs for the as-sprayed samples are shown in Fig. 4.3. These coatings are found to be free from any surface cracks. It can be observed that the as-sprayed NiCrAl and NiAlCrFeMo coatings have dark grey appearance with surface roughness values of 14 μm and 13 μm, respectively. The surface of the as-sprayed NiCrFeSiB coatings has dull green appearance, and that of the WC-Co/NiCrFeSiB coatings appears to be shining grey color. The measured surface roughness value for the NiCrFeSiB and WC-Co/NiCrFeSiB coatings are found to be 7.5 μm and 7 μm, respectively.

4.4 MEASUREMENTS OF COATING THICKNESSES

The coating thickness was measured from the Back Scattered Image (BSEI) obtained along the cross-section of the coated specimens (Figs. 4.11 and 4.12). The measured values of the coating thicknesses are tabulated in Table 4.1. The HVOF coating parameters used could provide the coatings of desired thickness range.

4.5 POROSITY AND DENSITY OF COATINGS

The porosity of the coatings is of prime importance in hot corrosion and erosion studies. The porosity analysis has been made with the help of image analyzing software. To determine the porosity, twenty fields of view per sample were taken at 250X magnification. The measured porosity values of the HVOF sprayed coatings used in the present study were found to be less than 2%. The densities of the coatings were measured by the method of water immersion in accordance with the standard ASTM test method designation C-135-96. The porosity and density of the coatings are reported in Table 4.1.

4.6 EVALUATION OF MICROHARDNESS

The micro-hardness values are the measures across the coating-substrate interface. The micro-hardness profile of all the coatings as a function of distance from the coating-substrate interface is shown in Figs. 4.4 and 4.5. As indicated by the microhardness profiles, the WC-Co/NiCrFeSiB coatings recorded higher hardness value of 1223 Hv with a standard deviation of 46. The average values of microhardness for the NiCrAl, NiAlCrFeMo, and
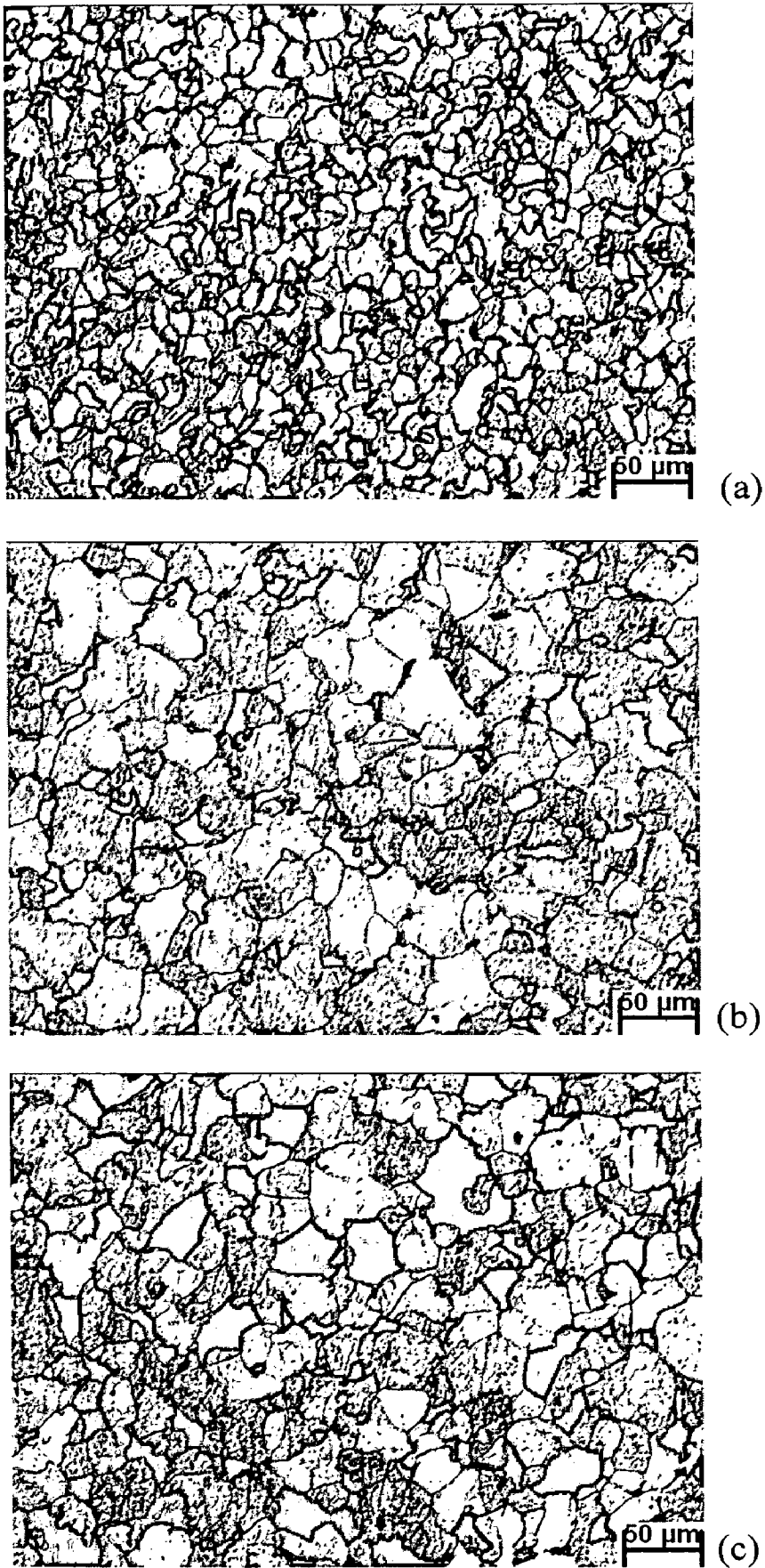
Fig. 4.1   Optical micrograph of substrate steels at 320X magnification
(a) ASTM-SA210-Grade A1 (b) ASTM-SA213-T11 (c) ASTM-SA213-T22
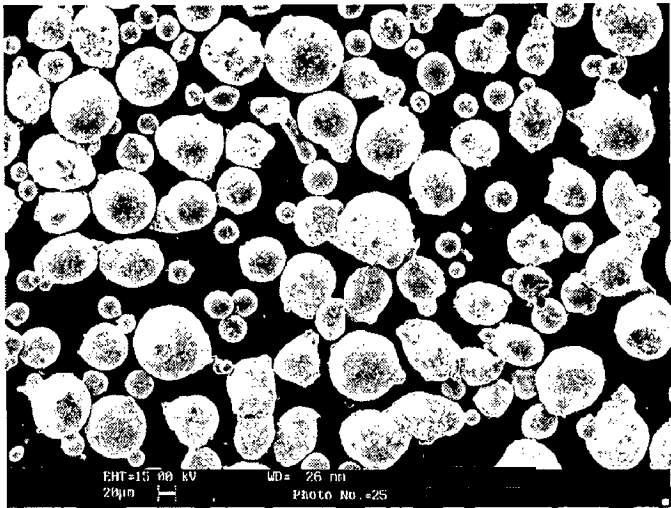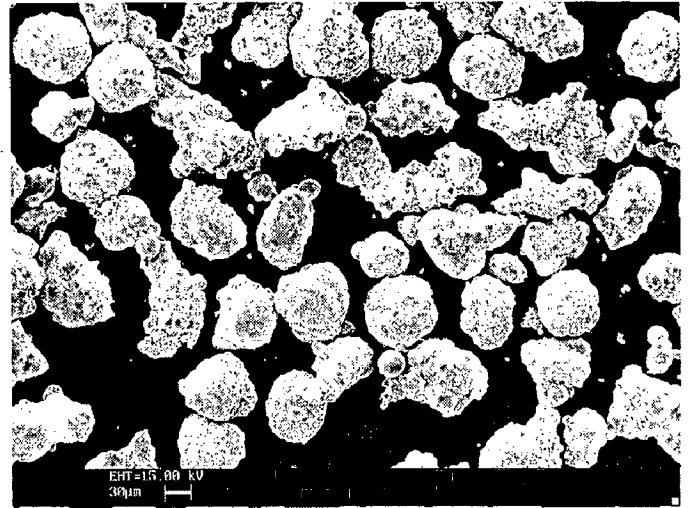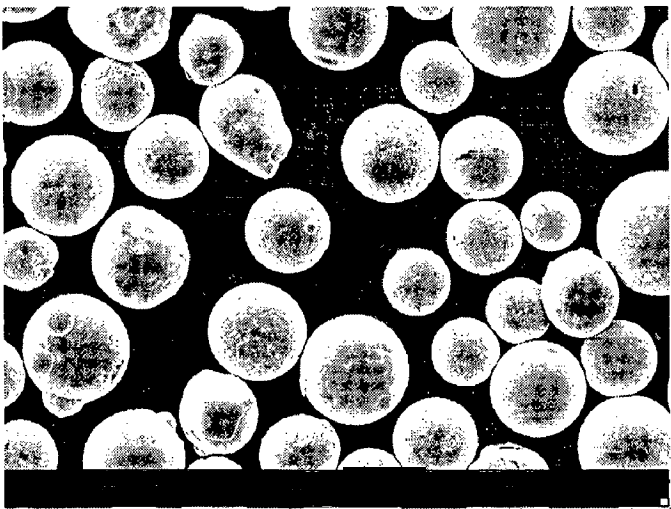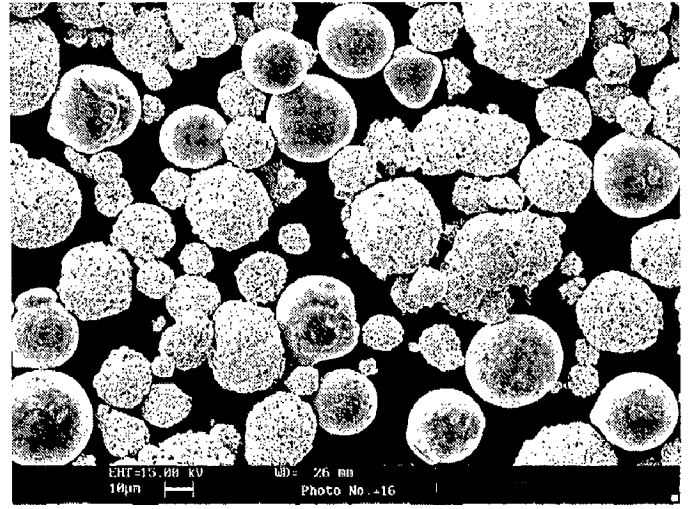
Fig. 4.2 Scanning electron micrograph of different coating powders:
(a) NiCrAl powder (b) NiAlCrFeMo powder
(b) NiCrFeSiB powder (d) WC-Co/NiCrFeSiB powder

55
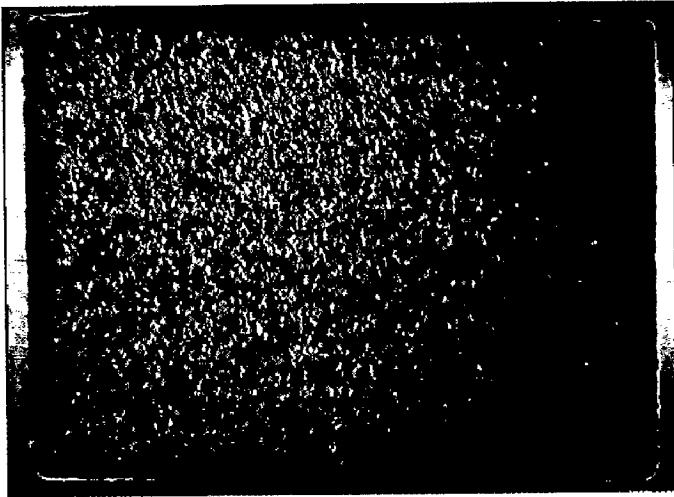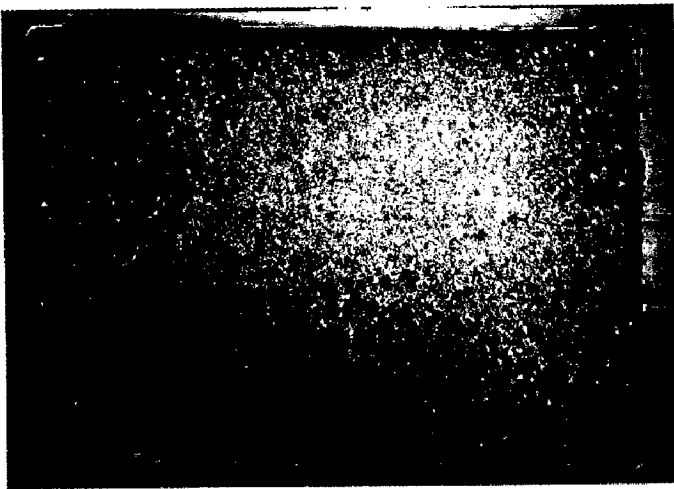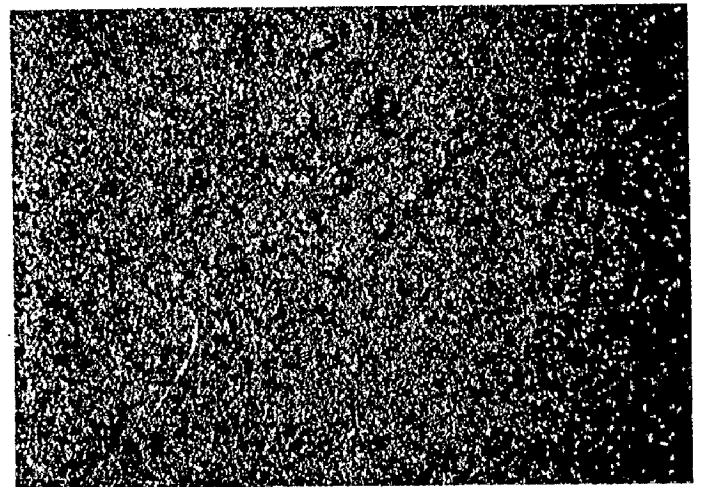
Fig. 4.3 Optical macrographs of as-sprayed coatings:
    (a) NiCrAl coating   (b) NiAlCrFeMo coating
    (b) NiCrFeSiB coating   (d) WC-Co/NiCrFeSiB coating
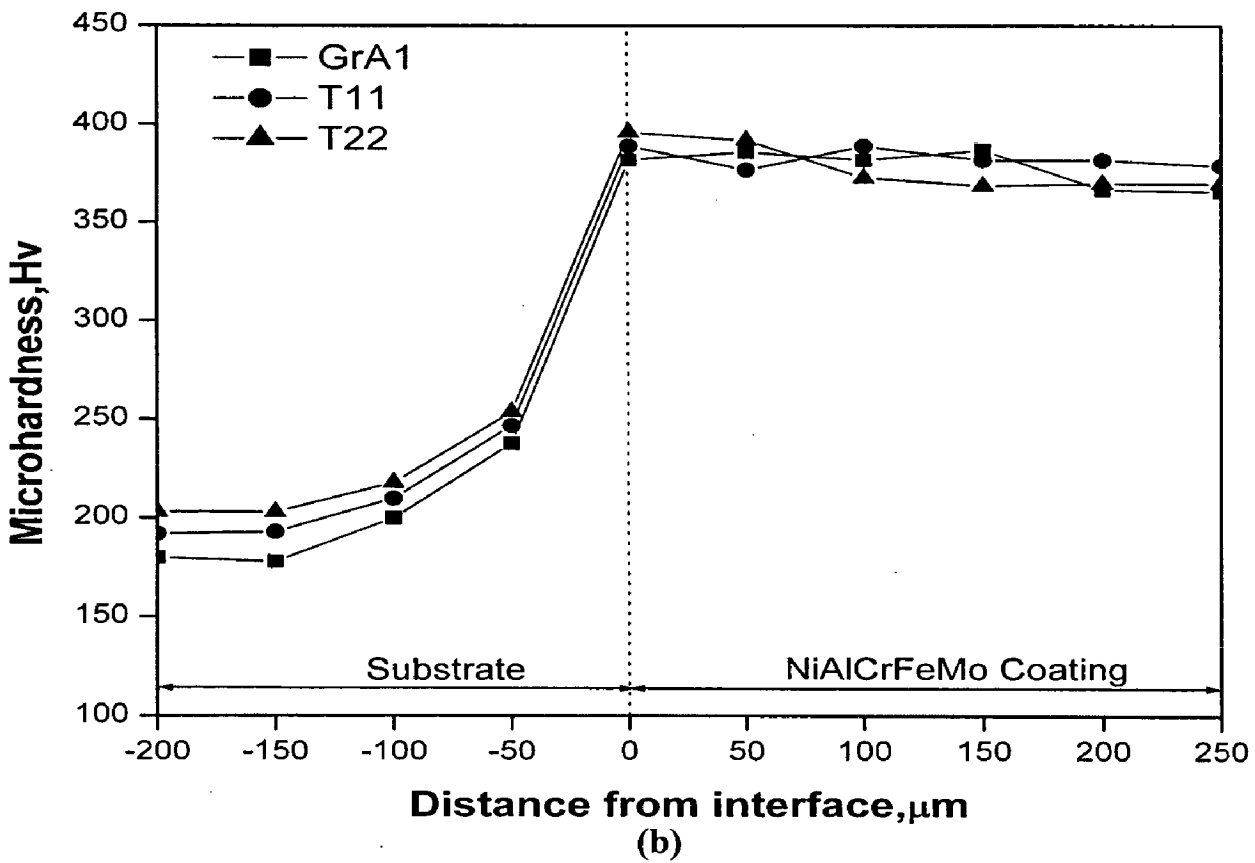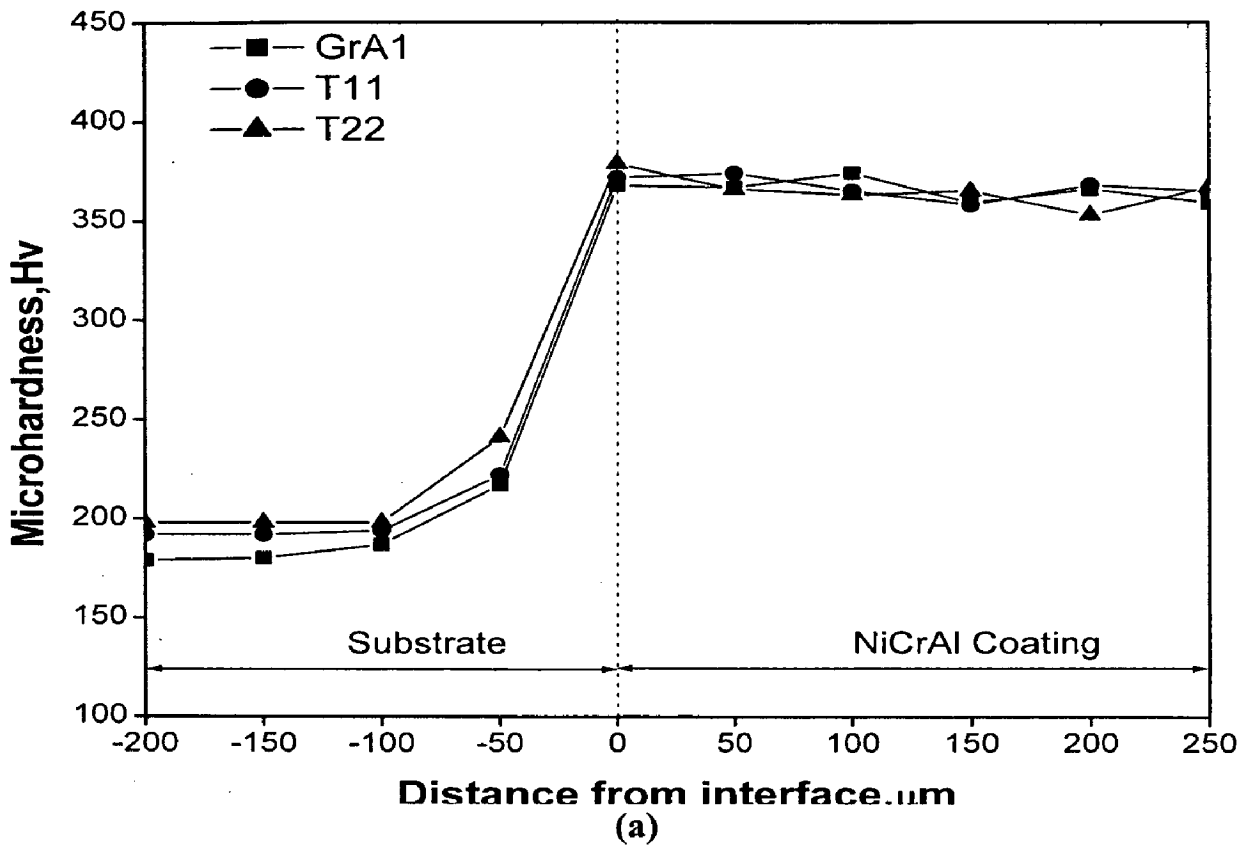
Fig. 4.4 Microhardness profiles of HVOF sprayed coatings for different substrate steels along the cross-section:

(a) NiCrAl coating (b) NiAlCrFeMo coating
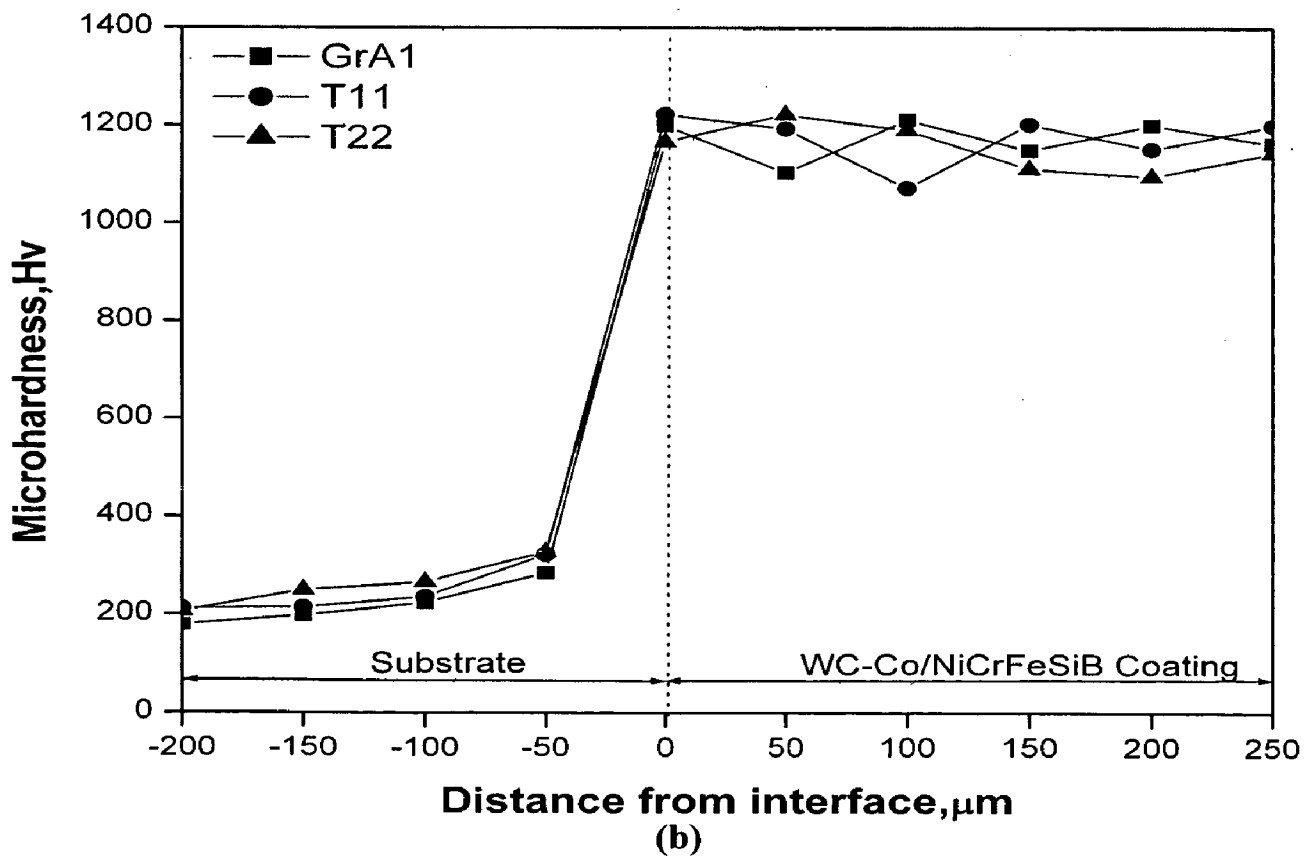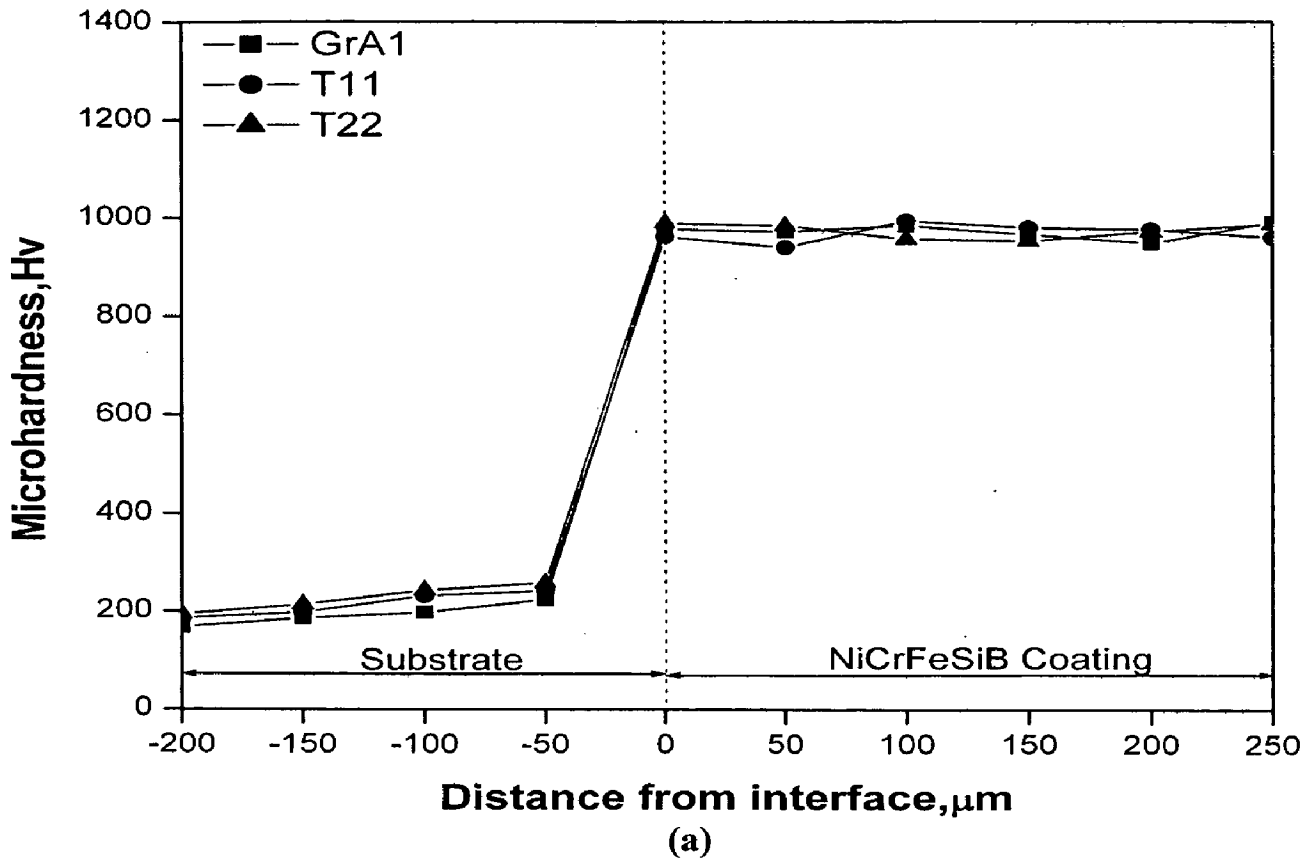
Fig. 4.5 Micro hardness profiles of HVOF sprayed coatings for different substrate steels along the cross-section:
(a) NiCrFeSiB coating (b) WC-Co/NiCrFeSiB coating

NiCrFeSiB coatings are found as 366 Hv, 380 Hv and 972 Hv, respectively with a standard deviation of less than 15 for all these coatings. The microhardness of the coatings is found to vary along the cross-section and, further, considerable increase in microhardness values are measured on the substrate region closer to the coating-substrate interface.

Table 4.1   Thickness, porosity, surface roughness, and density of sprayed coatings

Coating Type	Average Thickness (μm)	Porosity (%)	Surface Roughness (μm)	Density (g/cm^3)
NiCrAl	260	< 1	14	3.05
NiAlCrFeMo	270	< 1.5	13	3.48
NiCrFeSiB	295	< 0.5	7.5	4.96
WC-Co/NiCrFeSiB	290	< 0.5	7	7.26

Table 4.2   Phases identified by the XRD analysis of the as-sprayed coatings

Coating Type	Major Phases	Minor Phases
NiCrAl coatings	γ-Ni solid solution	$AlNi_3,Ni_2Al_3,Cr,Al_2O_3$
NiAlCrFeMo coatings	γ-Ni solid solution	$AlNi_3,Ni_2Al_3,Cr,Al_2O_3,FeNi_3$
NiCrFeSiB coatings	γ-Ni solid solution	$Ni_3Fe,Ni_3Si,CrB,CrSi$
WC-Co/NiCrFeSiB coatings	γ-Ni solid solution, WC, Co	$W_2C,Ni_3Si,CrSi,Cr$

4.7   XRD ANALYSIS

The X-ray diffraction patterns for the surfaces of the HVOF sprayed NiCrAl, NiAlCrFeMo, NiCrFeSiB and WC-Co/NiCrFeSiB coatings and the initial powders are shown in Figs. 4.6 and 4.7. The major and minor phases formed in the as-sprayed coatings are presented in Table 4.2. All the coatings exhibit almost similar peaks as compared to that of the powder indicating no change in their phase composition after spraying. The XRD patterns for all the powders and coating have a nickel-rich FCC structure as a principal phase. The NiCrAl and NiAlCrFeMo coated samples show the presence of weak intensity

peaks indexed to Al_2O_3, which indicate that a small amount of oxidation has occurred during spraying. The surface of the WC-Co/NiCrFeSiB coatings consists of W_2C phase besides WC, which illustrates that the minor decomposition of carbides has taken place during the HVOF spraying.

4.8   ADVANCED METALLOGRAPHIC STUDIES

The scanning electron micrographs showing surface morphologies along with the EDAX composition analysis, at the selected points, on the surface of the as-sprayed HVOF coatings are shown in Figs. 4.8 and 4.9. The surface of the NiCrAl and NiAlCrFeMo coatings consists of melted matrix distributed with globules of partially melted particles, which reflects overlapping of the individual splats. The partially melted particles are found to be rich in nickel and have similar size and shape as that of the powder. The compositional analysis of the light grey phases of the WC-Co/NiCrFeSiB coatings (Fig. 4.9b) show higher amount of tungsten and cobalt, which represents the distribution of carbides in the coating.

The optical micrographs showing the cross-sectional microstructures are reported in Fig. 4.10. The coatings have a typical laminar structure. The coatings were deposited on stationary substrate by moving the HVOF gun and the required thickness of the coating have been achieved by varying a number of passes. Hence, each layer of the coatings is supposed to represent one pass of the particle deposition over the other. Apparent from the images, the dark areas correspond to porosity, voids, and oxide formation. Very thin streaks of oxides appear to be oriented parallel to the substrate. Some dark areas appearing at the coating-substrate interface are the inclusions. The splat size is larger in case of the NiCrAl and NiAlCrFeMo coatings, and the light grey particles identified in the microstructure (Figs. 4.10a and 4.10b) are the partially melted particles. The microstructure of NiCrFeSiB coatings (Figs. 4.10c and 4.10d) has a dense and isotropic structure which consists of fine grains that are elongated in the longitudinal direction. The carbides in the WC-Co/NiCrFeSiB coatings (Fig. 4.10e) can be recognized by the black streaks dispersed in the matrix.

The BSE images were obtained at the cross-section of the coatings and the EDAX compositional analyses at different points along the cross-section of the as-sprayed coatings are shown in Figs. 4.11 and 4.12. The EDAX analysis at Point 4 of the NiCrAl coatings
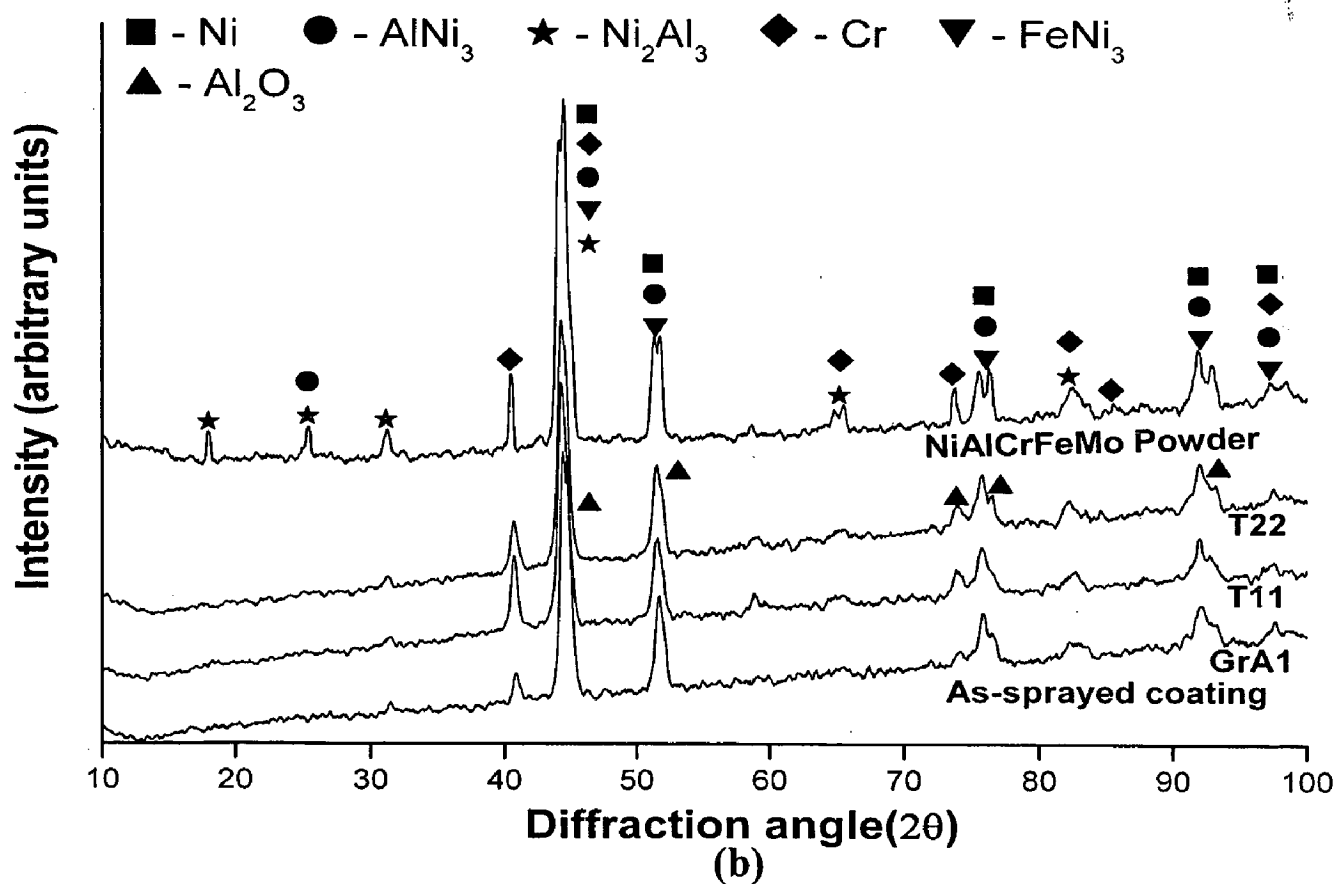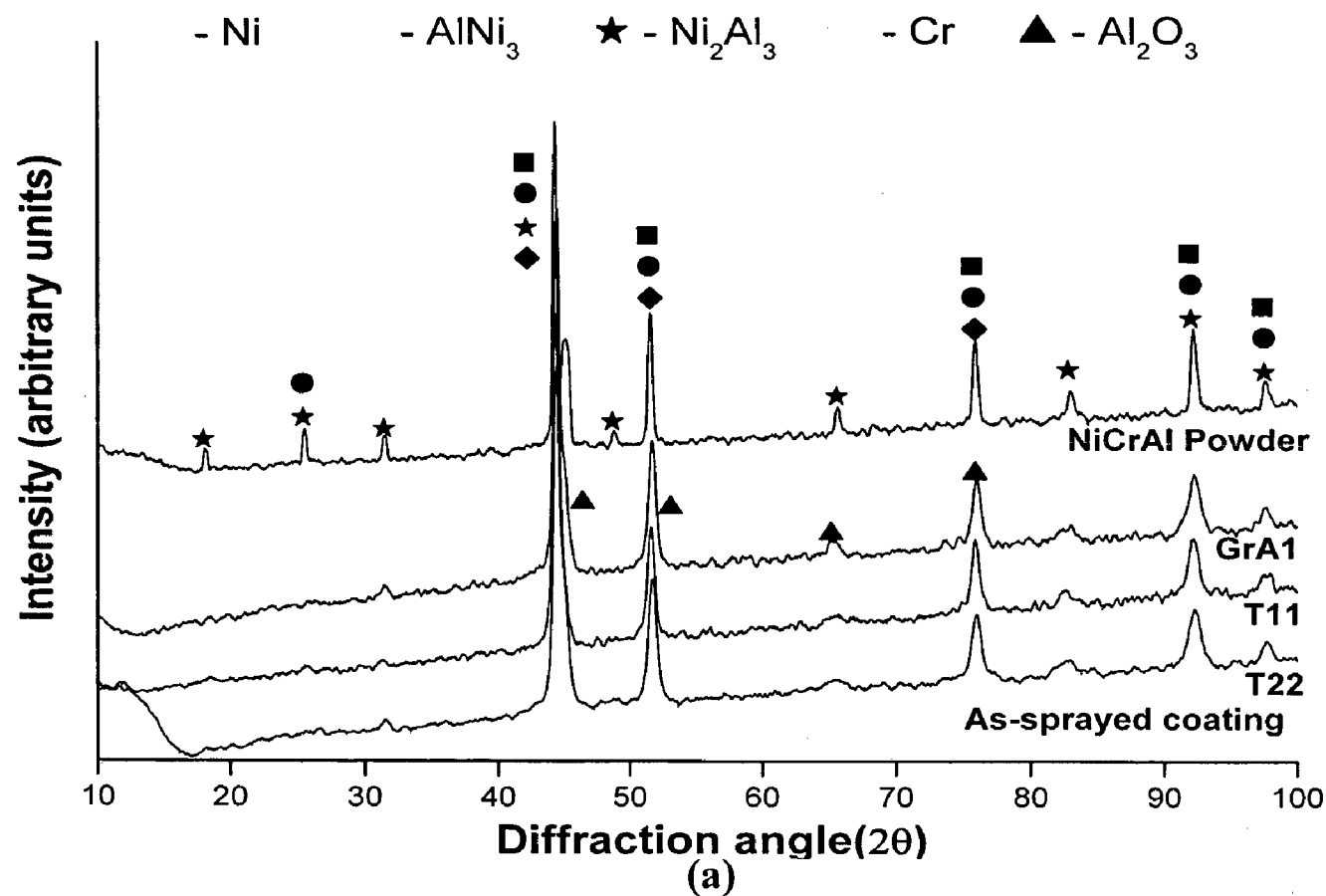
Fig. 4.6 X-ray diffraction patterns for powder and as-sprayed coatings
(a) NiCrAl coating (b) NiAlCrFeMo coating
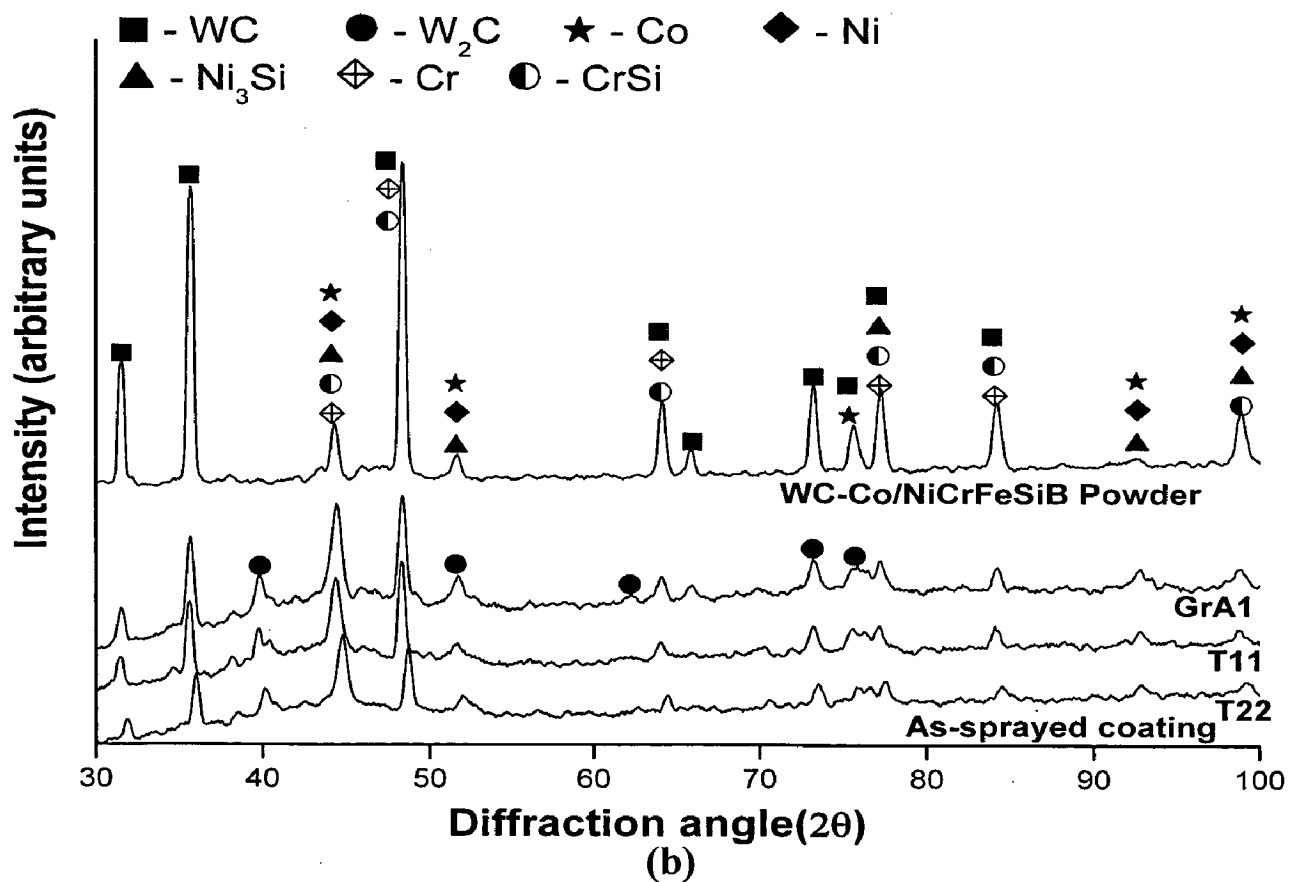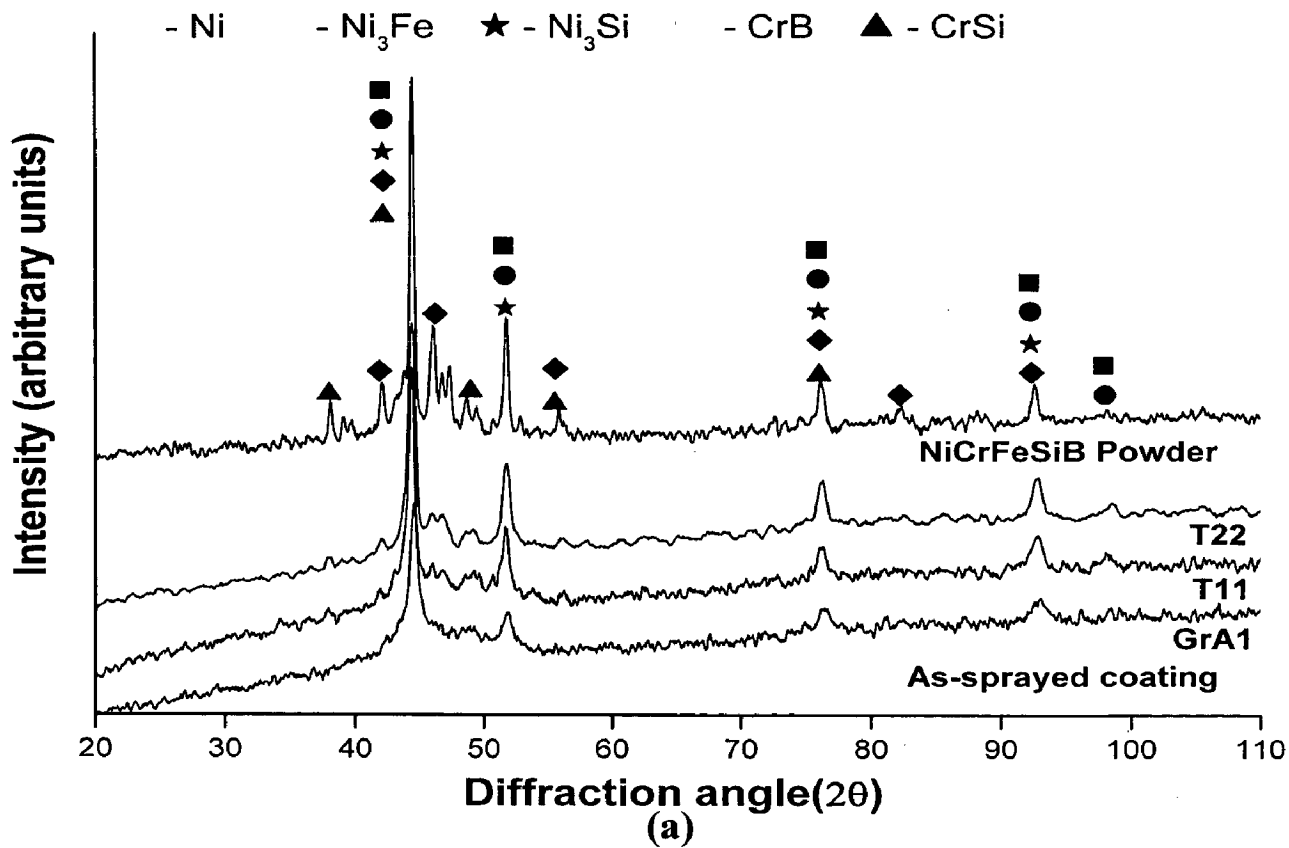
Fig 4.7   X-ray diffraction patterns for powder and as-sprayed coatings
(a) NiCrFeSiB coating (b) WC-Co/NiCrFeSiB coating
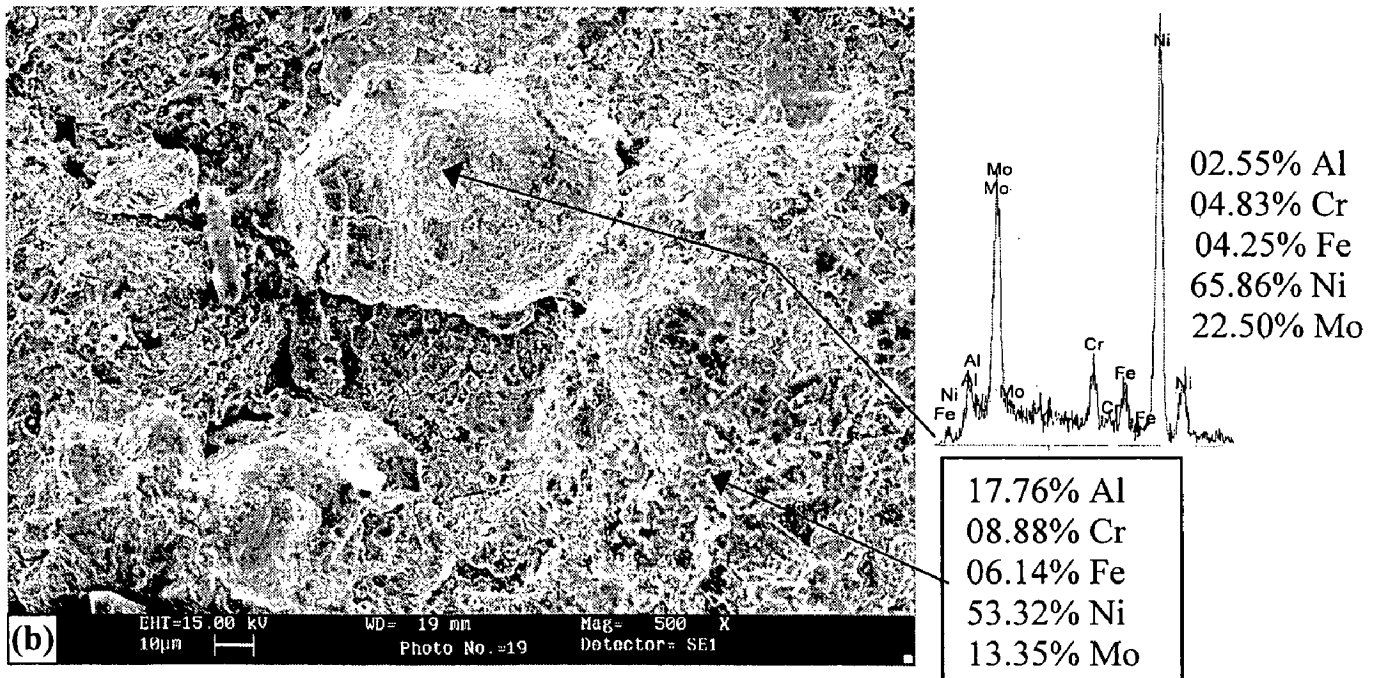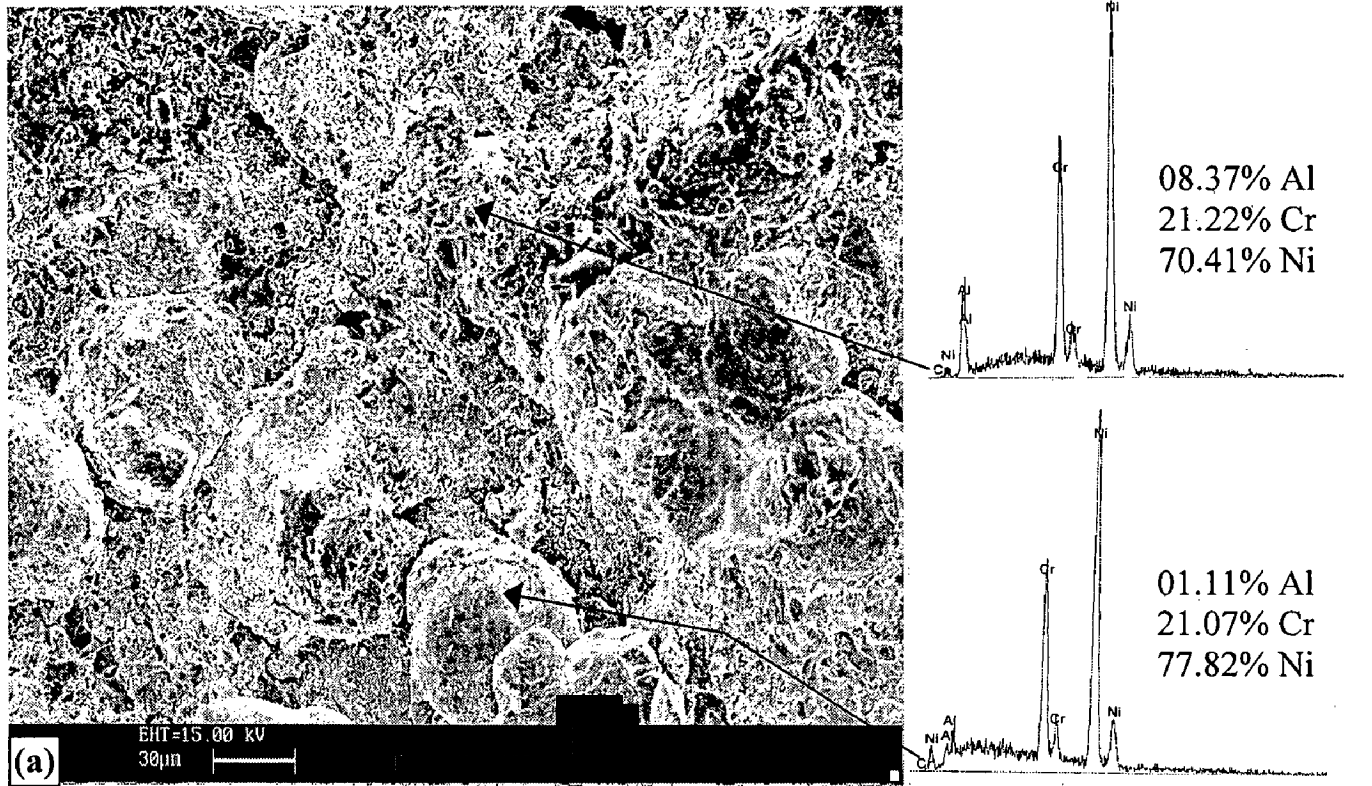
Fig. 4.8 SEM/EDAX analysis on surface of as-sprayed coating showing elemental composition (wt %) and spectra at selected points:
(a) NiCrAl coating (b) NiAlCrFeMo coatings
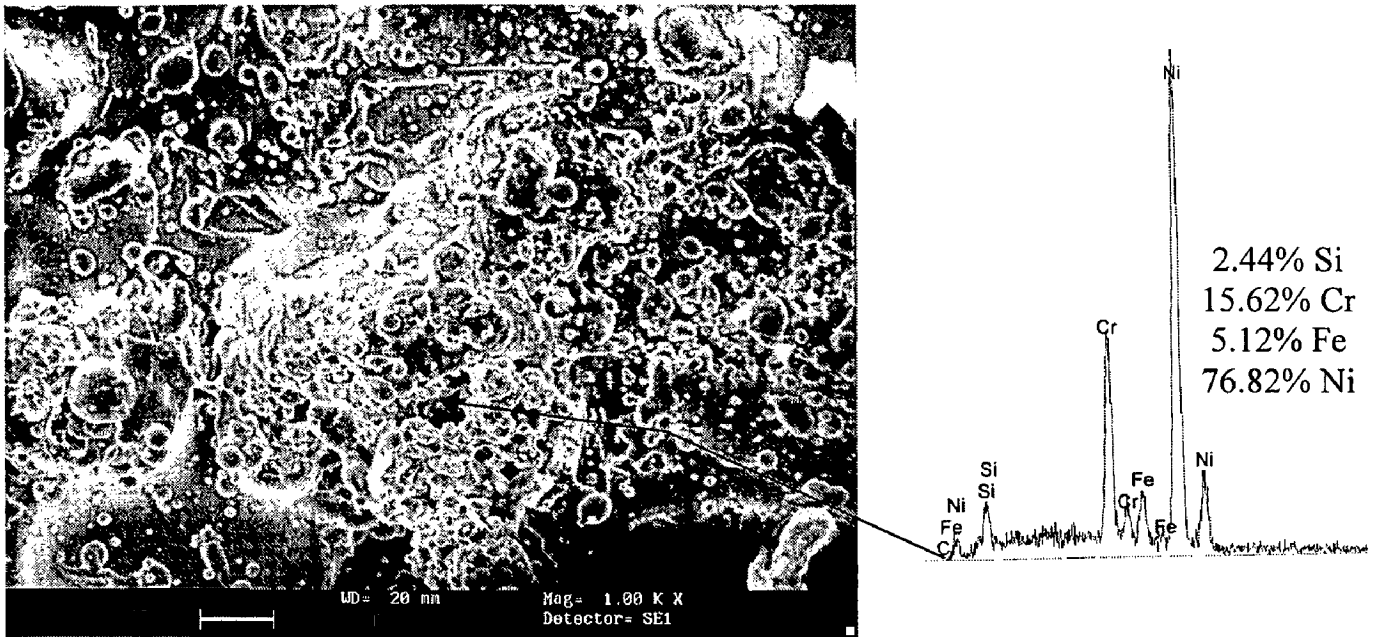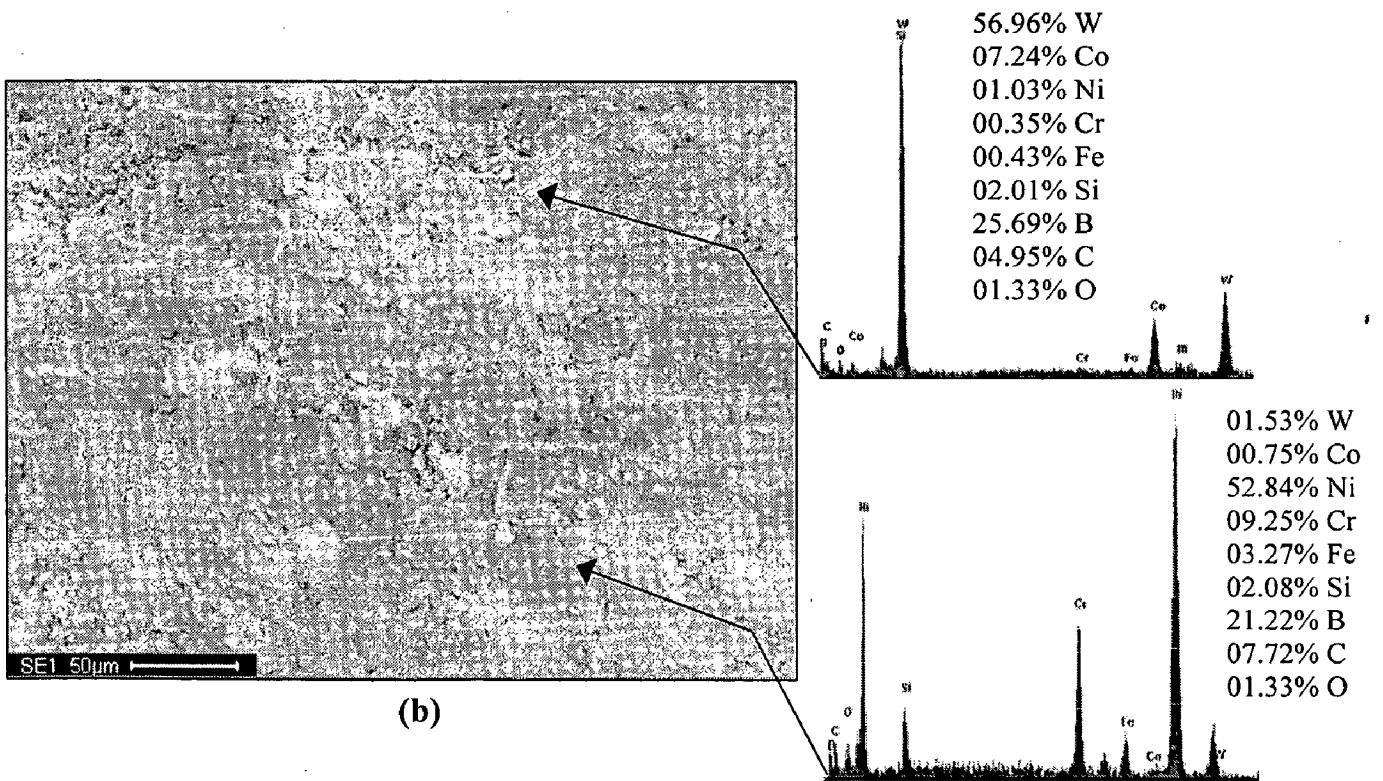
Fig. 4.9 SEM/EDAX analysis on surface of as-sprayed coating showing elemental Composition (wt %) and spectra at selected points:
(a) NiCrFeSiB coatings (b) WC-Co/NiCrFeSiB coatings
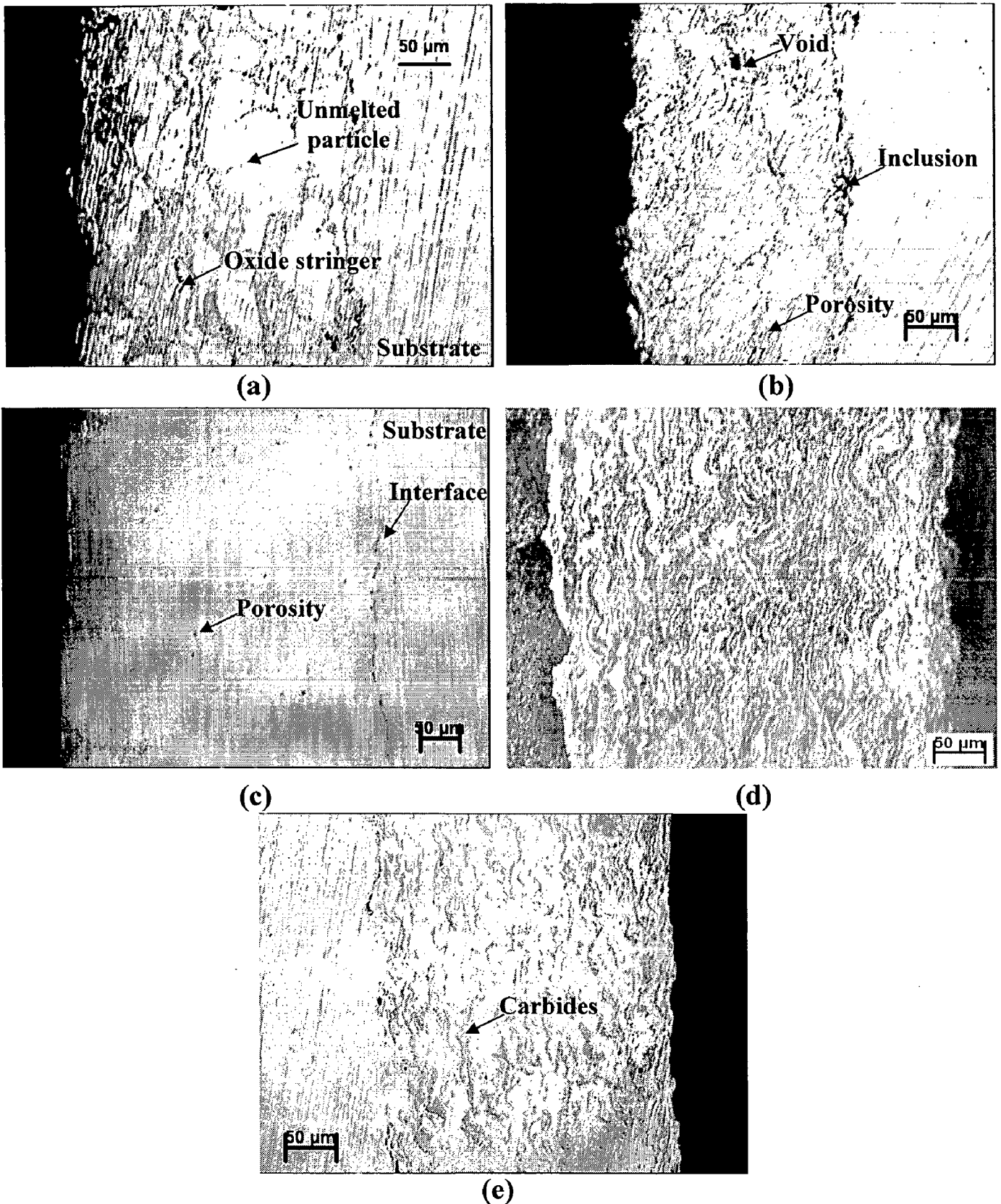
Fig. 4.10 Optical micrographs showing cross-sectional microstructures of coatings:
(a) NiCrAl coatings   (b) NiAlCrFeMo coatings
(c) NiCrFeSiB coatings   (d) NiCrFeSiB coatings (etched condition)
(e) WC-Co/NiCrFeSiB coatings

(Fig. 4.11a) and point 5 of the NiAlCrFeMo coatings (Fig. 4.11b) are found to be rich in nickel content which are identified as the partially melted splats. The chemical composition profile of the NiCrFeSiB coating (Fig. 4.12a) indicates homogeneous elemental concentration throughout the thickness of the coating. Further, the microstructure of the WC-Co/NiCrFeSiB coating (Fig. 4.12b) is characterized by WC+Co aggregates (Points 4 and 6) enveloped by the nickel alloy particles (point 5).

4.9   EPMA ANALYSIS

The qualitative X-ray mapping images for the as-sprayed coatings, which indicate the distribution chemistry of the various elements in the scanned area, are shown in Figs. 4.13 to 4.16. The intensity of the images gives an idea about the relative concentration of the element in a particular phase.

The EPMA analysis of the NiCrAl coating (Fig. 4.13) indicates that the coating primarily consists of nickel. The distinct splats enriched with partially melted nickel are also clearly visible in the elemental mapping for nickel. The distinct layer of aluminum tends to concentrate along the boundaries of nickel-rich splats. A uniform distribution is observed for chromium throughout the coating. A minor amount of nickel and aluminum appeared to be diffused from the coating into the substrate steel.

The elemental mapping for the NiAlCrFeMo coating (Fig. 4.14) shows higher intensity for nickel. The Aluminum shows a tendency to distribute mainly along the splat boundaries in the form of ridges. The clusters of molybdenum are also present at the splat boundaries. A uniform distribution is observed for chromium and iron along the splat boundary. It is evident from the observation across the coating-substrate interface that a minor amount of nickel and aluminum are diffused from the coating into the substrate steel.

Figure 4.15 shows the EPMA analysis of the NiCrFeSiB coating. The coating region is found to be rich in nickel. A uniform distribution is also observed for chromium, silicon, and iron along the nickel-rich intersplat boundaries of the coating. The WC-Co/NiCrFeSiB coating (Fig.4.16) show that the WC+Co particles are embedded into the nickel matrix. Further, the WC+Co grains exhibit a lamellar geometry which is almost parallel to the substrate surface.

4.10 DISCUSSION

The microstructure of the substrate steels, the ASTM-SA210-GrA1 consist of ferrite and pearlite, and that of ASTM-SA213-T11 and T22 show ferrite and bainite, which is usual for this grade of steels (ASM Handbook, 2001).

The thick coatings have better corrosion resistance (Heath et al., 1977); however, the self-disintegration of thicker coatings restricts the thickness of the coatings. A higher thickness may lead to cracks due to accumulation of residual stresses in the splat layers during spraying and coating solidification. In the present study, the desirable thicknesses of the coatings in the range of 250–300 μm (Table 4.3) have been successfully deposited on the steel substrate. For the HVOF sprayed nickel-based coating, the typical coating thicknesses are in the range of 250–300 μm as suggested by Nicholls (2000) and Sidhu (2003A). The roughness of the coating influences the wear rate (Picas et al., 2006). In comparison to the NiCrFeSiB and WC-Co/NiCrFeSiB coatings, the higher coating roughness of the order of 14 μm is observed for NiCrAl and NiAlCrFeMo coatings, which may be due to a greater size of the feedstock powder used for these coatings.

The maximum value of porosity measured along the cross-sectional area of all the coatings using the image analyzer software is found to be 1.83% (Table 4.1). The lower value of porosity obtained for the HVOF sprayed coatings may be related to higher kinetic energies of powder particles and to the melting behavior exhibited by the particles. The partially melted particles form an almost porosity-free coating when they reach the substrate at high velocity (Figs. 4.11 and 4.12). The measured values of the porosities are in good agreement with the findings of Sahraoui et al. (2003), Sidhu et al. (2006E), Aalamialeagha et al. (2003), Miguel et al. (2003), Planche et al. (2005), Vicenzi et al. (2006) and Miranda et al. (2001) for the HVOF sprayed Nickel chrome and composite coatings with nickel based self-fluxing alloy and a WC hard phase. The porosity of the coatings influence the corrosion-resistant behavior of the thermal spray coatings as pores form an interconnected network through which the corrosive species could reach the coating/substrate interface. The porosity may contribute to a reduced mechanical strength as well as the modulus of elasticity that leads to a higher erosive rate.
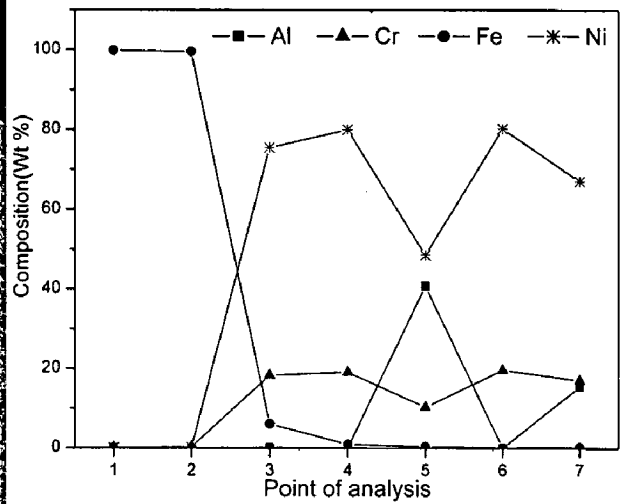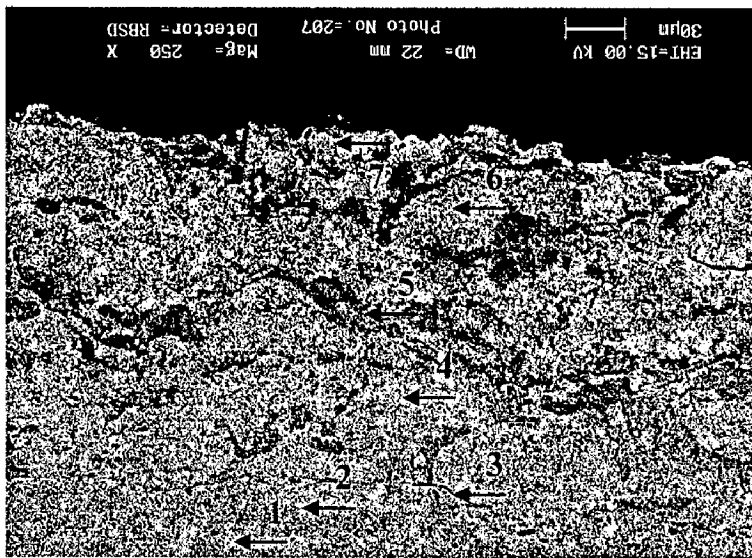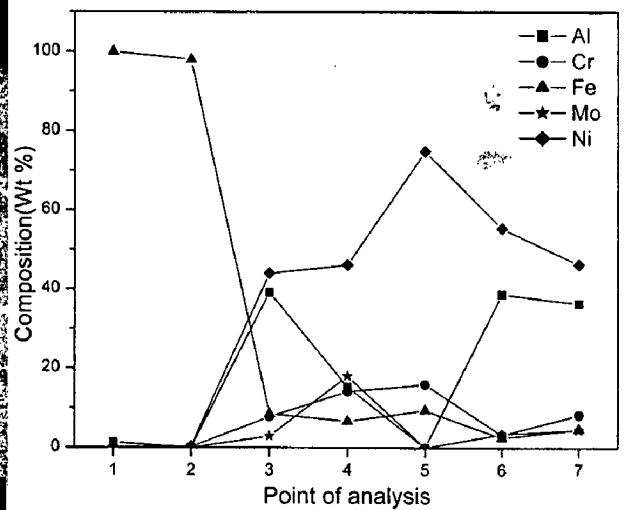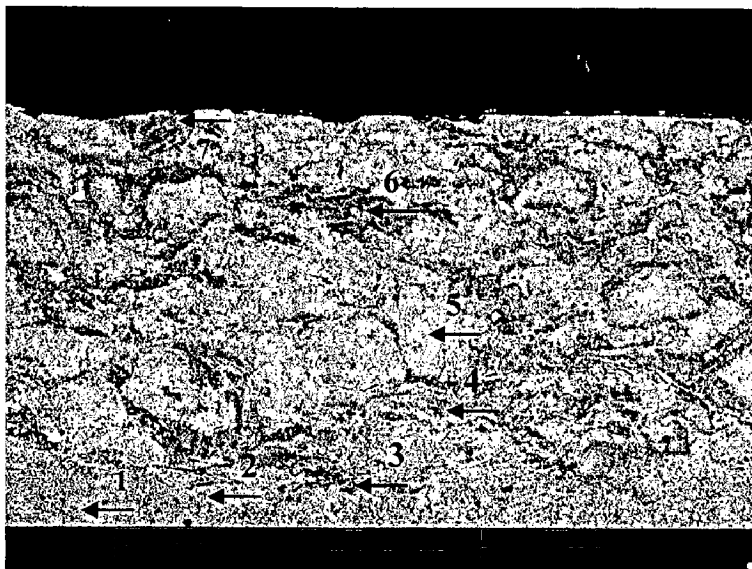
Fig. 4.11   Back scattered electron image and EDAX point analysis (wt %) across the cross-section of the as-sprayed coating deposited on T22 steels:
(a) NiCrAl coatings   (b) NiAlCrFeMo coatings
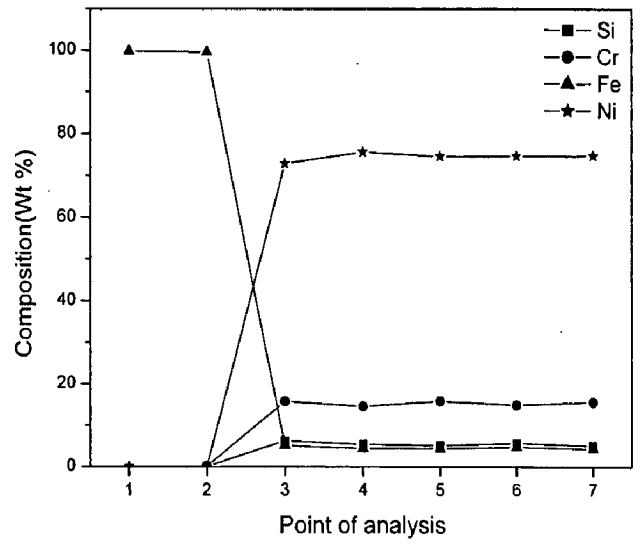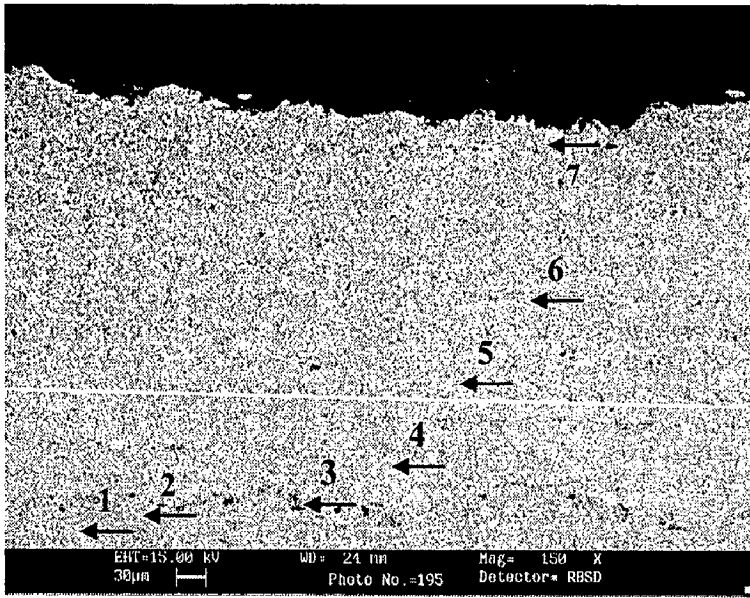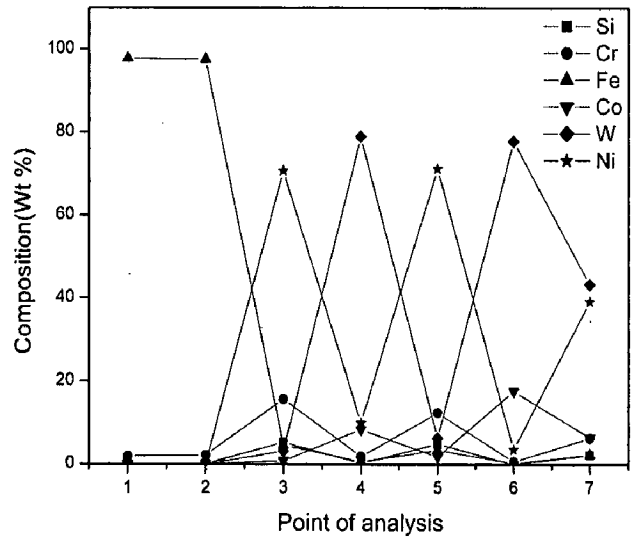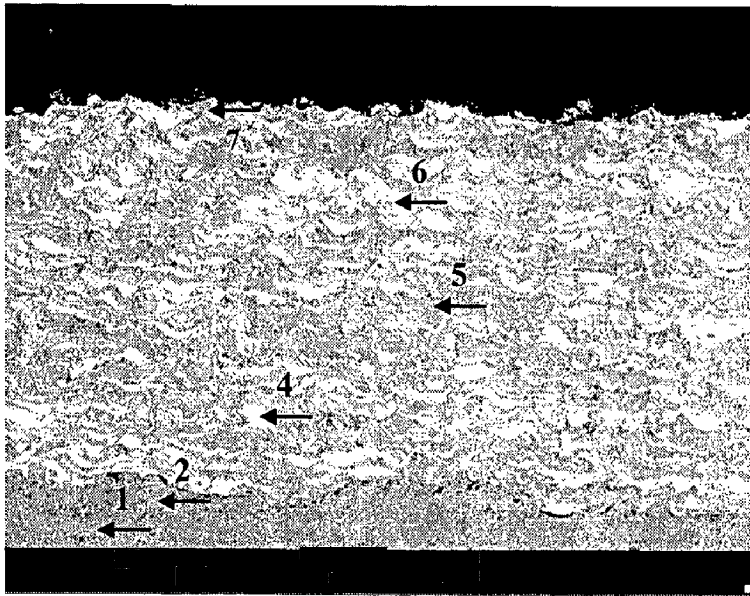
Fig. 4.12   Back scattered electron image and EDAX point analysis (wt %) across the
cross-section of the as-sprayed coatings deposited on T11 steels:
(a) NiCrFeSiB coatings   (b) WC-Co/NiCrFeSiB coatings
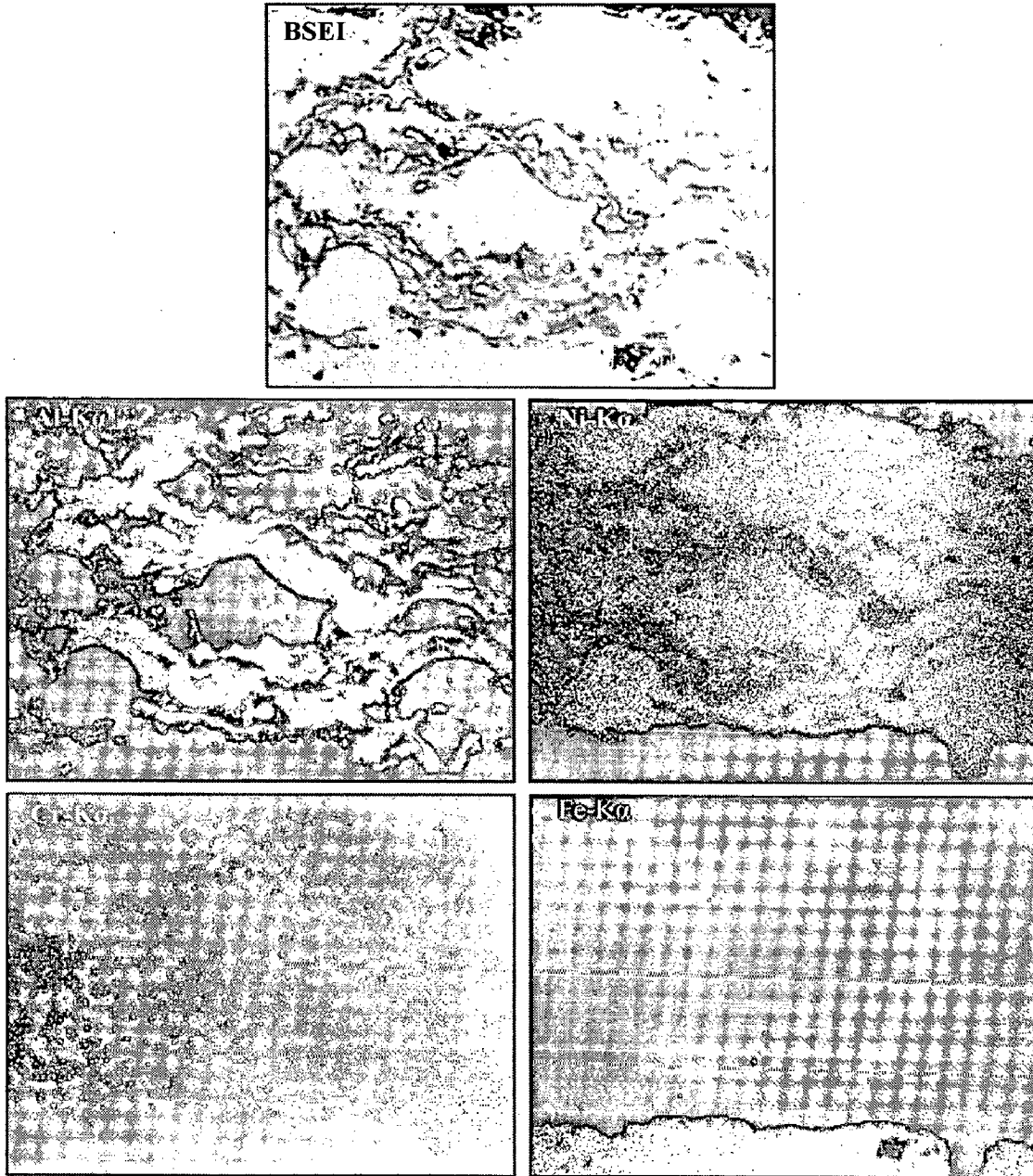
Fig. 4.13 BSEI and elemental X-ray mapping at the cross-section of the as-sprayed NiCrAl coating on T22 steel.
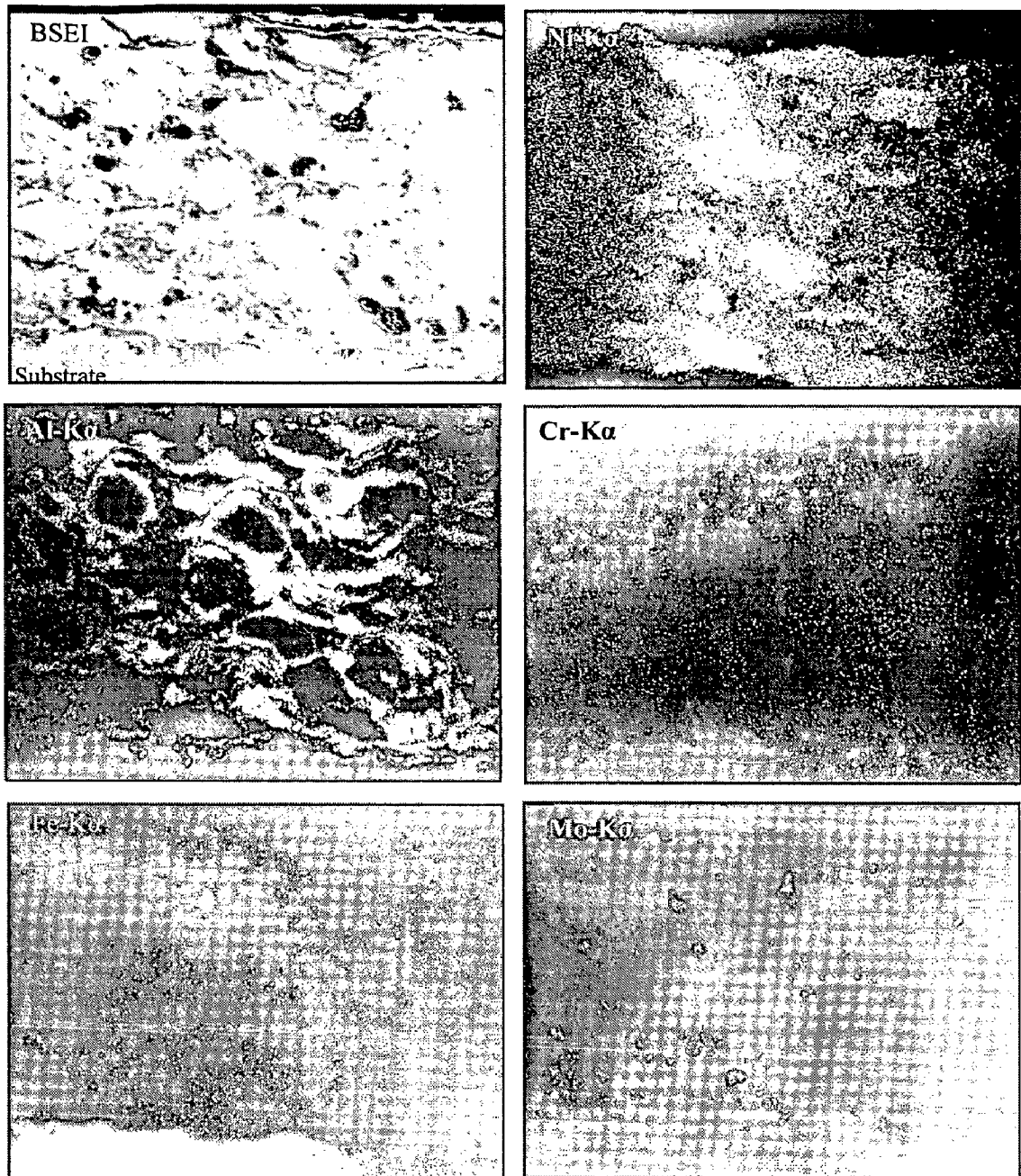
Fig. 4.14 BSEI and elemental X-ray mapping at the cross-section of the as-sprayed NiAlCrFeMo coating on T22 steel.
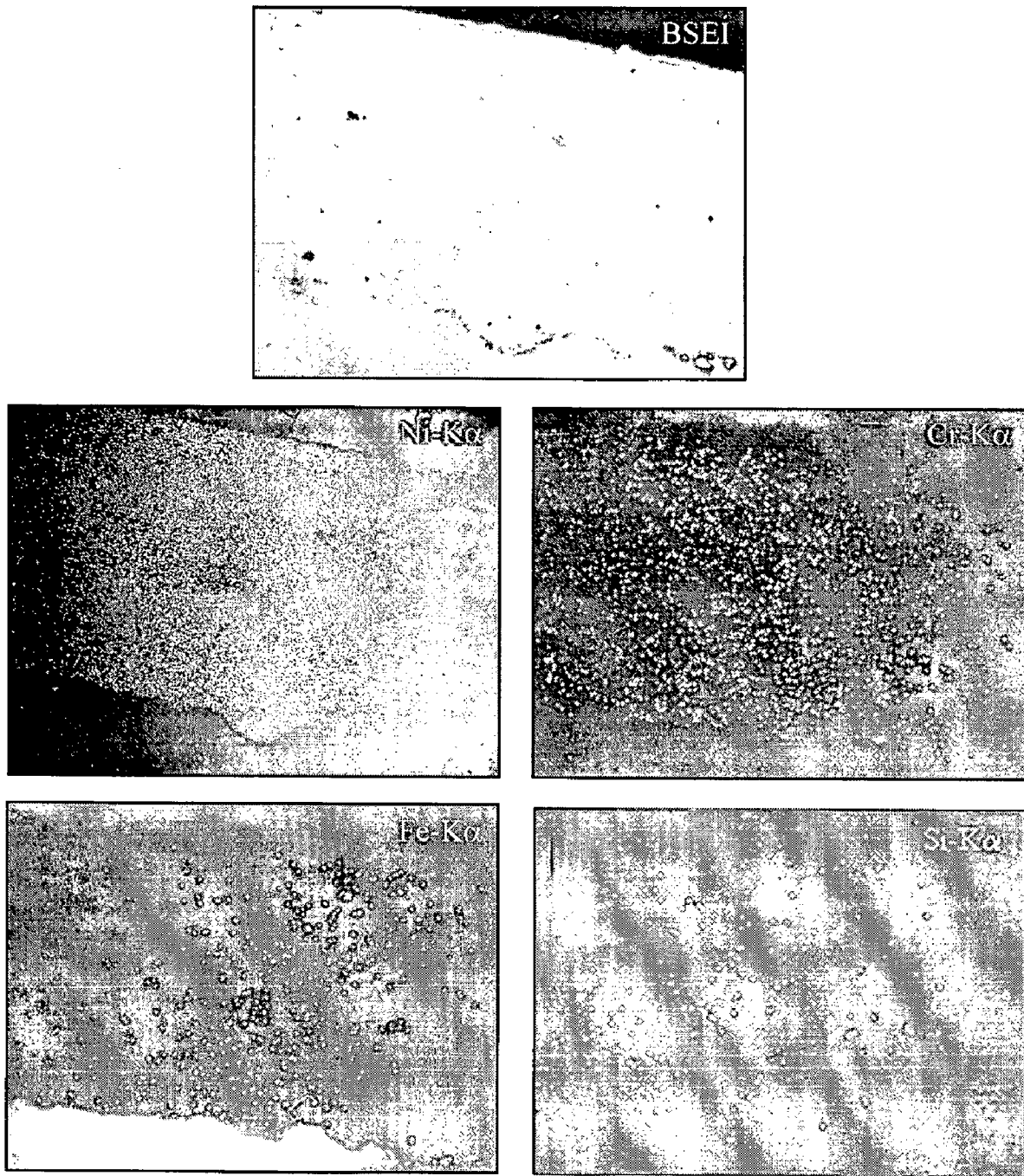
Fig. 4.15   BSEI and elemental X-ray mapping at the cross-section of the as-sprayed NiCrFeSiB coating on T11 steel.
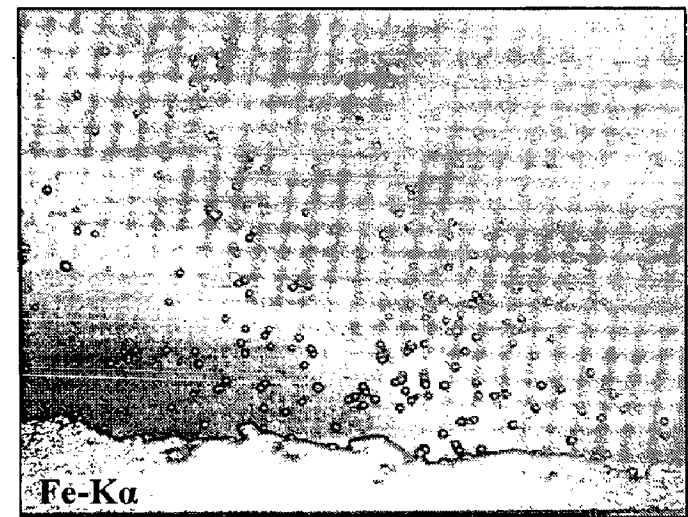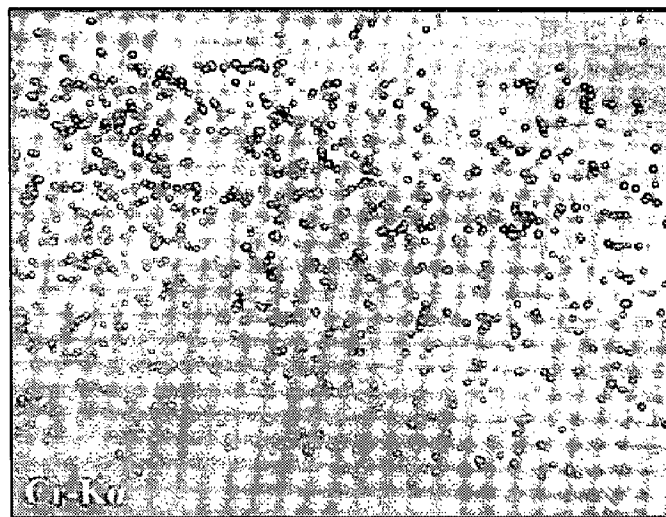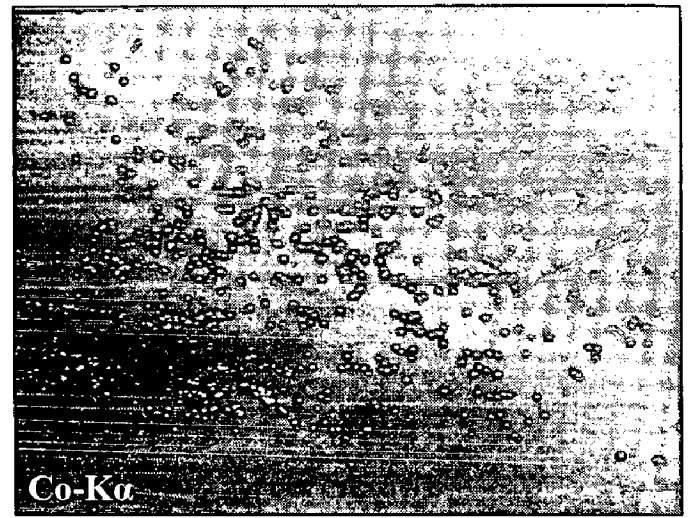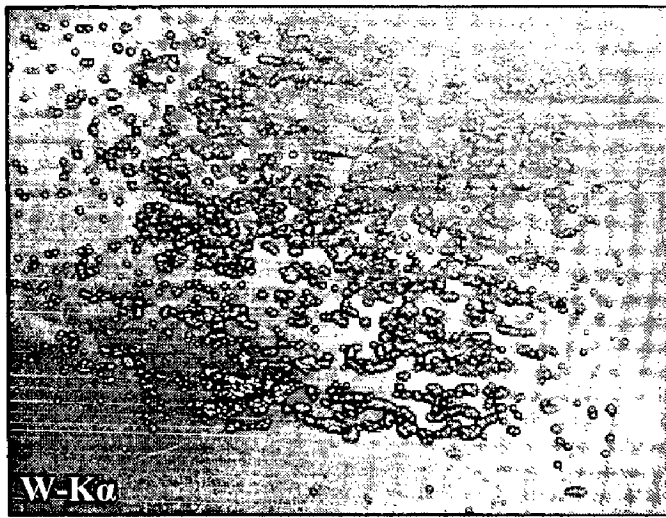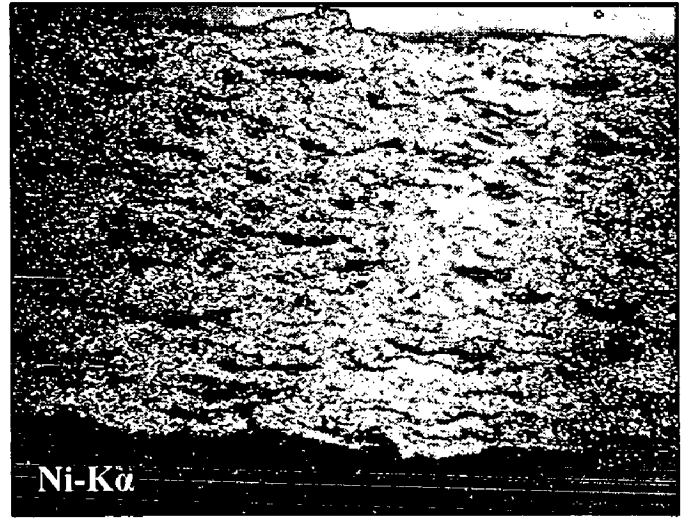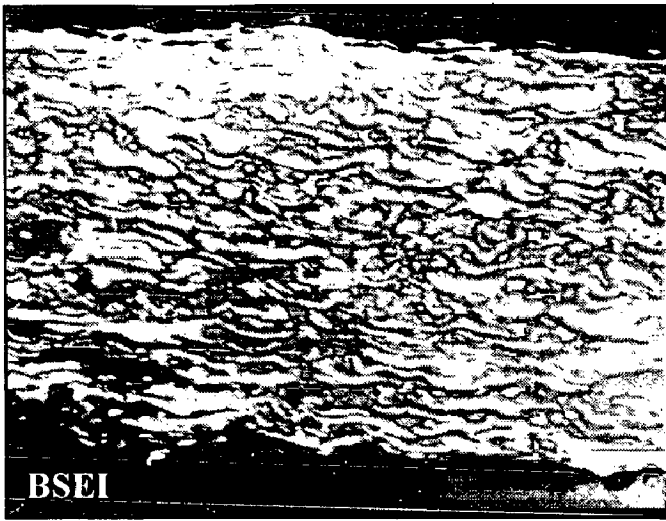
Fig. 4.16 BSEI and elemental X-ray mapping at the cross-section of the as-sprayed WC-Co/NiCrFeSiB coating on GrA1 steel.

The coatings obtained by the HVOF did not undergo significant phase transformations. It may be due to the supersonic speeds of the sprayed particles, which limits exposure of the particles to an oxidizing environment and to the fact that they are exposed to moderate heating. Hence, the XRD peaks for the coatings are almost similar to that of the powder.

The HVOF process hardens the coating due to its higher velocity of particle impact. The microhardness of the coating is found to vary with the distance from the coating-substrate interface. This significant variation in the micro-hardness along the thickness of the coatings might be due to the presence of porosity, oxides, unmelted and semi-melted particles, and inclusions in the microstructure of the coating as well as the layered structure of the coatings as observed in the optical micrographs (Fig. 4.10) and BSEI (Figs. 4.11 and 4.12). Similar observations are also reported by Ak et al. (2003) and Sidhu et al. (2006F) for the HVOF sprayed Ni-Cr coatings. During the HVOF spraying, the solidification rate varies for each layer deposited over each other. The first coating layer deposited on the substrate achieves the highest solidification rate, and the solidification rate decreases with the further deposition, mainly due to decrease in heat transfer rate from the molten material to the substrate. With respect to the WC-Co/NiCrFeSiB coating, the variation in the hardness across the thickness is due to the distribution of the WC hard phase in nickel alloy matrix. Further, the measured values of hardness for the WC-Co/NiCrFeSiB coatings are much higher than the hardness reported for similar coatings by Miranda et al. (2001), Hawthorne et al. (1999) and Clark et al. (1999). This may be due to a higher cohesive strength accompanied with lower porosity of the coating obtained by the optimum process parameter adopted for the HVOF spraying in the present study. Furthermore, a considerable increase in the microhardness values is measured on the substrate region closer to the coating. This increased hardness might be partially due to the high speed impact of the coating particles during the HVOF projection and partially due to the work hardening effect of the sandblasting of the substrate prior to the coating process. A similar trend of increased hardness in the austenitic and ferritic steel substrates during the HVOF coating has been discussed by Sundararajan et al. (2004) and Hidalgo et al. (2002).

The XRD analysis of the NiCrAl coating envisages the presence of nickel-rich FCC structure as the principal phase along with the minor phases of $AlNi_3$, Ni_2Al_3, Cr, and Al_2O_3. The strong peaks appearing in the pattern of the as-sprayed coating (Fig. 4.6a) shows an almost crystallized structure. Further, the EDAX analysis of the melted region in the microstructure of the coating (Figs. 4.8a and 4.11a) shows increased content of Al. This confirms the formation of Ni-Al intermetallic compounds like $AlNi_3$ and Ni_2Al_3. The presence of weak intensity peaks indexed to Al_2O_3 indicate that a small amount of oxidation has occurred during spraying. The oxide formation during the HVOF spraying has also been observed by Dent et al. (2001) and Sundararajan et al. (2003). The XRD patterns for the NiAlCrFeMo coating also shows the formation of γ-Ni solid solution as a principal phase along with the peaks of the $AlNi_3$, Ni_2Al_3, Cr, and $FeNi_3$. The presence of low intensity peaks of Al_2O_3 indicates that a small amount of oxidation occurred during spraying.

The X-ray pattern for the as-sprayed NiCrFeSiB coatings and powder (Fig. 4.7a) reveals that the Ni-rich FCC structure has a strong peak. The presence of CrSi and CrB phases indicate the melting of powder during spraying to the extent of dissolution of the borides and silicides in the liquid phase. The dissolution of B and Si makes the crystallization process impossible. Evidently, a very broad peak accompanied by reduction in peak intensity at 2θ of about 44.5° can be observed for the as-sprayed coating in comparison to the XRD pattern for the initial powder. This difference reveals the formation of amorphous matrix. The EDAX composition analysis across the coating cross-section (Fig. 4.12 a) shows the homogeneous elemental concentration, which indicates complete melting of the coating powder. Similar observations are reported by Eigena et al. (2005), Sundararajan et al. (2004), Planche et al. (2005), Sidhu (2006E) and Li et al. (2004).

The WC-Co/NiCrFeSiB coatings showed the crystalline peaks of WC and W_2C. Generally, the formation of W_2C phase is regarded as a product of decarburization in the thermal spraying. During the HVOF spraying, the flame temperature is usually less than 3000°C, and the particle speed can reach up to 800-1000 m/s. Therefore, the time of powder exposed in air is so short that the decomposition and decarburization of WC is not serious. The HVOF spraying leads to a high retention of WC in the matrix. The W_2C is more brittle

than WC and, hence, the hardness of the coating increases with increase in the content of W_2C. Similar observations are reported by Miranda et al. (2001) and Wang et al. (2004) for different combinations of WC hard phase in the nickel-alloy matrix.

The cross-sectional micrographs (Fig 4.10) of the coatings show the layered structure which reflects the building of coating thickness due to deposition and resolidification of molten or semi-molten droplets and the impacted splats, roughly oriented parallel to the substrate surface. The distinct splats enriched with partially melted nickel have been identified in the NiCrAl and NiAlCrFeMo coatings using the EPMA studies. This indicates that the powder particles were at lower temperature impact with the substrate. During spraying, the particles of different sizes might have different molten states, i.e., the particles of moderate sizes may get fully melted or partially melted at the point of impact on the substrate, and the particles of either small or large sizes are usually not melted as they hit the substrate. Similar observations regarding the microstructure of the HVOF sprayed coating containing partially melted particles were reported by Boudi et al. (2004), Hidalgo et al. (2002) and Mingheng et al. (2004).

Some inclusions are found to be present along the coating substrate interface. The inclusion at the coating substrate interface have been identified as alumina in the elemental X-ray mapping for aluminum, which got retained possibly during the grit blasting of the substrate surface before spraying and also would have induced during polishing of specimens. Similar observations of retained alumina powder during polishing have also been reported by Sundarajan et al. (2003). It is evident from the EPMA analysis across the coating-substrate interface (Figs. 4.13– 4.16) that a minor amount of nickel and aluminum have diffused from the coating into the substrate and the iron from substrate to the coating. This suggests that the adhesion between the coating and the substrate is due to the combined mechanical interlocking and metallurgical bonding effect.

This chapter describes the oxidation behavior of HVOF coated and uncoated steels. The cyclic oxidation was conducted in air for 50 cycles at an elevated temperature of 900°C. The specimens were visually examined at the end of each cycle during the course of the study. Thermogravimetry is used to study the reaction rate and kinetics of the oxidation process. The identification and structural investigation of reaction products of the oxidized specimens were made by means of the XRD, SEM/EDAX and EPMA techniques. The results have been compiled in different sections of the chapter to assess the performance of each coating.

5.1 RESULTS

5.1.1 Uncoated Steels

5.1.1.1 Thermo gravimetric studies

The macrographs of the GrA1, T11 and T22 steel specimens subjected to cyclic oxidation for 50 cycles at 900°C are shown in Fig. 5.1. All the steels developed a dark grey colored oxide scale. During the cyclic oxidation, the minimum spallation of scale was observed for the T11 steels as compared to the other steels. The scale formed on the T22 steel, found to be fragile and cracked from centre of the sample.

The plots of cumulative weight gain (mg/cm^2) as a function of time expressed in number of cycles are shown in Fig. 5.2. The weight gain for the GrA1, T11 and T22 steels at the end of 50 cycles are found to be 221.5, 165.9 and 197.7 mg/cm^2, respectively. Evidently, the GrA1 steel shows the maximum weight gain during the course of the study. Further, the weight gain square (mg^2/cm^4) data has been plotted as a function of time, as shown in Fig. 5.3, to establish law governing the corrosion. This plot shows the observable deviation from the parabolic rate law for all types of steel, which indicate that the oxide films were weakly protective at 900°C. The parabolic rate constant K_p was calculated by a linear least-square algorithm function in the form of $(\Delta W/A)^2 = K_p \times t$, where $\Delta W/A$ is the weight gain per unit area, and t is the oxidation time in seconds. The values of K_p for the

GrA1, T11 and T22 are found to be 29.14×10^{-8}, 15.87×10^{-8} and 22.54×10^{-8} g^2 cm^4 s^{-1} respectively.

5.1.1.2 X-ray Diffraction Analysis

The X-ray diffraction pattern for the steels, after exposure to air at 900°C for 50 cycles is compiled in Fig. 5.4. As obvious from the composition, all the steels show Fe_2O_3 as the major peak, whereas the minor peaks of Fe_3O_4, Cr_2O_3 and MoO_3 are found in the oxide scale of T11 and T22 steels. Further, the "d" values matched well with the rhombohedral mixed oxide of Fe and Cr, viz. $FeCr_2O_4$.

5.1.1.3 SEM/EDAX Analysis

The SEM micrograph showing the scale morphology along with the EDAX analysis is shown in Fig. 5.5. The iron oxide is the main constituent of the scale in case of all the steels. All other minor elements and chromium had depleted considerably. The surface scale, in case of the GrA1 and T11 steels show intergranular cracking. Figure 5.6 shows the BSEI taken along the cross section of the oxidized samples. Deep pits are seen along the metal-scale interface, which grows laterally, meets one another and leads to the formation of cracks. This crack allows the oxygen to reach the metal surface, and increased oxidation eventually ends in spalling of scale. The multi-laminations, as seen in the cross section of oxide scale, weaken its protection against oxidation. The EDAX point analysis (Fig. 5.6c) along the cross section confirms iron oxide as the major phase.

5.1.1.4 EPMA Analysis

The BSEI and X-ray mappings for a part of the oxide scale of T22 steels after oxidation in air for 50 cycles at 900°C are shown in Fig. 5.7. The Fe mapping indicates higher concentration of iron throughout the oxide layer. The chromium oxide is clearly seen in the inner layer of the oxide scale. The Mo and Mn seem to be homogeneous throughout the cross-section.

5.1.2 NiCrAl Coating

5.1.2.1 Thermo gravimetric studies

The macrographs of the HVOF-sprayed NiCrAl coatings on the GrA1, T11 and T22 steels subjected to cyclic oxidation for 50 cycles at 900°C are shown in Fig. 5.8. The
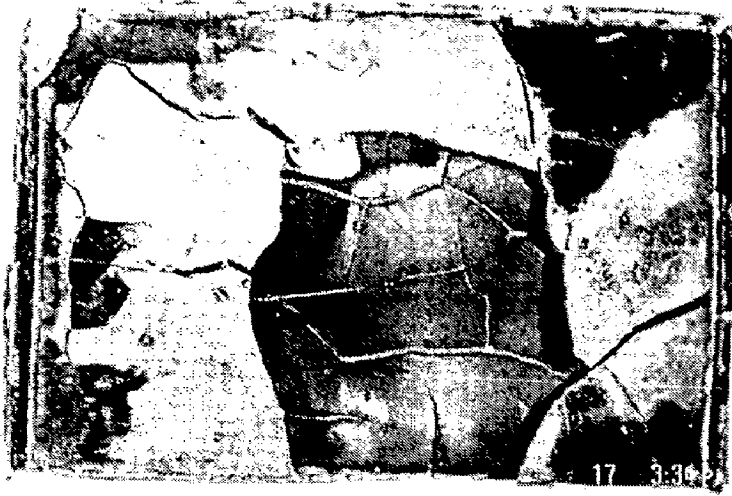
(a)

(b)

(c)

Fig. 5.1   Macrographs of bare boiler steels subjected to cyclic oxidation in air at
900°C for 50 cycles:
(a) GrA1 steels (b) T11 steels (c) T22 steels
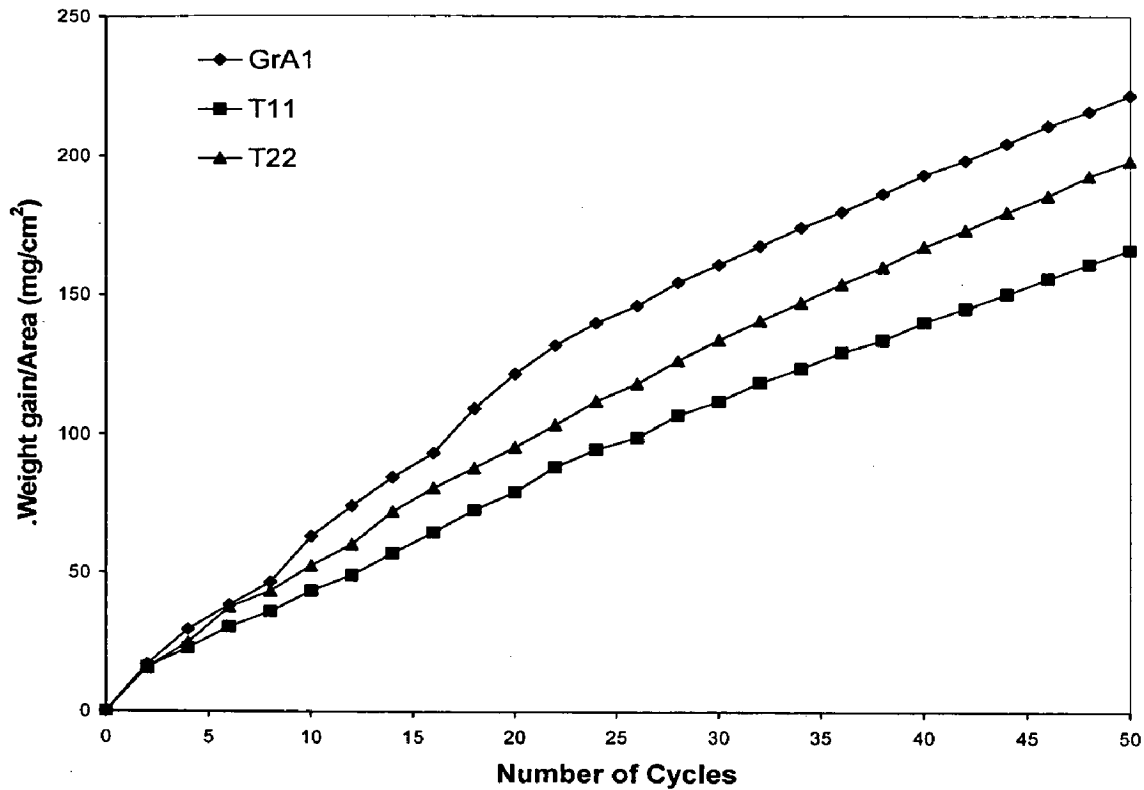
Fig. 5.2　　Weight gain vs. number of cycles plot for uncoated steels subjected to cyclic oxidation for 50 cycles in air at 900°C
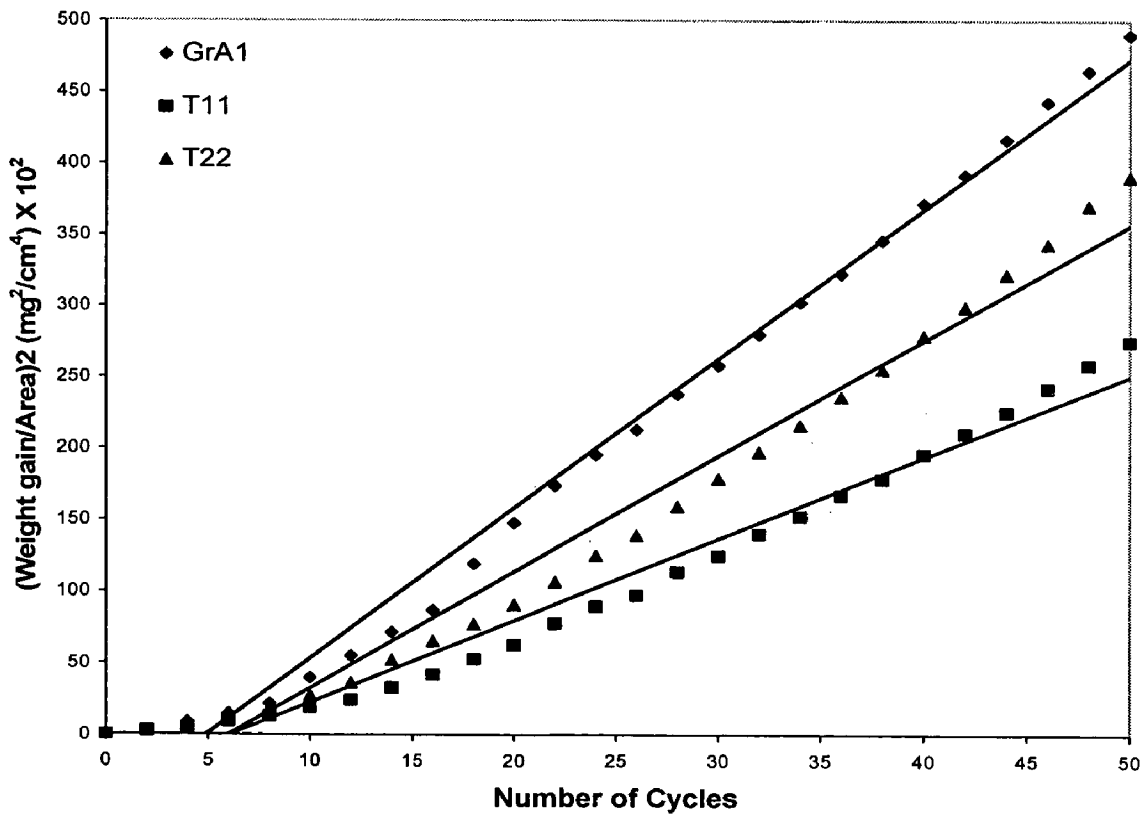
Fig. 5.3　　(Weight gain/area) ^{2} vs. number of cycles plot for uncoated steels subjected to cyclic oxidation for 50 cycles in air at 900°C
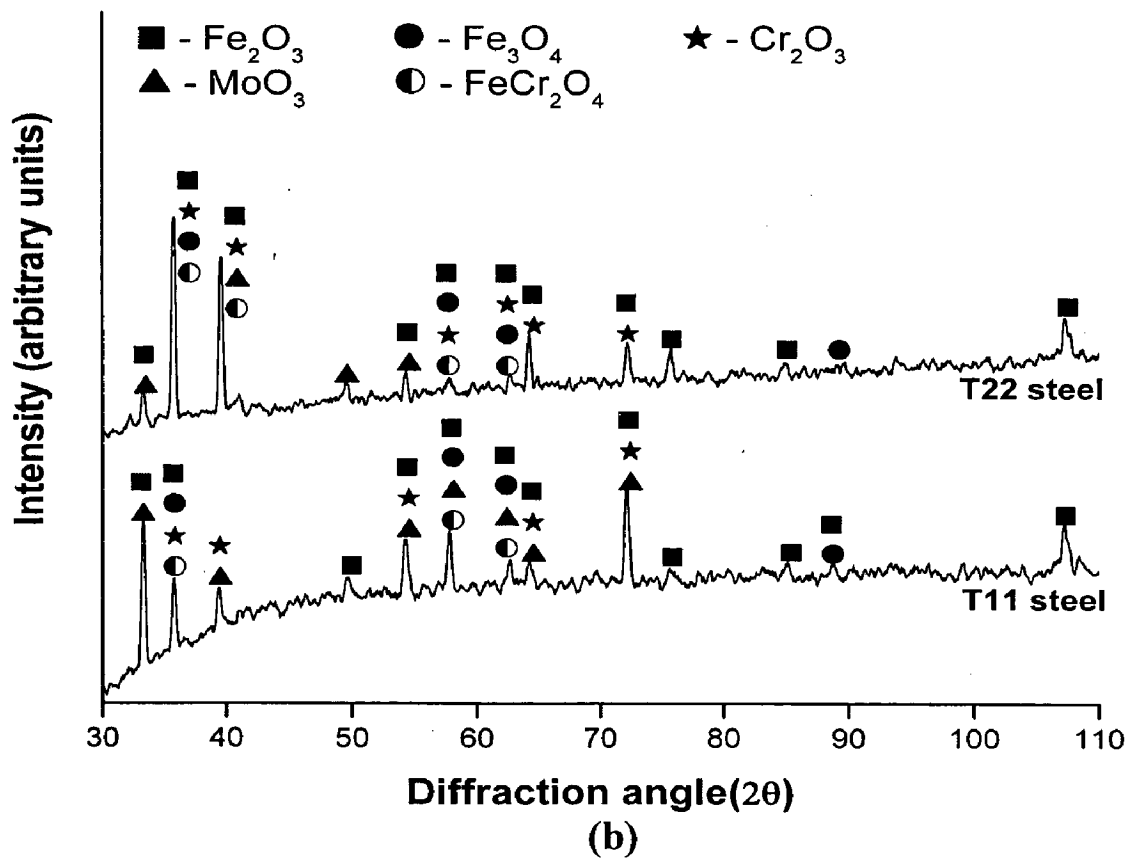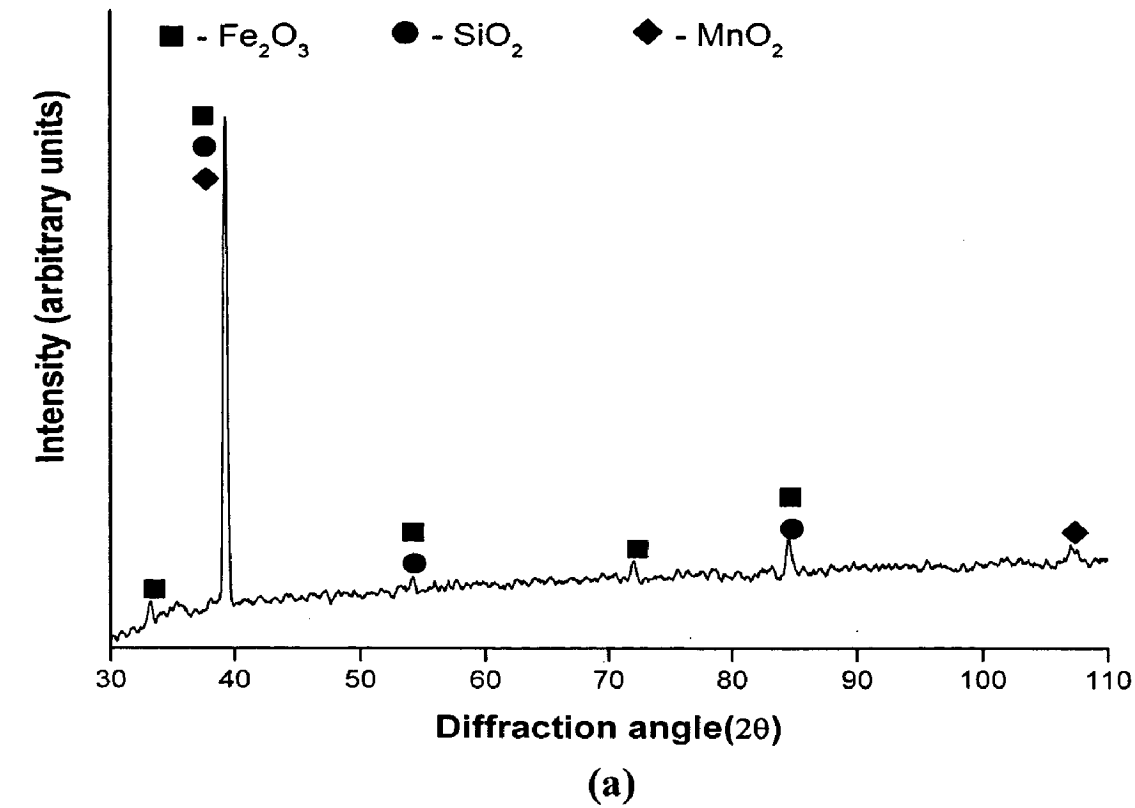
Fig.5.4   X-ray diffraction patterns for the uncoated steels subjected to cyclic oxidation for 50 cycles in air at 900°C:
(a) GrA1 Steel (b) T11 and T22 steels
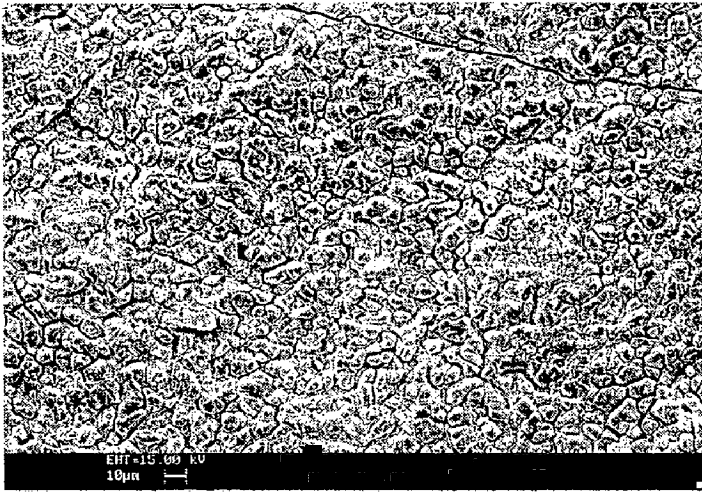
99.31% Fe_2O_3

(a)

97.51% Fe_2O_3
2.04%   MnO

(b)
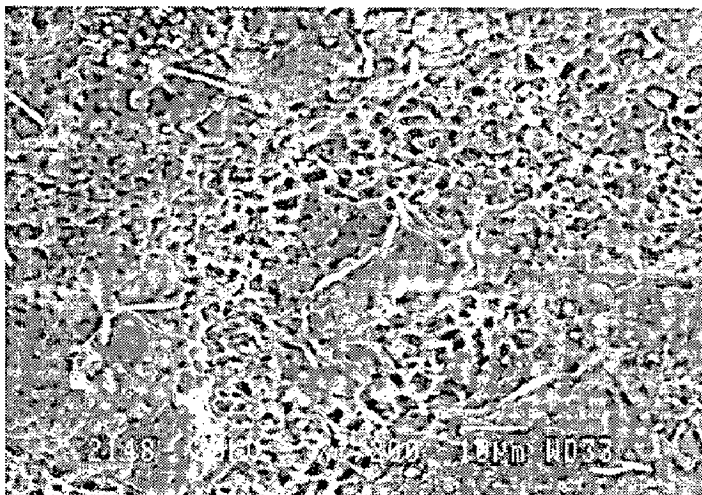
94.65% Fe_2O_3
2.96% Cr_2O_3
2.03%   MnO

(c)

Fig. 5.5   Surface scale morphology and EDAX area analysis for the uncoated steels
subjected to cyclic oxidation in air at 900°C for 50 cycles:
(a) GrA1 Steel   (b) T11 Steel   (c) T22 Steel
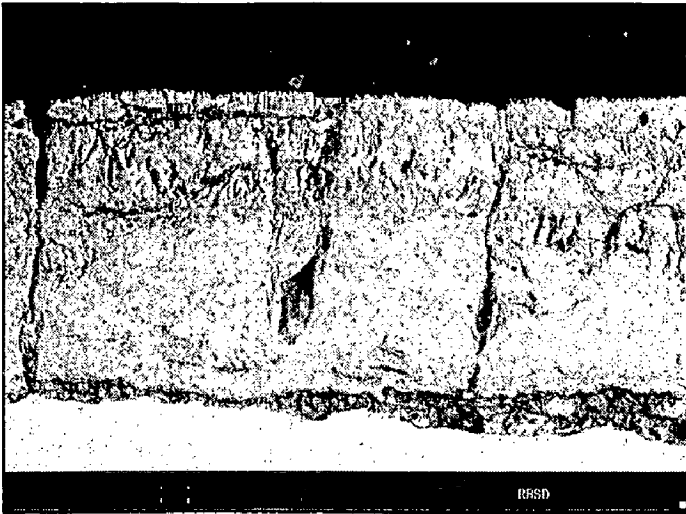
(a)
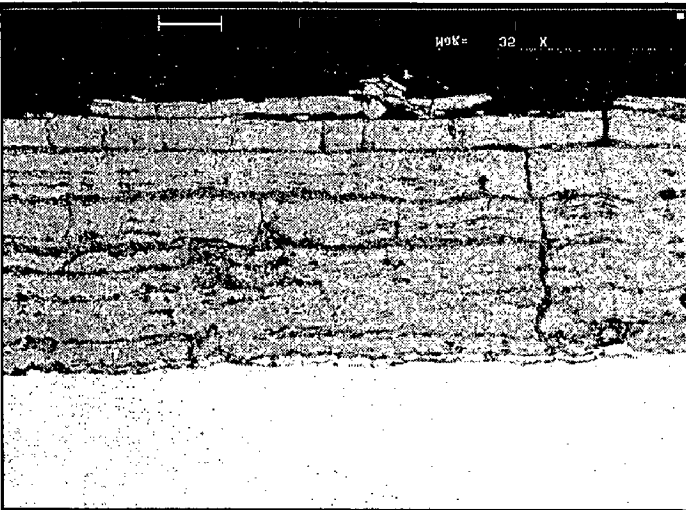
(b)
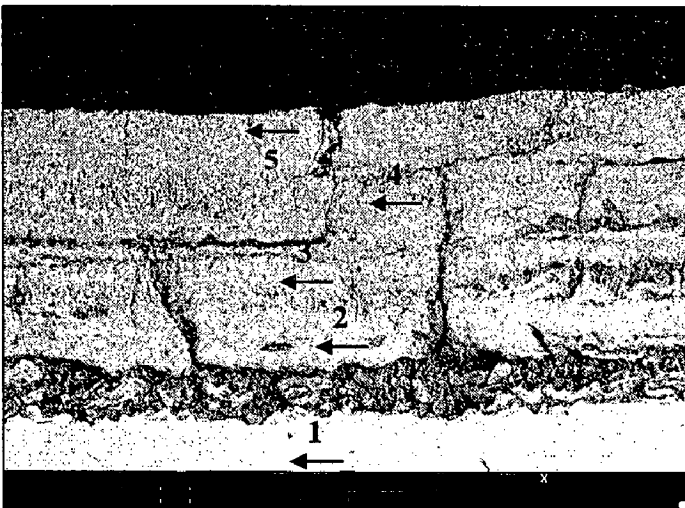
(c)
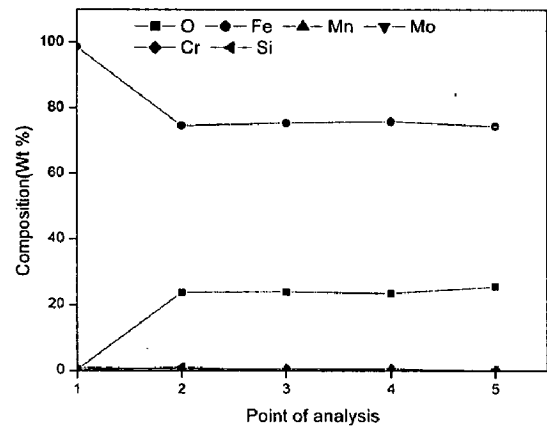
(d)

Fig.5.6   Back scattered images for the uncoated steels after cyclic oxidation in air at 900°C for 50 cycles

(a) GrA1 Steel   (b) T11 Steel   (c) T22 Steel

(d) EDAX point analysis along the cross-section of T22 steel
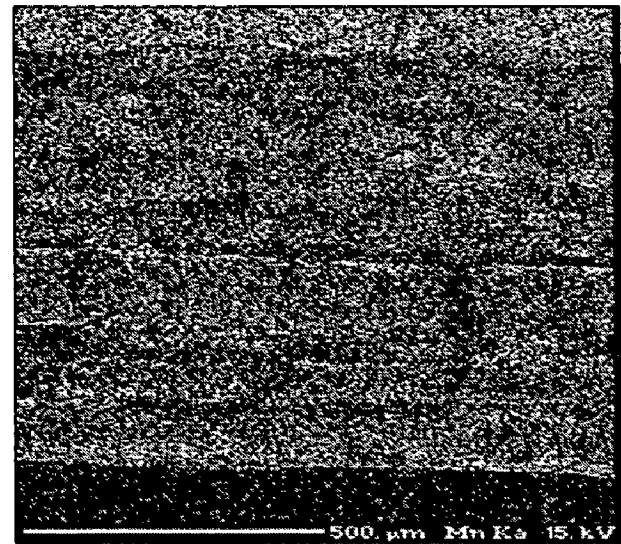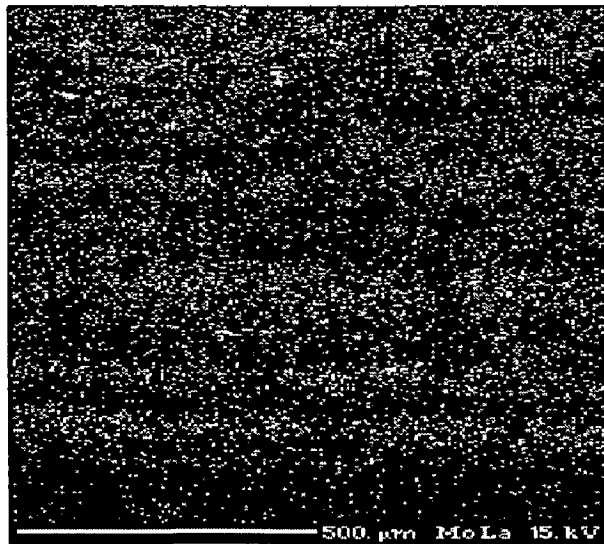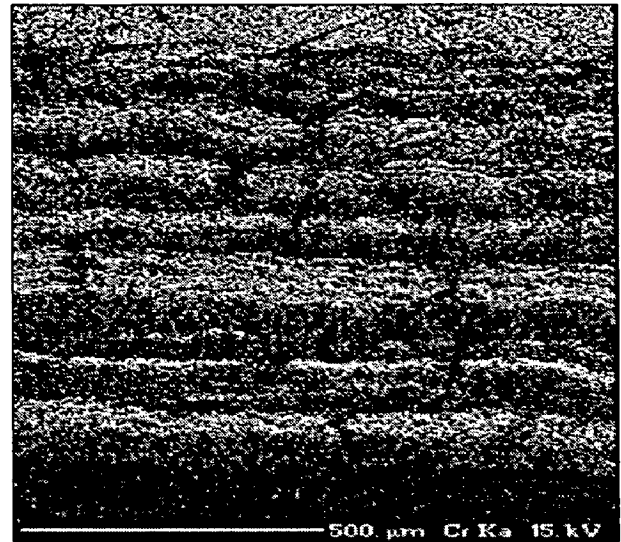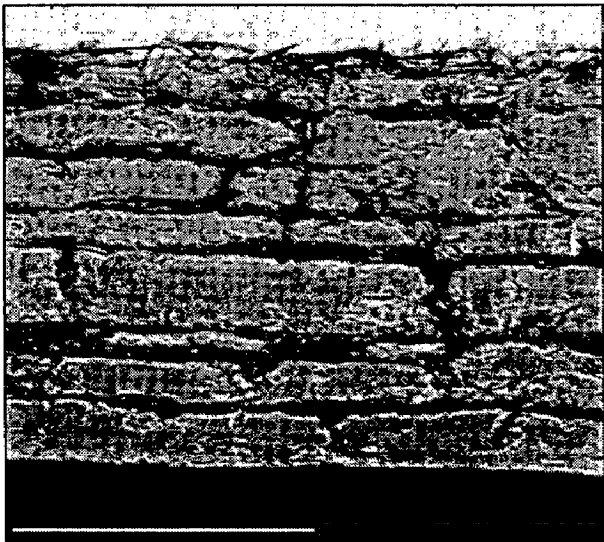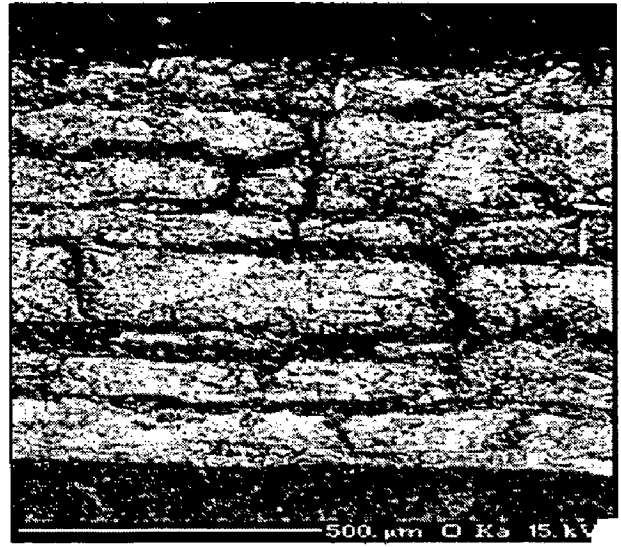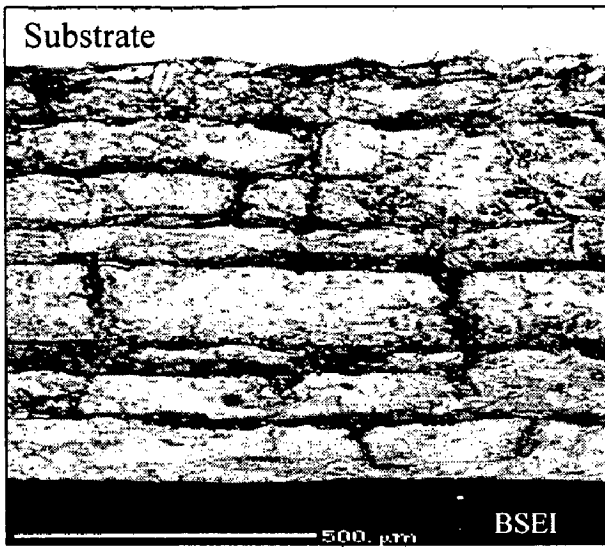
Fig.5.7 BSEI and X-ray mapping of the cross-section of T22 boiler steel subjected to cyclic oxidation for 50 cycles in air at 900°C
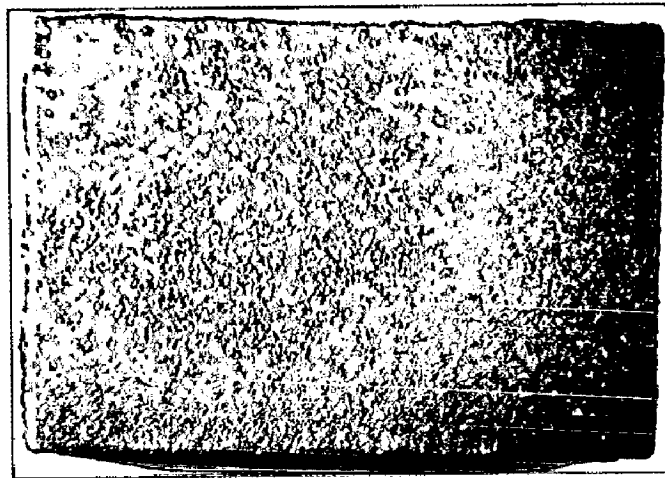
(a)
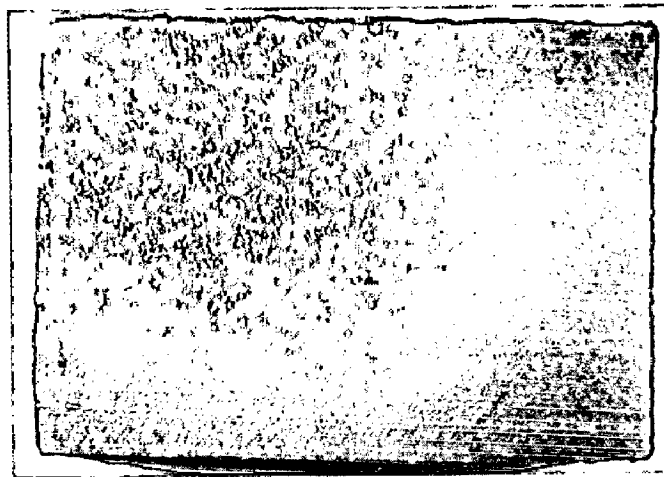
(b)

(c)

Fig.5.8   Macrographs of the NiCrAl coating subjected to cyclic oxidation in air for 50 cycles at 900°C:
(a) GrA1 steel   (b) T11 steel   (c) T22 steel

color of the oxide scale on the surface of all the three coated steels is greenish grey, close to dark green. The color of as-sprayed coatings was grey and with oxidation, firstly green tinges were observed which progressed with increasing duration of cycles and finally a greenish grey colored scale has been observed. The oxide scale found to be strongly adhered to the substrate, with no tendency for spalling. In case of the NiCrAl coated T22 steel, protrusions were seen after 12th cycle and these protrusions are of dark grey color.

The plots of cumulative weight gain (mg/cm^2) as a function of time expressed in number of cycles are illustrated in Fig. 5.9. The NiCrAl coated T22 steels showed a maximum weight gain in comparison to the coated GrA1 and T11 steels. Extents of weight gain in all the coated steels are similar up to the 12th cycle and, thereafter, the coated T22 showed a higher weight gain in comparison to the other coated steels. The weight gain for the coated GrA1, T11 and T22 steels at the end of 50 cycles of cyclic oxidation is found to be 6.7, 10.8 and 16.91 mg/cm^2, respectively.

Further, the weight gain square (mg^2/cm^4) data were plotted as a function of time, as shown in Fig. 5.10, to establish the rate law for oxidation. From Fig. 5.10, it can be envisaged that the oxidation behavior of the coated GrA1 and T11 steels is parabolic in nature up to 50 cycles. The plot for the coated T22 steels showed a perceptible deviation from the parabolic rate law. The parabolic rate constant K_p, as calculated from the slope of the linear regression fitted line for the NiCrAl coated GrA1, T11 and T22 steels is 0.027×10^{-8}, 0.075×10^{-8} and 0.164×10^{-8} g^2 cm^4 s^{-1}, respectively.

5.1.2.2 X-ray Diffraction Analysis

The X-ray diffraction patterns for the NiCrAl coated GrA1 and T11 steels are shown in Fig. 5.11 which revealed the phases of $\alpha-Al_2O_3$, Ni, $AlNi_3$ and mixed spinal-type oxide, $NiCr_2O_4$. The XRD plot for the NiCrAl coated T22 steel is shown in Fig. 5.12. The presence of Fe_2O_3 has been revealed along with the phases of $\alpha-Al_2O_3$, Cr_2O_3, and $NiCr_2O_4$.

5.1.2.3 SEM/EDAX Analysis

The SEM micrograph showing the scale morphology along with the EDAX analysis is demonstrated in Figs. 5.13–5.15. The surface of the oxide scale shows different morphologies of its constituents. The EDAX analysis on nearly spherical globule (Fig. 5.13b) on the surface corresponds to a higher amount of Ni and Cr oxides, while the

matrix (Fig. 5.13a) indicates an increased content of Al_2O_3. The EDAX area analysis on the surface of NiCrAl coated T11 steels (Fig. 5.14) also shows the protective oxides of Ni and Cr. The surface morphology of the coated T22 steels (Fig. 5.15) shows oxide protrusion, and the EDAX analysis on this protrusion confirmed that it is Fe_2O_3, which might have oozed out from the substrate.

Similarly, Fig. 5.16 shows the BSEI taken along the cross section of the oxidized NiCrAl coated steels and the EDAX composition analysis at the point of interest. Figure 5.16a shows the point analysis along the cross section of the oxidized NiCrAl coated GrA1 steel. The EDAX analysis at point 5 shows the presence of Al_2O_3 and the oxides of Ni and Cr. The presence of oxygen at point 3 indicates that the coating might have got oxidized along the splat boundaries, whereas the absence of oxygen at point 2 shows that the Ni-rich splat has not got oxidized.

The analysis for the oxidized NiCrAl coated T11 steels, as illustrated in Fig. 5.15b, shows that the outermost layer of the scale mainly consists of the oxides of Ni, Al, and Cr. The points 2 and 5 indicate Ni and Cr-rich splat in an unoxidised state, as oxygen is absent at this point. At points 3 and 5, the concentration of Cr, Al and O is high; which reveals about the internal oxidation along the splat boundary. The black phase present at the coating substrate interface (point 7) is found to be rich in elements Al and O and, therefore, it is an inclusion of the alumina particles as already discussed in Chapter 5.

Figure 5.16c shows the BSEI/EDAX analysis along the cross-section of the oxidized NiCrAl coated T22 steel. The EDAX analysis at the points 1, 2 and 3 revealed the presence of only Fe and O. This implies that iron oxide has oozed out from the substrate on to the surface of the coatings along the crack formed during the oxidation studies. The crack has followed the path along the splat boundary via the open porosity. Similarly, the point 5 shows the presence of Al_2O_3 and Cr_2O_3 along with a minor amount of Fe_2O_3. It is also observed that the corrosion of substrate occurred to a large extent near the area where the coating is cracked.

5.1.2.4 EPMA Analysis

The EPMA analysis for the NiCrAl coated T11 steel oxidized for 50 cycles (Fig. 5.17) shows a thin layer of oxide scale on the top of the coating. The X-ray mapping revealed that this adherent top most layer is rich in O and Al, which confirmed the
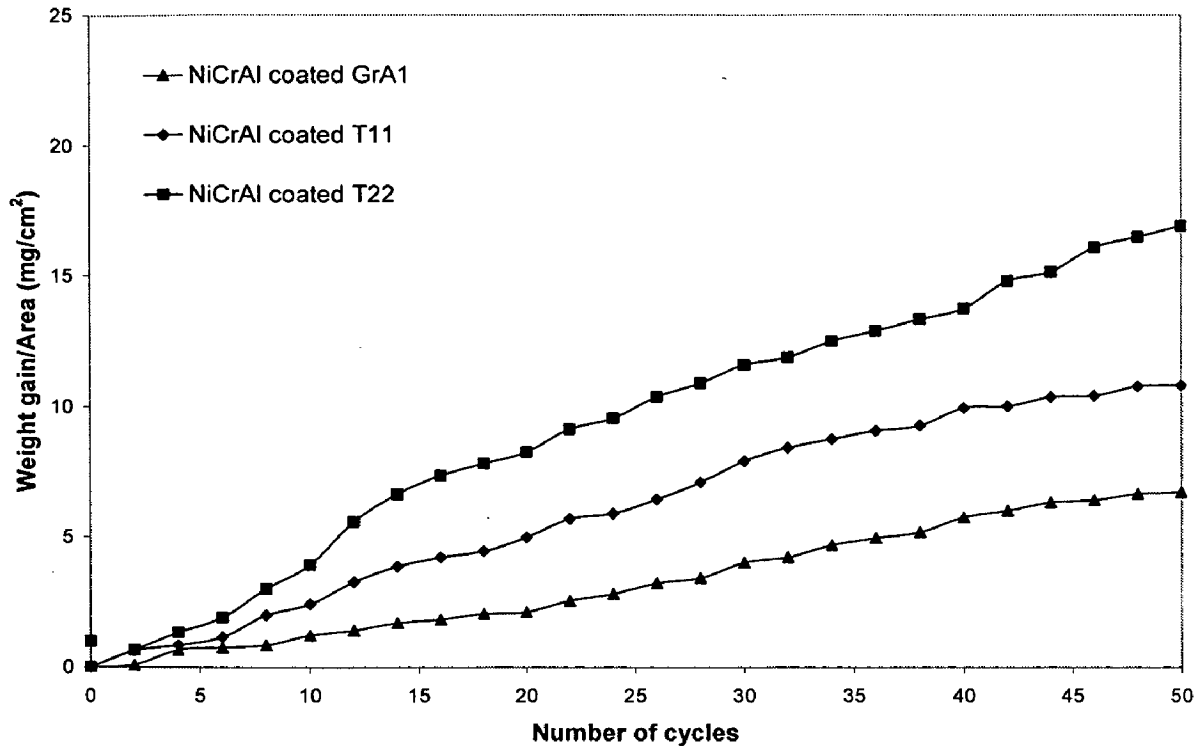
Fig.5.9 Weight gain vs. number of cycles plot for NiCrAl coated steels subjected to oxidation for 50 cycles in air at 900°C
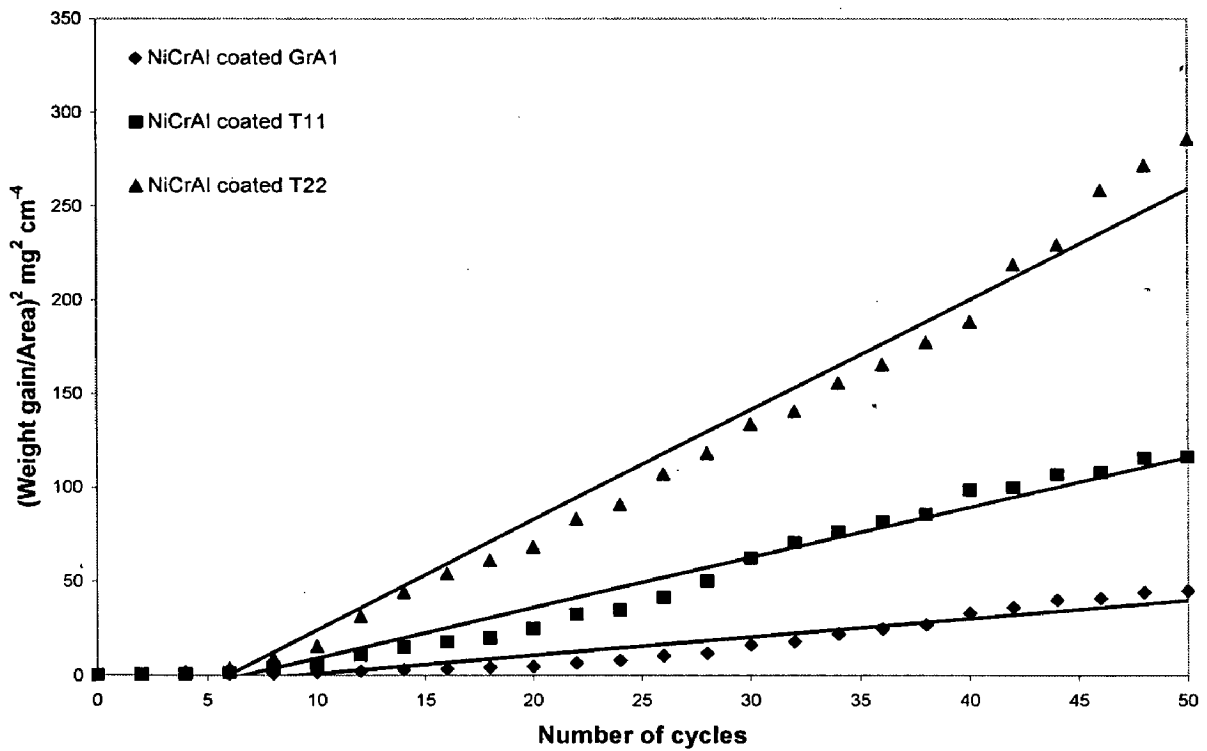
Fig.5.10 (Weight gain/area)^2 vs. number of cycles plot for NiCrAl coated steels subjected to oxidation for 50 cycles in air at 900°C
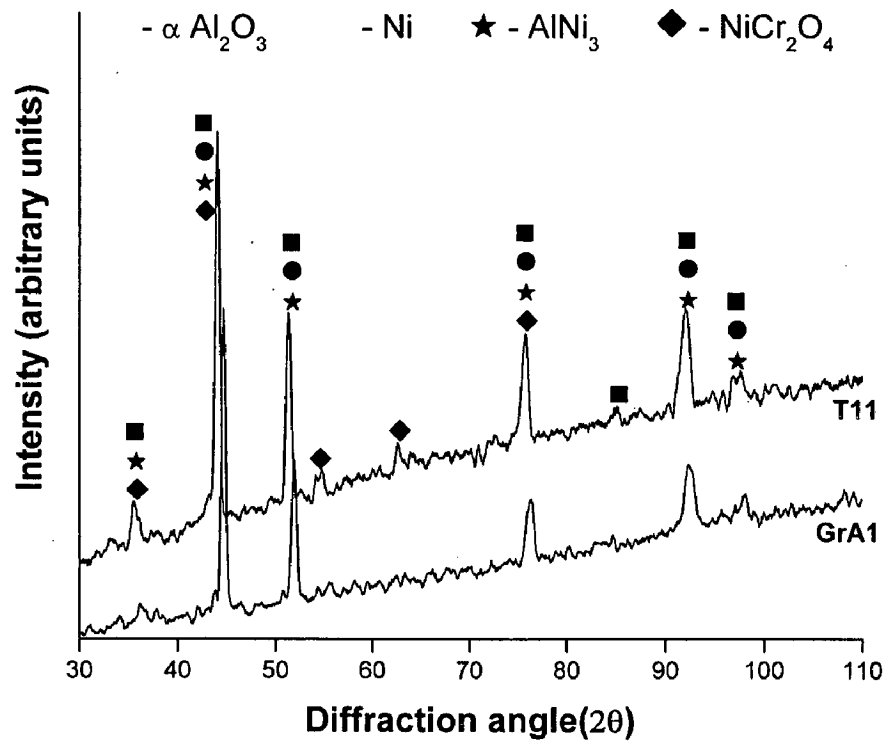
Fig.5.11   X-ray diffraction patterns for NiCrAl coated GrA1 and T11 steels subjected to cyclic oxidation in air for 50 cycles at 900°C

Fig.5.12   X-ray diffraction patterns for NiCrAl coated T22 steels subjected to cyclic oxidation in air for 50 cycles at 900°C

Element	Wt %
NiO	26.95
Al2O3	33.29
Cr2O3	39.75

(a)

Element	Wt %
NiO	33.67
Al2O3	14.60
Cr2O3	51.73

(b)
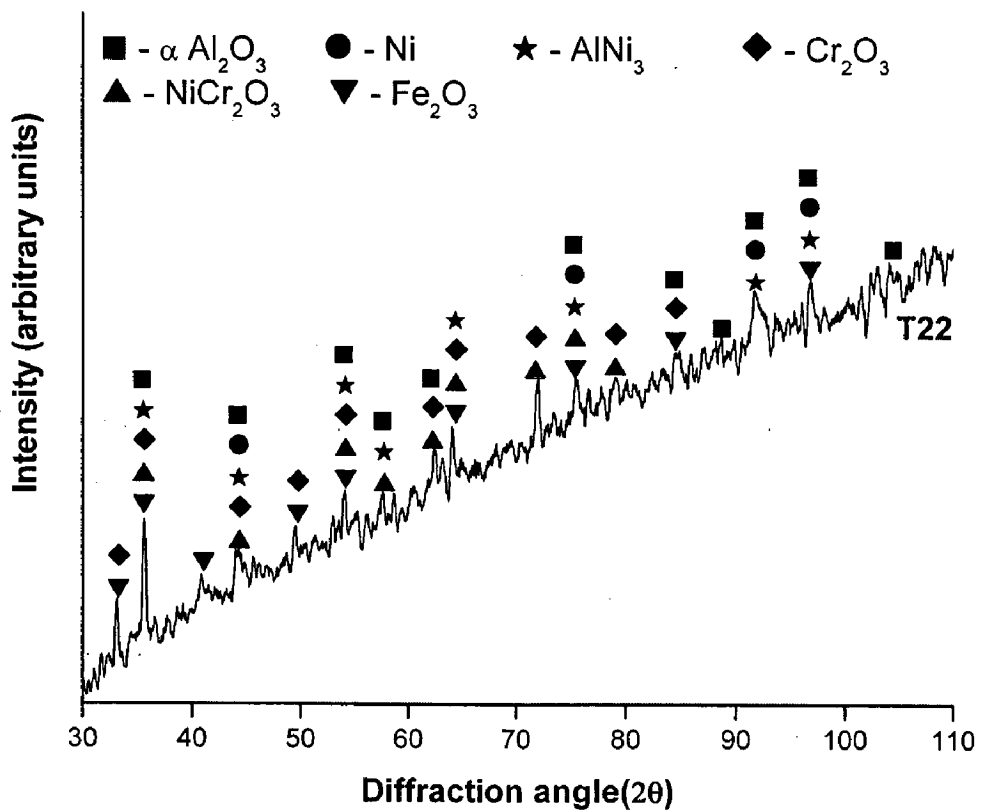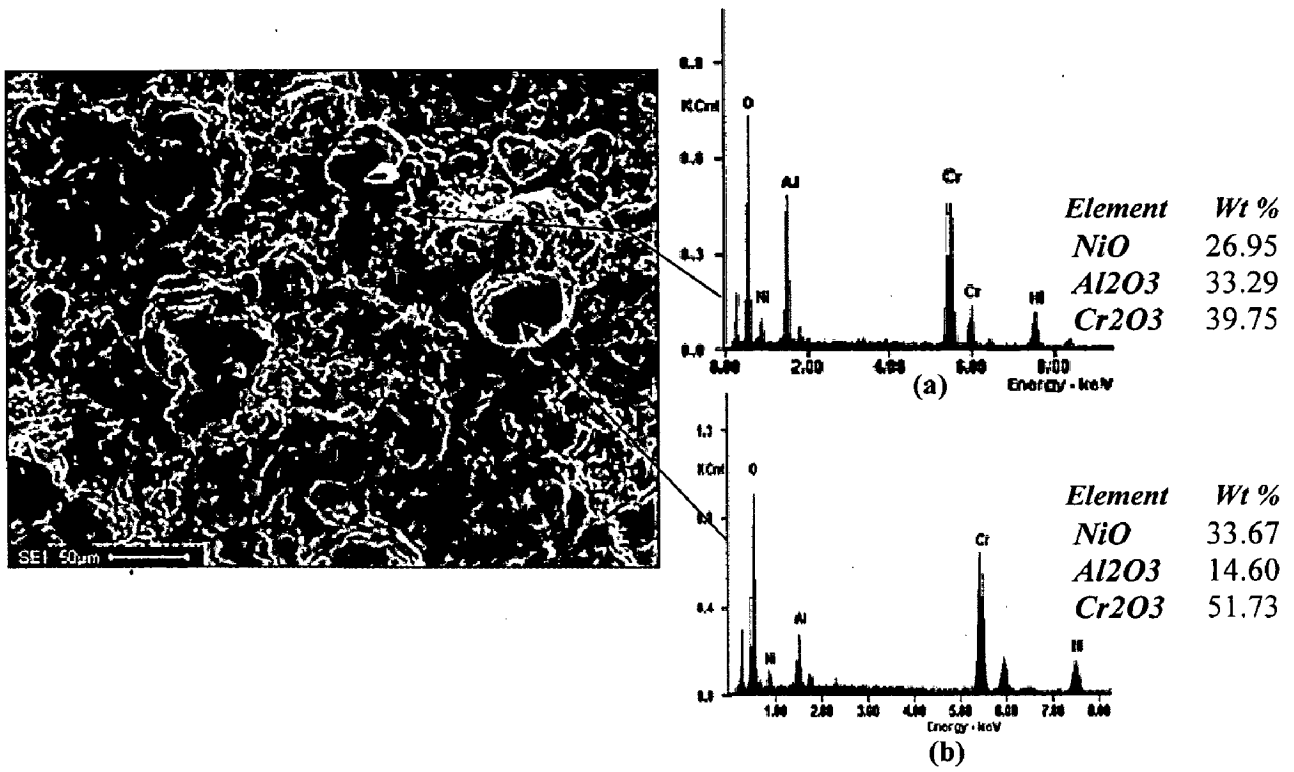
Fig.5.13   SEM and EDAX point analysis for NiCrAl coatings on GrA1 steel subjected to oxidation for 50 cycles in air at 900°C

Element	Wt %
NiO	25.47
Al2O3	33.7
Cr2O3	40.83
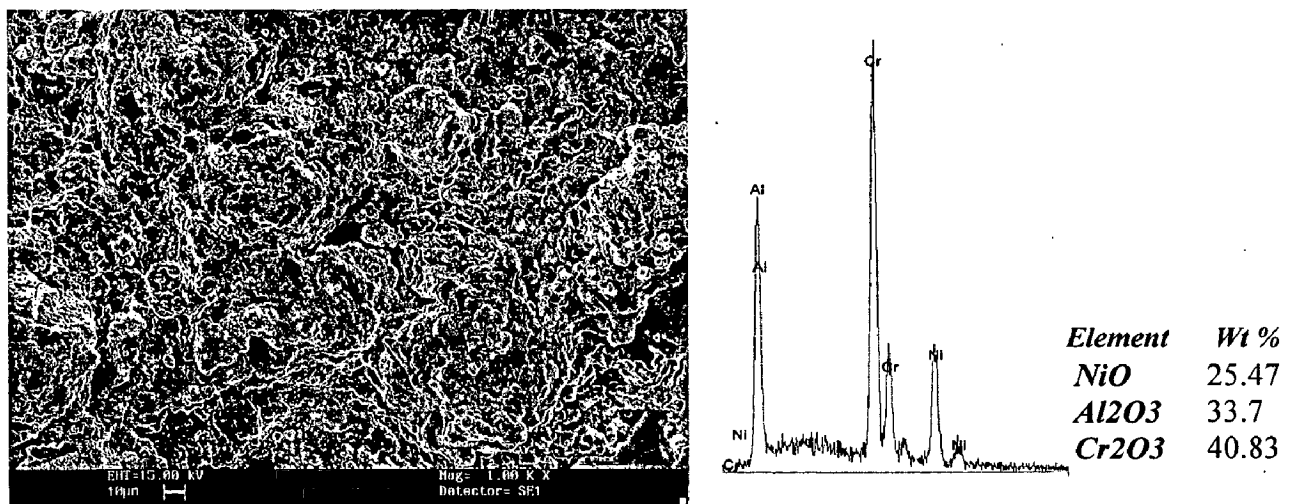
Fig.5.14   SEM and EDAX area analysis for NiCrAl coatings on T11 substrate steel subjected to oxidation for 50 cycles in air at 900°C
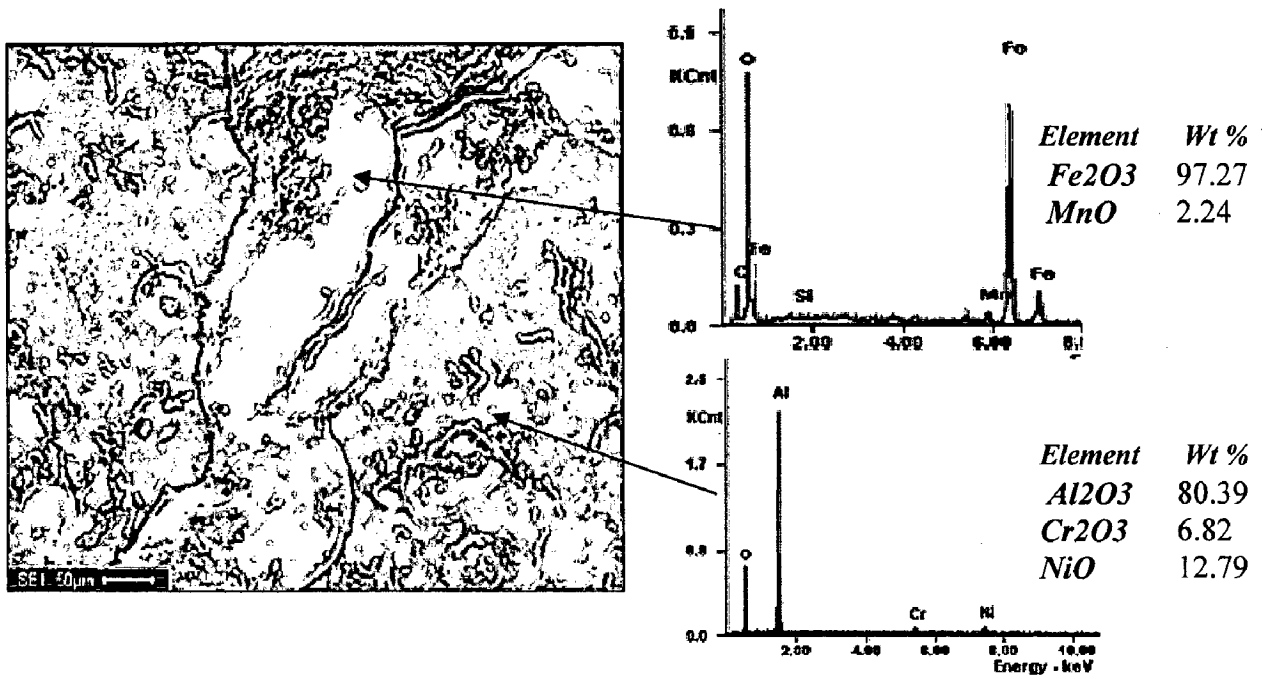
Fig.5.15 Surface scale morphology and EDAX point analysis for NiCrAl coatings on T22 steel subjected to oxidation for 50 cycles in air at 900°C
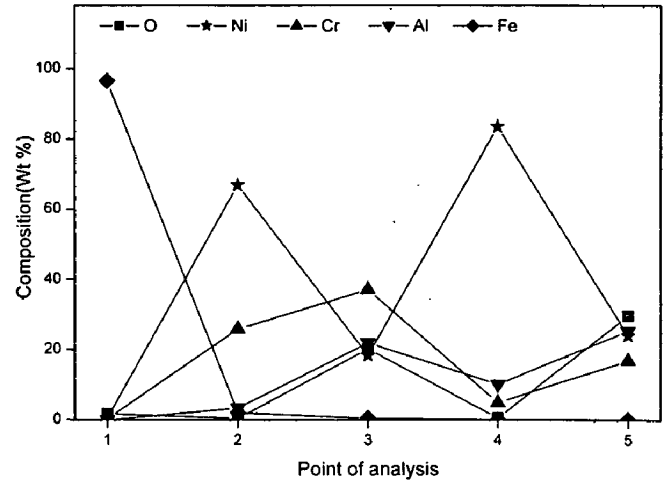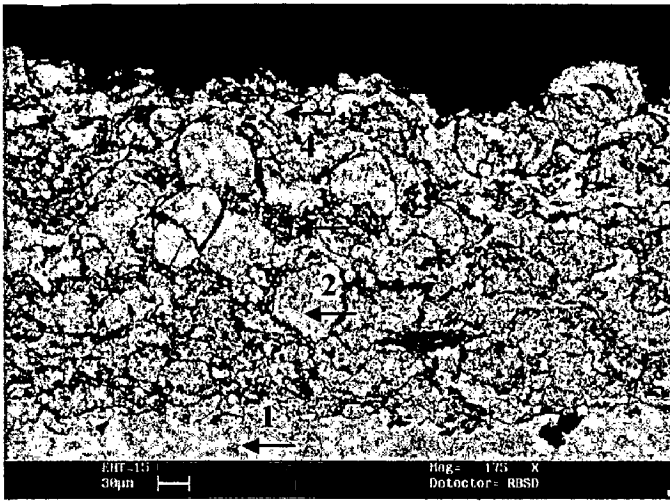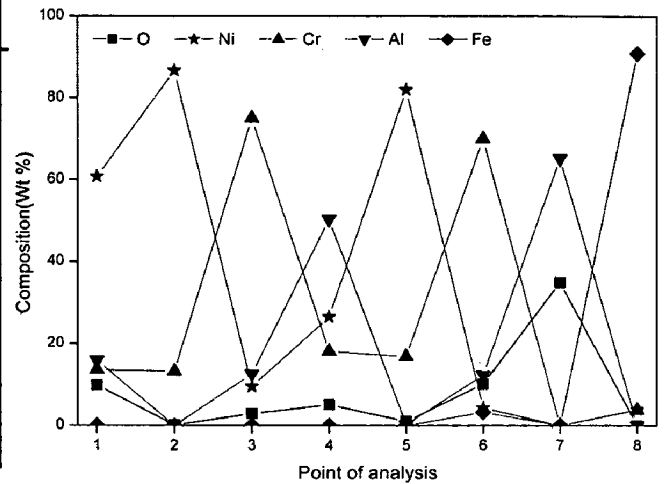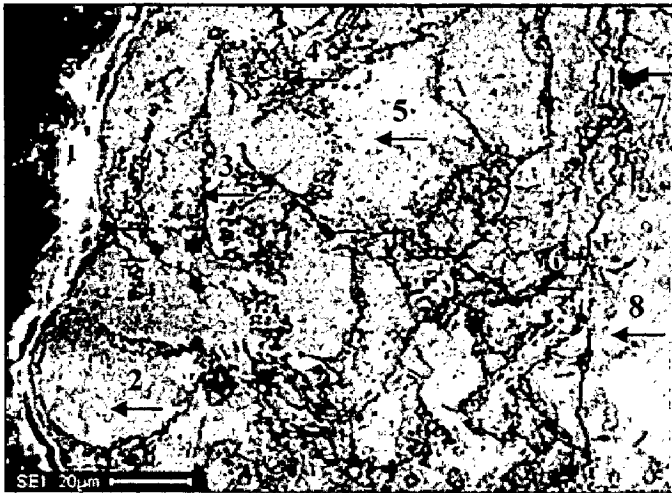
Fig. 5.16 Back scattered electron image and EDAX point analysis (wt %) across the cross-section of the NiCrAl coated steels subjected to cyclic oxidation for 50 cycles in air at 900°C : (a) GrA1 steel (b) T11 steel (c) T22 steel
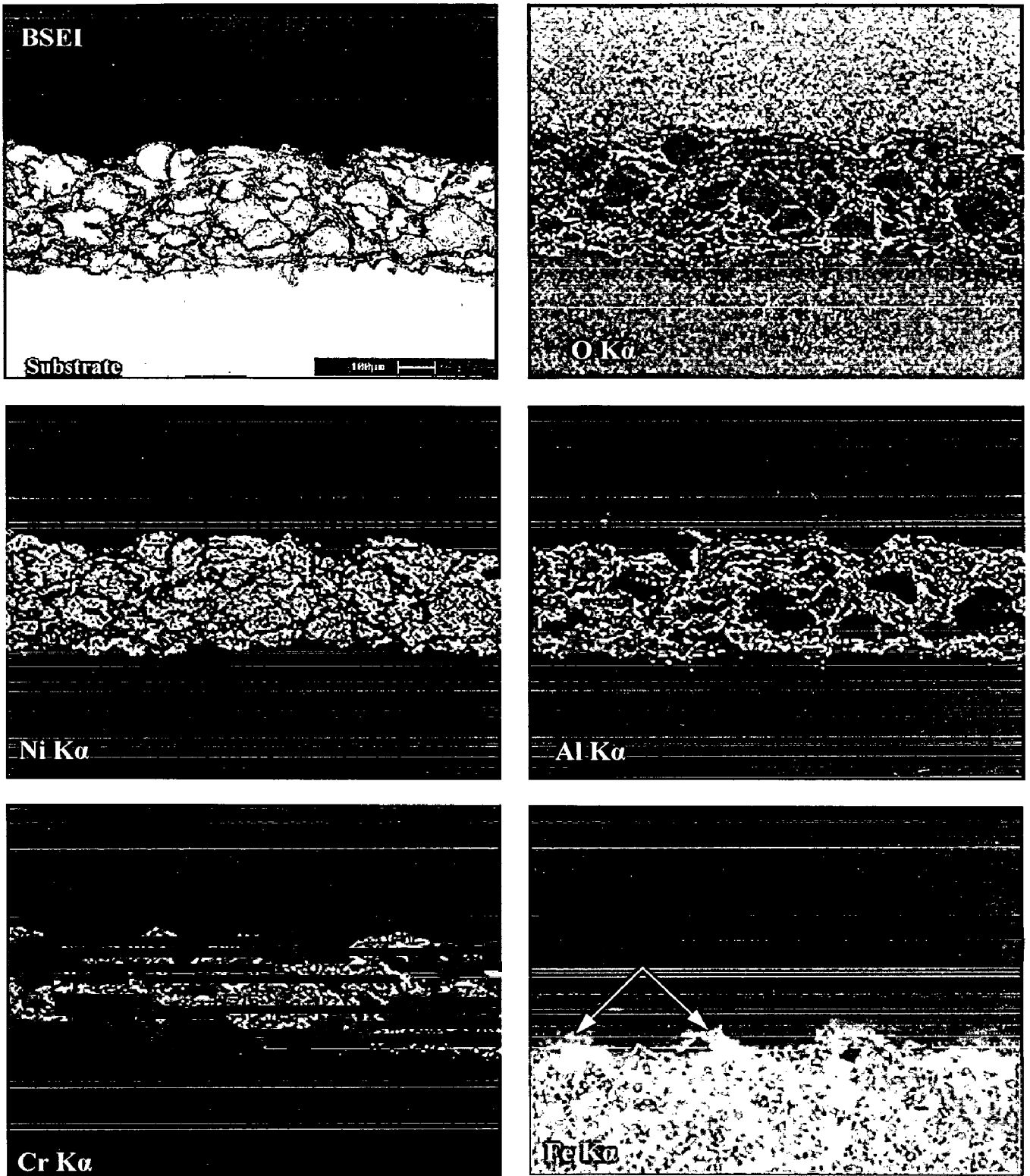
Fig.5.17   BSEI and elemental X-ray mapping at the cross-section of the NiCrAl coated T11 steels subjected to cyclic oxidation in air at 900°C

formation of a protective Al_2O_3 oxide scale. The mapping for the elements Al, Cr, and O clearly shows the selective oxidation of Al and Cr along the splat boundary. The absence of O in nickel-rich splats reveals that the nickel-rich splats are not oxidized at the end of 50 cycles of the oxidation studies. A minor diffusion of the substrate iron through the open pores along the splat boundary in to the coating is indicated by an arrow mark.

The X-ray mappings for the NiCrAl coated T22 Steel (Fig. 5.18) also reveal that the Ni and Cr-rich splats are in unoxidised condition. The top layer of the oxide scale mainly consists of the oxides of Al and Cr. The selective oxidations of Al and Cr have been observed along the nickel-rich splat boundary. It is interesting to see that the crack has been initiated in the substrate-coating interfaces and propagated along the splat boundary via the open pores into the coating. It is evident from the combined mapping for Fe and O that the iron oxide is protruding through this crack to the surface of the coating.

5.1.3 NiAlCrFeMo Coating

5.1.3.1 Thermo gravimetric studies

Fig.5.19 shows the macrographs of HVOF sprayed NiAlCrFeMo coatings on GrAl, T11 and T22 steels, after 50 cycles of oxidation studies at 900°C. Brown color oxide scale has been observed on the surface of all the three coated steels. The oxidized surface of coated GrAl steel found to be smooth and no spalling or cracks have been observed. Where as in case of coated T11 and T22 steels, dark grey colored protrusions have been observed, oriented parallel to the sides of the sample. These protrusions become more pronounced in coated T22 steel and are observed after 18th cycle of oxidation studies.

The plots of cumulative weight gain as a function of time are shown in Fig.5.20. NiAlCrFeMo coated T22 steel show higher weight gain in comparison to other coated steels. The weight gain for coated GrAl, T11 and T22 steels at the end of 50 cycles of oxidation found to be 8.6, 14.79 and 28.63 mg/cm^2 respectively. Further the weight gain square (mg^2/cm^4) data were plotted as a function of time, as shown in Fig 5.21. The kinetics of oxidation of coated GrAl and T11 steels are almost parabolic in nature. The parabolic rate constant K_p, as calculated from slope of the linear regression fitted line for coated GrAl and T11 steels are found to be 0.372×10^{-8} and 1.26×10^{-8} g^2 cm^{-4} s^{-1} respectively. The T22 Steel followed linear behaviour from 18th cycle of oxidation study.

5.1.3.2 X-ray Diffraction Analysis

The X-ray diffraction pattern for NiAlCrFeMo coated GrA1 and T11 steels (Fig.5.22) shows the phases of Ni, Al_2O_3, Cr_2O_3, NiO, $NiCr_2O_4$ and $FeO.Cr_2O_3$. The oxide scale formed on the NiAlCrFeMo coated T22 steel (Fig.5.23) mainly consisted of Al_2O_3, Cr2O3, NiO, Fe_2O_3, $NiCr_2O_4$ and $NiMoO_4$.

5.1.3.3 SEM/EDAX Analysis

Fig.5.24a shows the surface morphology of oxide scale formed on the oxidized NiAlCrFeMo coated GrA1 steel. Oxide scale consists of spherical globules dispersed in the non uniform matrix. The EDAX analysis revealed spherical globules as nickel rich splats (97.3% NiO) and the matrix composed of NiO (53.7%), Cr_2O_3 (23.3%), Al_2O_3 (12.36%) and Fe_2O_3 (8.05%).Corresponding analysis on the surface of coated T11 steel (Fig.5.24b) mainly consist of nickel oxide along with the oxides of Cr, Al and Fe. Protrusions formed on the surface of coated T22 steel is as shown in Fig.5.25a. The blown-up area on the protrusion (Fig.5.25b) clearly shows the growth oriented outwards on the surface. Iron rich area has been detected by EDAX analysis (Point 2) on the protrusions. EDAX analysis on the matrix (Point 1) shows the oxide layer consist of oxides of Ni, Cr, Al and Fe.

Back scattered electron image and EDAX point analysis across the cross-section of the NiAlCrFeMo coated steels subjected to cyclic oxidation for 50 cycles in air at 900°C is as shown in Fig.5.26. The oxidized coating seems to be compact and adherent. It is apparent from the BSE image for coated GrA1 steel (Fig.5.26a) that the thin outermost oxide layer has been formed and the EDAX analysis on this layer (Point 1) shows nickel oxide (52.45%) as a main constituent along with the oxides of Cr, Al and Fe. Also minor content of molybdenum oxide has been detected on the surface. The absence of oxygen at point 2 indicates nickel rich splats (Ni-85.83%) in an unoxidised condition. EDAX analysis at point 3 and 4 shows that the splat boundary got oxidized and contains relatively higher amount of oxides of Al and Cr.

Corresponding analysis for the oxidized NiAlCrFeMo coated T11 steel (Fig.5.26b) shows that the uppermost oxide scale mainly consisted of nickel oxide along with oxides of Cr, Al and Fe. Point 2 and 3 indicate nickel rich splat in an unoxidised state as oxygen is absent at this point. Internal oxidation along the splat boundary has been observed and composition at point 4, shows relatively higher amount of O, Al, Cr and Fe. The dark region (Point 5) along the coating-substrate interface found to be rich in Al and O, which
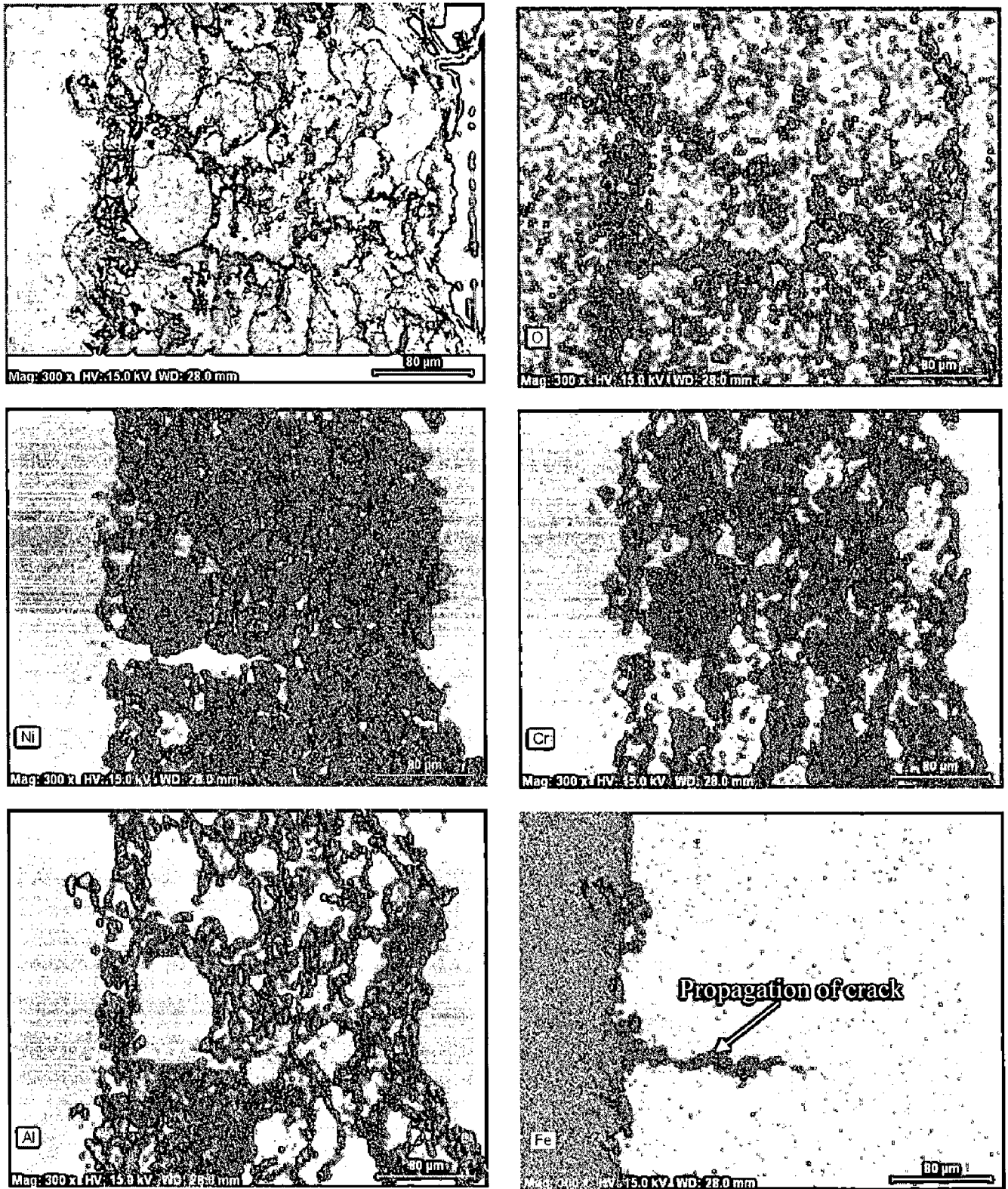
Fig.5.18   BSEI and elemental X-ray mapping at the cross-section of the NiCrAl coated T22 steel subjected to cyclic oxidation in air at 900°C
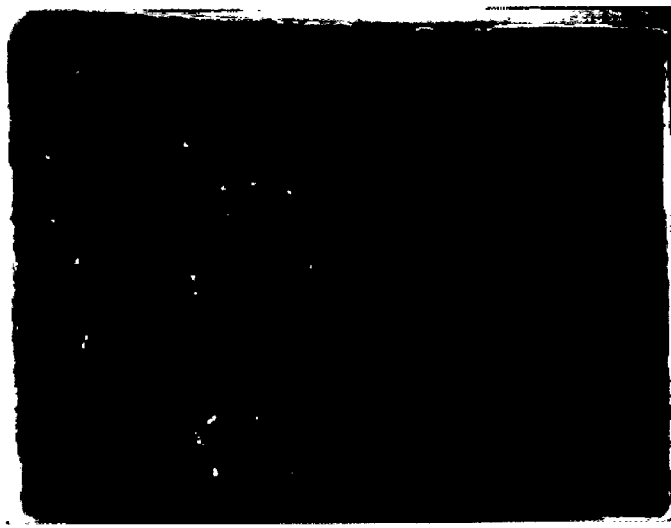
(a)

(b)

(c)

Fig.5.19   Macrographs of the NiAlCrFeMo coating subjected to cyclic oxidation in air for 50 cycles at 900°C:

(a) GrA1 steel   (b) T11 steel   (c) T22 steel
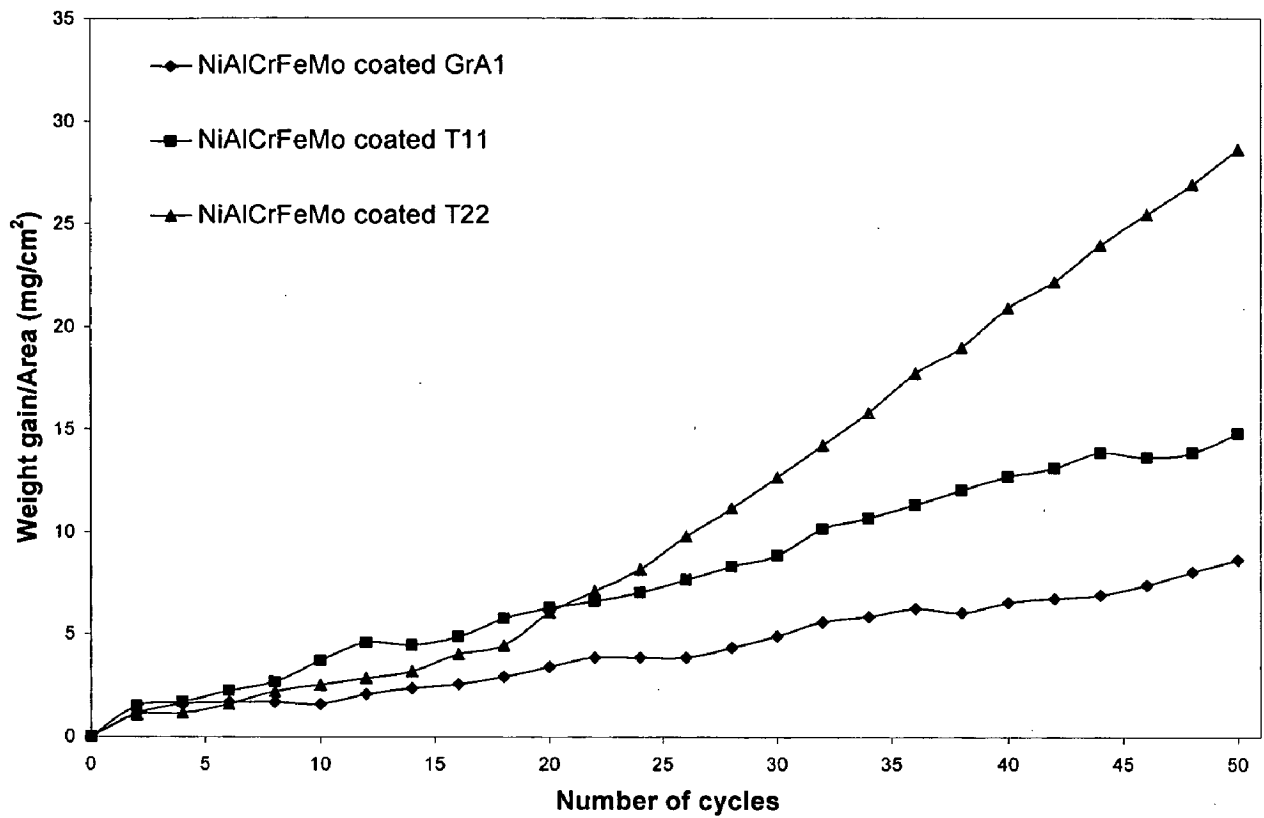
Fig.5.20   Weight gain vs. number of cycles plot for NiAlCrFeMo coated steels subjected to oxidation for 50 cycles in air at 900°C
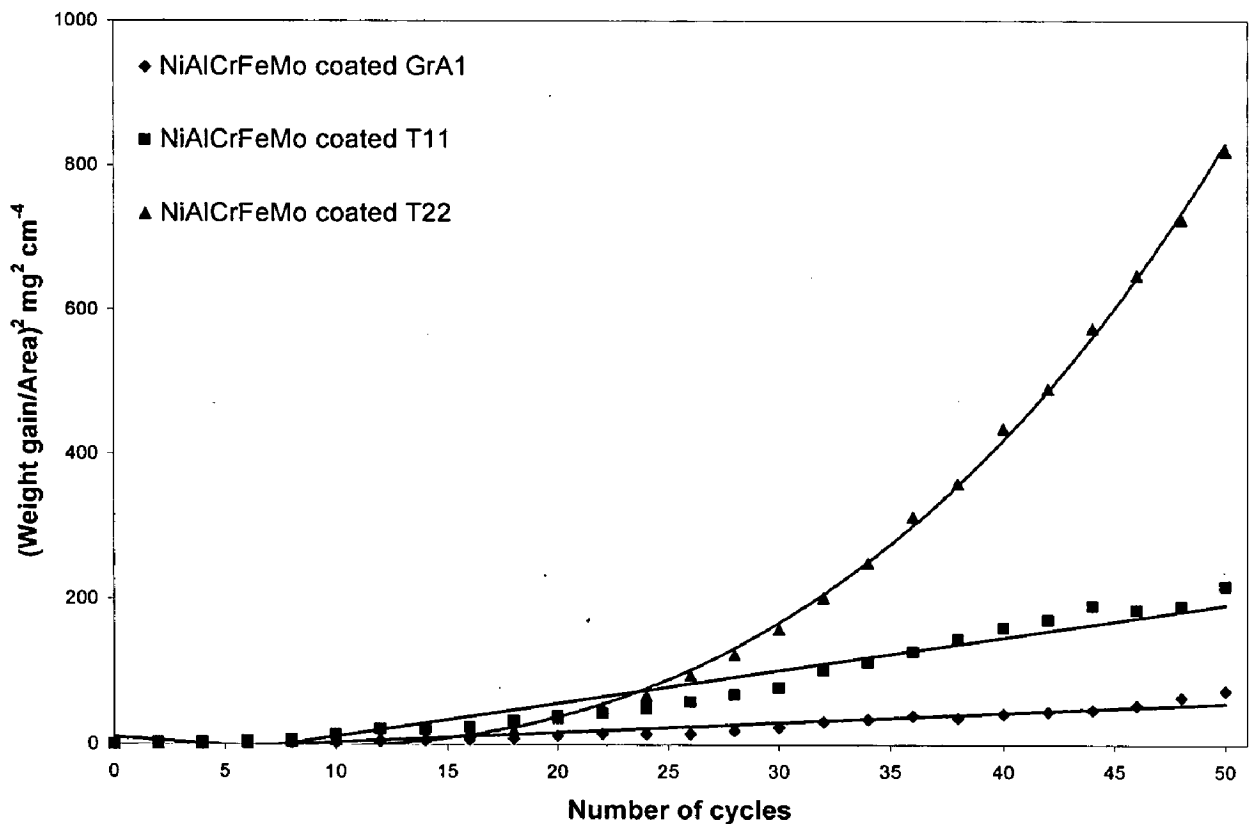
Fig.5.21   (Weight gain/area)^2 vs. number of cycles plot for NiAlCrFeMo coated steels subjected to oxidation for 50 cycles in air at 900°C

98
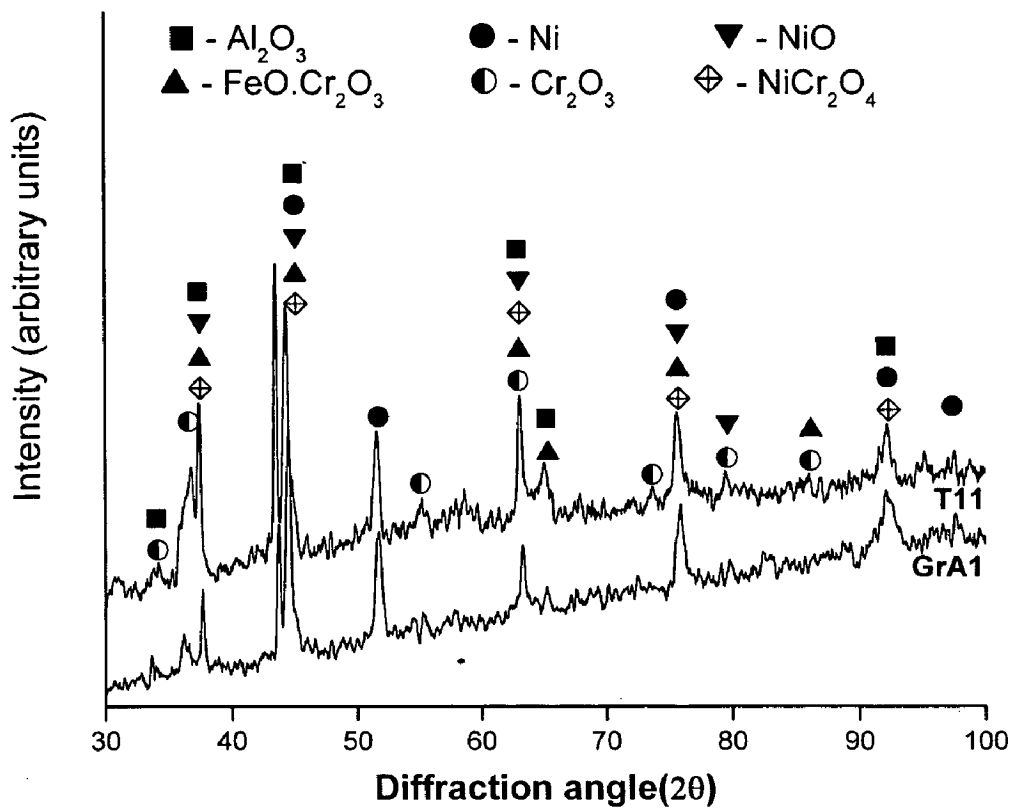
Fig.5.22 X-ray diffraction patterns for NiAlCrFeMo coated GrA1 and T11 steels subjected to cyclic oxidation in air for 50 cycles at 900°C

Fig.5.23 X-ray diffraction patterns for NiAlCrFeMo coated T22 steels subjected to cyclic oxidation in air for 50 cycles at 900°C

97.34% NiO
01.10% Cr_2O_3

EDAX analysis at point 1

53.73% NiO
23.33% Cr_2O_3
12.36% Al_2O_3
08.05% Fe_2O_3

EDAX analysis at point 2

(a)

52.99% NiO
22.21% Cr_2O_3
15.52% Al_2O_3
06.69% Fe_2O_3
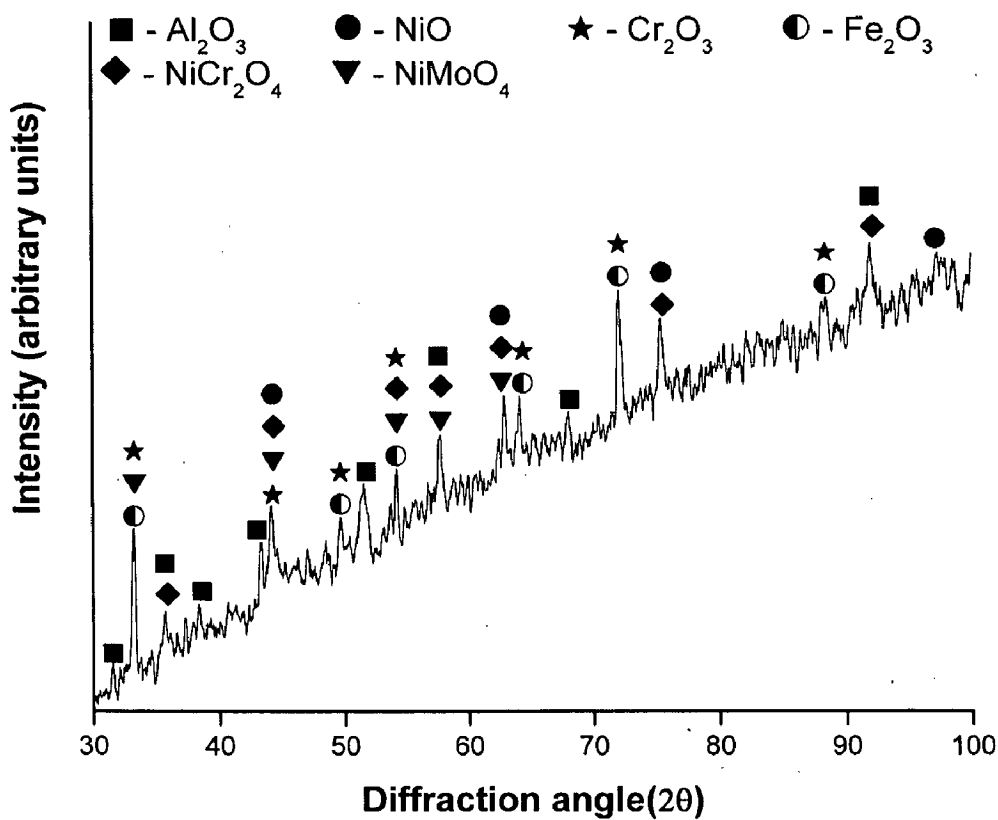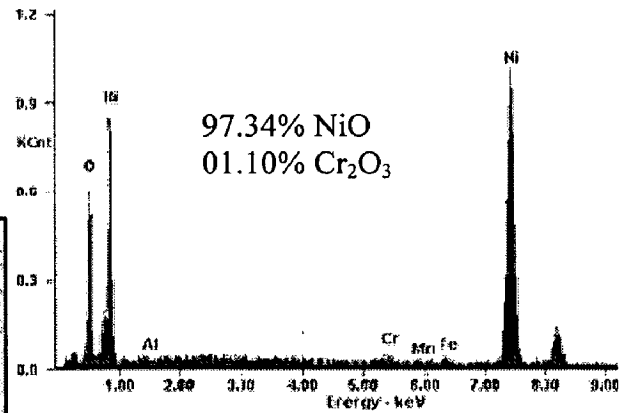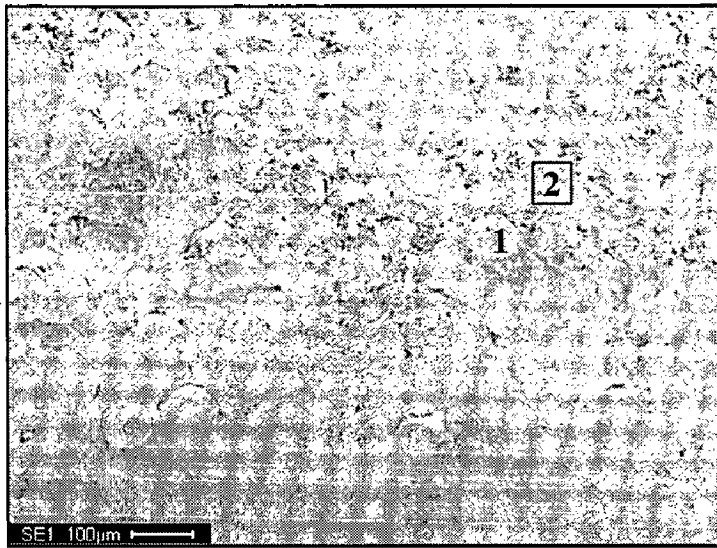
EDAX area analysis

(b)

Fig.5.24   Surface scale morphology and EDAX analysis for NiAlCrFeMo coated GrA1 and T11 steels subjected to oxidation for 50 cycles in air at 900°C
(a) GrA1 steel   (b) T11 steel
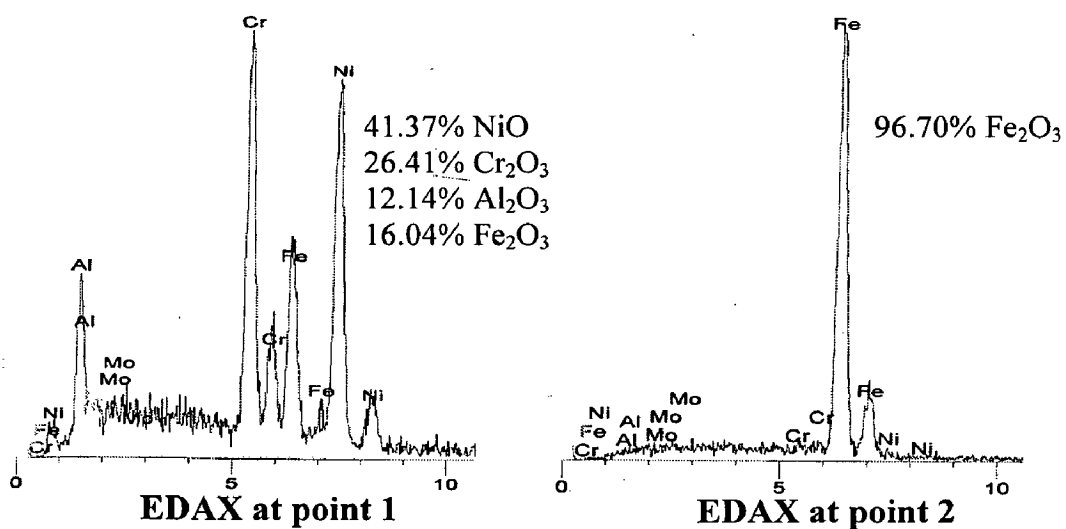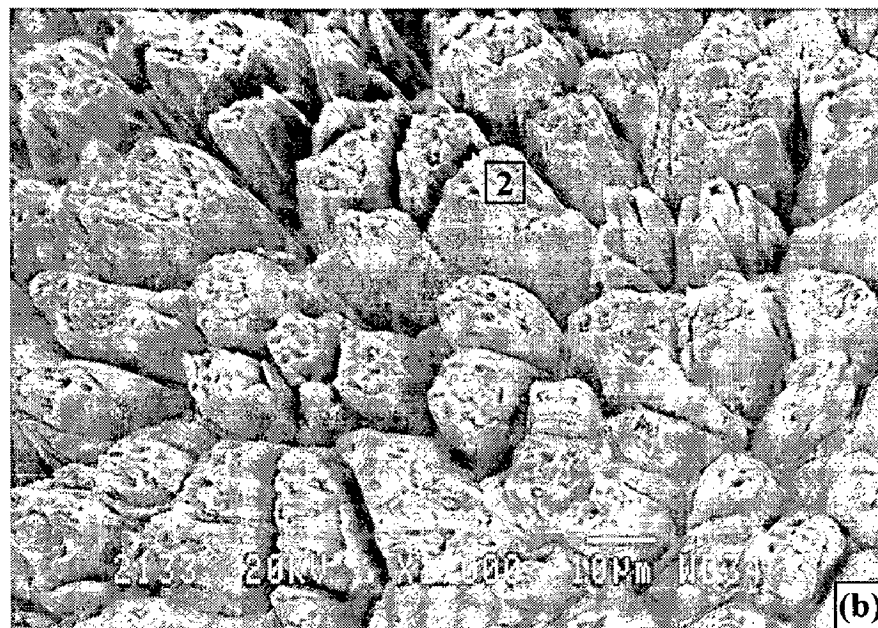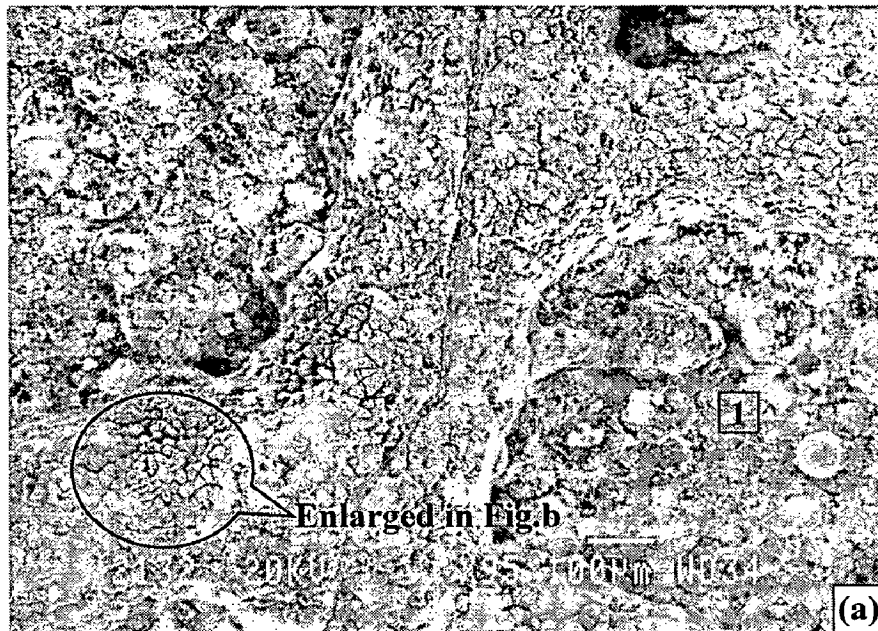
Fig.5.25   Surface scale morphology and EDAX point analysis for NiAlCrFeMo coated T22 steel subjected to oxidation for 50 cycles in air at 900°C
(a) Protrusion on coating surface (b) Enlarged image of marked region in Fig (a)

101
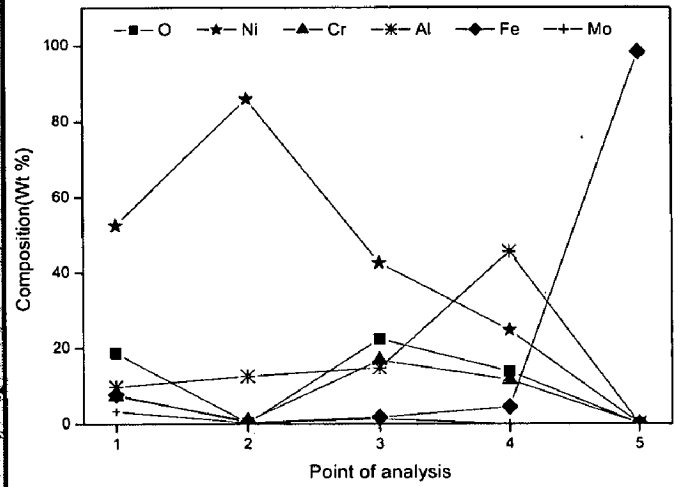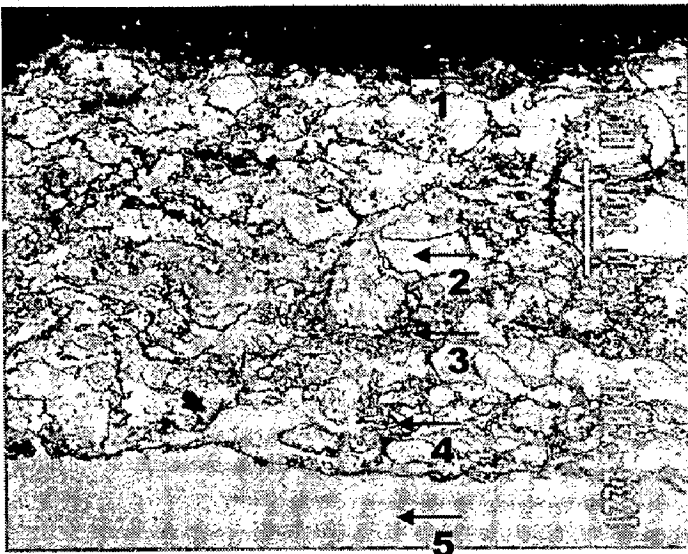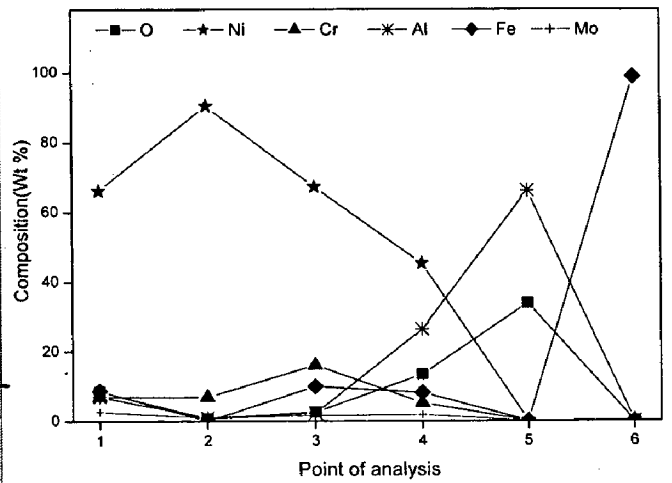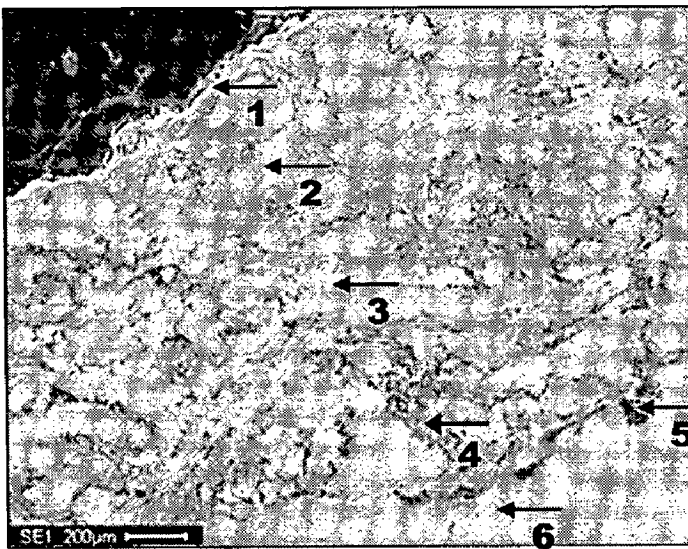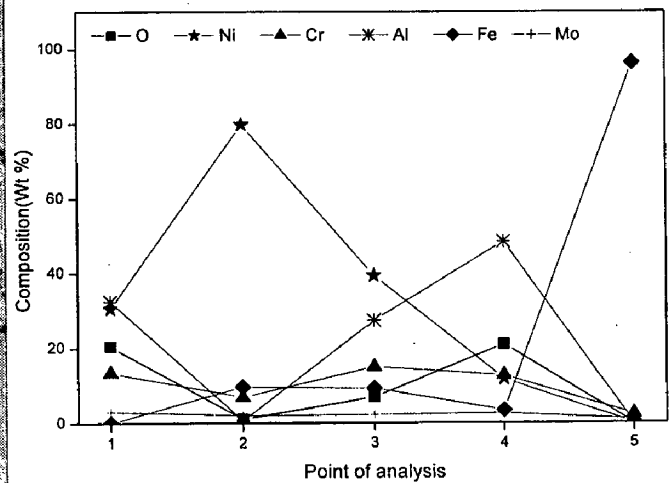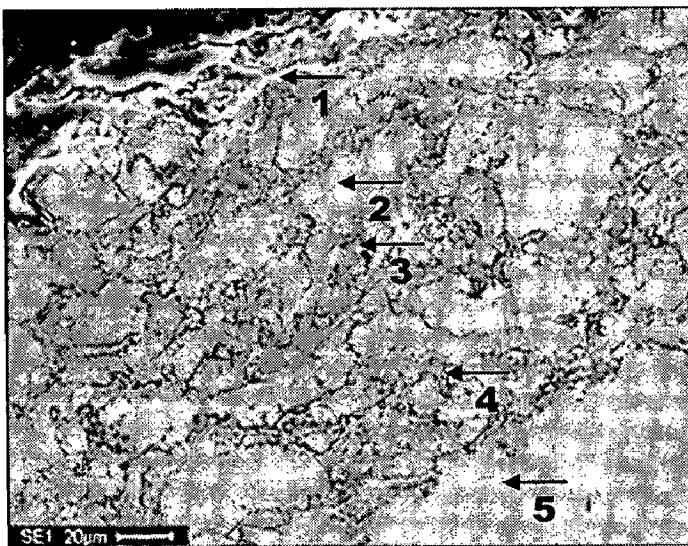
Fig.5.26 Back scattered electron image and EDAX point analysis (wt %) across the cross-section of the NiAlCrFeMo coated steels subjected to cyclic oxidation for 50 cycles in air at 900°C :
(a)Coated GrA1 steel   (b) Coated T11 steel   (c) Coated T22 steel

may be due to Al2O3 particles got retained possibly during grit blasting of the substrate surface before HVOF spraying as already discussed in chapter 4. Similar observations have been noticed for the NiAlCrFeMo coated T22 steel as shown in Fig.5.26c.

5.1.3.4 EPMA Analysis

Elemental X-ray maps for the NiAlCrFeMo coated GrA1 steel subjected to cyclic oxidation for 50 cycles at 900°C are shown in Fig.5.27. The mapping for oxygen indicates that the complete cross-section of coating has been oxidized along the splat boundary. The selective oxidation of aluminum, chromium and molybdenum along the splat boundary has been observed. Also during the early stage of oxidation, oxidising atmosphere penetrates into the coatings through open porosity (mostly located at splat boundary) until all the accessible internal surfaces have been oxidized. Subsequently the oxidation phenomenon takes place only on the outer surface of the coating due to formation of protective oxide layer. Elemental maps for O, Ni, Al and Cr, show a thin distinct oxide layer formed on the outer surface and mainly consists of oxides of Ni, Al and Cr. It is apparent from the mapping for oxygen and nickel that nickel rich splats remain unoxidised up to the end of 50 cycles of oxidation studies. Minor diffusion of nickel from the coating into the substrate can also be observed along the coating-substrate interface. Similar observations have been noticed for the oxide scale formed on NiAlCrFeMo coated T11 steel as shown in Fig.5.28. The top layer of the oxide scale mainly consisted of oxides of Ni, Al and Cr. The nickel rich splats remain unoxidised and the splat boundaries consist of oxides of Al, Cr and Mo.

BSEI and X-ray mapping for NiAlCrFeMo coated T22 steel have been shown in Fig.5.29. BSE image clearly shows the crack along the thickness of the coating. Localized corrosion of the substrate under the cracked coating can be observed. Combining the mapping for Fe and O, corroborated that the oxide protrusion reach the surface, along the crack formed in the coating mainly consist of iron oxide.

5.1.4 NiCrFeSiB Coating

5.1.4.1 Thermo gravimetric studies

The macrographs of the HVOF-sprayed NiCrFeSiB coatings on the GrA1, T11 and T22 steels subjected to cyclic oxidation for 50 cycles at 900°C are shown in Fig. 5.30. The color of the oxide scale formed on all the three coated steels was parrot green. The oxide

scale formed on the surface is found to be compact, adherent, and no spallation of scale was observed during the course of the study.

The plots of cumulative weight gain (mg/cm^2) as a function of time, expressed in number of cycles, are shown in Fig.5.31. The rapid weight gain of the coating has been observed in the initial oxidation period up to 10 cycles of study, thereafter, exhibits a gradual decrease in oxidation rate with exposure time. The total weight gain at the end of 50 cycles for the NiCrFeSiB coated GrA1, T11 and T22 steels are found as 1.65, 1.25 and 2.22 mg/cm^2, respectively.

Further, the weight gain square (mg^2/cm^4) versus the number of cycles are plotted in Fig. 5.32. The oxidation behavior of the coated GrA1, T11 and T22 steels were parabolic in nature up to 50 cycles. The parabolic rate constant K_p, as calculated from the slope of the linear regression fitted line for the NiCrFeSiB coated GrA1, T11 and T22 steels, were found to be 0.147×10^{-10}, 0.097×10^{-10} and 0.25×10^{-10} g^2 cm^{-4} s^{-1}, respectively.

5.1.4.2 X-ray Diffraction Analysis

The diffraction patterns for the NiCrFeSiB coated steels are shown in Fig. 5.33. The XRD results reveal the presence of the phases of NiO, Cr_2O_3, Ni, Ni_3B, Ni_3Si, Ni_2SiO_4, and Fe_2SiO_4. All the three coated steels have been found to have identical oxides on the surface. No peaks for SiO_2 are present.

5.1.4.3 SEM/EDAX Analysis

The SEM micrographs showing the scale morphology along with the EDAX spectra at the point of interest are shown in Figs. 5.34 and 5.35. It can be observed in Fig. 5.34 that the oxide scale has a glassy matrix with some coarse nodules dispersed uniformly. The EDAX compositional analysis of the glassy scale shows the dominant presence of Si and O peaks along with the minor peaks of Cr and B. This can be attributed to the formation of a SiO_2 glass scale. The results of the EDAX analysis of the dark nodules reveal that these are mainly rich in Ni and Cr and oxygen with some Fe. The most interesting point is that the O and Si contents in these dark nodules are low, while the Ni contents were rather high. This implies that the metallic Ni rich globules exist within the
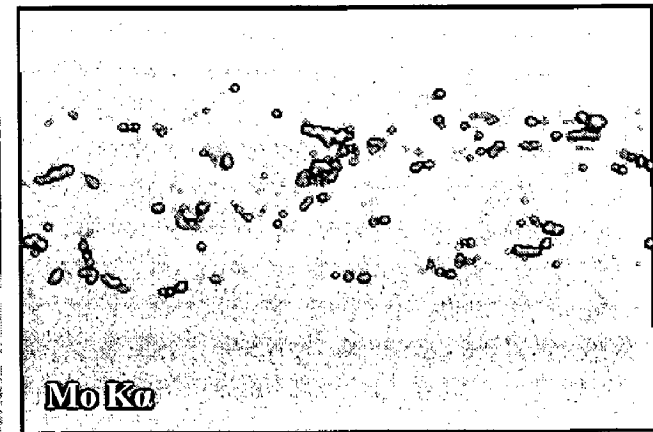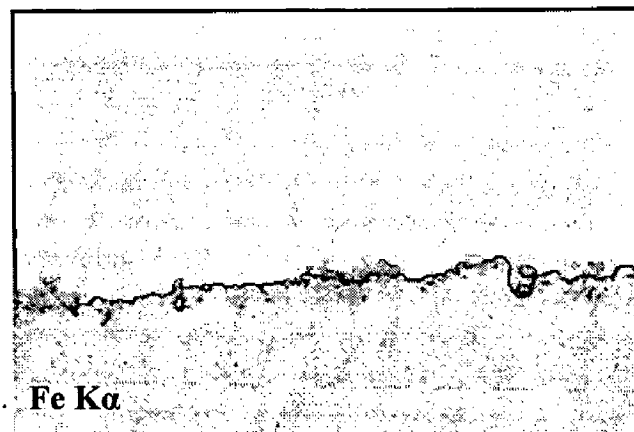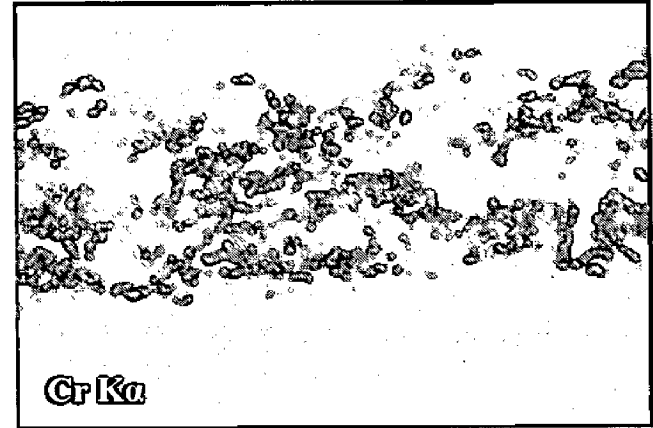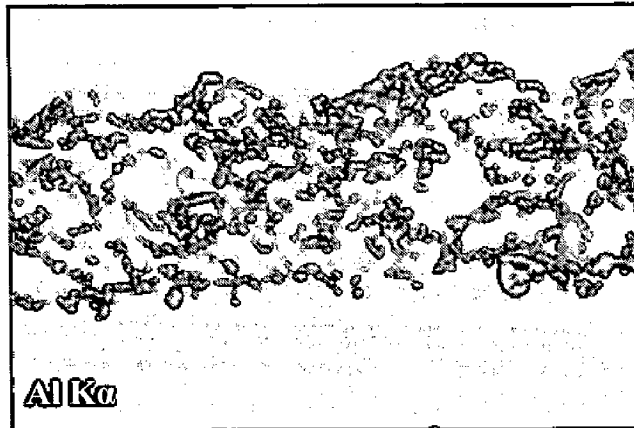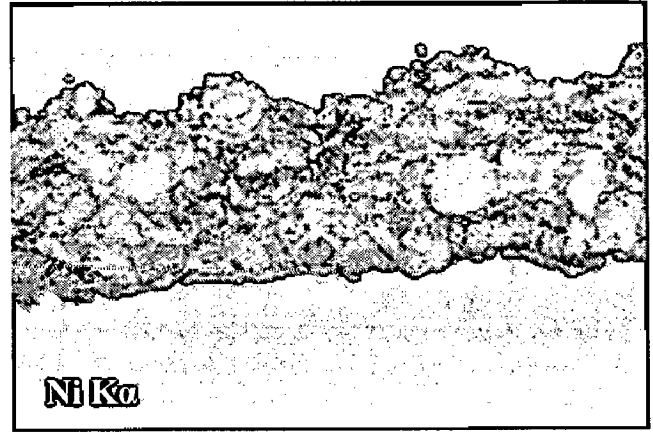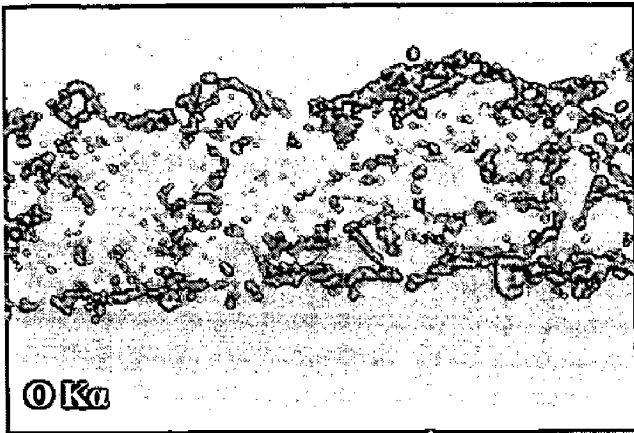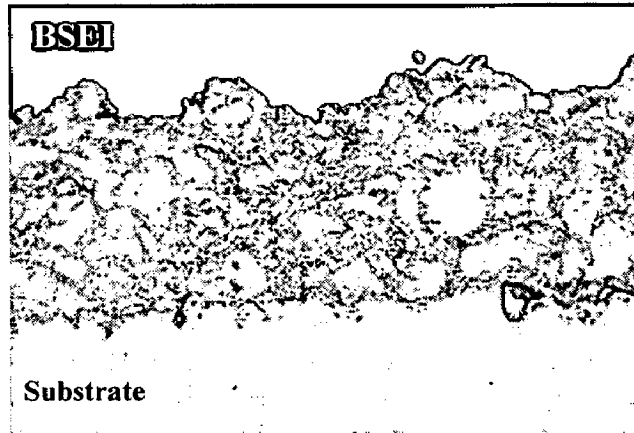
Fig.5.27 BSEI and elemental X-ray mapping at the cross-section of the NiAlCrFeMo coated GrA1 steels subjected to cyclic oxidation in air at 900°C
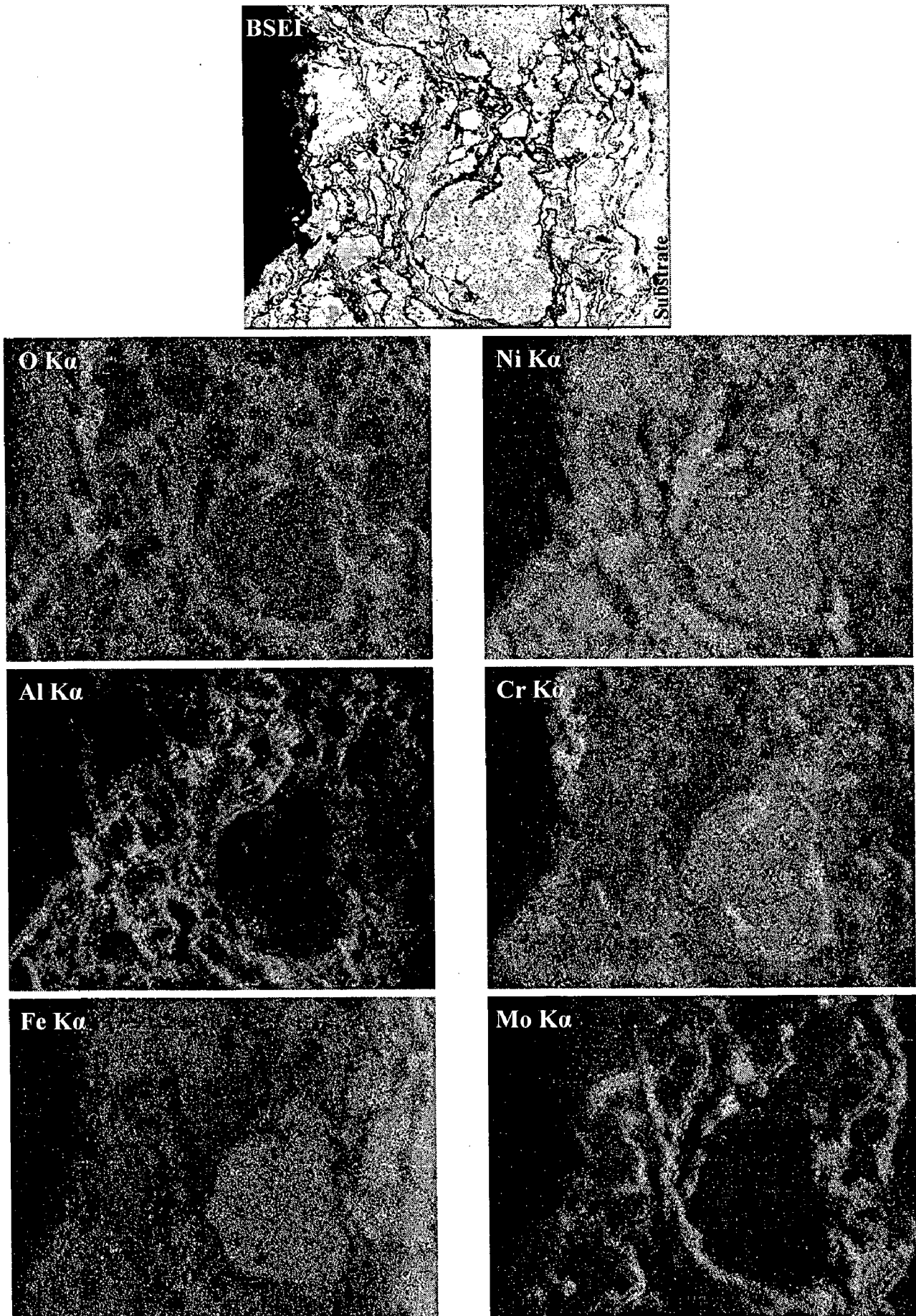
Fig.5.28   BSEI and elemental X-ray mapping at the cross-section of the
NiAlCrFeMo coated T11 steels subjected to cyclic oxidation in air at
900°C
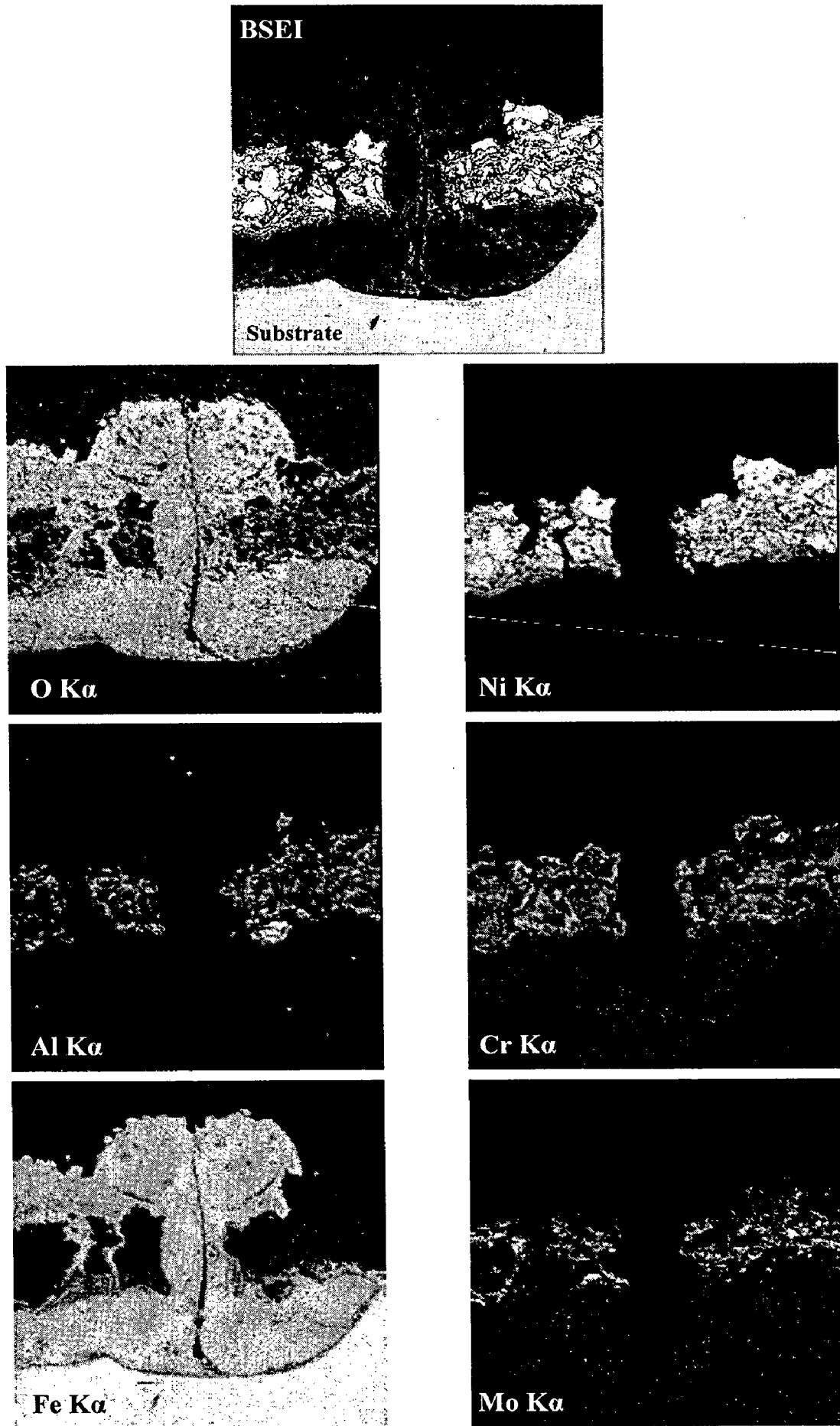
Fig.5.29 BSEI and elemental X-ray mapping at the cross-section of the NiAlCrFeMo coated T22 steel subjected to cyclic oxidation in air at 900°C
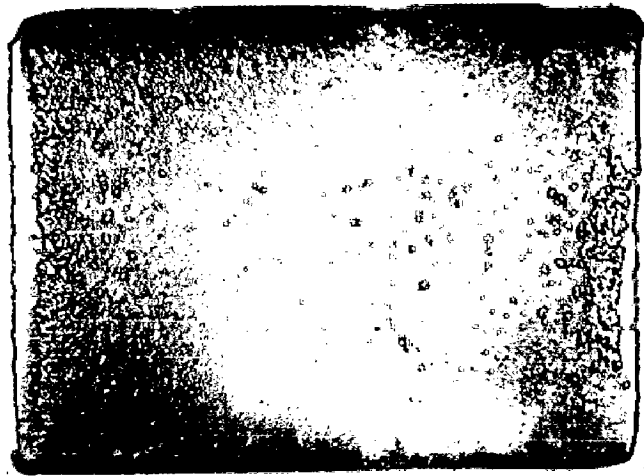
(a)
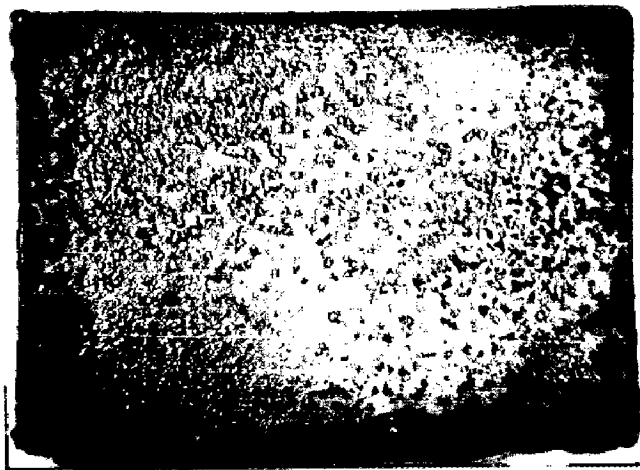
(b)
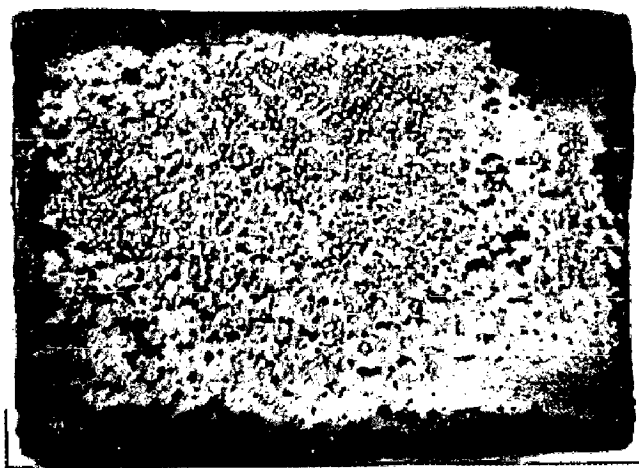
(c)

Fig.5.30   Macrographs of the NiCrFeSiB coating subjected to cyclic oxidation in air for 50 cycles at 900°C:

(a) GrA1 steel   (b) T11 steel   (c) T22 steel
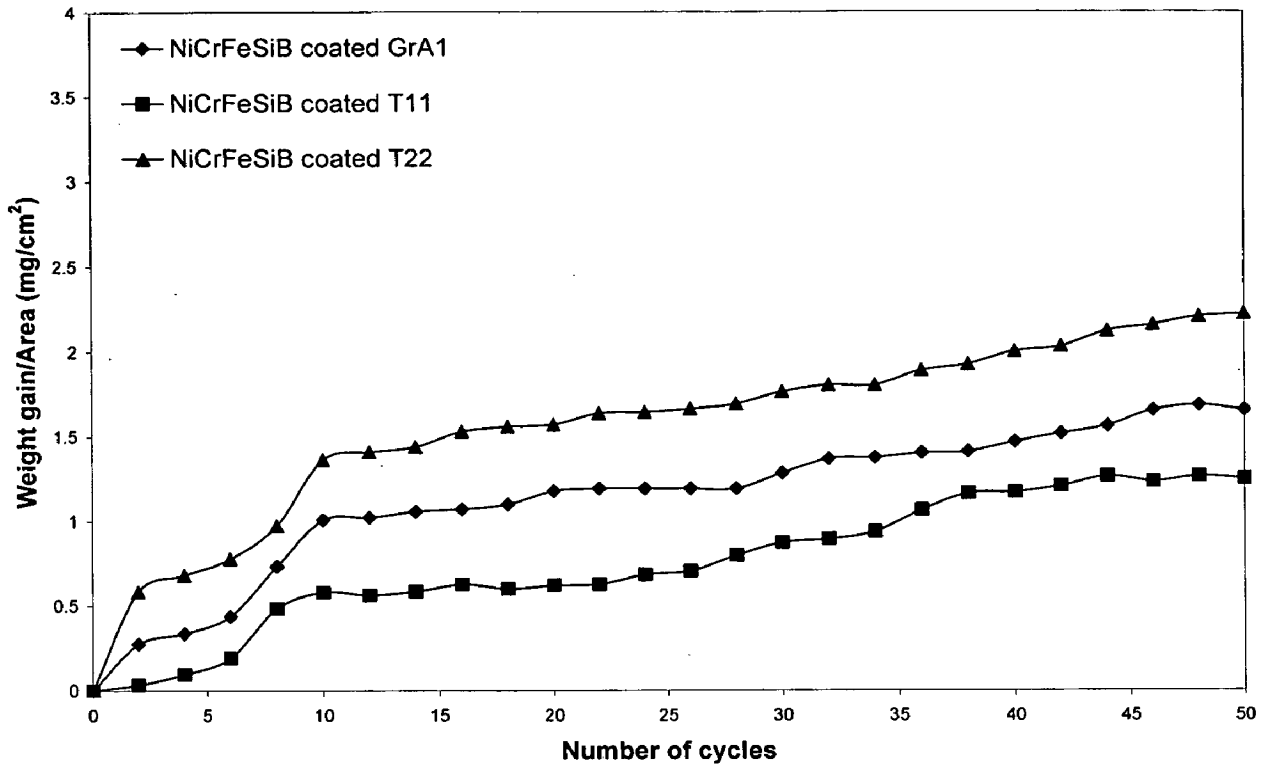
Fig.5.31   Weight gain vs. number of cycles plot for NiCrFeSiB coated steels subjected to oxidation for 50 cycles in air at 900°C
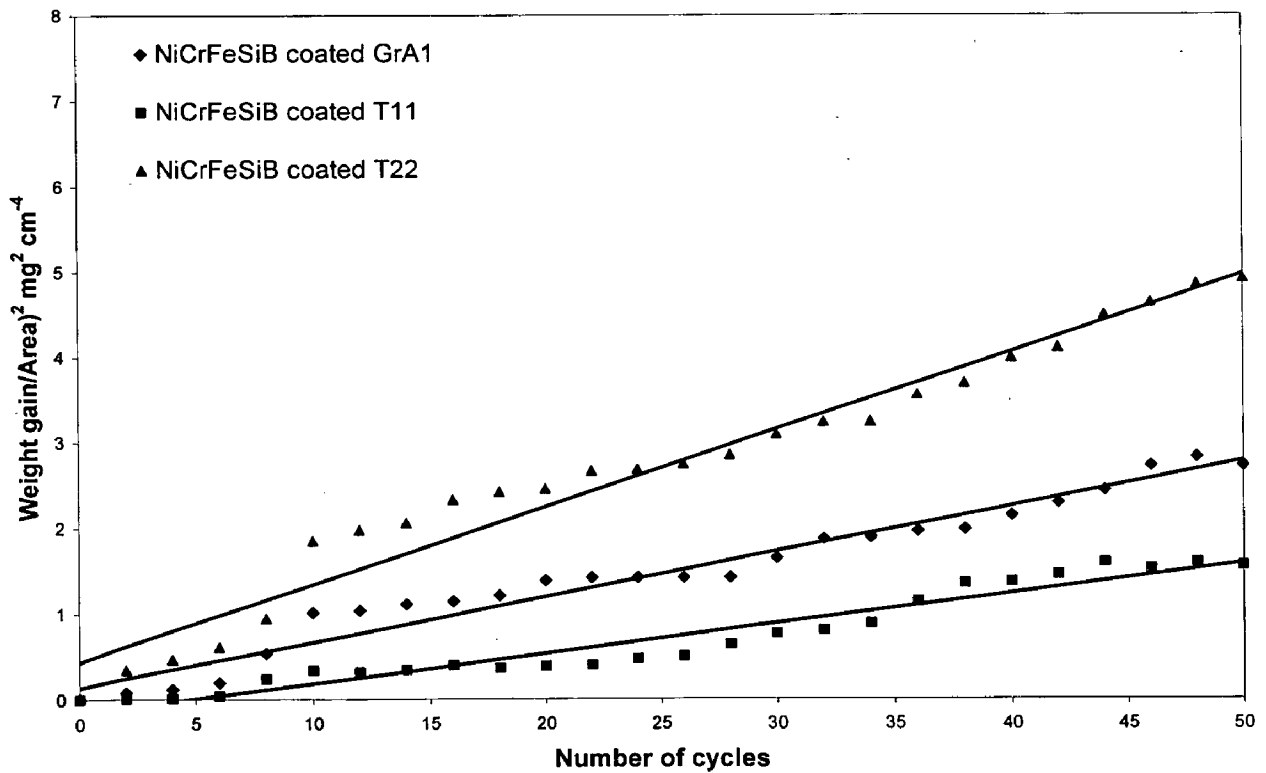
Fig.5.32   (Weight gain/area) ^{2} vs. number of cycles plot for NiCrFeSiB coated steels subjected to oxidation for 50 cycles in air at 900°C
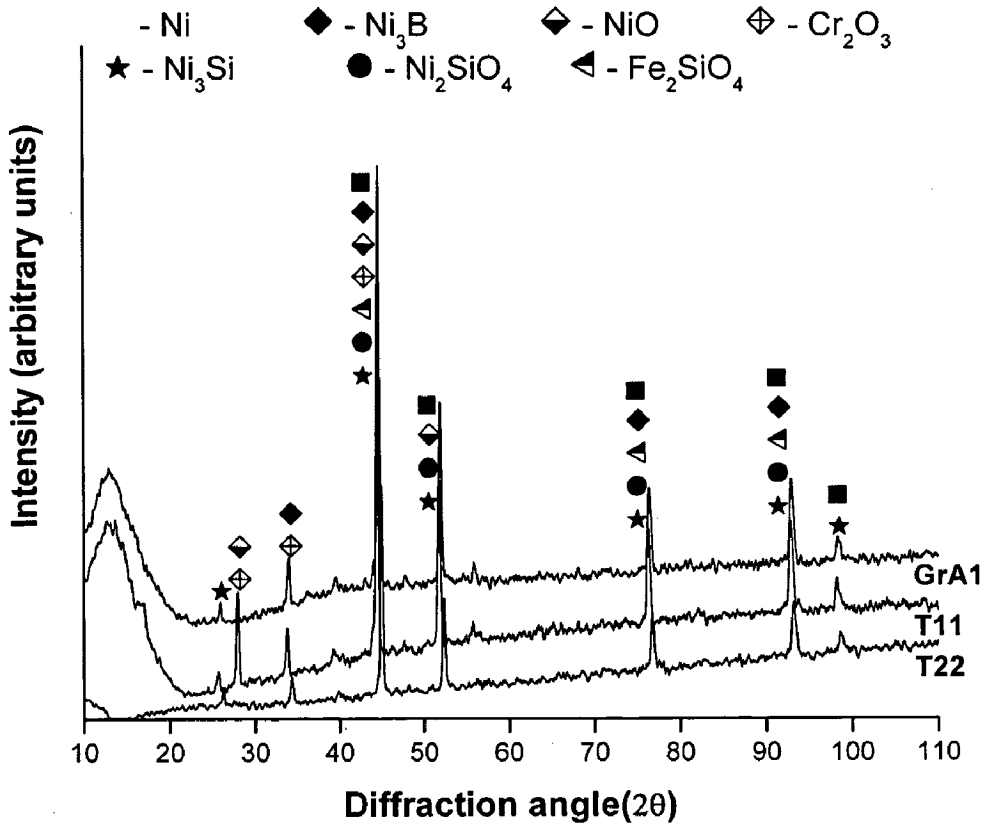
Fig.5.33 X-ray diffraction patterns for NiCrFeSiB coated GrA1, T11 and T22 steels subjected to cyclic oxidation in air for 50 cycles at 900°C
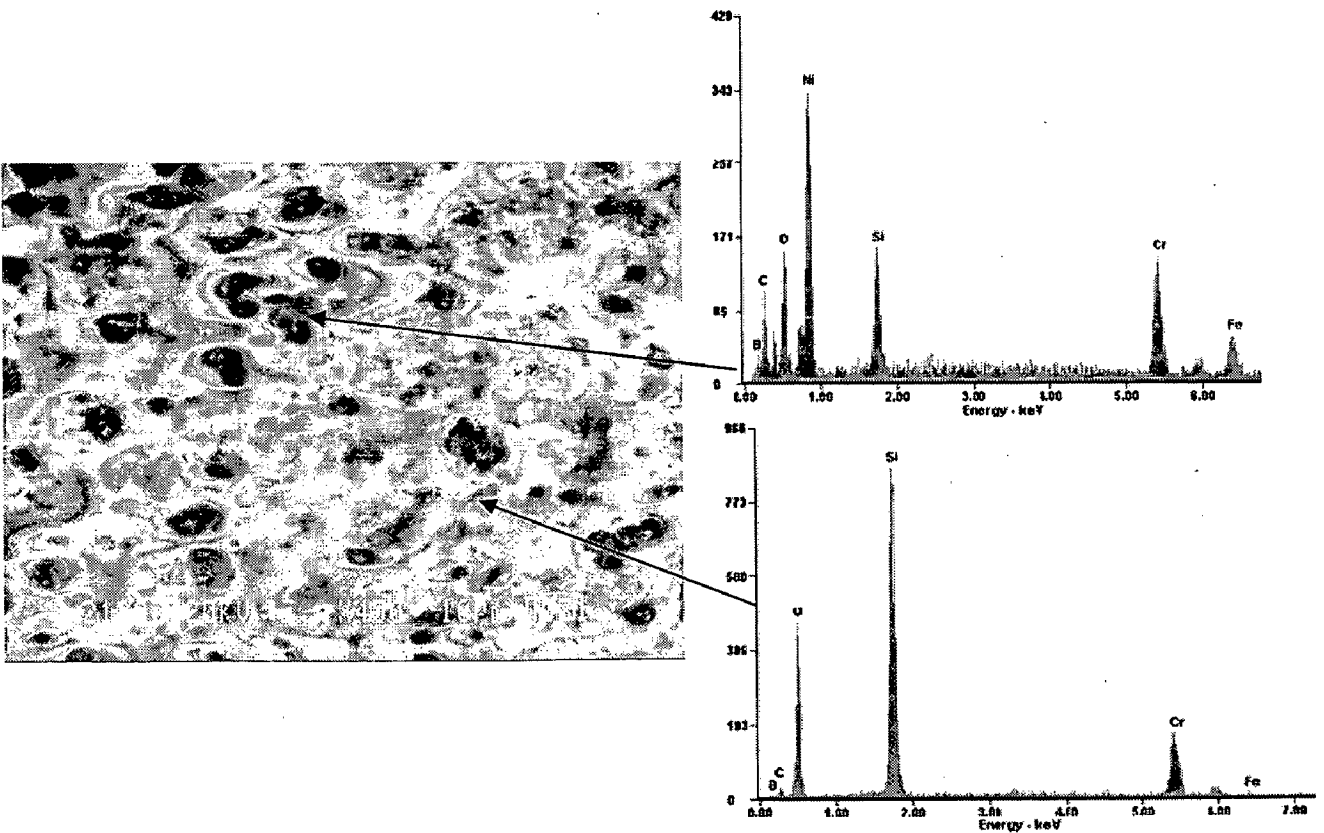
Fig.5.34 Surface scale morphology and EDAX point analysis for NiCrFeSiB coated GrA1 steel subjected to oxidation for 50 cycles in air at 900°C

glassy oxide scale. Similar observations are also noticed for the oxide scale formed on the NiCrFeSiB coated T11 and T22 steels as shown in Figs. 5.35.

Figure 5.36 depicts the BSE image along the cross section of the oxidized NiCrFeSiB coated GrA1 and T22 steels and the elemental composition at the point of interest are represented in the form of a graph. The oxide scale formed is compact and the structure of the oxidized coating appears similar to the as-sprayed coating. The EDAX analysis at point 1 (Figs. 5.36a and 5.36b) shows that the oxide scale formed on the surface is mainly composed of the oxides of Si, Ni and Cr. Points 2 and 3 represent the Ni-rich splats with a minor content of Cr, Si, and Fe. The absence of oxygen at these points indicates that oxidation has been restricted to the upper most layer, and the protective oxides of Si, Cr, and Ni formed on the surface acts as a barrier to the oxygen transport to the inside of coating. The dark region along the coating-substrate interface is found to be rich in Al and O which may be an inclusion of aluminum oxide during the surface preparation prior to the HVOF spraying since aluminum is neither present in composition of coating nor in the substrate.

5.1.4.4 EPMA Analysis

The BSEI and elemental X-ray maps for the NiCrFeSiB coated T11 steel after the cyclic oxidation for 50 cycles at 900°C are shown in Fig. 5.37. After combining the mappings for Si, Cr, and O, it can be substantiated about the formation of SiO_2 and Cr_2O_3 phases at the outermost surface of oxidized coating. This topmost oxide scale appears to be a thin and discontinuous layer. The coating region below the topmost oxide scale is in an unoxidised condition as seen from the elemental mapping for oxygen. It can be inferred from the silicon depleted layer near the coating-substrate interface that some degree of oxidation of Si has occurred at the oxide-gas interface by diffusion of Si to top of the scale. A careful observation of the coating-substrate interface suggests about the diffusion of Fe from the substrate into the coating which can be seen as a thick layer in the coating region, represented by an arrow mark in the X-ray mapping for Fe. Further, a distinct nickel-rich band can be noticed along the coating-substrate interface which implies the diffusion of nickel into the substrate. The elemental mapping for Mo demonstrates that there is a minor diffusion of Mo into the coating.

The EPMA analysis for the NiCrFeSiB coated T22 steel oxidized for 50 cycles at 900°C is shown in Fig. 5.38. A distinct thin oxide scale of SiO_2 can be seen on the uppermost part of the scale as revealed from the X-ray mapping for Si and O. Chromium and Ni shows a tendency to form a thin band in the subscale region. The absence of oxygen in the coating region below the surface oxide scale signifies the protective nature of the oxide scale formed during the cyclic oxidation. The interdiffusion of Fe from the substrate into the coating, and Nickel from coating to the substrate can be noticed as a thick diffusion layer along the coating-substrate interface. Further, a minor diffusion of Mo into the coating can be observed from the mapping for Mo.

5.1.5 WC-Co/NiCrFeSiB Coating

5.1.5.1 Thermo gravimetric studies

Macrographs of HVOF sprayed WC-Co/NiCrFeSiB coatings on GrA1, T11 and T22 steels subjected to cyclic oxidation for 50 cycles at 900°C are shown in Fig.5.39. With the progress of study the originally shining grey color as-sprayed coatings turned to green color gradually. The oxide scale formed on the surface of all the three coated steels found to be compact and adherent. In case of coated T22 steels, dark grey color protrusions are observed after 26th cycle of oxidation studies.

Figure 5.40 shows the weight change per unit area (mg/cm^2) for the oxidation of the coated steels in air at 900°C. During the initial cycles of study, all the three coated steels showed weight loss (up to 4th cycle), probably due to evaporation of W-oxides (WO_3) from the surface. The growth of protective oxides from the active elements of the coating stabilize the formation of volatile tungsten oxides, would result in the weight gain with subsequent oxidation cycles. After 8 cycles, gradual decrease in oxidation rate has been observed in case of coated GrA1 and T11 steels. Coated T22 steel showed a increased weight gain after 26th cycles of oxidation. Cumulative weight gain at the end of 50 cycles for WC-Co/NiCrFeSiB coated GrA1, T11 and T22 steels are 1.48, 1.72 and 2.86 mg/cm^2 respectively which is marginal. Coated T22 showed a higher weight gain where as weight gain values are not very different in case of coated GrA1 and T11 steels. So far, as the kinetics of the oxidation is concerned, it can be approximated by the parabolic rate law in all the cases, (Fig. 5.41). The calculated values of parabolic rate constant (K_p) for WC-
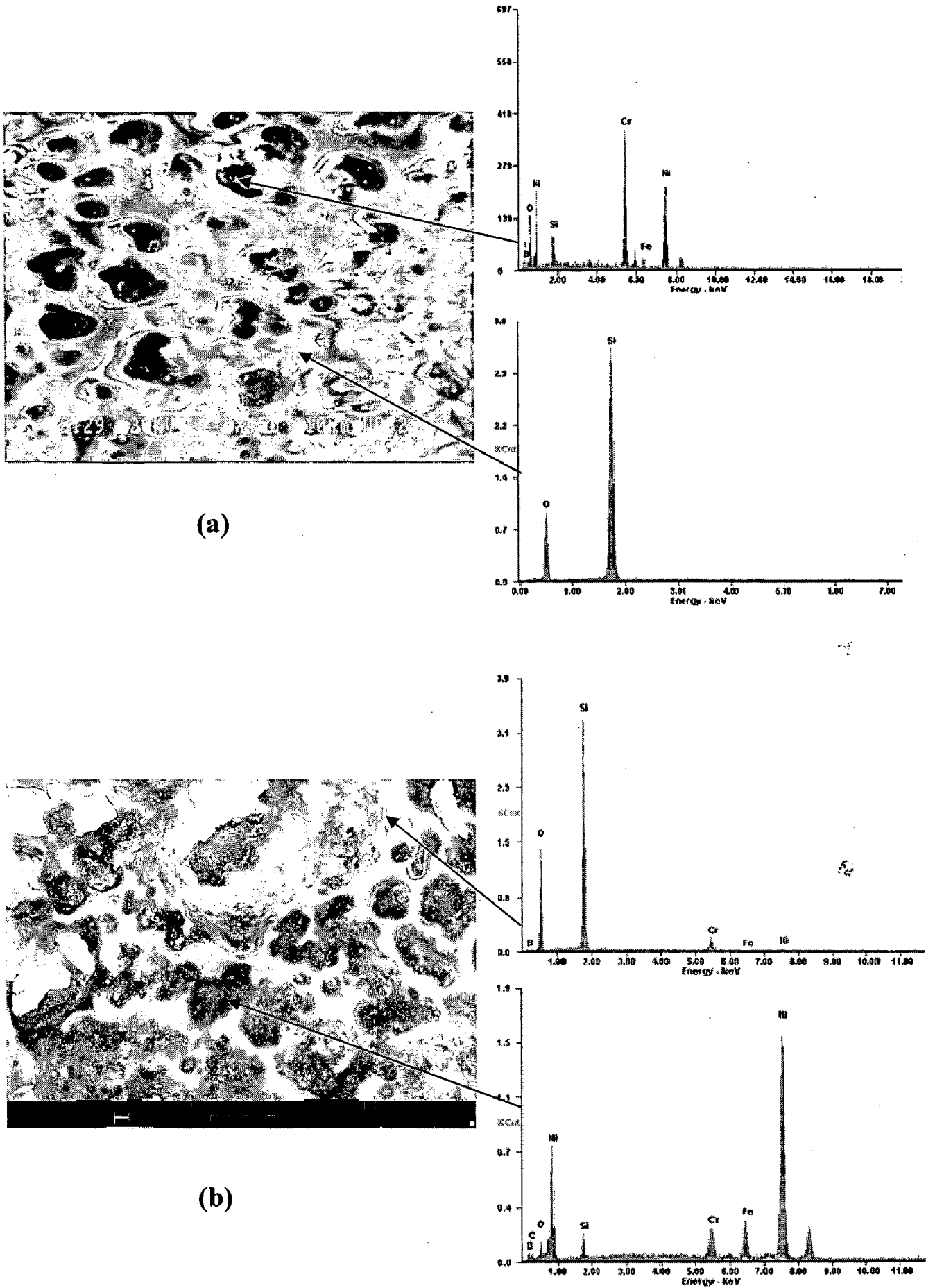
Fig.5.35   Surface scale morphology and EDAX point analysis for NiCrFeSiB coated T11 and T22 steels subjected to oxidation for 50 cycles in air at 900°C: (a) T11 steel   (b) T22 steel
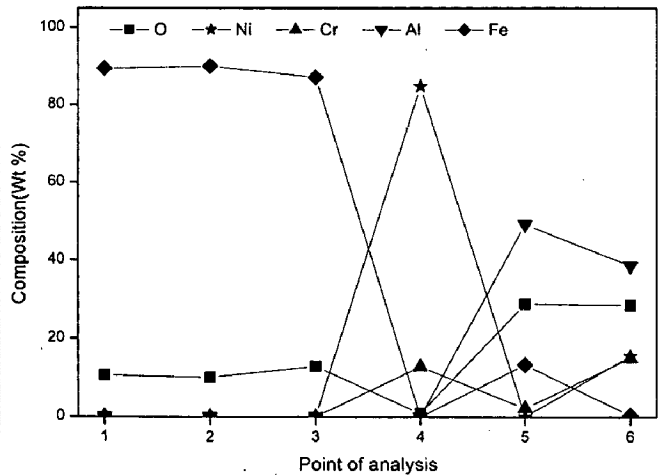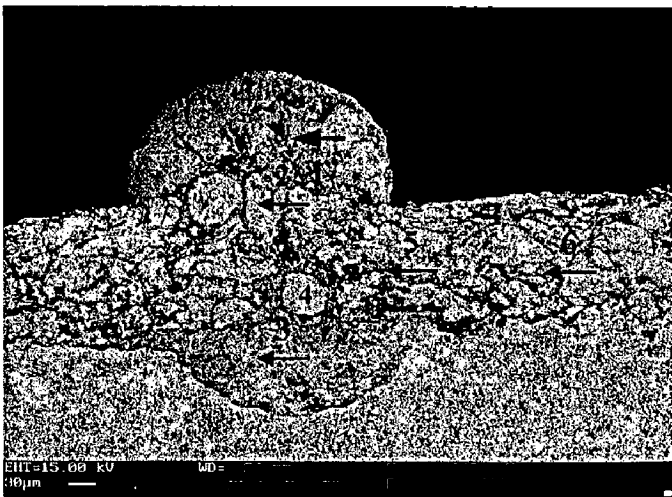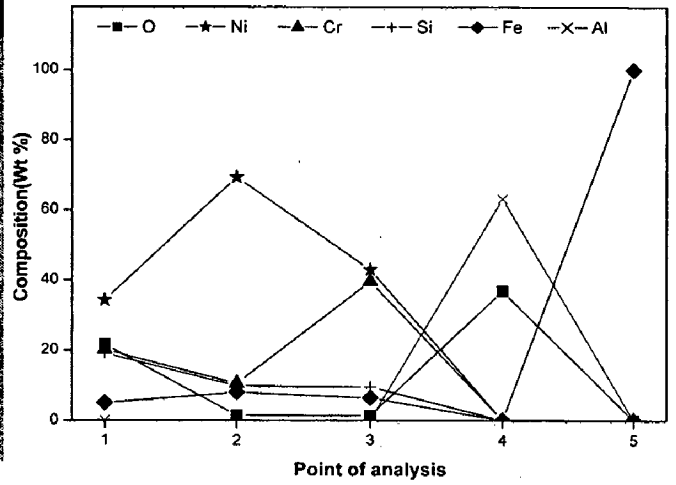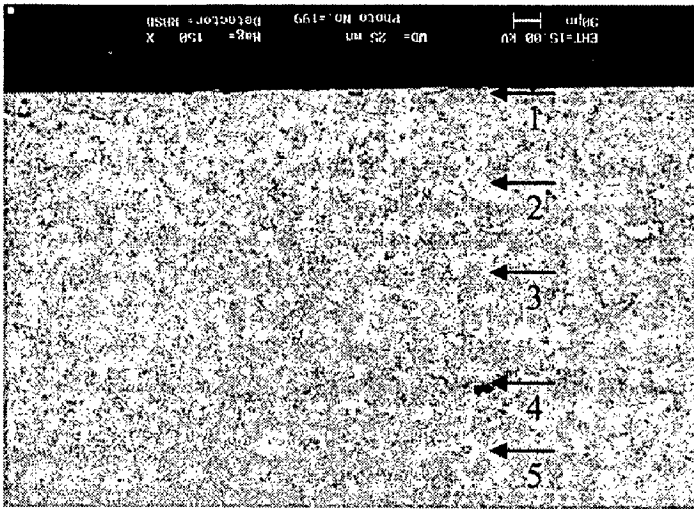
(a)
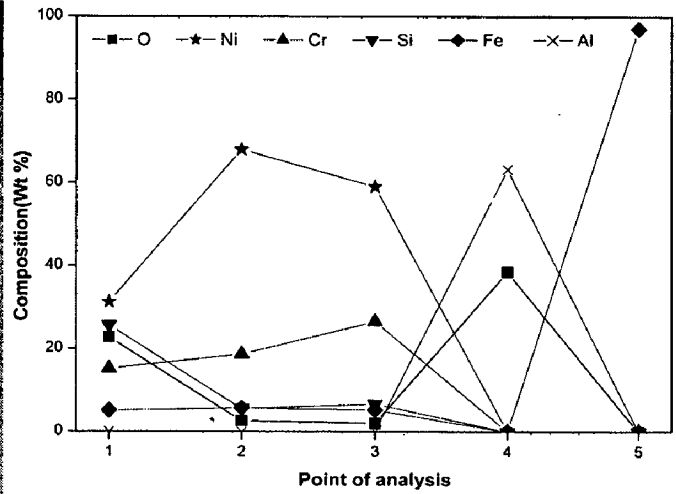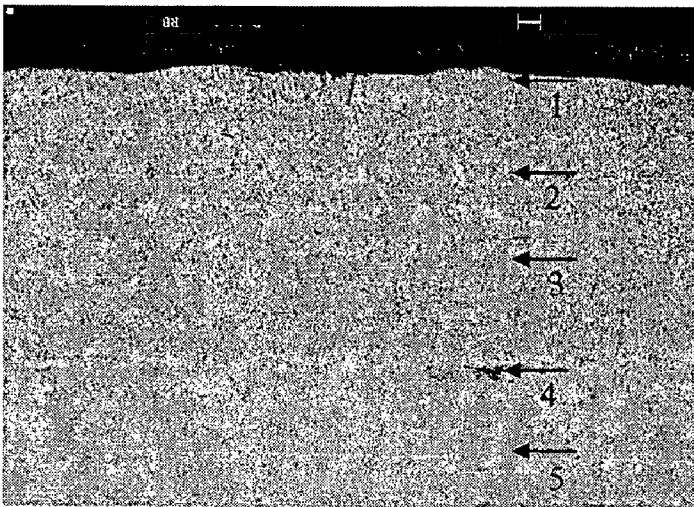
(b)

Fig.5.36   Back scattered electron image and EDAX point analysis (wt %) across the cross-section of the NiCrFeSiB coated steels subjected to cyclic oxidation for 50 cycles in air at 900°C: (a) GrA1 steel   (b) T22 steel
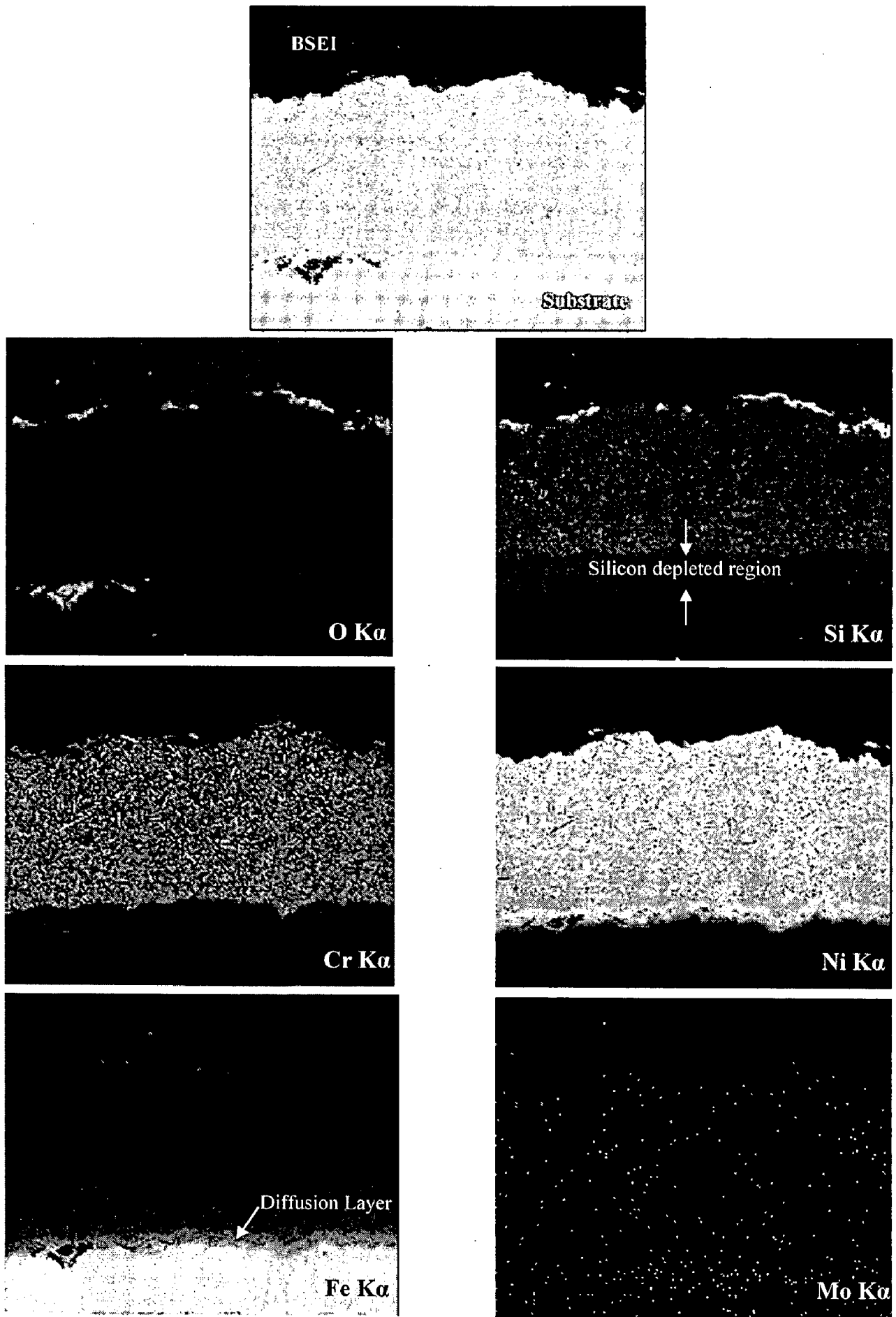
Fig.5.37 BSEI and elemental X-ray mapping at the cross-section of the NiCrFeSiB coated T11 steels subjected to cyclic oxidation in air at 900°C
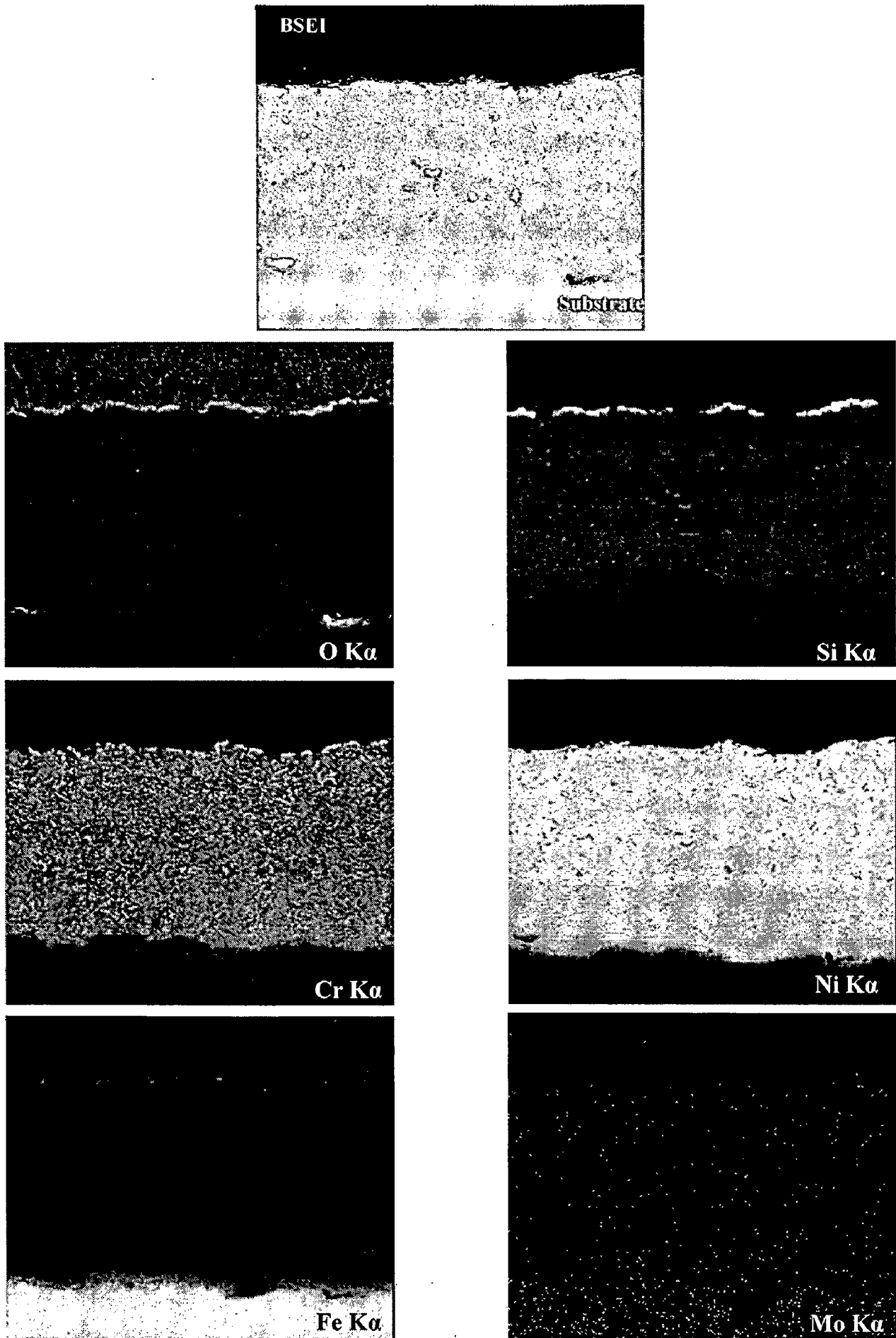
Fig.5.38   BSEI and elemental X-ray mapping at the cross-section of the NiCrFeSiB coated T22 steel subjected to cyclic oxidation in air at 900°C

116
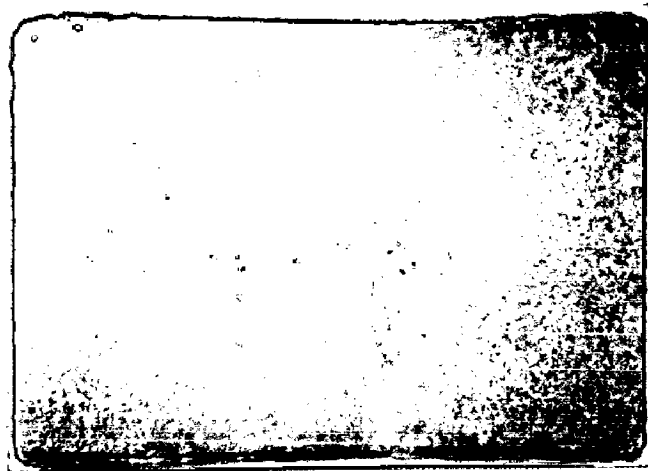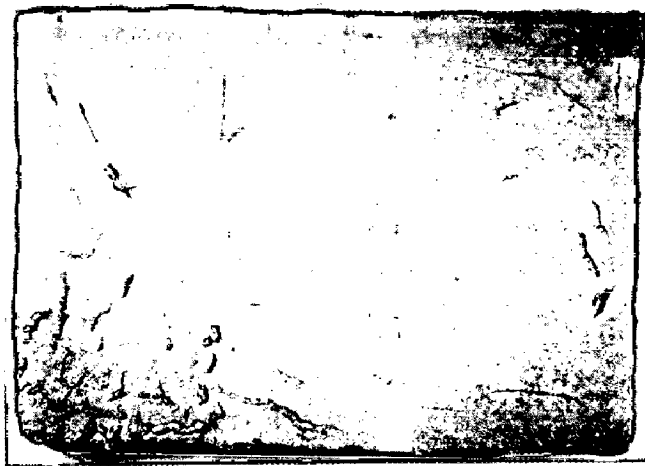
Fig.5.39   Macrographs of the WC-Co/NiCrFeSiB coating subjected to cyclic oxidation in air for 50 cycles at 900°C:
(a) GrA1 steel   (b) T11 steel   (c) T22 steel
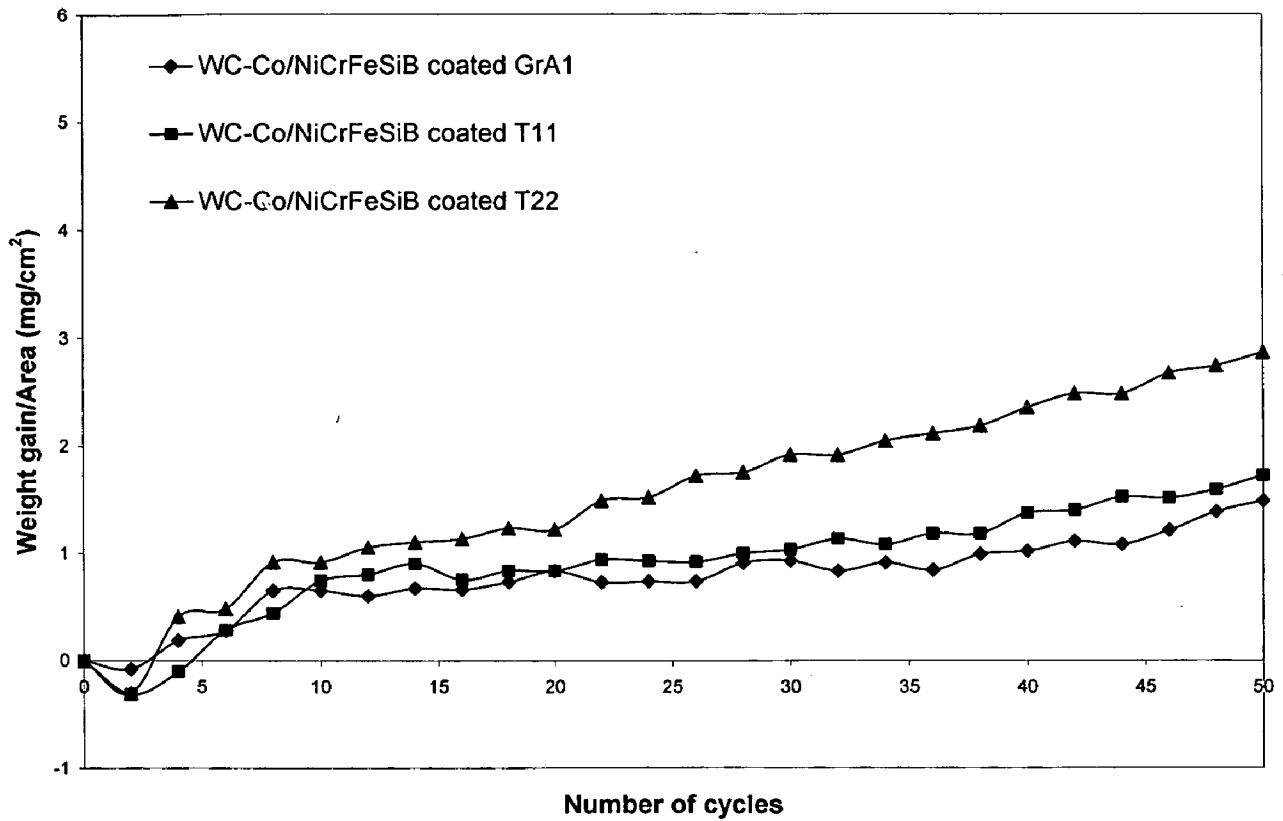
Fig.5.40   Weight gain versus number of cycles plot for WC-Co/NiCrFeSiB coated steels subjected to oxidation for 50 cycles in air at 900°C
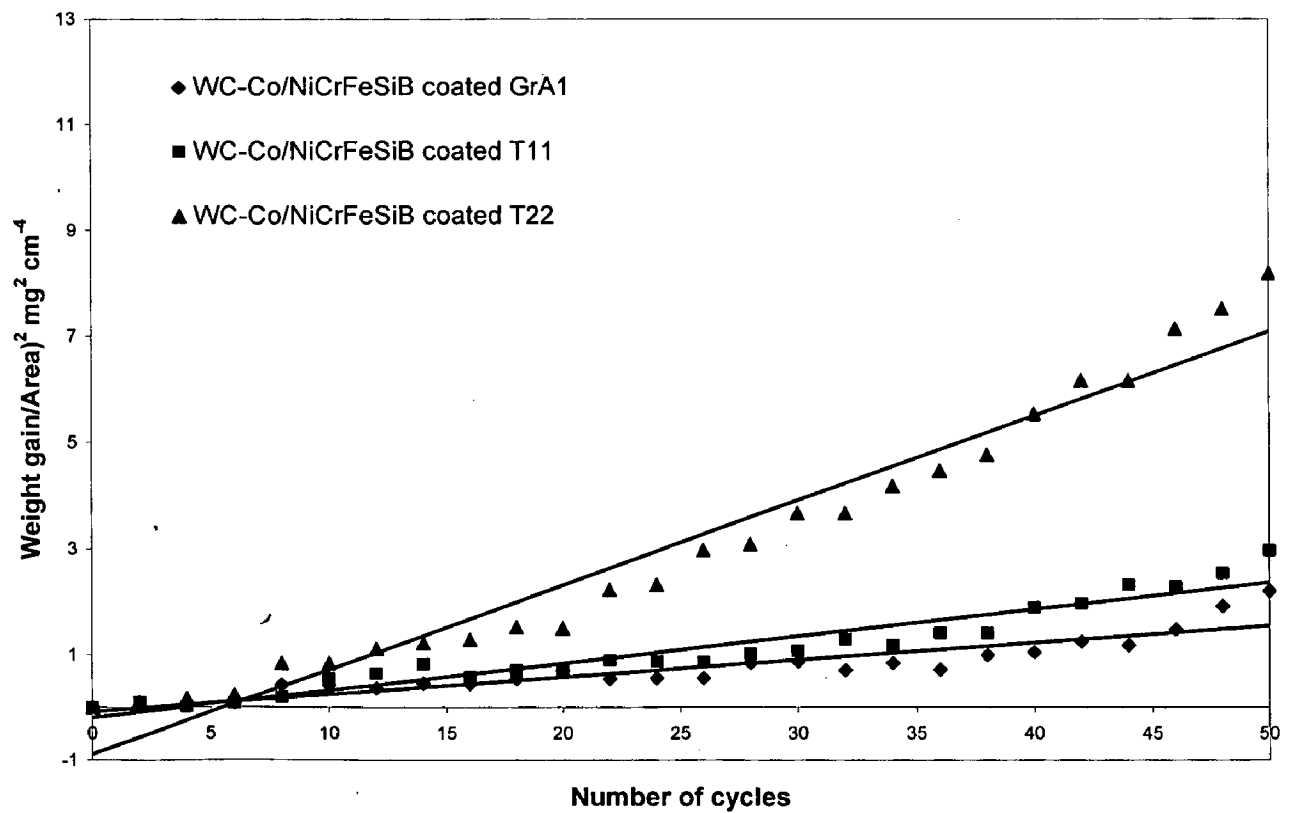
Fig.5.41   (Weight gain/area)^2 versus number of cycles plot for WC-Co/NiCrFeSiB coated steels subjected to oxidation for 50 cycles in air at 900°C

118

Co/NiCrFeSiB coated GrA1, T11 and T22 steels are 0.09×10^{-10}, 0.14×10^{-10} and 0.44×10^{-10} $g^2cm^{-4}s^{-1}$ respectively.

5.1.5.2 X-ray Diffraction Analysis

X-ray diffraction patterns of the oxide scale formed on the surface of oxidized WC-Co/NiCrFeSiB coated steels after cyclic oxidation in air at 900°C have been compiled in Fig. 5.42 and 5.43. The main XRD phases identified for the coated GrA1 and T11 steels are Co, Ni, Cr_2O_3, $CoCr_2O_4$, Co_2SiO_4 and $NiCr_2O_4$. In case of coated T22 steel, additional phases of Fe_2O_3 and Fe_2SiO_4 has been observed along with the phases mentioned above. No peaks for SiO_2 could be identified.

5.1.5.3 SEM/EDAX Analysis

The surface morphology of the oxidized WC-Co/NiCrFeSiB coated GrA1 steel (Fig.5.44a) shows the glassy oxide scale spread on the dark globular matrix. The EDAX analysis on the glass scale shows oxides of Si and Cr (57.25% SiO_2 and 30.34% Cr_2O_3) as the main constituent. The globular matrix contains relatively higher amount of cobalt oxide (37.50%) along with oxides of Cr (16.46%) and Si (28.84%). The dominant presence of Si, Cr and Co peaks supports the possibility of formation of spinels of mixed oxide of Si, Cr and Co on the surface of the oxidized coating. Also minor presence of Ni, W, and Fe oxides has been detected. Corresponding analysis on the oxidized WC-Co/NiCrFeSiB coated T11 steel (Fig.5.44b) illustrate similar oxide scale morphology which contain glassy oxide scale, mainly composed of oxides of Si (49.8%) and Cr (41.1%) dispersed on the globular matrix. Oxides of Co, Si and Cr are the main constituent revealed on the globular matrix.

SEM micrograph shows worm like oxide protrusion on the surface of WC-Co/NiCrFeSiB coated T22 steel (Fig.5.45). Compositional analysis revealed oxide protrusion primarily contains iron oxide (92.54%). Rest of the surface mainly composed of oxides of Si, Cr and Co.

Fig.5.46 shows the BSE image along the cross section of the WC-Co/NiCrFeSiB coated T11 steel oxidized at 900°C and elemental composition at the point of interest are represented in the form of graph. The external surface of the oxide scale (point1) mainly consisted of oxides of Cr Ni and Si. The absence of oxygen at point 2 shows nickel rich

splats in an unoxidised condition dark. White contrast region (point3) mainly composed of tungsten (78.2%) and Co (12.01%) and oxygen is not present in this region. WC+Co particles are arranged in a lamellar fashion, almost parallel to the substrate surface. The absence of oxygen at points 2 and 3 is an indicative of the fact that the oxidation has been restricted only to the uppermost layer and the rest of the coating remains unoxidised. Hence the protective oxides formed on the surface acts as a barrier to the oxygen transport into the coating. Point 4 shows the substrate coating interface rich in Fe and Ni which indicate the possibility of interdiffusion of Ni into the substrate and Fe from substrate into the coating. Analogous analysis across the cross section of the WC-Co/NiCrFeSiB coated T22 steel shows similar results and is shown in Fig.5.46b.

5.1.5.4 EPMA Analysis

Elemental X-ray maps for the WC-Co/NiCrFeSiB coated GrA1 steel subjected to cyclic oxidation for 50 cycles at 900°C are shown in Fig.5.47. X-ray mapping for oxygen shows thin layer of oxide scale formed on the external surface of the oxidized coating. It is evident that oxidation has been restricted only to the uppermost layer only and the rest of the coating remains unoxidised. Combining O and Si maps substantiate the formation of thin and discontinuous layer of SiO_2 on the external surface. Presence of continuous oxide layer of Cr, Co and their spinel can be corroborated from the mapping for O, Cr and Co. Distinct nickel rich band can be noticed along the coating-substrate interface, represented by an arrow mark in the Ni map, signify diffusion of Ni from coating into the substrate. A careful observation shows probable diffusion of Fe from the substrate into the coating. Corresponding analysis along the cross section of WC-Co/NiCrFeSiB coated T22 steel shows similar result and illustrated in Fig.5.48.
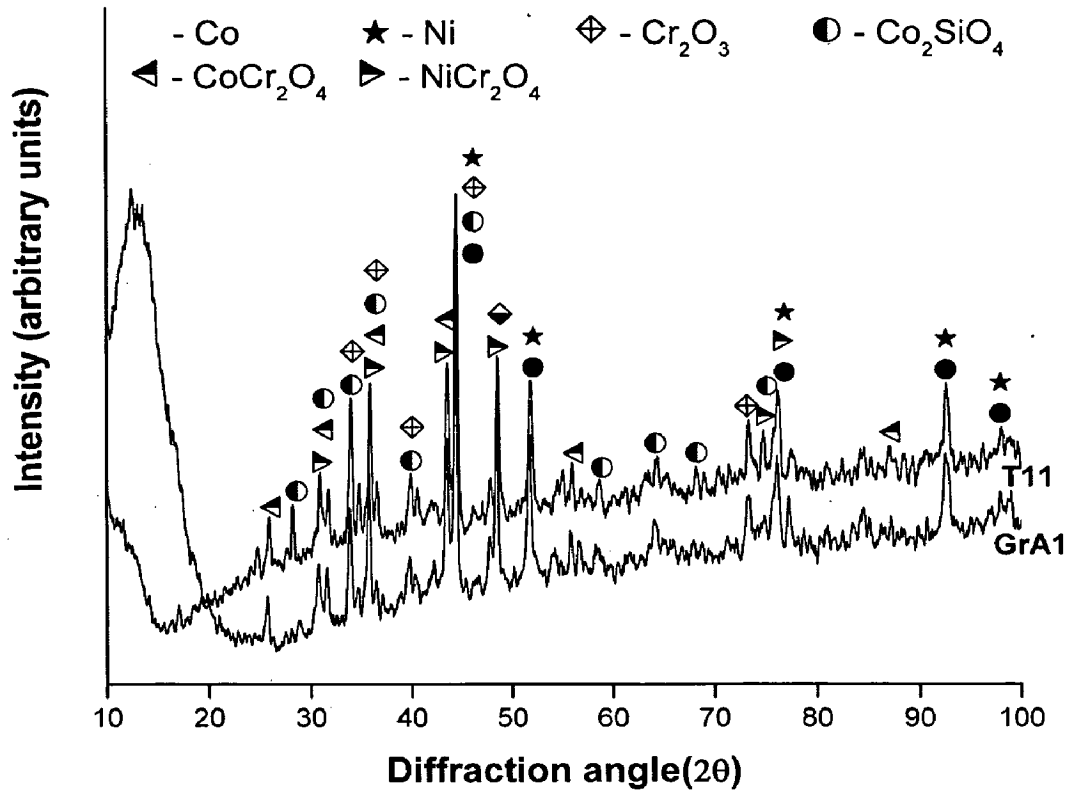
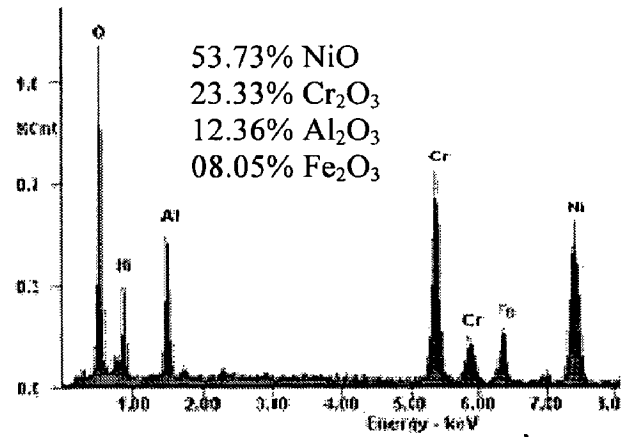**Fig.5.42**   X-ray diffraction patterns for WC-Co/NiCrFeSiB coated GrA1 and T11 steels subjected to cyclic oxidation in air for 50 cycles at 900°C

Fig.5.43   X-ray diffraction patterns for WC-Co/NiCrFeSiB coated T22 steels subjected to cyclic oxidation in air for 50 cycles at 900°C
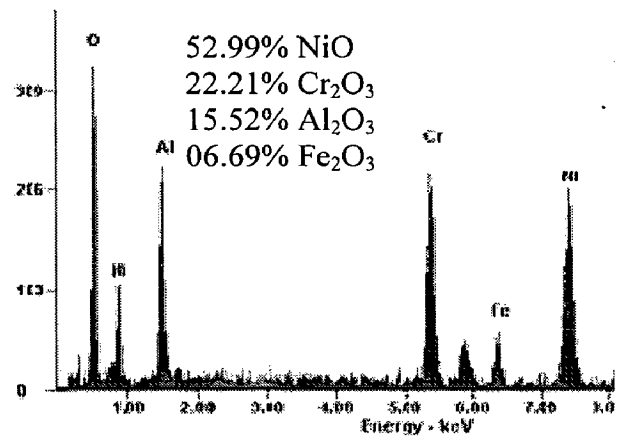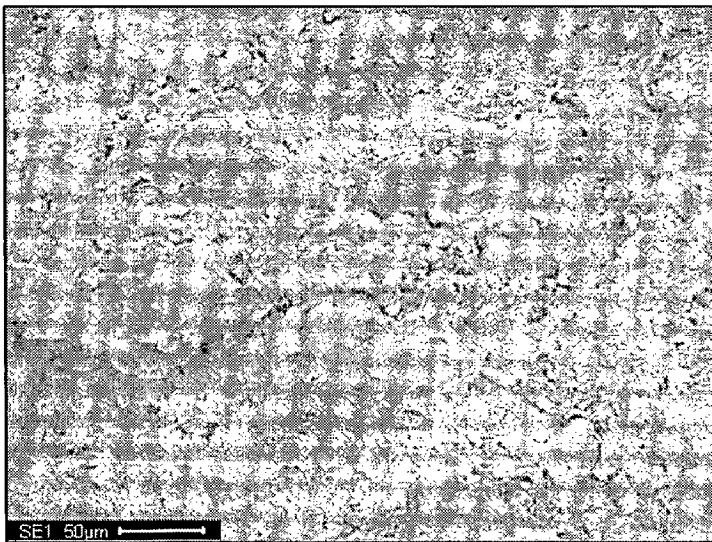
57.25% SiO$_2$
30.34% Cr$_2$O$_3$
04.47% NiO
05.88% WO$_3$

EDAX at point 1

28.84% SiO$_2$
16.46% Cr$_2$O$_3$
37.50% CoO
11.31% NiO
03.64% Fe$_2$O$_3$

EDAX at point 2

(a)

49.83% SiO$_2$
41.12% Cr$_2$O$_3$
04.38% NiO

EDAX at point 3

21.83% SiO$_2$
21.80% Cr$_2$O$_3$
20.13% CoO
11.89% NiO
18.85% WO$_3$

(b)

EDAX at point 4

Fig.5.44   Surface scale morphology and EDAX analysis for WC-Co/NiCrFeSiB coated steels subjected to oxidation for 50 cycles in air at 900°C
(a) GrA1 steel   (b) T11 steel

122

92.54% Cr_2O_3
06.32% CoO

33.21% SiO_2
31.18% Cr_2O_3
11.74% CoO
10.59% NiO
09.92% WO_3

EDAX at point 1

EDAX at point 2
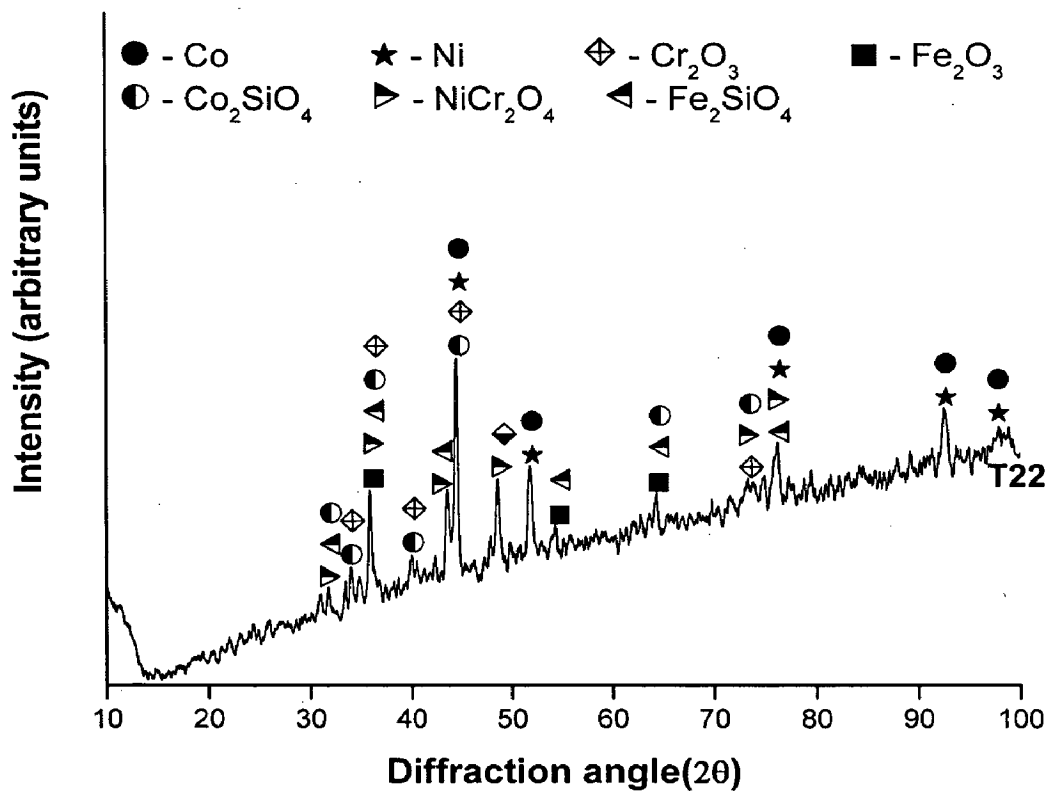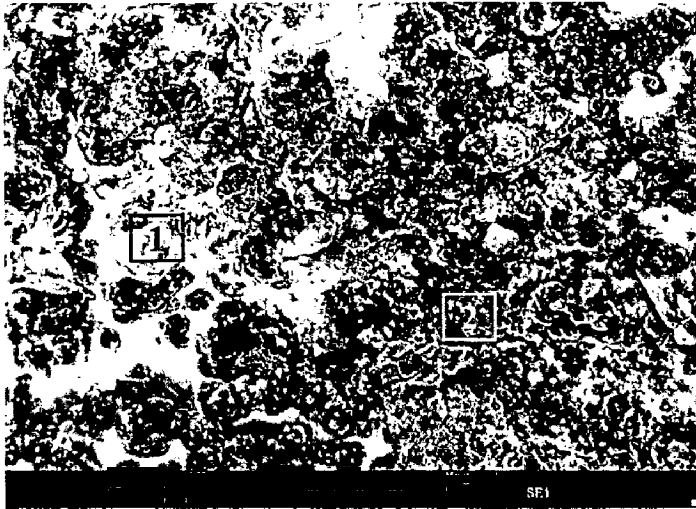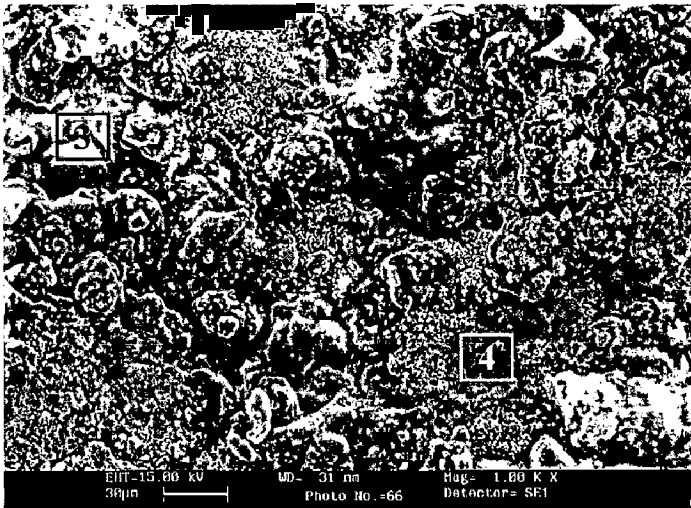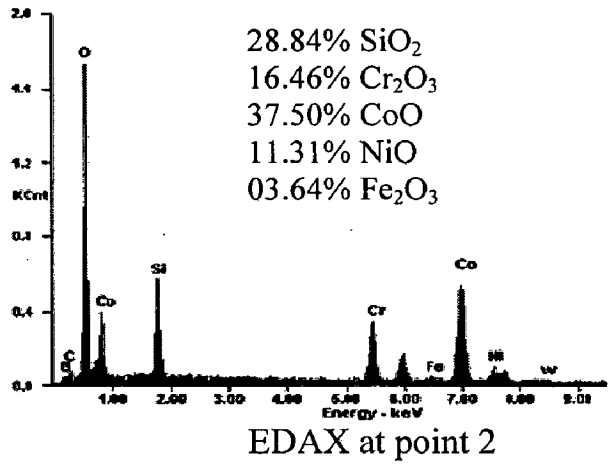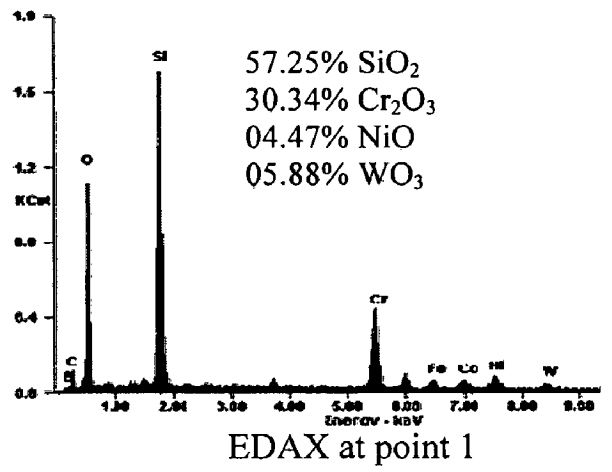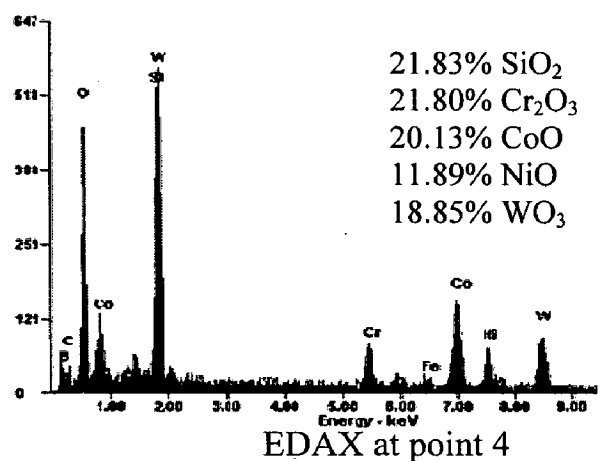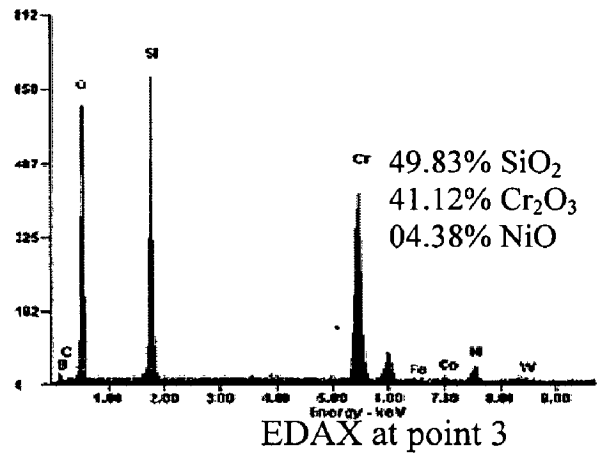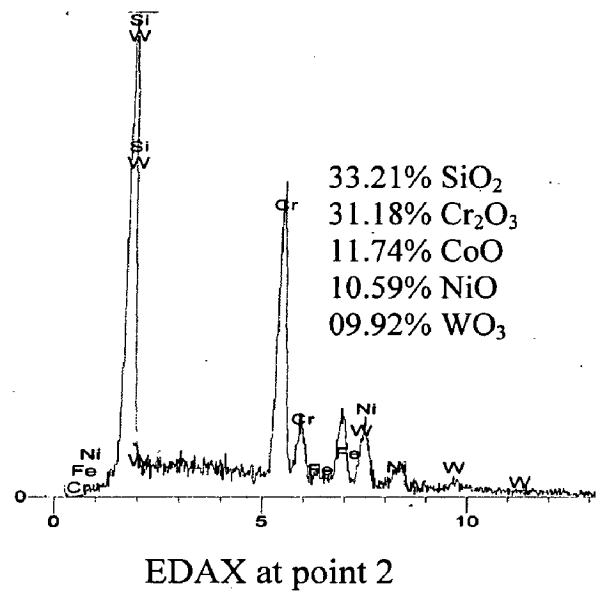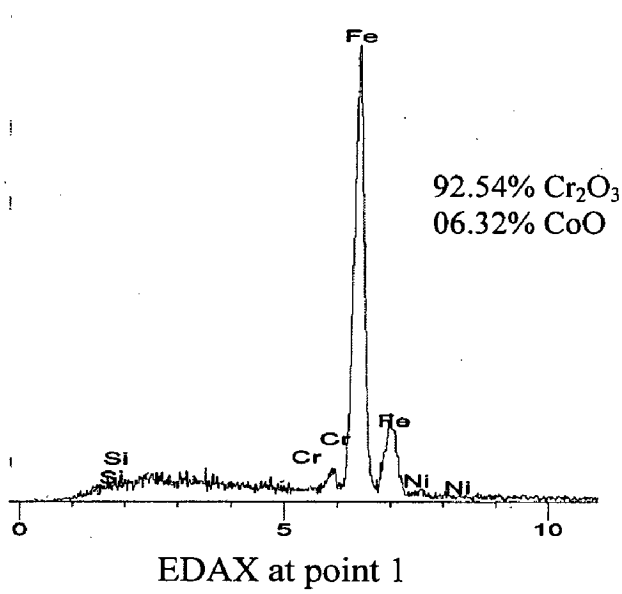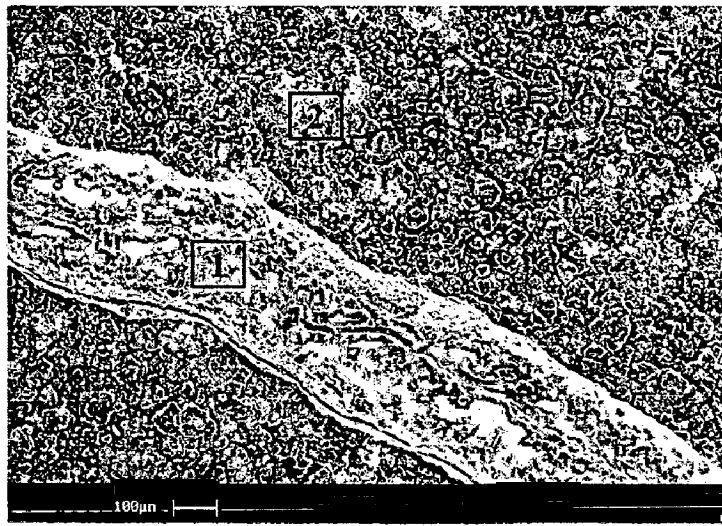
Fig.5.45   Surface scale morphology and EDAX analysis for WC-Co/NiCrFeSiB coated T22 steel subjected to oxidation for 50 cycles in air at 900°C
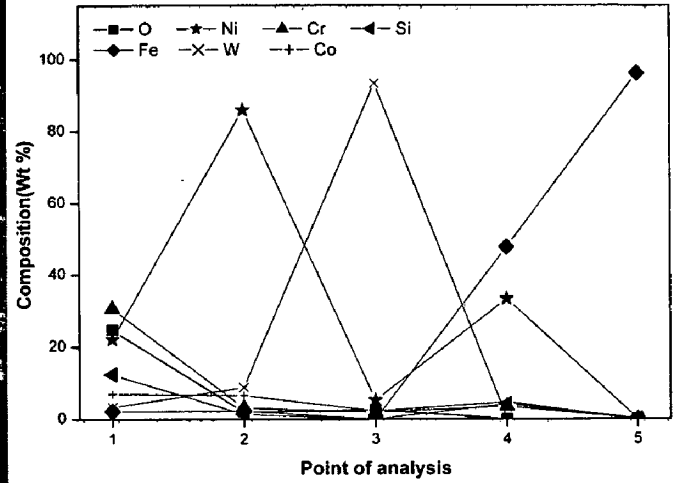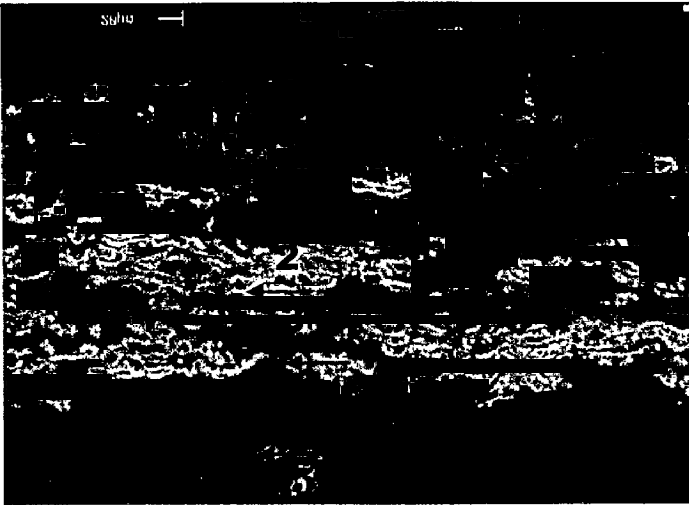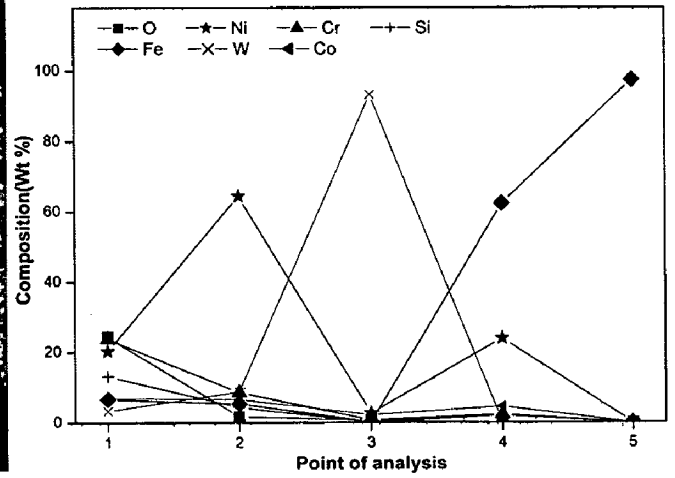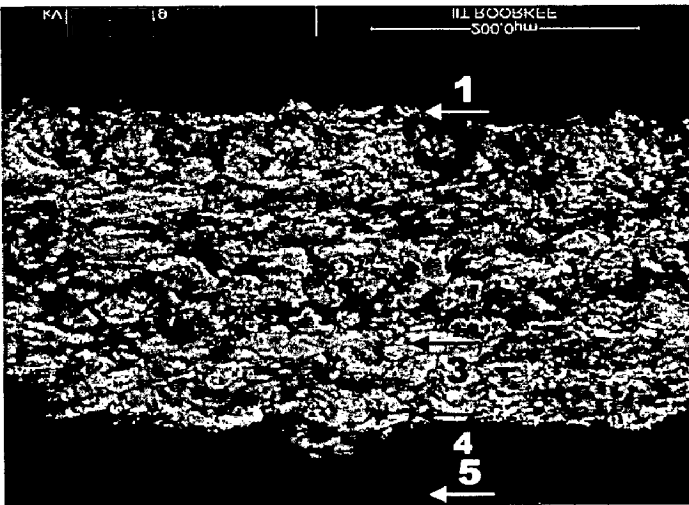
Fig.5.46 Back scattered electron image and EDAX point analysis (wt %) across the cross-section of the WC-Co/NiCrFeSiB coated steels subjected to cyclic oxidation for 50 cycles in air at 900°C: (a) T11 steel   (b) T22 steel
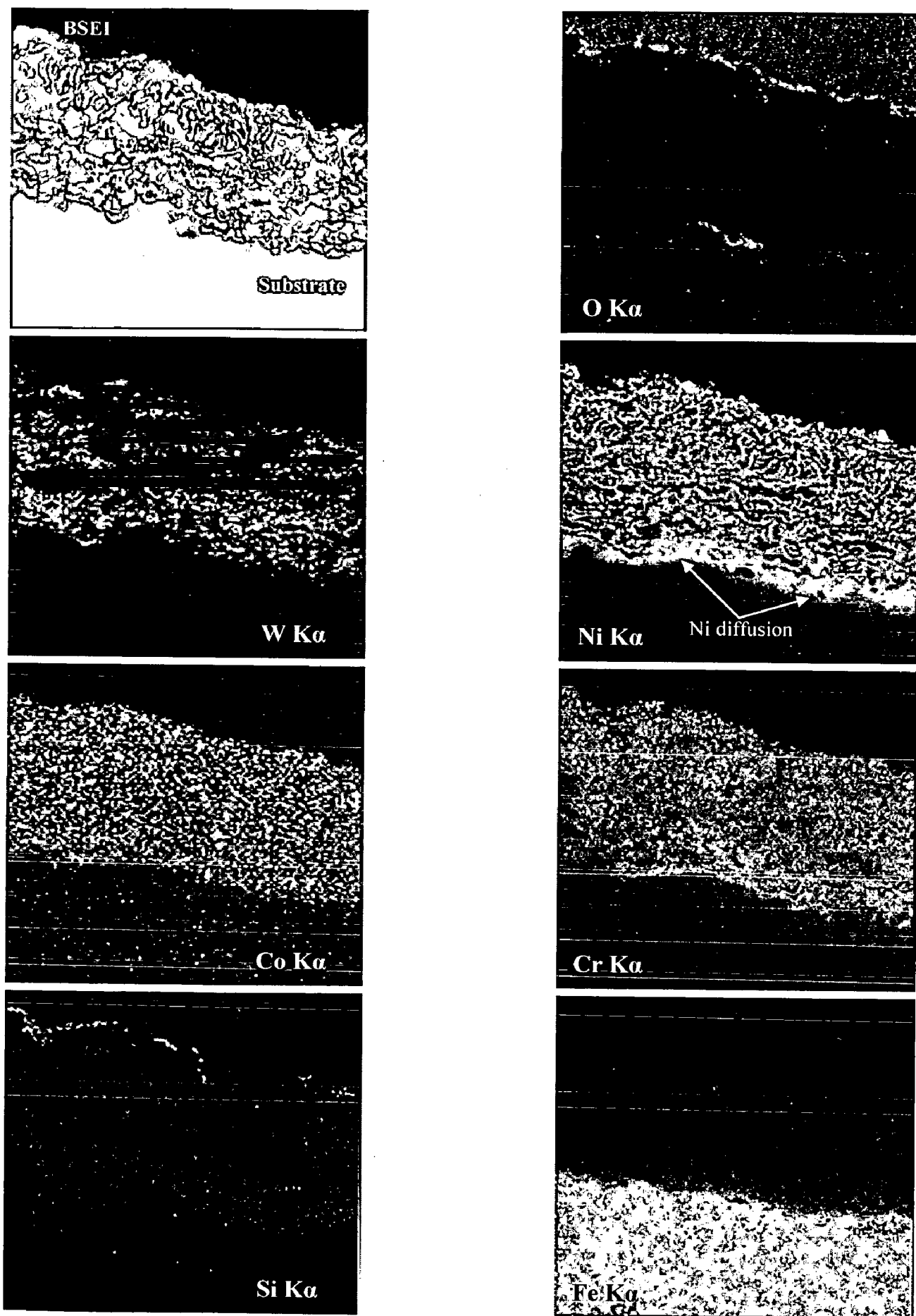
Fig.5.47 BSEI and WDS elemental X-ray mapping across the cross-section of the WC-Co/NiCrFeSiB coated GrA1 steel subjected to cyclic oxidation in air at 900°C
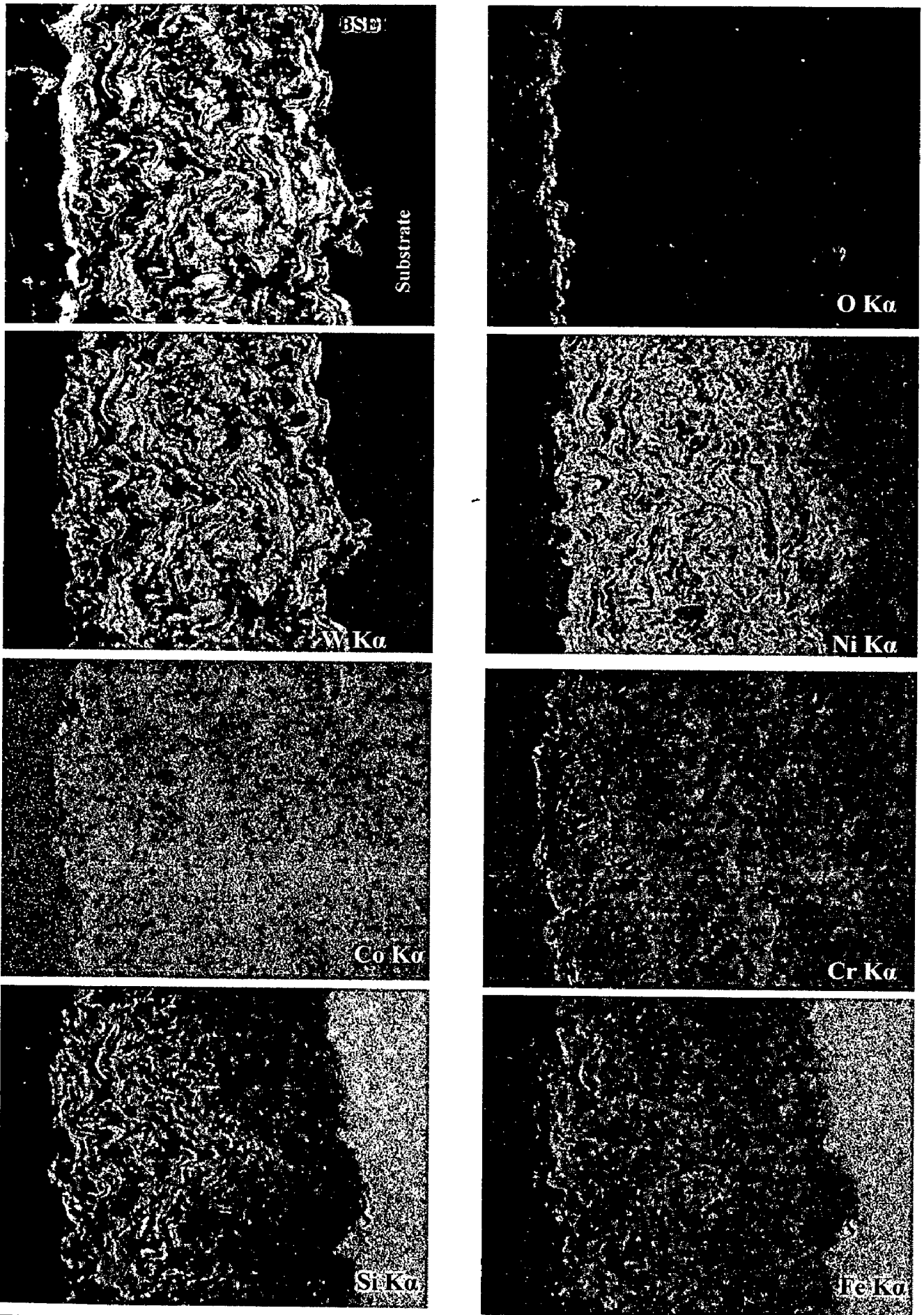
Fig.5.48   BSEI and WDS X-ray mapping at the cross-section of the WC-
Co/NiCrFeSiB coated T22 steel subjected to cyclic oxidation in air at
900°C

	T22	28.63	Linear behavior	Al_2O_3, $Cr2O_3$, NiO, Fe_2O_3, $NiCr_2O_4$ and $NiMoO_4$. .	the Mo content in the base steel. • Internal oxidation along the splat boundary has been observed across the entire cross section of the coating.
NiCrFeSiB coating	GrA1	1.65	0.0147	Ni, Ni_3B, Ni_3Si, Cr_2O_3, NiO, Ni_2SiO_4 and Fe_2SiO_4	• The color of oxide scale formed on all the three coated steels was parrot green. • EPMA & EDAX analysis corroborated the formation of a protective thin oxide scale of amorphous glassy SiO_2 and Cr_2O_3. • Silicon depletion region (Si map) just above the coating-substrate interface further support oxidation of Si at the oxide-gas interface by outward cation migration. • Coating region below the topmost thin oxide scale is in unoxidised condition
	T11	1.25	0.0097	Ni, Ni_3B, Ni_3Si, Cr_2O_3, NiO, Ni_2SiO_4 and Fe_2SiO_4	
	T22	2.22	0.025	Ni, Ni_3B, Ni_3Si, Cr_2O_3, NiO, Ni_2SiO_4 and Fe_2SiO_4	
WC-Co/ NiCrFeSiB Coating	GrA1	1.48	0.009	Co, Ni, Cr_2O_3, $CoCr_2O_4$, Co_2SiO_4 and $NiCr_2O_4$.	• The color of oxide scale formed on all the three coated steels was green. • In case of coated T22 steels, iron oxide protrusions are observed after 26th cycle of oxidation studies. • EDAX and EPMA analysis confirm that the thin protective oxide scale mainly composed of amorphous SiO2 along with the oxides of Cr and Co. • This oxide scale stabilizes the formation of volatile tungsten oxide. • Oxidation has been restricted only to the external surface up to few microns and rest of the coating below this protective oxide layer remains unoxidised.
	T11	1.72	0.014	Co, Ni, Cr_2O_3, $CoCr_2O_4$, Co_2SiO_4 and $NiCr_2O_4$.	
	T22	2.86	0.044	Co, Ni, Cr_2O_3, Fe_2O_3, Co_2SiO_4, $NiCr_2O_4$, Fe_2SiO_4.	

5.2 SUMMARY OF RESULTS

Results of oxidation studies reported in section 5.1 for coated and uncoated steels are summarized in Table 5.1, to elicit comparisons among the various coatings and substrate.

Table 5.1 Summary of the results for uncoated and coated steels subjected to oxidation in air for 50 cycles at 900^0C.

Coating	Substrate	Weight gain mg/cm^2	Parabolic constant, $K_p \times 10^{-9}$ g^{2}cm^{-4}s^{-1}	XRD phases	Remarks
Uncoated Steels	GrA1	221.5	291.4	Fe$_2$O$_3$	• Intense spalling of oxide scale is observed and it is multi laminated and cracked.
	T11	165.9	158.7	Fe$_2$O$_3$, Fe$_3$O$_4$, Cr$_2$O$_3$, MoO$_3$ and FeCr$_2$O$_4$	• In case of T11 and T22 steels, Chromium oxide is seen in the inner
	T22	197.7	225.4	Fe$_2$O$_3$, Fe$_3$O$_4$, Cr$_2$O$_3$, MoO$_3$ and FeCr$_2$O$_4$	layer of oxide scale
NiCrAl Coating	GrA1	6.7	0.27	α-Al$_2$O$_3$, AlNi$_3$ and NiCr$_2$O$_4$	• Greenish grey colored oxide scale is formed on all the coated steels. • In case of coated T22 steel, dark grey color iron oxide protrusions are
	T11	10.8	0.75	α-Al$_2$O$_3$, AlNi$_3$ and NiCr$_2$O$_4$	observed. • EDAX & EPMA confirms the formation of α-Al$_2$O$_3$ on the outermost surface along with the oxides of Cr and Ni.
	T22	16.91	1.64	α-Al$_2$O$_3$, Cr$_2$O$_3$, Fe$_2$O$_3$ and NiCr$_2$O$_4$	• Preferential oxidation of Al and Cr along the nickel rich splat boundaries has been observed.
NiAlCrFeMo coating	GrA1	8.6	3.72	Ni, Al$_2$O$_3$, Cr$_2$O$_3$, NiO, NiCr$_2$O$_4$ and FeO.Cr$_2$O$_3$	• Brown color oxide scale has been observed on the surface of all the three coated steels. • The outermost thin oxide layer mainly composed of oxides of nickel, chromium and aluminum.
	T11	14.79	12.6	Ni, Al$_2$O$_3$, Cr$_2$O$_3$, NiO, NiCr$_2$O$_4$ and FeO.Cr$_2$O$_3$	• In case of coated T11 and T22 steels, the extent of iron oxide protrusions observed on the corroded surface and the oxidation rate seems to be related to

5.3 DISCUSSION

5.3.1 Uncoated Steels

The weight gains for T11 and T22 steels during oxidation studies are found to be less than that of the GrA1 steels. In this case, the lesser weight gain values may be attributed to the presence of chromium up to 1.12% for T11 and 2.56% for T22 steels. These observations are similar to the findings of Lai (1990) who observed a significant increase in the oxidation resistance for the 0.5% Mo containing steels by increasing chromium from 1% to 9%.

The XRD results show an outer layer of scale which mainly consists of Fe_2O_3 in all the three steels. In T11 and T22 steels, an inner layer of scale contain predominantly Cr_2O_3 as diffusion of iron towards outside out weighs that of chromium (Fig.5.7). Furthermore, it is revealed by the XRD analysis that there is the presence of $FeCr_2O_4$ spinal along with Cr_2O_3. From the thermodynamic considerations, it is observed that the formation of $FeCr_2O_4$ requires a lower level of oxygen. As the availability of oxygen at the oxide metal interface was less, it favored the formation of spinal. Similar results are also reported by Khanna et al. (1982), Ahila et al. (1993) and Pinder (1981). Further, Lai (1990) has reported that the alloys having 2% chromium could only form the oxides of chromium along with iron oxide in the innermost layer.

It is a well known fact that the stresses developed due to a higher volume of oxides formed on the metal leads to scale cracking. The attainment of critical stress to cause scale rupture may be related to the critical thickness. The difference in the thermal coefficients of the oxide scale and the metal also contribute to the development of cracks in the scale. These cracks help in the internal oxidation and spalling of the scale. Similar observations are also observed by Khanna et al. (1982) and Ahila et al. (1994).

The weight gain for T22 is slightly higher in comparison to that of T11. The cause of this difference can be attributed to a significant variation in the amount of Cr and Mo in these two alloys. The XRD and EPMA analysis shows the presence of MoO_3 in the scale. This could have been produced structural destabilization of the protective layer leading to a higher weight gain in T22 than T11 at 900°C. Chatterjee et al. (2001) has reported that during the initial oxidation, Fe got oxidised and the oxide scale is protective in nature. With the progress of oxidation, Mo becomes

enriched at the alloy interface, leading to the formation of an inner layer of molten MoO_3 (m.p. = 795°C), which penetrates along the alloy-scale interface. Simultaneously, MoO_3 may exert dissolving action on other oxides, such as Fe_2O_3 and Cr_2O_3, and this fluxing may further get accelerated by the enthalpy of formation of Fe_2O_3 and Cr_2O_3 which tends to an increase in the temperature at the alloy-scale interface.

5.3.2 NiCrAl coating

The NiCrAl coated steels show marginally lower weight gain in comparison to the uncoated steels as reported in Section 5.1.1.1. Weight gain after 50 cycles of oxidation of NiCrAl coated GrAl, T11 and T22 steels are found to be 1/33, 1/15 and 1/10 fraction that of respective uncoated steel substrate. The parabolic rate constant (K_p) are lower for all the coated steels in comparison to the uncoated steels, thereby further indicating lower oxidation rates for the coated steels. The oxidation behavior of the coated steels is parabolic in nature up to 50 cycles and, hence, the oxide scales formed have shown the tendency to act as the diffusion barriers. Similar findings have been reported by Sidhu et al.(2005B), where they showed a better oxidation resistance of plasma sprayed NiCrAlY coatings in comparison to the substrate boiler steels oxidized in air at 900°C.

It is revealed from the XRD analysis on the surface of the oxidized coating (Figs. 5.11 and 5.12) that α-Al_2O_3 is a major phase. α-Al_2O_3 is the thermodynamically stable phase, having nearly a close-packed corundum structure which shows slow-scale growth kinetics during the oxidation (Zhenyu, 1998). Further EDAX (Figs.5.13-5.16) and EPMA analysis (5.17 & 5.18) confirmed the presence of thin layer of Al_2O_3 along with the oxides of Cr and Ni. The solid state reaction between initially grown NiO and Cr_2O_3 might have resulted in $NiCr_2O_4$. The XRD results also indicate the presence of $AlNi_3$ phase, which could have segregated during the oxidation. The segregation of $AlNi_3$ could restrict the diffusivity of Al and, hence, this supports forming a continuous α-Al_2O_3, by holding a larger amount of Al with slowing down the reaction. However, some Ni may easily get oxidized and form NiO, which is not a favorable oxide. During the initial oxidation period, the NiO and α-Al_2O_3 might have undergone the solid state reaction to form $NiAl_2O_4$. However, with the increase in oxidation time and transformation to thermally stable α-Al_2O_3, the spinal oxide $NiAl_2O_4$ could have overlaid by the growing

Al_2O_3. Hence, in the present study, it is not identified with the XRD analysis. This is substantiated by the results reported by Chen et al. (2000) during their study on the oxidation behavior of sputtered NiCrAl nanocrystaline coating.

The preferential oxidation of Al and Cr along the nickel-rich splat boundary has been observed (Figs. 5.16 to 5.18). The free energy of formation of oxide, affinity to oxygen, and flattened structure of the HVOF coatings are the governing factors in selective oxidation. The Aluminum ($\Delta G° = -1295.66$ kJ mol^{-1} at 925°C) in the coating oxidizes before Cr ($\Delta G° = -813.85$ kJ mol^{-1}) and Ni ($\Delta G° = -132.31$ kJ mol^{-1}) due to relatively high negative free energy of formation of oxide (Huo et al., 1999). During the initial stage of oxidation, the oxygen penetrates into the coatings through the open porosity located along the splat boundaries until all the accessible internal surfaces have been oxidized. Al and Cr are partially oxidized during the initial stage and reduced further oxygen ingress into the coating. Subsequently, the oxidation phenomenon takes place only on the external surface of the coating. Aluminum gets oxidized to α-Al_2O_3 and this retards further oxide growth, which results in a lower oxide scale thickness as observed in the present study. Sidhu and Prakash (2005B), Singh et al. (2006), Niranatlumpon et al. (2000), and Belzunce et al. (2001) also reported the internal oxidation via open pores during the early stages of oxidation for thermal-sprayed MCrAlY coating.

The above discussion is represented as sequence of equations and are as follows. In order to form α-Al_2O_3 scale, the thermodynamic conditions must be such that the following reaction is favorable on the surface of the alloy (Ajdelsztajn et al., 2002):

$$2Al + 3/2O_2 \rightarrow Al_2O_3$$
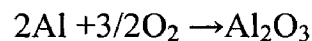
The initial supply of oxygen is such that the other oxides in addition to Al_2O_3 are also formed via reactions of this type.

$$M + 1/2O_2 \rightarrow MO$$
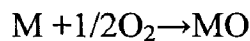
Where M indicates other metallic elements. For the Al_2O_3 to develop as a continuous scale, the following additional reaction must be favorable:

$$2Al + 3MO \rightarrow Al_2O_3 + 3M$$
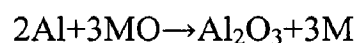
Usually, the Al_2O_3 develops continuity beneath some of the MO layer. With further oxidation, when the coating experiences a severe Al depletion, it will become favorable

to form other oxides and spinal as follows (Wang et al., 2002A; Evan et al., 2001; Niranatlumpong et al., 2000):

$$Al_2O_3 + 2Cr \rightarrow 2Al + Cr_2O_3$$

or

$$Al_2O_3 + 1/2O_2 + Ni \rightarrow NiAl_2O_4$$
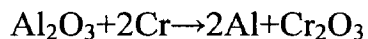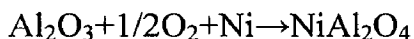
Furthermore, Cr atoms substitute for Ni atoms in the NiO that had formed in the initial oxidation, thus forming a certain amount of Cr_2O_3:

$$3NiO + 2\ Cr \rightarrow 3\ Ni + Cr_2O_3$$
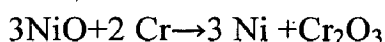
This nickel, apart from reacting with alumina to form $NiAl_2O_4$, may also have reacted with Al and Cr to form spinals:

$$Ni + 2\ Al + 2O_2 \rightarrow NiAl_2O_4$$

and

$$Ni + 2\ Cr + 2O2 \rightarrow NiCr_2O_4$$
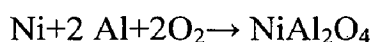
The weight gains in all the NiCrAl coated steels are not very different up to the 12th cycle of oxidation studies and, thereafter, the coated T22 shows a abrupt change in weight gain in comparison to other the coated steels, probably due to the development of crack. During the thermal cycle, stresses are developed in both the oxidized coating and the substrate as a result of mismatch between the thermal expansion coefficients of the oxide and the metal. The thermal expansion values of the metals are usually larger than oxides; hence, the oxide layer experiences a compressive stress during cooling and the metal substrate has a tensile stress. The thermally induced stresses may be simultaneously released in the form of cracks along the brittle oxide scale (Zhenyu et al., 1998). The initiation of the crack near the substrate-coating interface can be observed in Fig. 5.18. These cracks propagate along the splat boundary to the coating surface. Another probable cause of cracking of the scale can be attributed to the presence of molybdenum in this substrate steel. MoO_2 and MoO_3 have low melting points which are also liable to sublimate directly at more than 800°C. An increased volume of the sublimated gaseous products of MoO_2 and MoO_3 induces stress that leads to crack. These volatile oxides and the iron oxide formed ooze outwards through the cracks due to a greater specific volume. EDAX analysis (Fig. 5.15 & 5.16) of the protruded oxide shows a higher concentration of iron oxide. The T11 steel did not show cracks similar to the one observed for T22 steel and this might be attributed to the smaller content of molybdenum in T11 steels. Identical findings have also been reported by Sidhu et al.

(2003A), where they observed a similar oxidation behavior of NiCrAlY coated T22 steels. The minor diffusion of substrate iron through the open pores along the splat boundary into the coating is indicated by an arrow mark in Fig. 5.17. Fe has a faster diffusion rate in the Ni system as suggested by Sundarajan et al. (2003). Fig.5.49 shows the general oxidation mode based on the present study.

5.3.3 NiAlCrFeMo coating

HVOF sprayed NiAlCrFeMo coated steels shows lower weight gain in comparison to uncoated steels as reported in section 5.1.1.1. Weight gain at the end of 50 cycles of oxidation studies for NiAlCrFeMo coated GrA1,T11 and T22 Steels found to be 1/26, 1/11 and 1/7 times of similar uncoated steels respectively. Higher oxidation rate in case of coated T22 steel after 18th cycles of oxidation might be attributed to the cracks developed in the coating. The crack formed in the coating facilitates the oxidizing environment to reach the substrate. Fig.5.29 clearly shows the localized corrosion of the substrate under the cracked coating. Elemental mapping for iron and oxygen shows the protrusion of iron oxide from the substrate on to the surface of the coating through the cracks. EDAX analysis confirms that the protrusions observed on the surface mainly composed of iron oxide (96.70%). XRD analysis on the corroded surface of coated T22 steel, also show the presence of Fe_2O_3 phase. Blown-up image of the protrusion illustrates that the growth of Fe_2O_3 in the transverse direction. During cyclic oxidation at elevated temperature, stresses are developed in both the oxide and substrate as a result of mismatch between the thermal expansion of the oxide and the metal. The thermally induced stresses may be simultaneously released in several ways, including creep of the oxides, creep of the substrate metals, cracking of the brittle oxide scales and spallation of the oxide scales (Zhenyu et al. 1998).In the present case stresses were released by means of cracking of the oxide scale. Another probable cause of crack or the propagation of existing thermal cracks developed in the oxidized coating may be due to presence of Mo in the substrate steels. MoO_2 or/and MoO_3 not only have low melting points but also are liable to sublimate directly at a temperature more than 800°C and destroy the integrity of the scale (Huo et al. 1999). The oxide protrusion appeared from the beneath through cracks are perhaps of greater specific volume oxides consistent with observations of Bornstein et al, (1975). Further this oozing out of oxides from the beneath is supposed to seal the cracks and have contributed to prevent the further oxidation of base metal to a

certain extent. The oxide protrusions are more pronounce in coated T22 steel (Mo-1.1%) in comparison to T11 steel (Mo-0.52%). The extent of oxide protrusions observed on the surface and the oxidation rate seems to be related to the Mo content in the base steel. Sidhu et al. (2005B) also observed the protrusion of iron oxide from the plasma sprayed NiCrAlY coated ASTM-SA213-T11 and T22 steels during the oxidation studies at 900°C and reported the deleterious effect of Mo on the oxidation resistance of the coatings.

Analysis across the cross section of coated steels (Figs.5.26, 5.27 and 5.28) shows the outermost thin oxide layer mainly composed of oxides of nickel, chromium and aluminum. Further the XRD analysis on the surface confirms the protection of the substrate steel by the oxides of nickel, chromium and aluminum and mixed spinal oxide $NiCr_2O_4$. Internal oxidation along the splat boundary has been observed along the entire thickness of the coating. EDAX and elemental mapping revealed the oxidation of aluminum, chromium, iron and molybdenum along the splat boundary where as nickel rich splats remain unoxidised at the end of 50 cycles of oxidation studies. During the early stage of oxidation, oxidant atmosphere penetrates into the coatings through open porosity (mostly located at splat boundary) until all the accessible internal surfaces have been oxidized. Subsequently the oxidation phenomenon takes place only on the outer surface of the coating due to formation of protective oxide layer (Belzunce et al. 2001). Uusitalo et al. 2003, also observed the internal oxidation occurred at the splat boundaries of HVOF sprayed Ni21Cr9MoFe coatings. Minor diffusion of nickel from the coating in to the substrate can also been observed along the coating-substrate interface which perhaps provided good adherence of coating with substrate. Based upon the results, the general oxidation mode for NiAlCrFeMo coatings at 900°C is shown in Fig.5.50.

5.3.4 NiCrFeSiB coating

The EPMA analysis (Figs. 5.37 and 5.38) and the compositional EDAX analysis on surface (Figs. 5.34 and 5.35) as well as along cross-section (Fig. 5.36) corroborates that there is the formation of an external protective thin oxidized layer composed of SiO_2, Cr_2O_3, and a minor content of NiO. Further, the XRD analysis confirms about the existence of chromium and nickel oxides, whereas no peak corresponding to the Si-related oxide phase has been detected, probably because it is amorphous silica. Yu et al. (2007), Douglass et al. (1987), and Wu et al. (2005) have reported about the possibility

Air, 900°C

Preferential oxidation of Al & Cr

α-Al$_2$O$_3$ & Cr$_2$O$_3$ rich top scale

Ni rich splat in unoxidised condition

Fe^{3+} Fe^{3+}

Substrate
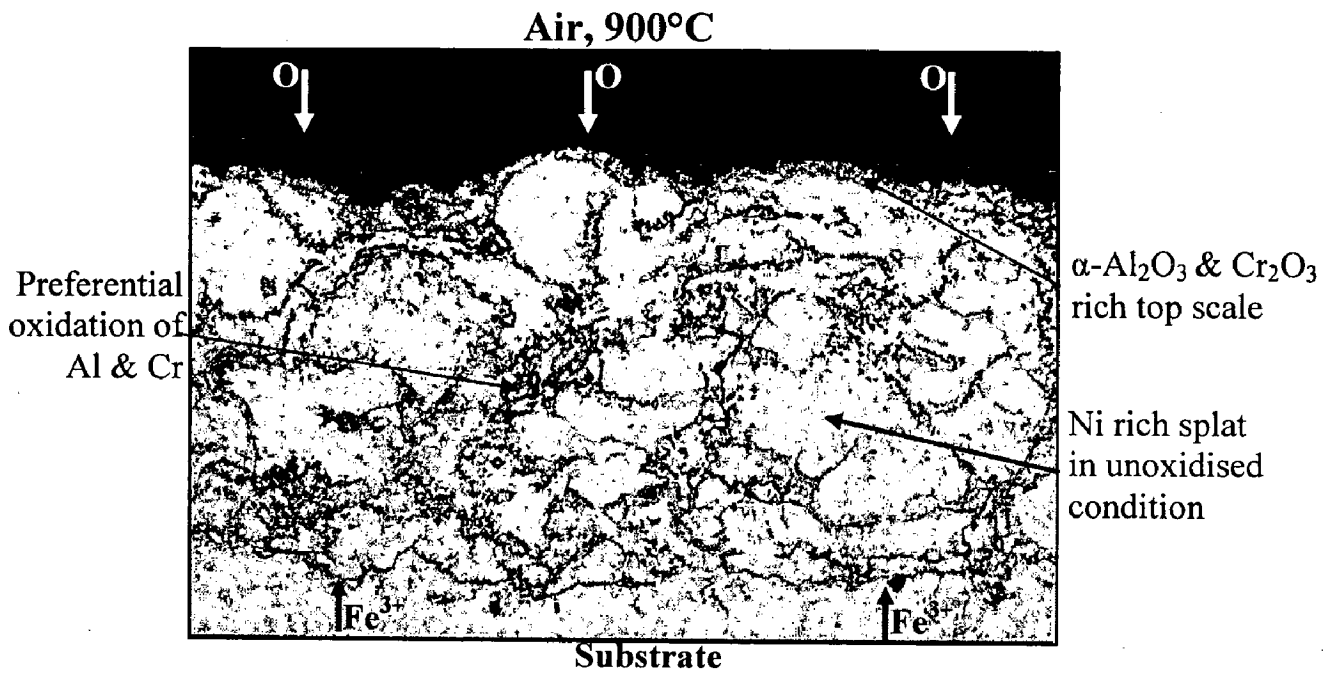
Fig.5.49   General oxidation mode of NiCrAl coated steels exposed to air for 50 cycles at 900°C

Air, 900°C

Severe internal oxidation along the splat boundary

Uppermost scale rich in oxides of Ni, Cr, Al and NiCr$_2$O$_4$

Ni rich splat in unoxidised condition

Fe^{3+} Substrate   Fe^{3+}
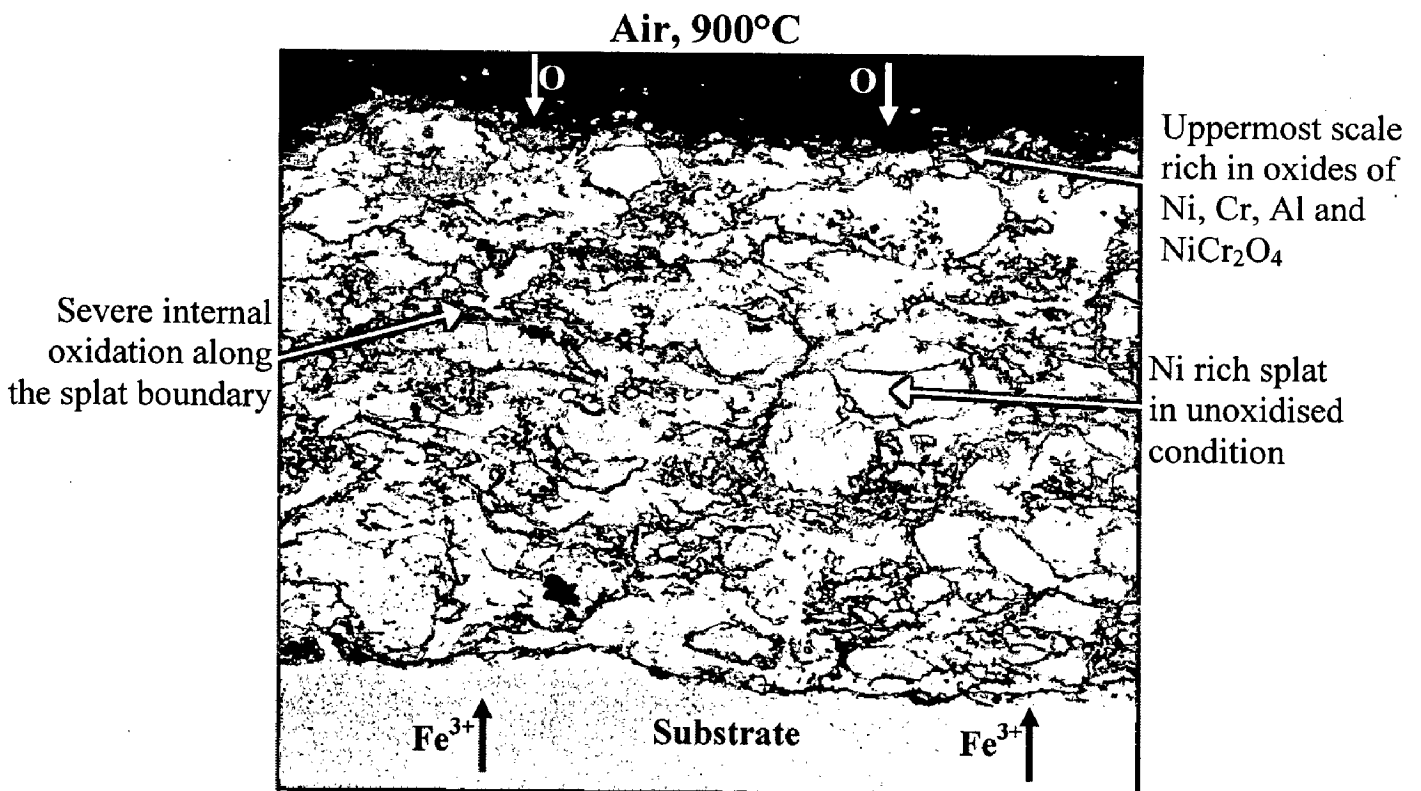
Fig.5.50   General oxidation mode of NiAlCrFeMo coated steels exposed to air for 50 cycles at 900°C

135

of formation of amorphous SiO_2 oxide scale using the energy dispersive X-ray micro analysis results during the oxidation of Ni-Si coatings and alloys. Lowell (1973) has identified the silicon as cristobalite at 1200°C and an amorphous discontinuous layer at 1100°C while studying the ternary system Ni-20Cr-3Si under cyclic and isothermal conditions. The mechanism of scale formation during the oxidation of Ni-Cr-Si alloy has been proposed by Rapp (1965) in three steps. Initially, an external scale is formed consisting of NiO and SiO_2 with Cr_2O_3 precipitates at the grain boundaries. The formation of SiO_2 lowers the oxygen potential, promoting the lateral growth of Cr_2O_3 rather than nucleation. After completion of the Cr_2O_3 external scale, more stable binary oxide formation replaces ternary oxides such as $NiCr_2O_4$ or Ni_2SiO_4, which have formed during the intermediate stages of oxidation. Grunling et al. (1982) suggested that SiO_2 affords a better protection than that of Cr_2O_3 scales which, in addition, becomes susceptible to vaporization loss via CrO_3 at a temperature of about 1000°C.

The investigations on the oxidation of Ni-Si based alloys as reported by Wu et al. (2005), Grunling et al. (1982) and Douglass et al. (1987) illustrate that at 1000°C, critical Si concentration is needed to form SiO_2 layer that ranges between 4-6 wt%. Further, Fitzer et al. (1978) have postulated that chromium can be replaced by half of the equivalent amount of silicon to maintain sufficient oxidation resistance for nickel based alloys. In the present study, 4.3% Si in the coating composition might have resulted in formation of silica oxide when oxidized coating at 900°C.

As the solid solubility of silicon in NiO is low, the inward-growing NiO rejects silicon and the slow diffusion of silicon in the alloy prevents back diffusion to eliminate the gradient. A build up of silicon occurs, eventually, giving rise to a displacement reaction (Douglass et al., 1987):

$$Si + 2NiO = SiO_2 + 2Ni$$
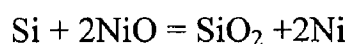
The above process occurs more rapidly at high temperatures. This means that a protective glassy film of silica forms rapidly during the present oxidation studies at 900°C. Fig. 5.33 shows a transient stage of oxidation where rapid weight gain of the coating has been observed in the initial oxidation period up to 10 cycles of study due to the formation of oxides of each and every active element present in the coating. Thereafter, the oxidation rate drops drastically due to the formation of glassy SiO_2 and Cr_2O_3 layer. Furthermore, the X-ray mapping for silicon shows that the silicon depletion region is just above the coating-substrate interface. This reveals the oxidation of Si at the

oxide-gas interface by the outward cation migration. The X-ray diffraction peaks for Ni, Ni_3B and Ni_3Si were more intense than NiO which implies a limited oxidation of Ni.

The surface EDAX analysis of the oxide scale reveals the presence of a small amount of B, and considering the earlier findings as reported by Wu et al. (2006), Grunling et al. (1982) and Hurricks (1972), the existence of SiO_2-B_2O_3 glass scale may be expected on the surface of the oxidized coating. SiO_2-B_2O_3 can improve the spalling resistance of the oxide scale due to its higher thermal expansion coefficients and lower softening temperature. Stronger evidence is necessary to confirm the existence of SiO_2-B_2O_3 in the oxide layer.

From the thermogravimetry data, the weight gain of NiCrFeSiB coated GrA1, T11 and T22 steels are much lower than that of the respective uncoated steels as reported in Section 5.1.1.1. Furthermore, the coated steels follow the parabolic rate law of oxidation up to 50 cycles and the parabolic rate constant (K_p) values are lower in comparison to the uncoated steels. Hence, it can be inferred that NiCrFeSiB coatings are successful in protecting the steels from the accelerated oxidation to a considerable extent. Kerr (1975) has reported that a significant drop in the parabolic oxidation rate was found with Ni-Cr alloys when silicon was added at low chromium concentrations. Si and B, which are distributed at the grain boundary, hinder the diffusion of Fe and Mo from the substrate into the coating along the grain boundary. A thick diffusion band has been observed at the substrate-coating interface (Figs. 5.37 and 5.38) which may be attributed to restricted inter-diffusion of Ni and Fe between coating and substrate, there by resulting in better bonding of coating and substrate. Fig 5.51 shows the general oxidation mode for NiCrFeSiB coatings subjected to oxidation in static air for 50 cycles at 900°C.

5.3.5 WC-Co/NiCrFeSiB coating

Thin oxide layer on the external surface of the oxidized coating, mainly composed of protective oxides of Si, Cr and Co has been identified with the help of EPMA analysis (Fig.5.47 and 5.48) and compositional EDAX analysis (Fig.5.44 to 5.46). Further XRD analysis on the outer surface confirms the presence of chromium oxide and not showed peaks corresponds to SiO_2. However EDAX and EPMA analysis confirm the existence of Si-related oxide phase, which should be present as amorphous SiO_2 on the surface of oxidized coating. Yu et al., (2007), Douglass et al., (1987), Wu et al., (2005) have

reported the possibility of formation of amorphous SiO_2 oxide scale using energy dispersive X-ray micro analysis results during oxidation of Ni-Si coatings and alloys. XRD analysis also revealed the presence of mixed spinel type oxides of $CoCr_2O_4$, Co_2SiO_4 and $NiCr_2O_4$, further corroborated by the EDAX analysis on the oxide scale which shows the higher content of oxides of Si, Co and Cr. Luthra (1985) proposed that the formation of spinel $CoCr_2O_4$ in top scales may block the diffusion activities through the cobalt oxide (CoO) by suppressing the further formation of CoO, thereby increases the oxidation resistance of alloys. Further $CoCr_2O_4$ have thermal conductivities two orders of magnitude higher than Cr_2O_3 at 800°C (Deng et al. 2006). EDAX and EPMA analysis across the cross section suggest that oxidation has been restricted only to the external surface up to few microns and rest of the coating below the protective oxide layer formed remains unoxidised. Oxygen has not penetrated into the substrate steel, which further indicates that the protective oxides of Cr, Si, Co, Ni and their spinel oxides acts as diffusion barrier to the transportation of oxidizing species into the inside of coating. Hence coating provides necessary protection to the substrate steel.

The oxidation kinetics shows weight loss during the early cycles of oxidation studies probably due to evaporation of W-oxides (WO_3) in the absence of adequate protective oxide layer. Tungsten having a higher affinity for oxygen is preferentially oxidized as WO_x in the initial stage of oxidation (Espevik et al. 1980). The protective oxide layer of SiO_2 and Cr_2O_3 formed with the subsequent oxidation cycle, stabilize the formation of volatile tungsten oxide. Similar results of weight loss caused by the evaporation of tungsten oxide during high temperature oxidation of tungsten based coatings and alloys have been reported by Sidhu et al.(2006G), Wang et al. (2002B) and Lee et al. (2005). Espevik et al. (1980) suggested that the presence of tungsten in the alloy does not necessarily lead to the breakaway, catastrophic oxidation resulting from the formation of WO_3 liquid or vapor. Further they observed protective kinetics for Ni-Cr-3W ternary alloy oxidized at high temperature of 1250°C.

In case of coated T22 steel, dark grey color protrusions are observed after 26th cycle of oxidation studies which coincides with the increased weight gain plotted in Fig.5.40. The EDAX analysis revealed that these protrusions are mainly iron oxide. The probable cause of oozing out of iron oxide might be attributed to the presence of

molybdenum in the substrate steel. MoO_2 and MoO_3 have low melting points and also are liable to sublimate directly at more than 800°C. This gas due to increased volume, induce stress and leads to crack. Further thermal expansion mismatch among the nickel-rich splats and WC particles also generate cracks in the coating. These volatile oxides and iron oxide ooze outward through cracks due to greater specific volume. T11 steel has not showed the cracks similar to one observed for T22 Steel and this might be attributed to the smaller content of molybdenum in T11 steels. Similar iron oxide protrusions formed during oxidation of plasma sprayed stellite-6 coatings on T22 steels at 900°C have been reported by Sidhu et al. (2005B). WC-Co/NiCrFeSiB coated GrA1 and T11 steels have not showed any cracks or protrusions on the surface and weight gain values are not very different relative to each other.

HVOF sprayed WC-Co/NiCrFeSiB coated steels shows much lower weight gain in comparison to uncoated steels as reported in section 5.1.1.1. Weight gain at the end of 50 cycles of oxidation studies for WC-Co/NiCrFeSiB coated GrA1, T11 and T22 Steels are only 0.66%, 1.04% and 1.45% respectively than that of similar uncoated steels. Further oxidation kinetics of all the coated steel can be approximated to by parabolic rate law, which signifies necessary protection has been provided by the WC-Co/NiCrFeSiB coatings to the substrate steel. Fig.5.52 shows the overall view of oxidation mode for WC-Co/NiCrFeSiB coatings exposed to air at 900°C for 50 cycles.
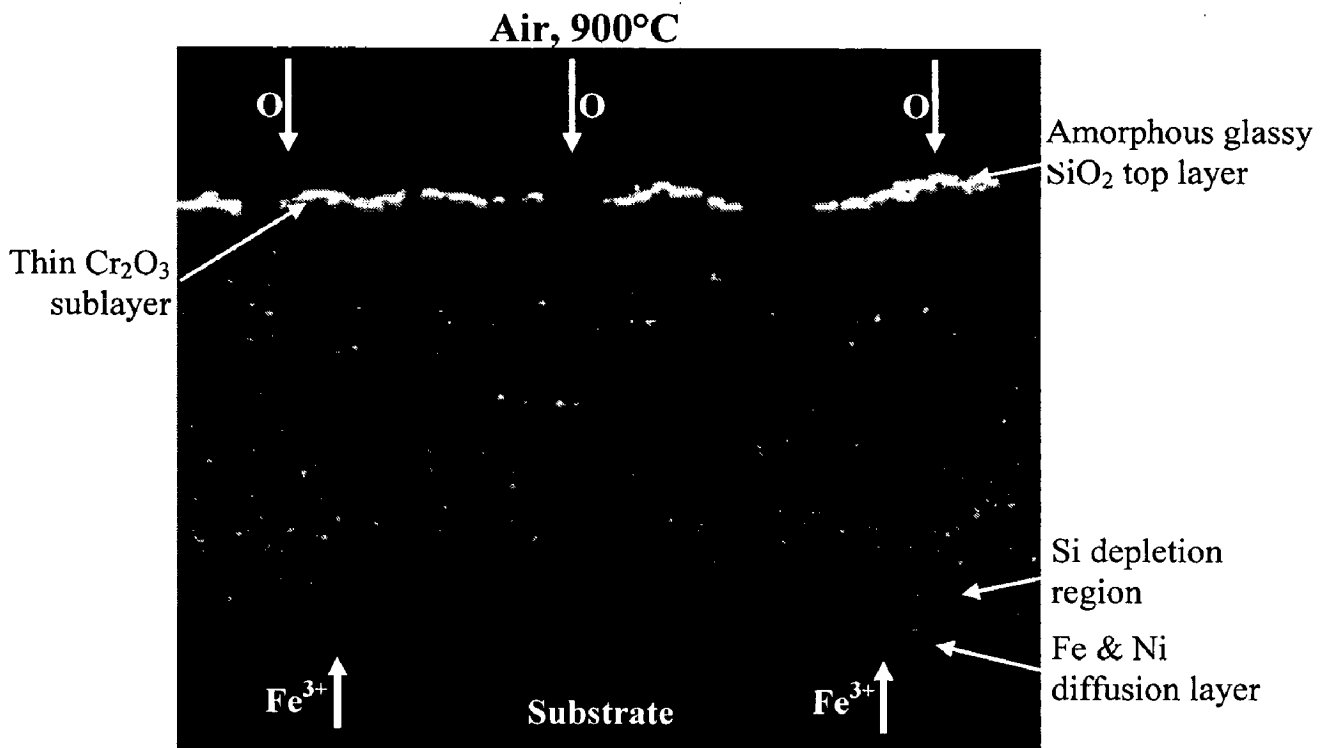
Fig. 5.51   General oxidation mode of NiCrFeSiB coated steels exposed to air for 50 cycles at 900°C
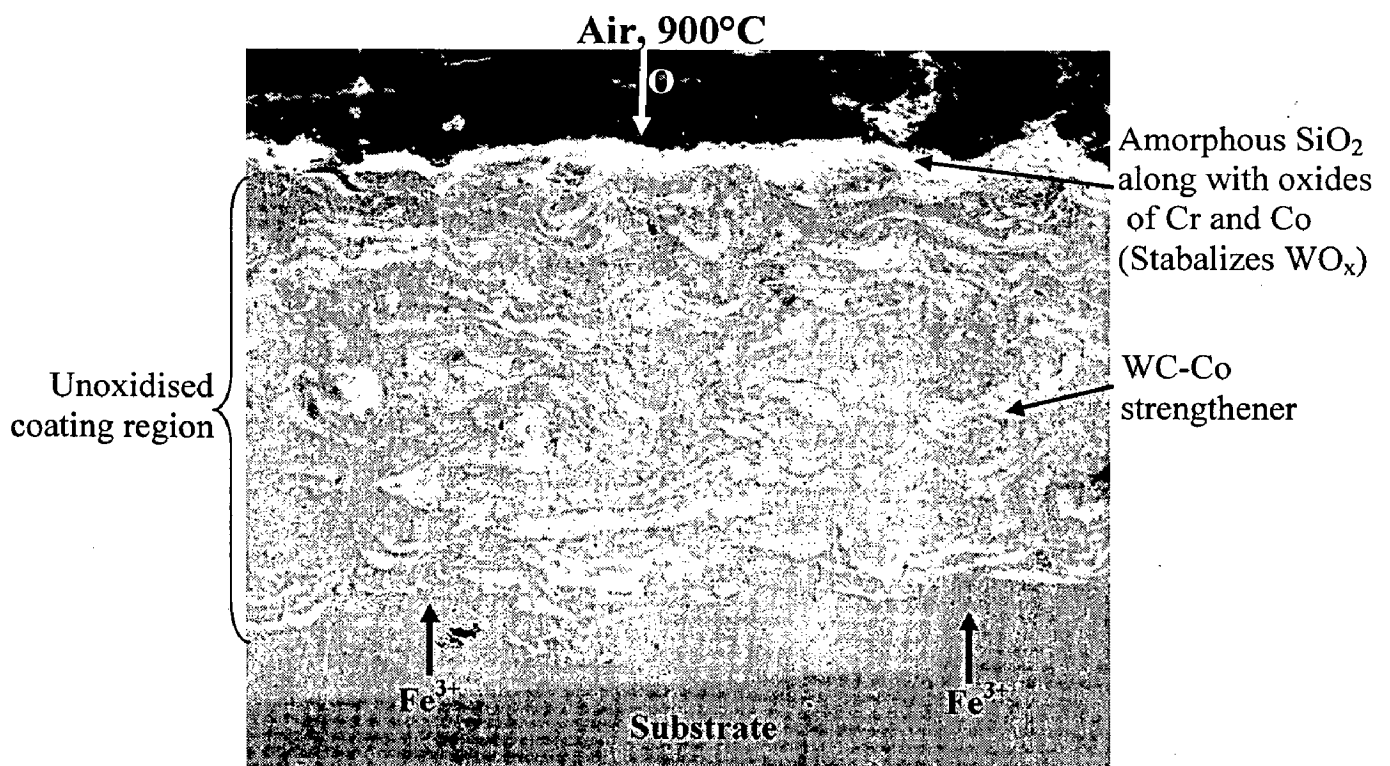
Fig. 5.52   General oxidation mode of WC-Co/NiCrFeSiB coated steels exposed to air for 50 cycles at 900°C

5.4 COMPARATIVE DISCUSSION

The cumulative weight gain (mg/cm^2) for uncoated and HVOF coated steels subjected to cyclic oxidation in air for 50 cycles at 900°C is shown in Fig.5.53. In general, it is evident from the bar chart that the weight gains for all the HVOF coated steels are considerably lower than that of uncoated steels. All the uncoated steels suffered intense spalling of oxide scale. The massive oxide scale formed on all the bare steels mainly consisted of iron oxide. The stresses developed due to higher volume of oxide scale leads to cracks, further these cracks help in internal oxidation and spalling of scale. Based on the thermogravimetric data, the relative oxidation resistance of the various coating under study can be arranged in the following sequence:

NiCrFeSiB > WC-Co/NiCrFeSiB > NiCrAl > NiAlCrFeMo

The superior performance of NiCrFeSiB coating is mainly attributed to continuous and protective thin oxide scale of amorphous glassy SiO$_2$ and Cr$_2$O$_3$ formed on the surface of the oxidized coatings. Build up of silicon oxide scale is more rapid at 900°C and it must be acting as a barrier to the oxygen transport to the inside of coating. Hence only a thin layer of oxides can be observed and the coating region beneath this oxide scale remains unoxidised. This is supported by the rapid weight gain observed during the initial oxidation cycles. X-ray mapping for silicon (Fig.5.37 & 38) shows silicon depletion region just above the coating-substrate interface which reveal oxidation of Si at the oxide-gas interface by outward cation migration. Hence 4.3% Si in the coating can be considered as the critical concentration to maintain sufficient oxidation resistance of the present coating. The oxidation kinetics of NiCrFeSiB coated GrA1, T11 and T22 steels follow the parabolic rate law upto 50 cycles and parabolic rate constant (K$_p$) values are much lower in comparison to uncoated steels and other coatings under study. Si and B present in the coating might have hindered the diffusion of Fe and Mo from substrate into the coating.

Resistance to oxidation in case of WC-Co/NiCrFeSiB coated steels are due to oxides and spinels of Si, Cr and Co formed into thin scale on the surface. EDAX and EPMA analysis confirm the presence of discontinuous scale of amorphous SiO$_2$ on the surface of oxidized coatings. This protective oxide scale stabilized the formation of volatile tungsten oxide. Oxidation has been restricted only to the external surface up to a depth of few microns and rest of the coating remains unoxidised. Further oxidation

kinetics of all the coated steel can be approximated by parabolic rate law. In case of Coated T22 steels, iron oxide protrusions are observed after 26th cycle of oxidation studied. The probable cause of oozing out of iron oxide might be attributed to the presence of molybdenum in the T22 steel substrate and is discussed in detail under section 5.3.5.

The protection offered by NiCrAl coatings can be attributed to the oxide layer of α-Al_2O_3 and Cr_2O_3 formed on the outermost surface. α-Al_2O_3 is thermodynamically stable phase having nearly close packed corundum structure and shows slow scale growth kinetics during oxidation (Zhenyu, 1998). Aluminum in coating will oxidize before Cr and Ni due to relatively high negative free energy of formation of oxide. Further $AlNi_3$ (segregated during HVOF spraying) could have restricted the diffusivity of Al and hence supports formation of continuous α-Al_2O_3, by holding larger Al and slowing down the reaction. Relatively higher weight gain observed for NiCrAl coated steels in comparison to NiCrFeSiB and WC-Co/NiCrFeSiB coated steels might be ascribed to the preferential oxidation of Al and Cr along the nickel rich splat boundary during the initial stage of oxidation. With further oxidation, formation of protective α-Al_2O_3 on the surface along with oxides at splat boundary block the transport of oxygen into the coating and thereby making the oxidation rate to reach steady state. The oxidation behavior of coated GrA1 and T11 steels is parabolic in nature where as coated T22 steels showed perceptible deviation from the parabolic rate law which might be attributed to iron oxide protrusions observed on the surface. The reason for oozing out of iron oxide in case of coated T22 steels are discussed in detail under the section 5.3.2.

NiAlCrFeMo coated steels show fairly higher weight gain as compared to other coated steels under study. This may be attributed, to some extent, to severe internal oxidation along the splat boundary. During the early stage of oxidation, oxidant atmosphere penetrates into the coatings through open porosity (porosity in NiAlCrFeMo coating is higher than other coatings under study) until all the accessible internal surfaces have been oxidized. Subsequently the oxidation phenomenon takes place only on the outer surface of the coating due to formation of protective oxide layer. Oxides of aluminum, chromium, iron and molybdenum have been revealed along the nickel rich splat boundary. The outermost oxide scale mainly composed of oxides of nickel, chromium and aluminum. Iron oxide protrusions have been observed on the surface of coated T11 and T22 steels. The oxide protrusions are more pronounce in coated T22 steel in comparison to T11 steel. The extent of oxide protrusions observed on the surface and the oxidation rate seems to be related to the Mo content in the base steel. The oxidation kinetics for coated T22 steel followed linear behavior.
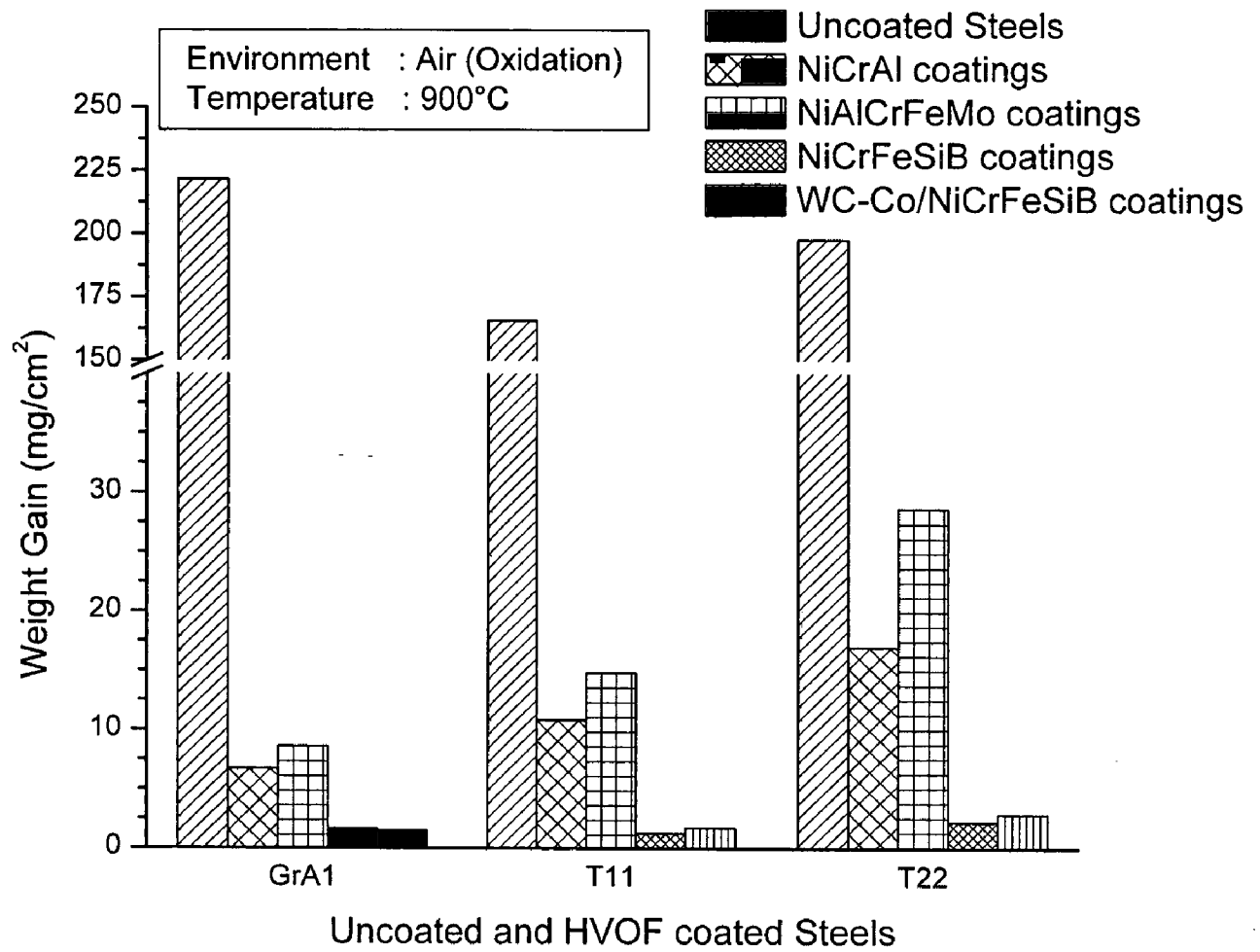
Fig.5.53   Bar chart showing cumulative weight gain (mg/cm²) for uncoated and HVOF coated steels subjected to cyclic oxidation in air for 50 cycles at 900°C

CHAPTER 6

HOT CORROSION STUDIES
IN MOLTEN SALT ENVIRONMENT

This chapter describes the hot corrosion behavior of the HVOF coated as well as the uncoated steels in an aggressive environment of molten salt (Na_2SO_4-60%V_2O_5) at 900°C under cyclic conditions. The specimens were visually examined at the end of each cycle during the course of study. The reaction rate and kinetics have been studied by means of thermogravimetry. The identification and structural investigation of reaction products of the corroded specimens are made by means of the XRD, SEM/EDAX, and EPMA techniques. The results are compiled in different sections of this chapter to evaluate the performance of each coating.

6.1   RESULTS

6.1.1   Uncoated Steels

6.1.1.1 Thermo gravimetric studies

The macrographs of GrA1, T11 and T22 steels subjected to hot corrosion in Na_2SO_4-60%V_2O_5 molten salt for 50 cycles at 900°C are shown in Fig. 6.1. It can be observed in Fig. 6.1 that there is an intense spalling of oxide scale for the T22 steel and after eighth cycle the scale starts separating from the substrate. For the GrA1 steel, the exfoliation of the oxide scale was observed from the 35th cycle onwards.

The plots of cumulative weight gain (mg/cm^2) as a function of time expressed in number of cycles are shown in Fig. 6.2. The weight gain for the GrA1, T11 and T22 steels at the end of 50 cycles are found to be 223.79, 200.91, and 428.12, respectively. Evidently, the T22 steel showed a maximum weight gain during the hot corrosion studies in molten salt environment as compared to the GrA1 and T11 steels, which is more than double the weight gain value for T22 subjected to oxidation in air at the same temperature (as reported in Chapter 5). Further, the weight gain square (mg^2/cm^4) data is plotted as a function of time in Fig. 6.3. The plot shows an observable deviation from the parabolic rate law for the T22 steel, which indicates that the oxide scale is not very protective in molten salt environment. It is evident from the plot that the GrA1 and T11

144

follow parabolic behaviour. The parabolic rate constants, K_p, for the GrA1, T11 and T22 steels are 28.41 x10^{-8}, 23.18 x10^{-8} and 118.33x10^{-8} g^2 cm^{-4} s^{-1}, respectively.

6.1.1.2 X-ray Diffraction Analysis

The X-ray diffraction patterns of the upper oxide scale, after its exposure to the molten salt environment at 900°C for 50 cycles are shown in Fig. 6.4. The oxide scale on all the steels under study consisted of Fe_2O_3 as a main constituent along with iron sulphide. The T11 and T22 steels showed the presence of Cr_2O_3 and $CrVO_3$ in the oxide scale.

6.1.1.3 SEM/EDAX Analysis

The SEM micrograph showing the scale morphology along with the EDAX analysis is illustrated in Fig. 6.5. Iron oxide was the main constituent of the outer layer of all the steels. The surface scale, in case of the T11 and T22 steels show intergranular cracking. Figure 6.6 shows the BSEI taken along the cross section of the oxidized samples. The EDAX point analysis (Fig. 6.6c) along the cross section of T22 steel shows that, throughout the scale thickness, the major constituent is iron oxide along with a small amount of Cr_2O_3.

6.1.1.4 EPMA Analysis

The BSEI and X-ray mappings along the cross section of oxide scale of T22 steels after hot corrosion for 50 cycles at 900^{0}C are shown in Fig. 6.7. The oxide scale mainly contains iron oxide as seen in the mappings for iron and oxygen. The inner layer of the scale contains a continuous layer of chromium oxide and streaks of molybdenum. The mapping for vanadium shows a distribution over a broad region of the outer layer. Furthermore, sodium seems to be homogeneous throughout the cross section.

6.1.2 NiCrAl Coating

6.1.2.1 Thermo gravimetric studies

The macrographs of the HVOF sprayed NiCrAl coatings on the GrA1, T11 and T22 steels subjected to hot corrosion in Na_2SO_4-60%V_2O_5 environment for 50 cycles at 900°C are demonstrated in Fig. 6.8. The color of the as-sprayed coating was dark grey which turned into black during the first cycle of exposure to salt environment. During the
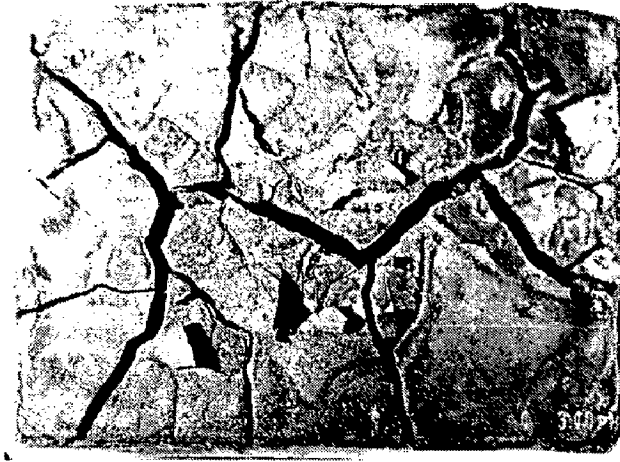
(a)
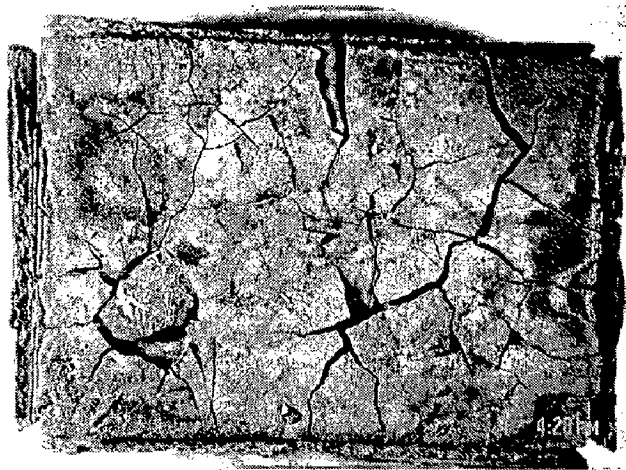
(b)
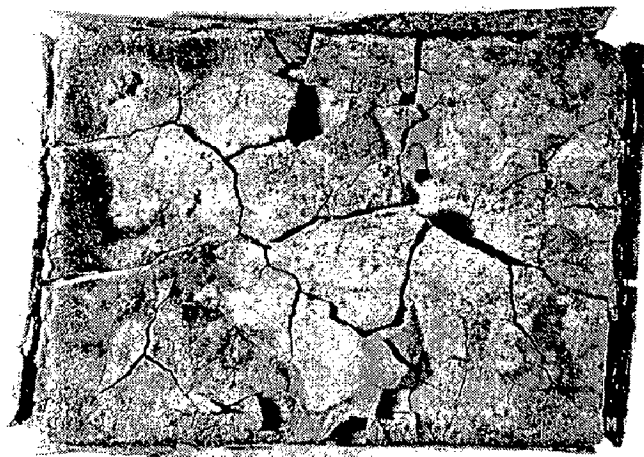
(c)

Fig.6.1   Macrograph of uncoated steel subjected to hot corrosion in Na2So4-
60%V2O5 at 900°C for 50 cycles:
(a) GrA1 steel   (b) T11 steel   (c) T22 steel
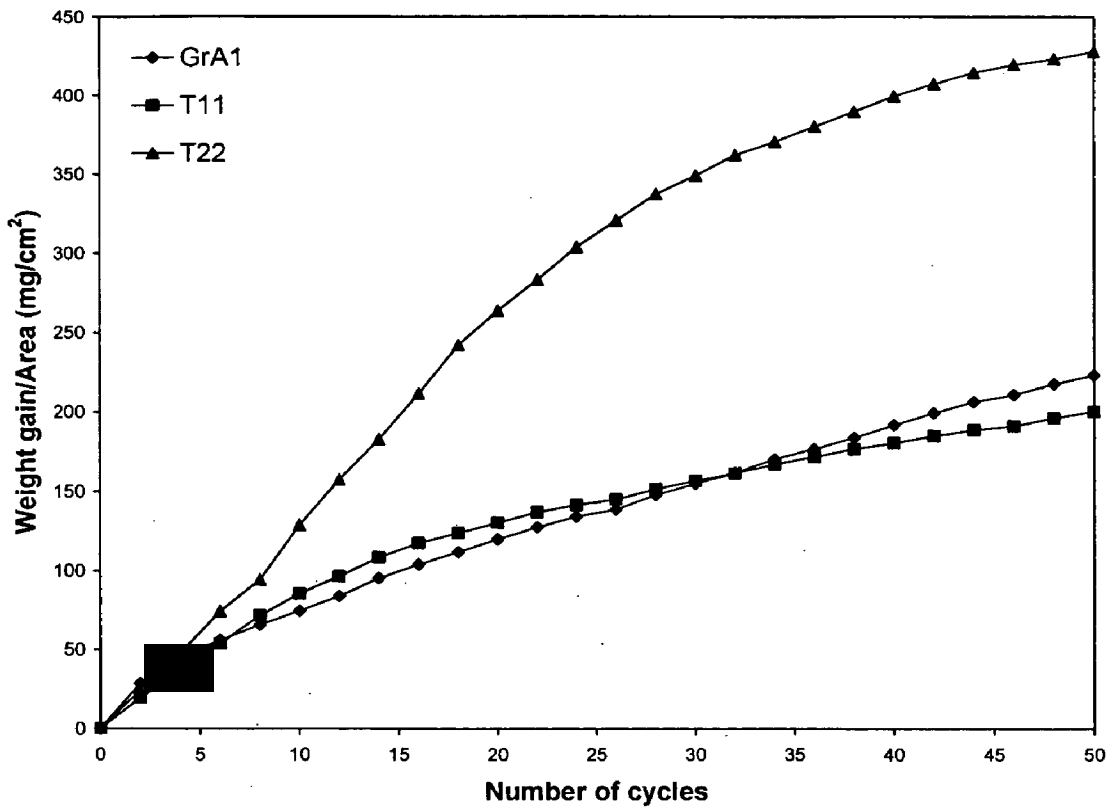
Fig.6.2   Weight change versus. number of cycles plot for uncoated steels subjected to hot corrosion for 50 cycles in Na_2SO_4-60% V_2O_5 environment at 900°C
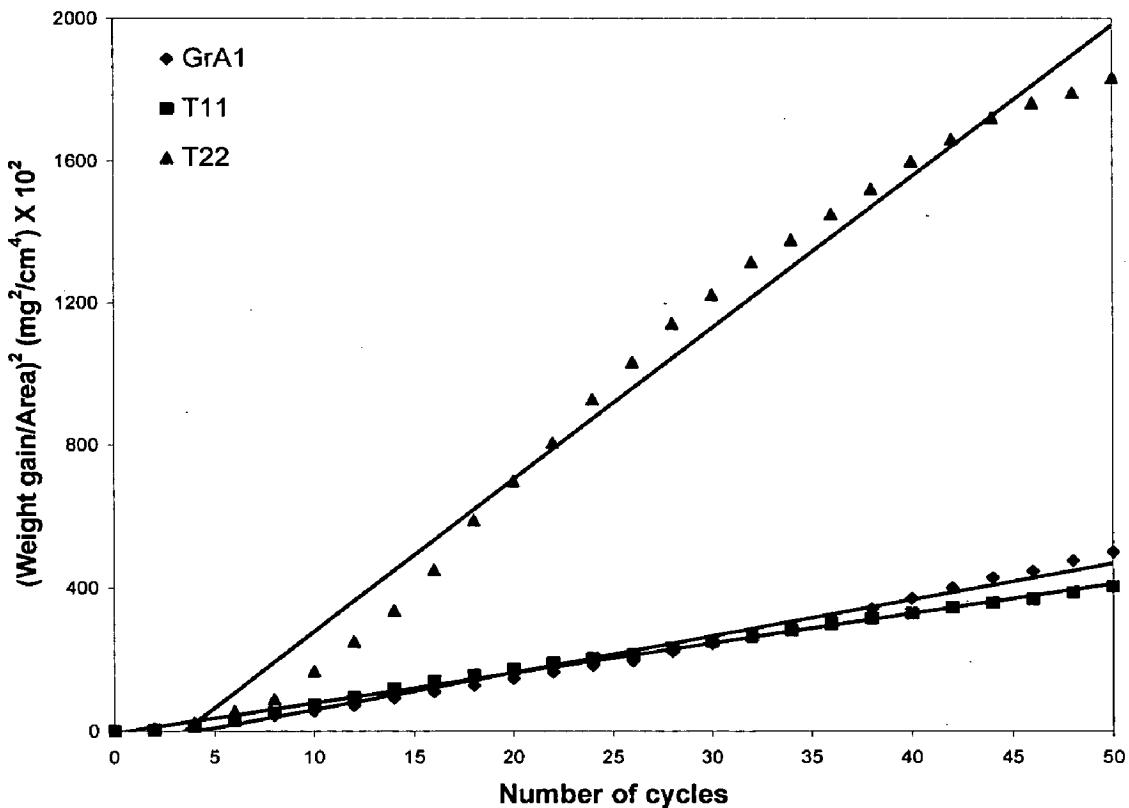
Fig.6.3   (Weight change/area)^2 vs. number of cycles plot for uncoated steels subjected to hot corrosion for 50 cycles in Na_2SO_4-60% V_2O_5 environment at 900°C
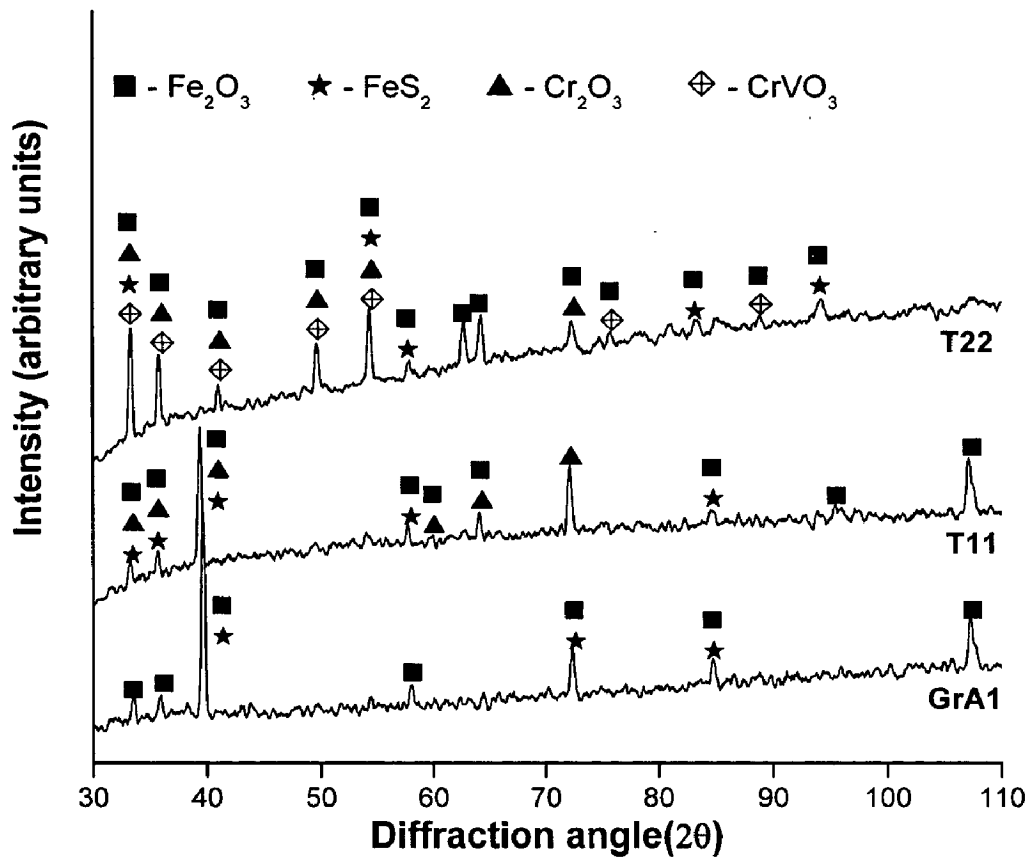
Fig. 6.4 X-ray diffraction patterns for the boiler steels subjected to hot corrosion for 50 cycles in Na_2SO_4-60%V_2O_5 environment at 900°C

94.34 % Fe_2O_3
05.41 % SO_3

(a)

93.04 % Fe_2O_3
04.50 % SO_3
01.10 % Cr_2O_3

(b)

97.51 % Fe_2O_3
01.52 % Cr_2O_3

(c)

Fig.6.5   Surface scale morphology and EDAX area analysis for the uncoated steels subjected to hot corrosion in Na_2SO_4-60%V_2O_5 environment at 900°C for 50 cycles:

(a) GrA1 Steel   (b) T11 Steel   (c) T22 Steel

149
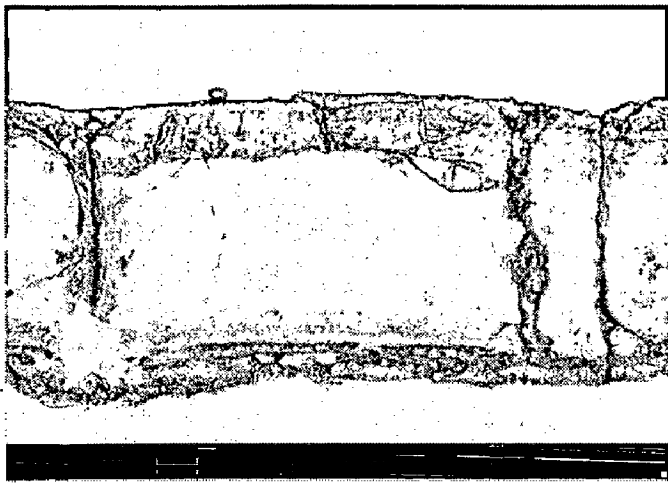
(a)
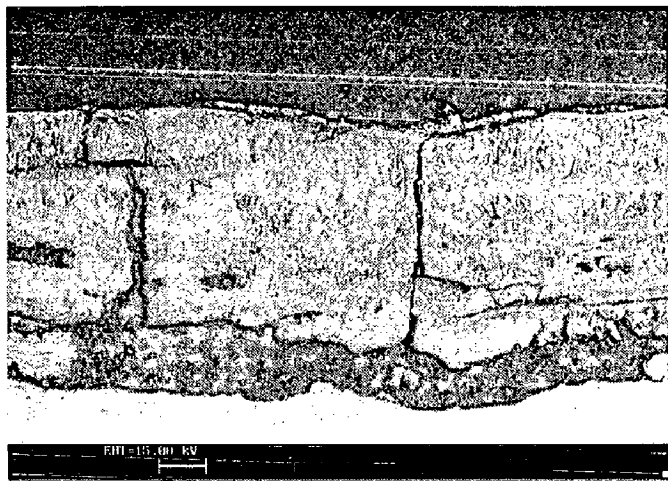
(b)
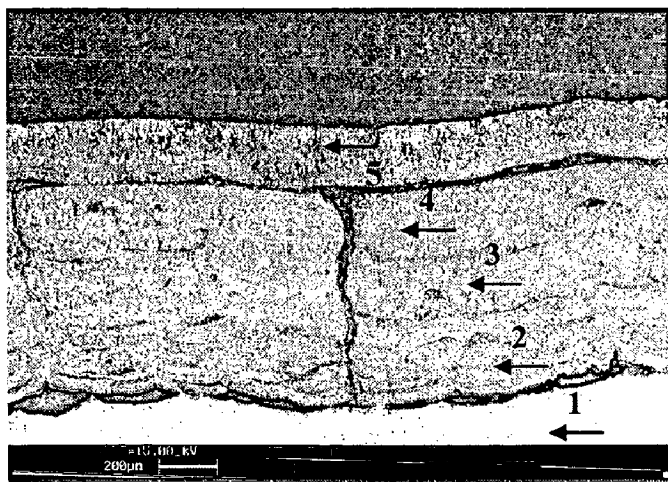
(c)
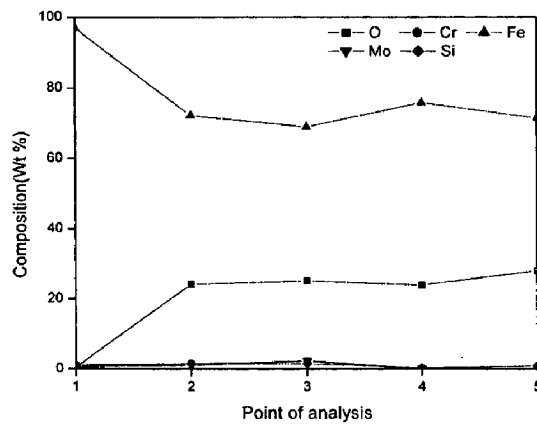
(d)

Fig.6.6   Back scattered images for the uncoated steels subjected to hot corrosion in
Na₂SO₄-60%V₂O₅ envirnoment at 900°C for 50 cycles
(a) GrA1 Steel   (b) T11 Steel   (c) T22 Steel
(d) EDAX point analysis along the cross-section of T22 steel

150
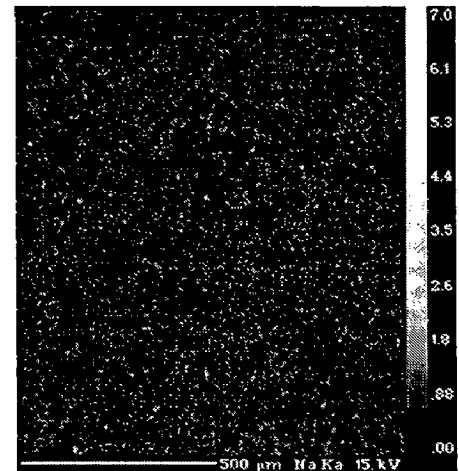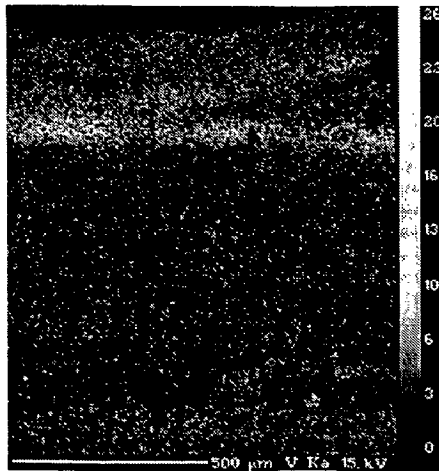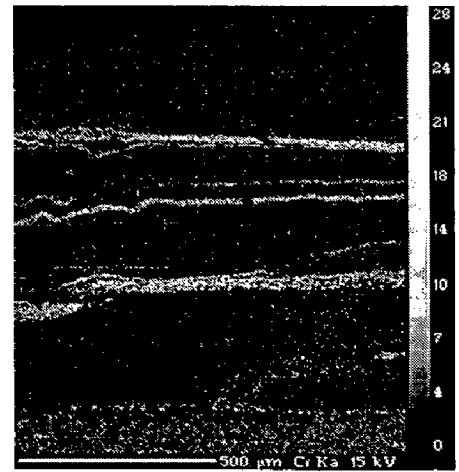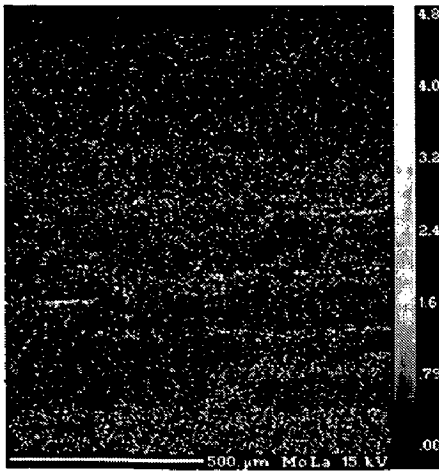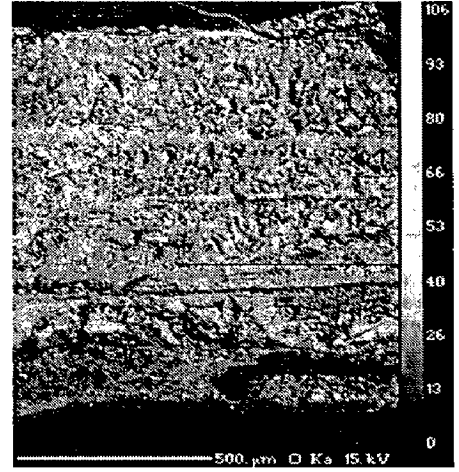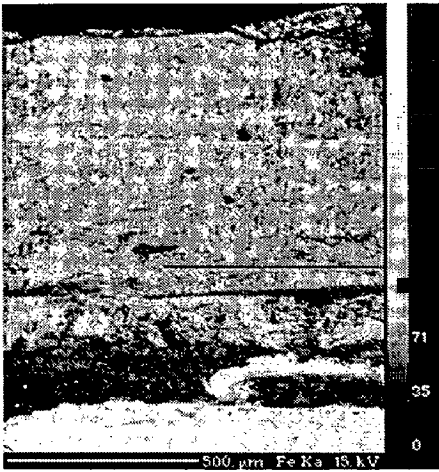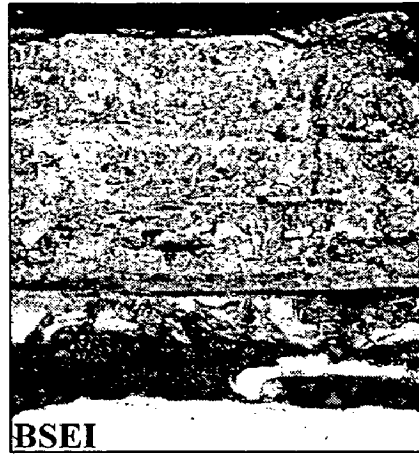
Fig.6.7 WDS X-ray mapping across the cross-section of the T22 steel subjected to hot corrosion in Na_2SO_4-60%V_2O_5 environment at 900°C for 50 cycles
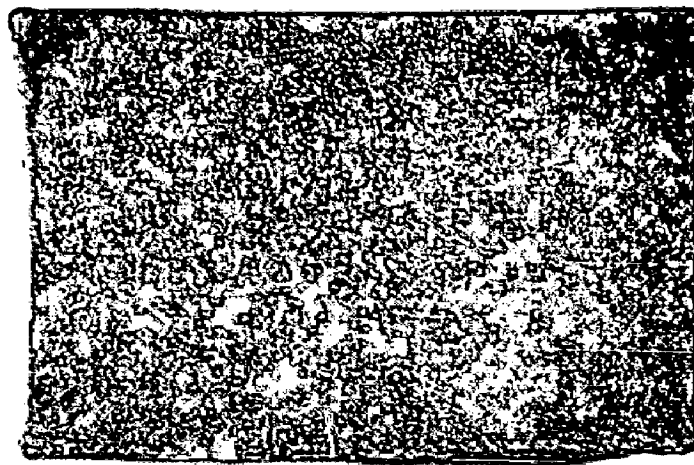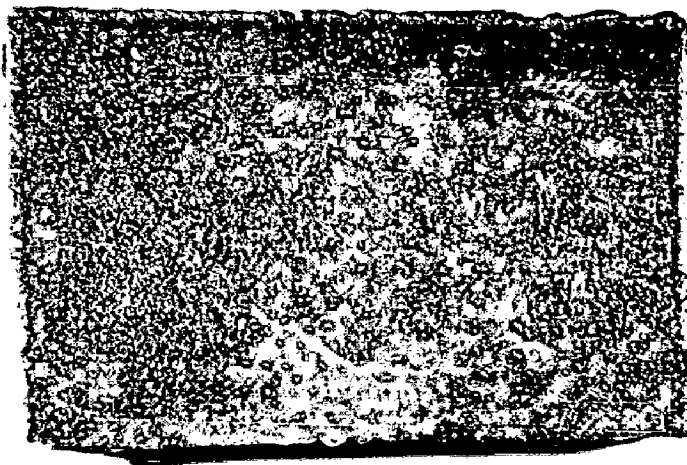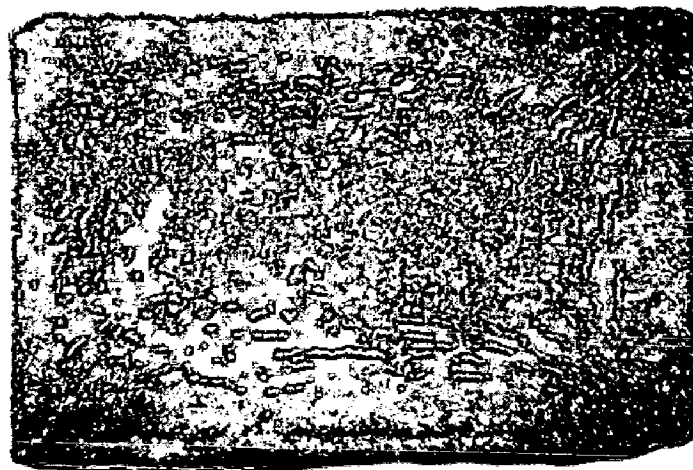
Fig.6.8 Macrographs of the NiCrAl coating subjected to hot corrosion in Na_2SO_4-60%V_2O_5 environment for 50 cycles at 900°C:
(a) GrA1 steel   (b) T11 steel   (c) T22 steel

17th cycle, the color of oxide scale turned into dark grey with tinges of green color appearing on the surface. These green tinges increased with the progress of oxidation, and at the end of 50 cycles, a greenish dark grey colored scale was observed. In case of the NiCrAl coated T22 steels, protrusions were seen after the 41st cycle on the surface of the corroded samples. These protrusions are of dark grey in color.

The plots of cumulative weight gain (mg/cm^2) as a function of time expressed in number of cycles are shown in Fig. 6.9. The values of overall weight gain after 50 cycles of hot corrosion for the NiCrAl coated GrA1, T11 and T22 steels are found to be 19.28, 26.14 and 30.52 mg/cm^2, respectively. Evidently, the coated T22 steel showed a maximum weight gain. The coated GrA1 and T11 steels followed nearly the parabolic behavior up to 50 cycles as can be inferred from the weight gain square (mg^2/cm^4) data plotted as a function of time, as shown in Fig. 6.10, whereas the coated T22 steel shows a perceptible deviation from the parabolic rate law. The parabolic rate constants (K_p in 10^{-8} g^2 cm^{-4} s^{-1}) for the NiCrAl coated GrA1, T11 and T22 steels are 0.229, 0.419 and 0.549, respectively.

6.1.2.2 X-ray Diffraction Analysis

The X-ray diffraction pattern for NiCrAl coated steels after exposure to molten salt environment for 50 cycles is as shown in Figs.6.11 and 6.12. The XRD results reveal δ-Al_2O_3, θ-Al_2O_3, NiO, Cr_2O_3, $NiCr_2O_4$ and $NiAl_2O_4$ as major phases along with minor phases of $Ni_3V_2O_8$, $AlVO_4$ and $CrVO_4$. In case of coated T22 steel additional phase of Fe_2O_3 have been revealed.

6.1.2.3 SEM/EDAX Analysis

The SEM micrograph showing the scale morphology along with EDAX analysis at some selected sites of interest on the surface of the corroded NiCrAl coated steels are shown in Fig. 6.13. The oxide scale has a blade-like structure with smooth patches (Fig. 6.13a). The EDAX analysis on these patches indicates a higher percent of Al_2O_3 (i.e., 58.83%), While the matrix has relatively a higher amount of Cr_2O_3 and NiO, the blade-like structure could correspond to θ-Al_2O_3. The polyhedral crystals on the oxide scale of the coated T11 steel (Fig. 6.13b) correspond to a higher amount of NiO (i.e., 51.78%) along with a relatively lower content of Cr_2O_3 and Al_2O_3. While the matrix has

comparatively a higher percent of Cr_2O_3 (i.e., 61.24%). Minor amount of V_2O_5 and Na_2O are also indicated on the surface of the oxide scale.

The surface morphology of the coated T22 steels (Fig. 6.13c) shows worm-like protrusion which is oriented parallel to the edges of the coating. The EDAX analysis on this protrusion shows higher amount of Fe_2O_3, which might have oozed out from the substrate through the cracks developed during the hot corrosion studies.

Figure 6.14 shows the BSEI taken along the cross section of the corroded NiCrAl coated steels and the EDAX composition analysis at the site of interest. A continuous and adherent thick layer of scale has been observed on the top of the corroded coating. The thickness of this outermost oxide layer as measured from the BSEI image is in the range of 25-50 µm after 50 cycles of hot corrosion studies. The EDAX analysis across this oxide layer indicates mainly the presence of NiO and Cr_2O_3 along with a lower percent of Al_2O_3 (Points 1 and 2 in Figs. 6.14a and 6.14b; and point 1 in Fig. 6.14c). The white grains (Point 3 in Figs. 6.14a–6.14c) underneath the uppermost oxide layer in the microstructure of all the coated steels corresponds to the nickel-rich splats in an unoxidized state, as oxygen is absent at this point. The EDAX analysis shows the light grey phases formed at the boundaries of these splats (point 4) consisted of mainly Cr, Al, Ni and O, which reveals that internal oxidation has occurred along the splat boundary. The presence of minor amount of iron at the coating substrate interface (point 5) explains the diffusion of Fe into the coating.

6.1.2.4 EPMA Analysis

The BSEI and X-ray maps for the NiCrAl coated steels after exposure to Na_2SO_4-60%V_2O_5 environment for 50 cycles at 900°C are shown in Figs. 6.15 to 6.17. The corroded NiCrAl coated GrA1 steel (Fig. 6.15) illustrates the formation of a thick uppermost oxide layer which mainly consisted of Ni and Cr oxides. The combined mapping for Al and O reveals thin stringers of aluminum oxide on top of the oxide scale. Moreover, the presence of a minor amount of V and Na in the uppermost oxide layer confirms the formation of corrosion products. The mapping for the elements Al, Cr, and O clearly shows the selective oxidation of Al and Cr along the splat boundary. The nickel rich splats are in unoxidised condition. The observation into the coating-substrate interface reveals the diffusion of iron into the coating along with the diffusion of coating elements Ni, Cr, and Al into the substrate which helps in better bonding. The presence of
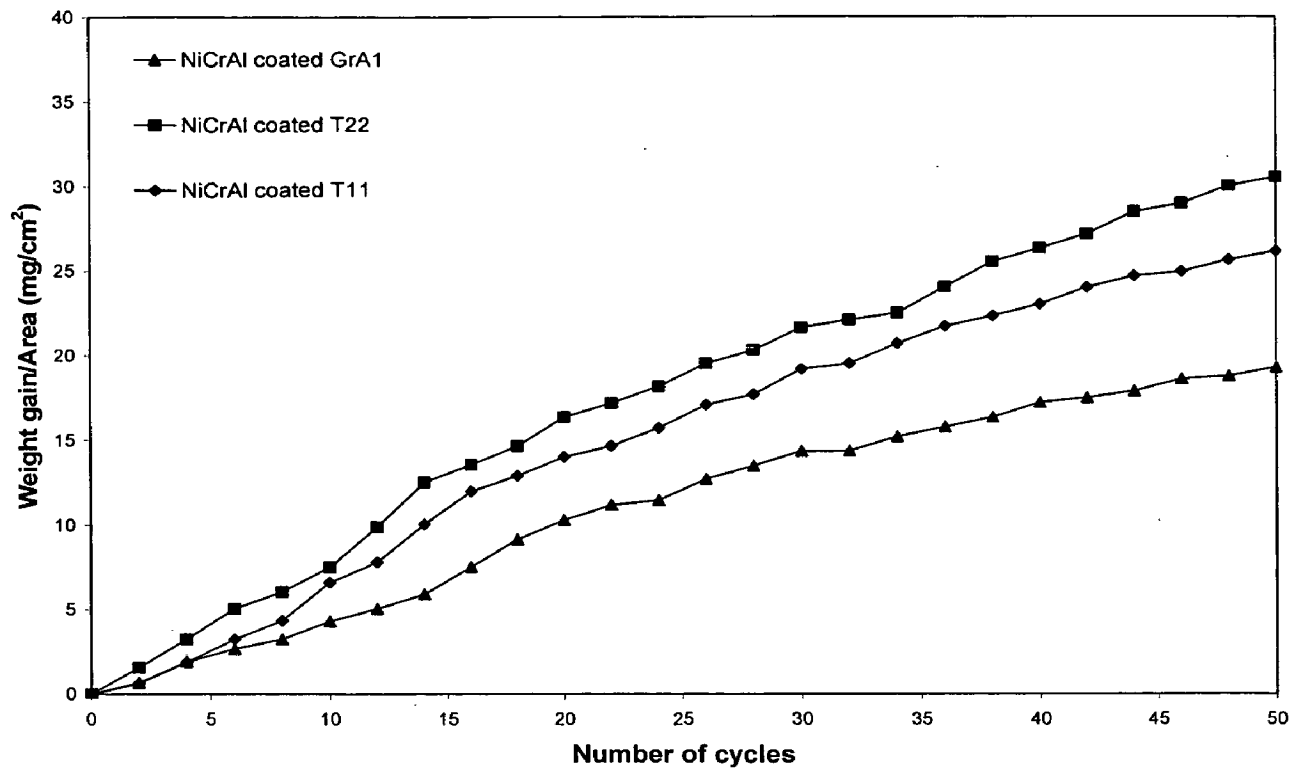
Fig.6.9 Weight gain versus number of cycles plot for NiCrAl coated steels subjected to hot Corrosion for 50 cycles in Na_2SO_4-60%V_2O_5 at 900°C
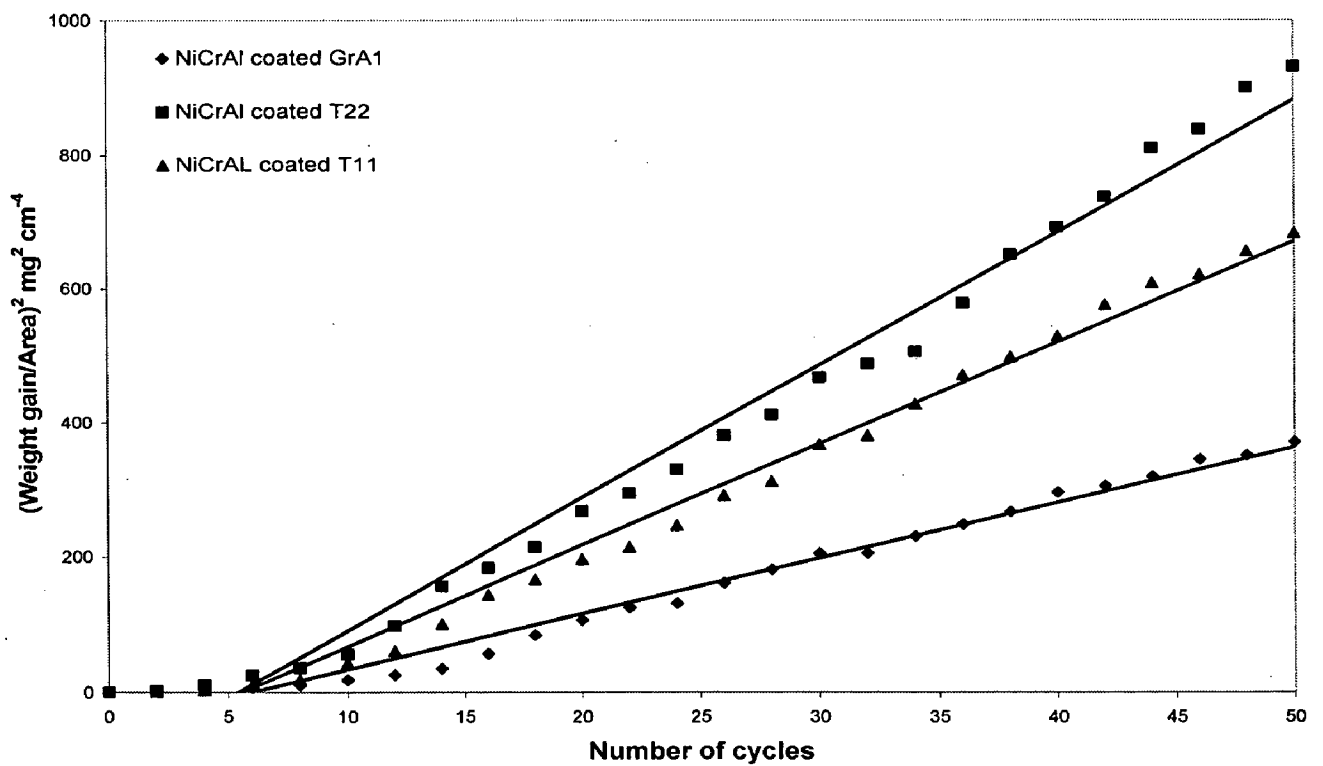
Fig.6.10 (Weight gain/area)^2 versus number of cycles plot for NiCrAl coated steels subjected to hot corrosion for 50 cycles in Na_2SO_4-60%V_2O_5 at 900°C

155
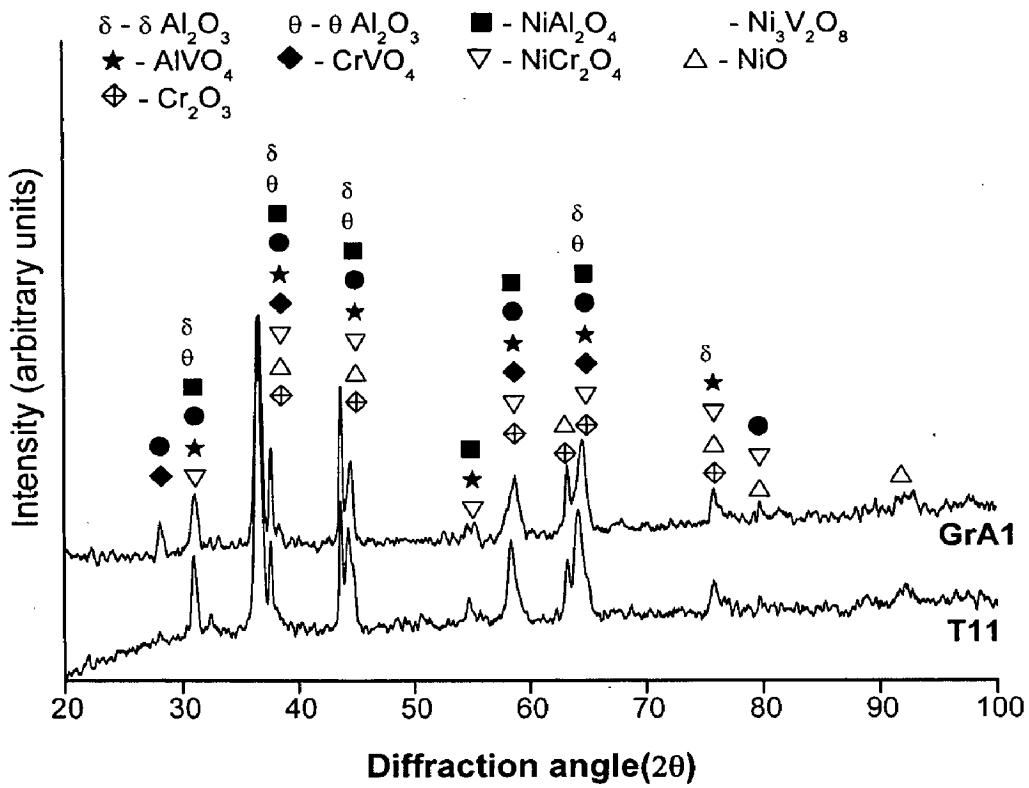
Fig.6.11   X-ray diffraction patterns for NiCrAl coated GrA1 and T11 steels subjected to hot corrosion in Na_2SO_4-60%V_2O_5 for 50 cycles at 900°C

Fig.6.12   X-ray diffraction patterns for NiCrAl coated T22 steels subjected to hot corrosion in Na_2SO_4-60%V_2O_5 for 50 cycles at 900°C

58.83% Al_2O_3
13.48% Cr_2O_3
19.72% NiO
04.58% Na_2O

09.01% Al_2O_3
48.91% Cr_2O_3
33.51% NiO
02.69% V_2O_5

(a)

02.62% Al_2O_3
61.24% Cr_2O_3
25.72% NiO
02.62% V_2O_5
01.49% Na_2O

05.11% Al_2O_3
37.05% Cr_2O_3
51.78% NiO

(b)

93.93% Fe_2O_3
02.20% Cr_2O_3
03.25% Na_2O

08.34% Al_2O_3
47.88% Cr_2O_3
39.04% NiO
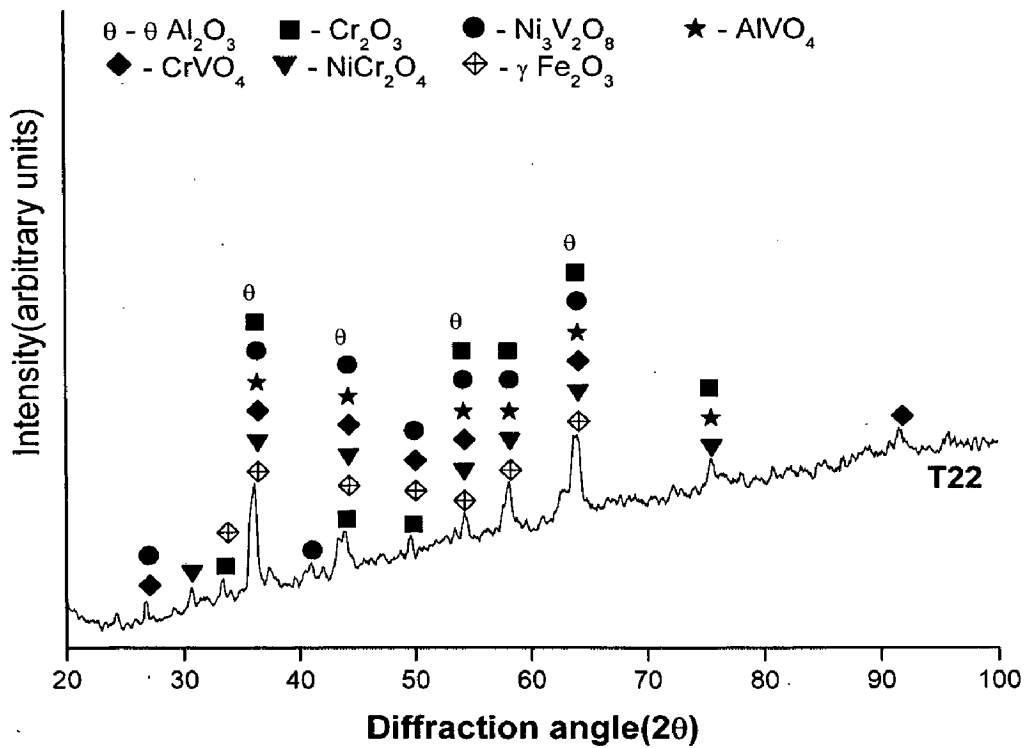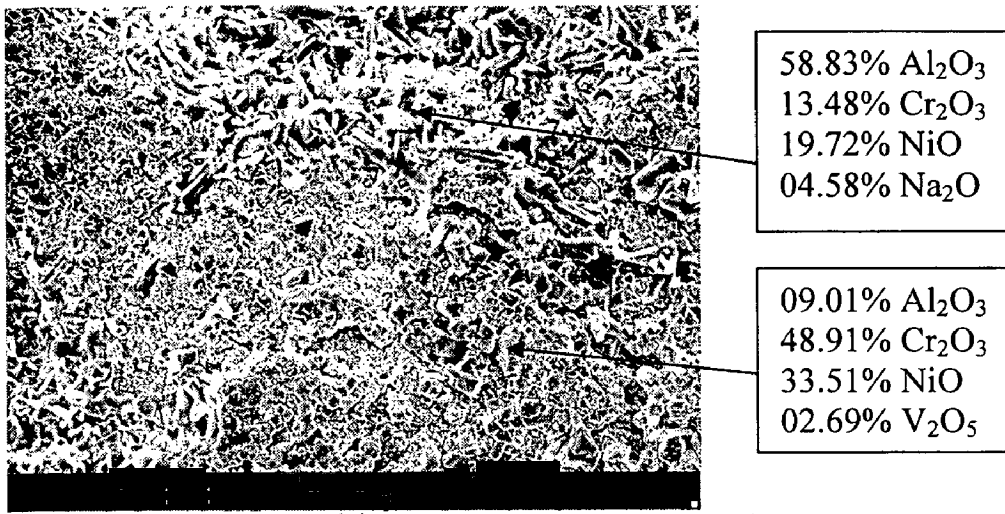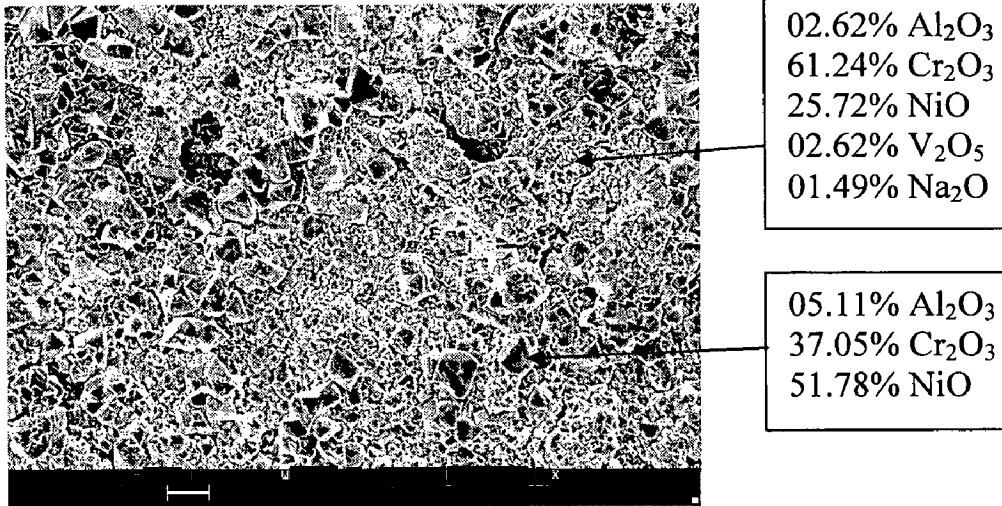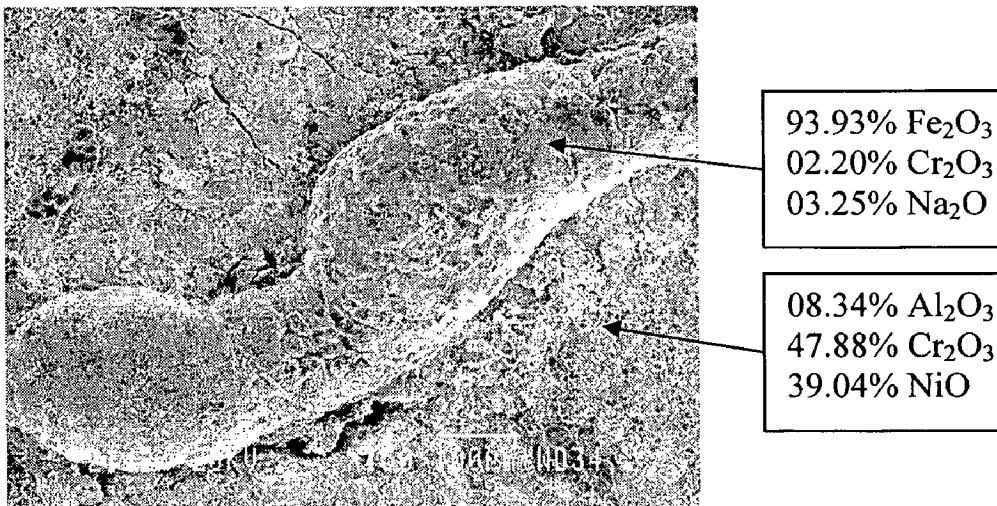
(c)

Fig.6.13   Surface scale morphology and EDAX point analysis for NiCrAl coated steels subjected to hot corrosion for 50 cycles in Na_2SO_4-60%V_2O_5 at 900°C:

(a) GrA1 steel   (b) T11 steel   (c) T22 steel
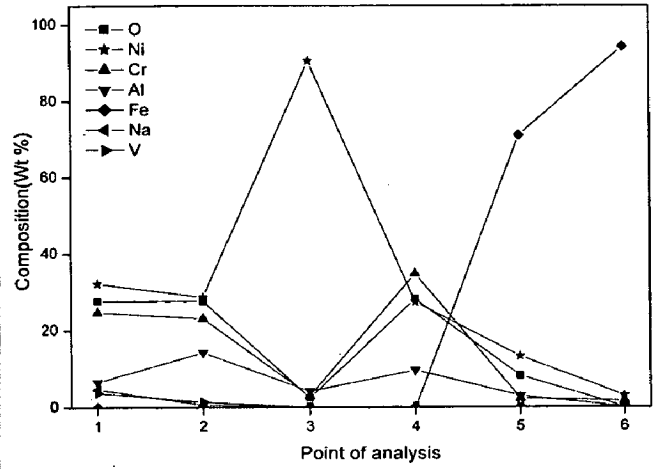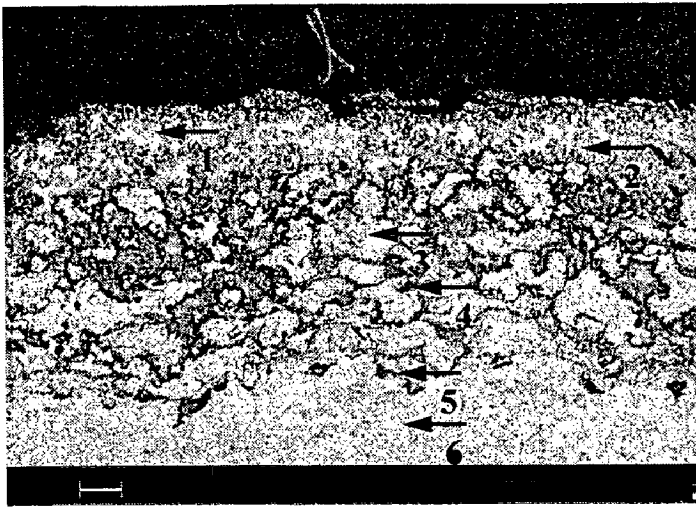
(a)
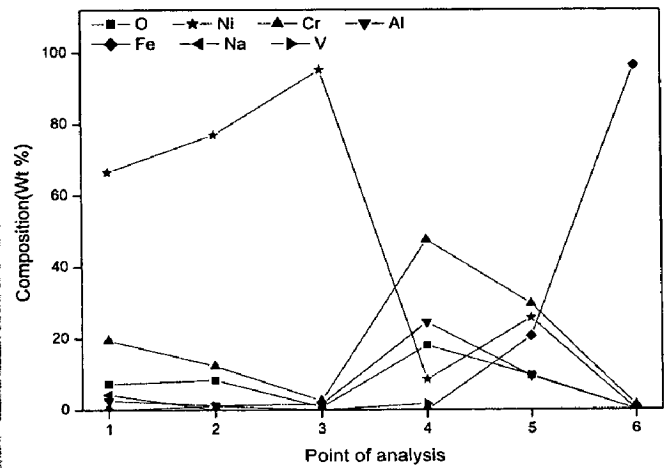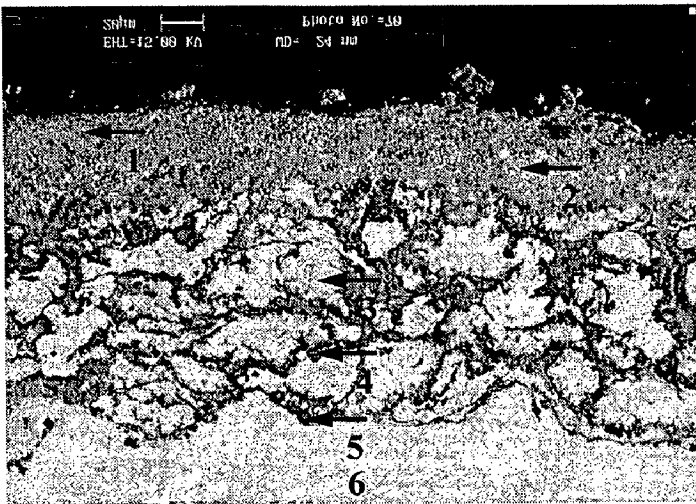
(b)
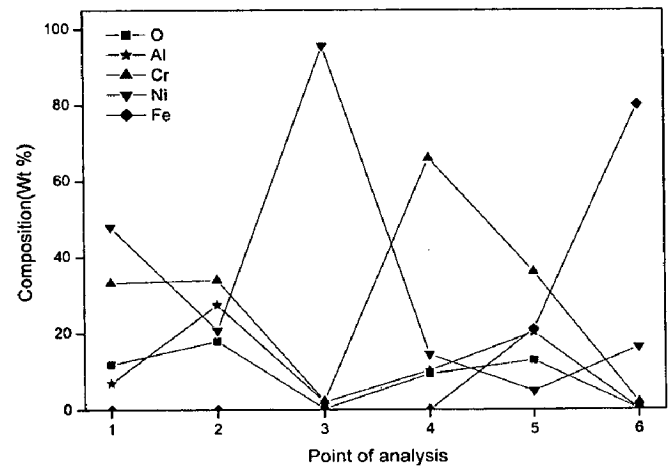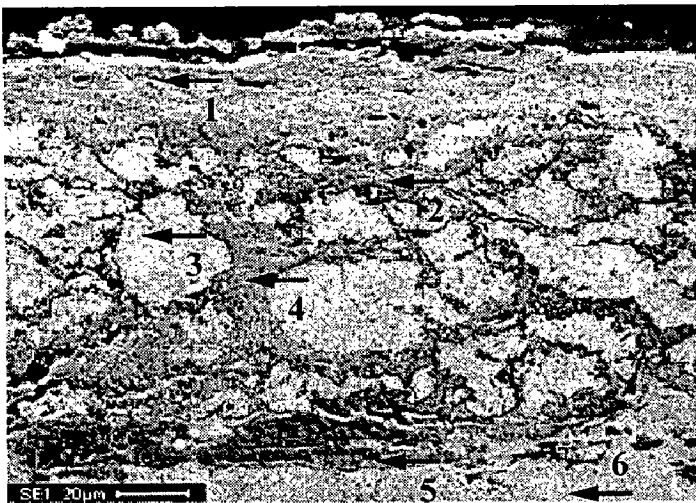
(c)

Fig.6.14   Back scattered electron image and EDAX point analysis (wt %) across the
cross-section of the NiCrAl coated steels subjected to hot corrosion in
Na_2SO_4-60%V_2O_5 environment for 50 cycles at 900°C :
(a) GrA1 steel   (b) T11 steel   (c) T22 steel
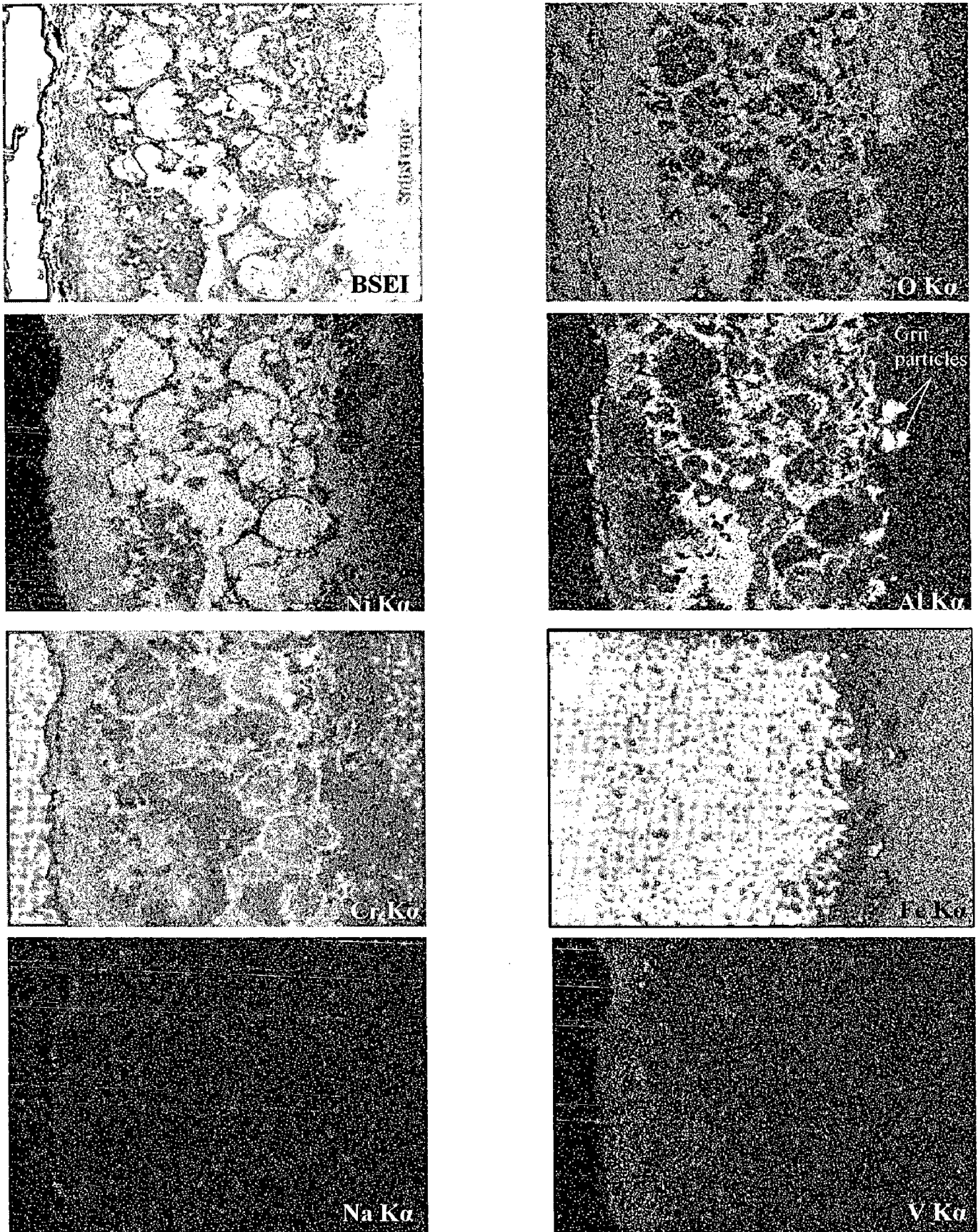
Fig.6.15 BSEI and elemental X-ray mapping along the cross-section of the NiCrAl coated GrA1 steels subjected to hot corrosion for 50 cycles in Na_2SO_4-60%V_2O_5 environment at 900°C

159
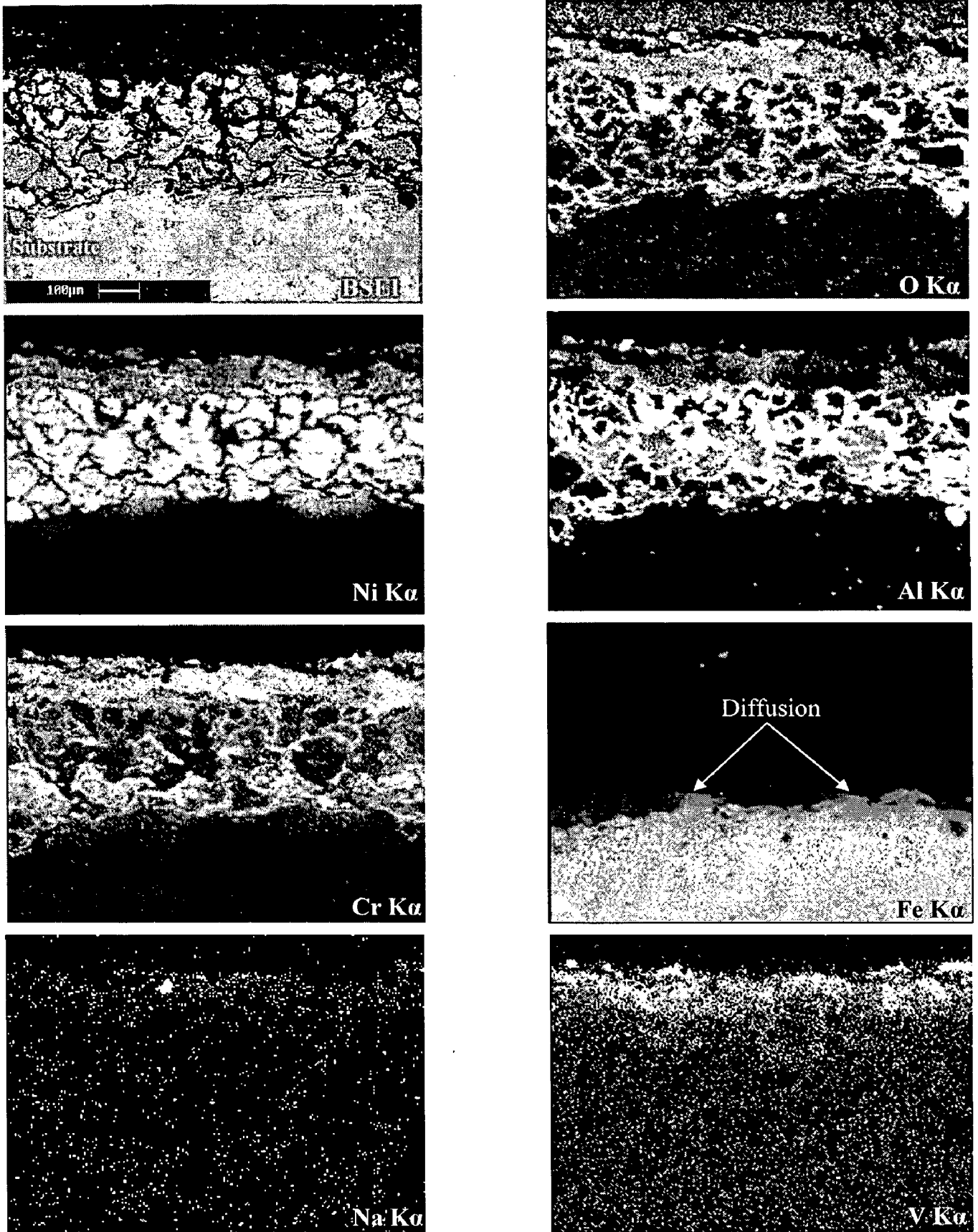
Fig.6.16 BSEI and elemental X-ray mapping along the cross-section of the NiCrAl coated T11 steels subjected to hot corrosion for 50 cycles in Na_2SO_4-60%V_2O_5 environment at 900°C

160
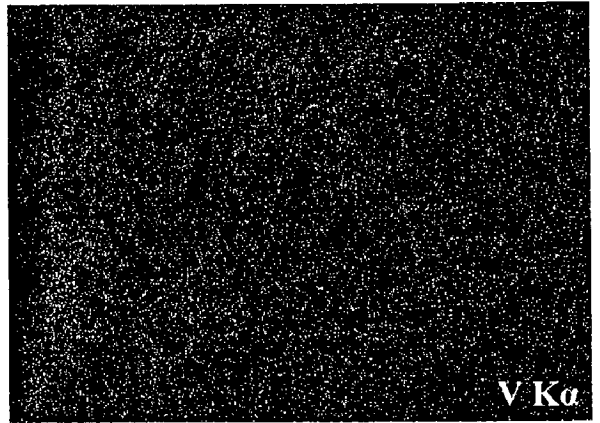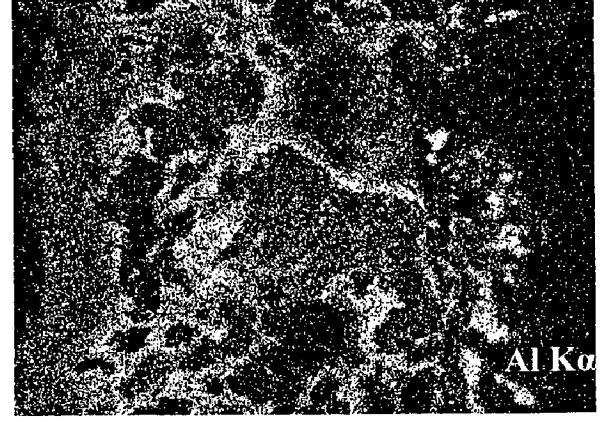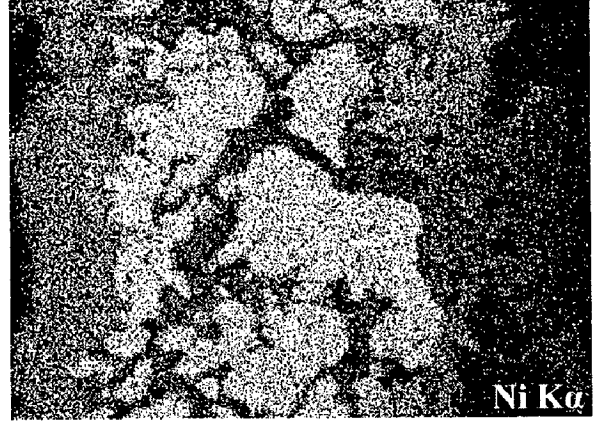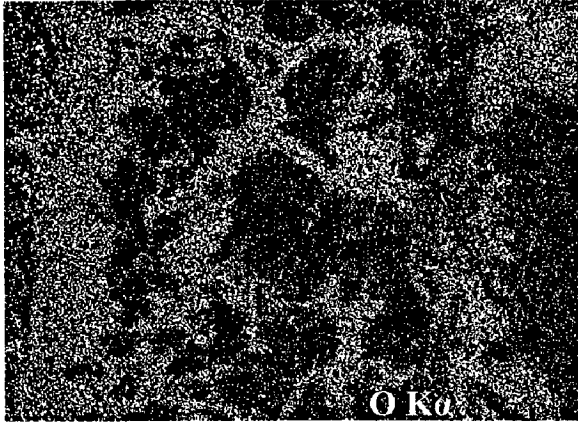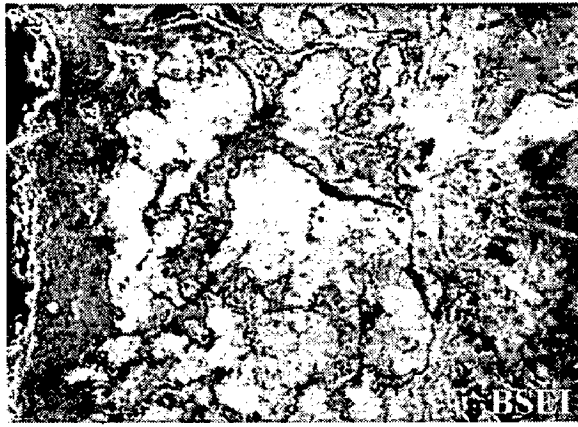
Fig.6.17 BSEI and elemental X-ray mapping along the cross-section of the NiCrAl coated T22 steels subjected to hot corrosion for 50 cycles in Na_2SO_4-60%V_2O_5 environment at 900°C

grit particles, as marked in the X-ray mapping for Al, is perhaps the residue of the surface preparation prior to the HVOF spraying. The EPMA analysis for NiCrAl coated T11 steel (Fig. 6.16) also shows the topmost thick adherent layer of oxide scale. The X-ray mapping revealed that this adherent topmost layer is rich in Nickel and Chromium oxides. Some patches of aluminum oxides are also seen in this oxide scale. The higher concentrations of V and Na are confined only to the surface and not penetrated much into the coating during the hot corrosion studies for 50 cycles. Al and Cr distributed along the splat boundaries got oxidized whereas Ni and Cr rich splats are in unoxidised condition. The minor diffusion of substrate iron into the coating is indicated by an arrow mark.

The X-ray mappings for NiCrAl coated T22 Steel (Fig. 6.17) shows a broader coating-substrate interface. Further, a higher diffusion of Ni, Cr, and Al into the substrate as well as the diffusion of iron into the coating has been observed after 50 cycles of exposure. The oxygen penetrates deeper inside and oxidized the substrate to a certain extent in case of the coated T22 steel.

6.1.3   NiAlCrFeMo Coating

6.1.3.1 Thermo gravimetric studies

Macrographs of HVOF sprayed NiAlCrFeMo coated steels subjected to hot corrosion in Na_2SO_4-60%V_2O_5 environment for 50 cycles at 900°C are shown in Fig.6.18. Green colored oxide scale has been observed on the corroded surface of all the three coated steels. Minor spalling of the oxide scale in the form of tiny flakes has been noticed in case of coated GrA1 and T11 steels where as coated T22 steel exhibited comparatively intense spalling of oxide scale on the surface. Contrast grey color protrusions were observed on corroded surface of all the three coated steels. These protrusions were seen after 43rd cycles in case of coated GrA1 steel and after 17th cycle in case of coated T11 and T22 steels. These protrusions become more pronounced in coated T22 steel as compared with other coated steels.

The plots of cumulative weight gain (mg/cm^2) as a function of time are shown in Fig.6.19. It can be inferred from the thermogravimetric data that the necessary protection against hot corrosion has been provided by the NiAlCrFeMo coating, as the weight gain values for the coated steels are smaller than those for respective uncoated steels as reported in section 6.1.1.1. The total weight gain values for the coated GrA1, T11 and T22 steels at the end of 50 cycles of hot corrosion studies are found to be 38.49, 43.16

and 99.35 mg/cm^2 respectively. Further the weight gain square (mg^2/cm^4) data were plotted as a function of time, shown in Fig.6.20. The GrA1 and T11 steels followed the parabolic behaviour and the parabolic rate constants calculated are 8.15 x 10^{-9} and 10.19 x 10^{-9} g^2 cm^{-4} s^{-1} respectively. The coated T22 steel followed linear behaviour.

6.1.3.2 X-ray Diffraction Analysis

X-ray diffractograms for the corroded surfaces of NiAlCrFeMo coated steels after cyclic studies in molten salt are shown in Fig.6.21. All the coated GrA1, T11 and T22 steels indicated the formation of similar phases. The main phases revealed by XRD analysis are NiO, NiCr$_2$O$_4$, Ni$_3$V$_2$O$_8$, AlV$_2$O$_4$, Al$_2$O$_3$, Fe$_2$O$_3$ and NiMoO$_4$.

6.1.3.3 SEM/EDAX Analysis

The surface morphologies of the corroded NiAlCrFeMo coated steels along with EDAX analysis at some points of interest are shown in Figs.6.22 and 6.23. Oxide scales formed on the surface seem to be porous and cracks are observed at some region. Grey colored phases (Fig.6.22a) dispersed on the dark matrix has been identified to be nickel rich splats. While the matrix has relative higher concentration of oxides of Cr, Al, Fe and Mo. The exact sulphur content of the oxide scale could not be quantified with EDAX analysis, since the EDS peaks of Mo (L-peak) and S (K-peak) overlap at ~2.35 KeV makes accurate quantification difficult and hence the peak corresponds to the presence of both S and Mo. Similarly presence of both V (K-peak) and Cr (K-peak) at ~5.5 KeV can be expected even though the accurate quantification is difficult with EDAX analysis. Similar observations have been noticed for the oxide scale formed on NiAlCrFeMo coated T11 and T22 steels as shown in Fig.6.22b and Fig.6.23.

The back scattered electron image along the cross section of coated GrA1 steel (Fig.6.24a) subjected to hot corrosion in molten salt environment, shows a discontinuous and fragmented oxide scale formed on the uppermost surface and EDAX analysis on this scale (Point1) revealed oxides of Ni and Cr as the main constituent. Analysis at point 2 and 3 shows that the oxidation occurred at the splat boundary and oxides rich in Cr, Al and Fe were detected. The absence of oxygen at point 4 shows nickel rich splat in an unoxidised state. Presence of minor quantity of Ni and Cr at point 5 shows the diffusion

(a)
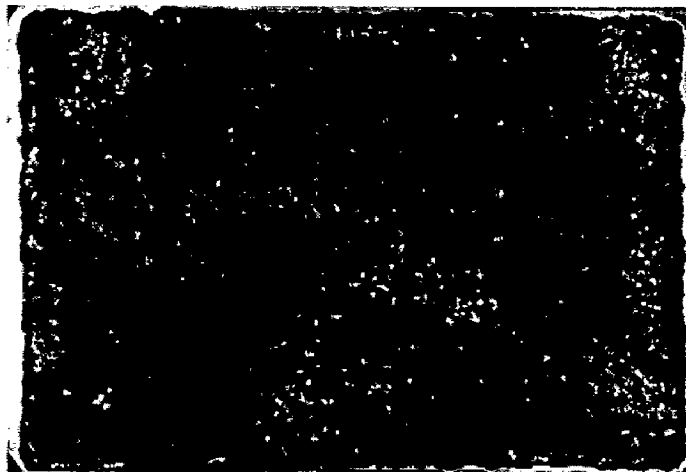
(b)

(c)

Fig.6.18   Macrographs of the NiAlCrFeMo coating subjected to hot corrosion in
Na₂SO₄-60%V₂O₅ environment for 50 cycles at 900°C:
(a) GrA1 steel   (b) T11 steel   (c) T22 steel

164
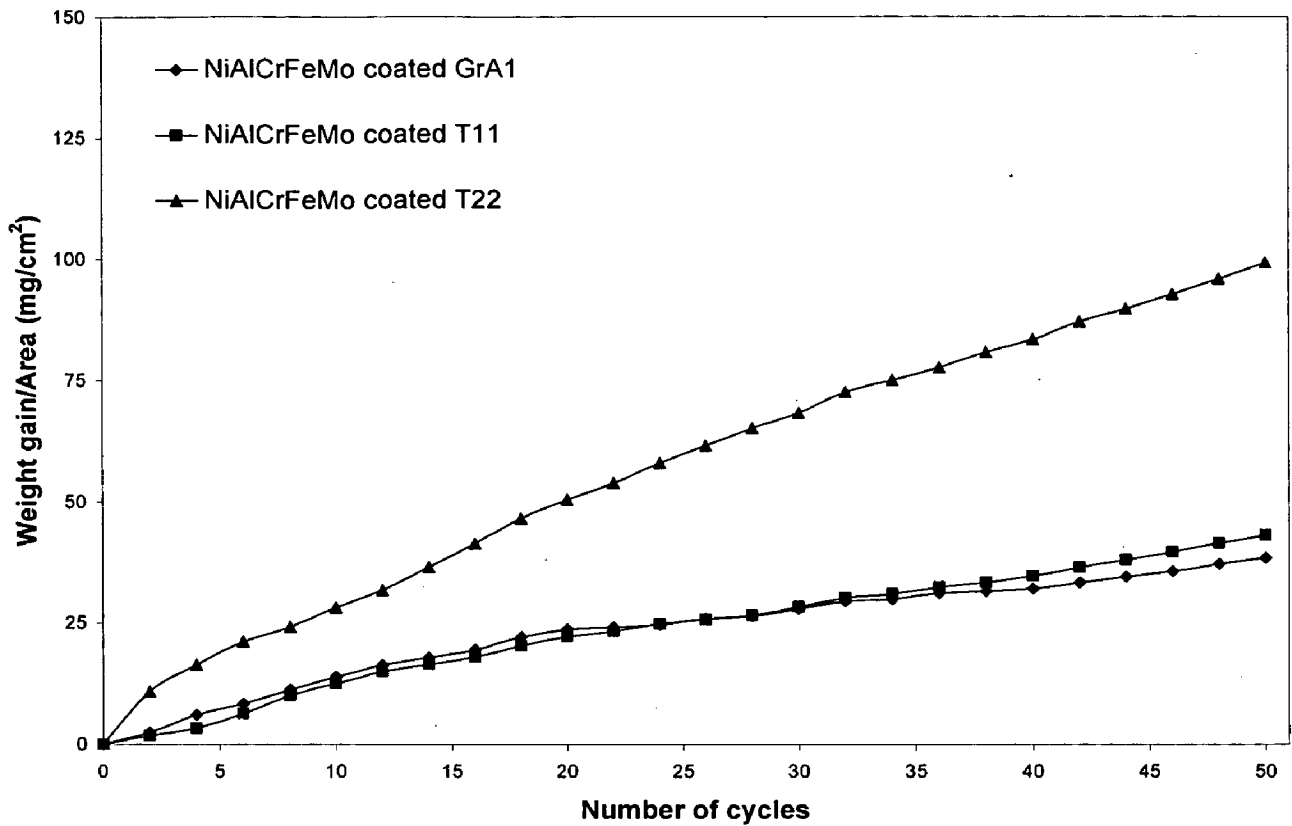
Fig.6.19   Weight gain versus number of cycles plot for NiAlCrFeMo coated steels subjected to hot Corrosion for 50 cycles in Na_2SO_4-60%V_2O_5 at 900°C
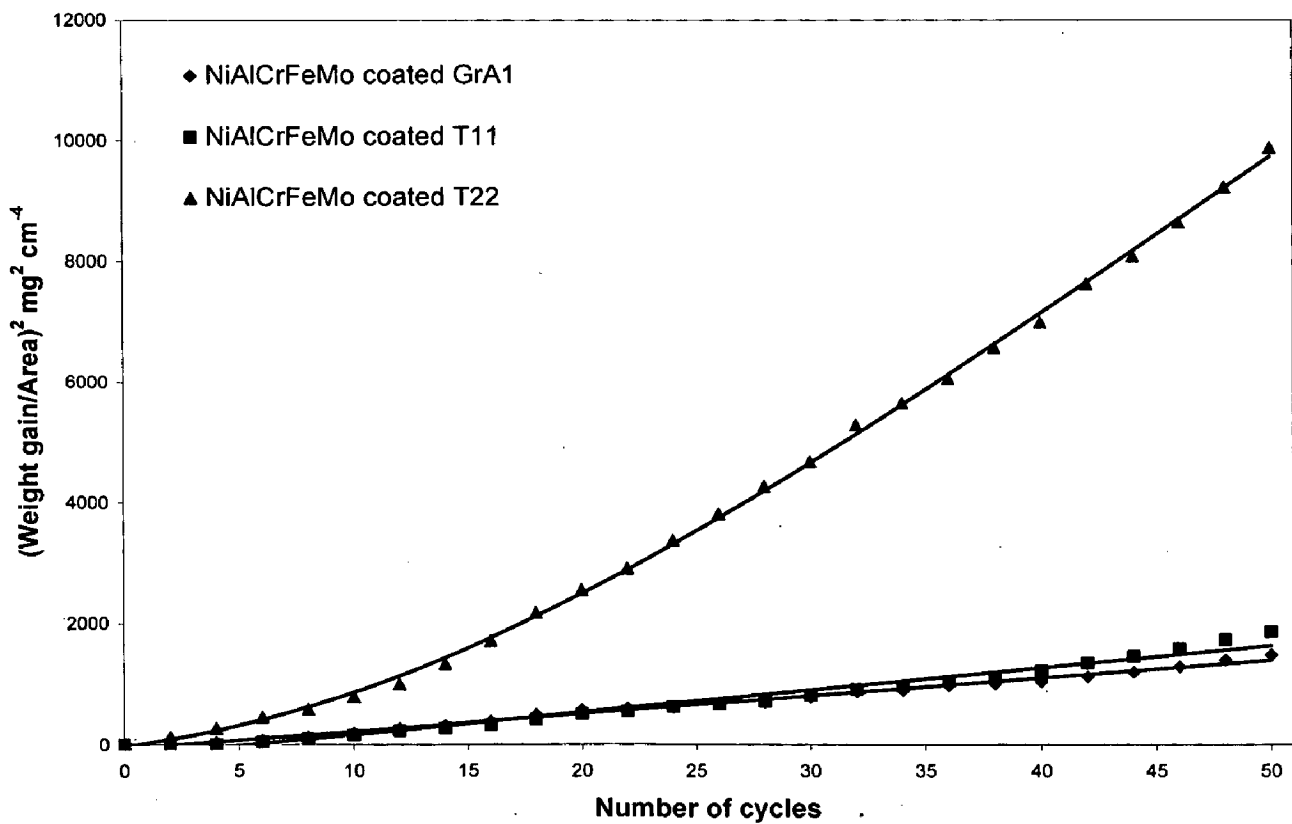
Fig.6.20   (Weight gain/area)^2 versus number of cycles plot for NiAlCrFeMo coated steels subjected to hot corrosion for 50 cycles in Na_2SO_4-60%V_2O_5 at 900°C
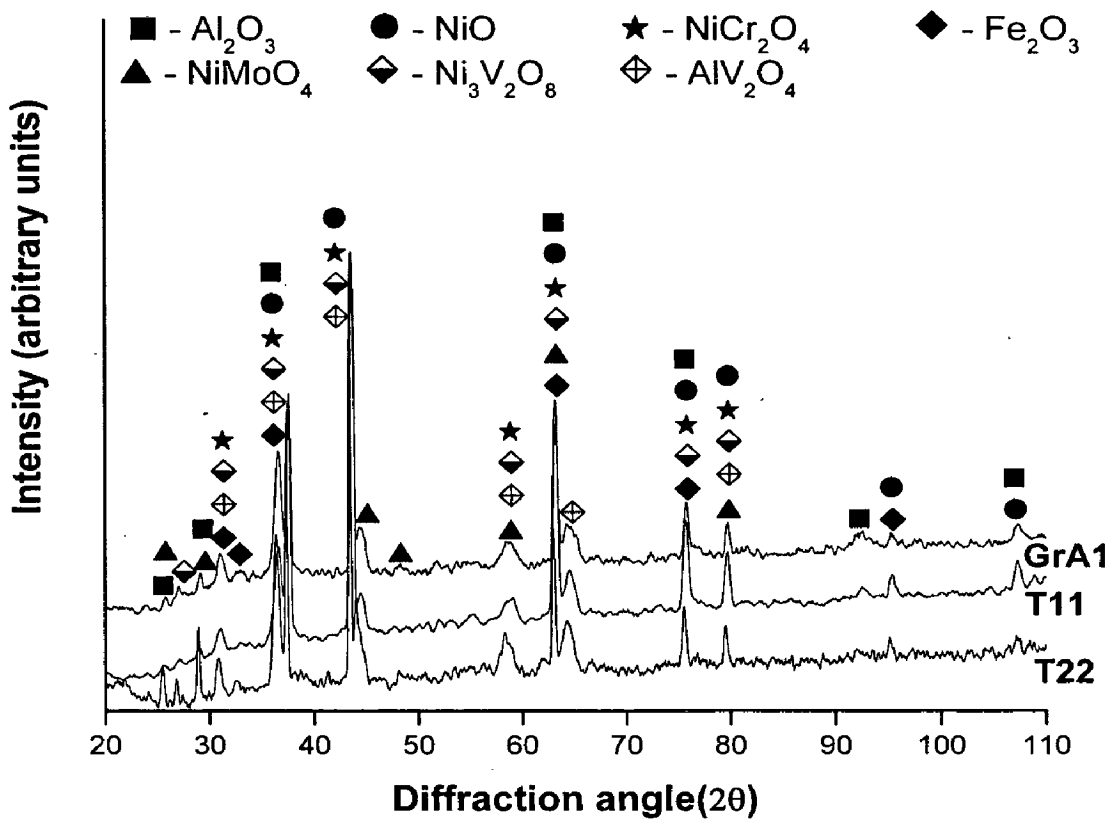
Fig.6.21 X-ray diffraction patterns for NiAlCrFeMo coated GrA1, T11 and T22 steels subjected to hot corrosion in Na_2SO_4-60%V_2O_5 for 50 cycles at 900°C
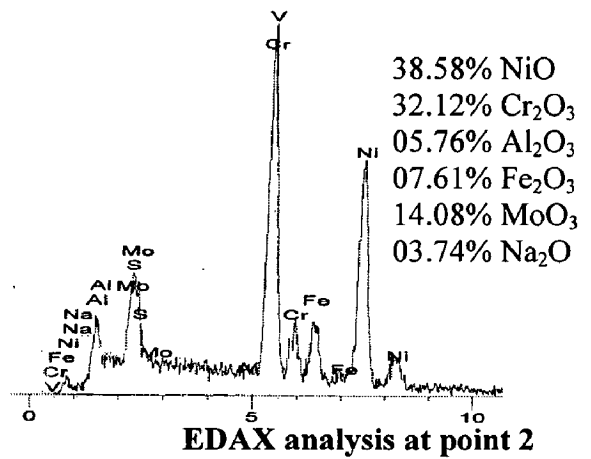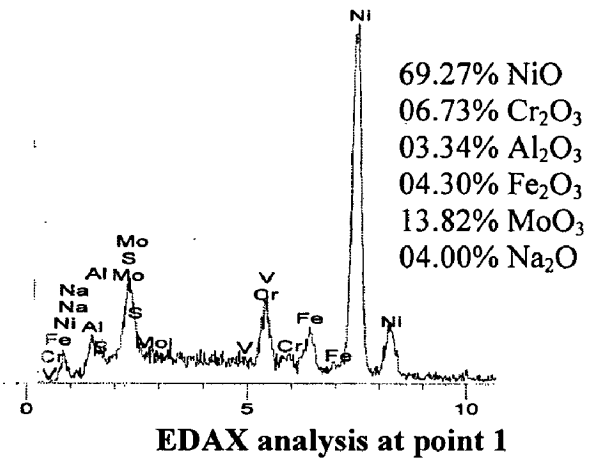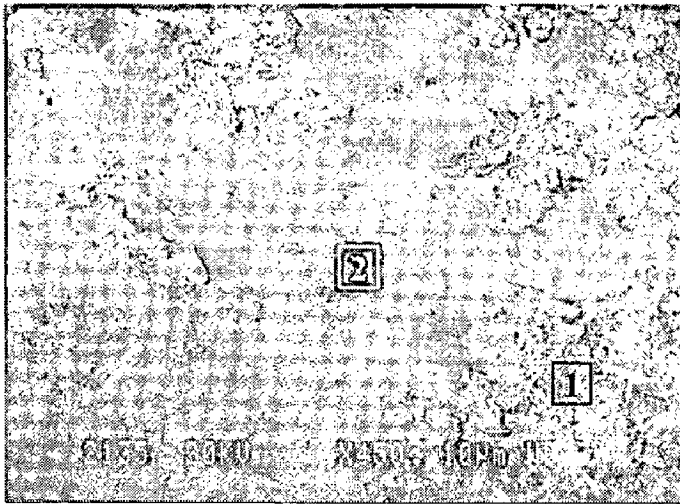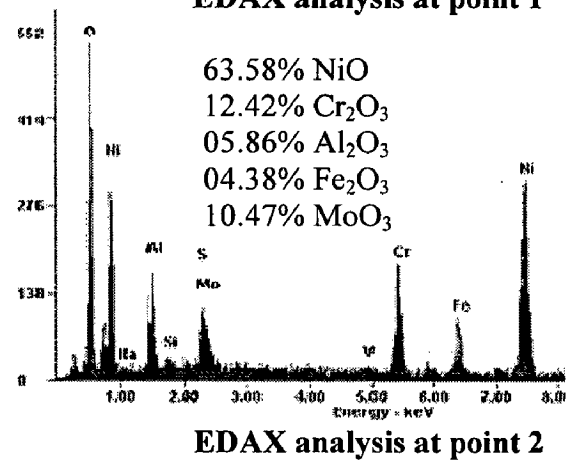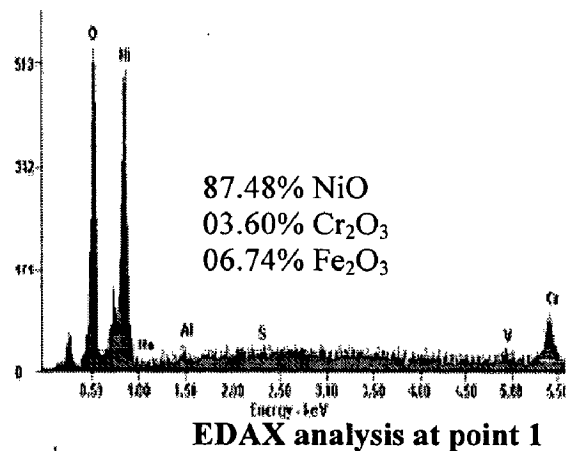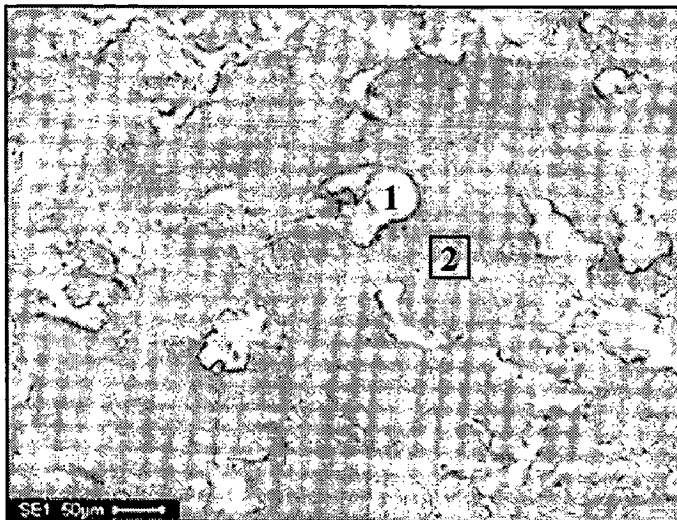
Fig.6.22   Surface scale morphology and EDAX analysis for NiAlCrFeMo coated GrA1 and T11 steels subjected to hot corrosion for 50 cycles in Na_2SO_4-60%V_2O_5 at 900°C:

(a) Coated GrA1 steel   (b) Coated T11 steel

59.95% NiO		30.06% NiO
08.54% Cr_2O_3		15.87% Cr_2O_3
04.98% Al_2O_3		06.29% Al_2O_3
10.59% Fe_2O_3		09.79% Fe_2O_3
08.30% MoO_3		36.22% MoO_3
03.35% Na_2O		02.04% Na_2O
02.84% SO_3		

EDAX at point 1   **EDAX at point 2**

Fig.6.23   Surface scale morphology and EDAX point analysis for NiAlCrFeMo
coated T22 steel subjected to hot corrosion for 50 cycles in Na_2SO_4-
$60\%V_2O_5$ at 900°C

168
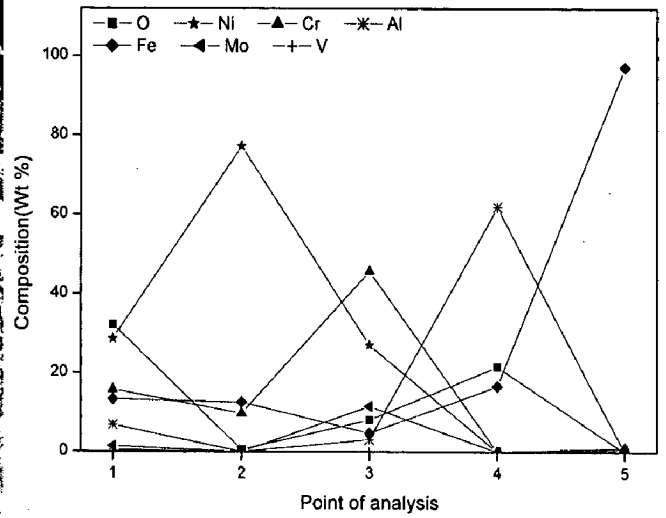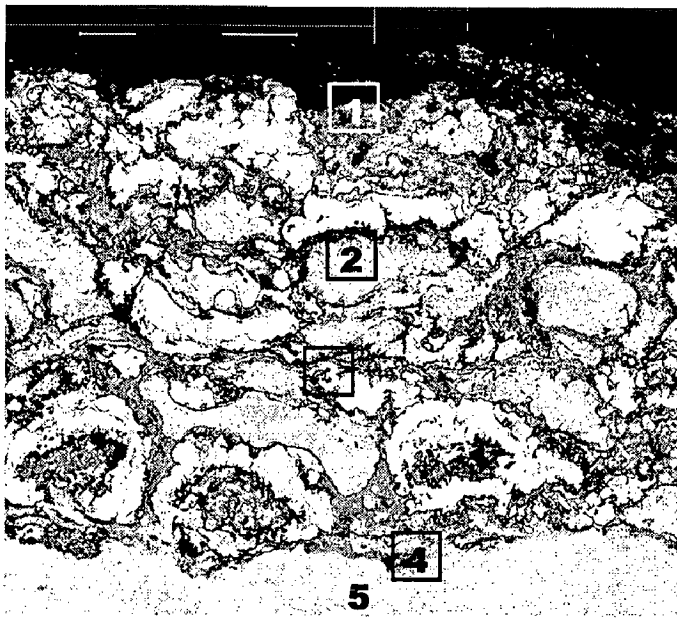
Fig.6.24   Back scattered electron image and EDAX point analysis (wt %) across the
cross-section of the NiAlCrFeMo coated steels subjected to hot corrosion
in Na$_2$SO$_4$-60%V$_2$O$_5$ environment for 50 cycles at 900°C :
(a) Coated GrA1 steel   (b) Coated T11 steel

of these elements from the coating into substrate Similar results have been noticed for the corroded NiAlCrFeMo coating on T11 steel, as shown in Fig.6.24b.

6.1.3.4 EPMA Analysis

Elemental X-ray maps for the NiAlCrFeMo coated T22 steel after exposure to oxidation in Na_2SO_4-60%V_2O_5 environment for 50 cycles at 900°C has been compiled in Fig. 6.25. As can be noticed from the mapping for oxygen, the entire cross-section of the coating has been oxidized. The outermost surface of the corroded coating mainly shows the presence of oxides of Ni and Cr and perhaps their spinels. Aluminum and iron have been oxidized around the nickel rich splat boundary. Penetration of vanadium into the coating is observed from the X-ray map for vanadium. Higher concentration of the vanadium distributed at the uppermost surface of the corroded coating, substantiate the formation of spinel oxides with Ni, Cr and Al. Presence of higher concentration of Mo at the bottom portion of the coating suggest that the Mo has been consumed at the surface in the formation of volatile oxides. X-ray maps for Ni and O show nickel rich splats in unoxidised form, distributed at some region of coating.

6.1.4 NiCrFeSiB Coating

6.1.4.1 Thermo gravimetric studies

Figure 6.26 shows the macrographs of the HVOF sprayed NiCrFeSiB coatings on GrA1, T11 and T22 steels subjected to hot corrosion in Na_2SO_4-60%V_2O_5 environment for 50 cycles at 900°C. The dull green appearance of the as-sprayed coatings changed to reddish brown (oily appearance) color after their exposure to the molten salt environment. The oxide scale formed on the corroded coatings seem to be compact, adherent, and dense with absence of scale spalling or cracking during 50 cycles of hot corrosion studies.

The plots of cumulative weight gain (mg/cm^2) as a function of time expressed in number of cycles are shown in Fig. 6.27. The weight gain in all the NiCrFeSiB coated GrA1, T11 and T22 steels vary in a narrow range. The corrosion behavior of the coated steels can be distinguished as a transient stage up to 3 cycles of exposure where rapid weight gain has been observed probably due to the accelerated oxidation influenced by

the molten salt environment that promotes rapid formation of oxides of active elements present in the coating. Thereafter, the rate of oxidation gradually reduces with time which implies the possible formation of a protective film that restricts the diffusion of O_2 or other corrosive elements through it. The slow rate of oxidation shows that the reaction rate is diffusion limited. This can be substantiated from the weight gain square (mg^2/cm^4) data plotted as a function of time (Fig. 6.28), which shows the parabolic behavior of all the coated steels. The parabolic rate constants (K_p) for the NiCrFeSiB coated GrA1, T11 and T22 steels are found to be (8.99, 9.22 and 9.98) x 10^{-10} g^2 cm^{-4} s^{-1}, respectively.

6.1.4.2 X-ray Diffraction Analysis

Figure 6.29 shows the X-ray diffraction pattern of the surface scale formed on corroded NiCrFeSiB coated steels in the molten salt environment. The XRD analysis reveals the phases of SiO_2, Cr_2O_3, $NiCr_2O_4$ $FeCr_2O_4$, NiO, $Ni_3V_2O_8$, Na_4FeO_3 and $CrVO_4$ present on the surface oxide scale.

6.1.4.3 SEM/EDAX Analysis

The surface morphology of the oxide scale along with the EDAX compositional analysis at some salient points is shown in Figs. 6.30 and 6.31. It can be observed in Figs. 6.30 and 6.31a that the oxide scale features a white matrix having dark globules embedded in it. The EDS spectra obtained from these regions indicates that an exclusive silicon oxide layer is formed on the surface of the NiCrFeSiB coated GrA1 and T11 steels after the accelerated oxidation in the molten salt environment of Na_2SO_4-60%V_2O_5 at 900°C. The dark globules contain relatively a higher amount of oxides of Cr, Ni, Fe, and V. The presence of a less amount of boron oxide in the oxide scale is also detected. The EDAX area analysis on the surface oxide scale of the coated T22 steel (Fig.6.31b) also corroborates about the formation of a continuous layer of protective silica oxide on the corroded coating.

The salt induced high temperature corrosion of NiCrFeSiB coatings yield a bulky oxide scale of about 110 µm to 140 µm, measured from the BSE image (Fig. 6.32) acquired along the cross section of the corroded coatings. The EDAX composition analyses at the points along the cross-section are represented in the form of a graph. Figure 6.31a depicts the BSEI image of the coated GrA1 steel. The EDAX analyses on

171
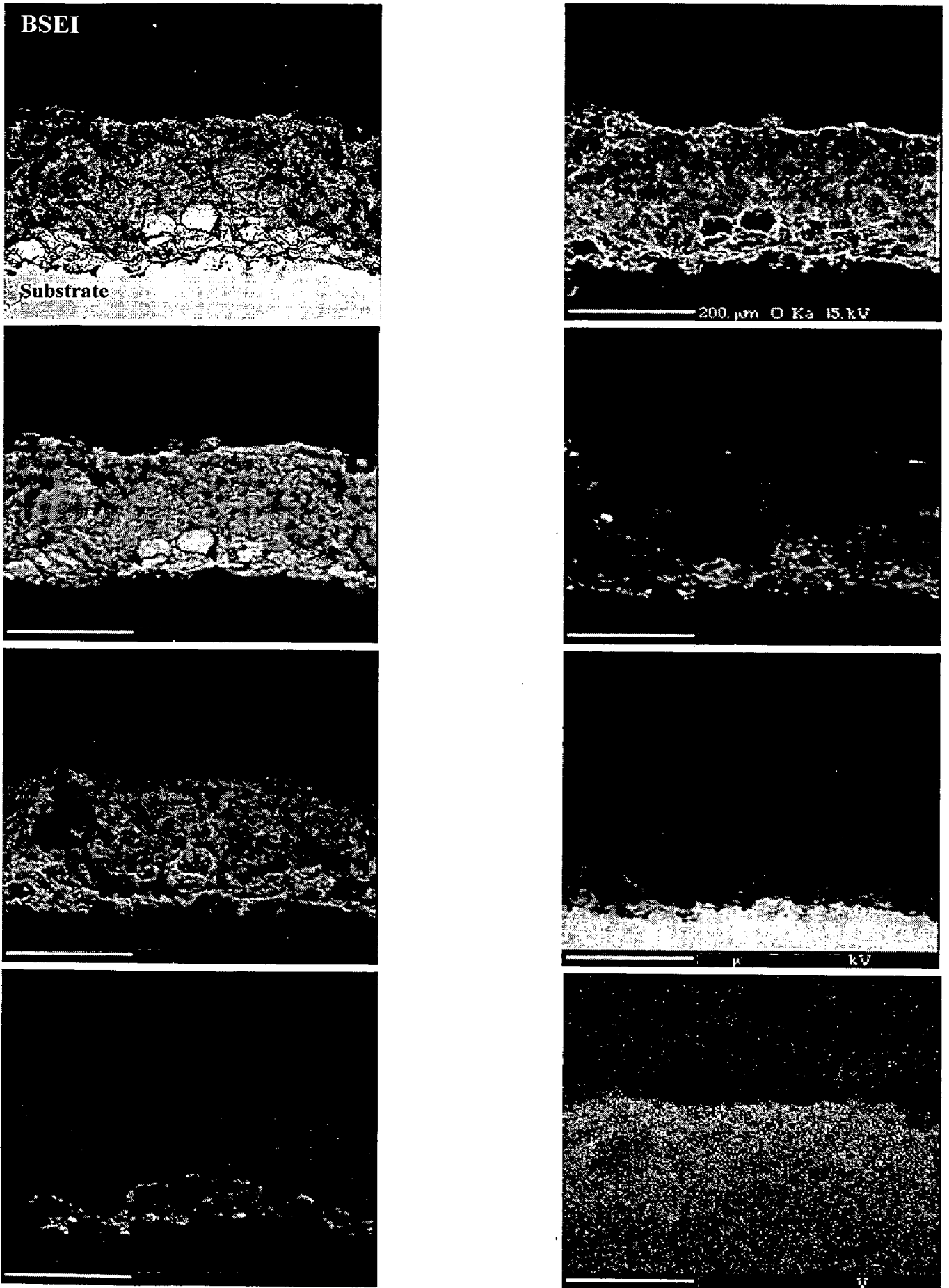
Fig.6.25 BSEI and elemental X-ray mapping along the cross-section of the NiAlCrFeMo coated T22 steels subjected to hot corrosion for 50 cycles in Na$_2$SO$_4$-60%V$_2$O$_5$ environment at 900°C
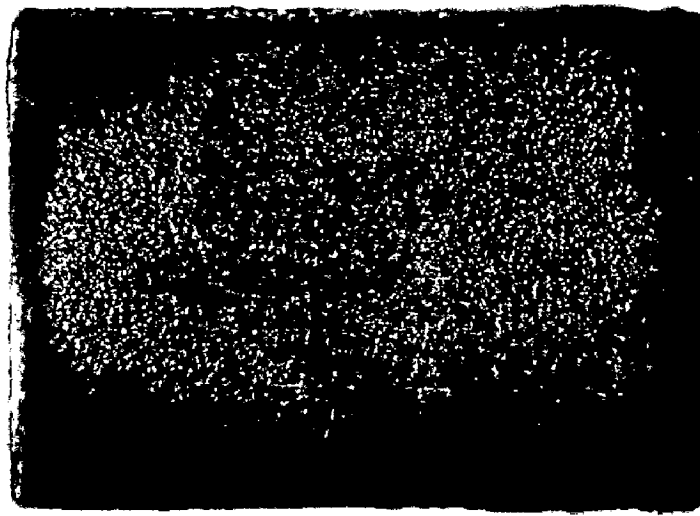
(a)
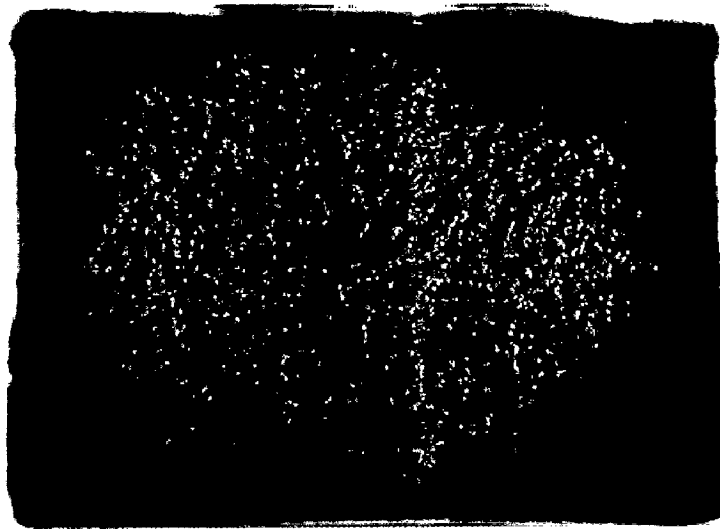
(b)
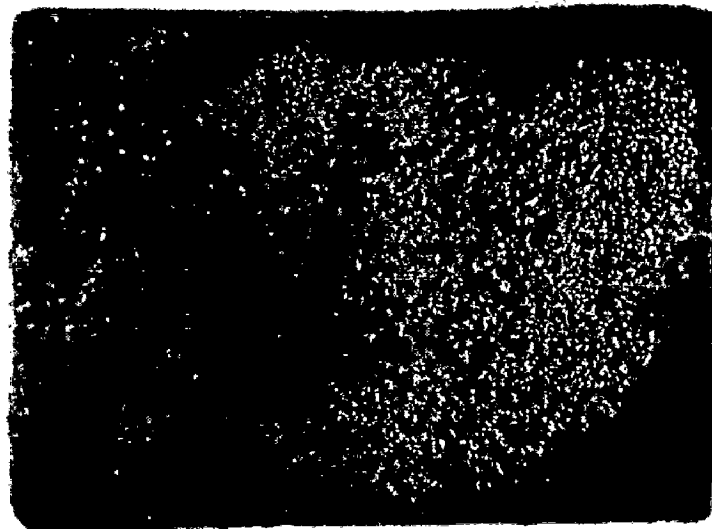
(c)

Fig.6.26   Macrographs of the NiCrFeSiB coating subjected to hot corrosion in
Na$_2$SO$_4$-60%V$_2$O$_5$ environment for 50 cycles at 900°C:
(a) GrA1 steel   (b) T11 steel   (c) T22 steel
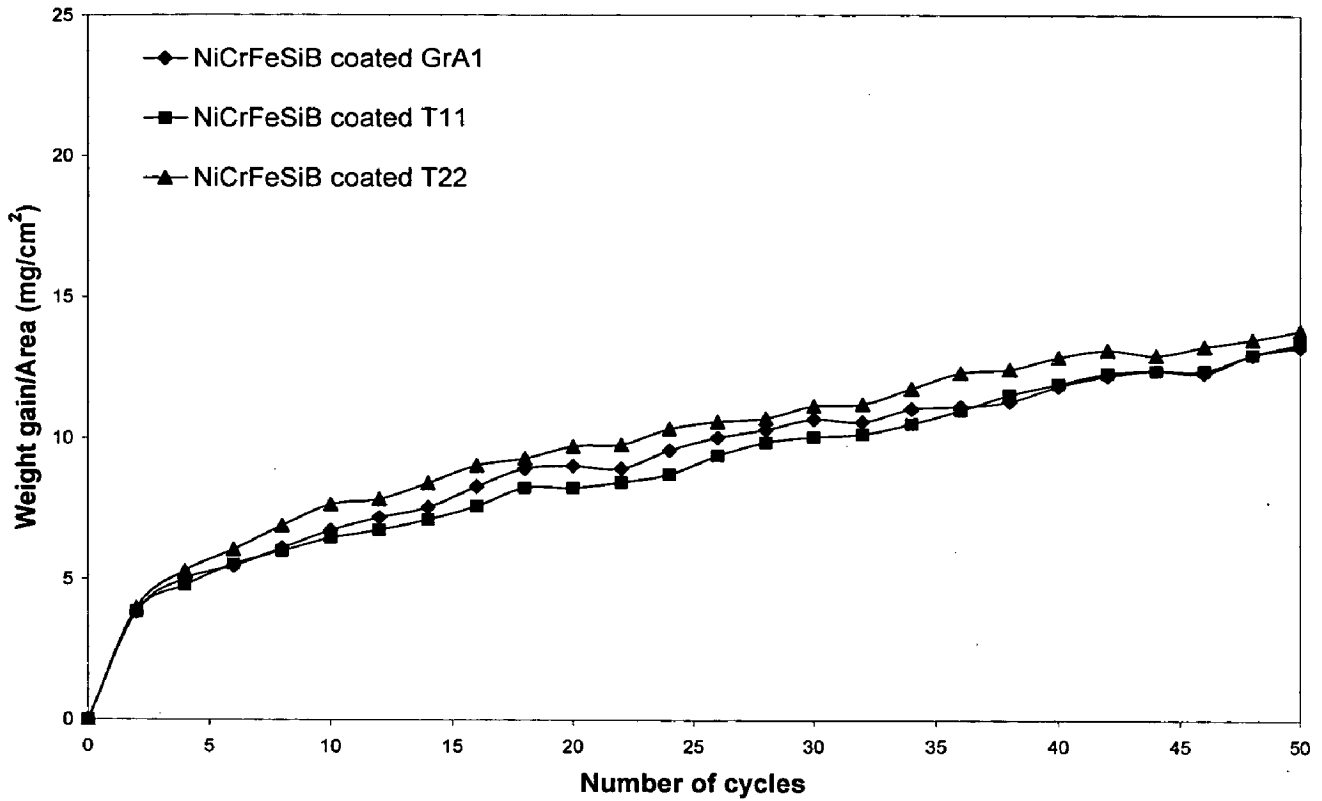
Fig.6.27 Weight gain vs. number of cycles plot for NiCrFeSiB coated steels subjected to hot Corrosion for 50 cycles in Na_2SO_4-60%V_2O_5 at 900°C
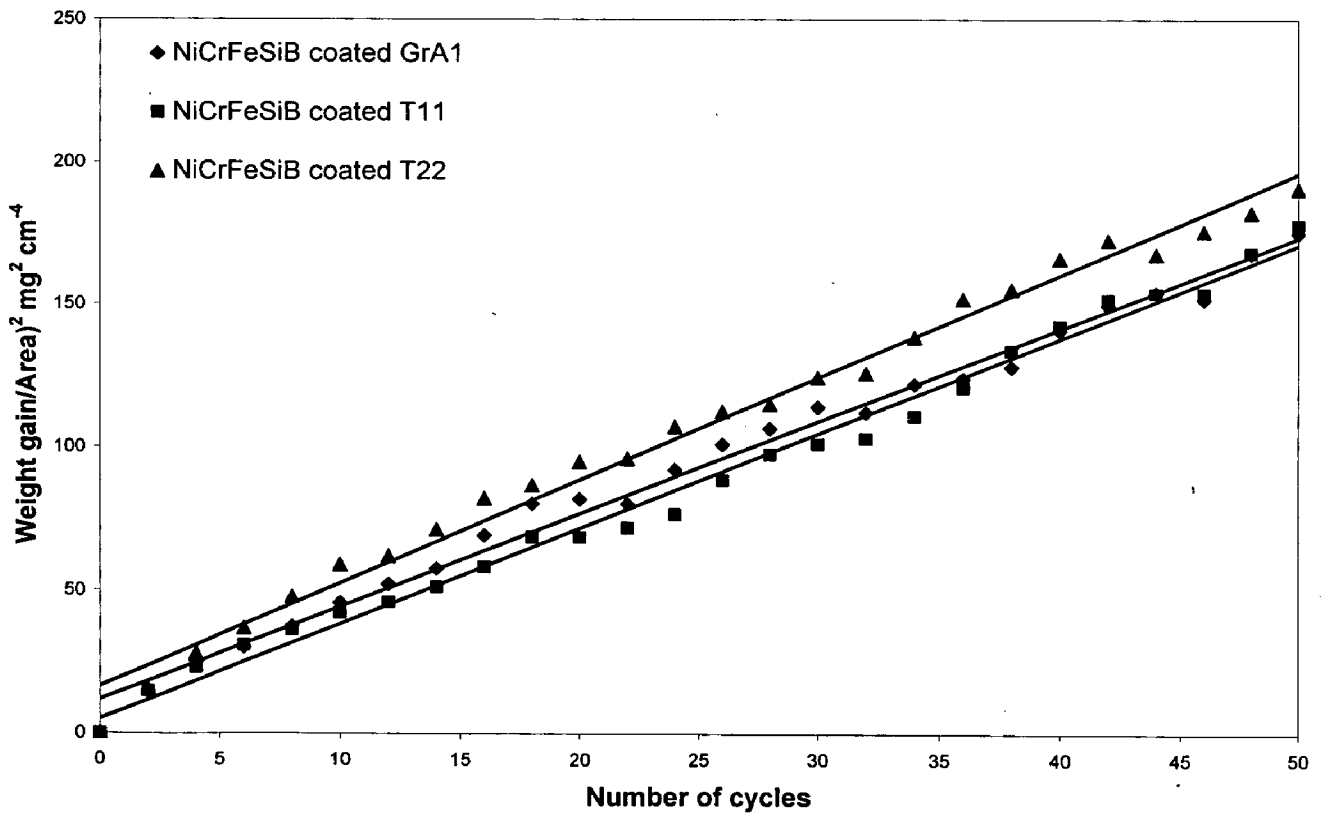
Fig.6.28 (Weight gain/area)^2 vs. number of cycles plot for NiCrFeSiB coated steels subjected to hot corrosion for 50 cycles in Na_2SO_4-60%V_2O_5 at 900°C
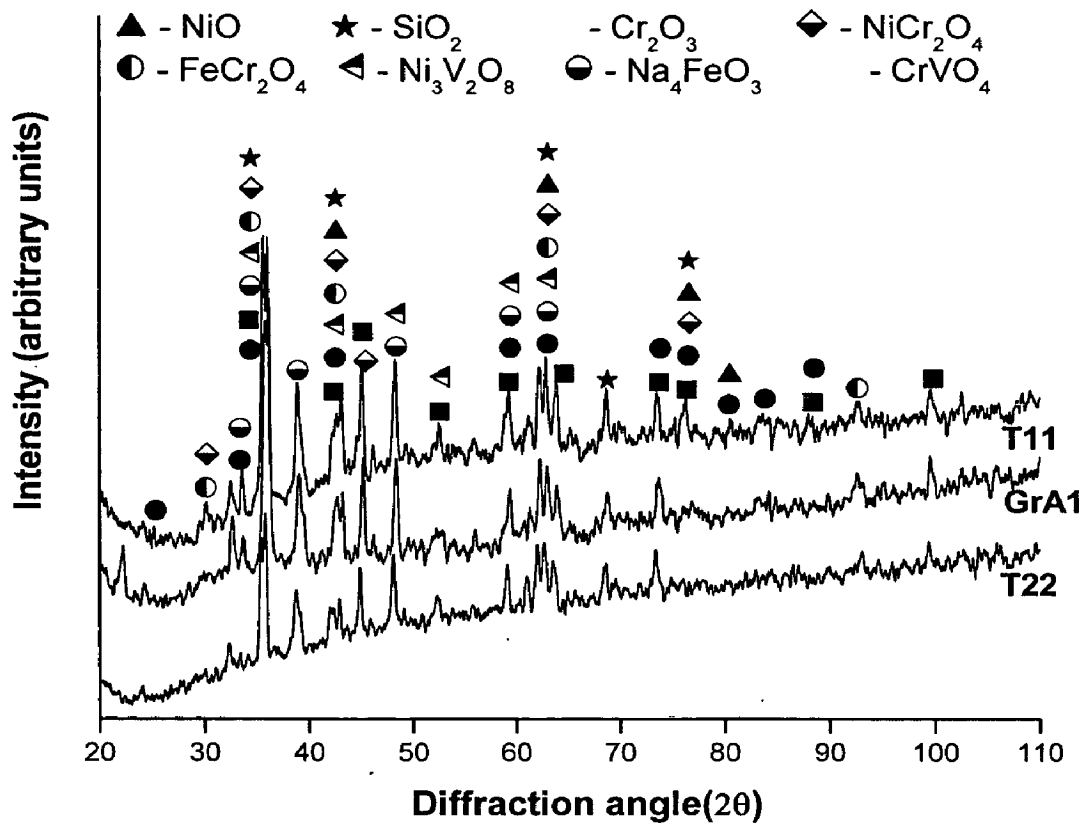
Fig.6.29   X-ray diffraction patterns for NiCrFeSiB coated GrA1, T11 and T22 steels subjected to hot corrosion in Na_2SO_4-60%V_2O_5 for 50 cycles at 900°C
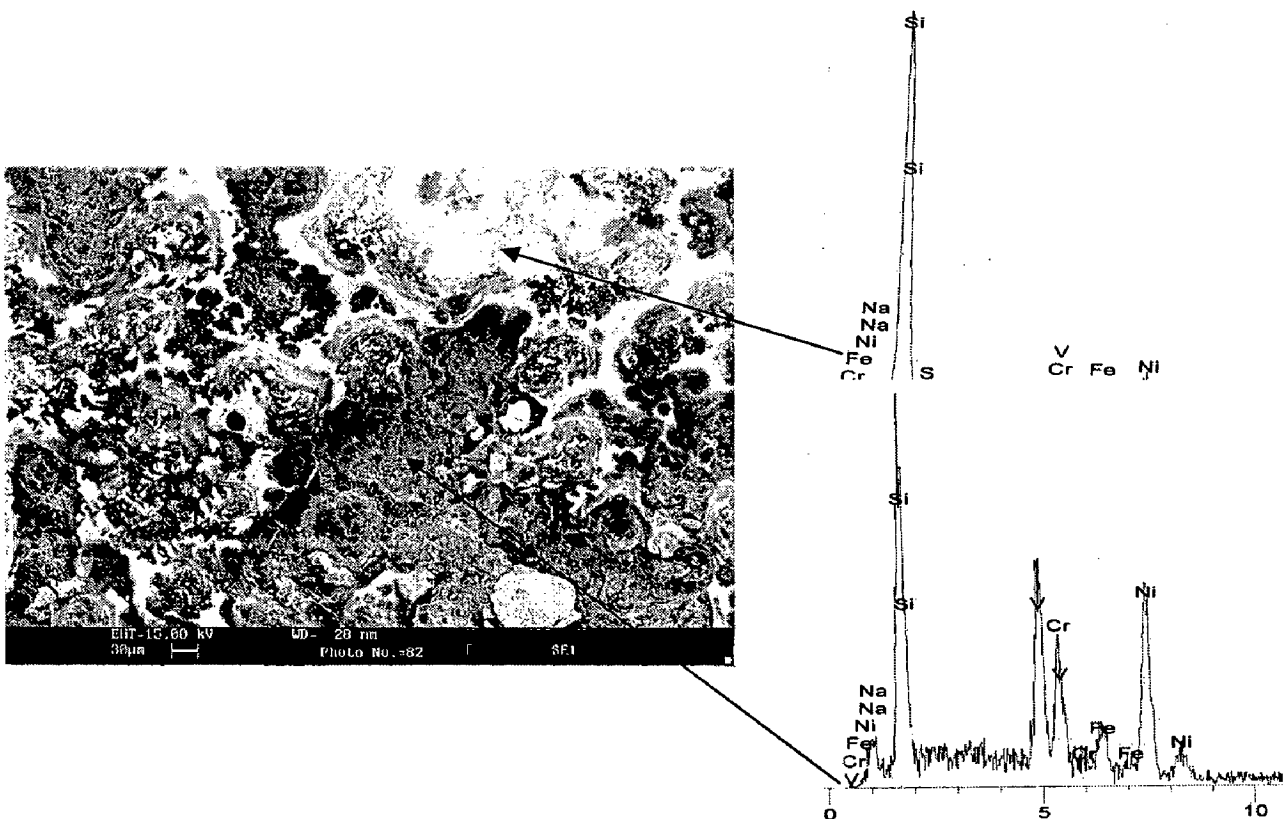
Fig.6.30   Surface scale morphology and EDAX area analysis for NiCrFeSiB coated GrA1 steel subjected to hot corrosion for 50 cycles in Na_2SO_4-60%V_2O_5 at 900°C

175
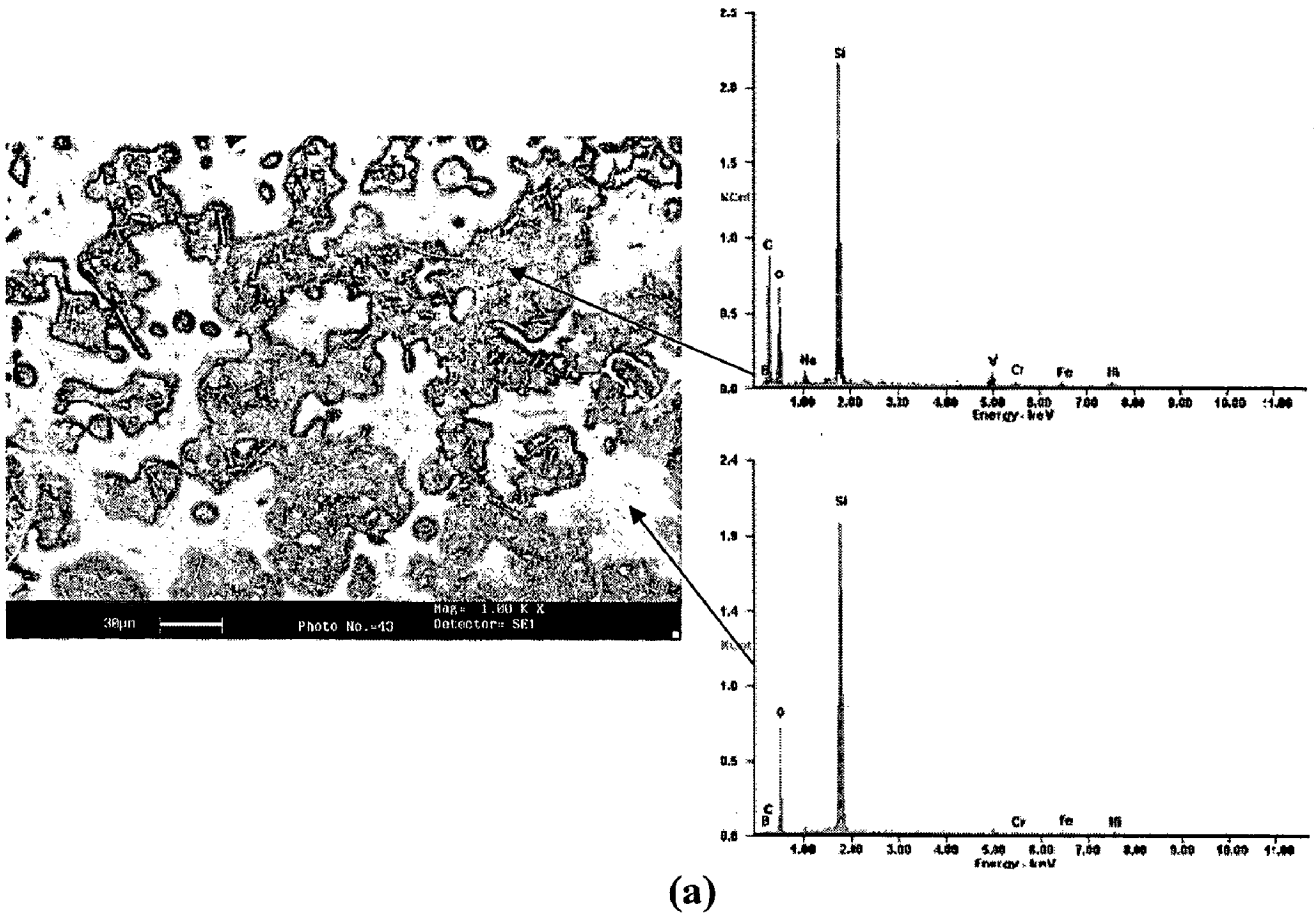
(a)
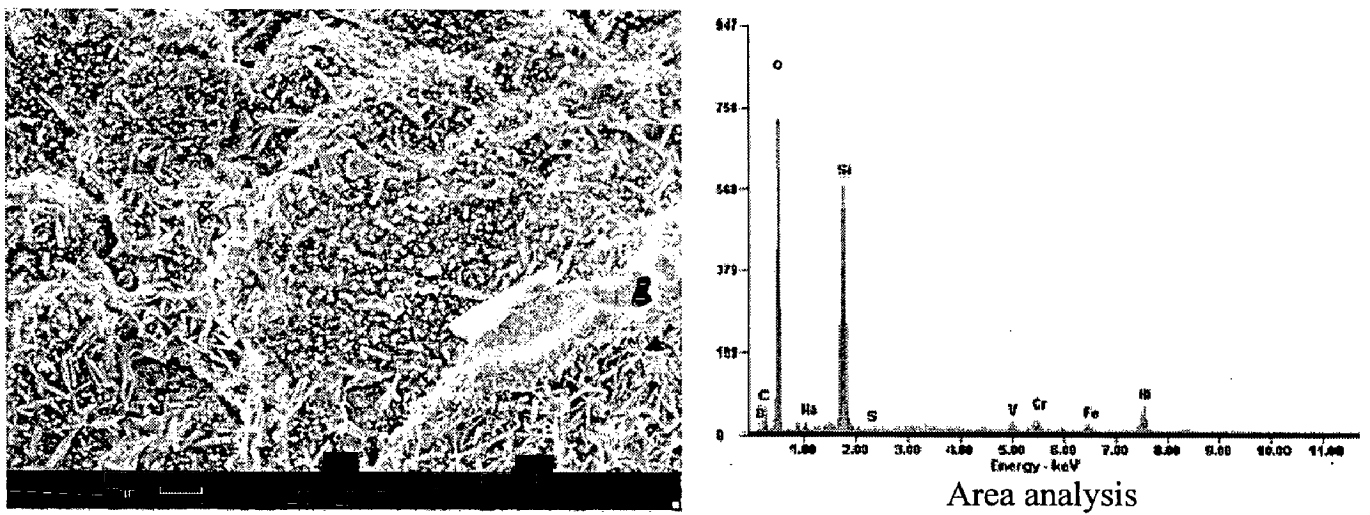
Area analysis

(b)

Fig.6.31   Surface scale morphology and EDAX analysis for NiCrFeSiB coated steels subjected to hot corrosion for 50 cycles in Na_2SO_4-60%V_2O_5 at 900°C: (a) T11 steel   (b) T22 steel

176
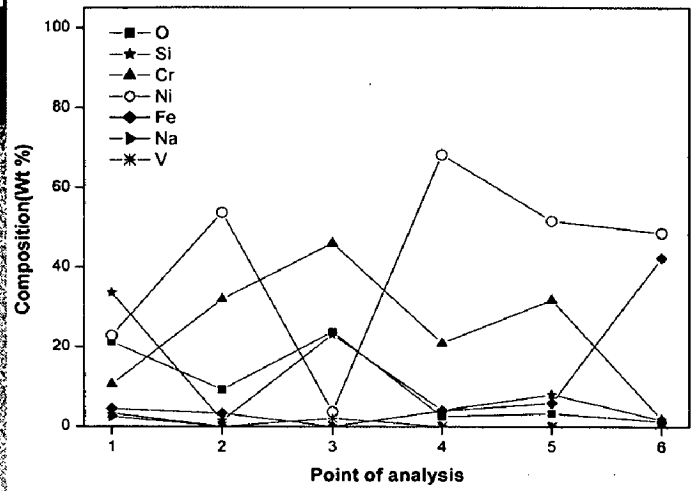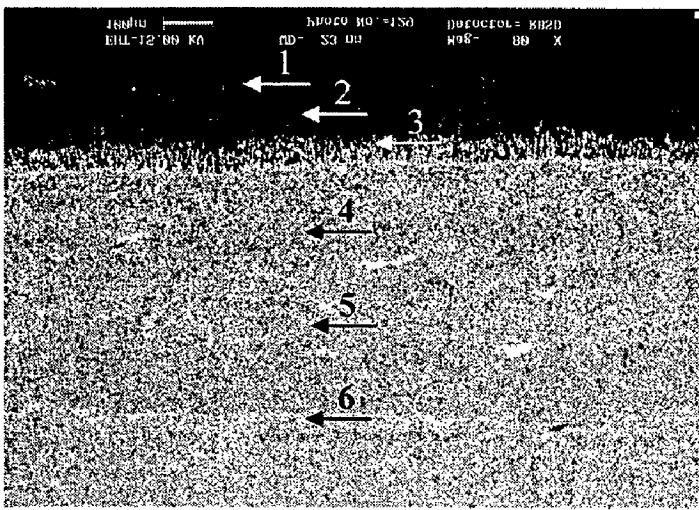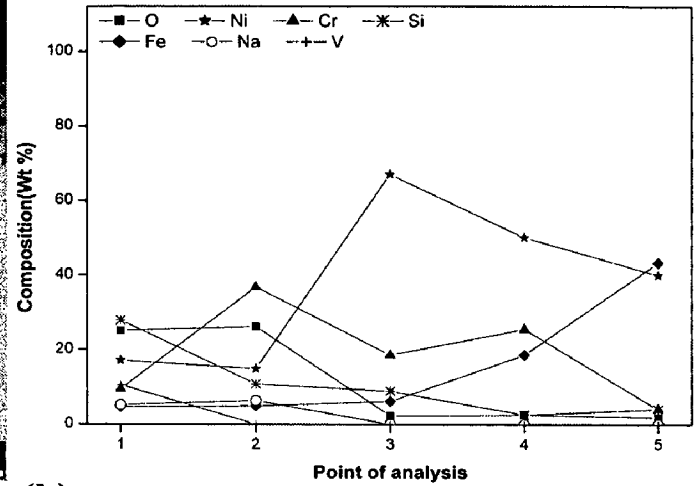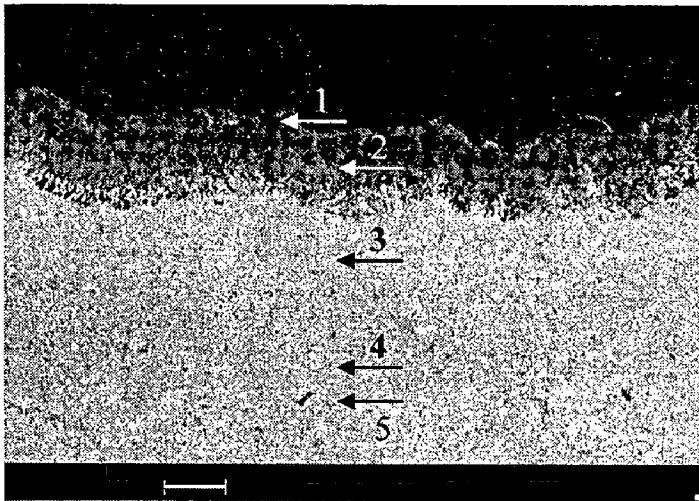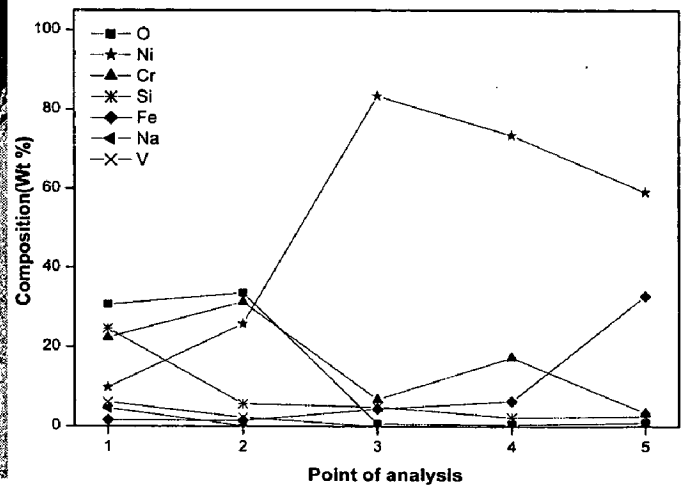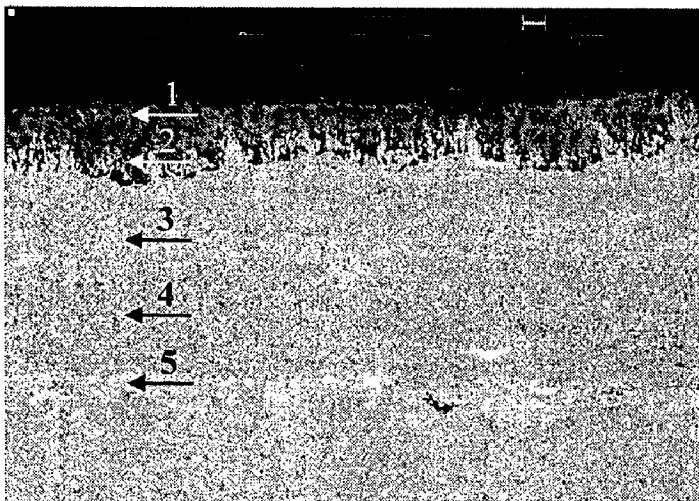
Fig.6.32   Back scattered electron image and EDAX point analysis (wt %) across the cross-section of the NiCrFeSiB coated steels subjected to hot corrosion in Na_2SO_4-60%V_2O_5 environment for 50 cycles at 900°C :

(a) GrA1 steel   (b) T11 steel   (c) T22 steel

the topmost layer of the oxide scale (Point 1) reveal that there is a higher content of SiO_2 along with a small amount of oxides of Cr and Ni. The presence of V and Na has also been indicated in this outermost layer. The Point 2 just below the topmost layer has been dominated by the oxides of Ni and Cr. The Point 3 at the bottom of the oxide scale shows the presence of a higher amount of oxides of Cr and Si. The coating region below the oxide scale (Points 4 and 5) shows a negligible amount of oxygen which infers that this region remained unoxidised. The oxide scale formed on the surface acts as a barrier to the inward diffusion of oxygen and other corrosive species which is proved to be protective. The thick band along the coating-substrate interface (Point 6) shows the presence of Fe and Ni, which signifies the interdiffusion of these elements along the interface. Similar results have been observed in case of the NiCrFeSiB coated T11 and T22 shown in Figs.6.32b and 6.32c.

6.1.4.4 EPMA Analysis

Figure 6.33 shows the elemental X-ray maps for the NiCrFeSiB coated GrA1 steel after its exposure to the Na_2SO_4-60%V_2O_5 environment for 50 cycles at 900°C. It is apparent from the BSE image that the thick oxide scale is formed on the corroded coating which consists of three distinct regions based on the oxides developed. The topmost region mainly consists of SiO_2, as silicon and oxygen co-exist in their respective X-ray maps. The presence of V and Na in this region also indicate the possibility of formation of corrosion products with Ni, Cr, and Fe. The intermediate region is dominated with the presence of Cr_2O_3 along with the uniform distribution of oxides of Ni and Fe. The formation of $FeCr_2O_4$ and $NiCr_2O_4$ spinal phase can also be expected. The underlying region just below this consists of unoxidised nickel-rich splats surrounded by oxides of mainly chromium and silicon. As can be observed from the X-ray mapping for oxygen, the coating is oxidized partially which is restricted to few microns on the surface at the end of 50 cycles of hot corrosion studies in the molten salt environment. The inter-diffusion of Fe from the substrate into the coating, as well as, Ni from the coating into the substrate can be observed along the coating-substrate interface which forms a thick band that is rich in nickel and iron. Similar oxide scales has also been observed for the NiCrFeSiB coated T22 steels which is illustrated in Fig. 6.34. It can be observed from

the mapping of Mo that there is a minor diffusion of Mo from the substrate into the coating.

6.1.5 WC-Co/NiCrFeSiB Coating

6.1.5.1 Thermogravimetric studies

Macrographs of HVOF sprayed WC-Co/NiCrFeSiB coatings on GrA1, T11 and T22 steels subjected to hot corrosion in Na_2SO_4-60%V_2O_5 environment at 900°C are shown in Fig.6.35. Pale brown color oxide scale has been observed on the corroded surface of all the coated steels. Open bud-shaped protrusions appeared on the surface scale during the first cycle of exposure to salt environment. Superficial cracks accompanied by spalling of oxide scale from the edges have been noticed in all the three coated steels. Spalling of oxide scale in case of coated T11 steel was relatively higher in magnitude in comparison to other coated steels.

Weight change of the WC-Co/NiCrFeSiB coated steels (mg/cm^2) plotted as a function of time is as shown in Fig. 6.36. Cumulative weight gain at the end of 50 cycles of hot corrosion studies for coated GrA1, T11 and T22 steels are found to be 59.35, 61.97 and 80.18 mg/cm^2 respectively. Coated T22 steel shows relatively higher weight gain, where as weight gain for coated GrA1 and T11 steels are not very different. Further the weight gain square (mg^2/cm^4) data was plotted as a function of time, shown in Fig.6.37. Coated GrA1 and T11 steels followed nearly the parabolic behavior up to 50 cycles and the parabolic rate constants calculated are (18.99 and 20.81) x 10^{-9} g^2 cm^{-4} s^{-1} respectively. The coated T22 steel shows parabolic rate up to 28th cycle thereafter oxidation rate increased continuously with time and followed nearly linear oxidation behavior.

6.1.5.2 X-ray Diffraction Analysis

Figure 6.38 shows similar XRD profiles for all WC-Co/NiCrFeSiB coated steels subjected to hot corrosion in salt environment for 50 cycles at 900°C. The phases revealed by XRD analysis are Cr_2O_3, NiO, SiO_2, $NiWO_4$, $CoCr_2O_4$, $NiCr_2O_4$, Ni_2SiO_4, $Ni_3V_2O_8$, and $FeVO_4$.
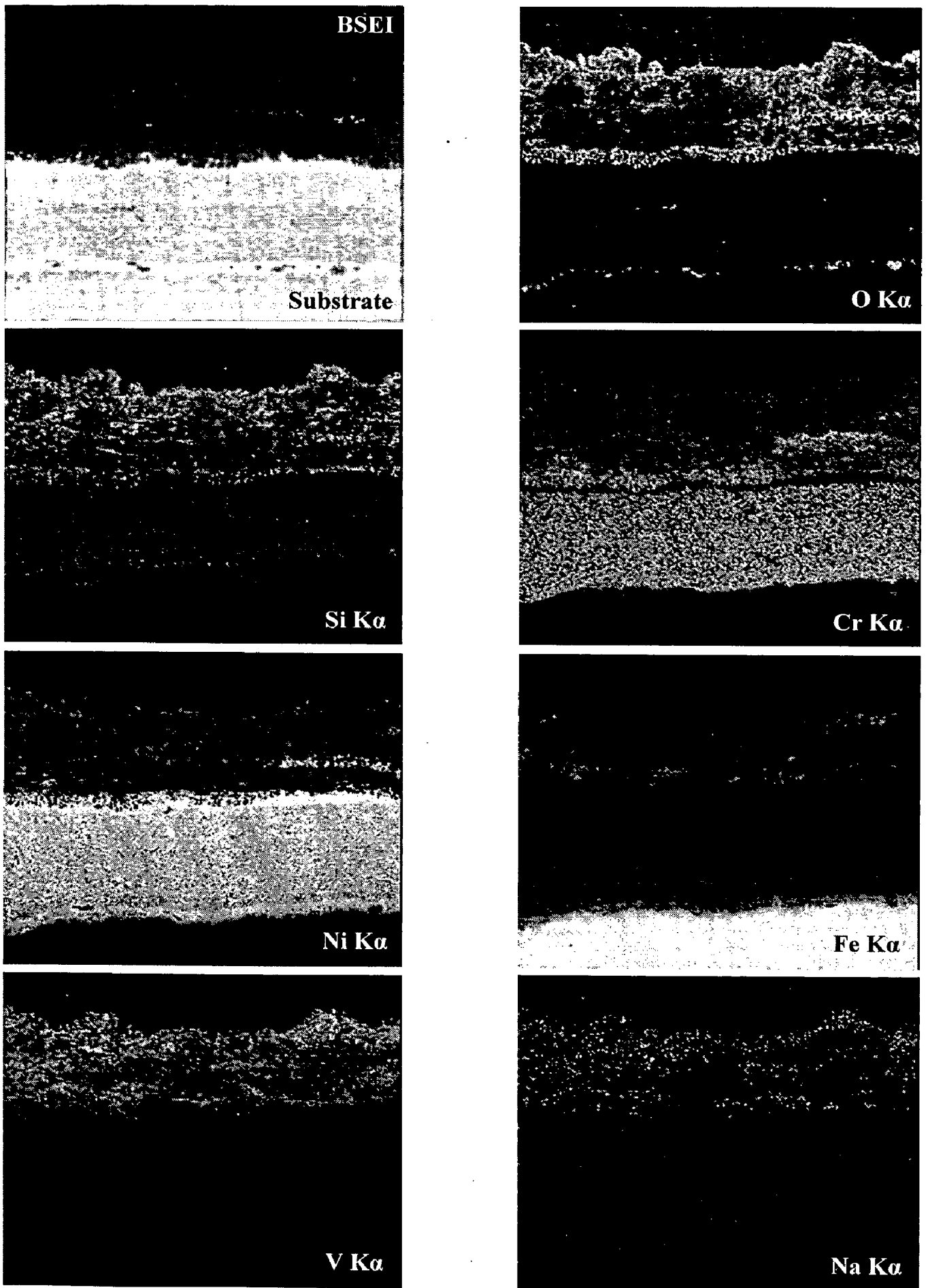
Fig.6.33   BSEI and elemental X-ray mapping along the cross-section of the
NiCrFeSiB coated GrA1 steels subjected to hot corrosion for 50 cycles in
Na₂SO₄-60%V₂O₅ environment at 900°C
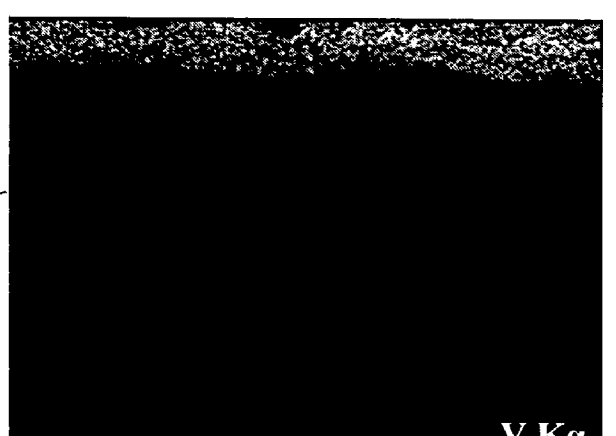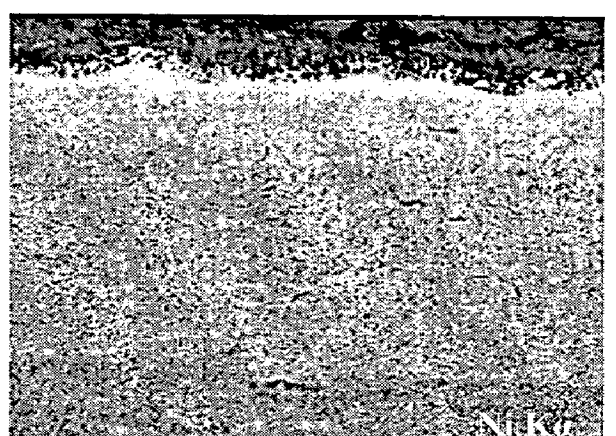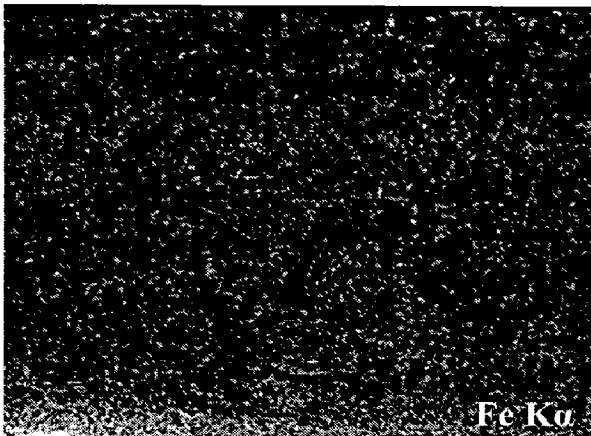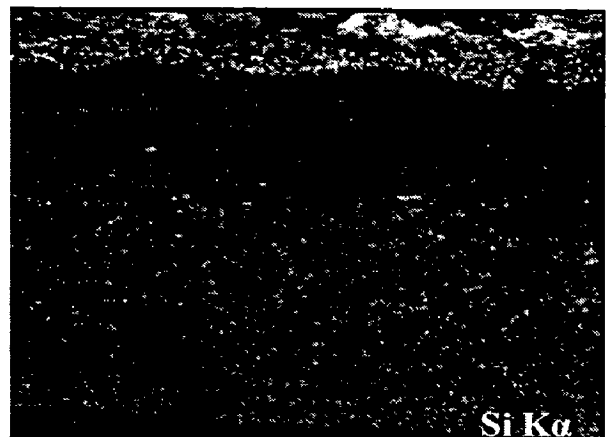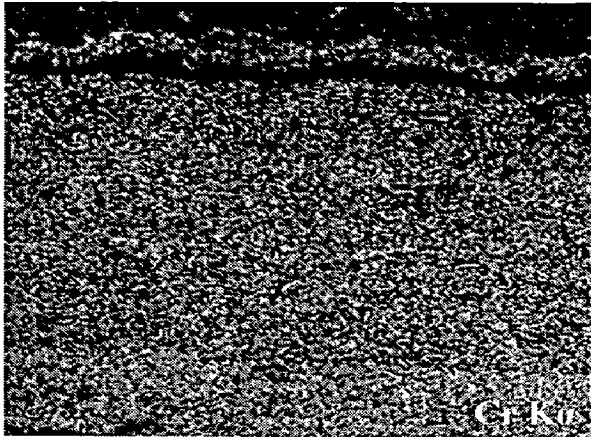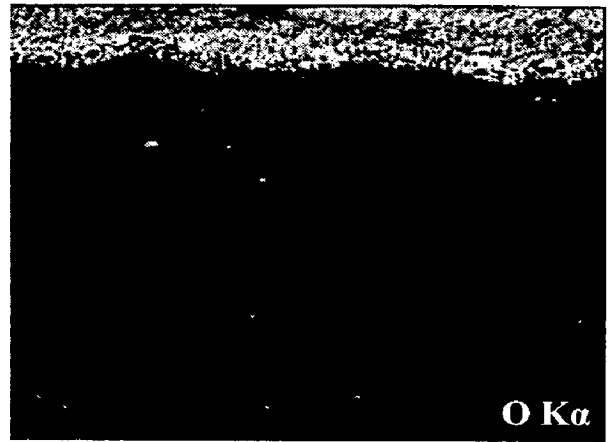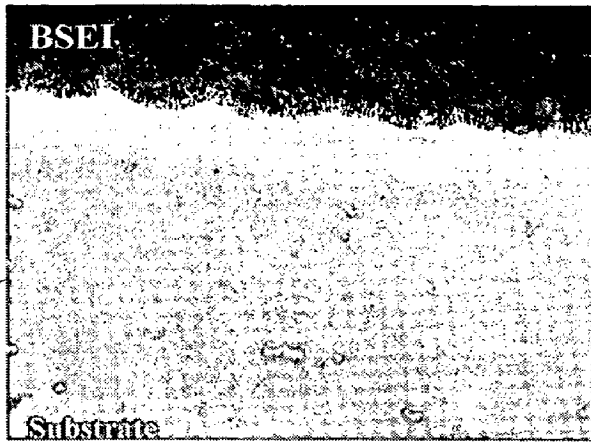
Fig.6.34 BSEI and elemental X-ray mapping along the cross-section of the NiCrAl coated T22 steels subjected to hot corrosion for 50 cycles in Na_2SO_4-60%V_2O_5 environment at 900°C

181
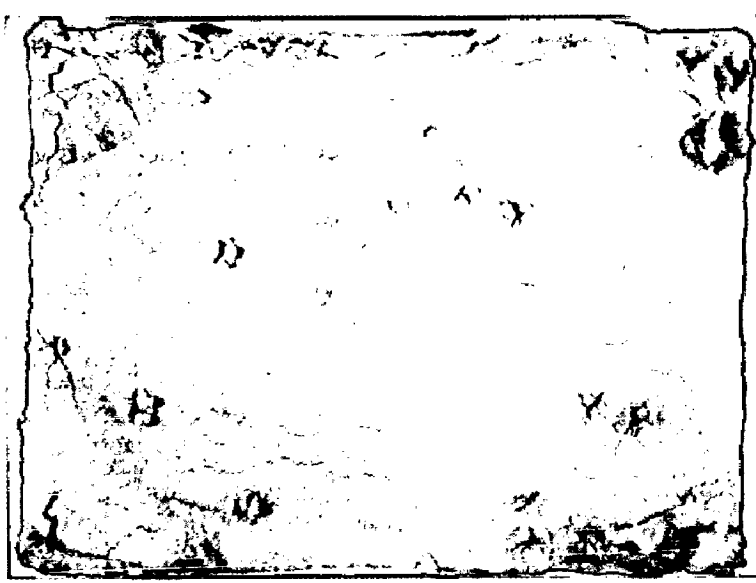
(a)
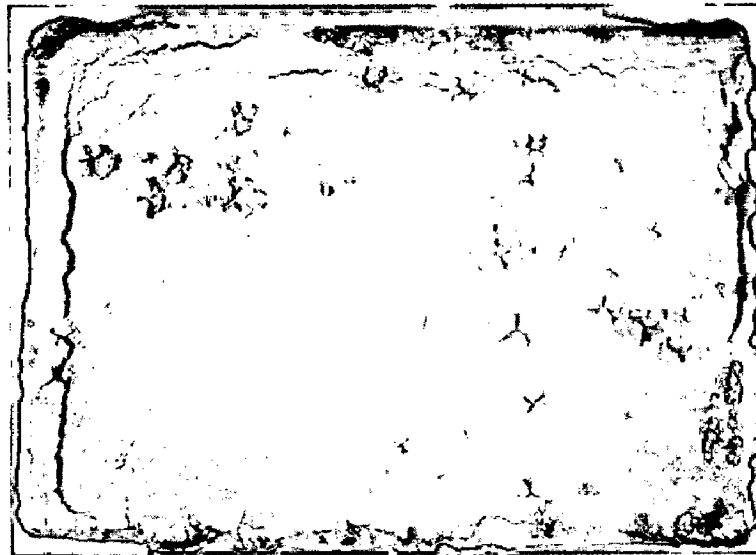
(b)
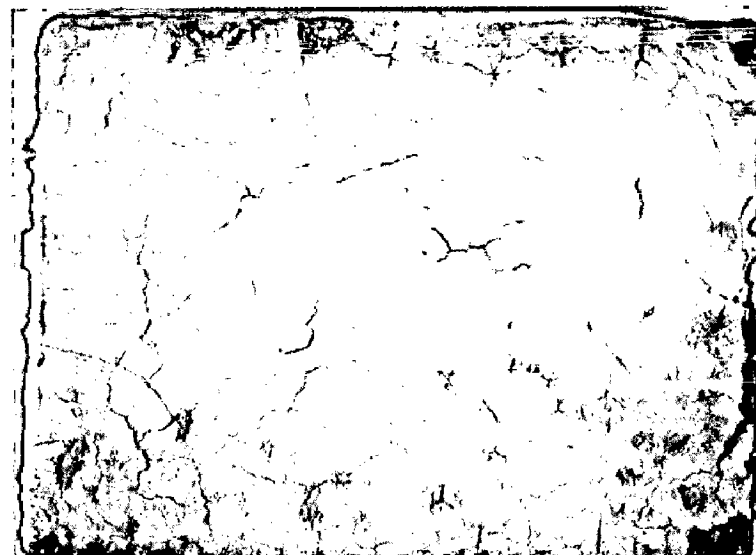
(c)

Fig.6.35   Macrographs of the WC-Co/NiCrFeSiB coating subjected to hot corrosion in Na_2SO_4-60%V_2O_5 environment for 50 cycles at 900°C:
(a) GrA1 steel   (b) T11 steel   (c) T22 steel
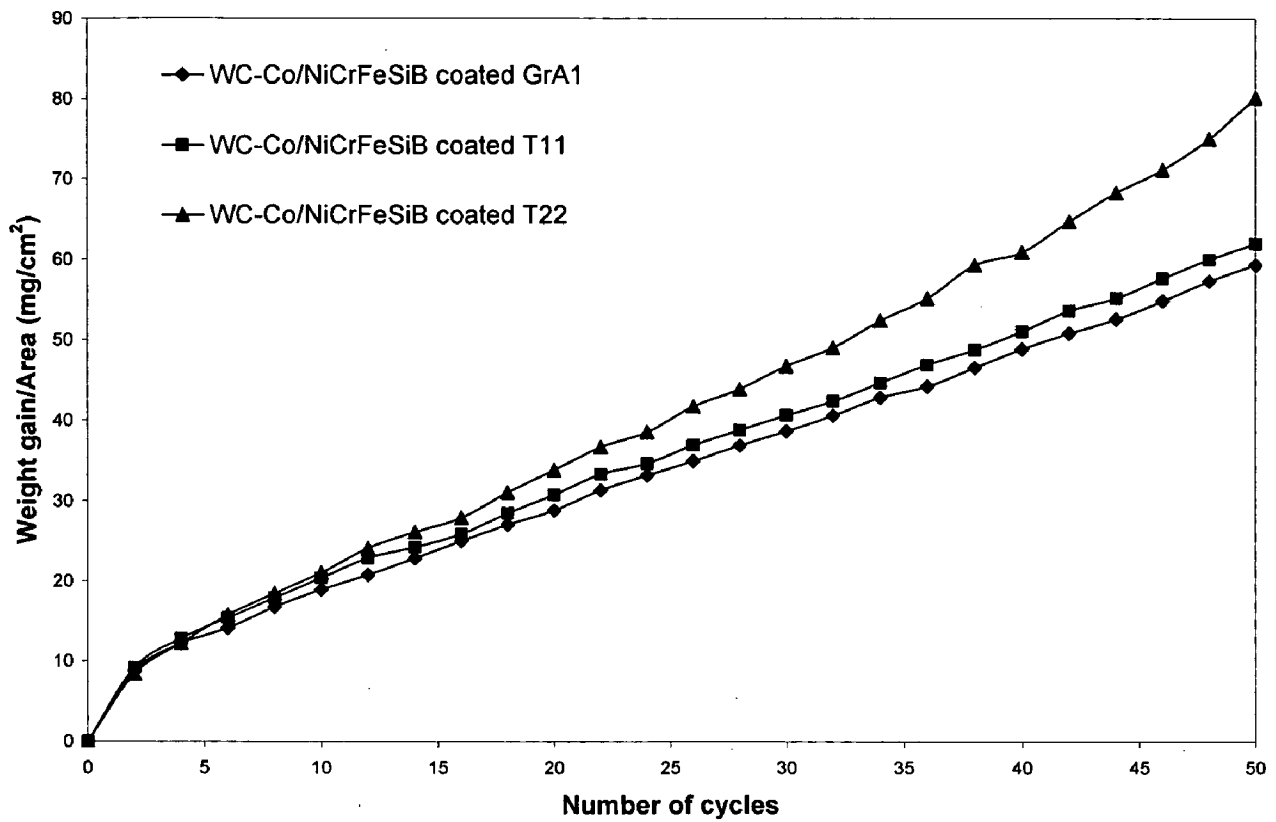
Fig.6.36   Weight gain versus number of cycles plot for WC-Co/NiCrFeSiB coated steels subjected to hot Corrosion for 50 cycles in Na_2SO_4-60%V_2O_5 at 900°C
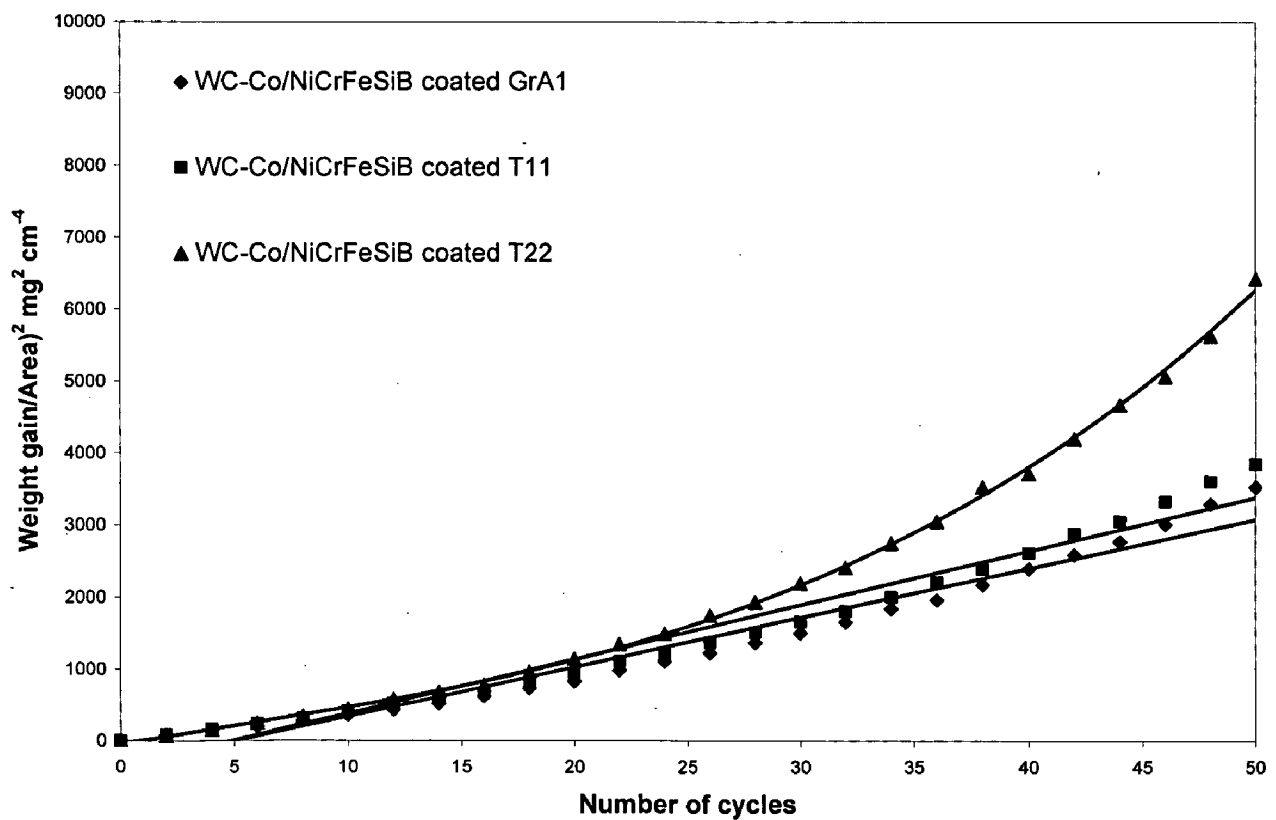
Fig.6.37   (Weight gain/area)^2 versus number of cycles plot for WC-Co/NiCrFeSiB coated steels subjected to hot corrosion for 50 cycles in Na_2SO_4-60%V_2O_5 at 900°C
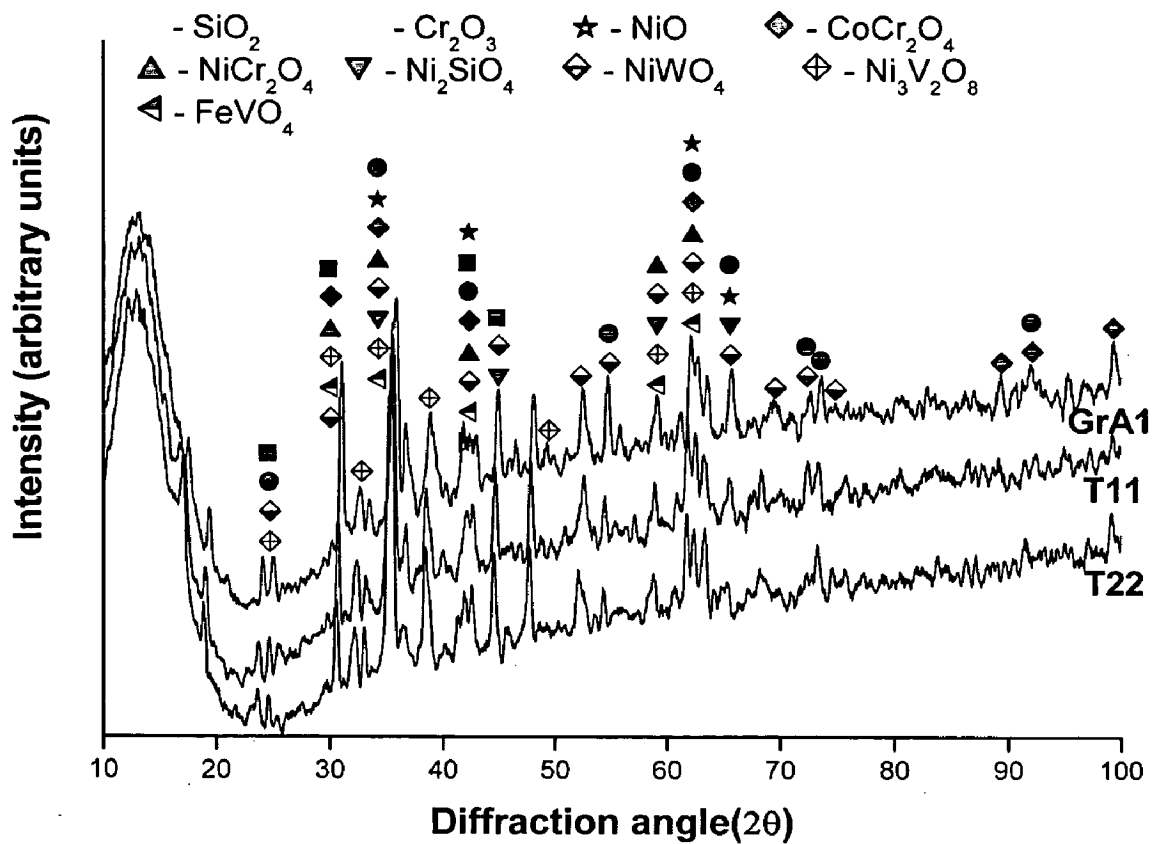
Fig.6.38 X-ray diffraction patterns for NiCrFeSiB coated GrA1, T11 and T22 steels subjected to hot corrosion in Na$_2$SO$_4$-60%V$_2$O$_5$ for 50 cycles at 900°C

EDS area analysis

58.58% NiO
16.40% Cr$_2$O$_3$
07.97% WO$_3$
06.53% CoO
08.41% Fe$_2$O$_3$
02.97% SiO$_2$
02.11% V$_2$O$_5$
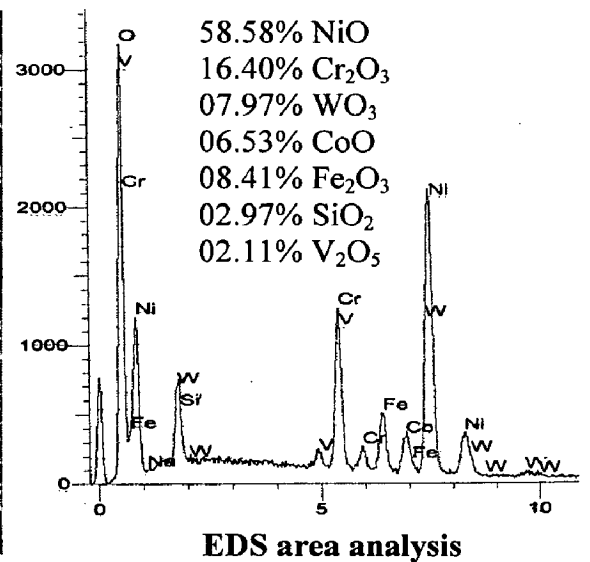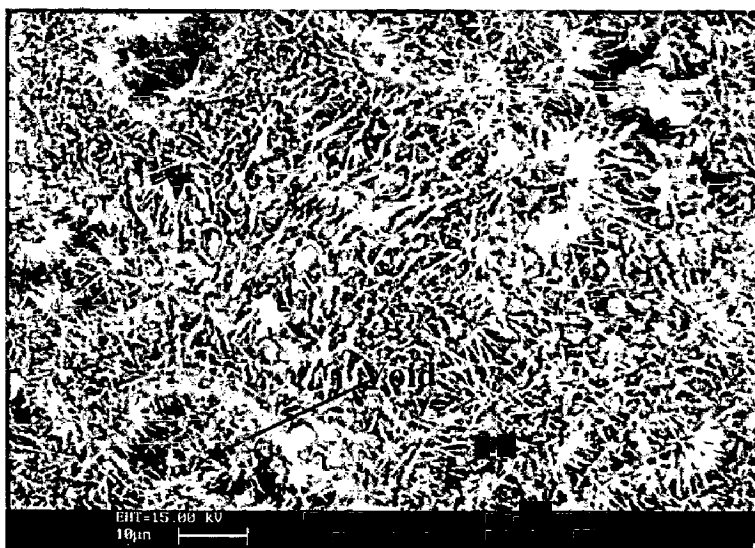
Fig.6.39 Surface scale morphology and EDAX analysis for WC-Co/NiCrFeSiB coated GrA1 steel subjected to hot corrosion for 50 cycles in Na$_2$SO$_4$-60%V$_2$O$_5$ at 900°C

184

6.1.5.3 SEM/EDAX Analysis

The surface morphology of the corroded WC-Co/NiCrFeSiB coated GrA1 steel (Fig.6.39) shows the formation of nonuniform loosely held scale consisting of voids. The loosely held microstructure illustrates the formation of porous oxide layer on the surface of the corroded coating. The compositional EDS analysis on the surface area reveals the dominating presence of nickel oxide (58.58%) along with the oxides of Cr (16.4%), W (7.97%), Co (6.53%) and Fe (8.41%).Minor amount of oxides of silicon and vanadium have also been detected.

The surface morphology of coated T11 steels (Fig.6.40a) shows the flakes and open bud protrusion oozed out perhaps at the region where protective oxide scale failed. Cracks can be noticed around the protrusion. Compositional analysis of the protrusion reveals the presence of oxides of Ni (56.6%), Cr (14.8%) and W (11.7%) as the main constituents. Area of the oxide scale enlarged in Fig.6.40b, shows loosely held needle structure, which might have resulted in formation of bulky oxide scale. EDAX analysis shows relatively lower amount of W (4.13%) when compared to composition of W in the protrusion. The oxide scale mainly composed of oxides of Ni, Cr, and Fe. Minor amount of sulphur and vanadium have also been detected in the surface scale. Corresponding analysis on the coated T22 steel shows non-uniform oxide scale with distinct globules, shown in Fig.6.40c.

Salt-induced high temperature corrosion yielded a bulky oxide scale on the surface of WC-Co/NiCrFeSiB coated GrA1 steel as seen from BSE image (Fig.6.41a) acquired along the cross section of corroded coatings. EDAX analysis at point 1 shows higher amount of oxides of Ni (38.9%) and W (31.8%), suggesting the presence of $NiWO_4$ spinel oxide. Composition at point 2 shows dominant presence of Ni oxide (62.1%) along with the oxides of Si (12.7%) and Cr (7.1%). The oxide scale at the vicinity of the coating (point 3) reveals the higher content of Ni and W. The outward diffusion of Ni from the coating resulted in enrichment of W at the subscale region and might have ended with the formation of spinel of mixed oxides of Ni and W. The contrast white elongated phases (point 4) which are oriented parallel to the substrate consist of 89.9% tungsten. Absence of oxygen at this point confirms WC particles are in an unoxidised condition. The EDAX analysis on the dark grey matrix (point 5) revealed

it as nickel rich splats (Ni-65.4%) which remained unoxidised. Higher concentrations of Ni and Fe along the coating-substrate interface (point 5) support the possibility of interdiffusion of Ni from the coating in to the substrate as well as Fe from the substrate in to the coating. Compositional analysis along the cross section elucidate that only external surface of the coating has been oxidized to form thick oxide scale and below which, coating remained unaffected.

BSE image along the WC-Co/NiCrFeSiB coated T22 Steel (Fig.6.41b) also shows the thick oxide scale formed on the surface of the coating, mainly consisting of oxides of Ni ,Cr and W (point 1 & 2). EDAX analysis at point 3 revealed the presence of significant amount of iron oxide (25.2%). Oozing out of Fe_2O_3 (point 4) from the substrate through the coating is evident from the micrograph. Iron oxide protrusions are subsided by the bulk oxide scale and are seen at the subscale layer. A localized molten salt corrosion of the substrate at the site of protrusion can be observed.

6.1.5.4 EPMA Analysis

Elemental X-ray mapping along the cross-section of the WC-Co/NiCrFeSiB coated T11 steel subjected to oxidation in Na_2SO_4-60%V_2O_5 environment for 50 cycles at 900°C is shown in Fig.6.42. Mapping for oxygen, shows the massive oxide layer formed on the surface of the corroded coating. Relatively higher intensities observed for Ni, Cr and W corroborated the formation of oxides and spinal oxides of Ni, Cr and W on the external surface. Nickel and silicon coexist at some regions in the external surface of the oxide scale which suggest the presence of discontinuous layer of SiO_2 and Ni_2SiO_4 spinel oxide. At these regions tungsten is absent. Close look into Ni and Fe maps indicate the interdiffusion of Ni from the coating in to the substrate as well as Fe from the substrate into the coating, It is clear from the EPMA analysis that only the upper portion of the coating has been oxidized and the coating below the oxide layer remains unoxidised. Hence the oxide scale formed seems to be effective in preventing the transport of corrosive species in to the substrate.

Similar oxide scale has been observed for WC-Co/NiCrFeSiB coated T22 steels which is characterized in Fig.6.43. Thin layer of iron oxide has been observed at the coating-oxide scale interface, which might be due to the iron oxide that oozed out from the substrate to spread along oxidized and unoxidised scale interface.

56.61% NiO
14.83% Cr_2O_3
11.73% WO_3
06.84% CoO
06.89% Fe_2O_3
01.33% SO_3
02.13% V_2O_5

EDS analysis at point 1

(a)

58.94% NiO
18.39% Cr_2O_3
04.13% WO_3
05.30% CoO
08.29% Fe_2O_3
00.74% SiO_2
02.77% SO_3
03.55% V_2O_5

EDS area analysis of Fig. b

(b)

59.26% NiO
15.26% Cr_2O_3
07.15% WO_3
05.59% CoO
08.79% Fe_2O_3
01.33% Na_2O
02.09% V_2O_5
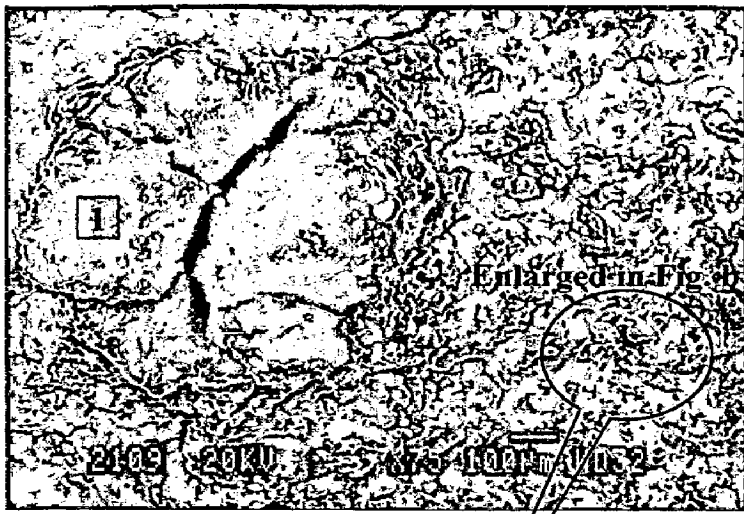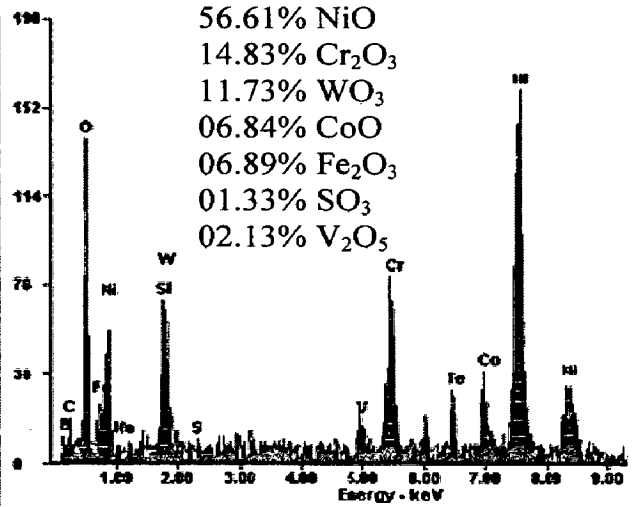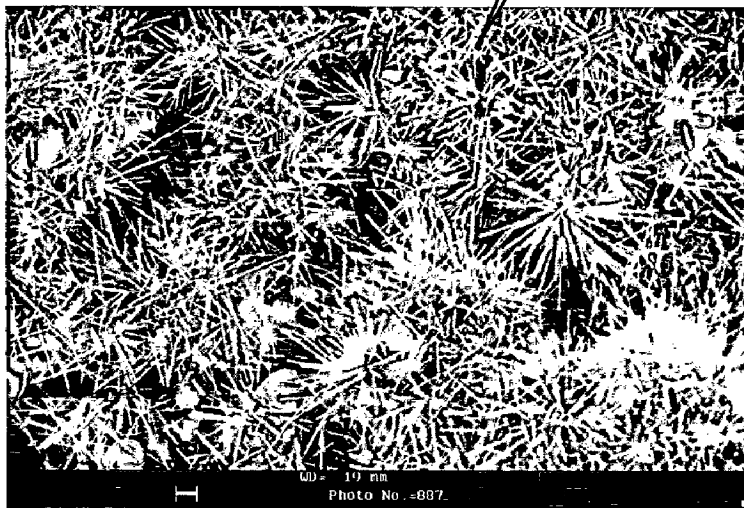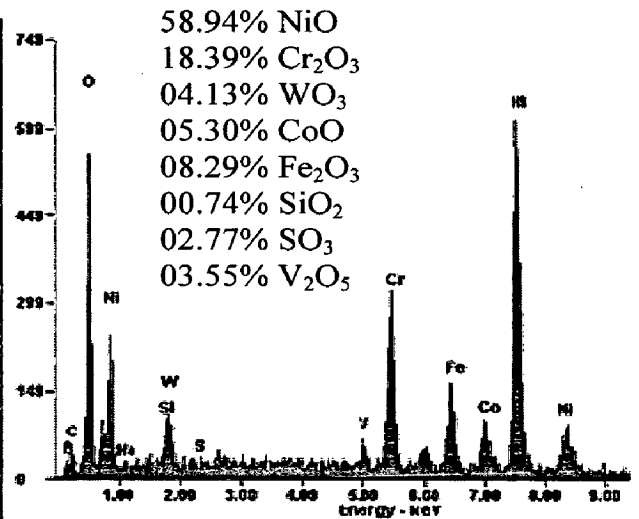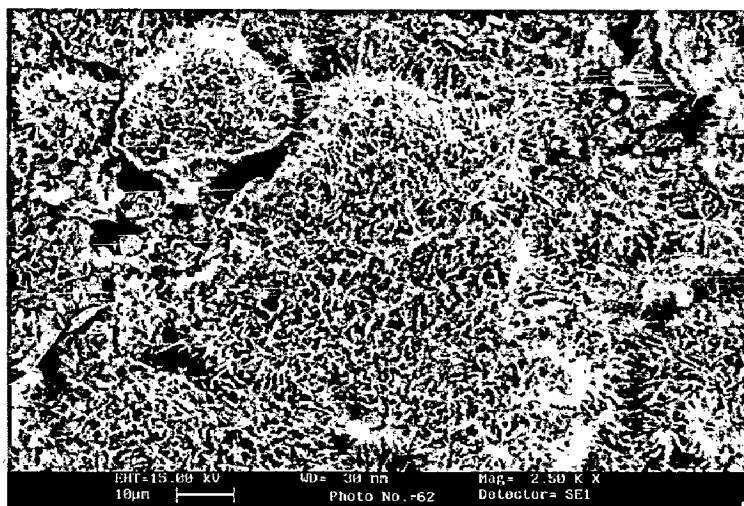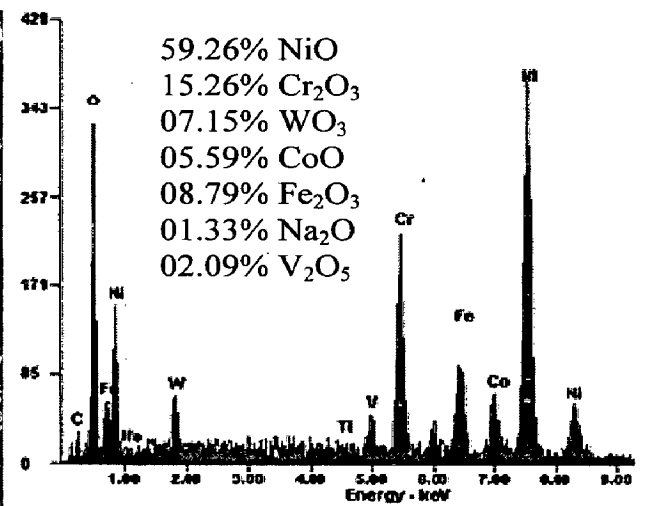
EDS area analysis of Fig. c
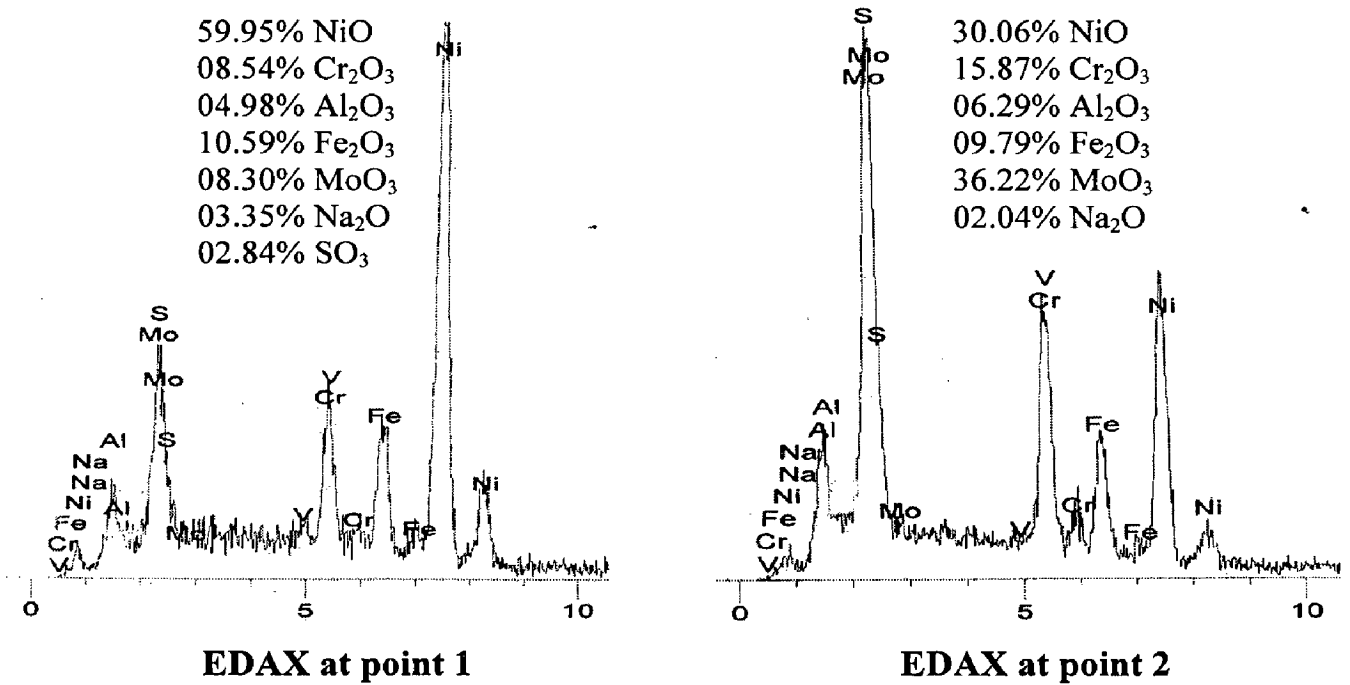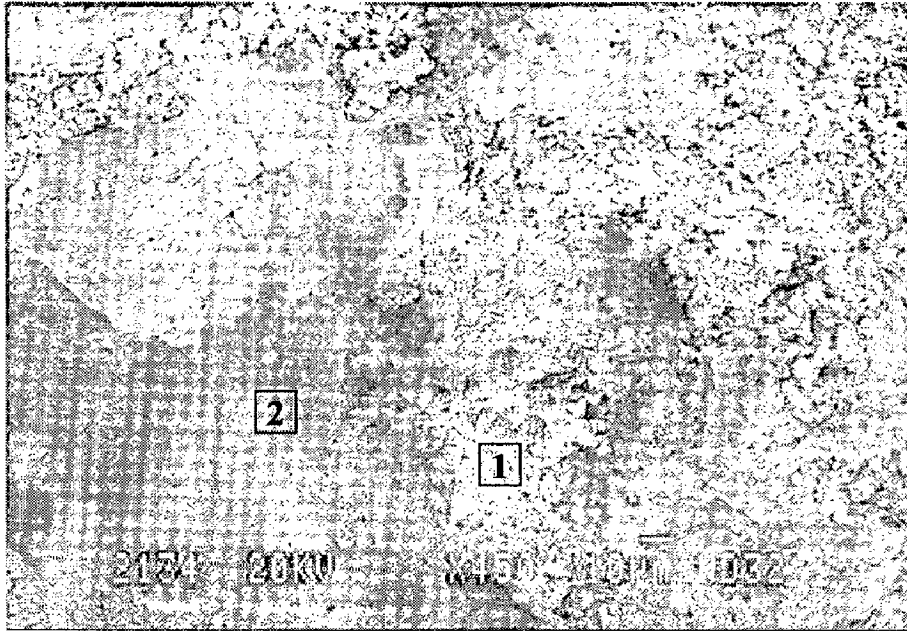
(c)

Fig.6.40   Surface scale morphology and EDAX analysis for WC-Co/NiCrFeSiB
coated steels subjected to hot corrosion for 50 cycles in Na_2SO_4-60%V_2O_5
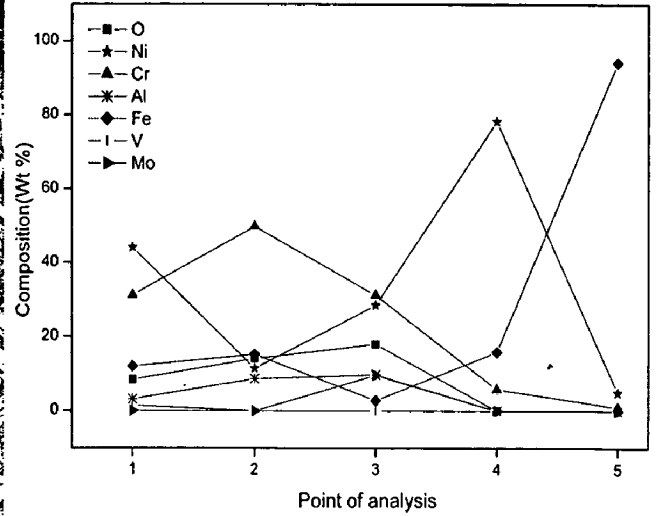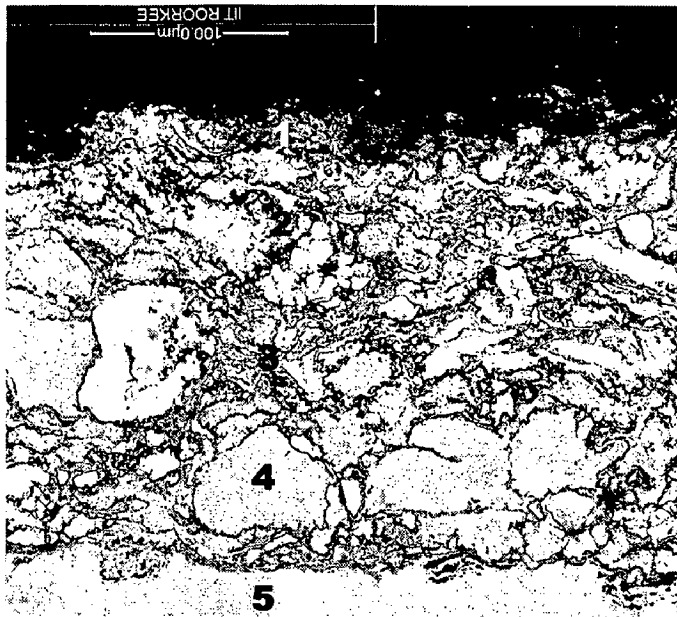at 900°C: (a) T11 steel   (b) Enlarged area of Fig. a
(c) T22 steel
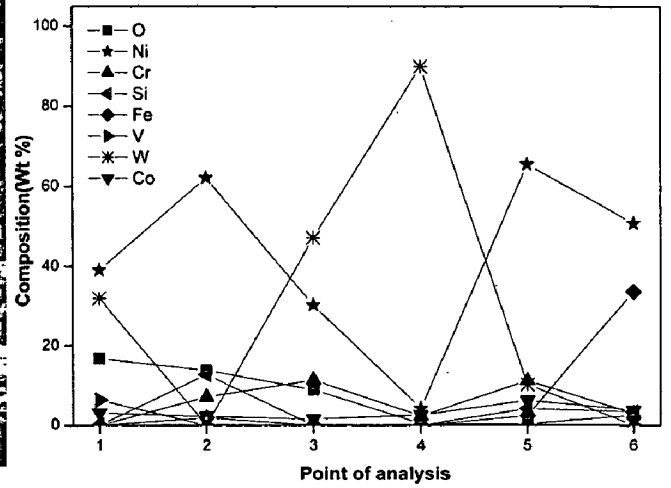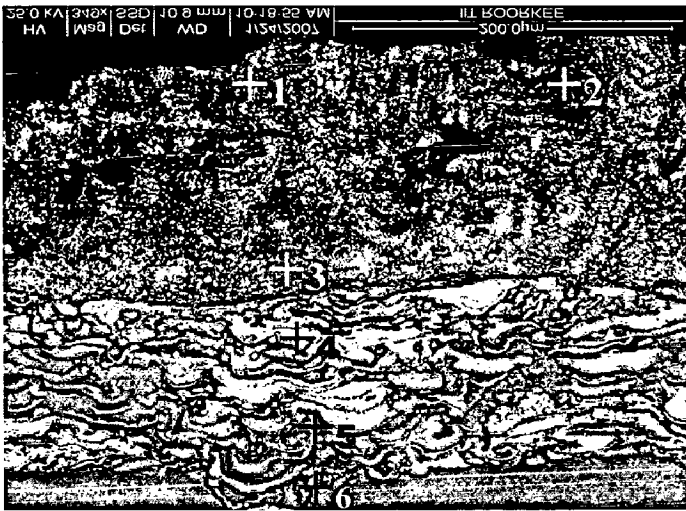
(a)
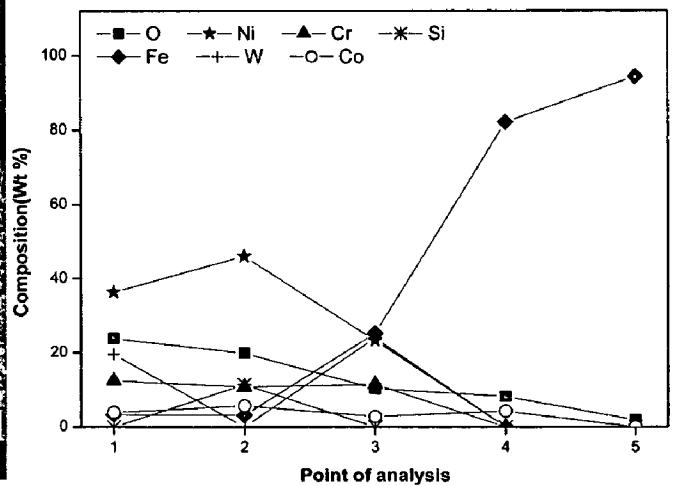
(b)

Fig.6.41   Back scattered electron image and EDAX point analysis (wt %) across the
cross-section of the WC-Co/NiCrFeSiB coated steels subjected to hot
corrosion in Na₂SO₄-60%V₂O₅ environment for 50 cycles at 900°C :
(a) GrAl steel   (b) T22 steel

188
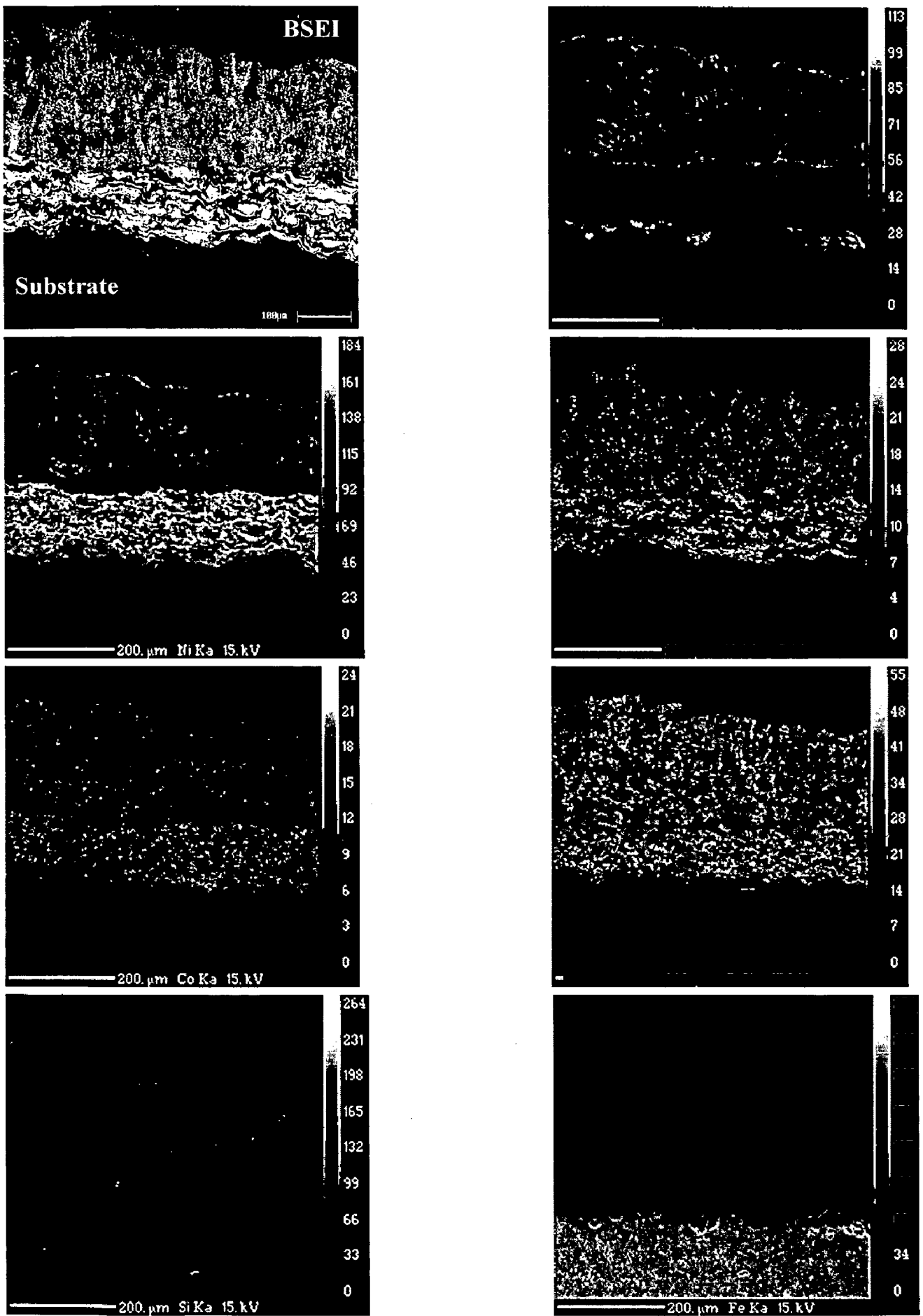
Fig.6.42 WDS X-ray mapping along the cross-section of the WC-Co/NiCrFeSiB coated T11 steels subjected to hot corrosion for 50 cycles in Na_2SO_4-60%V_2O_5 environment at 900°C

189
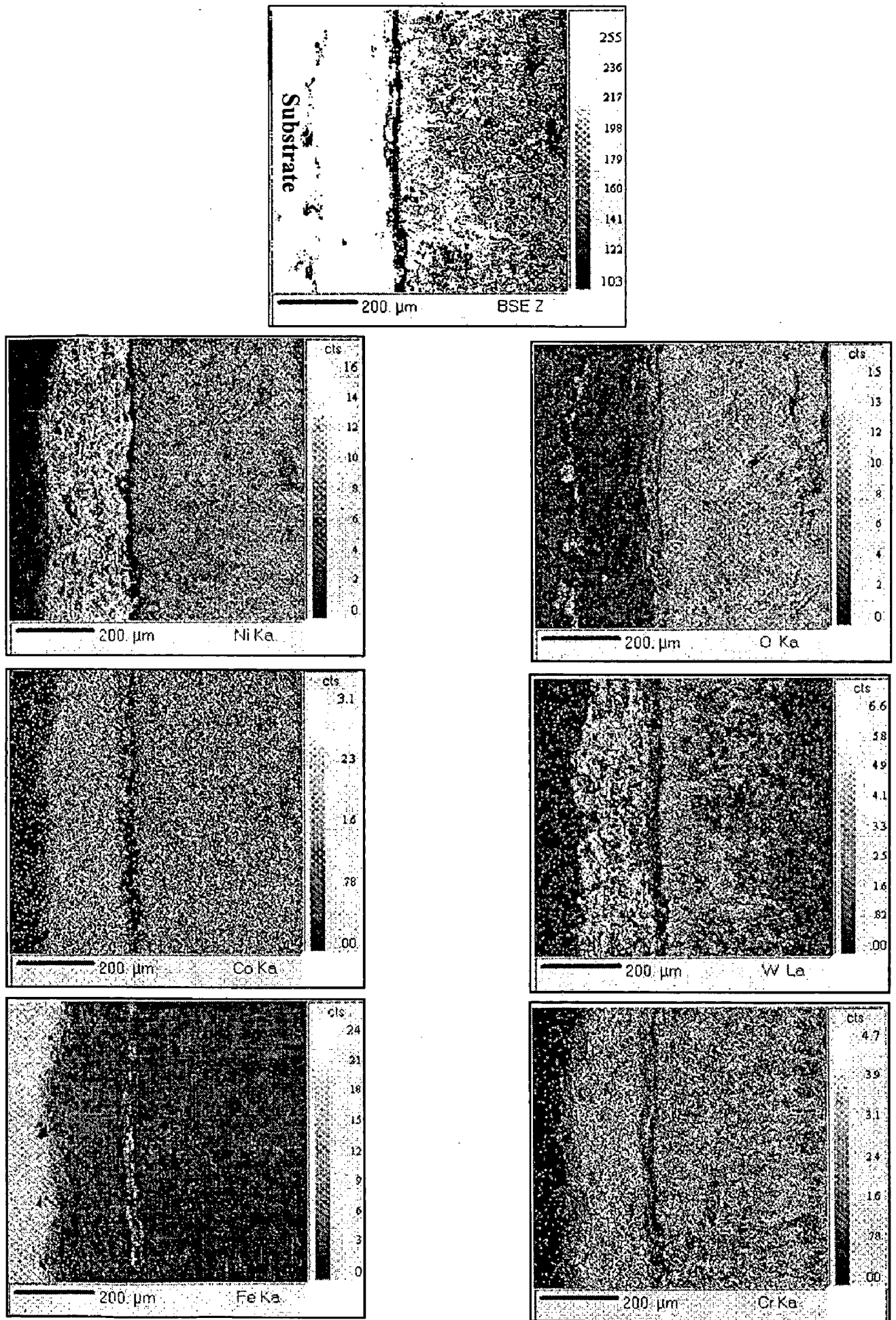
Fig.6.43   WDS X-ray mapping along the cross-section of the WC-Co/NiCrFeSiB coated T22 steels subjected to hot corrosion for 50 cycles in Na₂SO₄-60%V₂O₅ environment at 900°C

6.2 SUMMARY OF RESULTS

Results of Hot corrosion studies in molten Na_2SO_4-60%V_2O_5 eutectic mixture reported in section 6.1 for coated and uncoated steels are summarized in Table 6.1, to elicit comparisons among the various coatings and substrate.

Table 6.1 Summary of the results for uncoated and coated steels subjected to hot corrosion in Na_2SO_4-60%V_2O_5 molten salt for 50 cycles at 900^0C.

Coating	Substrate	Weight gain mg/cm^2	Parabolic constant, $K_p \times 10^{-9}$ $g^2cm^{-4}s^{-1}$	XRD phases	Remarks
Uncoated Steels	GrA1	223.79	284.1	Fe_2O_3, FeS_2	• Intense spalling of oxide scale is observed • The main constituent of oxides scale formed in all the steels is Fe_2O_3.
	T11	200.91	231.8	Fe_2O_3, Cr_2O_3, FeS_2	• In case of T11 and T22 steels, the inner layer of the scale contains continuous layer of Chromium oxide and streaks of molybdenum.
	T22	428.12	1183.3	Fe_2O_3, Cr_2O_3, FeS_2, $CrVO_3$	• X-ray mappings for T22 steel shows Cr, V and O co-exist together at the upper most oxide scale and confirmed the formation of chromium vanadate.
NiCrAl coating	GrA1	19.28	0.229	δ-Al_2O_3, θ-Al_2O_3, NiO, Cr_2O_3, $NiCr_2O_4$, $NiAl_2O_4$ $Ni_3V_2O_8$, $AlVO_4$ and $CrVO_4$.	• A thick greenish dark grey colored oxide scale (25-50μm) has been formed on the surface mainly consist of oxides of Ni, Cr and a thin stringers of aluminum oxide.
	T11	26.14	0.419		• Blade like structured θ-Al_2O_3 has been identified on the surface. • Preferential oxidation of Al and Cr along the nickel rich splat boundaries has been observed.
	T22	30.52	0.549	θ-Al_2O_3, Cr_2O_3, $NiCr_2O_4$, $Ni_3V_2O_8$, $AlVO_4$, $CrVO_4$, and Fe_2O_3	• Iron oxide protrusions are observed on the surface of coated T22 steel. • Presence of V and Na at the outermost oxide scale supports the formation of Corrosion products.

Coating	Steel			Phases	Observations
NiAlCrFeMo coating	GrA1	38.49	8.15	NiO, NiCr$_2$O$_4$, Ni$_3$V$_2$O$_8$, AlV$_2$O$_4$, Al$_2$O$_3$, Fe$_2$O$_3$ and NiMoO$_4$	• Iron oxide protrusions as well as spalling of the oxide scale in the form of tiny flakes has been noticed in case of coated GrA1 and T11 steels where as in case of coated T22,it is more pronounced. • Green color oxide scale at the outermost surface of the corroded coating mainly consists of oxides of Ni, Cr and perhaps their spinals. • The entire cross-section of the coating has been oxidized along the splat boundary • Mo has been consumed at the surface in the formation of volatile oxides.
	T11	43.16	10.19		
	T22	99.35	linear behavior		
NiCrFeSiB coating	GrA1	13.23	0.899	SiO$_2$, Cr$_2$O$_3$, NiCr$_2$O$_4$, FeCr$_2$O$_4$, NiO, SiO$_2$-B$_2$O$_5$, Ni$_3$V$_2$O$_8$, Na$_4$FeO$_3$ and CrVO$_4$	• Salt induced hot corrosion of coatings yield a bulky reddish brown oxide scale about 110 to 140 μm. • The uppermost portion of the oxide scale mainly consisted of continuous film of SiO$_2$ and the sub-scale found to be rich in Cr$_2$O$_3$. • Coating region below this thick oxide scale remain unoxidised. • Presence of V and Na also been indicated at the outermost layer. • Thick band along the coating-substrate interface shows the presence major amount of Fe and Ni, which signify the interdiffusion of these elements along the interface.
	T11	13.34	0.922		
	T22	13.82	0.998		
WC-Co/ NiCrFeSiB Coating	GrA1	59.35	18.99	Cr$_2$O$_3$, NiO, SiO$_2$, NiWO$_4$, CoCr$_2$O$_4$, NiCr$_2$O$_4$, Ni$_2$SiO$_4$, Ni$_3$V$_2$O$_8$, and FeVO$_4$.	• Open bud shaped protrusions are appeared on the corroded surface. • Massive, pale brown color oxide scale observed on the surface mainly consists of oxides and spinles of Ni, Cr and W. • EPMA analysis shows nickel and silicon coexists at some regions on the external surface of the oxide scale which suggest the presence of discontinuous layer of SiO$_2$ and Ni$_2$SiO$_4$ spinel oxide. • SEM shows loosely held needle microstructure illustrates the formation of porous oxide scale on the surface • Corrosion is restricted to upper part of the coating and portion below the thick oxide scale is in unoxidised condition.
	T11	61.97	20.81		
	T22	80.18	linear behavior		

6.3 DISCUSSION

6.3.1 Uncoated Steels

The results of thermogravimetry data demonstrates the accelerated kinetics induced due to Na_2SO_4-60%V_2O_5 eutectic mixture. Thick oxide scale formed on GrA1, T11 and T22 steels mainly consists of iron oxide. T22 steel shows a higher corrosion rate and intense spalling of oxide scale in comparison to T11 and GrA1 steels. The higher Corrosion rate of T22 steel can be attributed to the presence of Mo. X-ray mapping for this steel also shows streaks of Mo in the interior of the oxide scale, which might have formed Mo mixed oxides. Deleterious effect of Mo has been already discussed in section 6.1.1. The acidic nature of MoO_3 increases the acidity of the molten salt mixture (Na_2SO_4-60%V_2O_5) and this might have led to the acidic fluxing of the protective oxides and results in porous oxide scale, allowing the aggressive gas to reach the metal surface. Identical results have been reported by Sidhu et al.(2003B), Otero et al.(1996), Peters et al (1976), Fryburg et al. (1982), Pettit and Meier (1985) and Misra (1986). Further X-ray mapping for Cr, V and O revealed that these elements co-exists together at the upper part of the oxide scale, which supports the formation of chromium vanadates as a result of dissolution-reprecipitation process. This dissolution reaction would have caused breakdown of the initially formed chromium oxide film on the alloy surface. XRD and EDAX analysis also indicated the presence of iron sulfides on the surface.

In case of T11 and T22 steels, an inner layer of scale contain predominantly Cr_2O_3 due to continuous diffusion of iron towards upper layer of scale, out weights that of chromium. The formation of iron chromium spinal along with chromium oxide in the inner scale has been reported by Ahila et al. (1993) and Khanna et al. (1982).The protection offered by these iron chromium spinal and chromium oxide may be the reason for the lower weight gain for T11 steel compare to GrA1 steel.

The stress developed due to higher volume of the oxide scale leads to cracking and is as evident from Fig.6.6. The severe spalling of oxide scale during hot corrosion of T22 steel in Na_2SO_4-V_2O_5 molten salt and medium BTU coal gasifier environment has been reported by Sidhu et al. (2003B) and Wang (1988), where they observed more than 70% of the scale got spalled during their test. Further Misra (1986) reported the spalling of thick external porous scale which spalled off completely on cooling during corrosion experiments at 900°C and 950°C.

6.3.2 NiCrAl coating

The NiCrAl coated steels show lower weight gain in comparison to the uncoated steels as reported in Section 6.1.1.1., when exposed to Na_2SO_4-60%V_2O_5 molten salt environment. The weight gain after 50 cycles of exposure of the NiCrAl coated GrA1, T11 and T22 steels are found to be 1/11, 1/7 and 1/14, respectively, times the uncoated substrate steels of the same kind. The parabolic rate constant (K_p) decreases for all the coated steels in comparison to the uncoated steels and, therefore, it can be inferred that the necessary protection has been provided by the HVOF-sprayed NiCrAl coatings to the substrate steels. Similar findings have also been reported by Sidhu et al.(2006A) and Singh et al. (2005B) wherein they showed a better corrosion resistance of plasma-sprayed NiCrAlY coatings in comparison to the substrate boiler steels and Fe-based super-alloy exposed to Na_2SO_4-60%V_2O_5 environment at 900°C.

A continuous and thick compact layer of scale is formed on the top of the corroded coating (Fig. 6.14) which measured about 25–50 μm after 50 cycles of hot corrosion studies. The XRD analysis (Figs. 6.11 and 6.12) on the surface of the oxidized scale revealed the existence of δ-Al_2O_3, θ-Al_2O_3, NiO, Cr_2O_3, $NiCr_2O_4$, $NiAl_2O_4$ and traces of $Ni_3V_2O_8$, $AlVO_4$, and $CrVO_4$. The SEM of oxide scale has a blade-like structure with smooth patches (Fig. 6.13a). The EDAX analysis on these patches indicates a higher percent of Al_2O_3 (58.83%). The blade-like structure could correspond to θ-Al_2O_3 as identified by the XRD. The Al_2O_3 formed as a thin layer which is confined to the topmost portion of the oxide scale as seen in the EPMA analysis (Figs. 6.15 to 6.17). Due to the accelerated oxidation induced by the molten salt, which acts as a catalyst and oxygen carrier, it is expected that the metastable Al_2O_3 has formed in the initial cycles of the studies that shows polymorphic transformation. Similar results showing the formation of metastable modifications of Al_2O_3 during the oxidation of HVOF-sprayed MCrAlY coatings and sputtered NiCrAl nanocrystaline coating is also reported by Brandl et al. (1998) and Guofeng et al. (1999). The EPMA and the EDAX analysis on the surface and along the cross section of the corroded coating show that the top layer is rich in NiO, Cr_2O_3, and their spinals due to discontinuous Al_2O_3 layer. Further, NiO and spinal oxides prevent the exclusive development of Cr_2O_3 layer, although the Cr concentration is 17.92% in the coating. This was substantiated by the results of Singh et al.(2005A) and Longa et al. (1992), wherein they identified NiO and $NiCr_2O_4$ along with relatively small quantities of Cr_2O_3 phase for flame-sprayed NiCrAl

and plasma-sprayed NiCrAlY coating oxidized in Na_2SO_4-60%V_2O_5 at 900°C. The formation of a continuous layer of NiO on the top scale is in accordance with the results reported by Sidhu et al. (2006A) and Seiersten et al. (1987).

The EPMA and EDAX analysis along the cross section shows the distribution of Na and V on the uppermost oxide scale. and, hence, the acidic fluxing by Na_2SO_4-60%V_2O_5 mixture may be expected. Based on the available thermodynamic data, Na2SO4 can react with V_2O_5 to increase the acidity of melt by the formation of vanadates $NaVO_3$ (m.p.$\approx$ 610°C) as per following reaction at 900°C (Kolta et al., 1972):

$$Na_2SO_4 + V_2O_5 \rightarrow 2NaVO_3 \, (l) + SO_2 + \frac{1}{2} \, O_2$$

This $NaVO_3$ acts as a catalyst and the acidic dissolution of NiO, Al_2O_3, and Cr_2O_3 probably might have occured according to the reactions (Longa et al., 1996; Hwang et al., 1989):

$$3 \, NiO + 2 \, NaVO_3 \rightarrow Ni_3(VO_4)_2 + Na_2O$$

$$Al_2O_3 + 2NaVO_3 \rightarrow 2AlVO_4 + Na_2O$$

$$Cr_2O_3 + 2NaVO_3 \rightarrow 2CrVO_4 + Na_2O$$
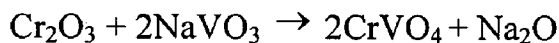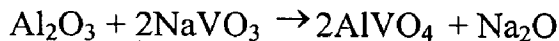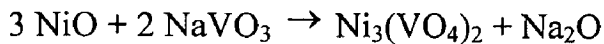
These dissolution reactions could have caused breakdown of the initially formed oxide film on the coating surface. The XRD and EPMA results also corroborated the formation of these metal vanadates which are concentrated mainly in the top scale.

The preferential oxidation of Al and Cr along the nickel-rich splats boundaries as revealed by the EPMA analysis acts as a diffusion barrier to the inward diffusion of the corrosive species. The nickel-rich splats are not oxidized during the high temperature corrosion studies for 50 cycles. The observation into the coating-substrate interface (Figs. 6.14 to 6.16) reveals the diffusion of iron into the coating along with the diffusion of coating elements Ni, Cr, and Al into the substrate which helps in better bonding. The presence of grit particles along the coating-substrate interface are the residues of the surface preparation prior to the HVOF spraying (Evans et al. 2001).

The weight gain in NiCrAl coated T22 steels is higher than that of the GrA1 and T11 steels and this may be attributed to the development of cracks after the 41st cycle of hot corrosion studies in molten salt environment for 50 cycles. The thermal shocks generated due to the differences in thermal expansion coefficients of coatings, substrate, and oxides may be responsible for the development of cracks. The surface morphology of the coated T22 steels (Fig. 6.13c) shows a worm-like protrusion on the surface of the oxide scale and the EDAX analysis on this protrusion confirmed that it mainly consisted

of Fe_2O_3, which is oozed out from the substrate through the cracks developed during the hot corrosion studies. The protrusion of Fe_2O_3 from the beneath of NiCrAl coated T22 steels exposed to the salt environment is identical to the results observed during the oxidation of NiCrAl coated T22 steel in air which has been discussed in Section 6.3.2 in detail. Sidhu et al. (2006A) also reported similar corrosion behavior of the NiCrAlY coated T22 steels in Na_2SO_4-60%V_2O_5 environment at 900°C. Fig.6.44 shows the general hot corrosion mode for NiCrAl coatings exposed to molten salt environment at 900°C.

6.3.3 NiAlCrFeMo coating

The surface morphology of the corroded coatings (Fig.6.22 and 6.23) as well as the backscattered image across the cross section (Fig.6.24) shows that the oxide scale formed on the surface of the corroded coatings are porous and non adherent. This might be due to acidic fluxing of the oxide scale induced by the eutectic Na_2SO_4-60%V_2O_5 molten salt mixture at 900°C during the early stage of oxidation studies. Based on the available thermodynamic data, Na_2SO_4 can react with V_2O_5 to increase the acidity of melt through the formation of liquid vanadates $NaVO_3$ (m.p.$\approx$ 610°C) at 900°C (Kolta et al, 1972). Further when the alloy contains a small amount of Mo, one of the main reactions is the formation of molybdenum oxide (MoO_3). The molten salt melt becomes more acidic due to acidic character of MoO_3 and combined effect causes catastrophic self-sustaining hot corrosion via acidic fluxing. MoO_3 reacts with the oxides present on the coating surface such as Cr_2O_3 and NiO, to form nickel and chromium molybdates which are low melting point compounds according to equations (Santorelli et al. 1989 and Peters et al. 1976). In this case, molten salt plays an important role in kinetics of the reaction:
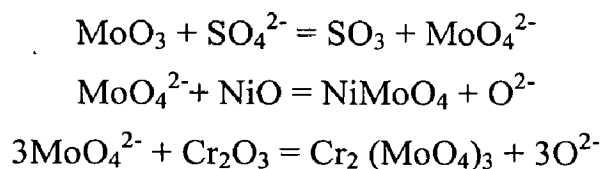
$$MoO_3 + SO_4^{2-} = SO_3 + MoO_4^{2-}$$
$$MoO_4^{2-} + NiO = NiMoO_4 + O^{2-}$$
$$3MoO_4^{2-} + Cr_2O_3 = Cr_2 (MoO_4)_3 + 3O^{2-}$$

These molybdates usually form a liquid phase at 900°C and induce formation of a highly friable and porous scale, thereby held to be responsible for the enhancement in attack. The EPMA and EDAX compositional analysis on the surface oxide layer revealed oxides of Ni and Cr as the main constituents. The XRD results (Fig.6.21) also show the presence of $NiMoO_4$ on the surface of corroded coatings along with the major phases of

Na$_2$SO$_4$-60%V$_2$O$_5$, 900°C

Patches of θ-Al$_2$O$_3$

Corrosion Products AlVO$_4$ and CrVO$_4$

Ni rich splat in unoxidised condition

Thick oxide scale rich in NiO,Cr$_2$O$_3$ and NiCr$_2$O$_4$

Preferential oxidation of Al & Cr along the splat boundary

Fe^{3+} Substrate   Fe^{3+}
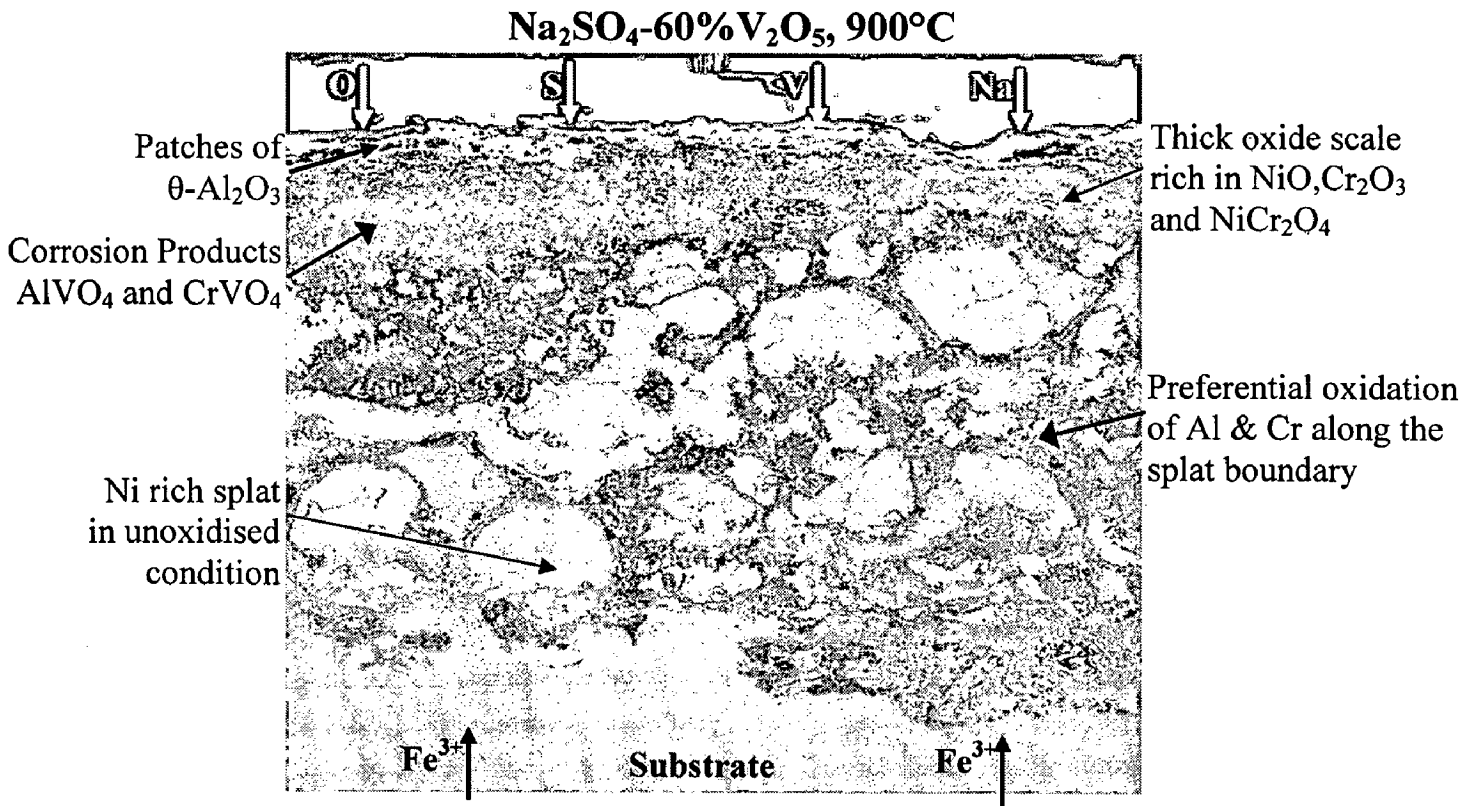
Fig.6.44   Hot corrosion mode of NiCrAl coated steels exposed to Na$_2$SO$_4$-60%V$_2$O$_5$ environment for 50 cycles at 900°C

Na$_2$SO$_4$-60%V$_2$O$_5$, 900°C

Corrosion Products Ni$_3$V$_2$O$_8$ and AlV$_2$O$_4$

Ni rich splat in unoxidised condition

Oxide scale rich in NiO, NiCr$_2$O$_4$, and NiMoO$_4$

Mo consumed in upper part of coating

Severe internal oxidation along the splat boundary/pores
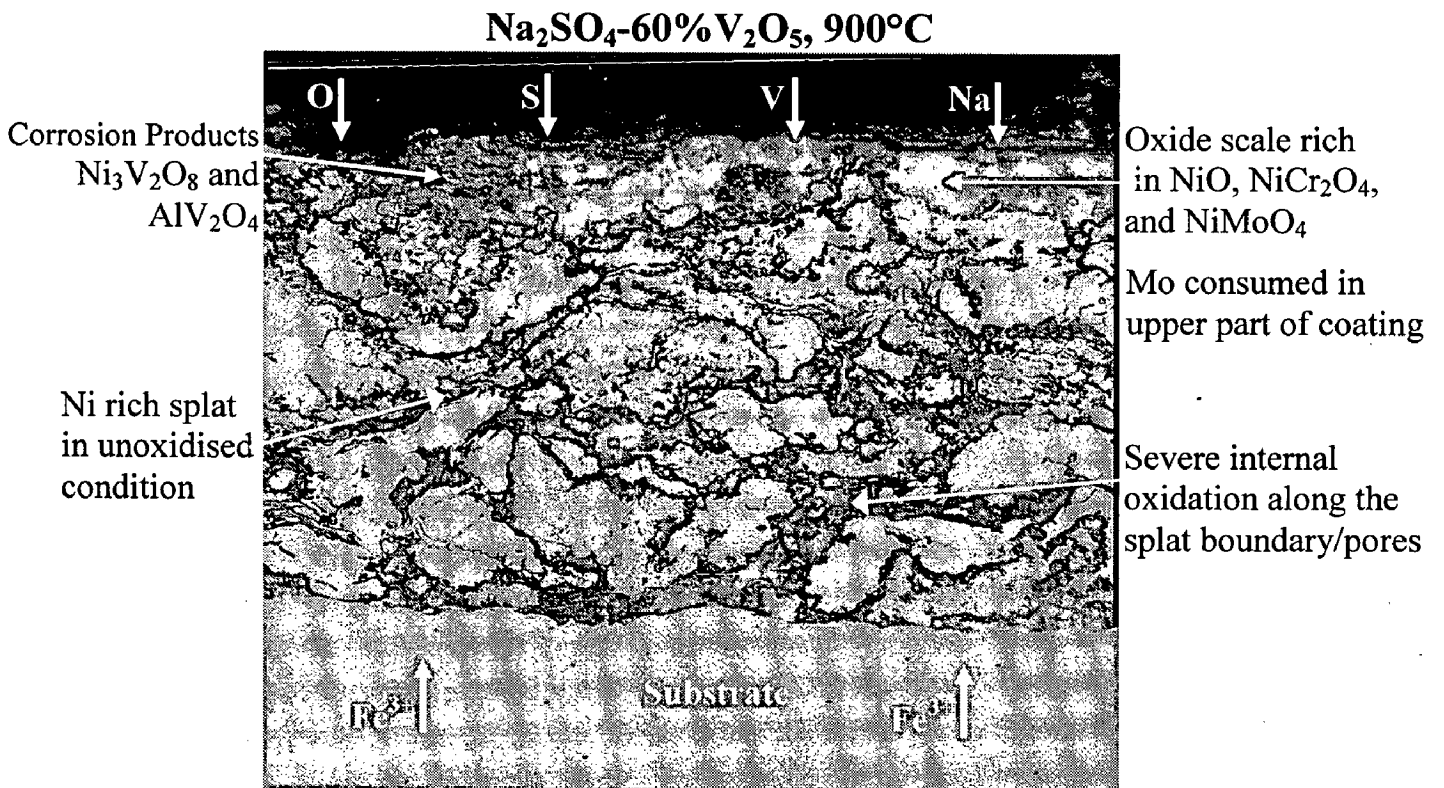
Fig.6.45   Hot corrosion mode of NiAlCrFeMo coated steels exposed to Na$_2$SO$_4$-60%V$_2$O$_5$ environment for 50 cycles at 900°C

197

NiO and $NiCr_2O_4$. It can be explained that Mo has been consumed in the surface layer only at the early oxidation stage and with the progress of oxidation cycles, it has to be transported from the depth of the coating and hence corrosion rate reduced with time. X-ray mapping for the Mo (Fig.6.25) shows relatively lower concentration of the Mo at the surface than at the bottom of coating. Niranatlumpong et al. (2000) also suggested that spalling and adhesion loss in case of chromia and alumina forming alloys may also be due to chemical failure of these protective layers and formation of porous Ni-rich oxides above them.

The formation of fresh protective oxides of Ni, Cr and Al at the subscale level with the progress of oxidation might have resulted in the parabolic behaviour of coated GrA1 and T11 steels (Fig.6.19 and 6.20). The observed severe protrusions on the surface of the corroded T22 steels (Fig.6.18) scaleoff the porous oxide layer formed during initial stage of oxidation and leads to extensive spalling of scale. Protrusion of Fe_2O_3 from beneath of NiAlCrFeMo coated T22 steel exposed to salt environment is identical to the results observed during oxidation of NiAlCrFeMo coated T22 steel in air and it has been discussed in section 6.3.3 in detail. This might be the reason for linear corrosion kinetics of coated T22 steels. The weight gain for NiAlCrFeMo coated GrA1, T11 and T22 steels are 1/6, 1/5, and 1/4 fractions that of similar uncoated steels respectively and hence it can be concluded that necessary protection have been provided by HVOF sprayed NiAlCrFeMo coatings for the substrate steels.

Higher concentration of the vanadium distributed at the uppermost surface of the corroded coating (Fig.6.25), substantiates the formation of thick layer of corrosion products containing $Ni_3V_2O_8$ and AlV_2O_4 and further confirmed by XRD analysis on the surface. Deb et al.1996, observed decrease in the corrosion rate of Ni based superalloys subjected to hot corrosion in vanadium containing salt mixture due to reprecipitation of refractory $Ni_3V_2O_8$. Based on the present study, the general hot corrosion mode for NiAlCrFeMo coatings are shown in Fig.6.45.

6.3.4 NiCrFeSiB coating

The NiCrFeSiB coatings developed a thick oxide scale which is of about 110 μm to 140 μm due to the accelerated oxidation in the given molten salt environment at 900°C. The uppermost portion of the oxide scale mainly consisted of a continuous film of SiO_2 and the subscale is found to be rich in Cr_2O_3. The nucleation and growth of NiO

uniformly occur throughout the oxide scale, because most of the oxygen is primarily used in formation of SiO_2 and Cr_2O_3. The minor phases of the mixed spinal oxides of $FeCr_2O_4$ and $NiCr_2O_4$ have also been identified by the X-ray diffraction analysis. The characterization of oxide scale to validate the presence of the above said phases has been done using the XRD (Fig. 6.29), the Energy Dispersive X-ray microanalysis on the surface (Figs. 6.30 and 6.31) as well as along the cross-section (Fig. 6.32) and the EPMA analysis (Figs. 6.33 and 6.34). These oxides act as a barrier to the diffusion of O_2 and the corrosive species of the molten salt into the inside of the coating, thereby, contributed for the hot corrosion resistance of NiCrFeSiB coatings. It is also corroborated from Figs. 6.32 to 6.34 that the coatings have been partially oxidized and the corrosion is restricted to a depth of few microns on the surface at the end of 50 cycles of hot corrosion studies. The absence of oxygen as well as Na and V is observed in the region below the surface oxide layer. This can be further substantiated from the weight gain square (mg^2/cm^4) data plotted as a function of time (Fig. 6.27), which shows a parabolic behavior of all the coated steels.

Further, the coefficients of thermal expansion of SiO_2 ($8.06 \times 10^{-6}/°C$), Cr_2O_3 ($8.06 \times 10^{-6}/°C$), NiO ($14.5 \times 10^{-6}/°C$), Ni ($13.3 \times 10^{-6}/°C$), and Fe ($11.7 \times 10^{-6}/°C$) are close to each other and, hence, the cooling and reheating stresses are minimized during the thermal cycles. In the present study, the oxide scale formed on the corroded coatings seem to be compact, adherent, and dense without any indication of scale spalling or cracking during 50 cycles of hot corrosion studies at 900°C.

Elliott et al. (1977) reported that the SiO_2 scales developed on the Si based coating seems to promote the formation of chromium oxide subscale barrier layer under vanadic attack. Sidhu et al. (2006E) has also showed the SiO_2 and Cr_2O_3 sub-scale formed during the hot corrosion studies of Ni-Si based coatings. Nicoll (1982) opinioned that the modification of standard M-Cr-Al-Y coating systems with silicon additions of upto 2.7% leads to an improvement in the oxidation resistance as well as the hot corrosion resistance.

The dissolution of the protective oxides in Na_2SO_4-60%V_2O_5 melt at 900°C could have caused breakdown of the initial formed oxide film on the coating substrate. Moreover, SiO_2 appears to have a better corrosion resistance in the given environment. The main reason for this good performance is that V_2O_5 renders the Na_2SO_4 melt, more acidic and, in the highly acidic melts, SiO_2 scales have the minimal solubility.

Furthermore, silicon and vanadium apparently do not form any compounds with each other. The corrosion products of $CrVO_4$, Na_4FeO_3, and $Ni_3V_2O_8$ have been identified in the XRD analysis.

The NiCrFeSiB coated steels show a lower weight gain in comparison to the uncoated steels as reported in Section 6.1.1.1. The weight gain after 50 cycles of corrosion studies for the NiCrFeSiB coated GrA1,T11 and T22 steels are found to be 1/17, 1/15 and 1/30 fractions that of uncoated substrate steels of the same kind respectively. Therefore, it can be inferred that the necessary protection to the substrate steels is provided by the HVOF sprayed NiCrFeSiB coatings.

The distribution of Si and B at the splat boundary blocked the outward diffusion of Fe and Mo from the substrate into the coating, resulting in a diffusion band along the coating-substrate interface as shown in Figs. 6.33 and 6.34. These results are in agreement with the investigations reported by Wu et al. (2006). Based on the results, general hot corrosion mode for NiCrFeSiB coatings are shown in Fig.6.46.

Further, the protective behaviour of the NiCrFeSiB coatings can be attributed to the following effects:

i.   Formation of SiO_2 external layer and Cr_2O_3 sub-layer.

ii.   Low diffusivity of molecular oxygen, Na and V across the coatings.

iii. Close values of thermal expansion coefficients of the active oxides and elements eliminate spalling tendency.

iv. SiO_2 scale found to be passive in the molten $NaVO_3$ melt.

6.3.5 WC-Co/NiCrFeSiB coating

Accelerated oxidation of WC-Co/NiCrFeSiB coatings in Na_2SO_4-60%V_2O_5 salt environment at 900°C resulted in the formation of massive oxide layer on the surface. EPMA analysis (Fig.6.41) shows nickel and silicon coexist at some regions on the external surface of the oxide scale which suggest the presence of discontinuous layer of SiO_2 and Ni_2SiO_4 spinel oxide. Preferential oxidation of W and Cr during the initial stage of the oxidation lowers the oxidation rate of Si and hence continuous layer of SiO_2 might have not formed. The refractory element tungsten oxidized at 900°C exhibits an extremely high vapour pressure as WO_3 molecules (Espevik et al 1980). WO_3 decreases the oxide ion activity ($WO_3 + O^{2-} = WO_4^{2-}$) of the molten salt environment to a level where acidic fluxing of SiO_2, Cr_2O_3, CoO and NiO can occur. Infact, acidic fluxing

initiate at the tungsten rich particles in the coating, since the activity of WO_3 in the given environment is much higher in these area. The heavily localized attack appeared as open bud shaped protrusion on the surface (Figs.6.34 and 6.39) is an evidence of the acidic fluxing attack. The open bud protrusions appeared at the region where the surface oxide scale has failed due to over growth of duplex oxides. Similar fluxing mechanism have been reported by Gurappa (1999) and wang et al. (2002B) during their studies on hot corrosion behavior of tungsten containing superalloys (CM 247 LC and MAR M247) in Na_2SO_4 and NaCl environments. EDAX composition analysis of the protrusion (Fig.6.39a) reveals the presence of major oxides of Ni (56.6%), Cr (14.8%) and W (11.7%).

The compositional analysis of the oxide scale revealed the presence of major oxides of Ni, Cr and W and their spinel oxides. With progress of hot corrosion the Ni gets oxidized in the surface of the coating and as more and more Ni gets oxidized, living behind W-enrich region. Composition analyses at the subscale of the corroded coatings substantiate the presence of higher amount of tungsten (47.05%) and are as shown in Fig.6.40. XRD analysis on the external surface of the corroded coatings also confirmed the formation of mixed oxide type spinel of $NiWO_4$, $CoCr_2O_4$, $NiCr_2O_4$ and metal vanadates. These non protective spinel oxides induce formation of a highly friable and porous scale which was held to be largely responsible for the enhancement in attack. Since $NiWO_4$ is the compound of NiO and WO_3, $NiWO_4$ would have poor oxidation resistance in molten salt environment. Similar observations have been reported by Peters et al (1976) and Lee et al (2005).

EPMA and EDAX analysis along the cross section of the corroded coating reveal that only the external surface of the coating has been oxidized to form thick oxide scale and below this, coating remain unoxidised. The coating might have protected by the oxides of Si and Cr and provided the necessary protection to the substrate steels against hot corrosion.

WC-Co/NiCrFeSiB coated T22 steel shows relatively higher weight gain (Fig.6.35) in comparison to other coated steels under study. Observation into coating cross section, revealed the oozing out of iron oxide from the substrate through unoxidised coating. Thermal shocks due to differences in thermal expansion coefficients of nickel rich splats, WC particles and substrate may generate cracks. Another possible cause of the scales cracking might be attributed to the presence of molybdenum in this T22 substrate steel (Mo-1.1%). MoO_2 and MoO_3 have low melting points and also are

Na₂SO₄-60%V₂O₅, 900°C

Corrosion products
Ni₃V₂O₈ & CrVO₄

Unoxidised
Coating

Top scale rich
in SiO₂

Cr₂O₃ rich
subscale

Fe & Ni
diffusion band

Fe³⁺   Substrate   Fe³⁺
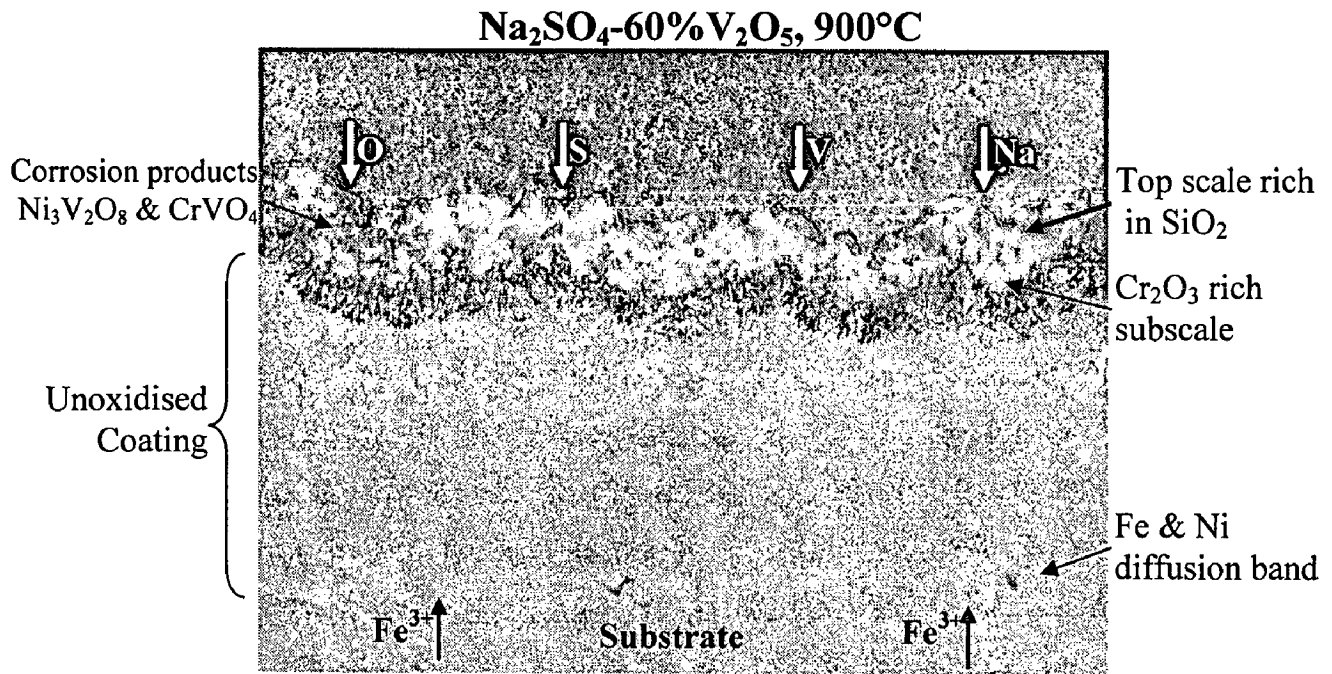
Fig.6.46   Hot corrosion mode of NiCrFeSiB coated steels exposed to Na₂SO₄-60%V₂O₅ environment for 50 cycles at 900°C

Na₂SO₄-60%V₂O₅, 900°C

Discontinuous
presence of SiO₂

Corrosion Products
Ni₃V₂O₈ and
FeVO₄

Unoxidised
coating region

Massive and porous
scale consist of
oxides and spinels
of Ni, Cr and W

Fe³⁺   Substrate   Fe³⁺
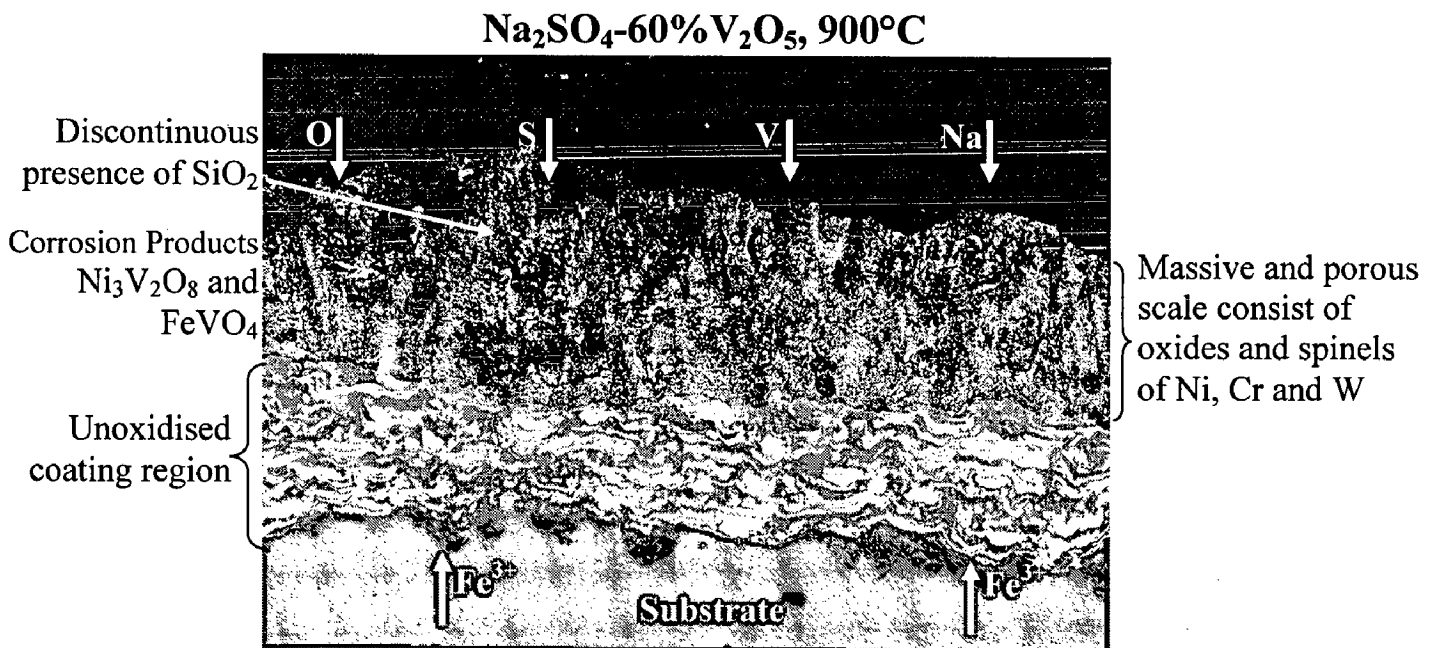
Fig.6.47   Hot corrosion mode of WC-Co/NiCrFeSiB coated steels exposed to Na₂SO₄-60%V₂O₅ environment for 50 cycles at 900°C

liable to sublimate directly at more than 800°C. This gas due to increased volume, induce stress and leads to crack or propagate the thermal cracks existing in the coating. These volatile oxides and iron oxide ooze outward through the cracks due to greater specific volume. Distribution of iron oxide has been identified at the vicinity of unreacted coating-oxide scale interface with the help of EDAX analysis and EPMA analysis across the cross section. This is the reason for para-linear kinetic behavior of coated T22 steel. Oxidation kinetics of WC-Co/NiCrFeSiB coated GrA1 and T11 steel followed nearly parabolic behavior. The minor deviation from the parabolic rate law in this case can be attributed to the formation and rapid growth of inhomogeneous oxides and their dissolution due to the fluxing action of the molten salt.

From the corrosion kinetics data, it can be inferred that WC-Co/NiCrFeSiB coatings show much lower weight gain in comparison to uncoated steels reported in section 6.1.1.1. The weight gain for WC-Co/NiCrFeSiB coated GrA1, T11 and T22 steels are 1/4, 1/3 and 1/5 fractions that of similar uncoated steels respectively. Hence on the basis of thermogravimetric measurements as well as by analyzing the oxide scale developed by the coating, it can be concluded that necessary protection to substrate steel, against high temperature corrosion have been provided by the coatings. Based on the present study, the general hot corrosion mode for WC-Co/NiCrFeSiB coatings exposed to Na_2SO_4-60%V_2O_5 environment at 900°C is shown in Fig.6.47

6.4 COMPARATIVE DISCUSSION

The cumulative weight gain (mg/cm^2) for uncoated and HVOF coated GrA1,T11 and T22 steels subjected to hot corrosion in Na_2SO_4-60%V_2O_5 molten salt environment for 50 cycles at 900°C is shown in Fig.6.48. From the bar charts, it can be inferred that the weight gains for all the HVOF coated steels are significantly lower than that of uncoated steels in molten salt environment. Uncoated steels suffered a higher corrosion rate and intense spalling of oxide scale is observed. The main constituent of oxide scale formed on all the steels is iron oxide. The acidic fluxing of the oxides by the molten salt mixture has resulted in massive, porous oxide scale. The stress developed due to higher volume of the oxide scale leads to cracks, in turn resulted in spallation. Uncoated T22 steel shows higher corrosion rate in comparison to uncoated GrA1 and T11 steels. Presence of chromium vanadate indicated the dissolution of initially formed chromium oxide film on the surface of T22 steel.

Based on the thermogravimetric data it can be inferred that the NiCrFeSiB coating provides the highest hot corrosion resistance where as WC-Co/NiCrFeSiB coating indicates the least resistance to the molten salt environment. The relative hot corrosion resistance of the various coating under study can be arranged in the following sequence:

NiCrFeSiB > NiCrAl > NiAlCrFeMo > WC-Co/NiCrFeSiB

The superior hot corrosion resistance of NiCrFeSiB can be attributed to the thick protective oxide scale developed on the surface. The uppermost layer of the oxide scale mainly consisted of continuous film of SiO_2 and the sub-scale found to be rich in Cr_2O_3. SiO_2 scales have minimal solubility in highly acidic Na_2SO_4-60%V_2O_5 melt. Furthermore silicon and vanadium apparently do not form any compounds with each other and found to be passive in the given environment (Grunling et al. 1982). These oxides act as barrier to the diffusion of O_2 and corrosive species of molten salt into the inside of coating, hence coating region beneath this oxide scale remain unoxidised. Corrosion products are confined to the outermost oxide scale. The close values of thermal expansion coefficients of the active oxides eliminate spalling tendency during the exposure. Slow oxidation kinetics observed during the thermogravimetric studies shows that the reaction rate is diffusion limited and all the three coated steels indicated parabolic behavior. The distribution of Si and B at the splat boundary blocked the outward diffusion of Fe and Mo from the substrate into the coating, thereby, resulting in diffusion band rich in Ni and Fe along the coating-substrate interface.

A continuous, compact and thick oxide scale has been formed in case of NiCrAl coated steels. The surface morphology of oxide scale shows smooth patches of blade like

structured θ-Al_2O_3, which indicate the metastable modifications of Al_2O_3 due to accelerated oxidation induced by the molten salt during the initial cycles of studies. This unstable alumina resulted in a thicker oxide scale consisting of oxides and spinel of Ni and Cr. Further acidic dissolution of these oxides resulted in formation of metal vanadates, which are concentrated mainly in the top scale. Preferential oxidation of Al and Cr along the Ni-rich splat boundary have been observed over the entire cross-section of the coating .These factors might have leads to higher weight gain in comparison to NiCrFeSiB coatings. Coated GrA1 and T11 steels followed nearly the parabolic behavior up to 50 cycles where as coated T22 steel shows perceptible deviation from the parabolic rate law after 41st cycle. This can be attributed to the Fe_2O_3 protrusions observed on the surface and it has been discussed in section 6.3.2 in detail.

Comparatively lower hot corrosion resistance of NiAlCrFeMo coatings can be ascribed to spalling of the oxide scale in the form of tiny flakes. At the earlier cycles, oxidation of Mo to MoO_3 increases the acidity of the molten salt melt and causes catastrophic self-sustaining hot corrosion via acidic fluxing. MoO_3 reacts with the oxides present on the coating surface such as Cr_2O_3 and NiO, to form nickel and chromium molybdates which are low melting point compounds. These molybdates usually form a liquid phase at 900°C and induce formation of a highly friable and porous scale. The corrosion rate reduces once the entire available Mo consumed at the surface. GrA1 and T11 coated steels followed parabolic rate law. Severe iron oxide protrusions in case of coated T22 steel resulted in linear corrosion kinetics.

The least hot corrosion resistance of the WC-Co/NiCrFeSiB coatings in comparison to the coatings under study can be attributed to the massive, loosely held needle microstructure of the oxides formed on the surface. Preferential oxidation of W and Cr during the initial stage impedes the formation of continuous protective layer of SiO_2. Tungsten got oxidized at 900°C and decreases the oxide ion activity of the molten salt environment to a level where acidic fluxing of SiO_2, Cr_2O_3, CoO and NiO can occur. Acidic fluxing initiate at the tungsten rich particles in the coating and the heavily localized attack appeared as open bud shaped protrusion on the surface. The thick oxide scale mainly consists of oxides of Ni, Cr and W and their spinel oxides. The coating region beneath this oxide scale remains unoxidised. Oxidation kinetics of WC-Co/NiCrFeSiB coated GrA1 and T11 steel followed nearly parabolic behavior. In case of coated T22 steel iron oxide has been oozed out and distributed at the vicinity of unoxidised coating and oxide scale interface. This might be the reason for para-linear kinetic behavior of T22 coated steel.
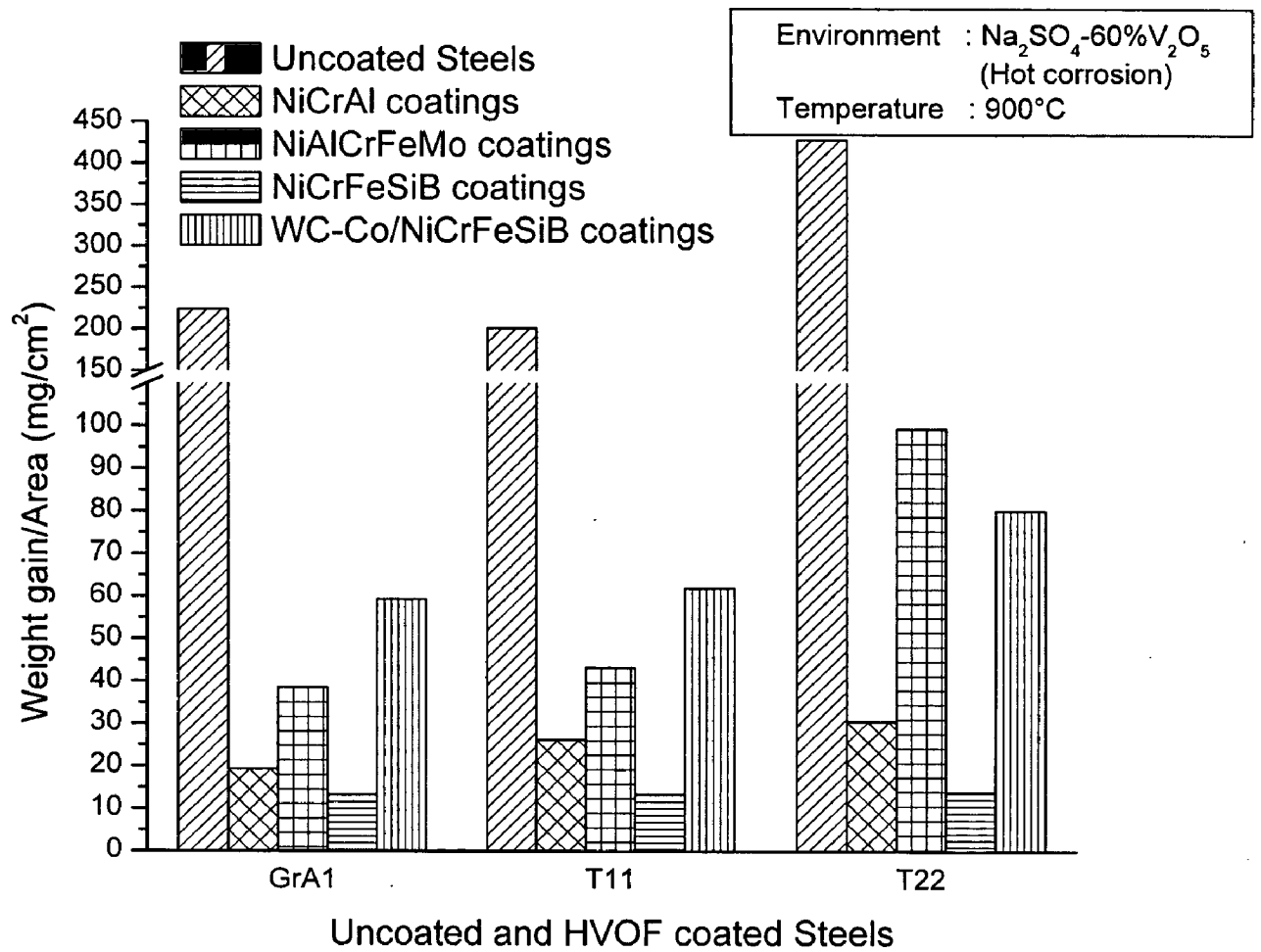
Fig.6.48   Bar chart showing cumulative weight gain (mg/cm²) for uncoated and
HVOF coated steels subjected to hot corrosion in Na₂SO₄-60%V₂O₅ salt
environment for 50 cycles at 900°C

206

CHAPTER 7

EROSION-CORROSION STUDIES
IN INDUSTRIAL ENVIRONMENT

This chapter focuses on the erosion-corrosion studies in industrial environment. The HVOF coated and uncoated steel samples studied herein were exposed to actual service conditions of a boiler. The samples were tested in the platen super heater region of the coal-fired boiler of Guru Gobind Singh Super Thermal Plant, Ropar, Punjab, India. This region is an area prone to high flue-gas corrosion. The flue gas temperature in this region is about 778±20°C. The experiments were conducted for 10 cycles, each cycle consisted of 100 hours of exposure, followed by cooling at ambient conditions. The extent of erosion-corrosion has been monitored by measuring the thickness loss in the samples after the total exposure of 1000 hours. The exposed samples are analyzed by XRD, SEM, and EDAX techniques. The results thus obtained are analyzed to evaluate the performance of the coatings in the given environment.

7.1 RESULTS

7.1.1 Uncoated Steels

7.1.1.1 Thermo-gravimetric studies and thickness monitoring

The macrographs of the GrA1, T11 and T22 steels after 1000 hours of exposure to the platen super heater zone of the coal-fired boiler are shown in Fig. 7.1. The scale developed on the GrA1 steel is fragile and showed intense spalling during the course of study. The GrA1 and T11 steels developed a dark grey colored scale, whereas, the light colored scale is observed in T22 steel.

The plots of weight change (mg/cm^2) as a function of time are shown in Fig. 7.2. During the exposure to actual industrial environment, the weight gain of the sample owes to the formation of the oxide scale and the weight loss is due to the continuous impact of fly ash, results in spalling, as well as, high temperature corrosion of the oxide scale. The GrA1 and T11 steels suffered weight loss throughout the study, whereas, T22 steel showed a weight gain up to 600 hours of exposure with a minor spalling in the later cycle of study.

The extent of the combined erosion-corrosion is measured in terms of metal thickness lost at the end of 1000 hours of exposure to platen super heater region. The thickness of metal lost is found to be 0.245 mm, 0.105 mm and 0.089 mm for GrA1, T11 and T22 steels respectively (Fig.7.3). The corresponding degradation rates expressed in mils per year (mpy) are found as 84.49 mpy, 36.21 mpy and 30.69 mpy respectively.

7.1.1.2 X-ray Diffraction Analysis

The X-ray diffraction pattern for the steels, after exposure to boiler environment for 1000 hours, is shown in Fig. 7.4. All the steels showed Fe_2O_3 and Fe_3O_4 as major peaks. Sulphide deposit is also found on the scale surface. The presence of Al_2O_3 and SiO_2 phases indicate the deposition of fly ash on the surface of exposed steel. Presence of Cr_2O_3 has been indicated in the oxide scale in case of T11 and T22 steels.

7.1.1.3 SEM/EDAX Analysis

The surface scale morphology and the EDAX analysis for steels exposed to platen super heater region of the coal-fired boiler for 1000 hours are shown in Fig. 7.5. All the steels reveal Fe_2O_3 as a main constituent of the surface scale. The white phase of the scale that appears like the spherical particles distributed along the cracks and the pits formed on the oxide scale may be attributed to the impact of fly ash. The EDAX analysis of these particles consist mainly of SiO_2, Al_2O_3, Fe_2O_3, TiO_2 and Na_2O, which are the constituents of fly ash and they may become a site of active corrosion later on.

The BSE images and the EDAX analysis at some points of interest across the cross section of the exposed NiCrAl coated steels are shown in Fig. 7.6.The appearance of the scale formed on the GrA1 steel is highly porus and cracked along the scale thickness, whereas the bulk scale appears on the T11 and T22 steels. The EDAX analysis at the selected points along the scale thickness of T22 is illustrated in Fig.7.6d. The point analysis on the top of the scale shows the higher content of SiO_2 and Al_2O_3. It is found that minor concentration of Cr and Mo oxides are distributed throughout the cross section.

7.1.1.4 EPMA Analysis

The BSEI and X-ray mappings for a part of the oxide scale of T22 steels after exposure to boiler environment is shown in Fig.7.7. The Fe mapping indicates a higher concentration of iron throughout the oxide layer. Surface oxide scale mainly consists of
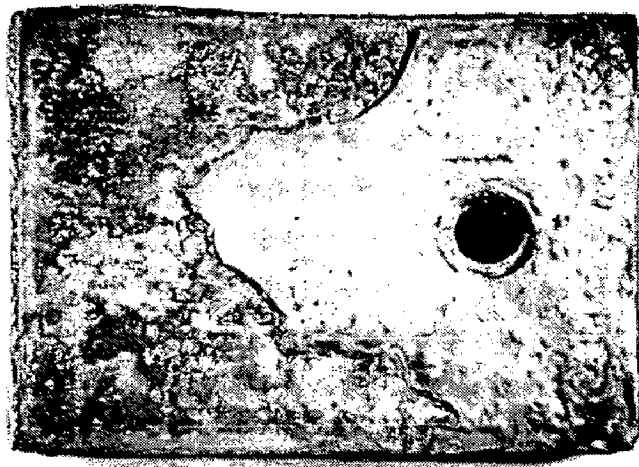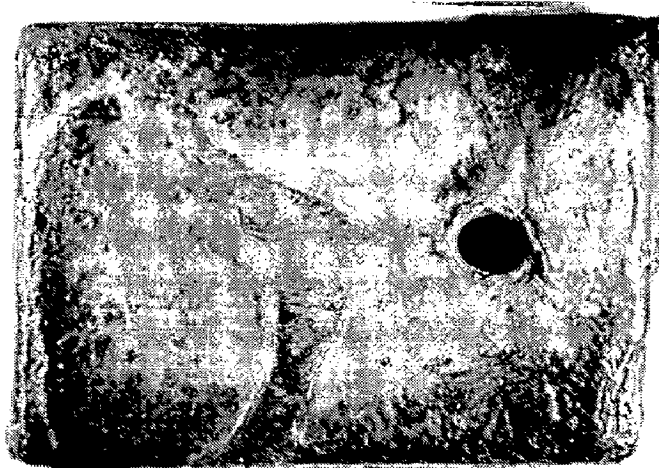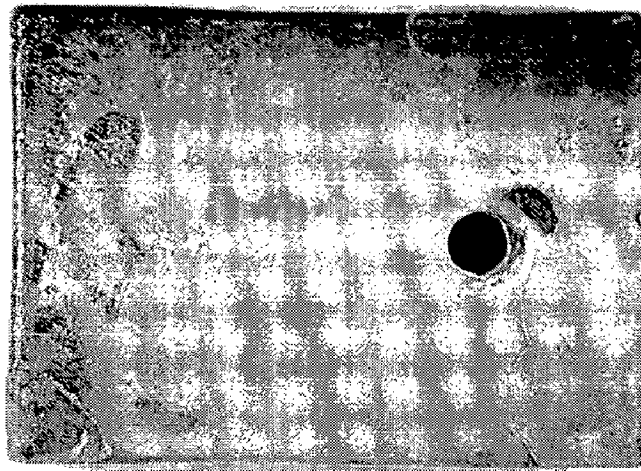
Fig.7.1   Macrograph of uncoated steel after 1000 hrs exposure to super heater zone of
           the coal fired boiler at 900°C:
           (a) GrA1 steel   (b) T11 steel   (c) T22 steel
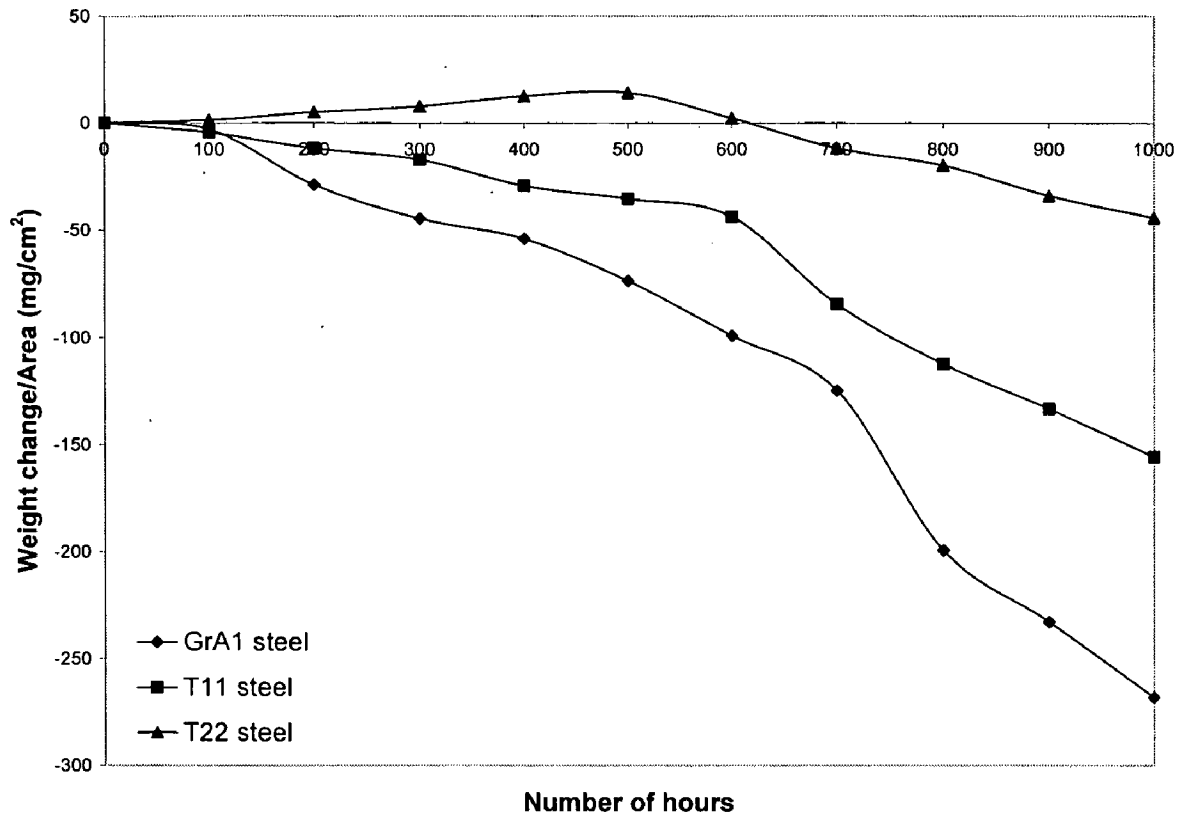
Fig.7.2   Weight change vs. time plot for uncoated steels subjected to 1000 hours cyclic exposure to super heater zone of the coal fired boiler
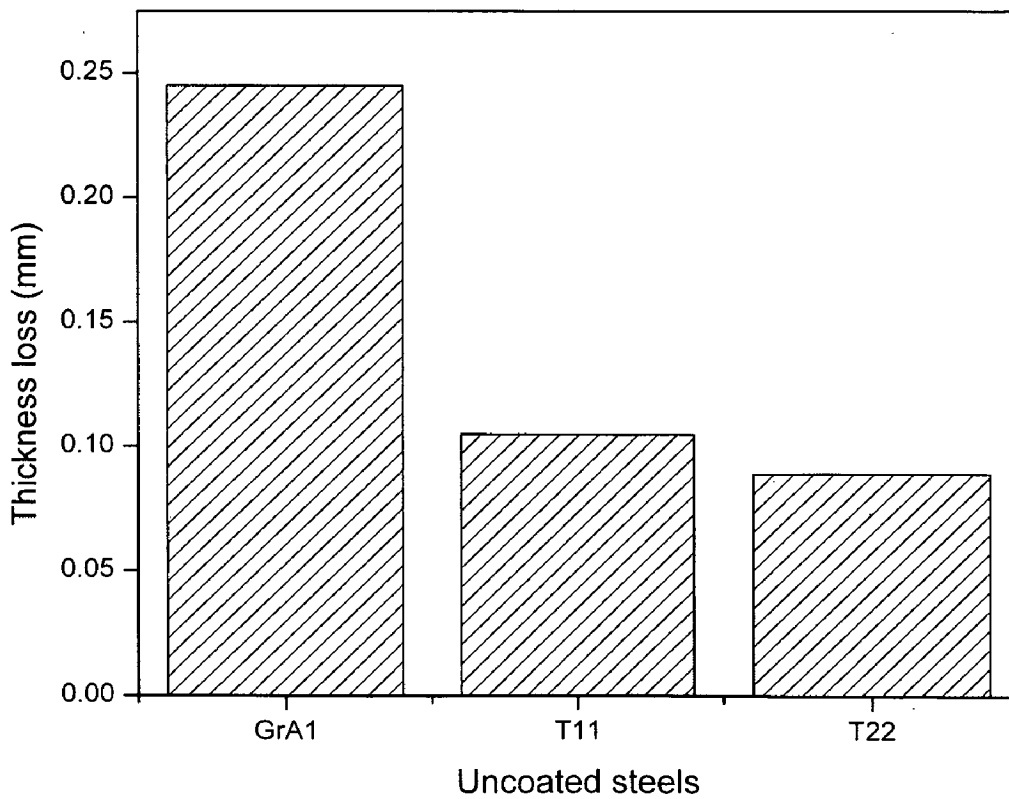
Fig.7.3   Bar chart indicating the thickness lost in mm for the uncoated steels after 1000 hours of exposure to super heater zone of coal fired boiler.

210
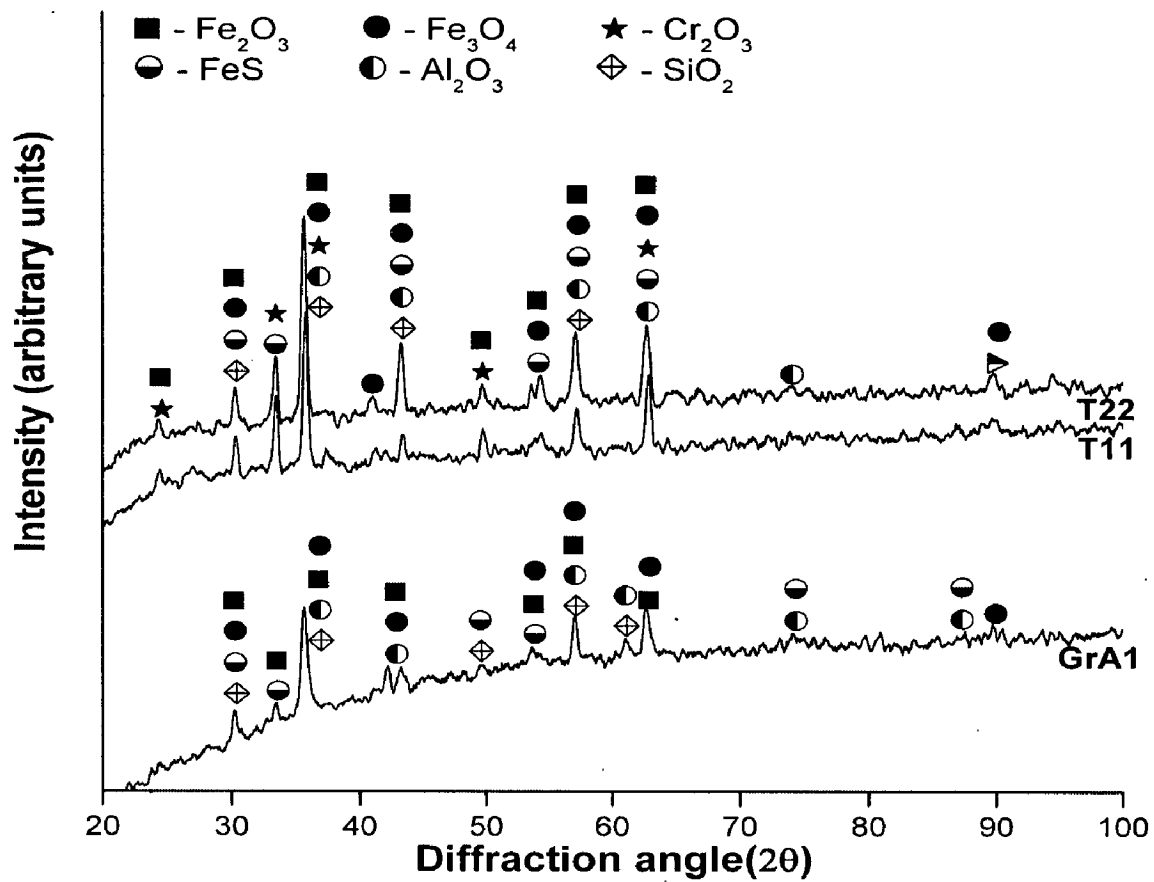
Fig.7.4 X-ray diffraction patterns for the boiler steels after 1000 hours of exposure to super heater zone of coal fired boiler
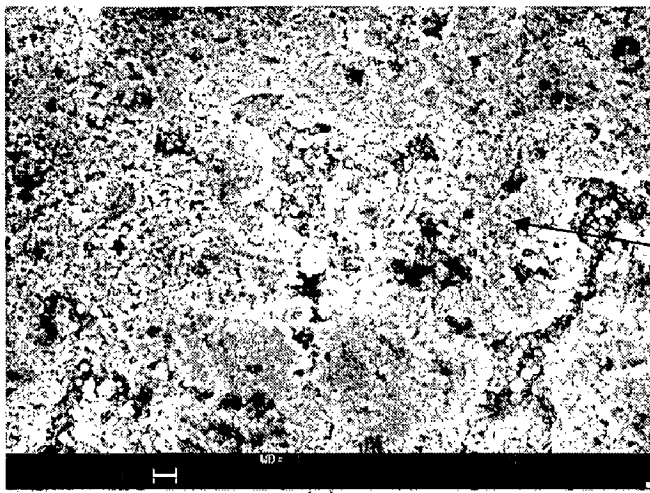
211
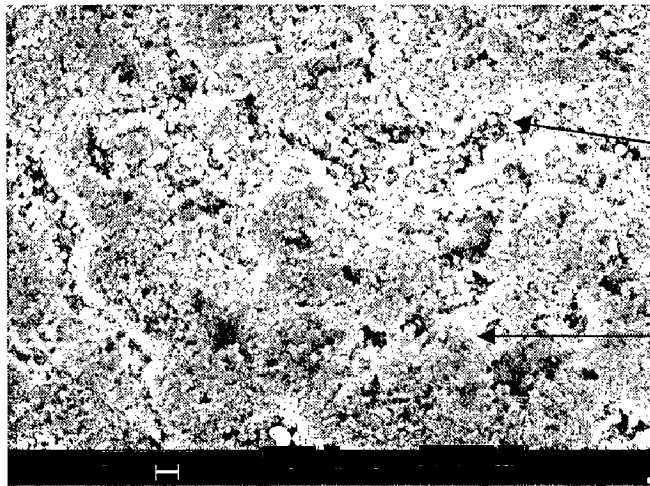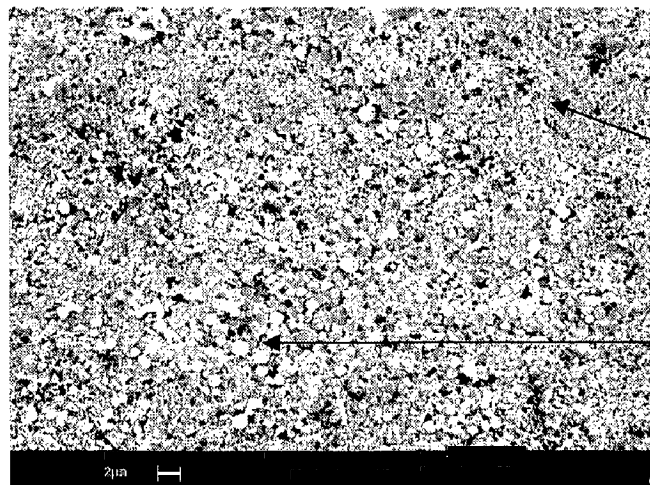
Fig.7.5 Surface scale morphology and EDAX analysis for boiler steels exposed to super heater of the coal fired boiler for 1000 hours:
(a) GrA1 steels (b) T11 steels (c) T22 steels

(a)

(b)

(c)

(d)
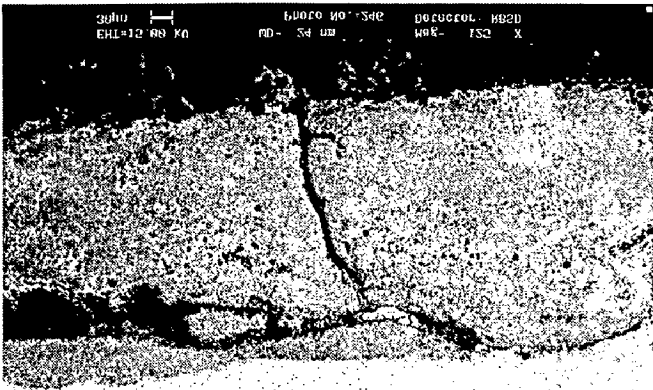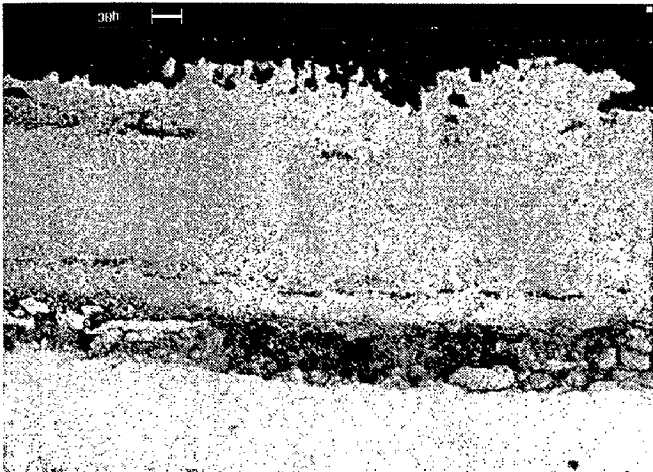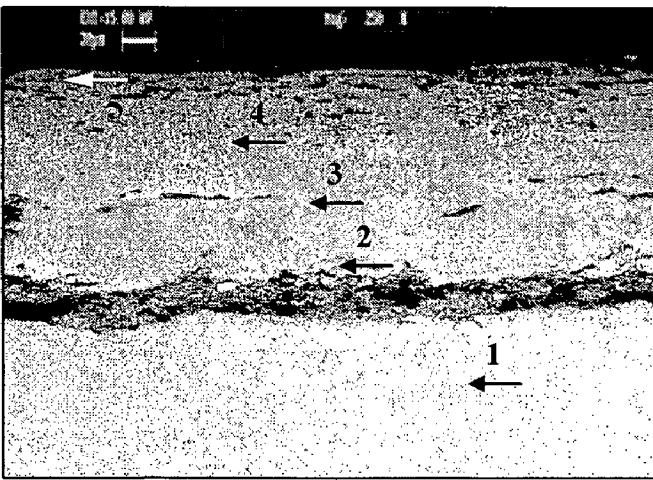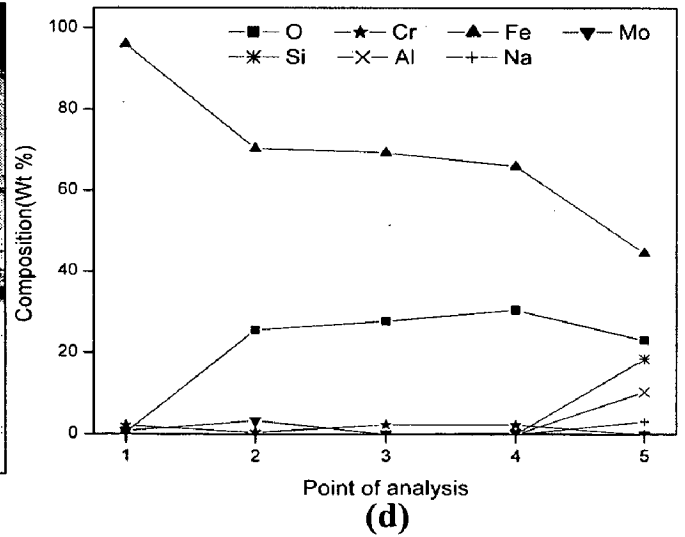
Fig.7.6   Back scattered images for the uncoated steels after 1000 hours of cyclic exposure to superheater zone of coal fired boiler:
(a) GrA1 Steel   (b) T11 Steel   (c) T22 Steel
(d) EDAX point analysis along the cross-section of T11 steel

213
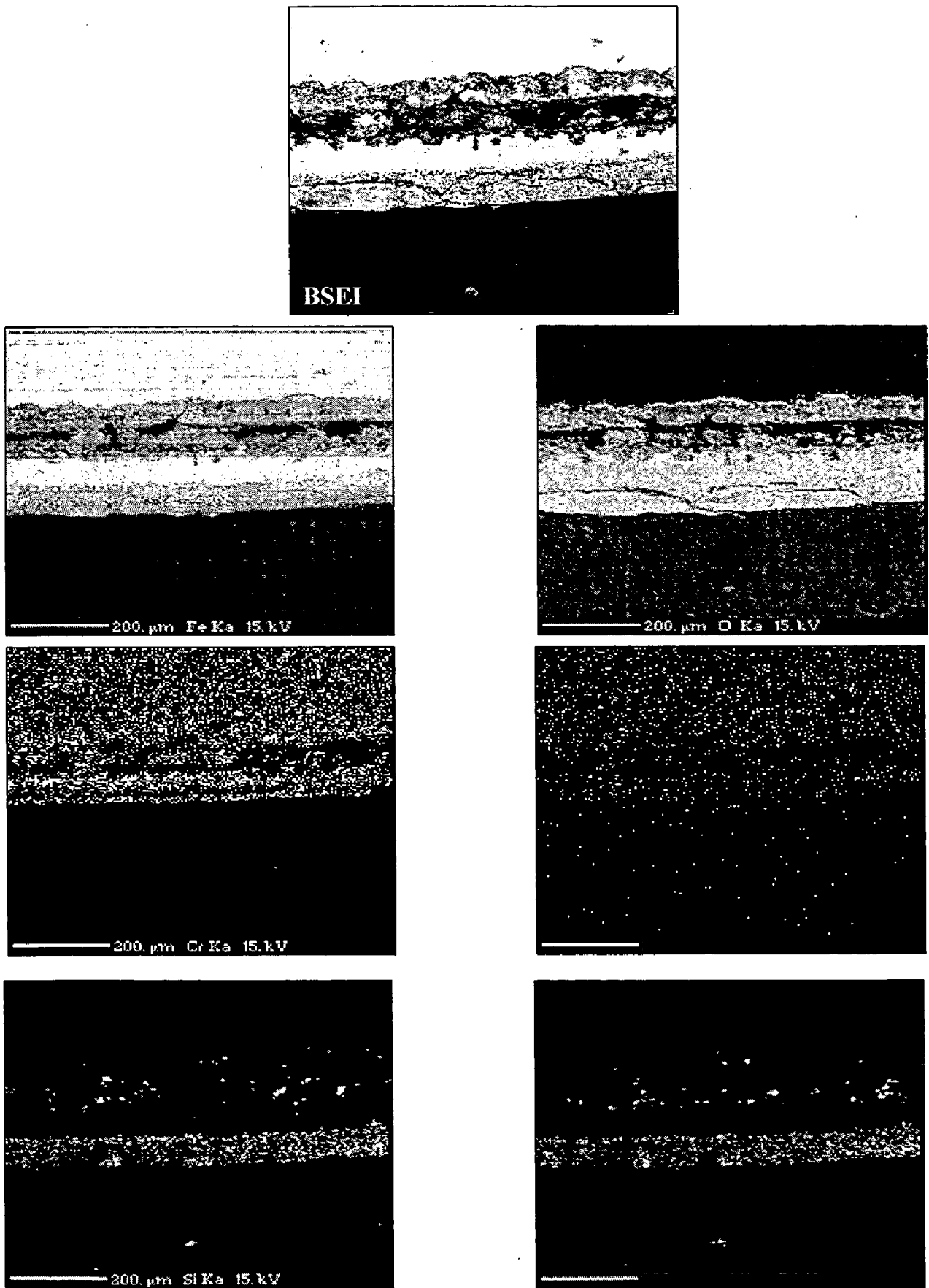
Fig.7.7   BSEI and X-ray mapping across the cross-section of the boiler steel T22 after 1000 hours of exposure to super heater zone of the coal fired boiler

oxides of Fe, Si and Al which reveals the embedment of ash particles. Further, a band of chromium oxide is clearly seen in the inner layer of the oxide scale. However, Mo seems to be homogeneous throughout the cross section.

7.1.2 NiCrAl Coating

7.1.2.1 Thermo-gravimetric studies and thickness monitoring

The macrographs of the HVOF-sprayed NiCrAl coatings on the GrA1, T11 and T22 steels after 1000 hours of exposure to superheater zone of the coal-fired boiler are shown in Fig. 7.8. The brownish grey color formed during the first cycle of exposure, subsequently changed to yellowish appearance with green tinges on the surface of the NiCrAl-coated GrA1, T11 and T22 steels. The smoothed surfaces in the centre of sample due to erosion by the impact of fly ash particle have been observed for all the samples. After 1000 hours of exposure, the scale formed on the coating was intact, adherent and did not show any crack or spallation tendency.

The weight change per unit area (mg/cm^2) versus time plots for 1000 hours exposure of the NiCrAl-coated steels exposed to the boiler environment is shown in Fig. 7.9. The coated T22 steel showed a maximum weight gain in comparison to the coated GrA1 and T11 steels. The weight gain values for the coated GrA1, T11 and T22 steels at the end of 1000 hours of exposure are found to be 4.38, 4.63 and 6.24 mg/cm^2, respectively. However, the uncoated GrA1, T11 and T22 steels suffer a weight loss and scale thickness loss during the exposure which is reported in Section 7.1.1.1. Hence, it is evident from the weight gain data that the NiCrAl coated steels have provided the necessary protection against corrosion and erosion in the industrial environment. Further, the weight gain square (mg^2/cm^4) data plotted as a function of time is shown in Fig. 7.10. The plot shows the observable deviation from the parabolic rate law. The parabolic rate constants K_p, calculated from the slope of the linear regression fitted line for NiCrAl coated GrA1, T11 and T22 steels, are obtained as 0.063×10^{-10}, 0.068×10^{-10} and 0.126×10^{-10} g^2 cm^{-4} s^{-1} respectively.

The bar chart indicating the thickness loss of the NiCrAl-coated steels after 1000 hours of exposure to the boiler environment is shown in Fig. 7.11. The erosion-corrosion loss of the exposed NiCrAl coated GrA1, T11 and T22 steels are found as 0.025 mm, 0.023 mm and 0.028 mm, respectively, and the corresponding degradation rates

expressed in mils per year are obtained as 8.62 mpy, 7.93 mpy and 9.66 mpy, respectively.

7.1.2.2 X-ray Diffraction Analysis

The X-ray diffraction pattern for the NiCrAl coated GrA1, T11 and T22 steels are shown in Fig. 7.12. The XRD results reveal the presence of major peaks of α-Al_2O_3, Cr_2O_3, Ni and $AlNi_3$. The presence of minor peaks of NiO, SiO_2, Na_2O, $Ni_3V_2O_8$ and FeS phases indicates the fly ash deposits on the surface of exposed steel.

7.1.2.3 SEM/EDAX Analysis

The SEM micrograph of the NiCrAl coated steels showing the scale morphology along with EDAX analysis is illustrated in Figs.7.13. The scale formed on the surface is adherent without any indication of crack. The EDAX analysis on the dark grey region of scale confirms the formation of protective oxide layer, which consists of oxides of Al and Cr. The white contrast region on the scale shows the presence of Al_2O_3, SiO_2, Fe_2O_3, Na_2O and CaO. It can be inferred that the composition of white phase is similar to fly ash composition which is deposited during the exposure to superheater zone of coal fired boiler environment.

The BSE images and EDAX analysis at some selected points of interest across the cross-section of the corroded NiCrAl coated steels are shown in Fig. 7.14. A thin and adherent scale is formed without any indication of crack along the cross section at the end of 1000 hours of exposure. Figure 7.14a shows the point analysis along the cross section of corroded NiCrAl coated GrA1 steel. The EDAX analysis on the surface (Points 1 and 2) shows that, the top most layer mainly consisted of oxides of Al and Cr, along with a minor amount of Si (3.02%). The presence of sulphur is also identified along the splat boundary (Point 4). Point 5 indicates the presence of Ni rich splat and absence of oxygen at these points suggests that the Ni-rich splats are in the unoxidised state. The black contrast region along the splat boundary is rich in Al, Cr and O, which indicates the oxidation of Al and Cr along the splat boundaries. Point 6 shows that the coating substrate interface containing Al_2O_3 grit particles.

Figure 7.14b which demonstrates the corresponding analysis for the exposed NiCrAl coated T11 steels shows that the outermost layer of the scale (Points 1 and 2) is mainly consisting of oxides of Ni, and Cr along with minor amounts of Al, Si and Na
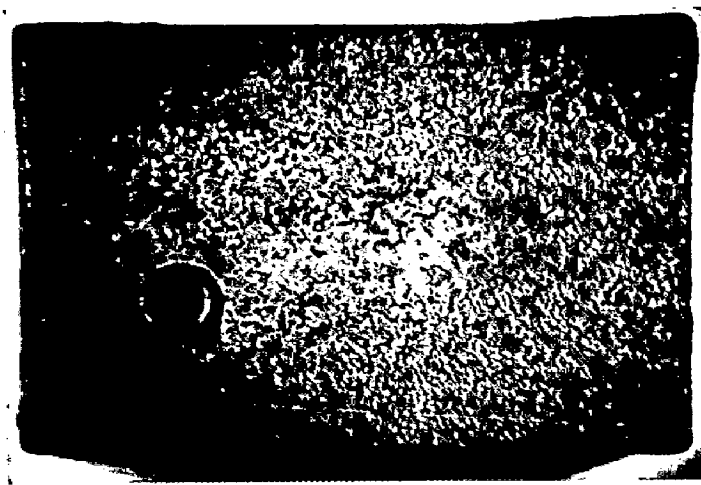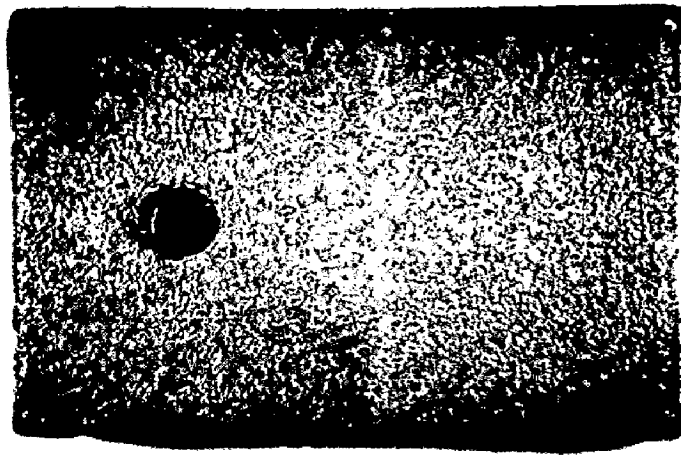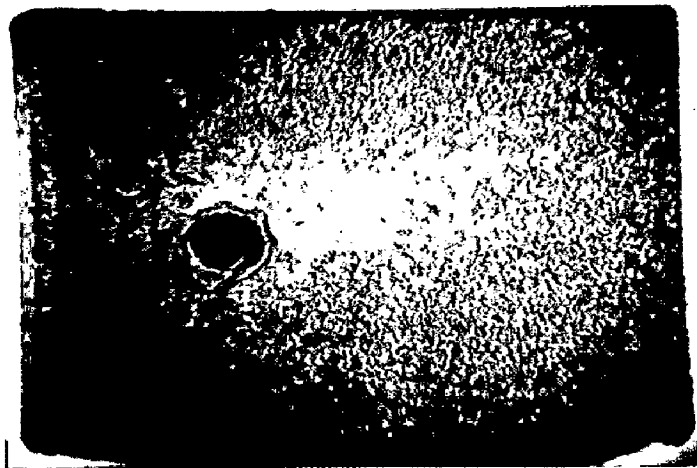
Fig.7.8   Macrographs of the NiCrAl coating exposed to superheater zone of coal fired boiler for 1000 hours:
(a) GrA1 steel   (b) T11 steel   (c) T22 steel
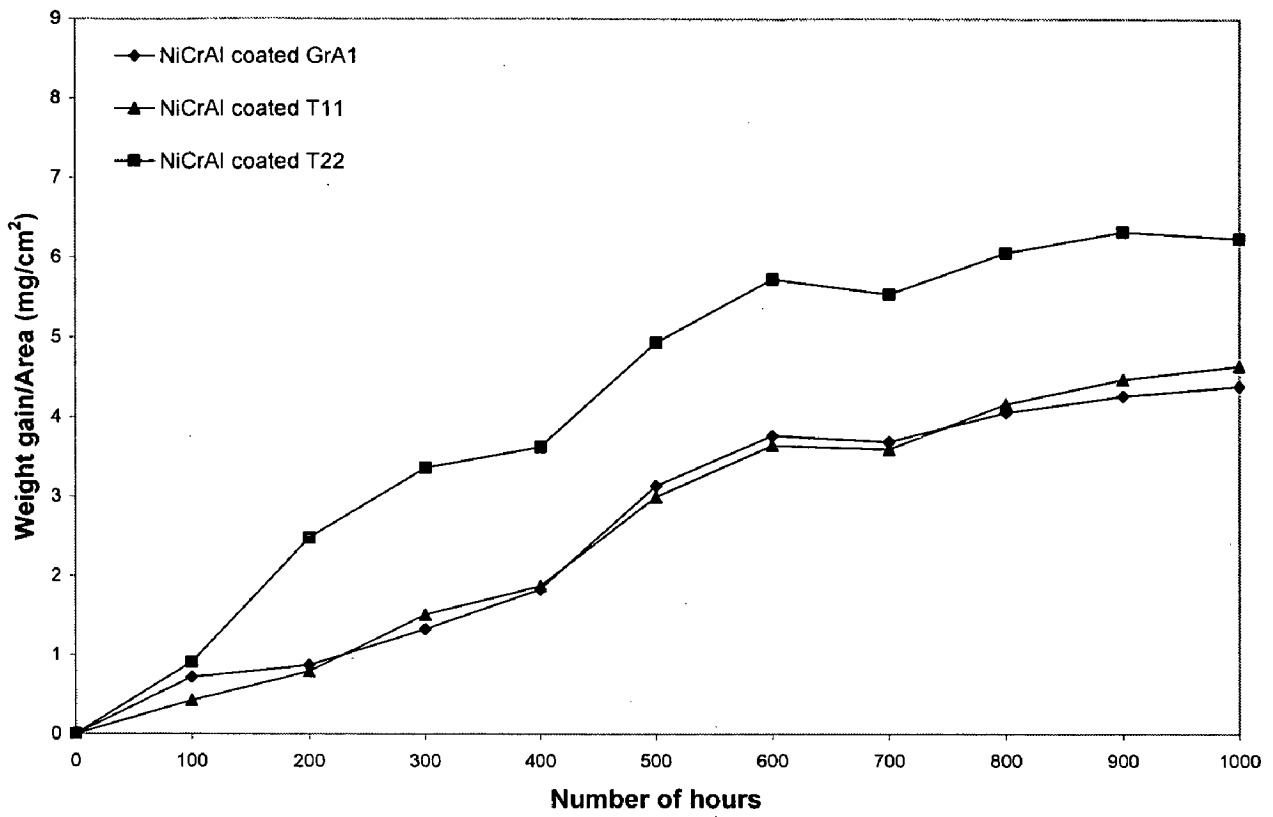
Fig.7.9   Weight change plot for NiCrAl coated steels exposed to super heater zone of coal fired boiler for 1000 hours
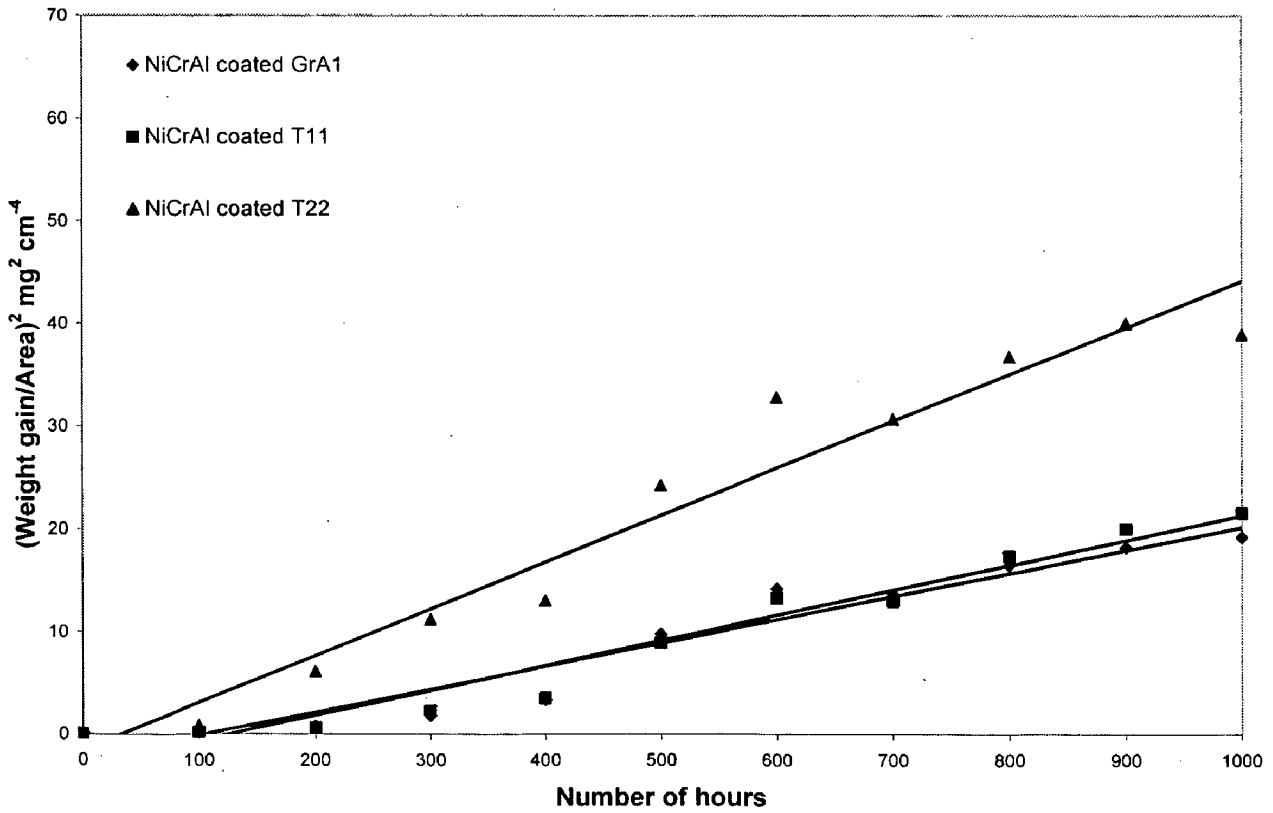
Fig.7.10   (Weight change/area)^2 plot for NiCrAl coated steels exposed to super heater zone of coal fired boiler for 1000 hours
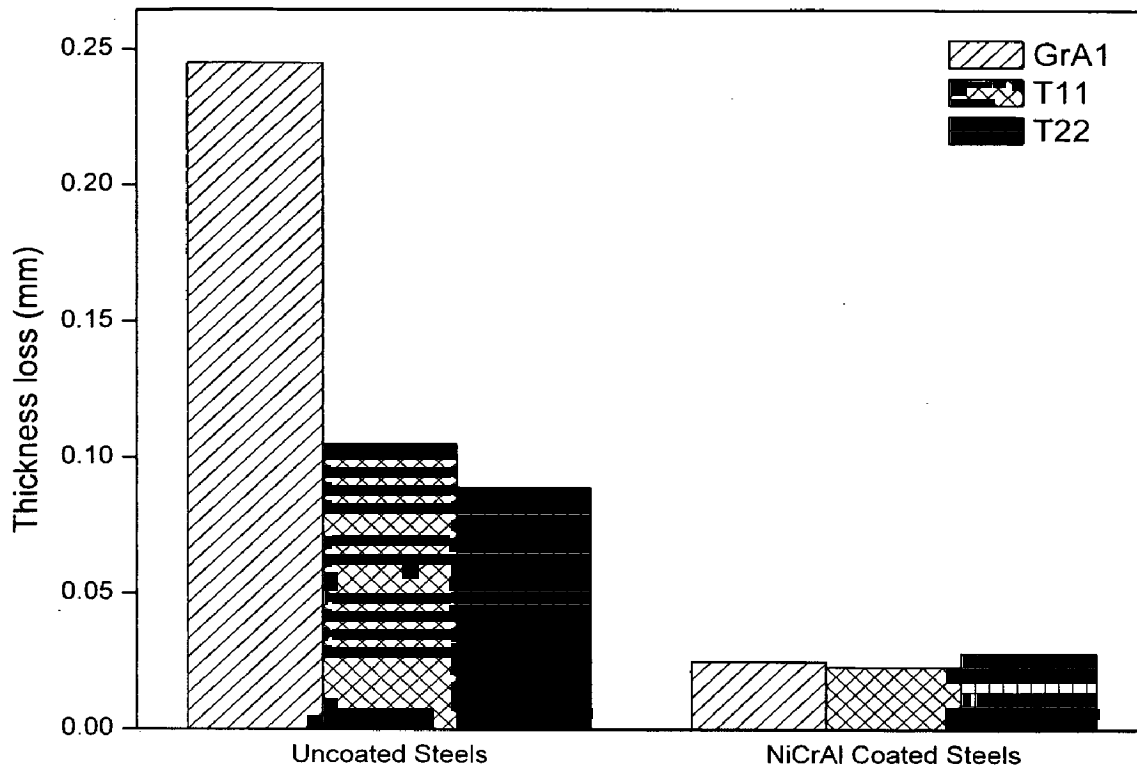
Fig.7.11 Bar chart indicating the thickness lost in mm for the uncoated and NiCrAl coated steels after 1000 hours of exposure to super heater zone of coal fired boiler.

Fig.7.12 X-ray diffraction patterns for NiCrAl coated GrA1, T11 and T22 steels Exposed to super heater zone of coal fired boiler for 1000 hours.

219

37.10% Al_2O_3
28.86% SiO_2
10.18% Cr_2O_3
06.67% NiO
02.02% SO_3

38.52% Al_2O_3
51.50% SiO_2
04.79% Fe_2O_3
02.29% Na_2O

(a)

74.38% SiO_2
12.65% Al_2O_3
03.14% CaO
02.70% V_2O_5

59.56% Al_2O_3
11.98% SiO_2
22.40% Cr_2O3
04.68% NiO
02.72% Na_2O

(b)

32.57% Al_2O_3
28.78% SiO_2
18.24% Cr_2O_3
08.32% Fe_2O_3
04.26% NiO
02.13% Na_2O

22.19% Al_2O_3
35.29% SiO_2
14.81% Fe_2O_3
18.65% Na_2O
04.15% CaO
01.34% V_2O_5
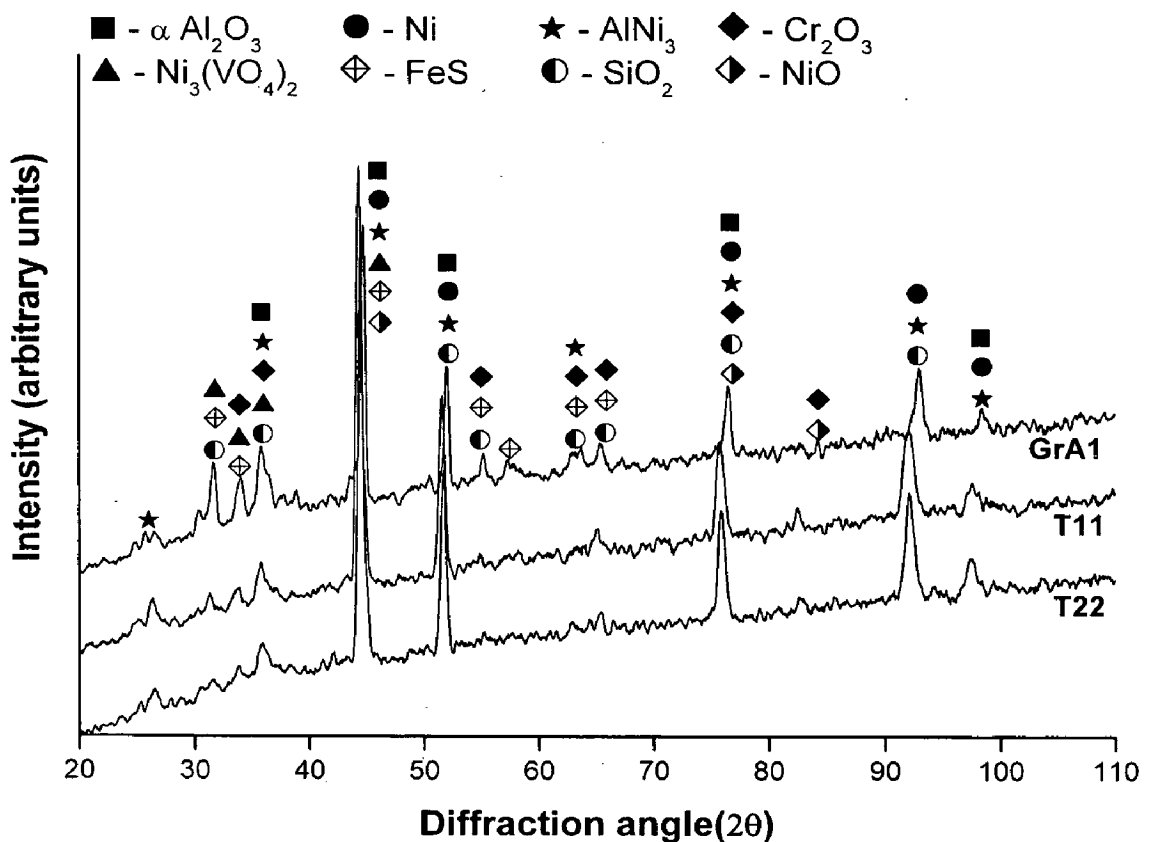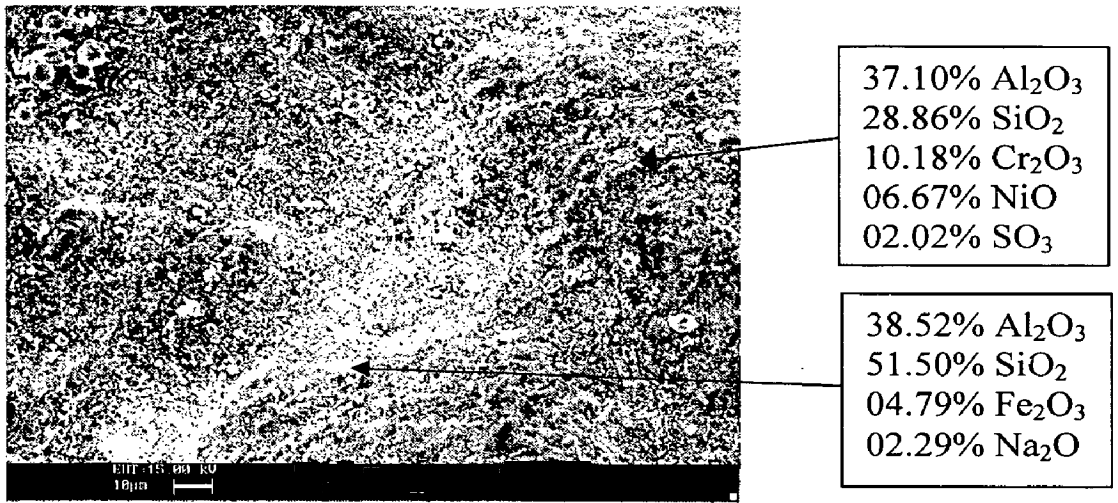
(c)

Fig.7.13 Surface scale morphology and EDAX point analysis for NiCrAl coated steels exposed to super heater zone of coal fired boiler for 1000 hours: (a) GrA1 steel (b) T11 steel (c) T22 steel
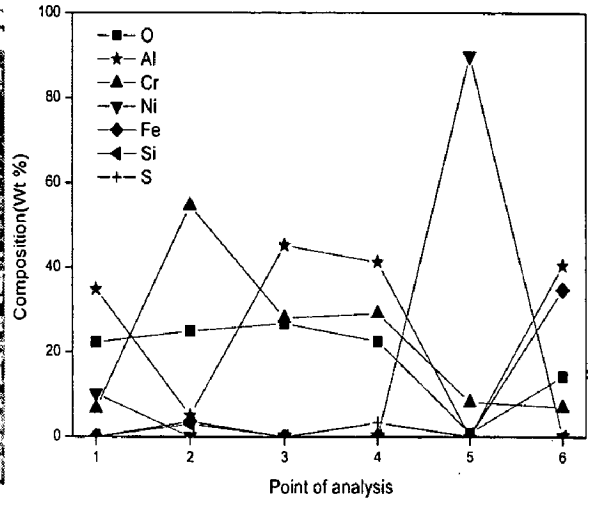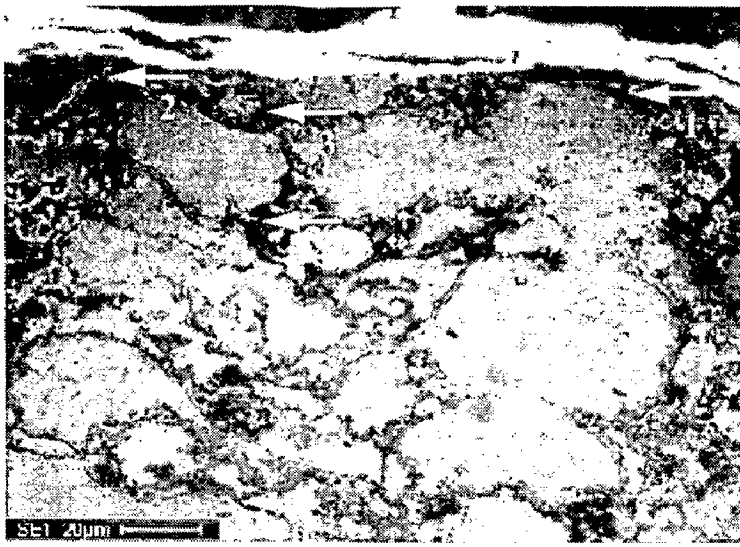
(a)
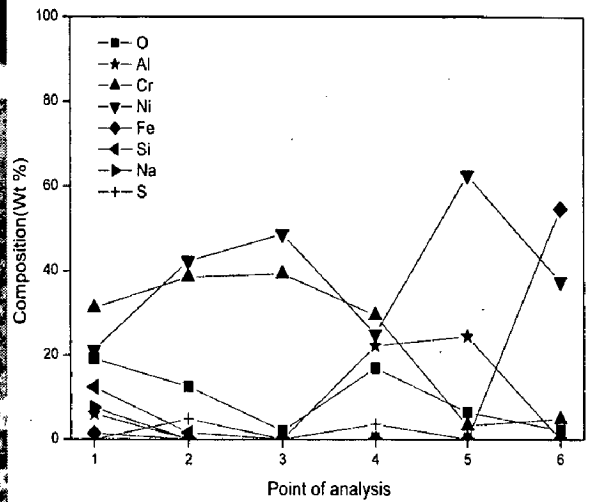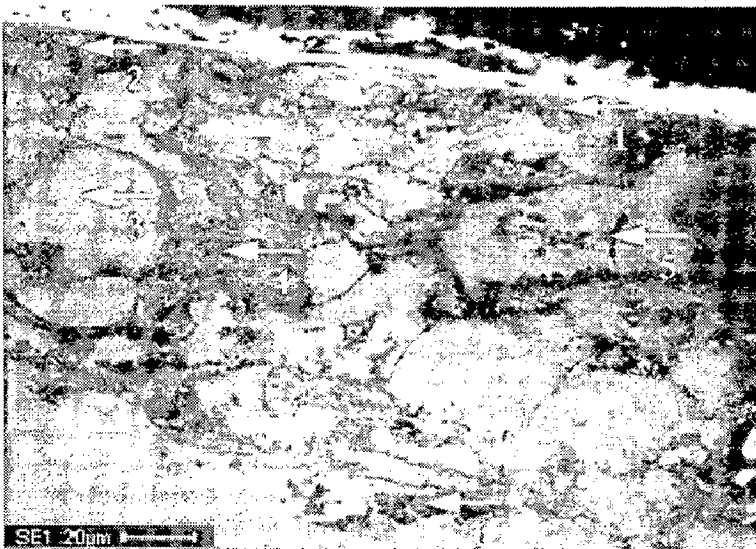
(b)
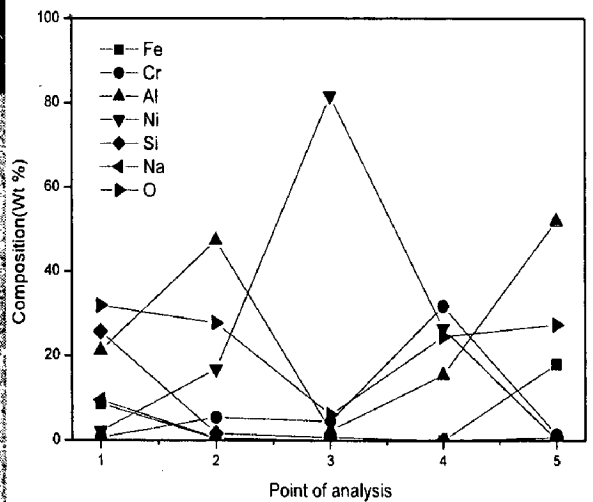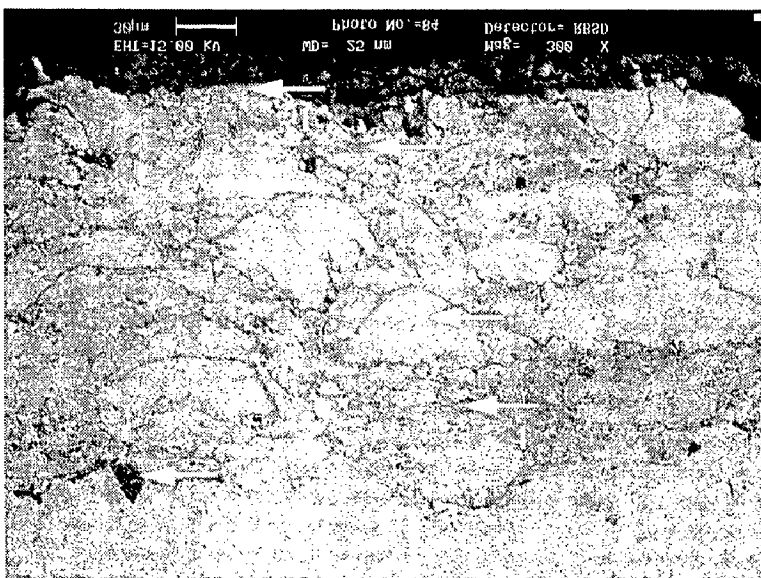
(c)

Fig.7.14 Back scattered electron image and EDAX point analysis (wt %) across the cross-section of the NiCrAl coated steels exposed to super heater zone of coal fired boiler for 1000 hours:

(a) GrA1 steel (b) T11 steel (c) T22 Steel

221

oxides. Point 3 indicates the Ni and Cr-rich splat in an unoxidised state, as oxygen is absent at this point. At point 4, the high concentrations of Cr, Al, Ni and O reveal the internal oxidation along the splat boundary. The presence of sulphur in this region suggests the penetration of corrosive species along the splat boundary. The coating-substrate interface (Point 6) shows the presence of a higher amount of Ni and Fe with minor amount of O, indicating the possible inter-diffusion between the coating and substrate. Figure 7.14c shows the BSEI/EDAX analysis along the cross section of the corroded NiCrAl coated T22 steel. The EDAX analysis at point 5 shows higher amount of Al and O, which reveals the embedment of grit particle during the surface preparation prior to the HVOF spraying.

7.1.2.4 EPMA Analysis

The BSEI and X-ray maps for the NiCrAl coated T22 steels after exposure to superheater zone of coal fired boiler are shown in Fig.7.15. The mapping for the elemental oxygen reveals the thin oxide layer at the outermost exposed surface of the coating. The outermost layer mainly consists of Al, Si and Fe, that reveals deposition of ash particles during the exposure to industrial environment. Chromium and Aluminum co-exists with oxygen and forms a continuous thin protective layer of Cr_2O_3 and Al_2O_3, just beneath the topmost layer. The selective oxidation of Al and Cr is observed mainly along the nickel-rich splat boundary. Combining the mapping for Ni and O, shows that the Ni-rich splats are not oxidized at the end of 1000 hours of exposure to industrial environment. The mapping for Fe and Ni corroborated about the inter-diffusion of Fe from the substrate into the coating and the Ni and Cr from coating into the substrate.

The X-ray mappings for the NiCrAl-coated T11 steel (Fig. 7.16) also reveals that the Ni and Cr-rich splats remain in un-oxidized state, whereas aluminum and chromium preferentially forms their oxides at the splat boundary. The presence of a thin layer of Si at the top of the corroded coating might be the indication of ash deposition. The exclusive islands of Al which coexists with oxygen along the scale-substrate interface are the inclusions of Al_2O_3.

7.1.3 NiAlCrFeMo Coating

7.1.3.1 Thermo gravimetric studies and Thickness Monitoring

Figure 7.17 depicts the macrographs of HVOF sprayed NiAlCrFeMo coated steels exposed to superheater zone of the coal fired boiler for 1000 hours. Yellowish brown color oxide scale has been observed on the surface of exposed coatings. The oxide scale formed on the surface found to adherent and has not showed any cracking or spallation tendency.

The plot of weight change per unit area as a function of exposure time is as shown in Fig.7.18. The observed fluctuations in the weight change data might be due to erosion-corrosion of the coatings accompanied with falling off and regeneration of the ash deposits on the surface of the exposed samples. The total weight gain at the end of 1000 hours of exposure for NiAlCrFeMo coated GrA1, T11 and T22 steels is 5.004, 7.04 and 6.59 mg/cm^2 respectively. Evidently, coated T22 steels showed a maximum weight gain, in comparison to other coated steels. All the coated steels showed noticeable deviation from the parabolic rate law, as shown in Fig.7.19. The parabolic rate constant, calculated by a linear least square algorithm function for coated GrA1,T11 and T22 steels, found to be 0.081 x 10^{-10}, 0.142 x 10^{-10} and 0.124 x 10^{-10} g^2 cm^{-4} s^{-1} respectively.

The histogram (Fig.7.20) indicates extent of erosion-corrosion measured in terms of thickness loss from the exposed coatings. Erosion-corrosion loss for NiAlCrFeMo coated GrA1, T11 and T22 steels are 0.039, 0.045 and 0.043 mm respectively and the corresponding degradation rate expressed in mils per year are 13.45, 15.52 and 14.82 mpy respectively.

7.1.3.2 X-ray Diffraction Analysis

X-ray diffraction pattern on the surface of NiAlCrFeMo coated steels exposed to environment in superheater zone of the coal fired boiler for 1000 hours are shown in Fig.7.21. The prominent phases revealed by XRD analysis are α-Al$_2$O$_3$, Cr$_2$O$_3$, NiO, NiCr$_2$O$_4$ and FeCr$_2$O$_4$.The minor phases of SiO$_2$, Na$_2$O$_2$ and FeS$_2$ indicated the fly ash deposit formation on the surface.

7.1.3.3 SEM/EDAX Analysis

Figure 7.22a shows the surface morphology of the NiAlCrFeMo coated T11 steel. The undulation observed on the surface might be due to erosion caused by the impacting
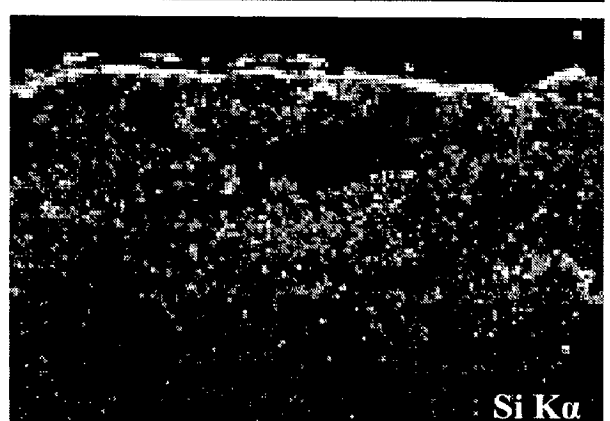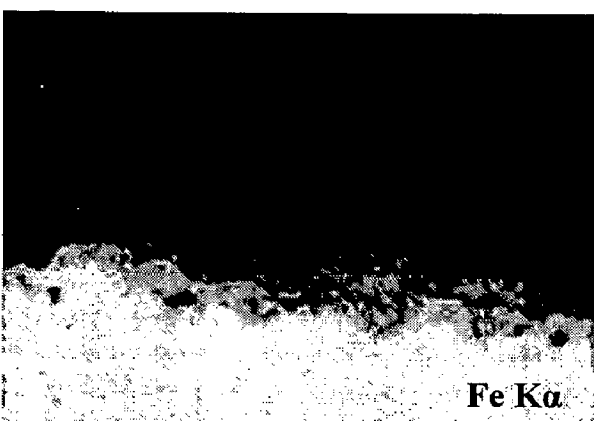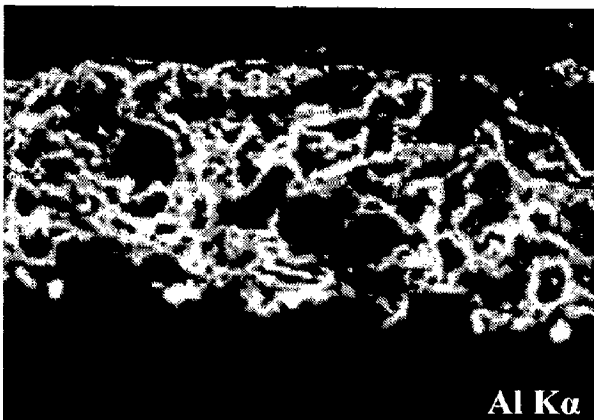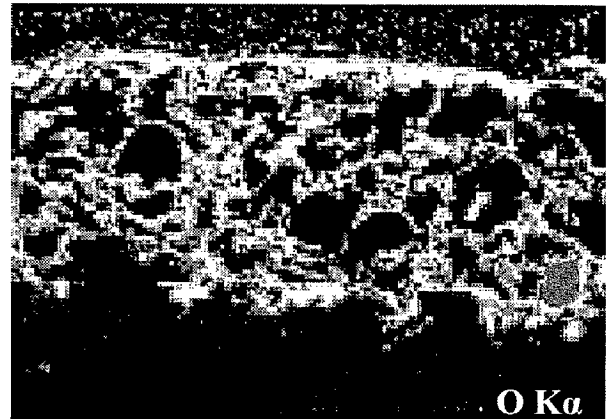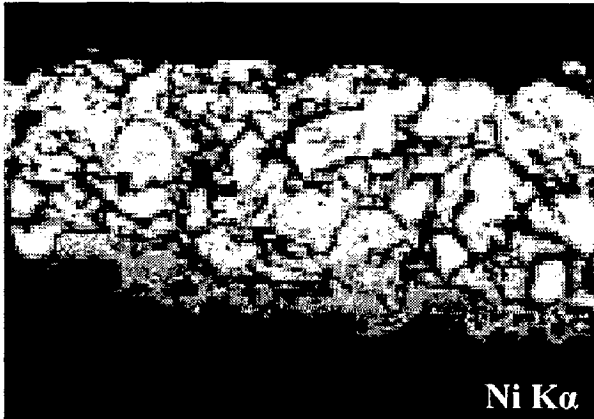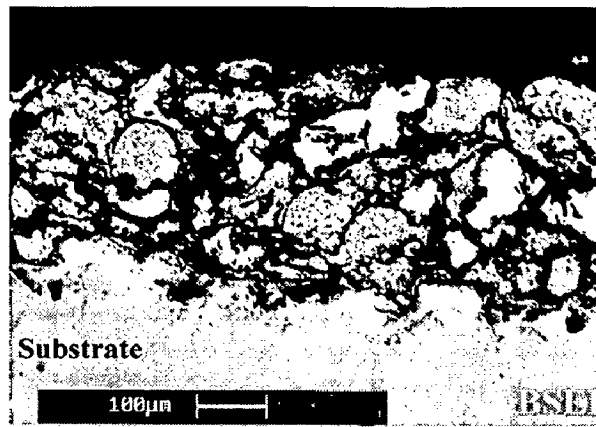
Fig.7.15 BSEI and elemental X-ray mapping along the cross-section of the NiCrAl coated T22 steels exposed to superheater zone of coal fired boiler for 1000 hours

224
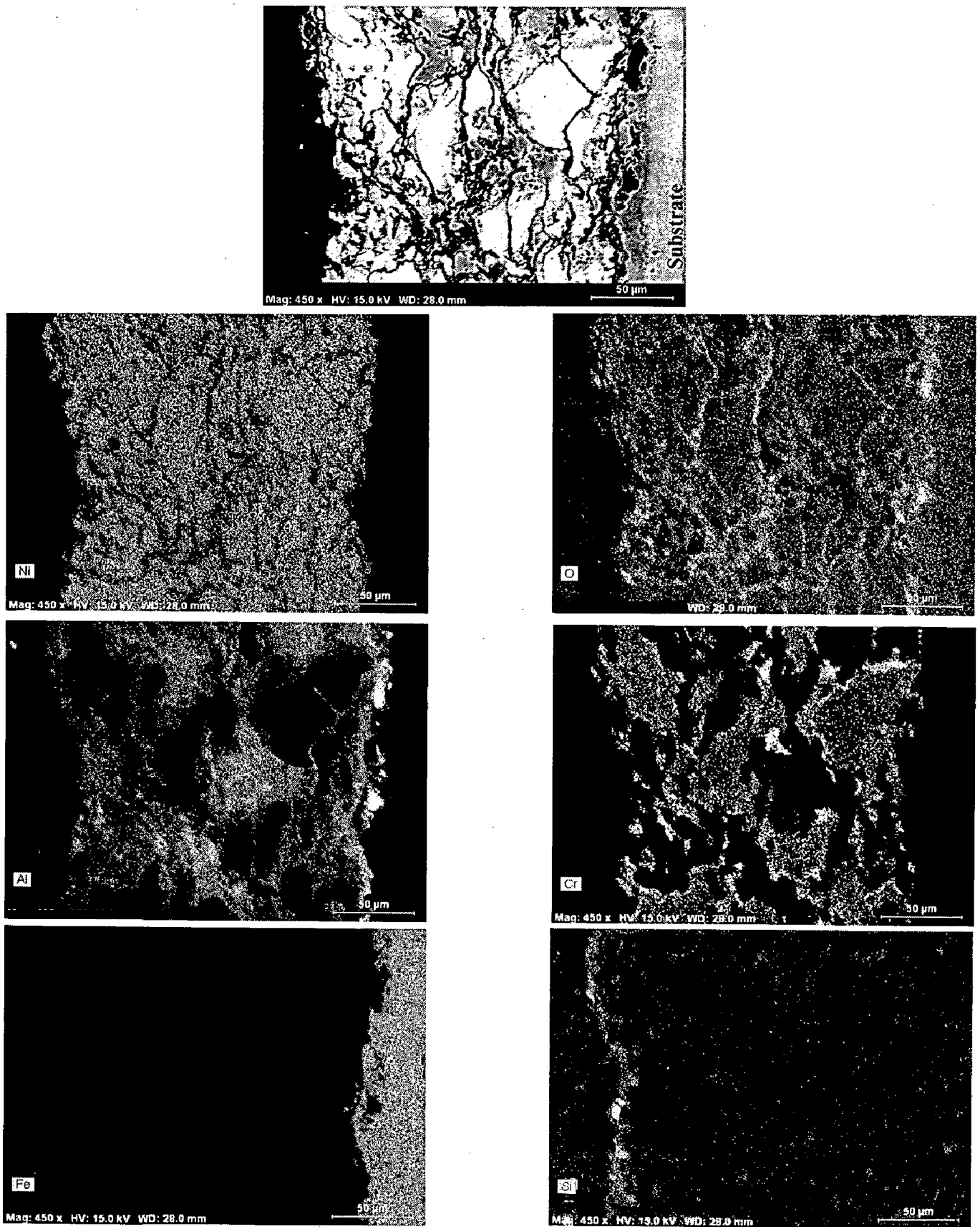
Fig.7.16　　BSEI and elemental X-ray mapping along the cross-section of the NiCrAl coated T11 steels exposed to superheater zone of coal fired boiler for 1000 hours
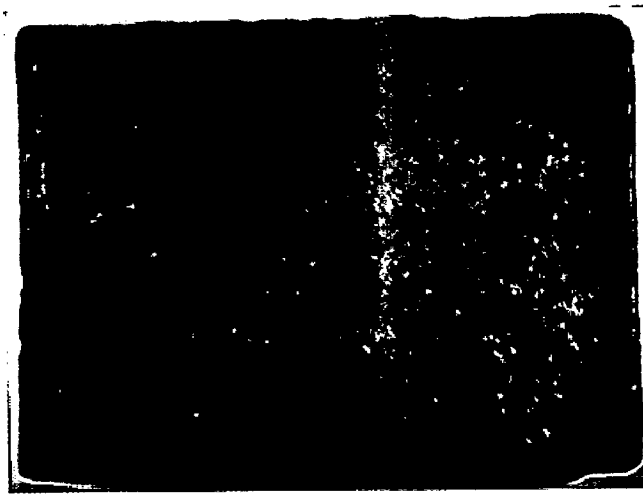
(a)

(b)

(c)

Fig.7.17   Macrographs of the NiAlCrFeMo coating exposed to superheater zone of coal fired boiler for 1000 hours:

(a) GrA1 steel   (b) T11 steel   (c) T22 steel
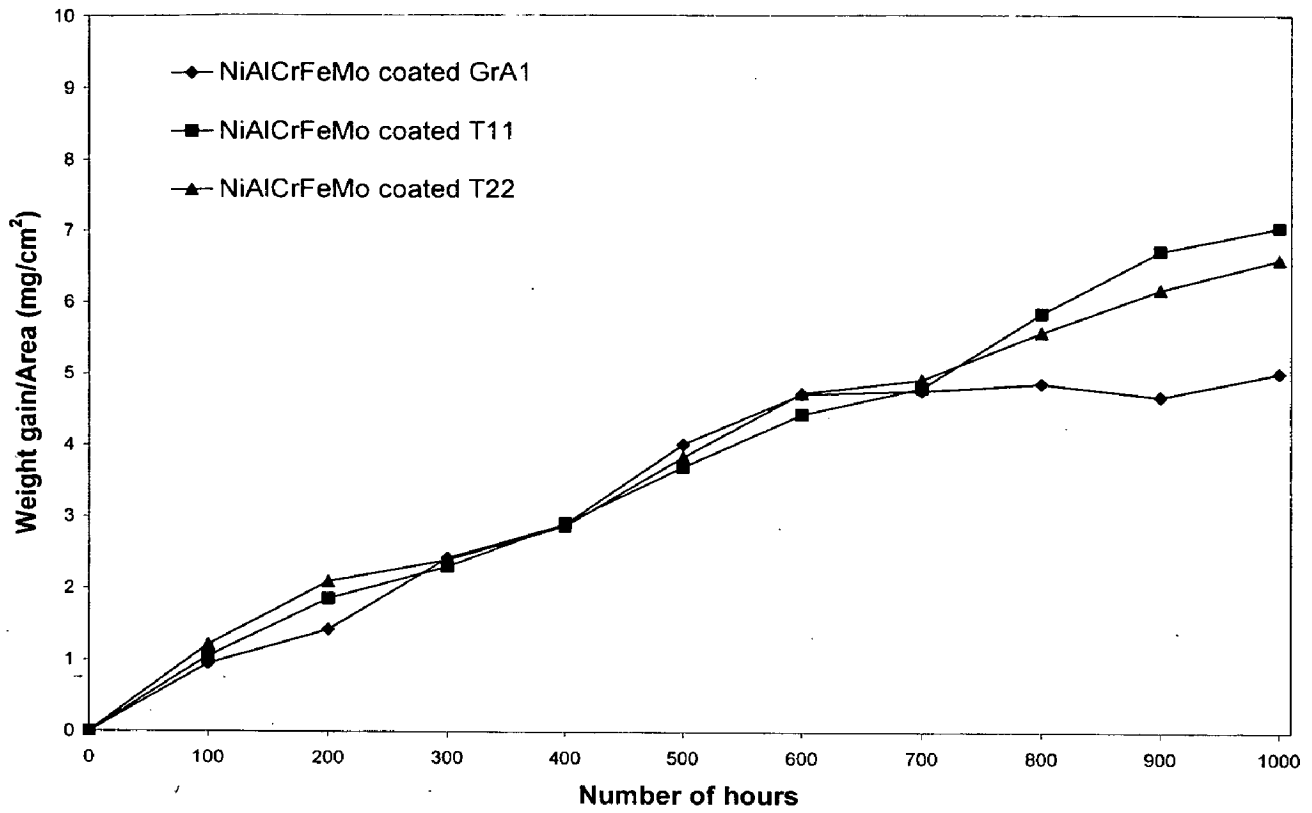
Fig.7.18   Weight change plot for NiAlCrFeMo coated steels exposed to super heater zone of coal fired boiler for 1000 hours
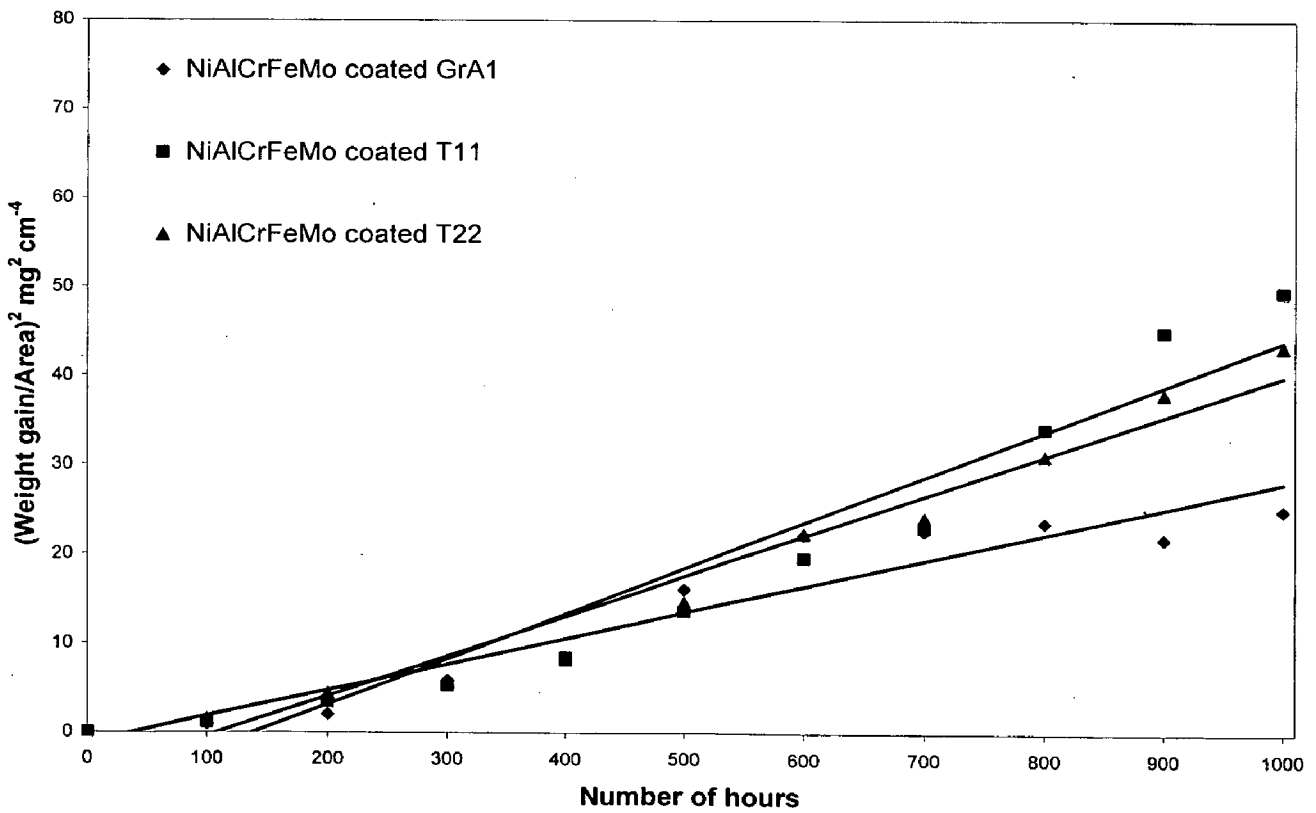
Fig.7.19   (Weight change/area) ^{2} plot for NiAlCrFeMo coated steels exposed to super heater zone of coal fired boiler for 1000 hours

Fig.7.20 Bar chart indicating the thickness lost in mm for the uncoated and NiAlCrFeMo coated steels after 1000 hours of exposure to super heater zone of coal fired boiler.

Fig.7.21 X-ray diffraction patterns for NiAlCrFeMo coated GrA1, T11 and T22 steels exposed to super heater zone of coal fired boiler for 1000 hours.

Box 1 (top, panel a):
14.19% Al$_2$O$_3$
24.88% SiO$_2$
26.32% Cr$_2$O$_3$
08.67% NiO
08.82% Fe$_2$O$_3$
12.87% Na$_2$O
01.35% MoO3

Box 2 (panel a):
15.76% Al$_2$O$_3$
30.54% SiO$_2$
16.99% Fe$_2$O$_3$
06.41% Na$_2$O
17.02% TiO$_2$
05.57% SO$_3$
04.22% CaO

Box 3 (panel b):
20.75% Al$_2$O$_3$
63.40% SiO$_2$
04.61% Fe$_2$O$_3$

Box 4 (panel b):
11.73% Al$_2$O$_3$
32.94% SiO$_2$
15.16% Cr$_2$O$_3$
08.81% NiO
10.53% Fe$_2$O$_3$
11.89% Na$_2$O
02.72% V$_2$O$_5$
01.05% SO$_3$
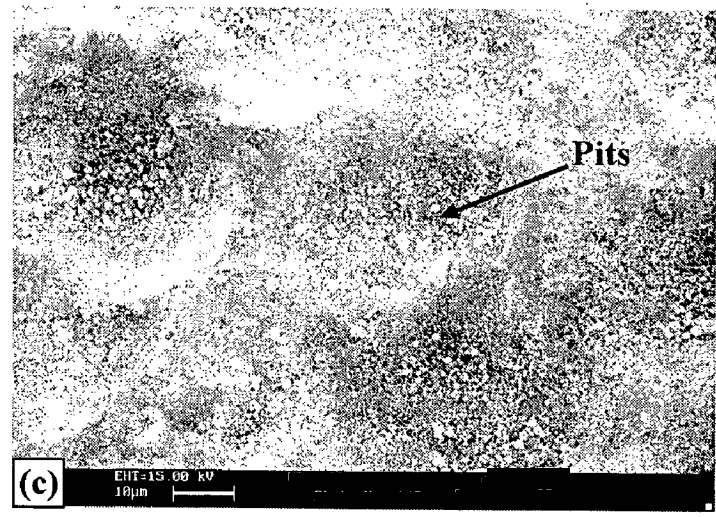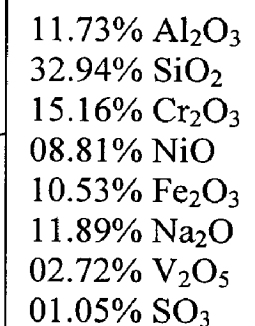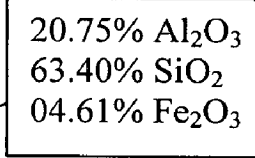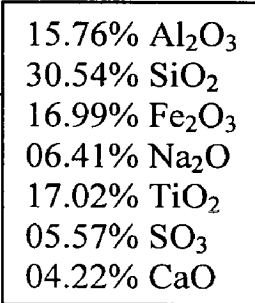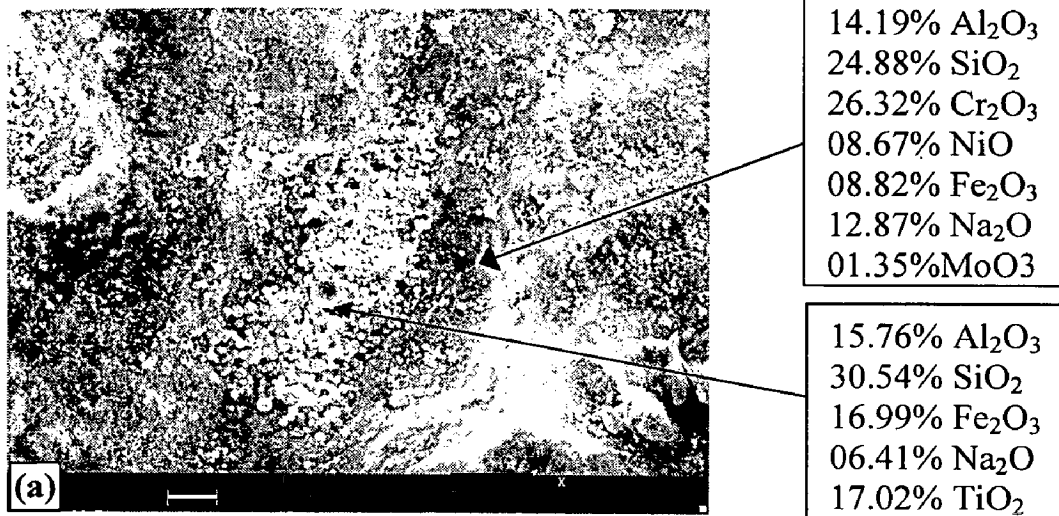
Fig.7.22 Surface scale morphology and EDAX point analysis for NiAlCrFeMo coated steels exposed to super heater zone of coal fired boiler for 1000 hours:
(a) Coated T11 steel   (b) Coated T22 steel   (c) Coated GrA1 steel

fly ash. The EDAX analysis on the dispersed white particles on the surface revealed the composition 15.76% Al_2O_3, 30.54% SiO_2, 16.99% Fe_2O_3, 06.41% Na_2O, 17.02% TiO_2, 05.57% SO_3 and 04.22% CaO. These phases are the main constituents of flyash and show the ash embedment into the open pores of coatings and pits formed on the surface. The Na and S present in the boiler environment can form low melting point compounds such as alkali metal-trisulphates, which can cause fluxing of the protective oxide scale as discussed in section 7.3.1. The compositional analysis on the dark matrix shows mainly the protective oxides of Cr_2O_3 (26.32%) and Al_2O_3 (14.19%) along with relatively lesser concentrations of NiO (08.67%) and Fe_2O_3 (08.82%) formed by the coating elements. Analogous analysis on the surface of coated T22 steel (Fig.7.22b) also shows the presence of white condensed phases of the boiler atmosphere, of which, composition is similar to flyash. The matrix shows the presence of oxides of Cr, Ni, Al and Fe. The surface morphology of coated GrA1 steel (Fig.7.22c) shows the pits formed due to impact of flyash on the surface.

The BSE images and EDAX analysis at some selected points of interest across the cross-section of the corroded NiAlCrFeMo coated GrA1 steel is shown in Fig.7.23a. Compositional analysis on the uppermost surface of the corroded coating (Point 1 and 2), mainly consist of oxides of Al and Cr along with relatively lower concentration of Ni, Fe and Mo oxides. The absence of oxygen at point 2 signifies nickel rich splats in unoxidised condition. From the EDAX analysis along the dark contrast region (point 3), it can be inferred that nickel rich splats are surrounded by the oxides of Cr, Al, Fe and Mo at their splat boundaries. Corresponding analysis along the cross-section of the NiAlCrFeMo coated T11 steel is shown in Fig.7.23b.The external surface of the corroded coating (Point 1) mainly composed of oxides of Cr, Al and Ni. Small quantity of sulphur can be found in the surface scale, indicating the possibility of chemical interaction of the corrosive boiler environment. Oxidation of the entire cross-section of the coating along the splat boundary can be observed and mainly aluminum and chromium got oxidized along the splat boundary (point2). Elongated nickel rich splats had remained unoxidised.

7.1.3.4 EPMA Analysis

Elemental X-ray maps for NiAlCrFeMo coated T11 steel after exposure to superheater zone of coal fired boiler are shown in Fig.7.24. A thin layer of oxide scale at the surface of the corroded coating can be observed form the oxygen map. This layer

mainly comprises of protective oxides of Al and Cr. Distribution of oxides of Si on the external surface indicates the embedment of fly ash deposit on the coating. The entire cross section of the coating has been oxidized along the splat boundary. The mapping for O, Cr and Al corroborated the preferential oxidation of Cr and Al along the splat boundary. Also minor amount of Mo and Fe oxides have been observed along the splat boundary. Combining the mapping for Ni and O, it can be concluded that the nickel rich splats are in unoxidised condition. Minor diffusion of Fe in to the coating can be observed along the substrate-coating interface. Similar results have been observed for NiAlCrFeMo coated T22 steel exposed to boiler environment and illustrated in Fig.7.25.

7.1.4   NiCrFeSiB Coating

7.1.4.1 Thermo gravimetric studies and Thickness Monitoring

Fig.7.26 shows the macrographs of HVOF sprayed NiCrFeSiB coated GrA1, T11 and T22 steels exposed to superheater zone of the coal fired boiler for 1000 hours. As-sprayed coatings with initial dull green appearance changed to brownish green color after exposure to industrial environment. Oxide scale formed on the coatings seems to be intact with out any cracks present on the surface.

The plot of weight change versus time is shown in Fig.7.27. The fluctuation in the weight change data as observed from the plot might be due to fly ash erosion and suspected spalling of formed oxide scale accompanied with falling off and regeneration of the ash deposits on the surface of the exposed sample. Coated T11 steel showed a maximum weight gain followed by coated T22 and GrA1 steels. Weight gain square curve (Fig.7.28) shows considerable deviations from the parabolic rate law. The parabolic rate constant K_p for NiCrFeSiB coated GrA1,T11 and T22 steels are found to be 0.01 x 10^{-10}, 0.027 x 10^{-10} and 0.018 x 10^{-10} g^2 cm^{-4} s^{-1} respectively.

Erosion-corrosion in terms of thickness loss from the surface of exposed samples is represented in bar chart (Fig.7.29). Degradation rate at the end of 1000 hours of study for NiCrFeSiB coated GrA1, T11 and T22 steels are found to be 6.2, 8.62 and 7.24 mpy respectively which are very small.

7.1.4.2 X-ray Diffraction Analysis

Fig.7.30 shows the X-ray diffraction pattern of the surface of exposed NiCrFeSiB coated steels. The main phases identified on the surface were Ni, NiO, Cr_2O_3, and Fe_3O_4
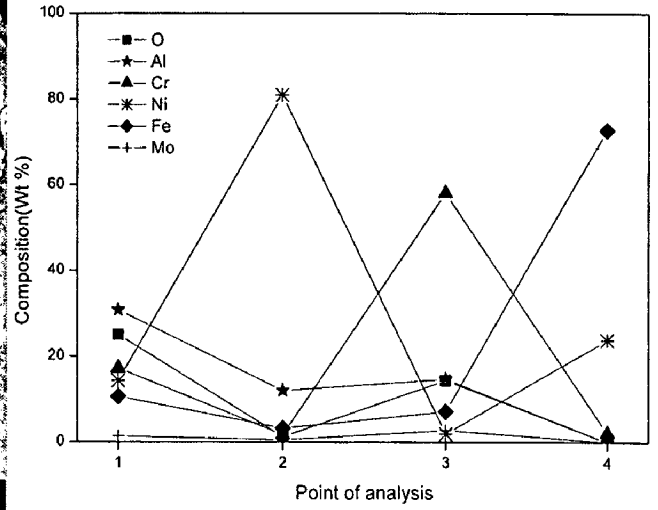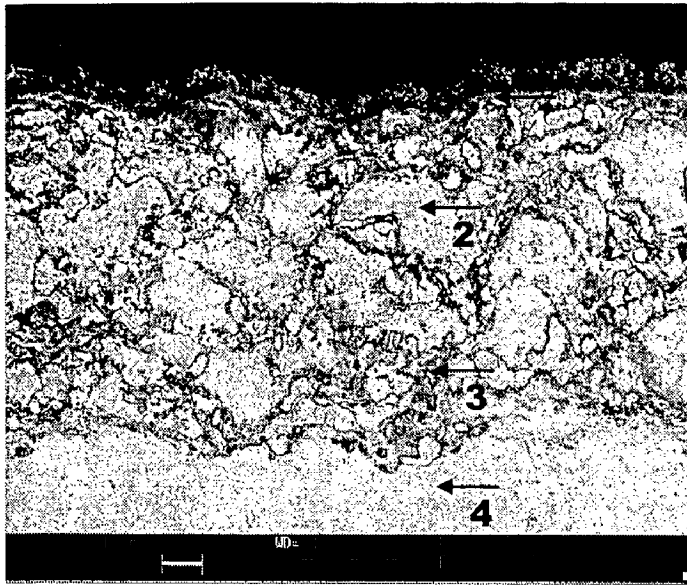
(a)
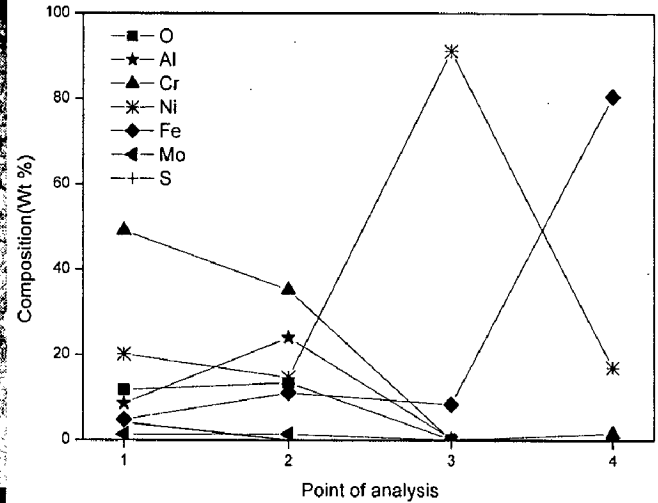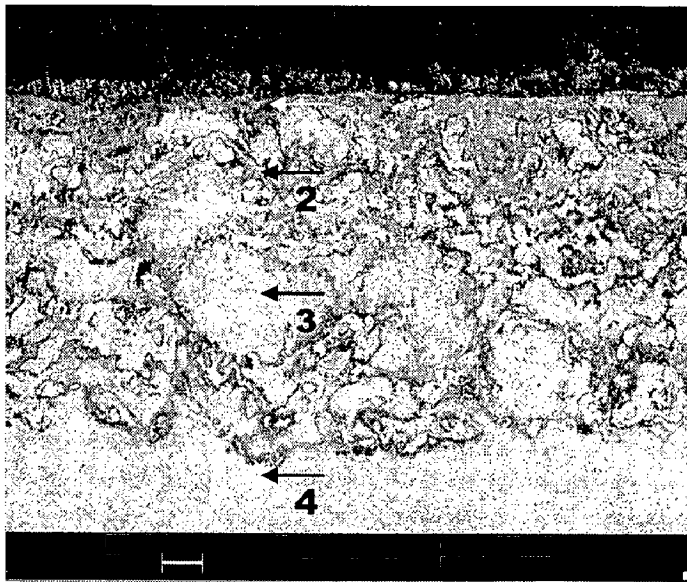
(b)

Fig.7.23   Back scattered electron image and EDAX point analysis (wt %) across the cross-section of the NiAlCrFeMo coated steels exposed to super heater zone of coal fired boiler for 1000 hours:

    (a) Coated GrA1 steel   (b) Coated T11 steel

232
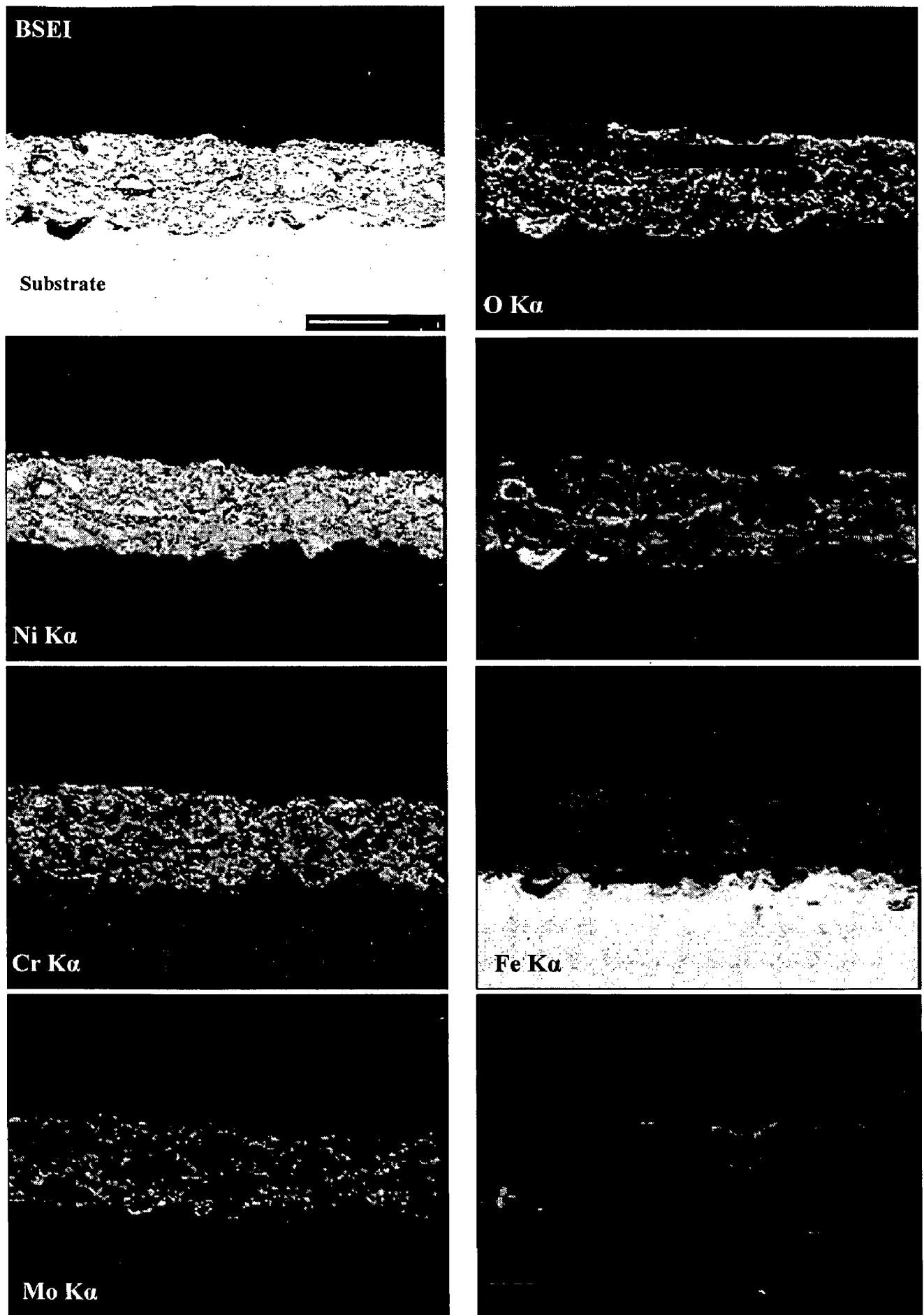
Fig.7.24 BSEI and elemental X-ray mapping along the cross-section of the NiAlCrFeMo coated T11 steels exposed to superheater zone of coal fired boiler for 1000 hours
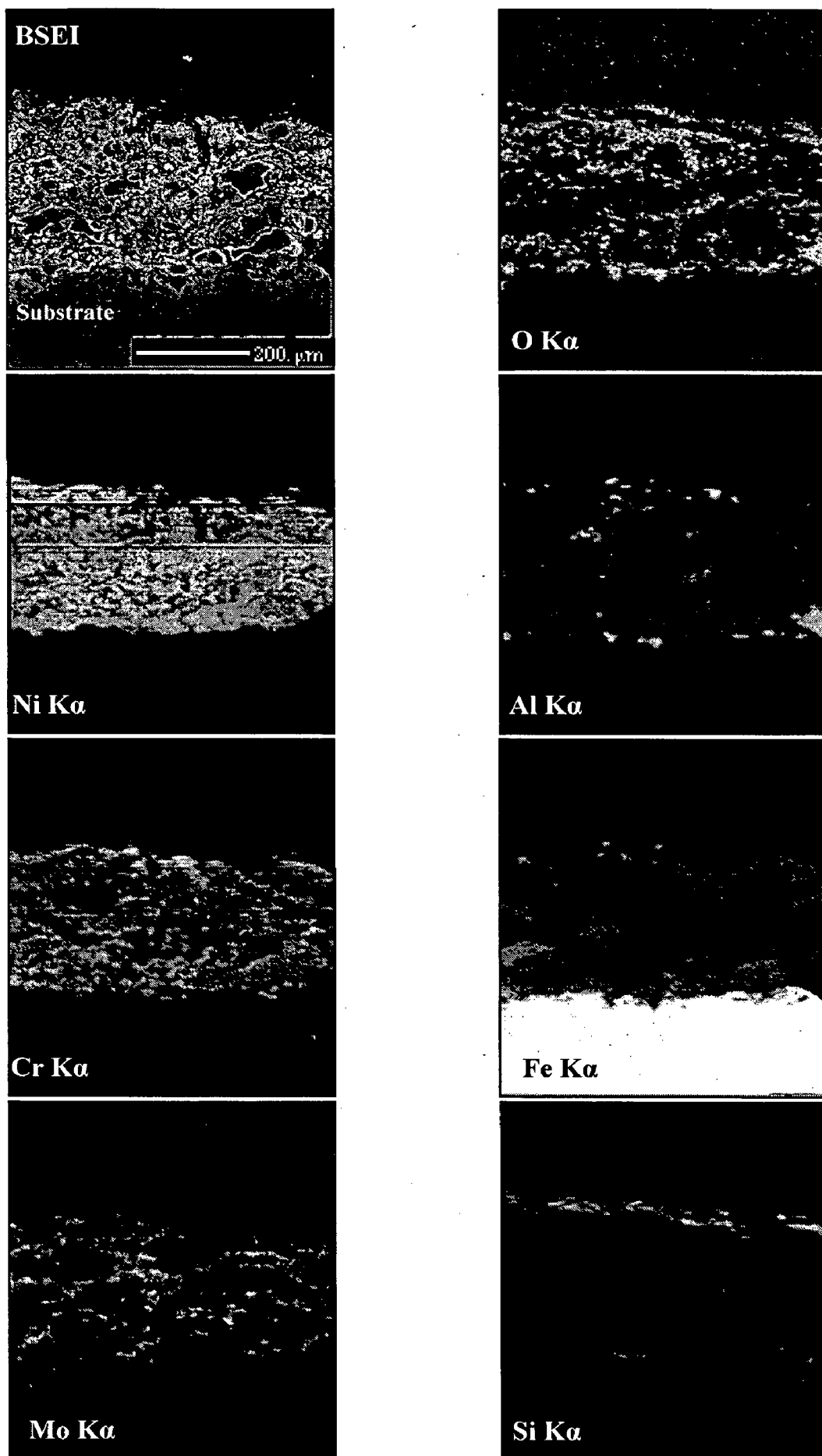
Fig.7.25 BSEI and elemental X-ray mapping along the cross-section of the NiAlCrFeMo coated T22 steels exposed to superheater zone of coal fired boiler for 1000 hours
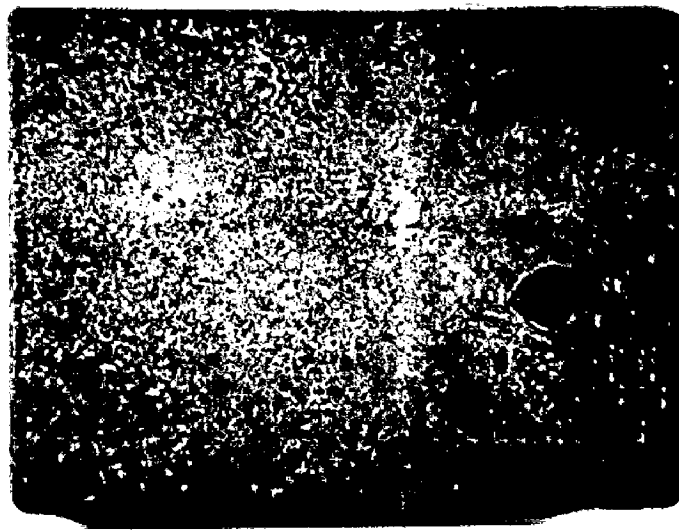
(a)
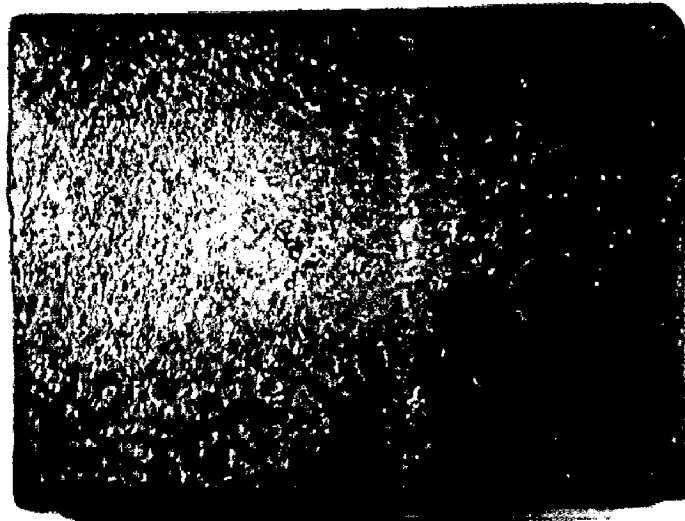
(b)

(c)

Fig.7.26   Macrographs of the NiCrFeSiB coating exposed to superheater zone of coal fired boiler for 1000 hours:
(a) GrA1 steel   (b) T11 steel   (c) T22 steel
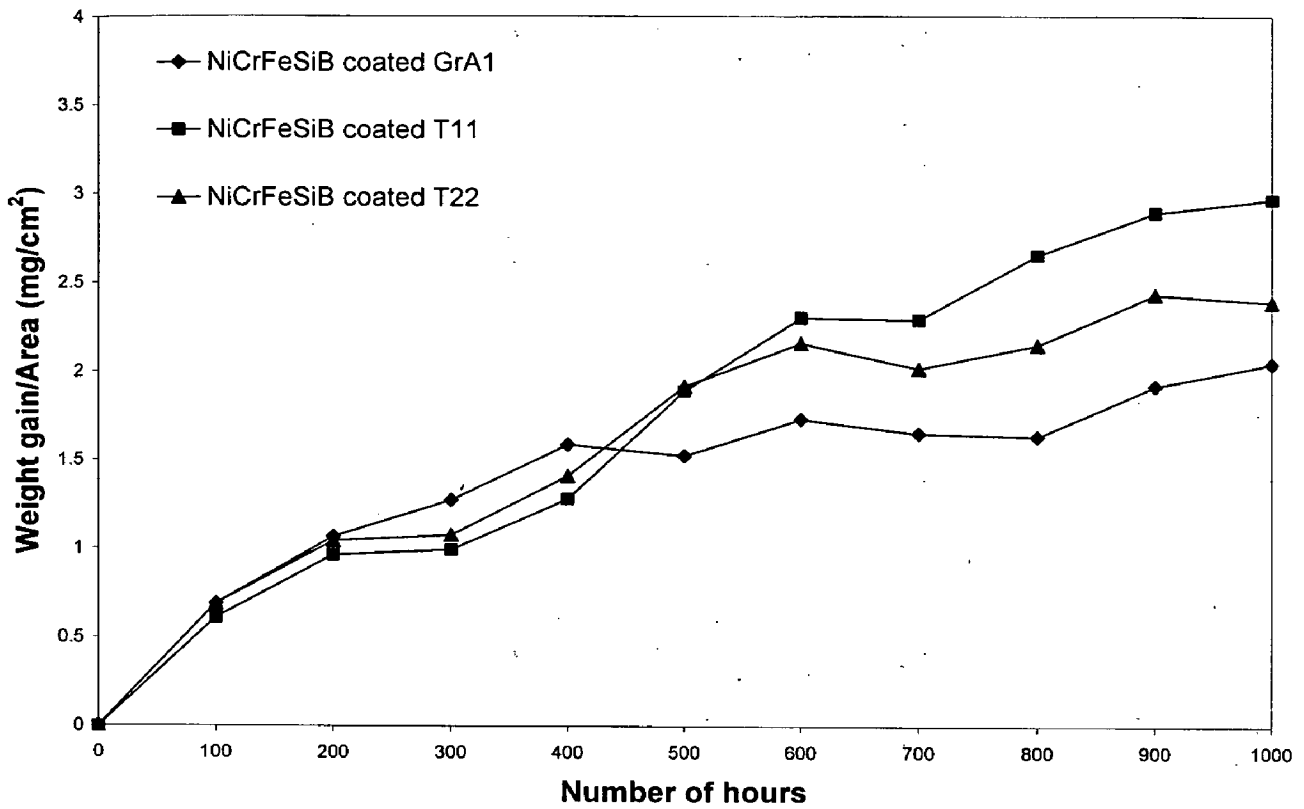
Fig.7.27   Weight change plot for NiCrFeSiB coated steels exposed to super heater zone of coal fired boiler for 1000 hours
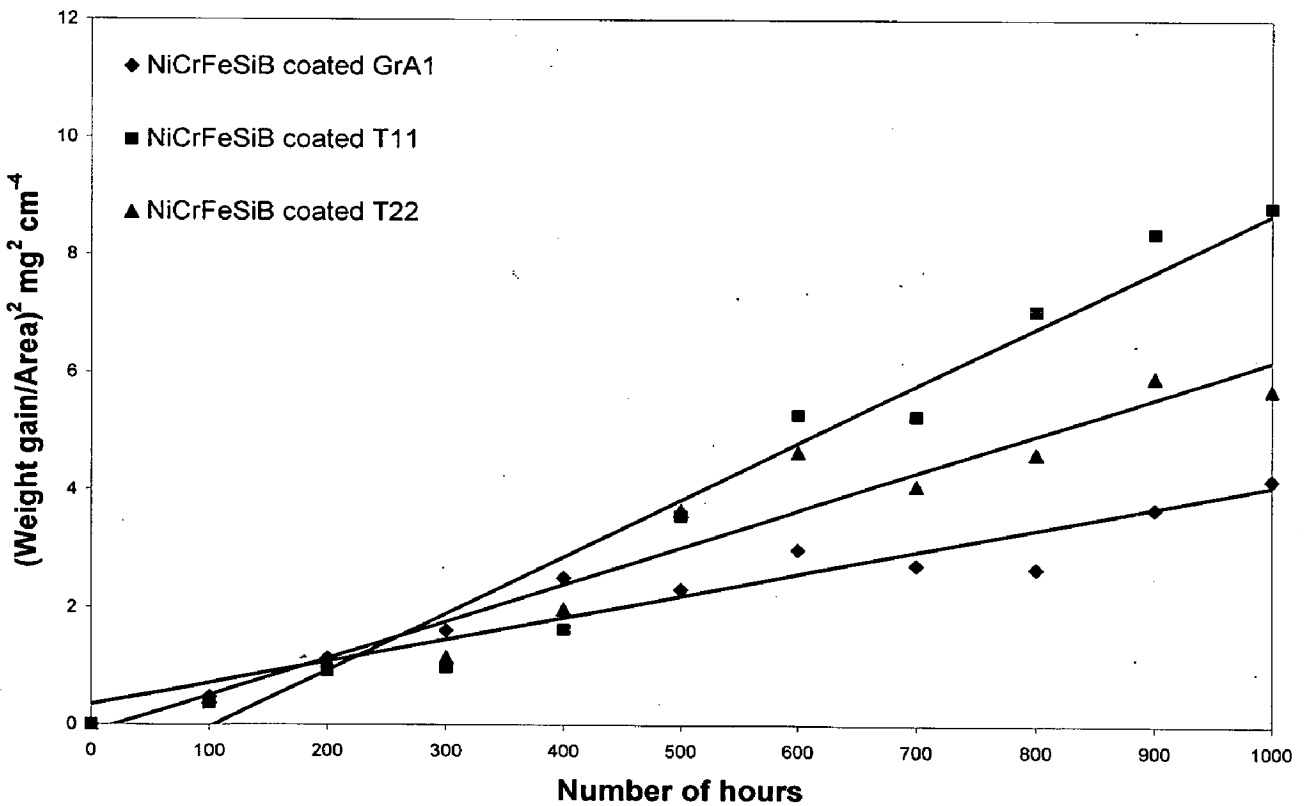
Fig.7.28   (Weight change/area)^2 plot for NiCrFeSiB coated steels exposed to super heater zone of coal fired boiler for 1000 hours

236
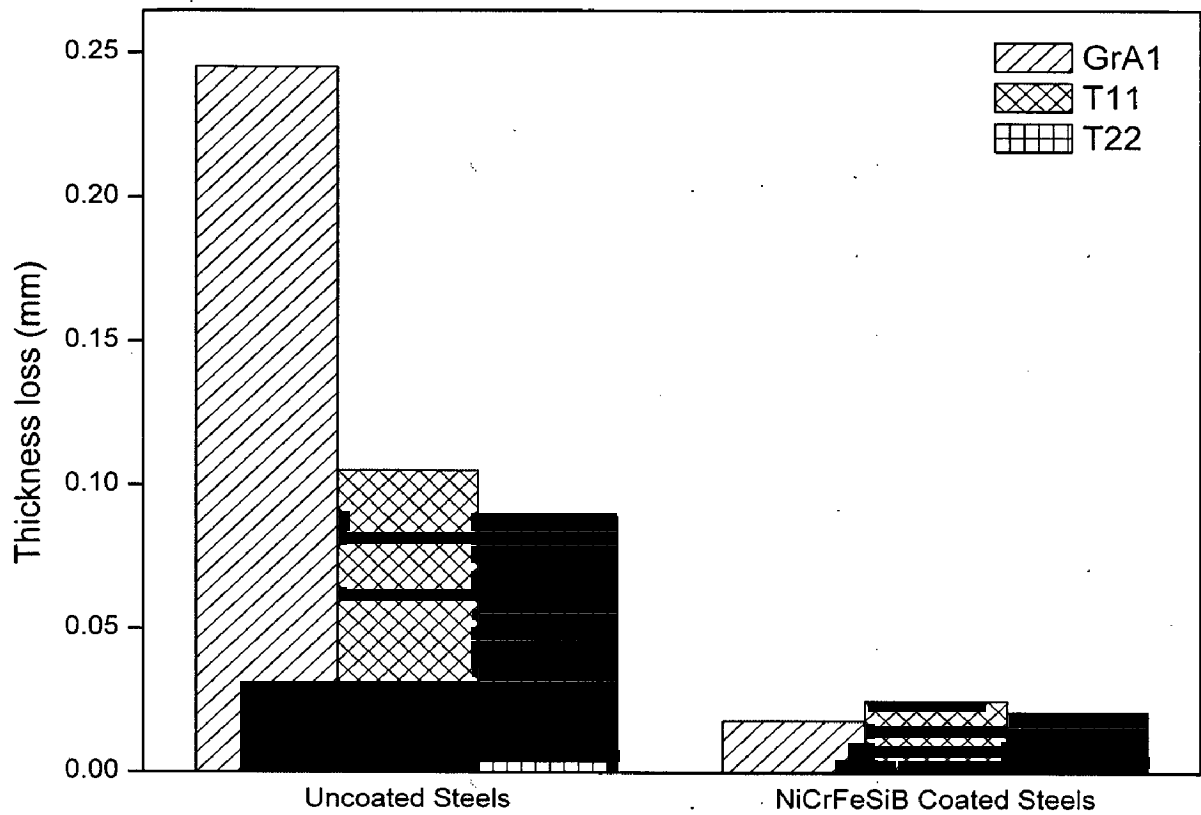
Fig.7.29   Bar chart indicating the thickness lost in mm for the uncoated and NiCrFeSiB coated steels after 1000 hours of exposure to super heater zone of coal fired boiler.
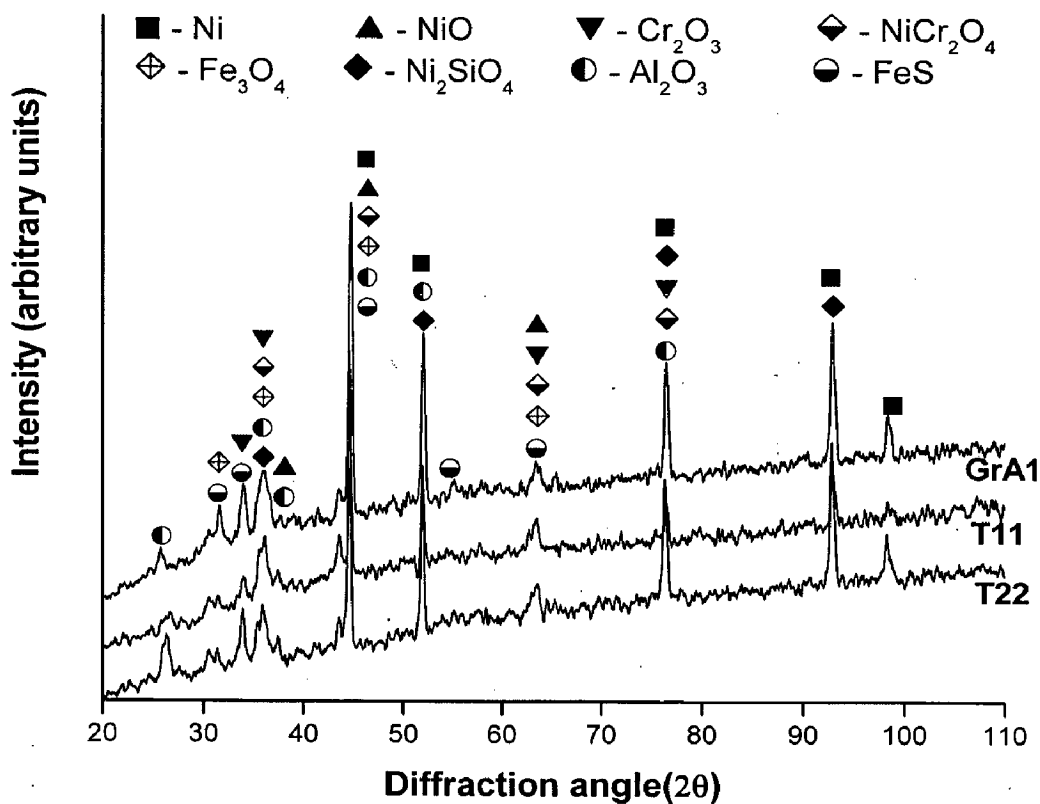
Fig.7.30   X-ray diffraction patterns for NiCrFeSiB coated GrA1, T11 and T22 steels Exposed to super heater zone of coal fired boiler for 1000 hours.

237

along with mixed oxide spinals $NiCr_2O_4$, and Ni_2SiO_4. XRD result also shows the presence of Al_2O_3 and FeS phases indicates the fly ash deposits on the surface of exposed coated steels.

7.1.4.3 SEM/EDAX Analysis

SEM/EDAX analysis on the surface of the exposed NiCrFeSiB coated steels are shown in Figs.7.31 & 7.32. Pits observed on the surface (Fig. 7.31 a & b) might be due to impact of fly ash resulting in spalling of oxide scale. This is further confirmed from the EDAX analysis on the white colored deposit distributed on the oxide scale, mainly composed of Al_2O_3, SiO_2, Fe_2O_3, Na_2O, CaO and TiO_2, which is almost similar to ash composition. The EDAX analysis on the pit region shows relatively higher amount of Cr_2O_3, SiO_2 and NiO, oxides formed on oxidized coatings. Corresponding analysis on NiCrFeSiB coated T22 steels (Fig.7.32) also shows that the white patches have a composition similar to fly ash. The dark matrix mainly shows the peaks for O, Si, Cr and Ni, which confirms the oxides and their spinels, have formed during oxidation of coating elements.

The BSE images (Fig.7.33 a) along the cross-section of NiCrFeSiB coated GrA1 steel showed thin and continuous oxide scale formed on the surface of corroded coating. EDAX analysis at point 1 reve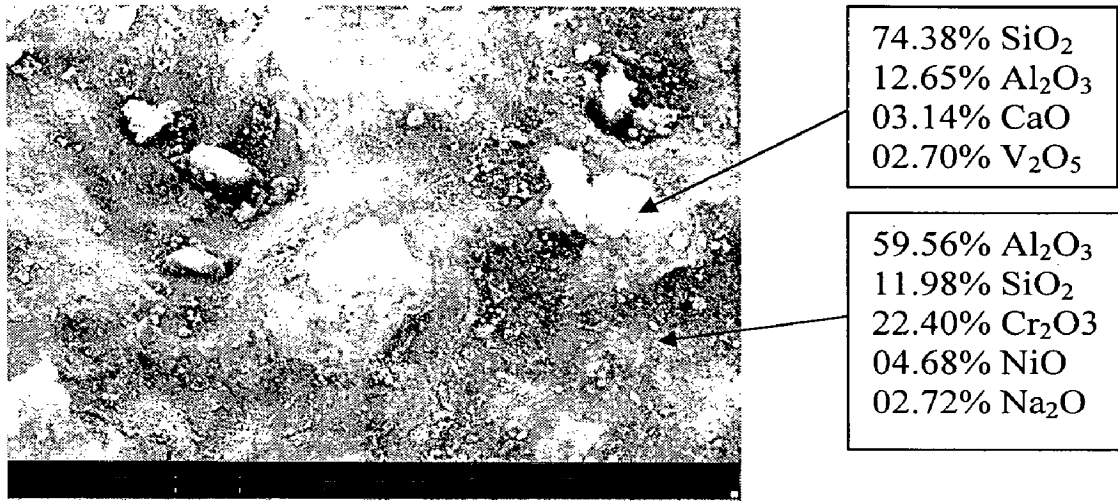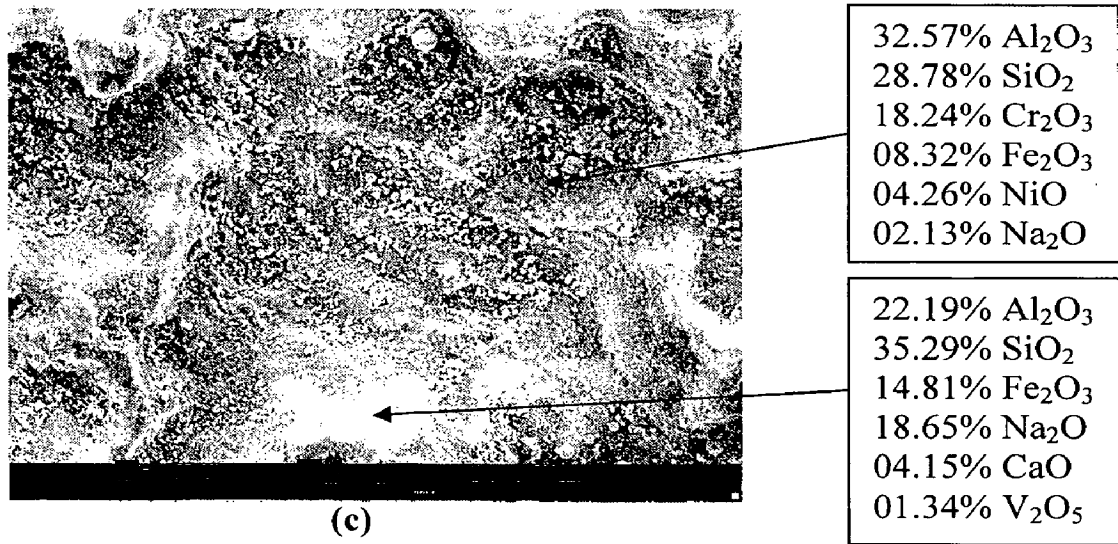aled that the oxide scale mainly consisted of oxides of Si, Cr and Ni along with the minor presence of Al (from ash deposit).The absence of oxygen at Point 2, 3 and 4 indicate that the coating region below the thin oxide layer has remained unoxidised and hence the oxides formed on surface act as barrier to diffusion of oxygen and other corrosive species of the boiler environment. The homogeneous concentration of coating elements at these points indicates that the coating region below the oxide scale is similar to as-sprayed coatings. Figs.7.33 b & c show the similar analysis on NiCrFeSiB coated T11 and T22 steels. Point 1 in both figures shows the minor presence of S, Na and Al on the surface of oxide scale, which shows ash deposit, got embedded in the oxide scale. Point 4 of Fig.7.33b shows the presence of Al_2O_3, which might have been included during surface preparation prior to HVOF spraying. The coating-substrate interface (Point 5 of Fig.7.33 c) shows continuous thin band of Ni and Fe, which shows the possibility of interdiffusion of these elements across the interface.

7.1.4.4 EPMA Analysis

Elemental X-ray mapping for the NiCrFeSiB coated T11 steel after exposure to superheater zone of coal fired boiler is shown in Fig.7.34. By combining the maps for O, Si and Cr, it is revealed that, thin oxide layer of SiO_2 and Cr_2O_3 formed on the surface of corroded coating. Presence of SiO_2 in the surface scale might be formed from the oxidation of coating element and partly due to formation of condensed phases from boiler environment (Fly ash deposit). A thin streaks of Ni co-exists with O, confirm the presence of NiO. The presence of patches of Na and S on the surface provides the evidence of interaction of ash with the oxide scale. The arrow mark shown on the Fe map indicates the outward diffusion of Fe from the substrate in to the coating. The absence of oxygen and other corrosive species beneath the uppermost oxide scale indicates protective behavior of the NiCrFeSiB coating in the given environment. Similar oxide scale has been observed for NiCrFeSiB coated T22 steels which is characterized in Fig.7.35.

7.1.5 WC-Co/NiCrFeSiB Coating

7.1.5.1 Thermo gravimetric studies and Thickness Monitoring

Macrographs of HVOF sprayed WC-Co/NiCrFeSiB coated GrA1, T11 and T22 steels exposed to superheater zone of the coal fired boiler for 1000 hours is shown in Fig.7.36. Brownish-green color oxide scale has been observed on all the three corroded coatings. The surface appears to be free from cracks and the coatings are found to be intact at the end of 1000 hours of exposure.

The plot of weight change as a function of time is shown in Fig.7.37. Marginal fluctuation observed in the plot might be due to fouling of the exposed samples by fly ash deposit. The weight gain at the end of 1000 hours of exposure for coated GrA1, T11 and T22 steels are 2.02, 2.86, and 2.49 mg/cm^2 respectively. Parabolic rate law has been assumed for the sake of simplicity, even though, minor deviation is observed in weight gain square versus time plot (Fig.7.38).The parabolic rate constant K_p calculated for coated GrA1,T11 and T22 steels are found to be 0.01 x 10^{-10}, 0.024 x 10^{-10} and 0.016 x 10^{-10} g^2 cm^{-4} s^{-1} respectively.

The bar chart (Fig.7.39) indicates the extent of combined erosion-corrosion measured in terms of thickness loss of the coated steels after 1000 hours of exposure to boiler environment. Thickness loss of coated GrA1, T11 and T22 steels are 0.031, 0.024,

41.90% Al_2O_3
51.69% SiO_2

10.22% Al_2O_3
22.03% SiO_2
30.05% Cr_2O_3
11.52% Fe_2O_3
12.50% NiO
07.22% Na_2O
03.28% MgO

(a)

31.04% Al_2O_3
39.60% SiO_2
08.93% Fe_2O_3
05.15% Na_2O
02.09% CaO
07.10% TiO_2

18.47% Al_2O_3
24.68% SiO_2
28.11% Cr_2O_3
07.39% Fe_2O_3
08.02% TiO_2
02.64% CaO
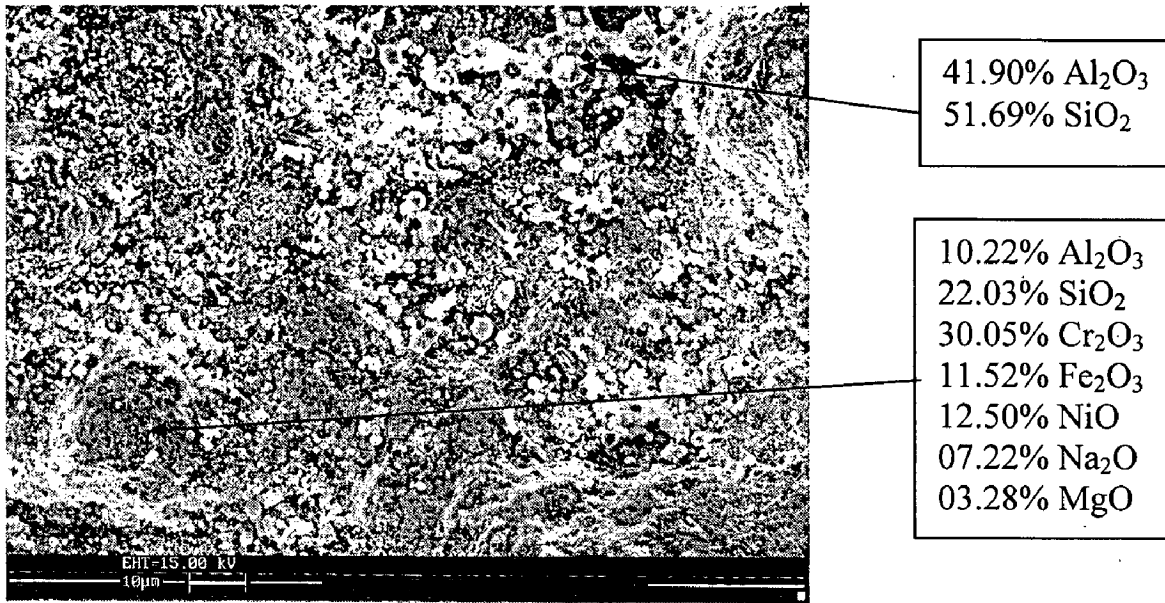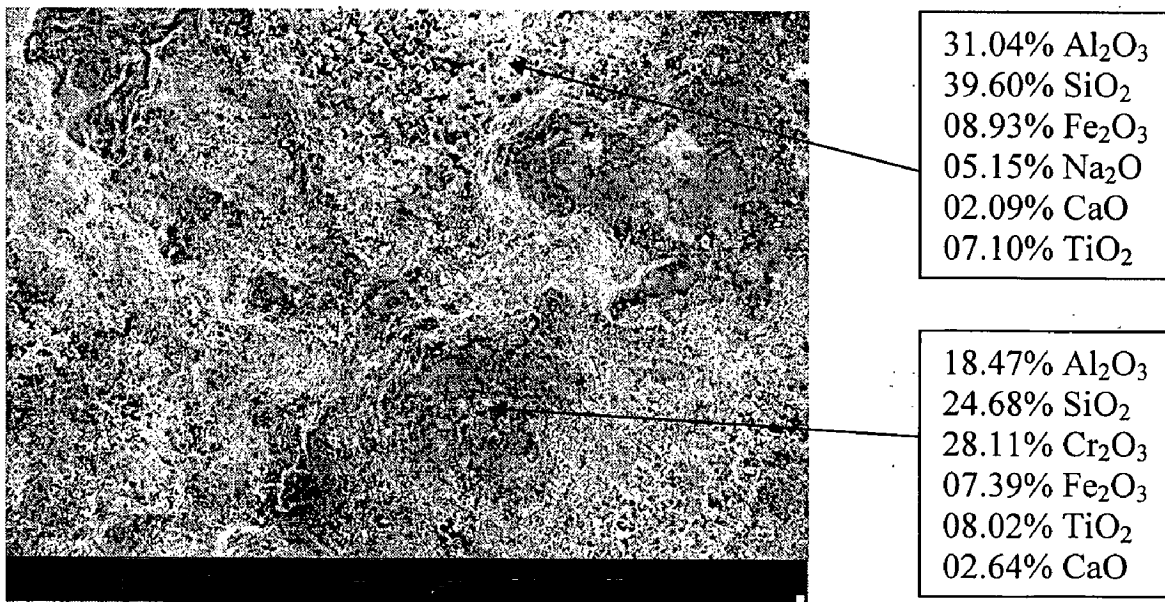
(b)

Fig.7.31   Surface scale morphology and EDAX point analysis for NiCrFeSiB coated steels exposed to super heater zone of coal fired boiler for 1000 hours:

(a) GrA1 steel   (b) T11 steel
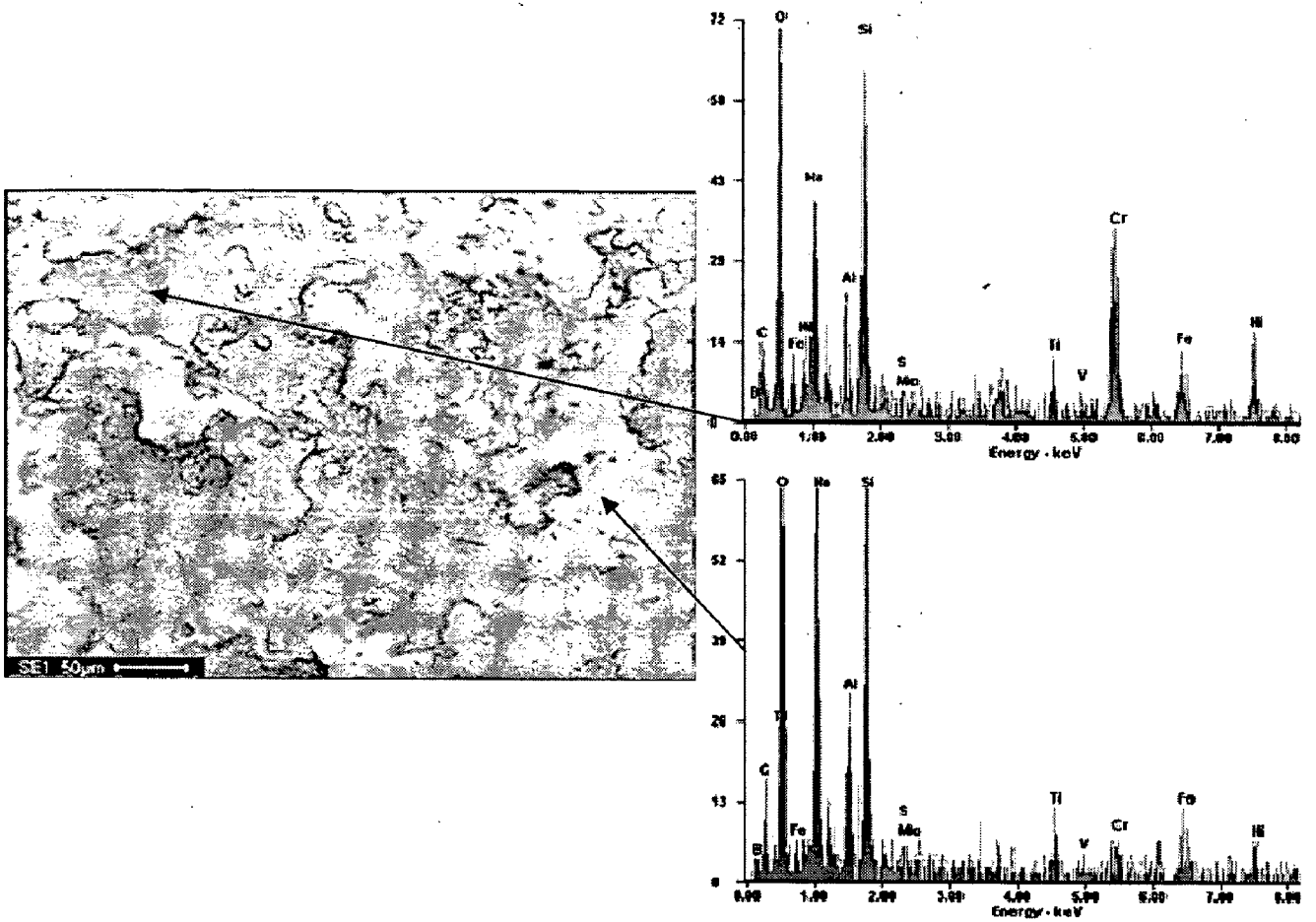
Fig.7.32   Surface scale morphology and EDAX point analysis for NiCrFeSiB coated T22 steel exposed to super heater zone of coal fired boiler for 1000 hours
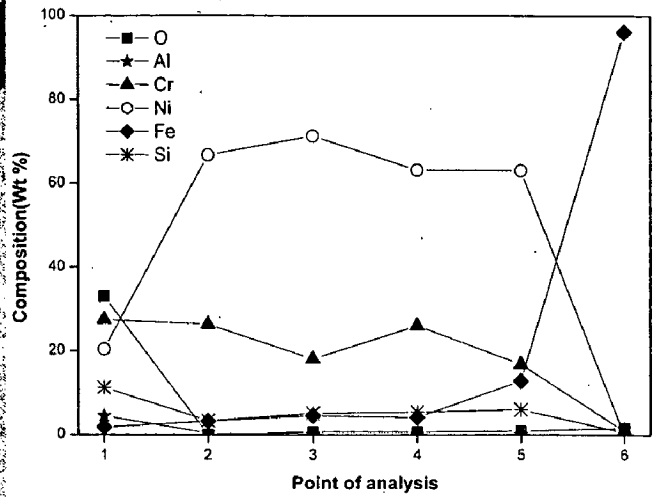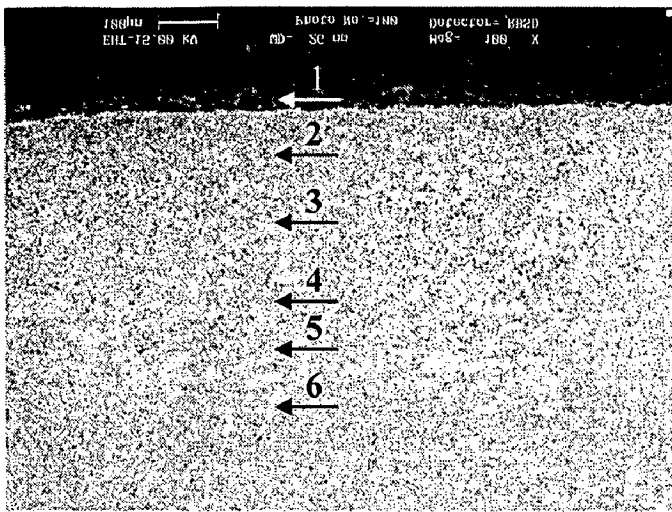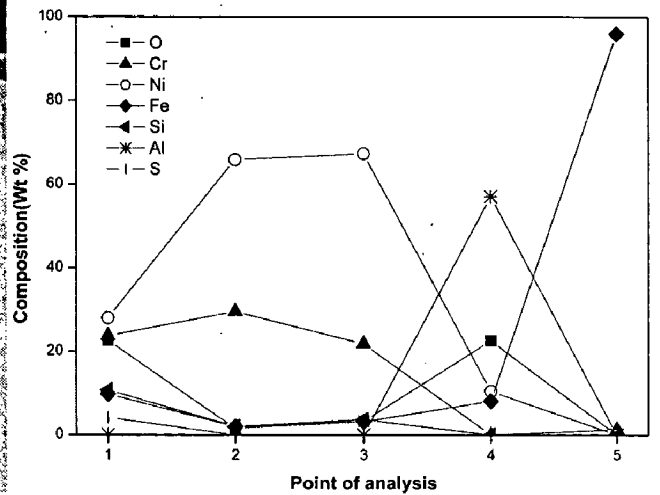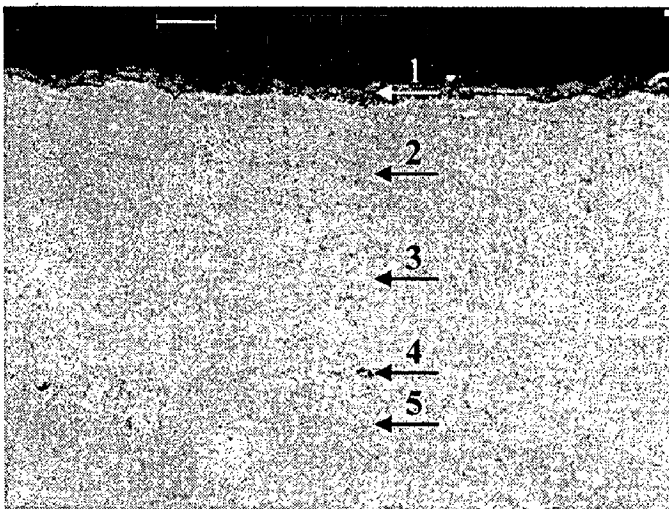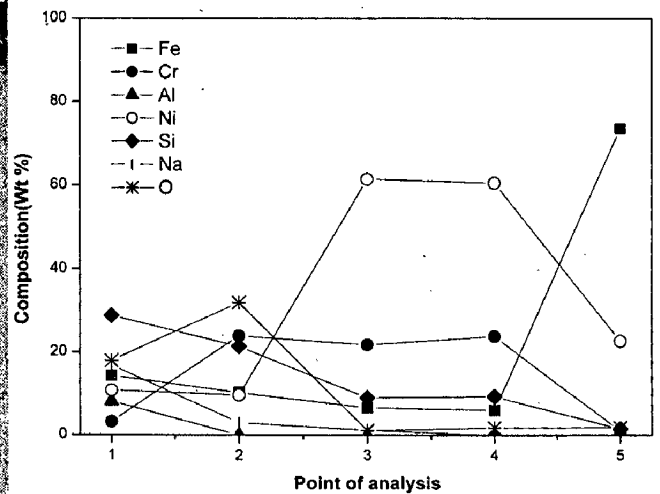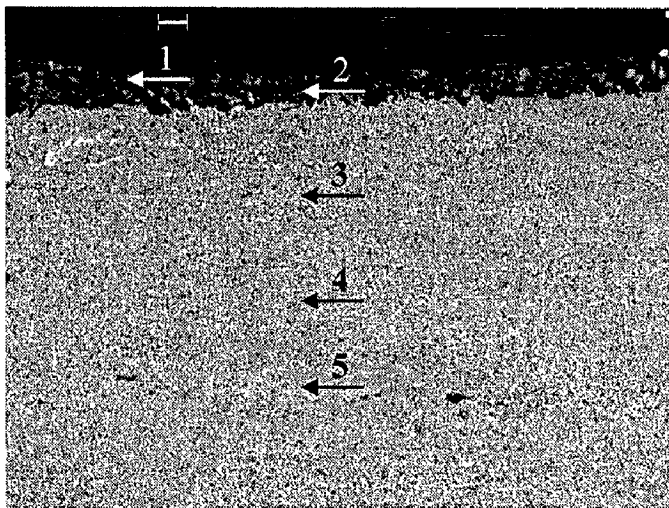
Fig.7.33 Back scattered electron image and EDAX point analysis (wt %) across the cross-section of the NiCrFeSiB coated steels exposed to super heater zone of coal fired boiler for 1000 hours:
(a) GrA1 steel   (b) T11 steel   (c) T22 Steel
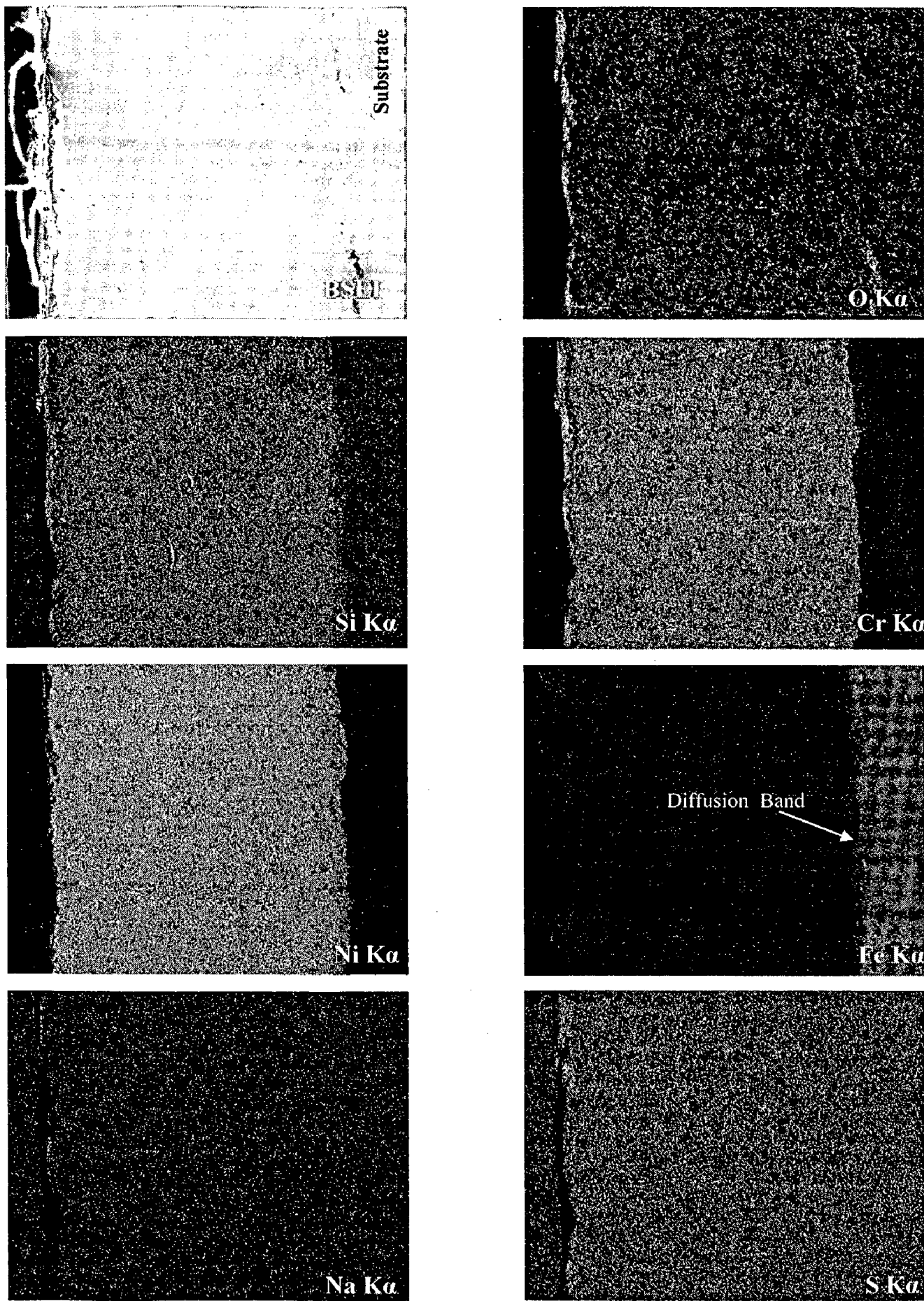
Fig.7.34   BSEI and elemental X-ray mapping along the cross-section of the
NiCrFeSiB coated T11 steels exposed to superheater zone of coal fired
boiler for 1000 hours

243
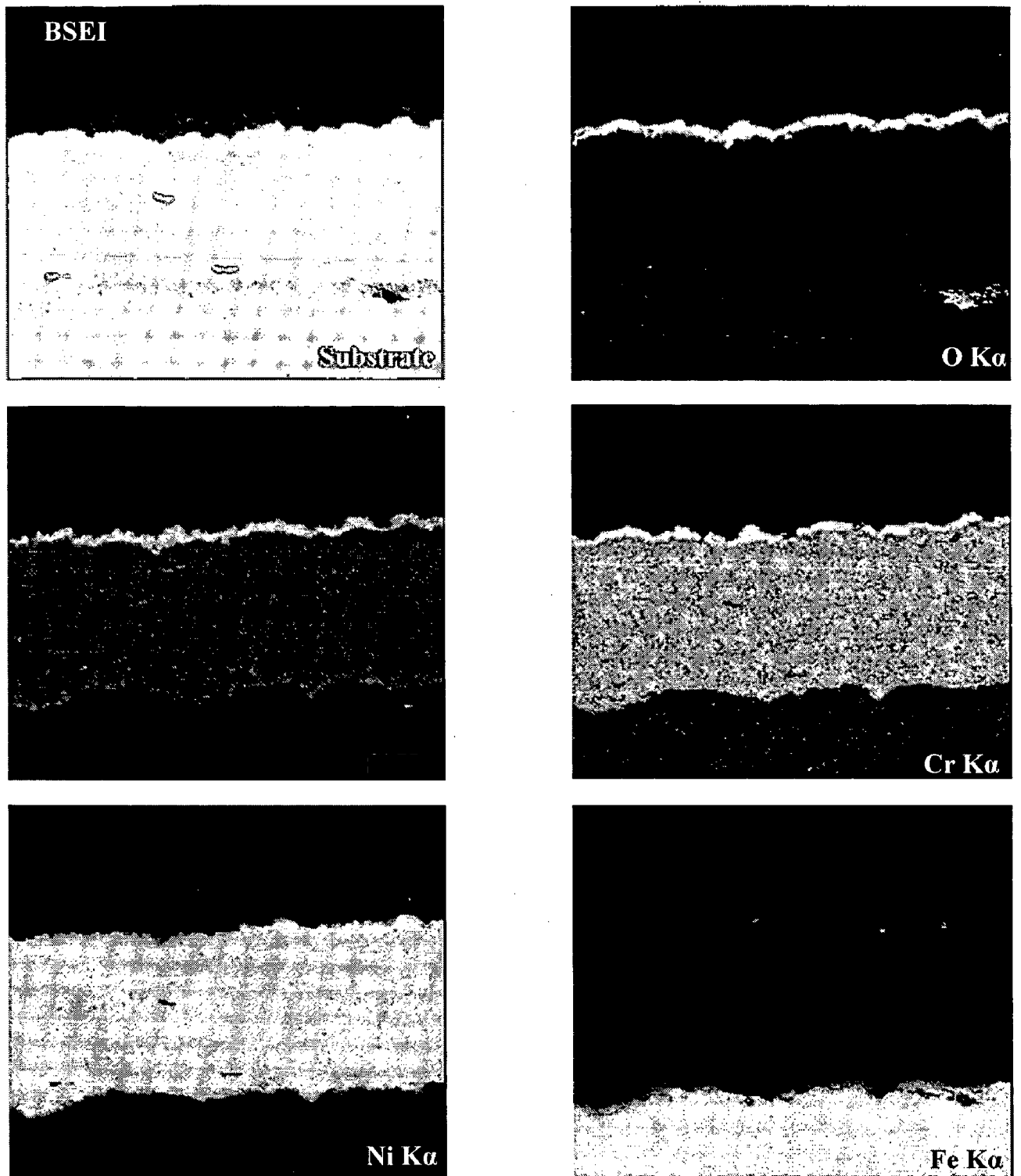
Fig.7.35 BSEI and elemental X-ray mapping along the cross-section of the NiCrFeSiB coated T22 steels exposed to superheater zone of coal fired boiler for 1000 hours
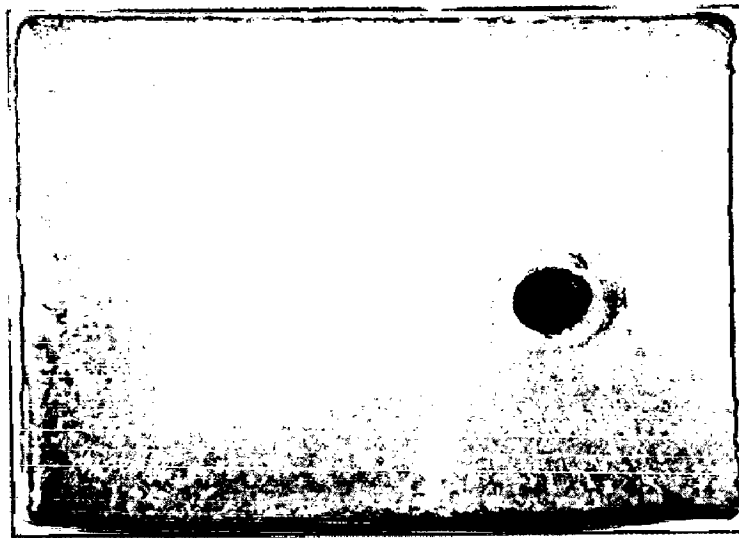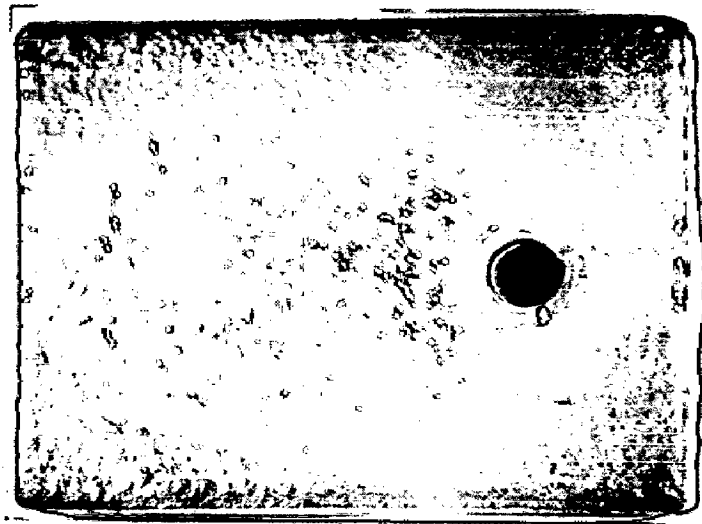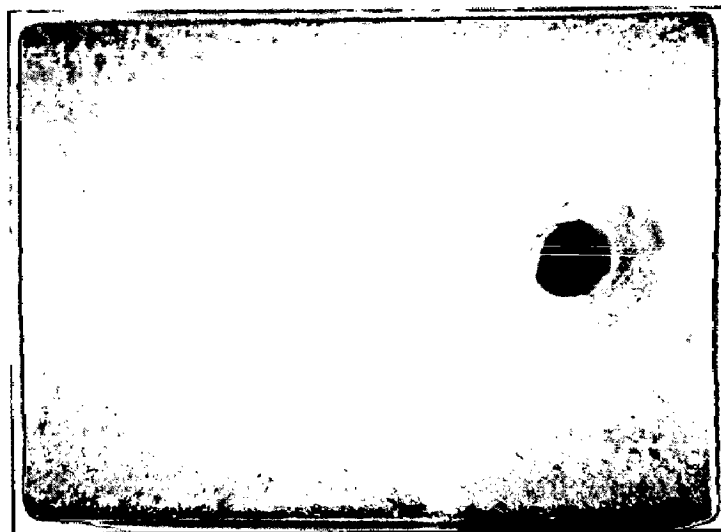
Fig.7.36   Macrographs of the WC-Co/NiCrFeSiB coating exposed to superheater zone of coal fired boiler for 1000 hours:
(a) GrA1 steel   (b) T11 steel   (c) T22 steel
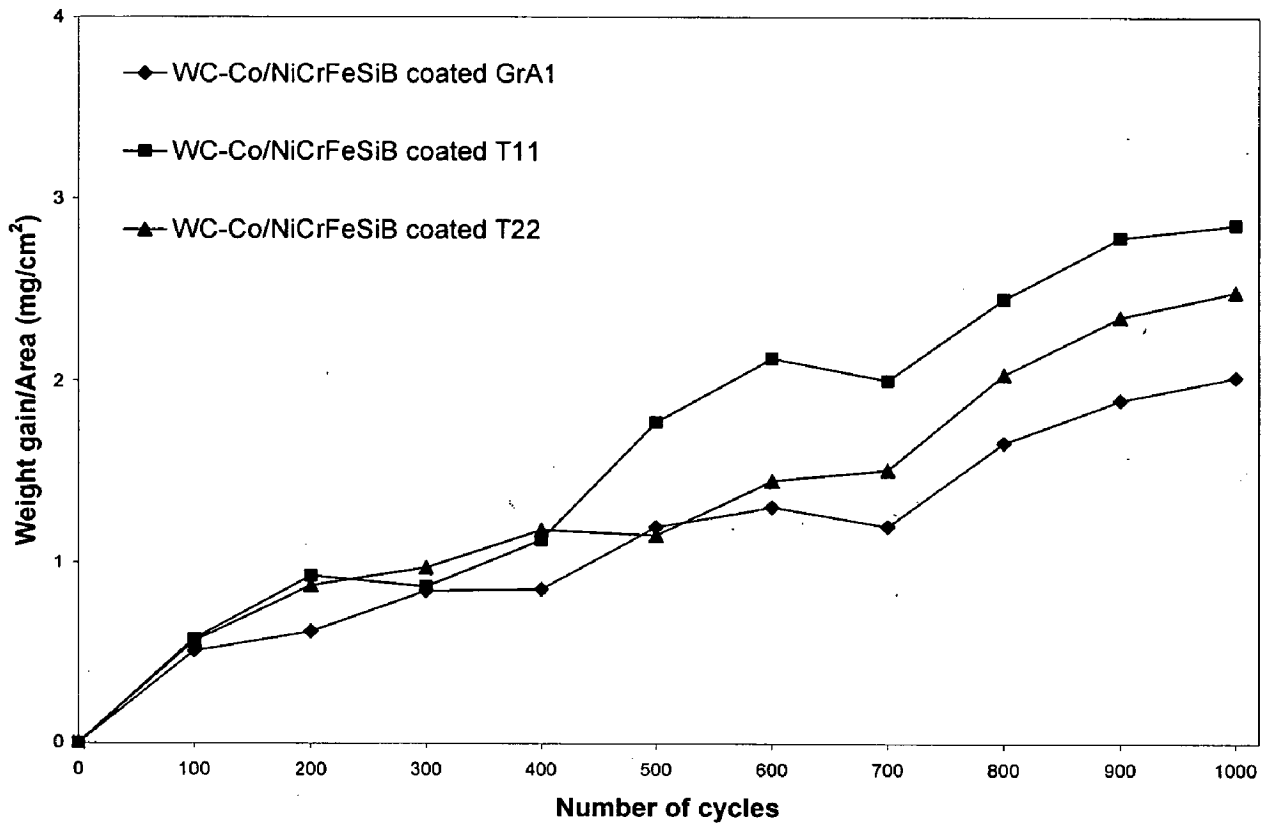
Fig.7.37 Weight change plot for WC-Co/NiCrFeSiB coated steels exposed to super heater zone of coal fired boiler for 1000 hours
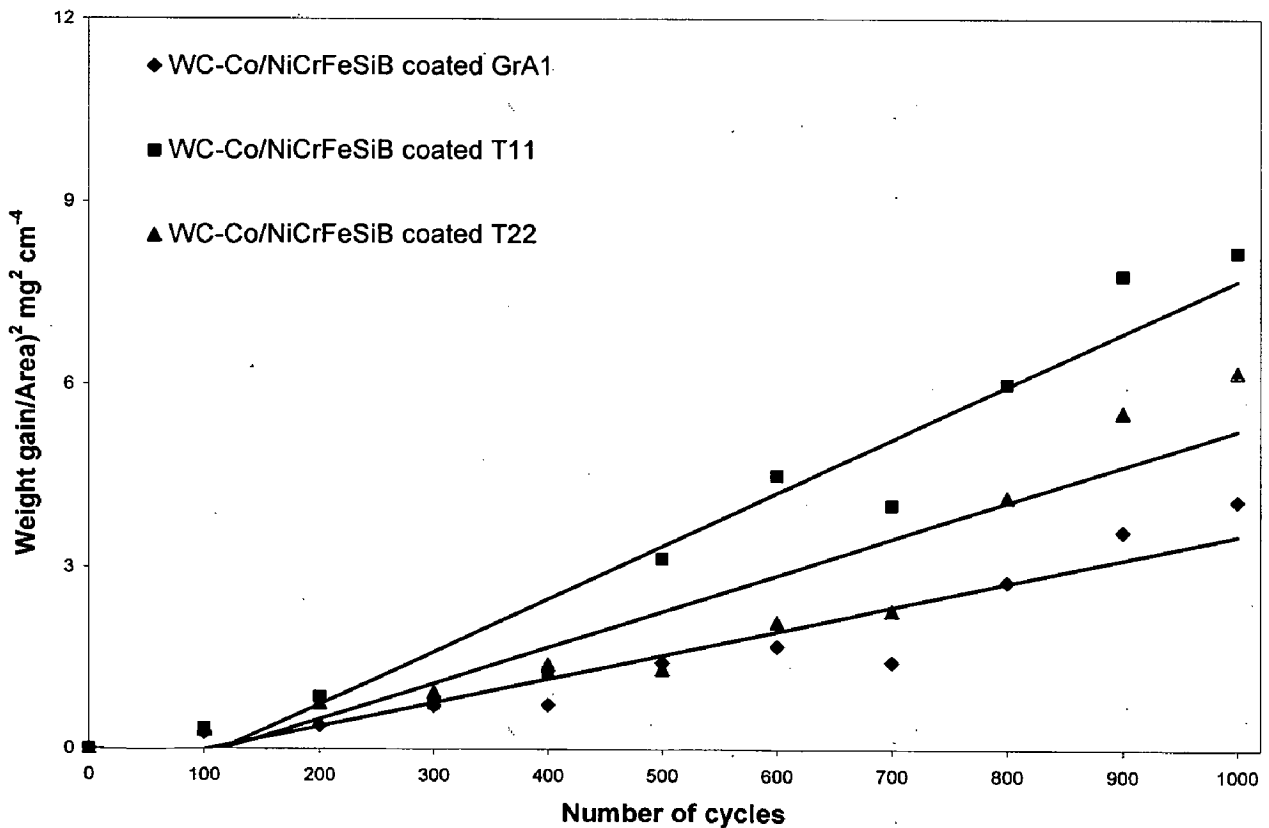
Fig.7.38 (Weight change/area) ^{2} plot for WC-Co/NiCrFeSiB coated steels exposed to super heater zone of coal fired boiler for 1000 hours

and 0.026 mm respectively and the corresponding degradation rate expressed in terms of mils per year are 10.69, 8.27, and 8.96 mpy respectively.

7.1.5.2 X-ray Diffraction Analysis

X-ray diffraction analysis for WC-Co/NiCrFeSiB coated GrA1, T11 and T22 steels, exposed to coal fired boiler environment is shown in Fig. 7.40. The prominent phases identified on the surface were WC, SiO_2, NiO, Cr_2O_3, Fe_2O_3, $NiCr_2O_4$ and Ni_2SiO_4. Presence of peaks for Al_2O_3 and FeS indicate the fly ash embedment on the surface of exposed samples.

7.1.5.3 SEM/EDAX Analysis

SEM on the surface of WC-Co/NiCrFeSiB coated GrA1 steel (Fig.7.41a) shows irregular morphology. The EDAX analysis on the contrast white phases dispersed on the surface revealed the composition of 44.92% SiO_2, 32.39% Al_2O_3, 10.23% TiO_2, 04.96% Na_2O and 03.33% Fe_2O_3. These phases are the main constituents of fly ash and indicated the ash embedment into the open pores of the coatings as well as fouling of exposed coatings due to condensed phases of the ash. The compositional analysis on the dark colored matrix shows the prominent oxides of Cr (26.72%), Si (18.29%), Ni (14.29%) and W (15.24%) formed from the active elements of the coating, and are protective by nature. Minor amount of sulphur has also been detected by the EDAX on the surface. Scanning electron micrograph on the surface of the coated T11 steel (Fig.7.41b) also shows the irregular morphology having hills and valleys, which indicated the likely erosion by impacting fly ash.
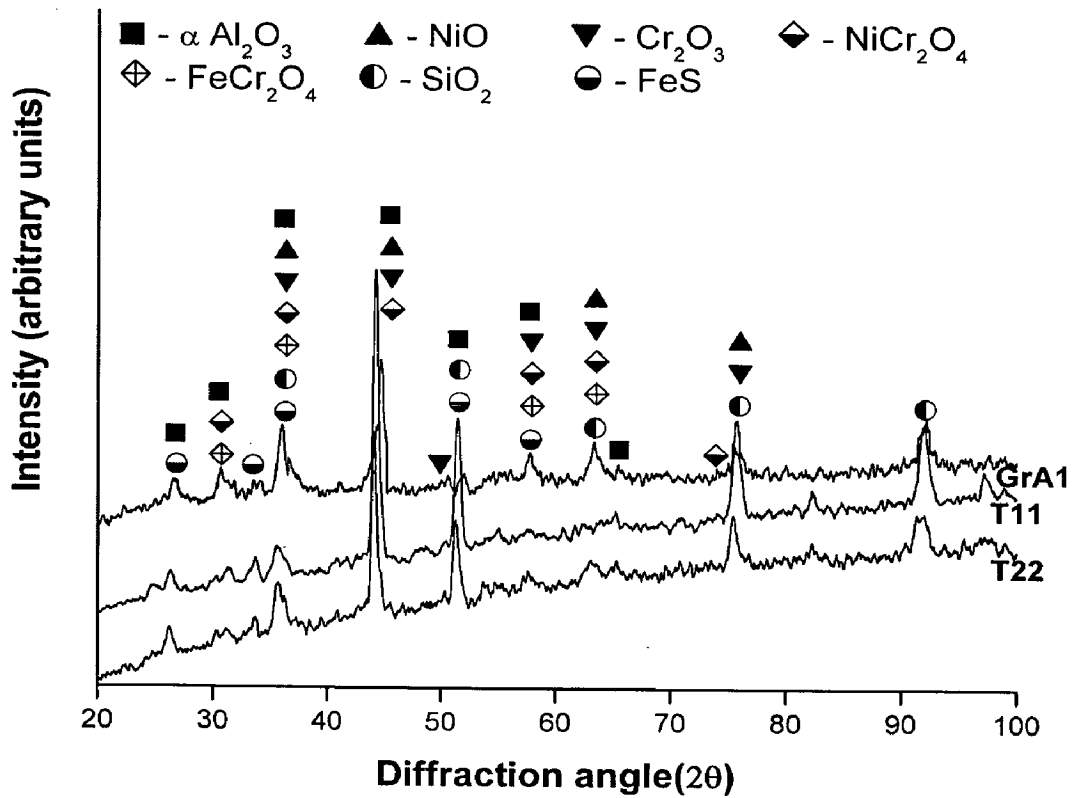
The back scattered image obtained along the cross section of WC-Co/NiCrFeSiB coated T11 steel (Fig.7.42a) shows minor cracks at the subsurface. The EDAX compositional analysis on the upper most surface of the corroded coating (point1) revealed the major constituents to be O (28.1%), Ni (29.8%), Cr (14.6%) and Si (11.5%) and supports the formation of protective oxide scale consisting of oxides and spinels of Ni, Cr and Si. White contrast elongated phases which are oriented parallel to the substrate have been identified as WC+Co aggregates (point2) and are dispersed in between the nickel rich (75.39%) splats (point3). It is noticed that oxygen is absent at point 2 and point 3. Hence, it can be concluded that, corrosion of the coating is limited to few microns on the uppermost surface and the rest of the coating remained unoxidised. EDAX analysis at darker region along the coating-substrate interface (point 4) shows

higher content of O and Al, which is not a part of coating and hence can be attributed due to embedment of grit particles during surface preparation prior to HVOF spraying. Presence of higher amounts of Ni (34.2%) and Fe (43.5%) along the interface (point5) suggests interdiffusion of Ni from the coating into substrate and Fe from substrate into the coating. Corresponding analysis along the cross section of WC-Co/NiCrFeSiB coated T22 steel shows similar results and is shown in Fig.7.42b.

7.1.5.4 EPMA Analysis

Elemental X-ray mapping for WC-Co/NiCrFeSiB coated GrA1 steels after exposure to superheater zone of coal fired boiler is shown in Fig.7.43. It is observed from the oxygen map that a thin layer of oxide scale is formed at the outermost surface of the corroded coating. The absence of oxygen below this oxide scale indicates the oxides formed at the surface, which, acts as a barrier to the ingress of oxidizing species into the coating. Combining maps of O, Cr, Si and Ni corroborated the presence of oxides and spinels of these elements. A continuous layer of SiO_2 has been observed from mapping for Si and can be partly attributed to the protective SiO_2 formed by the oxidation of Si present in the coating composition and partly due to fly ash deposit condensed on the coating surface, contains SiO_2. By combining Cr and O maps, discontinuous layer of chromium oxide can be identified on the outermost surface. Minor interdiffusion of Ni and Fe across the coating-substrate interface in the form of thick band can be perceived from Fe and Ni maps. Similar findings have been observed from X-ray mapping for WC-Co/NiCrFeSiB coated T22 steels which is characterized in Fig.7.44.
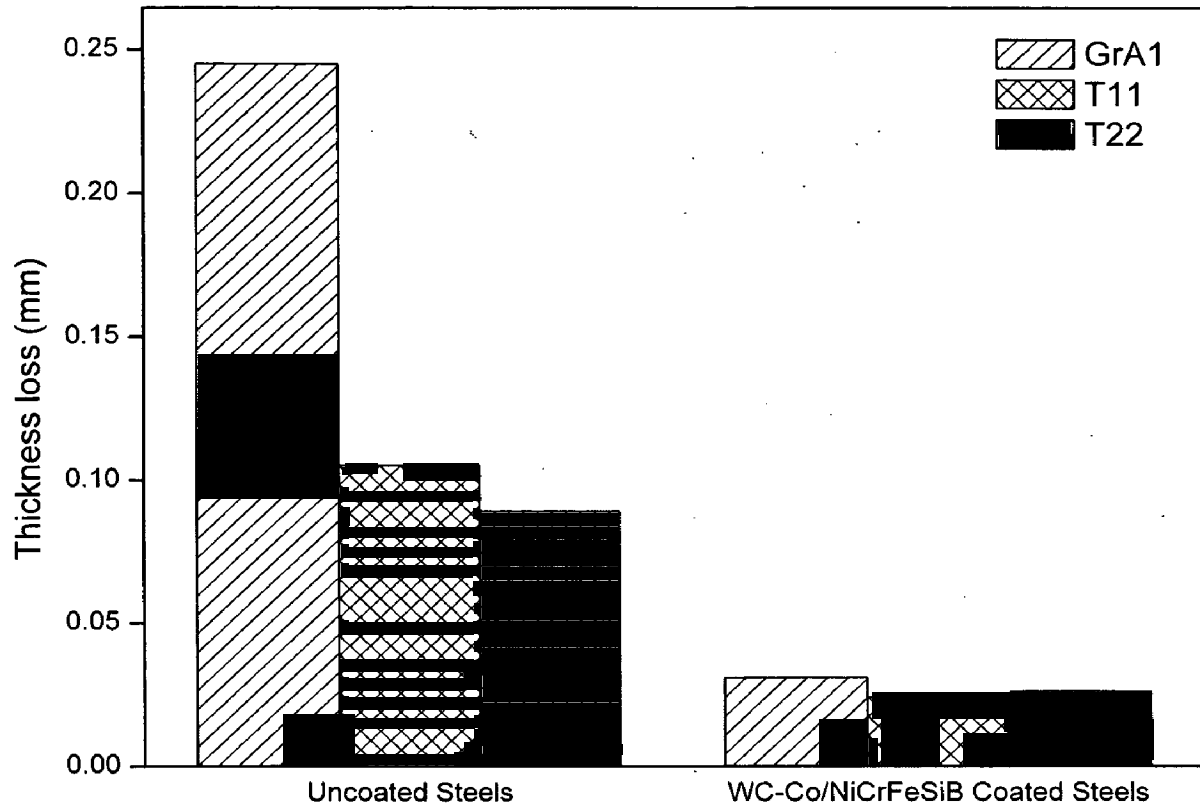
Fig.7.39   Bar chart indicating the thickness lost in mm for the uncoated and WC-Co/NiCrFeSiB coated steels after 1000 hours of exposure to super heater zone of coal fired boiler.

Fig.7.40   X-ray diffraction patterns for WC-Co/NiCrFeSiB coated GrA1, T11 and T22 steels exposed to super heater zone of coal fired boiler for 1000 hours.
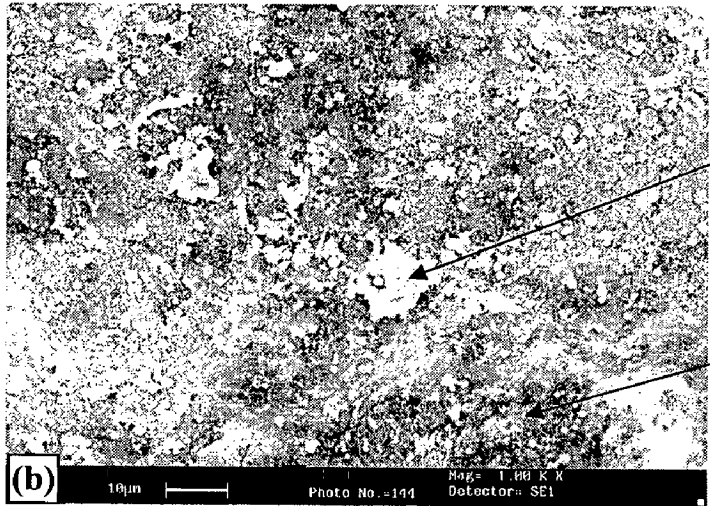
44.92% SiO_2
32.39% Al_2O_3
10.23% TiO_2
04.96% Na_2O
03.33% Fe_2O_3

EDS analysis at point 1

26.72% Cr_2O_3
14.29% NiO
18.29% SiO_2
15.24% WO_3
04.83% CoO
05.65% Fe_2O_3
06.06% Al_2O_3
02.66% SO_3
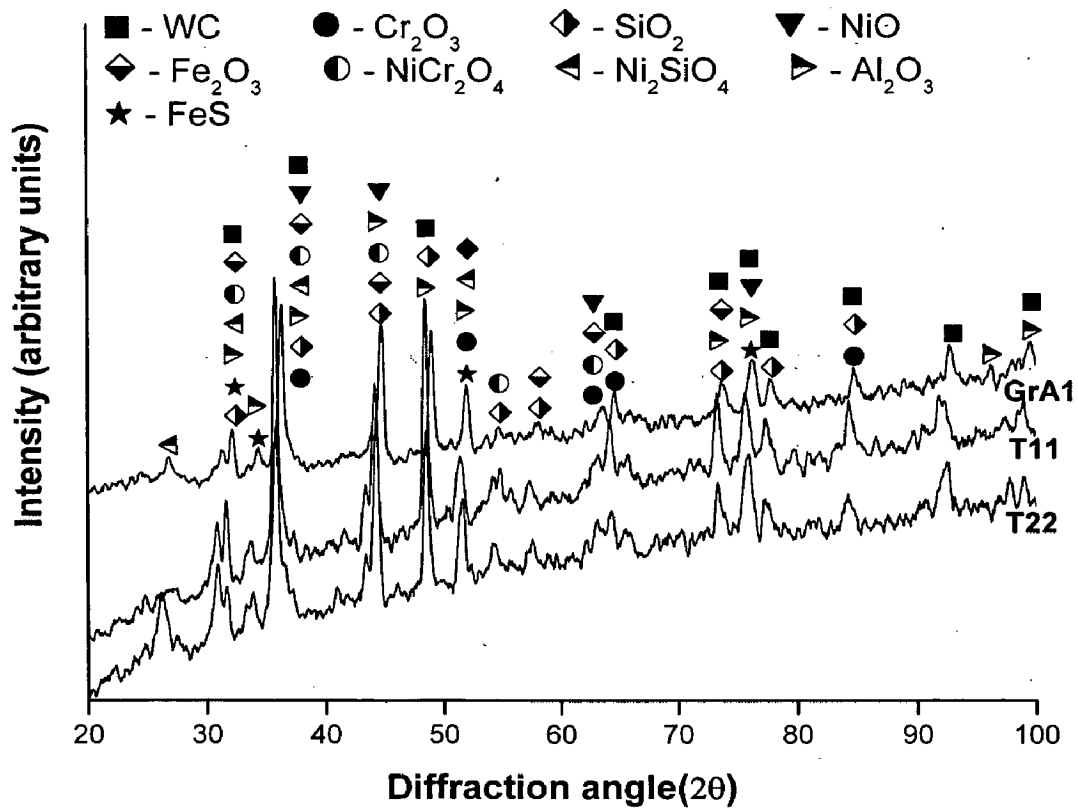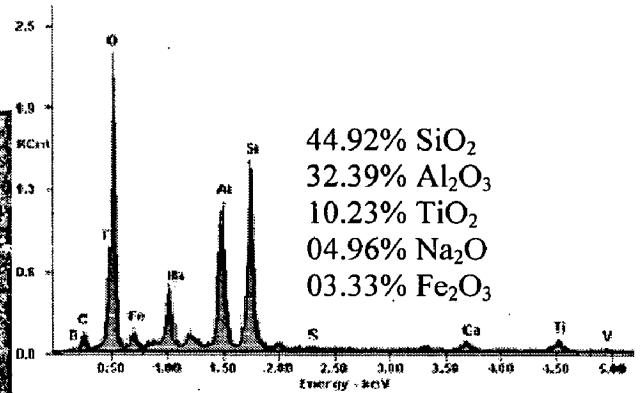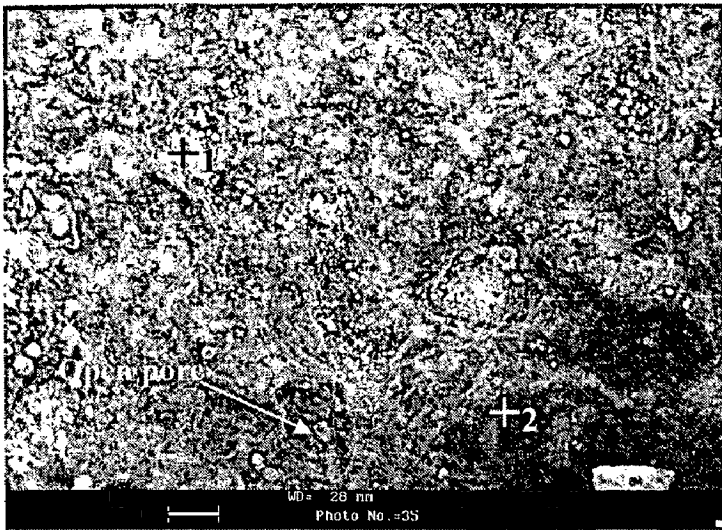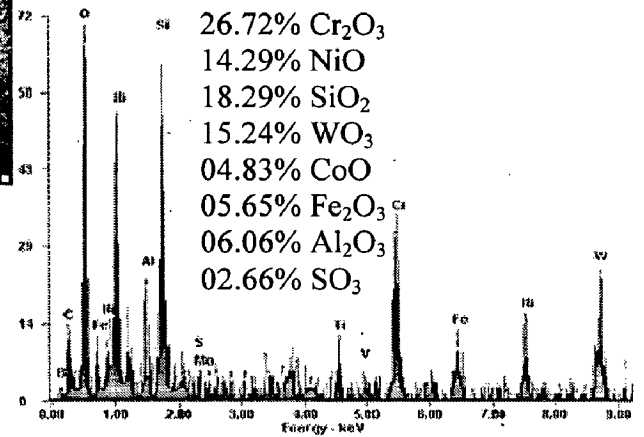
EDS analysis at point 2

(a)
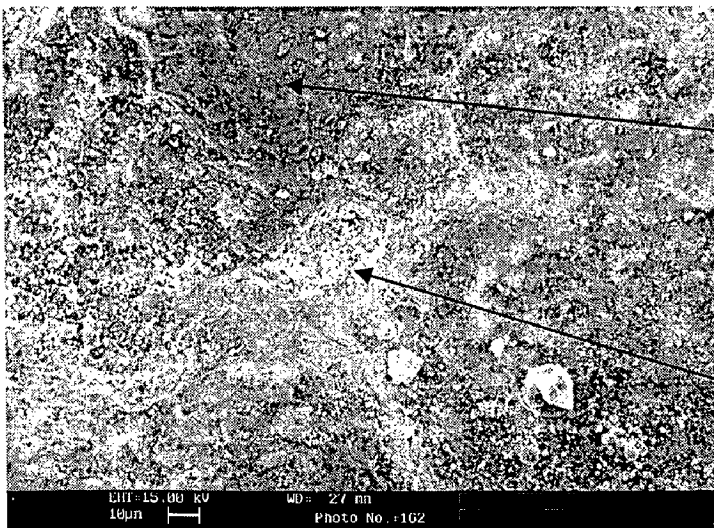
18.57% Cr_2O_3
05.47% NiO
28.48% SiO_2
22.70% WO_3
02.18% CoO
09.33% Fe_2O_3
04.23% Na_2O

66.46% SiO_2
10.86% TiO_2
12.44% Fe_2O_3
03.55% Na_2O

(b)

Fig.7.41 Surface scale morphology and EDAX analysis for WC-Co/NiCrFeSiB coated steels exposed to super heater zone of coal fired boiler for 1000 hours:
(a) GrA1 steel   (b) T11 steel
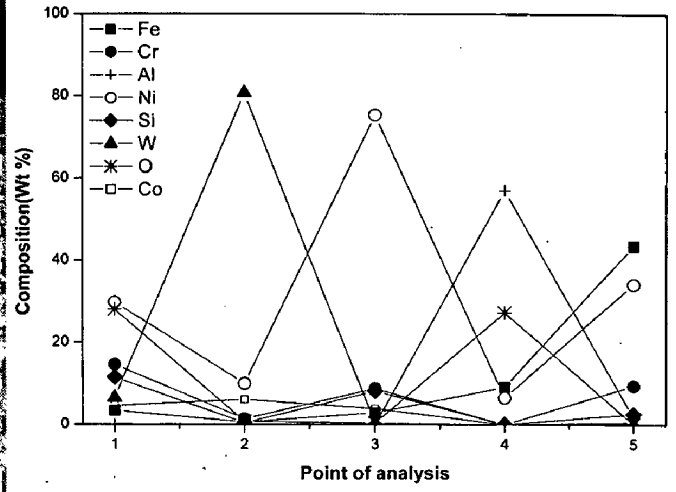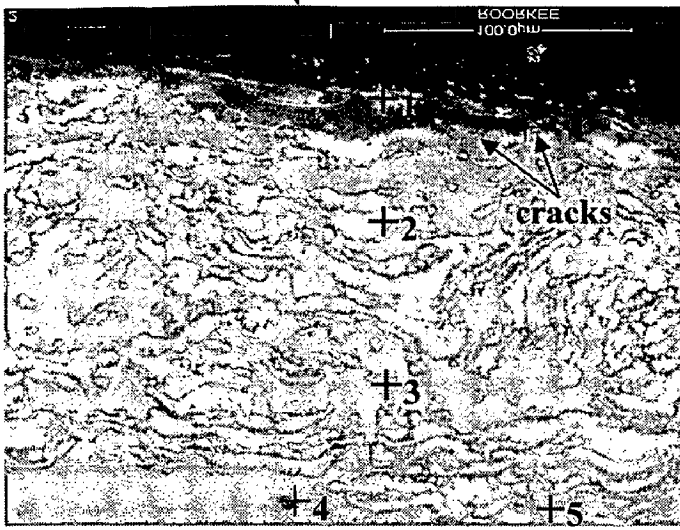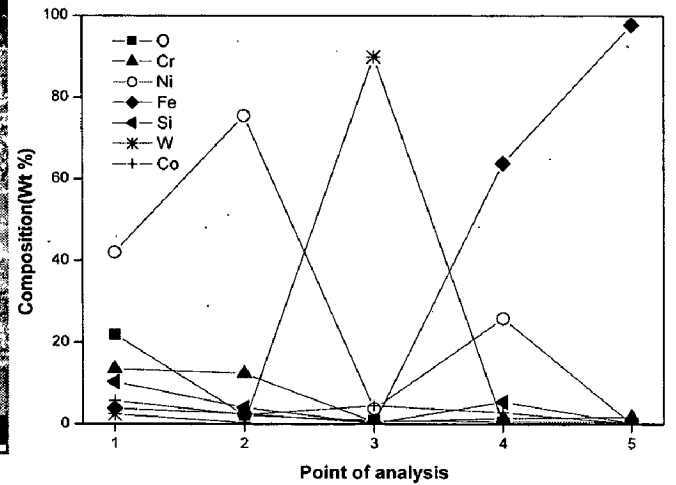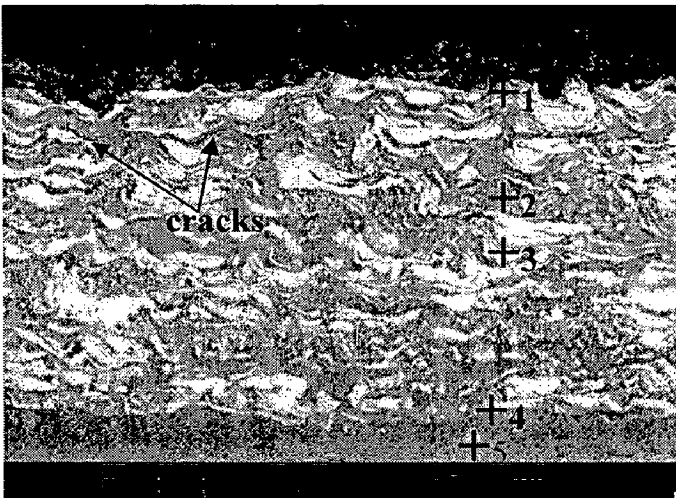
Fig.7.42 Back scattered electron image and EDAX point analysis (wt %) across the cross-section of the WC-Co/NiCrFeSiB coated steels exposed to superheater zone of coal fired boiler for 1000 hours:
(a) T11 steel   (b) T22 Steel
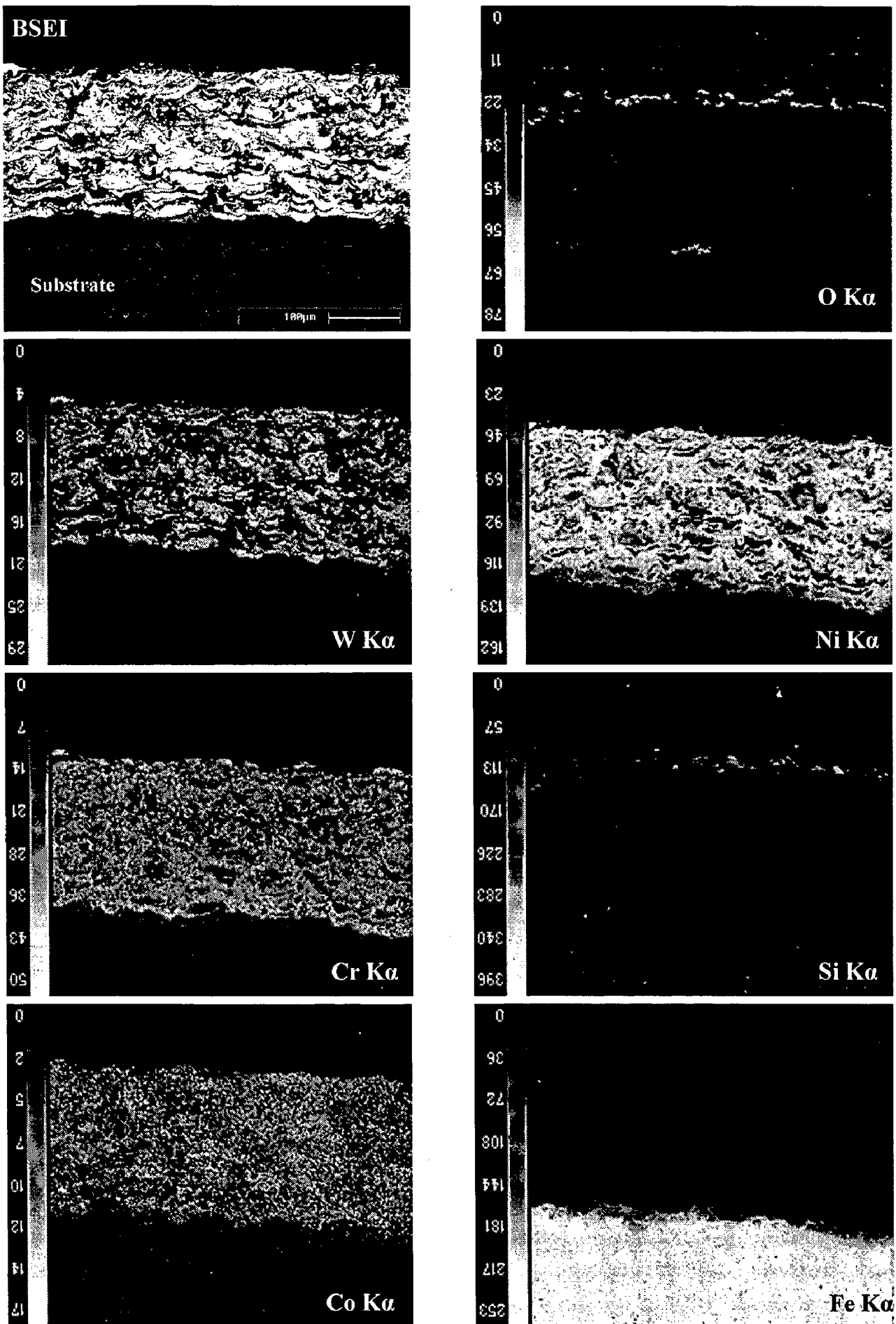
Fig.7.43   WDS X-ray mapping across the cross-section of the WC-Co/NiCrFeSiB
coated GrA1 steels exposed to superheater zone of coal fired boiler for
1000 hours
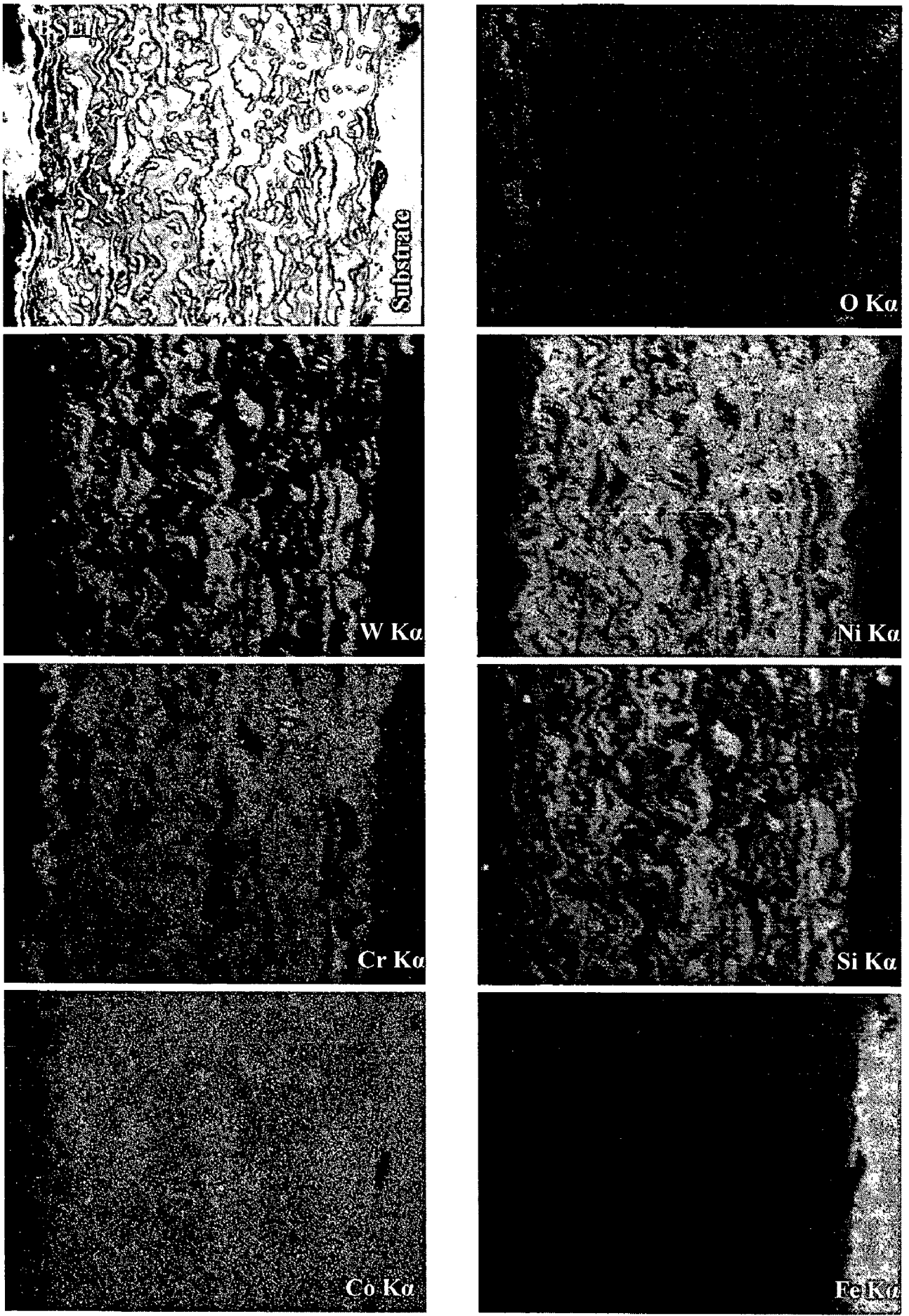
Fig.7.44 BSEI and elemental X-ray mapping along the cross-section of the WC-Co/NiCrFeSiB coated T11 steels exposed to superheater zone of coal fired boiler for 1000 hours

7.2 SUMMARY OF RESULTS

Results of studies in actual industrial environment where coated and uncoated steels are exposed to superheater zone of coal fired boiler for 1000 hours are summarized in table 7.1:

Table 7.1 Summary of the results for uncoated and coated steels exposed to superheater zone of coal fired boiler for 1000 hours.

Coating	Substrate	Weight gain mg/cm^2	K_p x10^{-10} g^{2}cm^{-4} s^{-1}	Thickness lost mm	Degradation rate mpy	XRD	Remarks
Uncoated Steels	GrA1	Weight loss	-	0.245	84.49	Fe$_2$O$_3$, Fe$_3$O$_4$, FeS, SiO$_2$, Al$_2$O$_3$	• The main constituent of oxide scale formed on all the steels is Fe$_2$O$_3$ and Fe$_3$O$_4$. • Scale formed on GrA1 steel is highly porous and showed intense spalling, where as bulk scale is observed on T11 and T22 steels. • Buildup of ash deposits on the surface of the oxide scale has been revealed. • Oxide scale formed on T11 and T22 steels contains continuous band of chromium oxide.
	T11	Weight Loss	-	0.105	36.21	Fe$_2$O$_3$, Fe$_3$O$_4$, Cr$_2$O$_3$, FeS, SiO$_2$, Al$_2$O$_3$	
	T22	Weight loss	-	0.089	30.69		
NiCrAl coating	GrA1	4.38	0.063	0.025	8.62	α-Al$_2$O$_3$, Cr$_2$O$_3$, Ni, AlNi$_3$,NiO, SiO$_2$, Ni$_3$V$_2$O$_8$ and FeS •	• Color of oxide scale formed on all the steels is greenish yellow. • Thin, protective oxide scale on the surface mainly consists of α-Al$_2$O$_3$ and Cr$_2$O$_3$. • Preferential oxidation of Al and Cr has been observed along the nickel rich splat boundary. • It is observed that the sulfur and Sodium has penetrated into the coating and has not affected the substrate steels. • Fly ash deposits have been observed on the surface.
	T11	4.63	0.068	0.023	7.93		
	T22	6.24	0.13	0.028	9.66		

NiAlCrFeMo coating	GrA1	5.004	0.081	0.039	13.45	α-Al_2O_3, Cr_2O_3, NiO, $NiCr_2O_4$, $FeCr_2O_4$, FeS and SiO_2.	• Yellowish brown color oxide scale has been observed. • The protective oxides formed on surface are mainly Al_2O_3 and Cr_2O_3 along with the discontinuous scale of NiO and Fe_2O_3. • Aluminum and chromium got oxidized along the splat boundary. • Flyash embedment into the open pores of coatings and pits formed on the surface is revealed.
	T11	7.04	0.142	0.045	15.52		
	T22	6.59	0.124	0.043	14.82		
NiCrFeSiB coating	GrA1	2.04	0.01	0.018	6.2	Ni, NiO, Cr_2O_3, Fe_2O_3, $NiCr_2O_4$, Ni_2SiO_4, Al_2O_3 and FeS	• Brownish green color oxide scale has been observed. • Thin and continuous oxide scale mainly composed of protective oxides of SiO_2 (amorphous), Cr_2O_3 and NiO. • Fly ash deposits found to be embedded into oxide scale. • Coating region beneath the uppermost oxide layer remained unoxidised. • Minor amount of Na and S on the surface have been noticed.
	T11	2.97	0.027	0.025	8.62		
	T22	2.39	0.018	0.021	7.24		
WC-Co/ NiCrFeSiB Coating	GrA1	2.02	0.01	0.031	10.69	WC, SiO_2, NiO, Cr_2O_3, Fe_2O_3, $NiCr_2O_4$, Ni_2SiO_4, Al_2O_3 and FeS	• Brownish-green color oxide scale has been observed. • Irregular surface morphology showing hills and valleys indicated the likely erosion by the impacting fly ash. Minor cracks are noticed at the subsurface. • EDAX & EPMA analysis revealed the major oxides of Si, Cr and Ni formed on the surface. • Coating region beneath surface oxide scale remained unoxidised.
	T11	2.86	0.024	0.024	8.27		
	T22	2.49	0.016	0.026	8.96		

7.3 DISCUSSION

7.3.1 Uncoated Steels

XRD analysis (Fig.7.4) of the scale formed on the steel after exposure to boiler environment mainly consists of Fe_2O_3 and Fe_3O_4. Once the oxidation occurs at the surface of the metal, resulting oxide scale acts as a barrier to the further growth of the oxide film. The growth of oxide scale occurs by both the diffusion of iron from the steel to the surface of the scale to react with oxygen and oxygen diffusion through the oxide scale to the metal-scale interface to react with iron (French, 1983). Prakash et al (2001) and Srikanth et al (2003) also reported greater volume of iron oxide scale on boiler steels during their failure analysis of super heater tubes of coal fired boilers. EDAX analysis (Fig 7.5 and 7.6d) shows the buildup of ash deposits on the surface of the scale, which is detrimental from a corrosion aspect. The EPMA analysis (Fig 7.7) shows a thin layer of oxides of Si, Al, and Fe, which further supports the interaction of ash with the oxide scale. Buecker (2002) and Harb et al. (1990) also reported the presence of higher concentration of oxides of Si, Al, and Fe in the outermost layer of the scale formed on the super heater tubes exposed to industrial environment. As ash deposits build up, volatile alkali sulphates (Na_2SO_4 or K_2SO_4) and sulphur trioxide (SO_3) produced during combustion diffuse through the ash to initiate corrosion reactions. These alkali sulphates, sulphur trioxide, and iron oxide (present in the oxide scale formed on tube wall or in the ash deposit itself), react to form complex alkali-metal-trisulphates on the cooler tube surface, according to the following reactions:

$$2\ Fe_3O_4 + 9\ M_2SO_4 + 9\ SO_3 + 1/2\ O_2 = 6\ M_3Fe\ (SO_4)_3$$

$$Fe_2O_3 + 3M_2SO_4 + 3\ SO_3 = 2M_3Fe\ (SO_4)_3$$
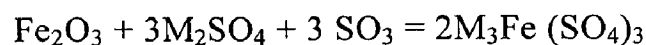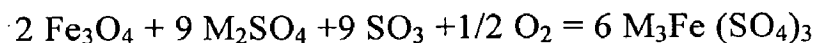
$$\text{where } M = Na \text{ or } K$$

These alkali-iron trisulphates are molten at the operating temperature of the boiler due to their low melting temperatures: 624°C for $Na_3Fe(SO_4)_3$, 618°C for K_3Fe $(SO_4)_3$, and 552°C for the mixed compound $(Na, K)_3Fe(SO_4)_3$, (Buecker 2002, French 1983, Srivastava et al.1997, Weulersse-Mouturat et al. 2004 and Harb et al. 1990). Sodium appears to be the prime culprit in causing deposit formation. These molten compounds can flux the scale or react with metallic iron resulting in the formation of massive amounts of FeS in corroded areas, as per the reaction given below:

$$2\ M_3Fe\ (SO_4)_3 + 6Fe = 3/2\ FeS + 3/2\ Fe_3O_4 + Fe_2O_3 + 3M_2SO_4 + 3/2\ SO_2$$
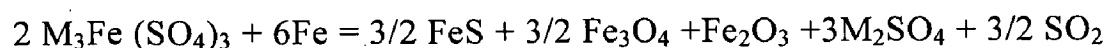
The above reactions account for the metal loss. In the present study, presence of FeS on the oxide scale has been revealed using XRD analysis.

The oxides formed by the reaction with the ash deposits are slightly different in character than those formed by reaction in air and molten salt environment, as discussed in chapter 5 and 6. The appearance of scale formed on GrA1 steel is highly porus, cracked along the scale thickness, and shows a weight loss throughout the exposure to the boiler environment for 1000 hours. The thickness of metal loss for GrA1 steel is very high which, is about 245 microns. Similar observations where, extensive weight loss in GrA1 steels, exposed to industrial environment, has been reported by Sidhu et al. (2005A).

The selective oxidation of chromium in T11 and T22 steels produce bulk protective oxide scale, resulting in a weight gain during the initial hours of exposure to boiler environment. This is further conformed by the X-ray mapping along the cross section of the scale, where a continuous band of chromium oxide is clearly seen in the oxide scale.

7.3.2 NiCrAl coating

HVOF sprayed NiCrAl coatings exhibit good resistance to corrosion both in the laboratory test, as well as, in the actual working environment of the coal fired boiler. The fluctuation in the weight gain data may be due to fly ash erosion and rapid thermal cycling, acting simultaneously on the exposed sample, which leads to increased oxidation rate. This is a result of gas temperature fluctuation and the fly ash deposit formation and fouling of the samples. The falling off and the regeneration of the ash deposits and oxide layer on the coating are repeated during the exposure of the sample. Palit et al., (1994), Mukhopadhyay et al., (1999), Kawahara (2006) and stringer (1995) have reported the incidence of fly ash erosion, fouling, and fireside deposit formation in pulverised coal fired boiler. The corrosion behavior of the NiCrAl coated steels follows nearly parabolic behaviour, whereas uncoated steels suffer a severe weight loss during the exposure to industrial environment. Hence, it can be inferred that the protection to the base metals has been provided by the NiCrAl coatings. Also coated steels show a minimum thickness loss by erosion corrosion during the exposure. Thickness lost in NiCrAl coated GrA1, T11 and T22 steels is around 1/10, 1/5, 1/3 times that of uncoated steels respectively. Similar observation has been reported by Sidhu et al. (2006C) and

Mishra (2006), where they showed lower thickness loss in case of plasma sprayed NiCrAlY and Ni-20Cr coating in comparison to substrate boiler steels and superalloys exposed to actual boiler environment. Yamada et al., (2002) reported that the wall thickness loss of detonation sprayed Ni-50%Cr alloy coatings was about 1/37 of carbon steel after 7 years of service in an actual refuse incineration plant.

The formation of α-Al_2O_3 and Cr_2O_3 upon exposure to the coal fired boiler environment as revealed by XRD analysis (Fig.7.12) and confirmed by EDAX/EPMA analysis (Fig.7.13 to 7.16) might have contributed to the protective nature of the NiCrAl coatings. The selective oxidation of Al and Cr along the splat boundary (as seen by combining the x-ray mapping for O, Al, and Cr) helps in blocking the open pores and voids, and these oxides serve as barrier to the inward diffusion of corrosive species along it. This is desirable since the corrosive species mostly propagate along the splat boundaries and through the pores and voids. Also, due to dense and flat splat structure of the coatings, the distance for the corrosive species to traverse from the coating surface to coating/substrate interface along splat boundaries is long. These combined advantages restrict the corrosive species reaching the substrate. Further, from EDAX/EPMA analysis it has been perceived that oxygen, sulphur, and sodium has penetrated upto the coating layer and has not affected the substrate steels. Also EPMA result corroborated the minor interdiffusion of Fe from substrate into the coating and Ni from coating into the substrate. Limited diffusion of elements can be attributed to the presence of uniformly distributed flat splats and low porosity of the coating.

Appearance of greenish tinge on the surface of the scale might be due to the presence of minor amount of NiO, identical to the findings of Wu, X. et al., (2001) and Sidhu (2003A). XRD analysis on the surface of the corroded coating revealed the presence of minor peaks of SiO_2, $Ni_3V_2O_8$, and FeS phases that indicate the fly ash deposits on the surface of the exposed steel. This is further conformed by EDAX analysis (Fig.7.13) at the white contrast regions on the surface of the exposed samples and EPMA analysis showed the outermost thin layer of SiO_2, Fe_2O_3, and Al_2O_3 deposition. Similar observation of the coal ash deposit on the surface of exposed coatings has been reported by Sidhu et al., (2006D) and Sidhu et al., (2005A). Vanadium oxide released in combustion, combined with alkali salts to form low melting compounds that accumulate on the tube surfaces. The following equation illustrates a typical reaction (Buecker, 2002).

$$Na_2SO_4 + V_2O_5 = 2NaVO_3 + SO_3$$
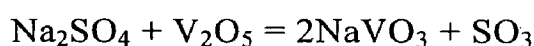
The low melting sodium vanadate (629°C) are corrosive and reacts with NiO formed on the oxidised coating to form corrosion product $Ni_3(VO_4)_2$ as per the reaction(Sidky et al. 1987).

$$2NaVO_3 + 3NiO = Ni_3(VO_4)_2 + Na_2O$$
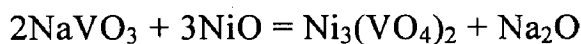
Presence of $Ni_3(VO_4)_2$ corrosion products has been revealed by XRD analysis which indicated the interaction of fly ash with the oxides formed on the coating surface.

7.3.3 NiAlCrFeMo coating

This coating has been successful in providing protection to substrate steel against combined erosion-corrosion prevailing in the actual working environment of the coal fired boiler. The BSE image (Fig.7.23) along the cross section shows that the corroded coating is continuous, intact and adherent without any indication of internal cracks. A thin oxide scale has been observed on the external surface. EPMA and EDAX analysis on the surface as well as along the cross section revealed that the oxide scale mainly consist of Al_2O_3 and Cr_2O_3 along with the discontinuous scale of nickel oxide. XRD results also confirmed the presence of α-Al_2O_3, Cr_2O_3 and NiO along with the spinels of mixed oxides of $NiCr_2O_4$ and $FeCr_2O_4$. These spinel oxides have much smaller diffusion coefficient of the cations and anions than those in their parent oxides and hence, thermodynamically lower solubility in the corrosive molten slat environment (Chatterjee et al. 2001). The entire cross section of the coating has been partially oxidized along the splat boundary. EPMA analysis corroborated the preferential oxidation of Cr and Al along the splat boundary. Minor amount of Mo and Fe oxides coexist with the oxides of Cr and Al along the splat boundary. Nickel rich splats remain unoxidised. It appeared that the oxides formed at splat boundaries also determine the protection capability of the coating by blocking the open porosities, which are the paths for the corrosive species to reach substrate. It is observed that the substrate steel remain unattached.

SEM micrograph indicates the embedment of fly ash into the open pores exist on the eroded surface of the coatings. The compositional analysis of the fly ash deposit formed on the surface reveal SiO_2 as the main constituent (most erosive species in the fly ash) along with minor quantities of sodium and sulphur. The Na and S present in the boiler environment can form low melting point compounds such as alkali metal-trisulphates, which can cause fluxing of the protective oxide scale as discussed in section

7.3.1. In the present study, the presence of FeS on the oxide scale has been identified by XRD analysis. The FeS has been identified as the promoter of sulphidation attack of metallic surfaces (Mayoral et al. 2006). Warren (1992) also reported the sulphide attack on plasma sprayed NiCrAlMoFe coatings exposed to boiler environment.

Figure 7.20 shows erosion-corrosion loss for NiAlCrFeMo coated GrA1, T11 and T22 steels, which are significantly lower than that of similar uncoated steels and the corresponding degradation rate expressed in mils per year, are 13.45, 15.52 and 14.82 mpy respectively. All the coated steels show conformance to parabolic rate of oxidation during cyclic exposure to boiler environment. Minor deviation from the parabolic rate law can be attributed to the fouling of the samples by the flyash deposits. Hence it can be inferred that the coatings showed a better performance against erosion-corrosion in the coal fired boiler environment.

7.3.4 NiCrFeSiB coatings

The problem of erosion of superheater and reheater tubing caused by fly ash cannot be ignored. Even though, fly ash consisted of very small particles, high velocity gas streams wear away or erode the leading tube (French 1983). Fig.7.31 show pits formed due to impact of fly ash on the surface of coated steels exposed to superheater zone of coal fired boiler. Ash particles (confirmed by EDAX analysis) appeared to be deposited or embedded on the surface may react with protective oxides. Hence, erosion rate is also dependent on the oxidation kinetics and erodent particle reactivity. In the present study, NiCrFeSiB coated GrA1,T11 and T22 boiler steels show better erosion-corrosion resistance and thickness loss was about 1/13,1/4,1/4 respectively that of uncoated steels. Degradation rate for coated GrA1, T11 and T22 steels, expressed in mils per year are 6.2, 8.62, and 7.24 mpy respectively. The weight change of the coated samples during 1000 hours of exposure (Fig.7.27) found to follow nearly parabolic behavior and hence the oxide scale formed on the surface act as barrier to the diffusion of oxidizing and corrosive species. Further EPMA (Fig.7.34&35) and EDAX (Fig.7.33) analysis along the cross-section confirm the absence of O, Na and S, beneath the uppermost oxide scale indicating protective behavior of the NiCrFeSiB coatings in the given environment. Although, 1000 hours of exposure to boiler environment is relatively short duration to extrapolate the obtained result to predict the coating performance in long term of service, the erosion corrosion

behavior of NiCrFeSiB coating is promising in comparison to substrate steels used in the present study.

The BSE images shows thin and continuous oxide scale formed on the surface of corroded coating. XRD, EDAX and EPMA analysis corroborate that the oxide layer mainly composed of protective oxides of SiO_2, Cr_2O_3 and NiO. Although, XRD analysis on the surface showed no peaks corresponding to Si-related oxide phases, EDAX and EPMA results supports the existence of SiO_2 in the oxide scale. The silica is obviously amorphous, might be formed from oxidation of coating element and partly from the condensed deposits of boiler environment on the surface of exposed sample. Presence of mixed spinal oxides of $NiCr_2O_4$, and Ni_2SiO_4 has been revealed by X-ray diffraction on surface. Wu et al, (2006) and Kerr (1975) have reported spinels Ni_2SiO_4 have similar crystallographic and thermodynamic properties as $NiCr_2O_4$, can hinder the ion diffusion effectively during oxidation and decrease the oxidation rate. Hidalgo et al., (2001B) reported the better oxidation and high temperature erosion of NiCrBSiFe coating on AISI 304 austenitic stainless steel in comparison with stainless steels, Ni-Cr alloys and Cr_3C_2 cermets under simulative industrial environment. Schneider et al., (1978) showed that better ductility and higher toughness of the nickel-chromium-silicon coating has prevented the spalling and cracking in service. Uusitalo et al., (2002A) showed better erosion-corrosion resistance of nickel based HVOF coating with high chromium content at elevated temperature in presence of chlorine.

Presence of Fe and Ni along the coating-substrate interface as indicated in EPMA and EDAX analysis along the cross section has shown the interdiffusion of Fe from substrate into coating and Ni from coating into substrate.

7.3.5 WC-Co/NiCrFeSiB coatings

WC-Co/NiCrFeSiB coatings found to be effective in providing necessary protection against erosion-corrosion and indicated insignificant degradation rate in comparison to substrate steels exposed to super heater zone of coal fired boiler for 1000 hours. The thickness loss observed for WC-Co/NiCrFeSiB coated GrA1, T11 and T22 steels are 1/8, 1/4 and 1/3 respectively that of uncoated steels reported in section 7.1.1.1. Degradation rate for coated GrA1, T11 and T22 steels, expressed in mils per year are 10.69, 8.27, and 8.96 mpy respectively. The corrosion kinetics (Figs.7.37 & 7.38) follows nearly parabolic rate law.

Compositional analysis on the surface of corroded coatings (Figs.7.40 &7.41) revealed the major oxides of Si, Cr and Ni formed on the surface of all the coated steels. Elemental X-ray mapping shows that, a thin layer of oxide scale is formed at the outermost surface of the corroded coating. Combined maps of O, Cr, Si and Ni corroborated the presence of oxides and mixed oxide spinels of these elements. XRD results (Fig.7.39) confirm the presence of these oxides on the surface. Further absence of oxygen and other corrosive species (S, Na, K etc.) in the coating core signify that the oxides of Si, Cr and Ni formed at the surface are protective and act as a barrier to the ingress of corrosive species into the coating. Minor cracks have been noticed at the subsurface. Cracks might have caused partially due to carbide particles pullout during the impact of fly ash and partially attributed to thermal mismatch between WC-Co particles and Ni rich matrix. Fukuda et al. (1995) also observed cracks in detonation gun sprayed WC-Co coatings tested in the superheater zone of coal fired boiler environment for one year.

Scanning electron micrographs shows fouling of exposed coatings due to condensed phases of the ash. Coal ash carried by the flue gas in the form of small particles form sintered and fused deposits on the superheater and reheater surfaces, thereby, providing the environment in which complex sulphates are formed causing metal wastages (Srivastava et al. 1997). EDAX analysis revealed the higher amount of SiO_2, Al_2O_3 and Fe_2O_3 present in the condensed ash deposits. These constituents have significant effect on erosivity (Wang, 1999). In addition, chemically active elements such as S and Na have been detected on the surface. Sulphide deposits (FeS) are also found in the corroded coating (Fig.7.39). The FeS has been identified as the promoter of sulphidation attack of metallic surfaces (Mayoral et al. 2006).

Presence of Fe and Ni along the coating-substrate interface suggests interdiffusion of Fe from substrate into coating and Ni from coating into substrate, which may be contributing to improve metallurgical bonding between substrate and coatings.

7.4 COMPARATIVE DISCUSSION

The HVOF coated and uncoated steels exposed to super heated zone of coal fired boiler are subjected to combined erosion and corrosion. The flue gas temperature in this region is about $778\pm20°C$ and high velocity gas stream carry many undesirable species. Scanning electron micrographs shows fouling of exposed samples due to condensed phases of the ash. Coal ash carried by the flue gas in the form of small particles form sintered and fused deposits on the superheater and reheater surfaces, thereby providing the environment in which complex sulphates are formed causing metal wastages. Compositional analysis revealed the higher amount of SiO_2, Al_2O_3 and Fe_2O_3 present in the condensed ash deposits. These constituents have significant effect on erosivity. In addition, chemically active elements such as S and Na have been detected on the surface. XRD analysis shows the presence of sulphide deposits (FeS) in the corroded coating. The FeS has been identified as the promoter of sulphidation attack of metallic surfaces (Mayoral et al. 2006). The observed fluctuation in the weight gain data can be attributed to fly ash erosion and rapid thermal cycling acting simultaneously, which leads to falling off and the regeneration of the ash deposit and oxide scale.

Figures 7.45 and 7.46 show a bar chart indicating the thickness loss and cumulative weight gain for coated and uncoated steels after 1000 hours of exposure to superheater zone of coal fired boiler. In general, all the HVOF coatings under study showed considerably lower thickness loss in comparison to uncoated steels. Scale formed on GrA1 steel is highly porous and showed intense spalling, where as bulk scale is observed on T11 and T22 steels. All the three uncoated steels suffered a weight loss. The main constituent of oxide scale formed on all the steels is Fe_2O_3 and Fe_3O_4.

NiCrFeSiB coatings showed minimum thickness loss as well as lower weight gain in comparison to other coatings under study. The superior performance of this coating can be attributed to the thin and continuous oxide scale of SiO_2 and Cr_2O_3 formed on the surface. Also, presence of mixed spinal oxides of $NiCr_2O_4$ and Ni_2SiO_4 has been revealed by X-ray diffraction on surface. Wu et al, (2006) and Kerr (1975) reported spinels of Ni_2SiO_4 have similar crystallographic and thermodynamic properties as $NiCr_2O_4$ and can hinder the ion diffusion effectively during oxidation and decrease the oxidation rate. Hence, the coating region beneath the uppermost oxide layer remained

unoxidised. The weight gains for WC-Co/NiCrFeSiB coated steels are almost equivalent to that of NiCrFeSiB coated steels. Further, absence of oxygen and other corrosive species (S, Na, K etc.) in the coating core signify that, the oxides of Si, Cr and Ni formed at the surface are protective and act as a barrier to the ingress of corrosive species into the coating. Minor cracks observed at the subsurface might have caused partially due to carbide particle pull out during the impact of fly ash and partially due to stresses developed as a result of thermal mismatch between Ni rich matrix and WC-Co particles. Thickness loss is marginally higher than that of NiCrFeSiB and NiCrAl coatings. The corrosion kinetics of all the coated steels shows nearly parabolic behavior.

The better performance of NiCrAl coatings can be credited to thin protective oxide scale of α-Al_2O_3 and Cr_2O_3, formed on the surface as well as preferential oxidation of Al and Cr along the nickel rich splat boundary. Selective oxidation along the splat boundary helps in blocking the open pores and voids, thereby restrict the inward diffusion of corrosive species. All the coated steels showed nominal erosion losses and oxidation kinetics and followed nearly parabolic rate law. NiAlCrFeMo coatings showed lower resistance to erosion-corrosion when compared to other coatings under study. This might be associated with relatively higher porosity content in the coating. The oxide scale formed on the surface consists of oxides and spinels of Al, Cr, Ni and Fe. The entire cross section of the coating has been partially oxidized along the splat boundary. All the coated steels show conformance to parabolic rate of oxidation during cyclic exposure to boiler environment.
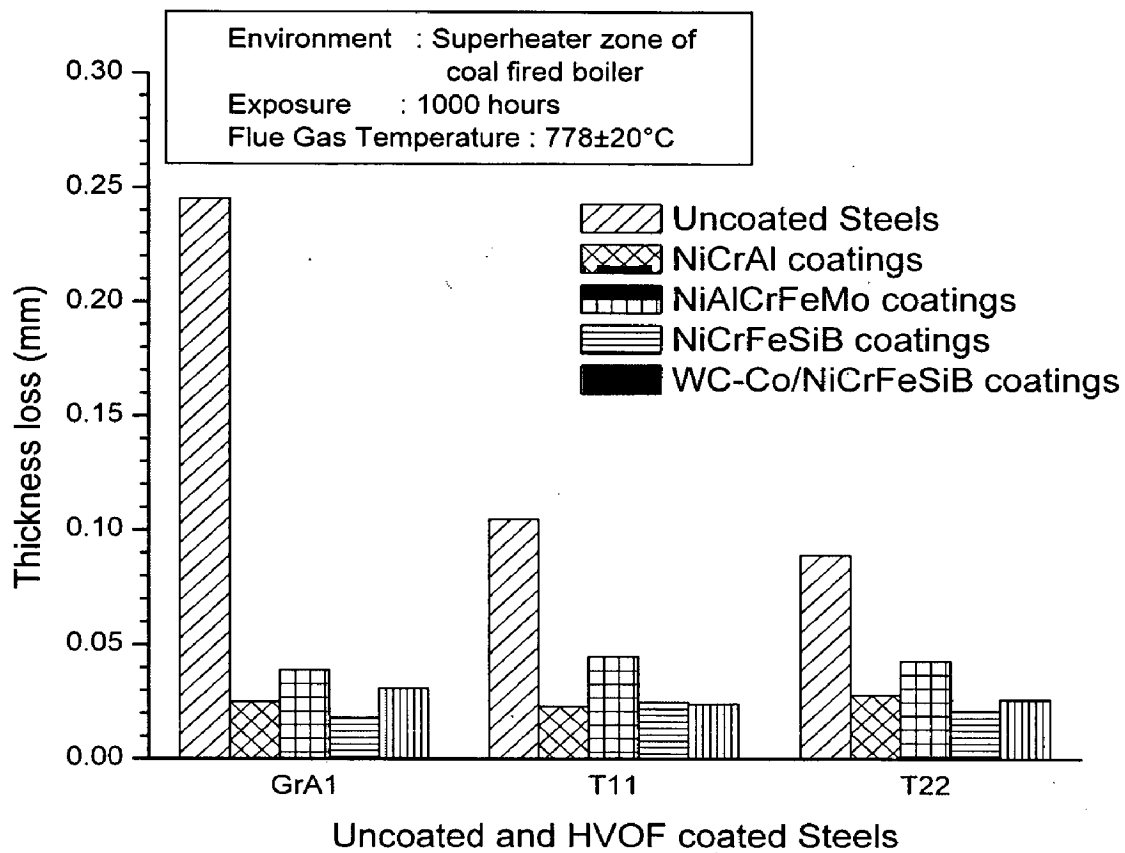
Fig.7.45 Bar chart indicating thickness lost in mm for uncoated and HVOF coated steels after 1000 hours of exposure to superheater zone of coal fired boiler.
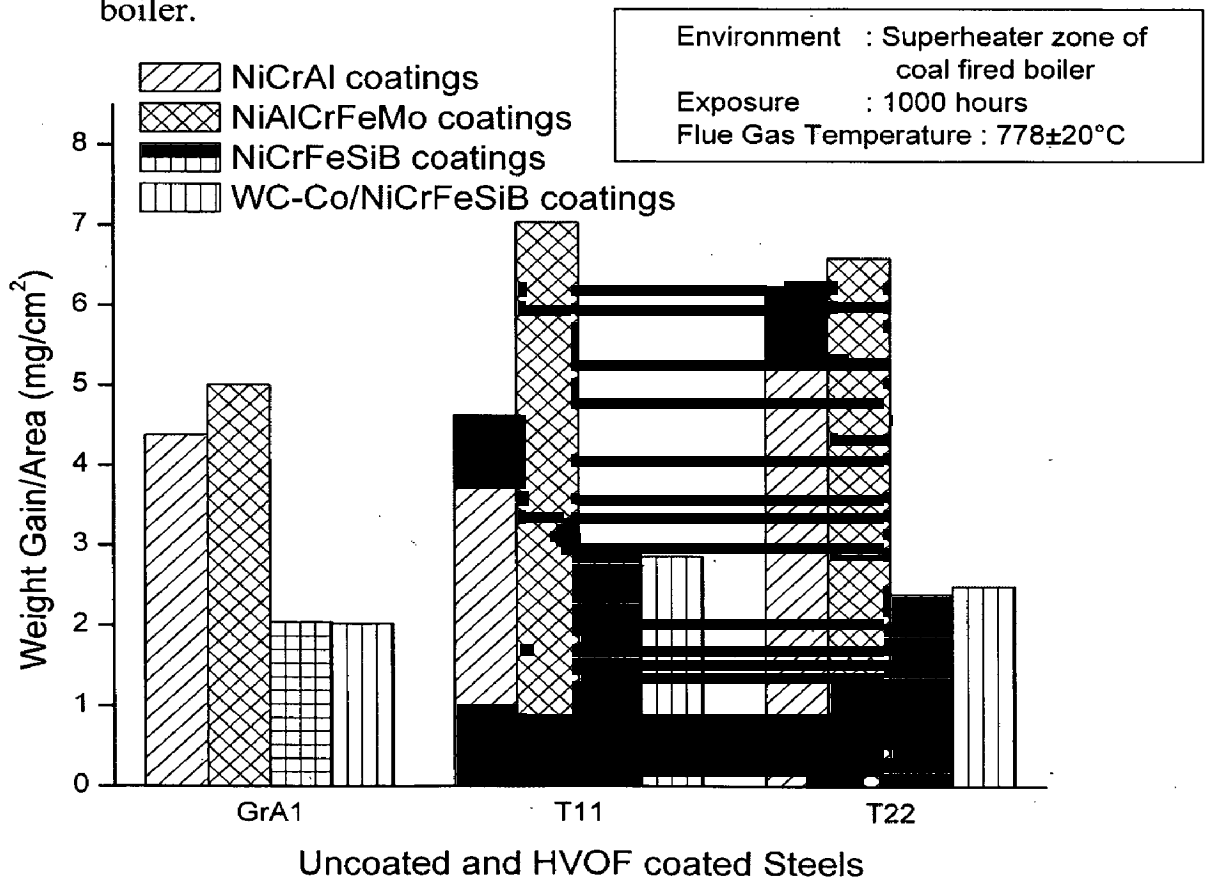
Fig.7.46 Bar chart indicating cumulative weight gain for HVOF coated steels after 1000 hours of exposure to superheater zone of coal fired boiler.

of 880 H_v and, for the GrA1 steel, it is 180 H_v. The ratio H_p/H_t is approximately 4.8, which cause the penetration of silica particles into the target material that act as a shield against impacting particles which leads to a lower wear loss of the GrA1 steel when compared to the coatings. Hutchings (1992) observed experimentally that abrasive particles of any shape will cause plastic scratching and indent the surface, only if $H_p/H_t > 1.2$. The SEM micrographs (Figs. 8.6d and 8.6e) on the surface of the eroded GrA1 clearly show the embedment of sand particle and the wear mechanism essentially involves the indentation induced severe plastic deformation. Mishra et al. (2006B) and Sidhu et al. (2007) also reported about the silica particle embedment on the surface of eroded superalloys and steels.

It is observed from the scanning electron micrographs (Figs. 8.6a–c) of the eroded surface at 30°C impact angle that the silica particles deform the surface by ploughing, displacing material to the side and in front of the particle in the form of lip due to severe plastic flow. With the subsequent impacts, these highly strained lips are vulnerable to be removed as micro-platelets. The crater formed by ploughing and lips at the rim of the crater are clearly visible in the micrograph. Since the erodent particles are being in contact for long time on the surface during sliding, the wear rate is much high. A careful observation of the eroded surface at the higher magnification also revealed the slip bands due to concurrence of the crater formed during repeated impacts. Similar erosion behavior of the ductile materials has also been reported by Hutchings (1992), Brown et al. (1981), Kumar et al. (2008) and Sidhu et al. (2007). Bellman (1981) has reported that these bands generally occur along the walls of the already formed craters where a fresh crater has been formed immediately adjacent to them. The particle impact cause plastic deformation of the new crater being formed on the unsupported surface of the already existing crater, resulting in slip band formation. The distance of these bands down the inclined surface of the existing crater is indicative of the depth to which the plastic deformation occurs as the result of repeated particle impact.

At normal impact, indentation crater along with existing impressions of impinging erodent are clearly seen in the scanning electron micrographs (Figs. 8.6d–f). It is also observed that sharp edged silica particles which are incrusted in the surface, forming a crater, extrude as micro-platelets at the sites of impacts. These platelets of metal that are locally attached to the crater rim are further forged by the subsequent impact of the erodent and will be strained to their critical plastic strain. The heavily

CHAPTER 8

SOLID PARTICLE EROSION STUDIES

The behavior of the HVOF coated and uncoated boiler steels subjected to solid particle erosion at room temperature is described in this chapter. The erosion experiments were carried out using the air-jet erosion test rig as per the ASTM-G76 standard. The impingement angles of 30° and 90° were selected to provide the maximum erosion condition for both the ductile and brittle materials under silica sand erodent.

The steady state erosion rates (volume basis) for different coatings and substrate steel were compared. The eroded samples were analysed using the scanning electron microscope and optical profilometer. Efforts have been made to understand the erosion mechanism.

8.1   RESULTS AND DISCUSSION

8.1.1   Uncoated Steels

The photographs and schematic diagram showing the erosion scar produced on the eroded surface at different impact angles of 30° and 90° are shown in Figs.8.1 - 8.3. The steady state volume erosion rate (Figs.8.4 and 8.5) of the GrA1 steel at 30°C impingement is higher than that at 90°C which is a characteristic behavior of the ductile materials, where material removal takes place predominantly by plastic deformation. In general, the incremental erosion rate curves follows the same forms as that for the ductile steels at 90°C, having a low initial rate, reaching a peak after 50 g of impacting particles and, subsequently, reaching a steady state erosion rate which is considerably lower than the peak rate (Murthy et al. 2001, Hutchings 1992, levy et al. 1986B).

In the present study, the GrA1 steels exhibit lower erosive loss when compared to all the HVOF coatings under similar test conditions (Fig.8.33). This may be due to the embedment of silica particles into the surface, which might bestow some shielding effect against further material loss. It is well established that the ratio of hardness of the erodent particles (H_p) to the target hardness (H_t), has a controlling influence in the erosion mechanisms (Lathabai et al. 1998, Hussainova et al. 1999, Shipway et al. 1996, Hearley et al. 1999). The silica particles used in the present study have an average hardness value
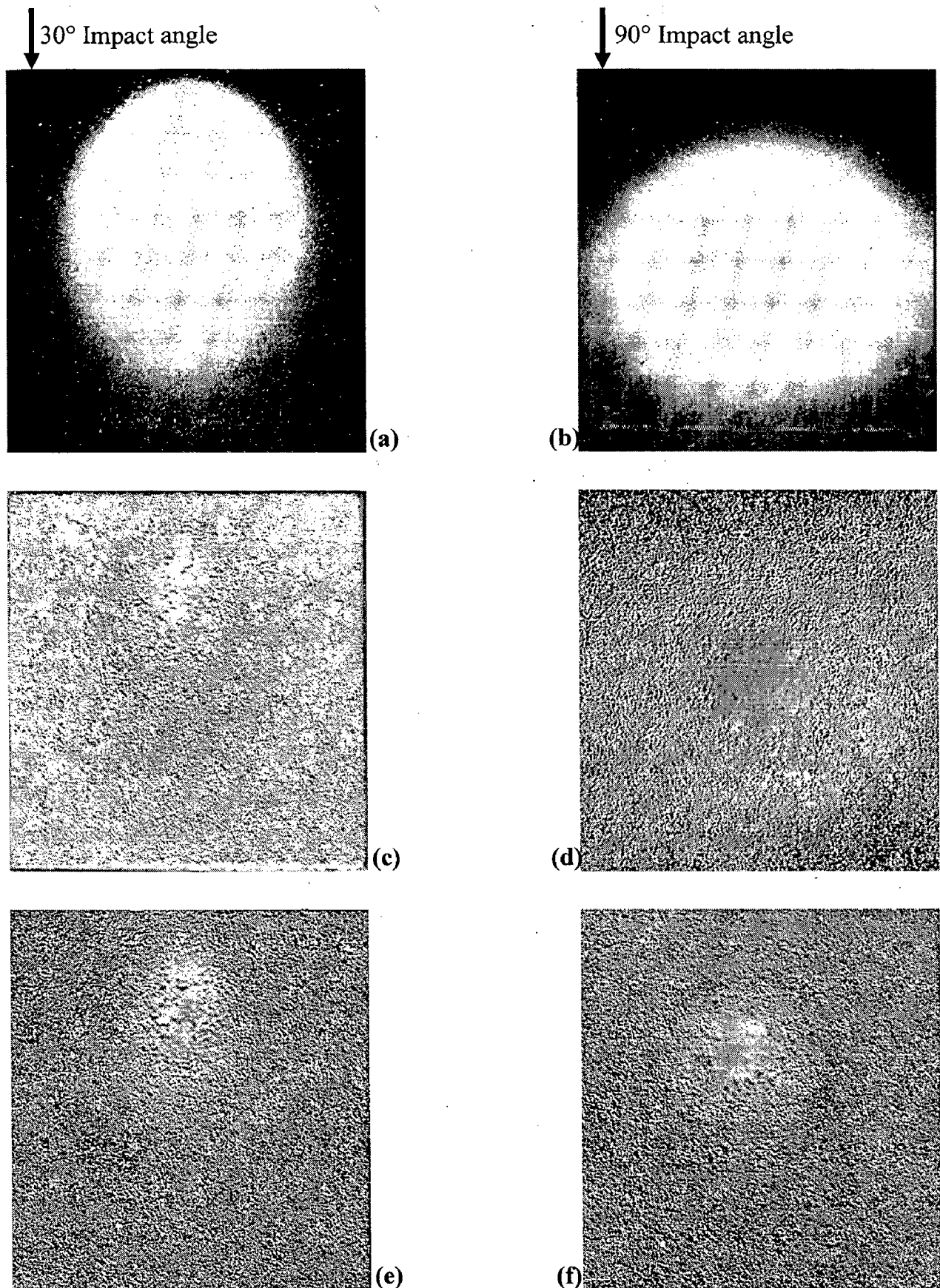
Fig.8.1 Camera macrographs of uncoated and coated steels impacted by silica erodent at different impact angles of 30° and 90°.(not to scale)
(a) and (b) uncoated steel; (c) and (d) NiCrAl coatings;
(e) and (f) NiAlCrFeMo coatings.
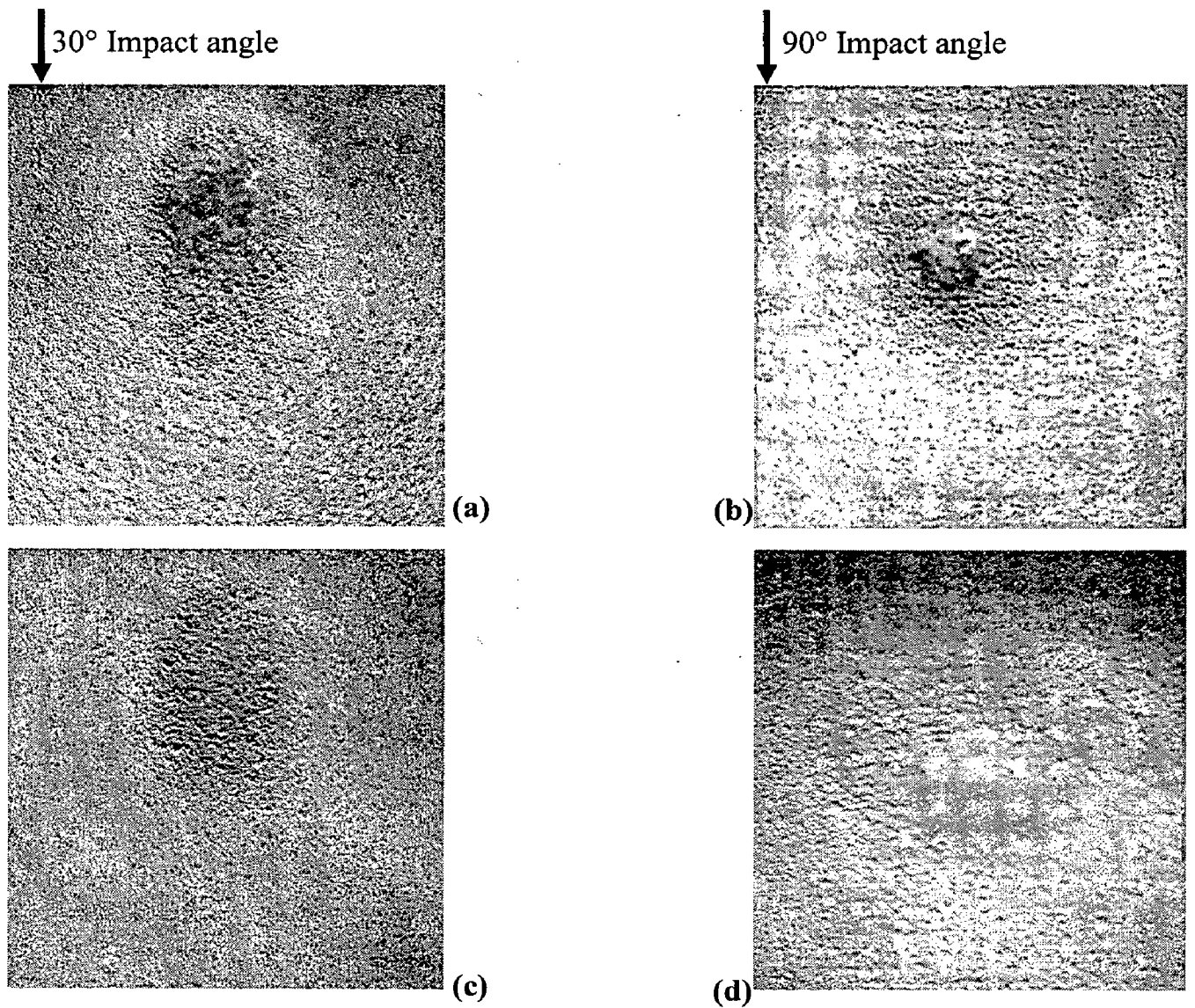
Fig.8.2   Camera macrographs of coated steels impacted by silica erodent at different impact angles of 30° and 90°.(not to scale)
(a) and (b) NiCrFeSiB coatings; (c) and (d) WC-Co/NiCrFeSiB coatings.
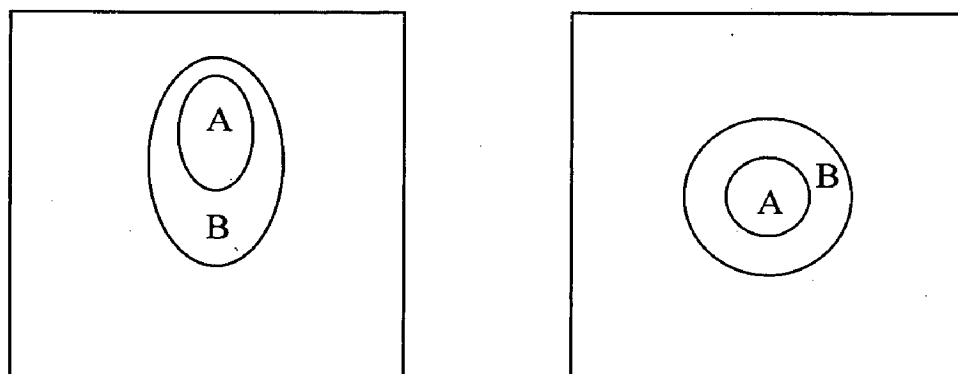
Fig.8.3   Schematic diagram showing the erosion scar produced, in general on the eroded surface at an impact angle of 30° and 90°.
Mark "A" represent localized region of material removed and
   "B" is the peripheral region of elastically loaded material

269
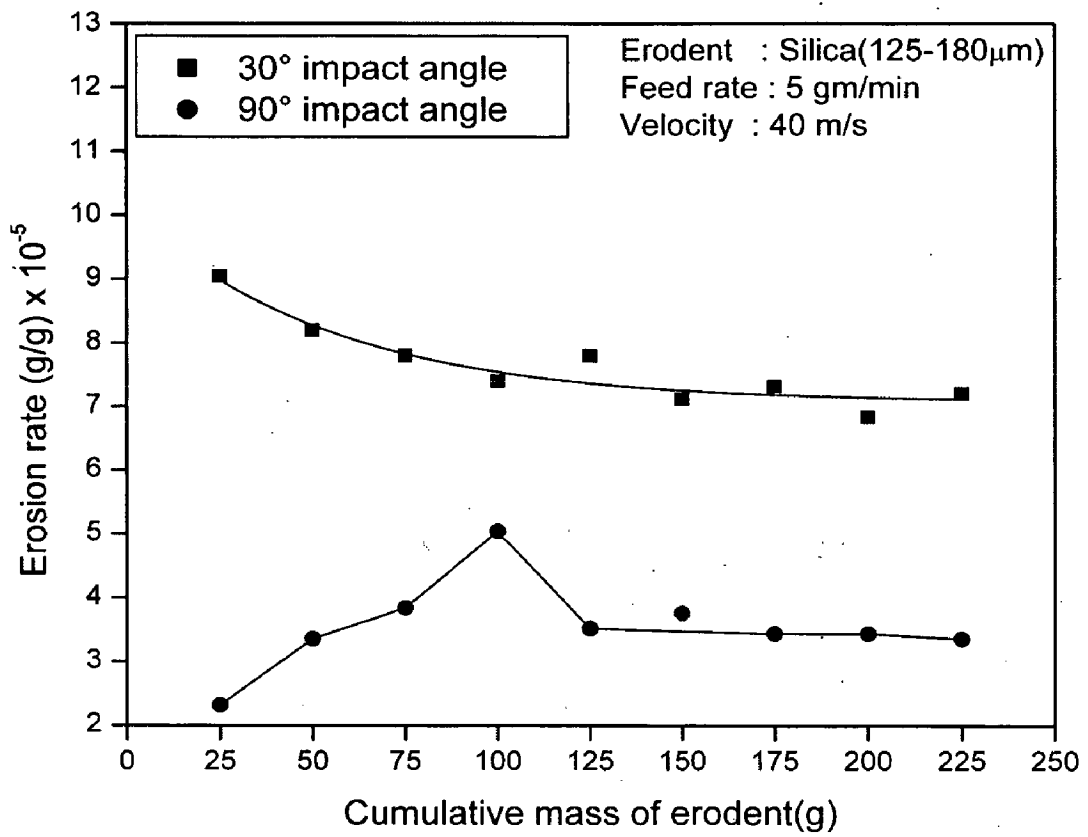
Fig.8.4   Variation of the Incremental erosion rate with the cumulative weight of
the erodent for uncoated steel at 30° and 90° impact angle.
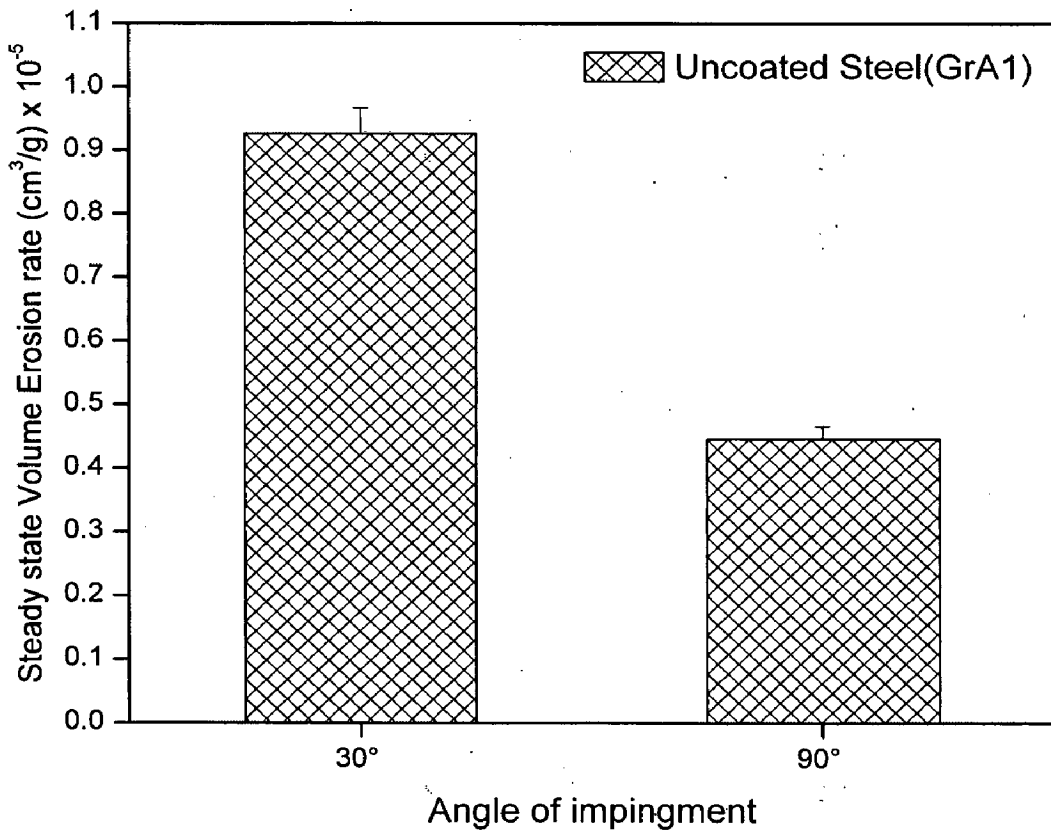
Fig.8.5   Histogram illustrating the steady state volume erosion rate of uncoated
steel (GrA1) at different impact angles.
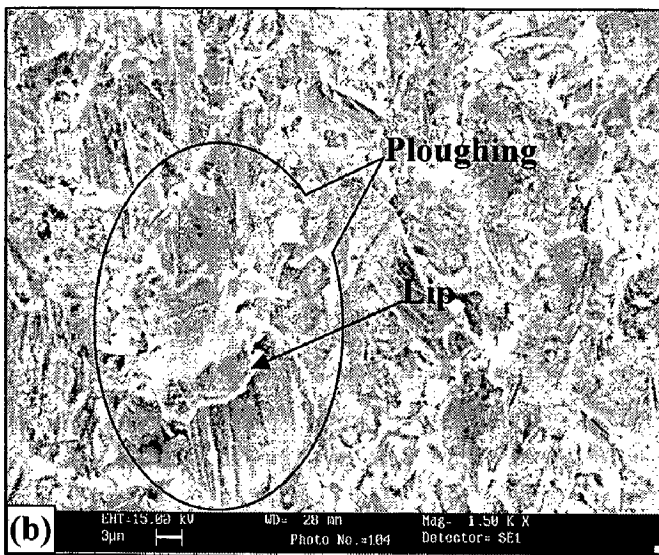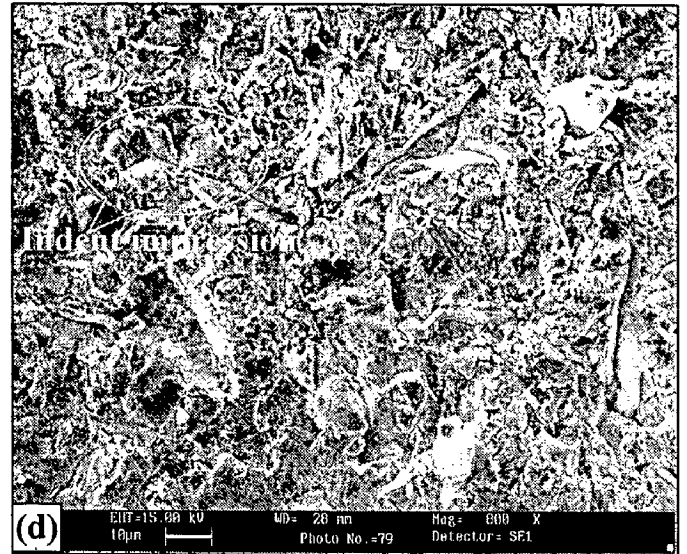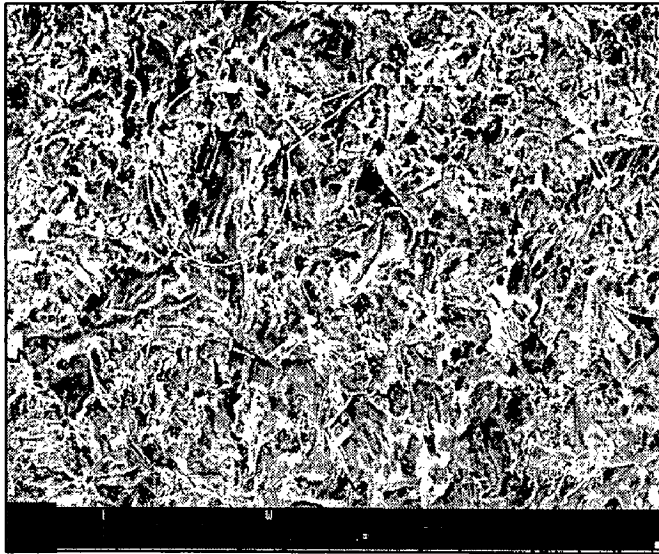
Fig.8.6   SEM micrographs showing the eroded surface morphology of GrA1 steel at different impact angle. Direction of particle impingement is from top to bottom of micrographs.

(a), (b) and (c) shows surface eroded at 30° impact angle

(d), (e) and (f) shows surface eroded at 90° impact angle

deformed platelets are detached by slow propagation of subsurface crack. Figure 8.7b shows the cracks at the subsurface of the platelets leading to ductile fracture. The deep indentation craters can be clearly seen in the cross-sectional micrograph. The erodent impacting at 90° will make the ductile metal to undergo work hardening and hence further impact of the particle will penetrate less. Thus, a ductile material at 90° shows lower erosion rate (Kumar et al. 2008).

The 3-Dimensional topography illustrating the surface roughness profile of the eroded steels is illustrated in Fig. 8.8. The surface roughness values of the eroded surface is found to be in the range of 1.29 μm and 1.13 μm for 30° and 90° impact angles, respectively. The channel like region shown in this figure reveals the material removal on the surface.

A severe plastic deformation occurs in the localized region around the points of impact of each particle in the form of lip and platelets which are detached resulting in loss of mass, in both the oblique and normal impacts. Similar mechanism of material removal has also been observed by Levy et al. (1984) for ductile metals, termed as the "Platelet mechanism". They have described it in terms of three distinct phases that which occur sequentially in the steady state condition. In the initial phase, an impacting particle forms a crater and the material is extruded or displaced from the crater to form a raised lip or mound. In the second phase, the displaced metal is deformed by subsequent impacts. This may lead to lateral displacement of the material which is part of the surface which can be accompanied by some ductile fracture in heavily strained regions. Finally, after a relatively few impacts, the displaced material becomes so severely strained that it is detached from the surface by ductile fracture.

8.1.2 NiCrAl Coating

Material wastage for the NiCrAl coatings tested at 30° impact angle is much higher than that tested at 90°(Figs. 8.9 and 8.10). Such a behavior is typical for the ductile materials (Hutchings, 1992). Initially high erosion rates are observed as a result of rough outer surface of the as-sprayed coatings. The globular protuberances on the as-sprayed surface are smoothed out by the impacting particles and the lower steady state erosion condition is reached with the increased cumulative mass of the erodent. Similar observations in case of erosion studies of the thermal-sprayed coatings are also observed by Levy et al. (1988) and Lathabai et al. (1998).

Figure 8.11 illustrates the surface morphology of the eroded surface at 30° impact angle. The eroded surface shows the evidence of severe plastic deformation. The smear creaters are dominant on the surface due to a large horizontal component of velocity that overwhelms the particle rotational tendency at the lower angle (Bellman et al., 1981). The EDAX analysis on the spherical particle seen on the micrograph (Fig. 8.11b) revealed it as Ni-rich unmelted particles. During spraying, the particles of different sizes might have different molten states, i.e., the particles of moderate sizes may be fully melted or partially melted at the point of impact on the substrate, and the particles of either small or large sizes are usually remain unmelted as they hit the substrate. A detailed characterization of these particles has already been reported in Chapter 4. The groove is formed with a relatively softer material around these particles, resulting in undercutting, which is subsequently loosened up and the unmelted particles may get pulled out of the surface. The pull out regions surrounded by lips or ridges suggests the strain localization which is a common feature in the ductile erosion behavior (Murthy et al., 2001). Further, the cross sectional view of the eroded area in Fig. 8.13a shows that the grove formed by the ductile mode of erosion along the splat boundary and leads to unmelted particle decohesion. A number of wider grooves can be seen on the eroded surface micrograph (Fig. 8.11a) and this event may lead to loss of mass. Furthermore, it is apparent from the micrographs that the material removal occurs from the ridges or lips which are formed on the bank of the crater or on the particle exit end of the crater, undergoing repeated deformation that is, subsequently, detached in the form of platelets.

The surface morphology of the coating eroded under 90° impingement (Fig. 8.12) demonstrates a number of crater sites created from individual impacting erodent silica particles. It is evident from the micrograph that repeated impacts by the silica particles resulted in a highly deformed platelets/flakes of material. The region associated with the cracks was analyzed for the composition using the EDAX and it is found that these regions are the Nickel-rich splats. There is no evidence of plastic deformation on these splats. The presence of indentation induced crack networks is an indicative of brittle fracture of some Ni-rich splats. The cross-sectional examination shows the surface hillocks and deep craters at various places which represent the portion of the material being removed from the surface of the coating. The 3-D optical profile (Fig. 8.14b) of the eroded surface reveals that there is a crater depth of 12.4 μm with a surface roughness value of 2.98 μm.
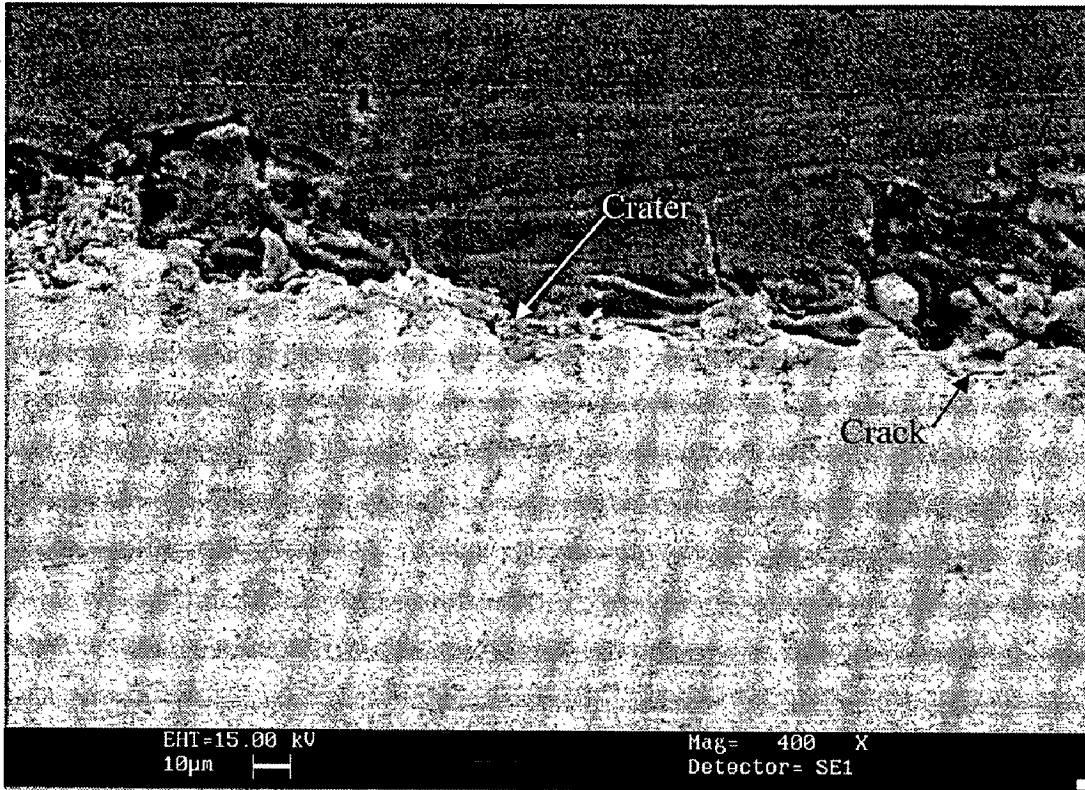
Fig.8.7   SEM micrographs across the cross-section of the eroded region of GrA1 steel eroded at 90° impact angle
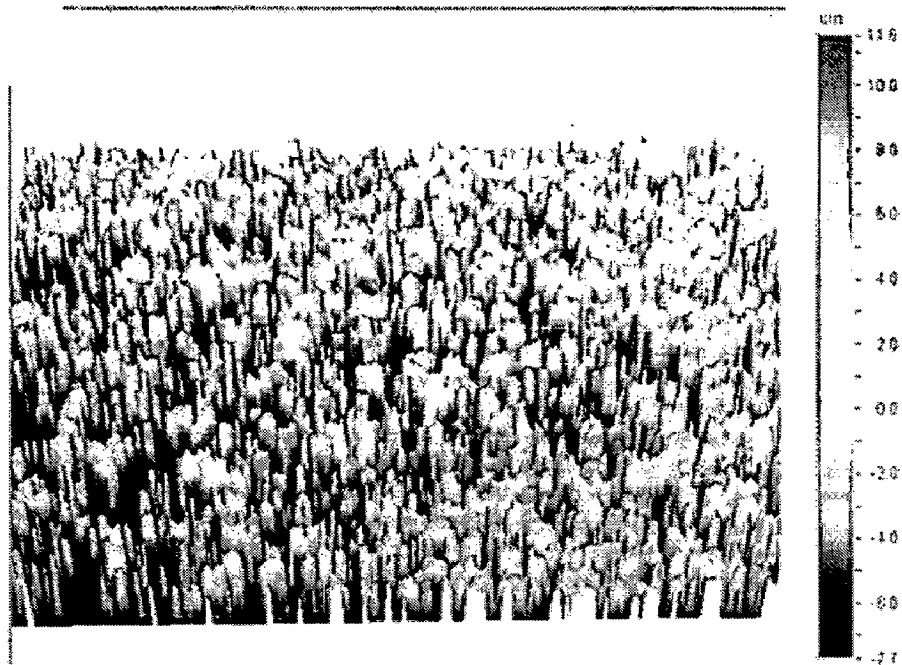
(a)
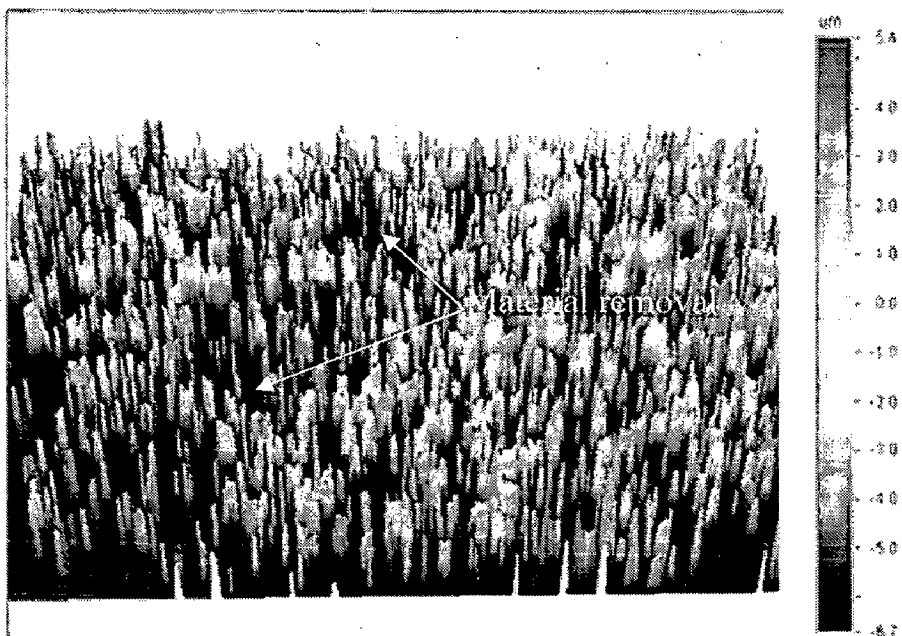
(b)

Fig.8.8   3D optical profile from the centre of an eroded GrA1 steel which shows depth profiles (Scanned area-591 X 449 μm)
(a) Eroded at 30° impact angle; (b) Eroded at 90° impact angle
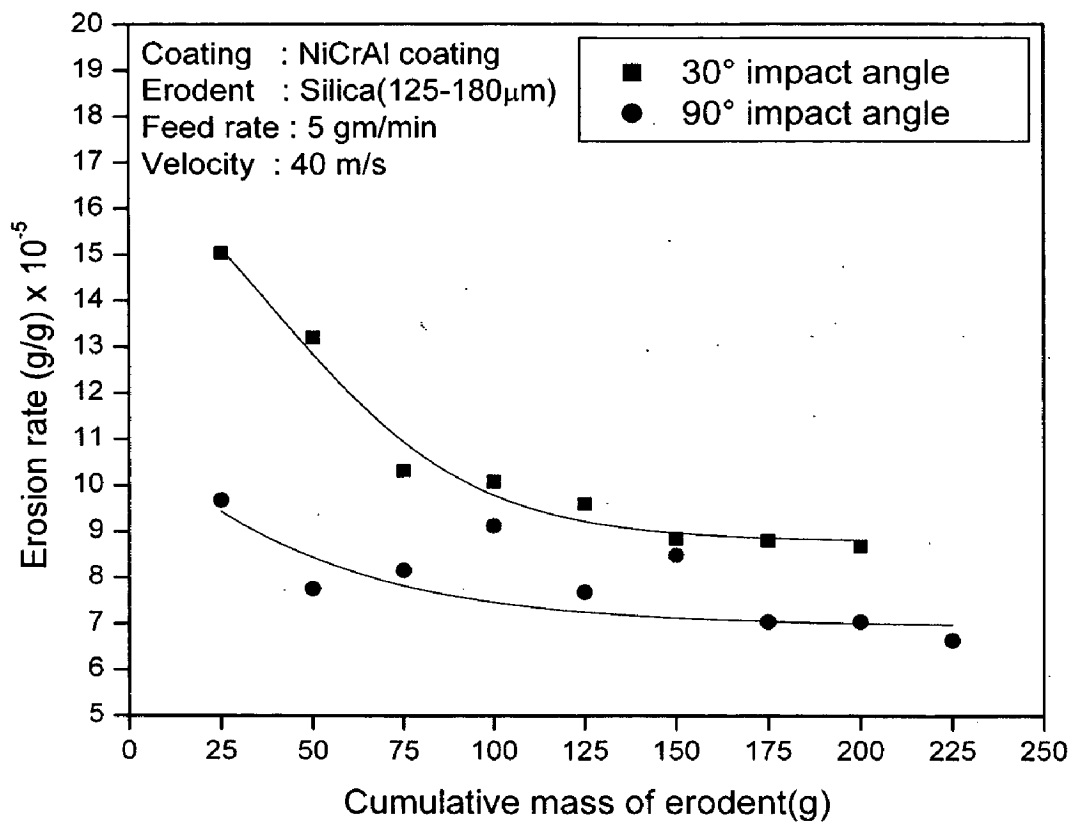
Fig.8.9   Variation of the Incremental erosion rate with the cumulative weight of the erodent for NiCrAl coatings at 30° and 90° impact angle.
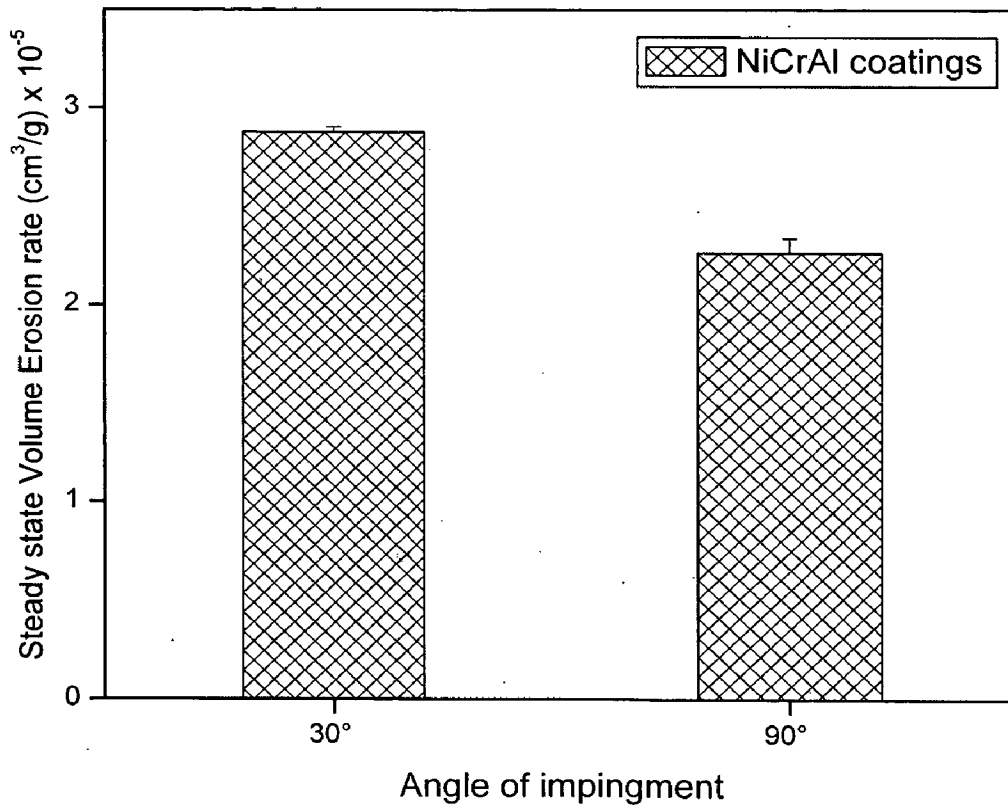
Fig.8.10   Histogram illustrating the steady state volume erosion rate of NiCrAl coatings at different impact angles.
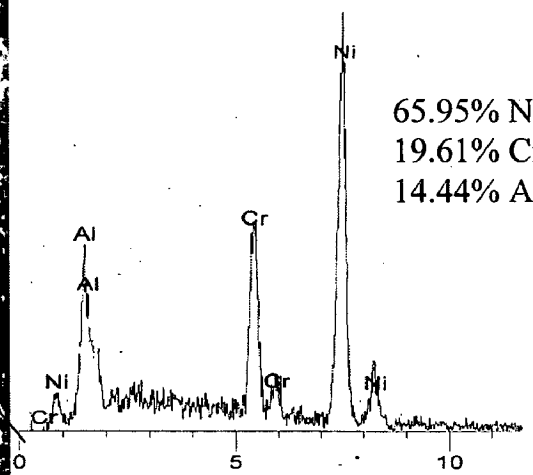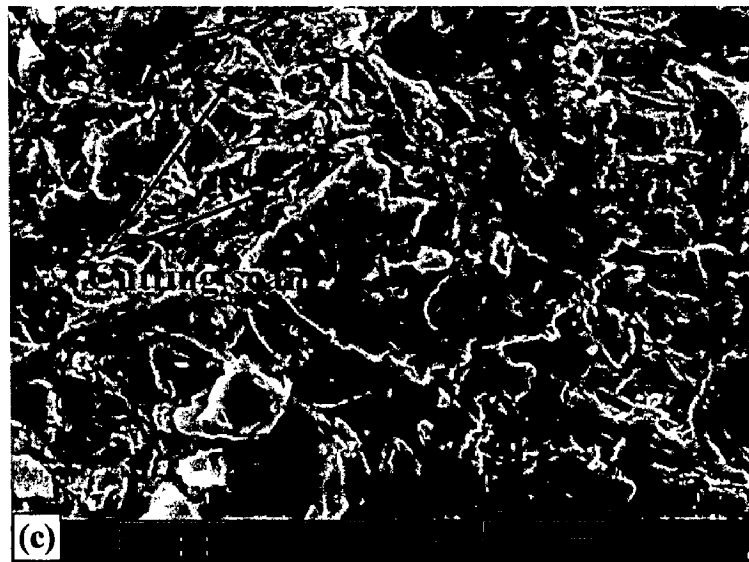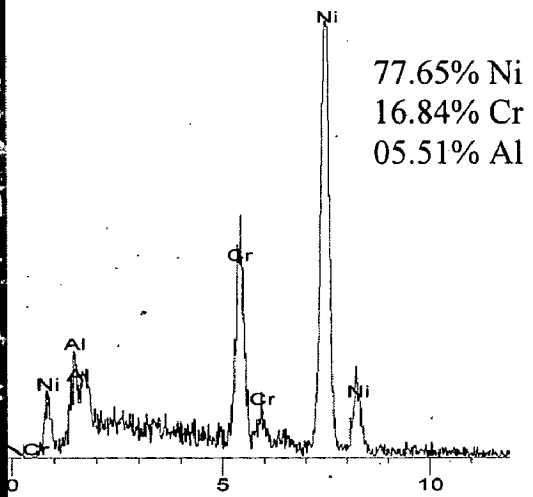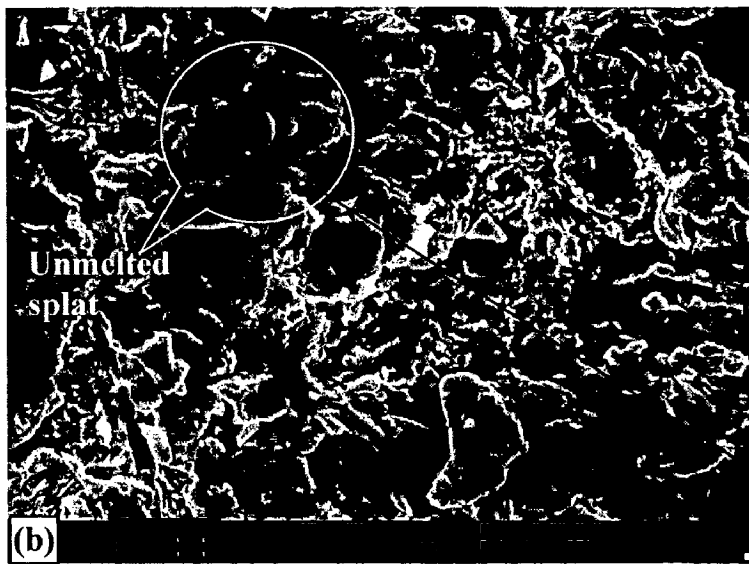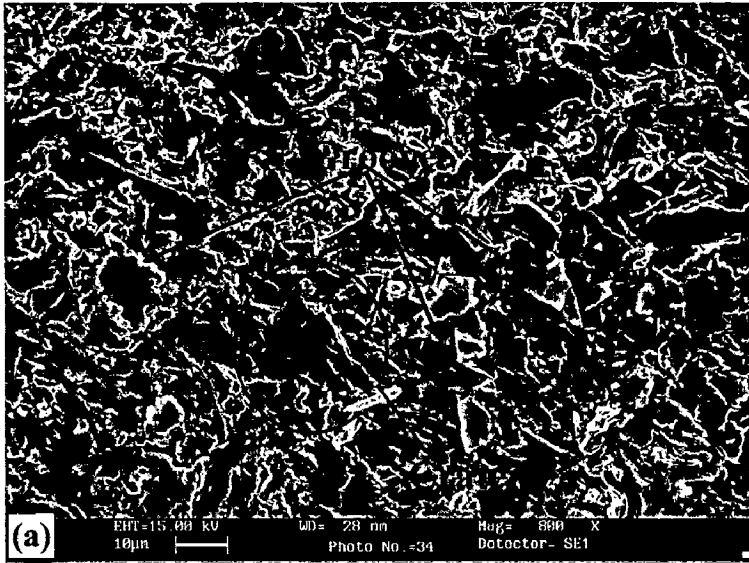
Fig.8.11 SEM micrographs showing the surface morphology and EDAX compositional analysis at some points on NiCrAl coated steels eroded at 30° impact angle.
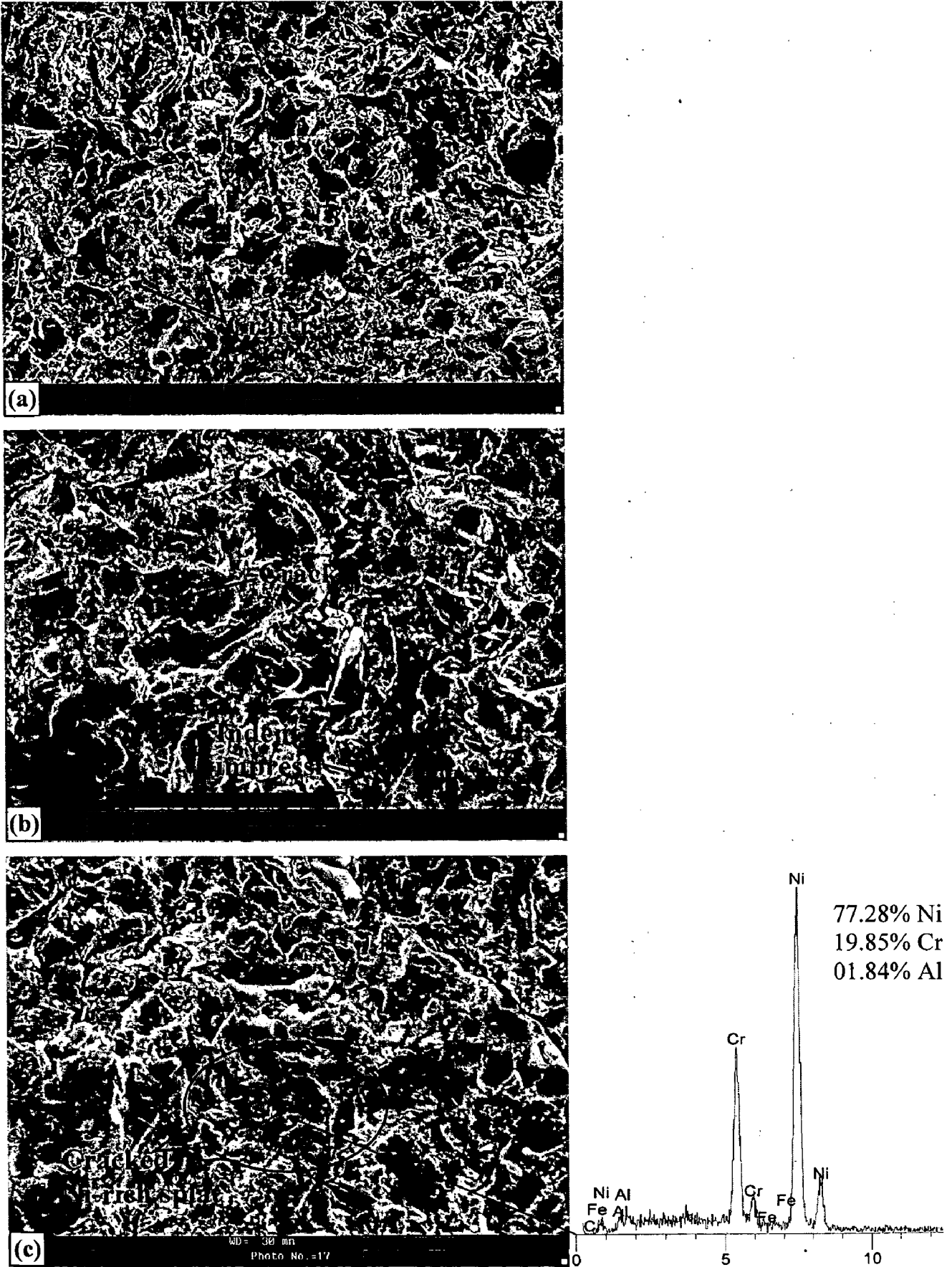
Fig.8.12 SEM micrographs showing the surface morphology and EDAX compositional analysis at some points on NiCrAl coated steels eroded at 90° impact angle.

278
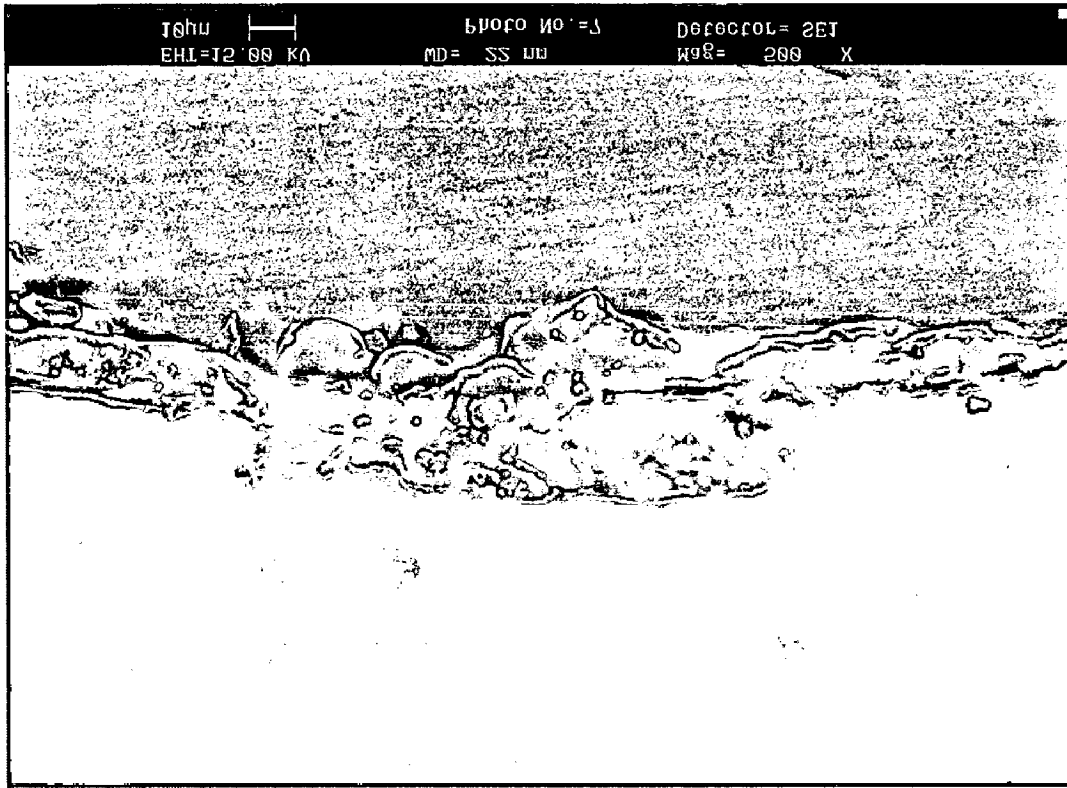
(a)

(b)

(c)

Fig.8.13   SEM micrographs across the cross-section of the eroded region of NiCrAl coatings.
(a) Eroded at 30° impact angle;
(b) Eroded at 90° impact angle   (c) Enlarged region marked in (b)
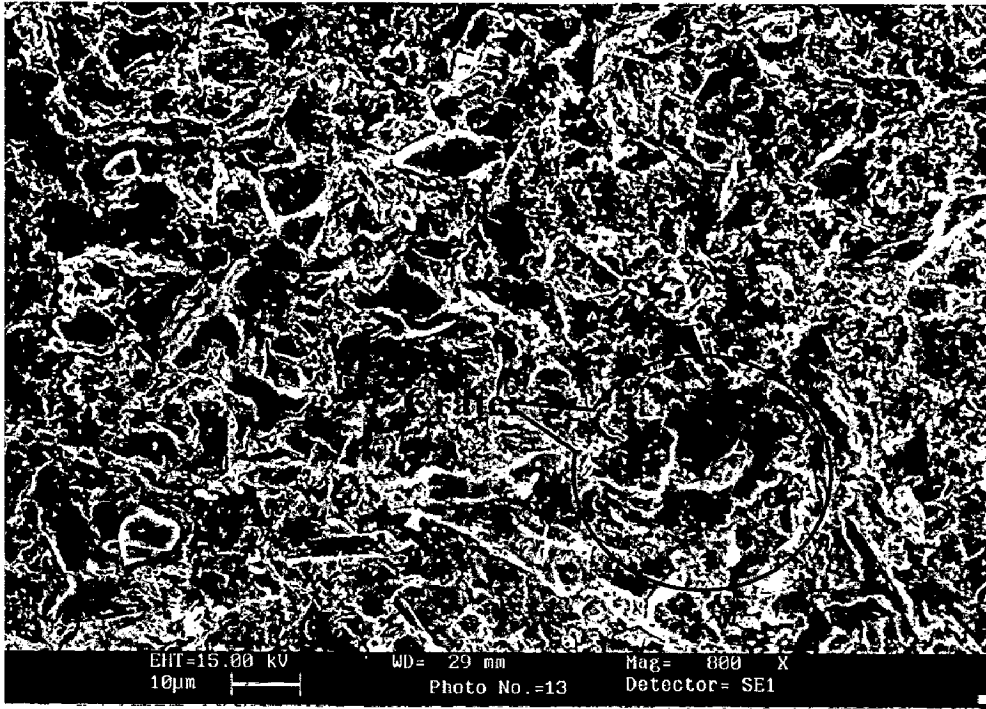
(a)
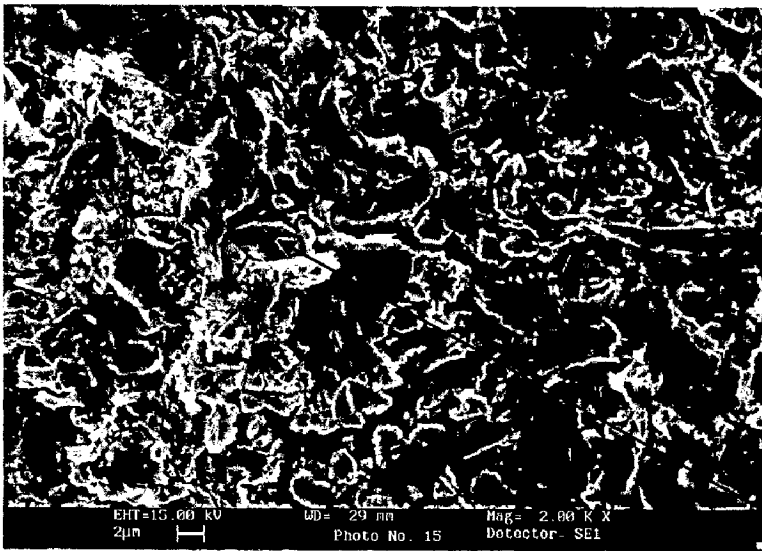
(b)

(c)

Fig.8.18   SEM micrographs showing the surface morphology and EDAX point analysis showing embedded sand particle on NiAlCrFeMo coated steels eroded at 90° impact angle.
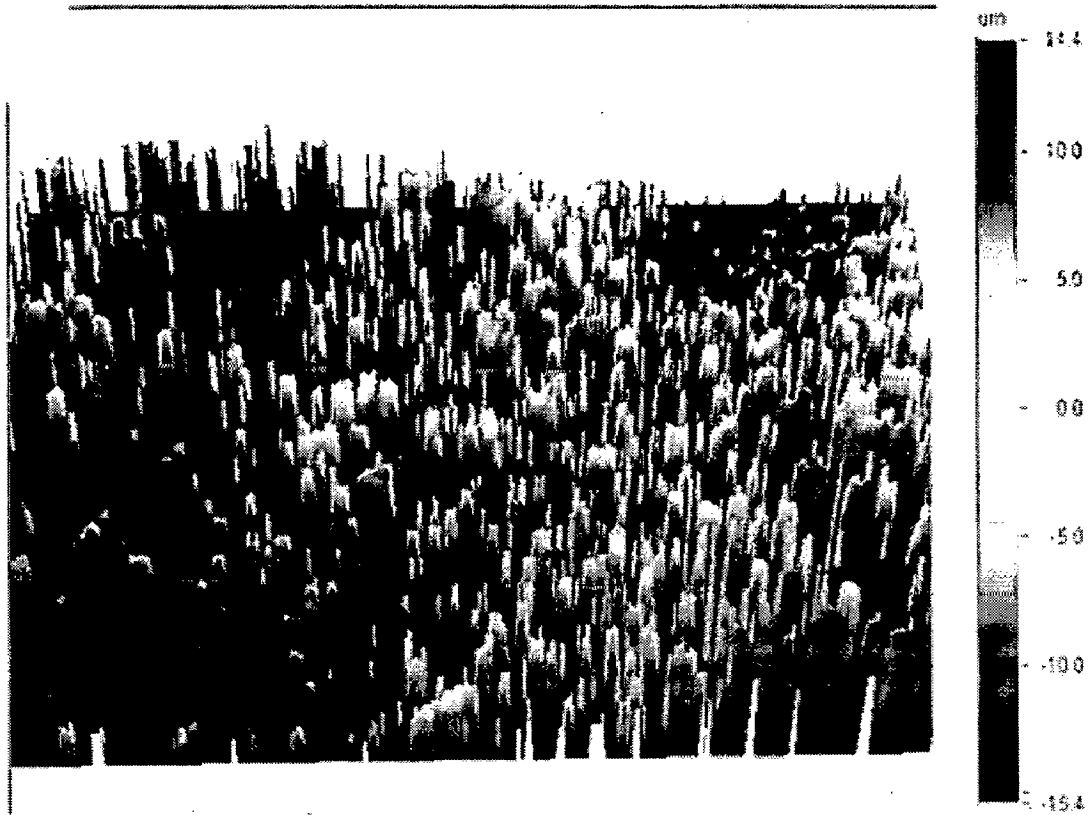
(a)
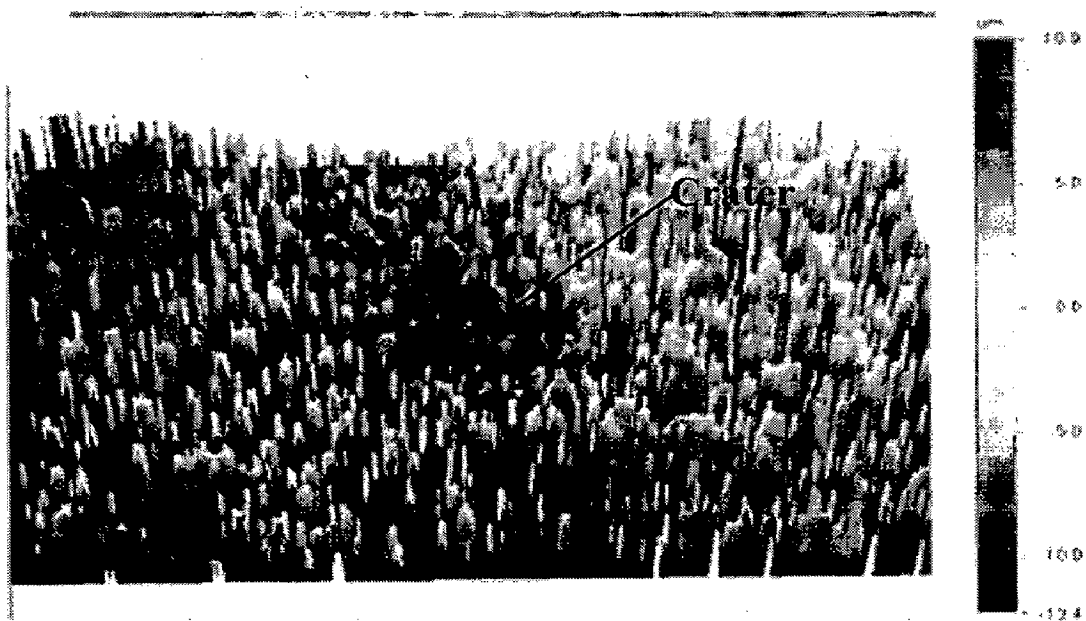
(b)

Fig.8.14   3D optical profile from the centre of an eroded NiCrAl coating which shows depth profiles (Scanned area-591 X 449 μm)
(a) Eroded at 30° impact angle; (b) Eroded at 90° impact angle

Although the microscopic observation of the eroded surface suggests about the composite ductile-brittle behavior of this coating, the predominant erosion has occurred by the plastic deformation and not by the fracture. Levy (1988) has reported that the thermally sprayed NiCrAl alloys have the best ductility at room temperature. Further, he has opined that the MCrAlY coatings and other primarily metallic coatings will erode as a result of the impacting particles causing localized plastic flow that exceeds the critical strain to failure in local areas.

8.1.3   NiAlCrFeMo Coating

The erosion rate curves along with the bar chart indicating the volumetric steady state wear loss is shown in Figs. 8.15 and 8.16. The HVOF-sprayed NiAlCrFeMo coatings showed a higher erosion rate at 30° impact angle than that at 90°, which is the typical characteristic erosion behavior of the ductile materials. Further, the leveling of surface protrusions on the as-sprayed coating results in higher erosion rate at the earlier stage of the experiment and gradually decreases to lower steady state rate. Levy et al (1986B) also observed the ductile behavior of NiCrAlMoFe coatings eroded with SiC particles impacted at 30 m/s.

Due to different impact angles of the silica particles, the eroded scars have different lengths and shapes. The surface morphologies of the eroded coatings at 30° impact angle (Fig. 8.17) show the smear craters forming lips at the exit end of the erodent, which is indicative of extensive plastic flow. Figure 8.17b clearly shows the lips formed under severe deformation which is detached from the bulk material in the form of microchips. Similar to the one observed in the previous section 8.1.2, the unmelted Ni-rich particles have pulled out by the erodent at shallow impact angle resulting in a deeper grove. It can be confirmed by the EDAX compositional analysis that the spherical particle is the unmelted splat, similar to one discussed during the characterization of the as-sprayed coatings in Chapter 4. Figure 8.18 shows the eroded surface morphology of the coatings under normal impact condition. The indentations, craters, and lips observed on the surface demonstrate the ductile type erosion behavior of the coatings. Although, each impact displaces the material from the indentations, it will often not become detached as micro platelets until it has experienced repeated plastic deformation. The lips are pancake forged and flattened by subsequent particle impact before they are finally knocked off. The embedded silica particles into open pores are clearly seen in the

micrograph (Fig 8.18b) and are further confirmed by EDAX analysis which shows a strong peak for silicon. The cross sectional view (Fig.8.19) along the eroded region shows the crater associated with subsurface cracks which propagates along splat boundary probably due to presence of porosity and oxide interface. Relatively higher porosity of NiAlCrFeMo coatings leads to higher erosion loses. 3D optical profile (Fig 8.20) at the centre of an eroded NiAlCrFeMo coating shows deep crater of 39.8 µm for the sample eroded at 90°. Higher roughness value of 6.88 and 13.24 µm as been observed on the surface eroded at 30° and 90° impact angle respectively.

8.1.4 NiCrFeSiB Coating

Fig 8.21 and 8.22 show the ductile behavior of NiCrFeSiB coating in which steady state erosion rate at 30° is higher than that at 90°. The higher erosion rate at the initial stage is due to surface texture of the as-sprayed coating containing protrusions on them which were vulnerable to being knocked off by the eroding particles.

The evidence of plastic deformation accompanied with ploughing and cutting has been observed on the eroded surface under both the test conditions, but became more pronounced at 30° impact angle. Fig 8.23 shows the scanning electron micrograph of the eroded surface at 30° oblique angle. It is apparent that plastic rupture of metal by the silica particle resulted in highly deformed platelets which are displaced by subsequent impacts. The cutting and platelet formation are clearly seen at higher magnification (Fig 8.23b). The EDAX analysis on the platelet formed shows relatively higher content of chromium and the composition on the groove are similar to that of coating. Fig 8.24 shows the micrograph of the eroded coating at 90° impact angle. Indentation-induced shallow craters along with deformed lips are observed at the impact site on the surface of coating. Fig.8.24 b shows the evidence of erosion damage localized at open pore region. It is clear from the micrograph that each impact displaces material from the impact site in to raised lips around the crater.

The cross sectional view at the eroded region of the coatings is shown in Fig.8.25. The coatings eroded at 30° impact angle shows crater formed from ploughing action, stretched out along its length where as those at normal impact show crater. The hillocks observed on the surface indicated the material removal by eroding silica particles. 3D optical profile (Fig.8.26) of eroded coating at shallow impact angle shows channel like regions indicating material removal from the crater and at normal impact it
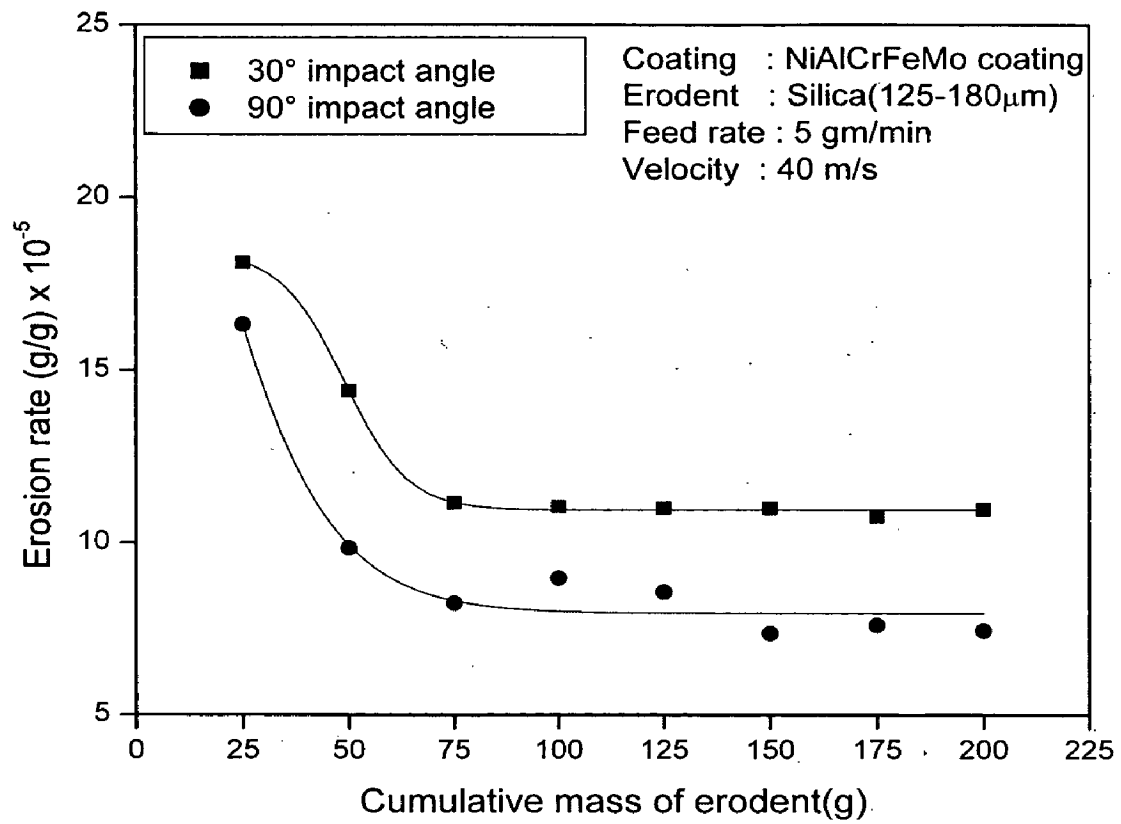
Fig.8.15   Variation of the Incremental erosion rate with the cumulative weight of the erodent for NiAlCrFeMo coatings at 30° and 90° impact angle.
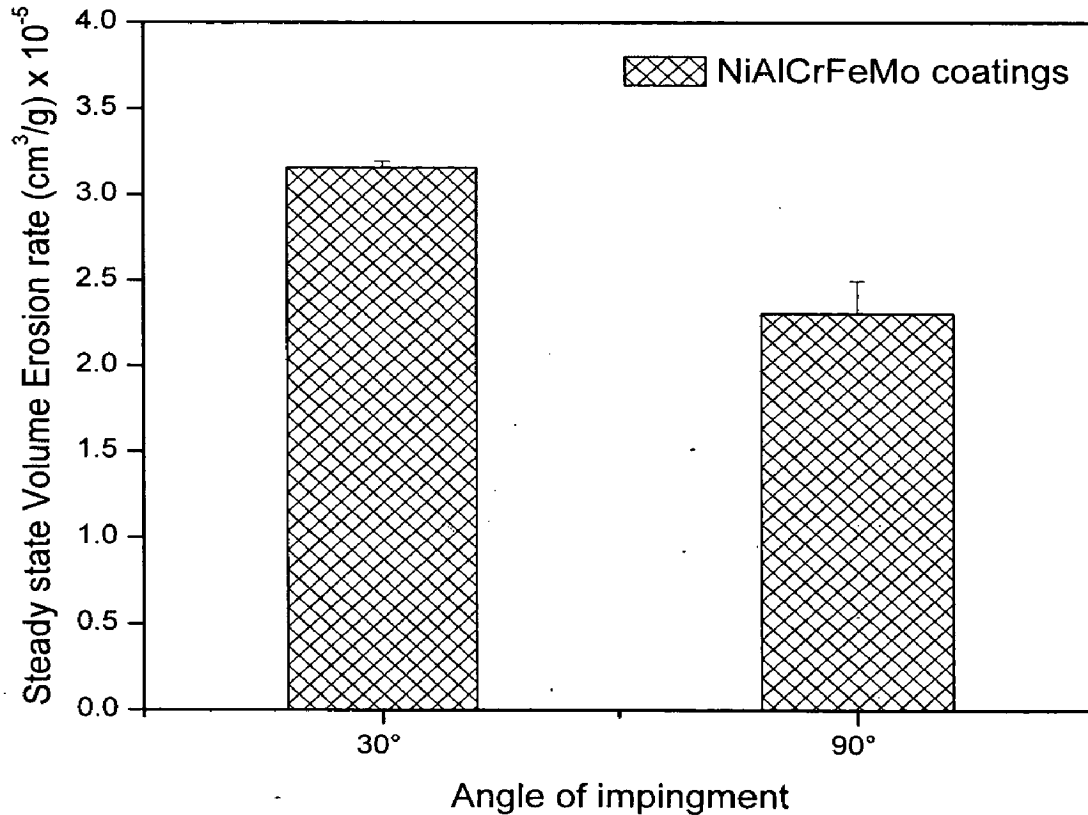
Fig.8.16   Histogram illustrating the steady state volume erosion rate of NiAlCrFeMo coatings at different impact angles.
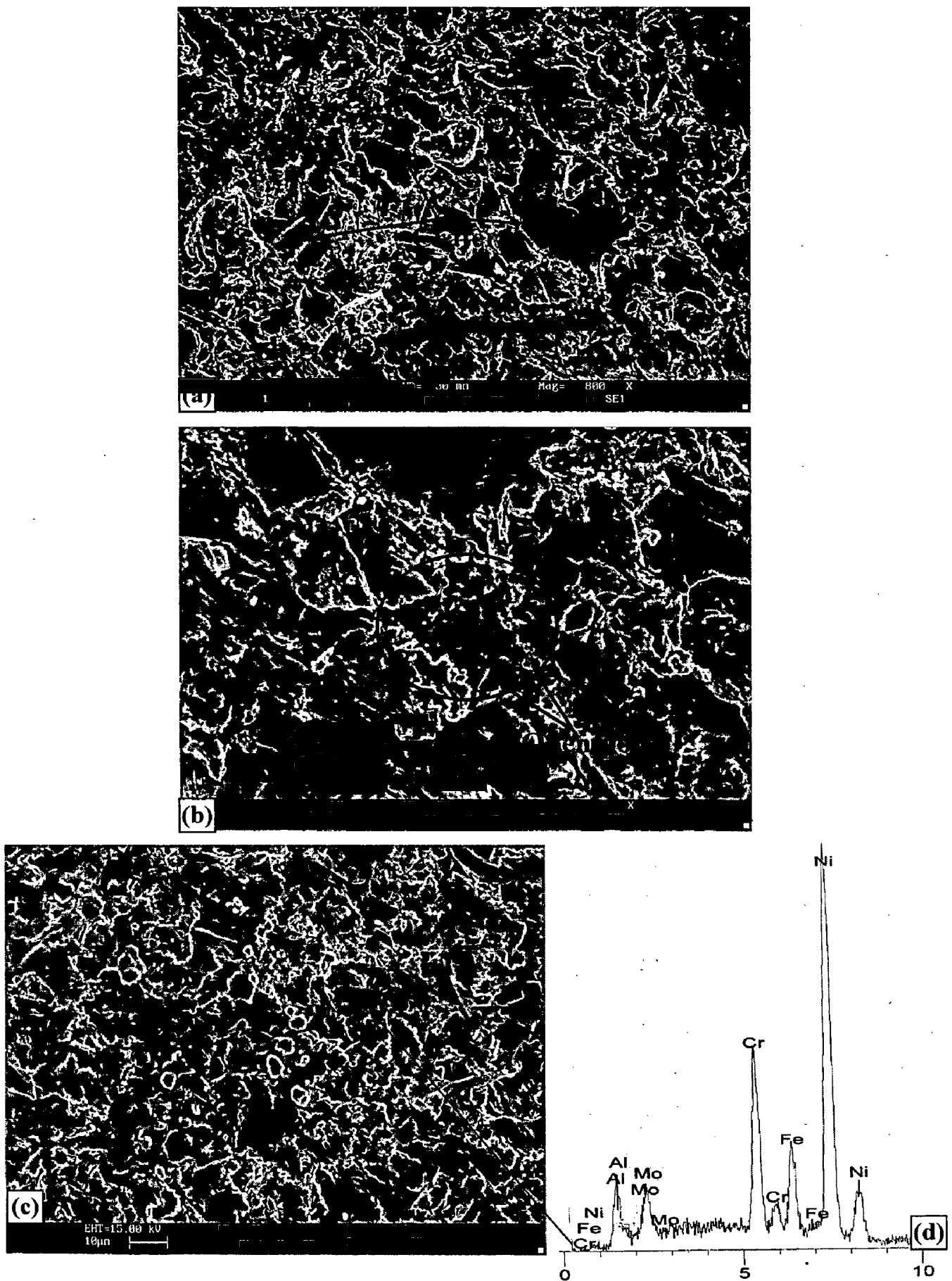
Fig.8.17 SEM micrographs are showing the surface morphology and EDAX point analysis on the unmelted particle of NiAlCrFeMo coated steels eroded at 30° impact angle.
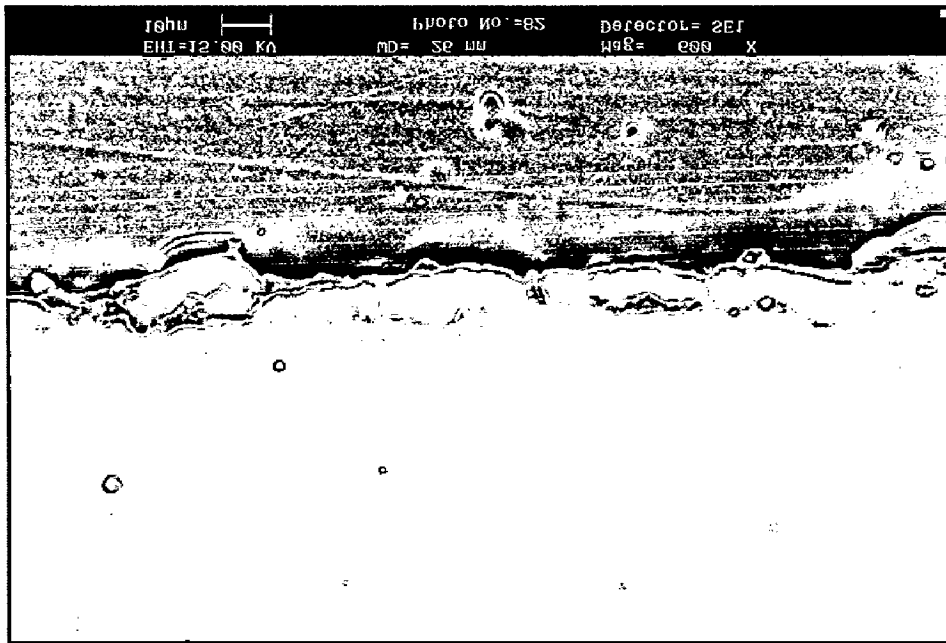
(a)
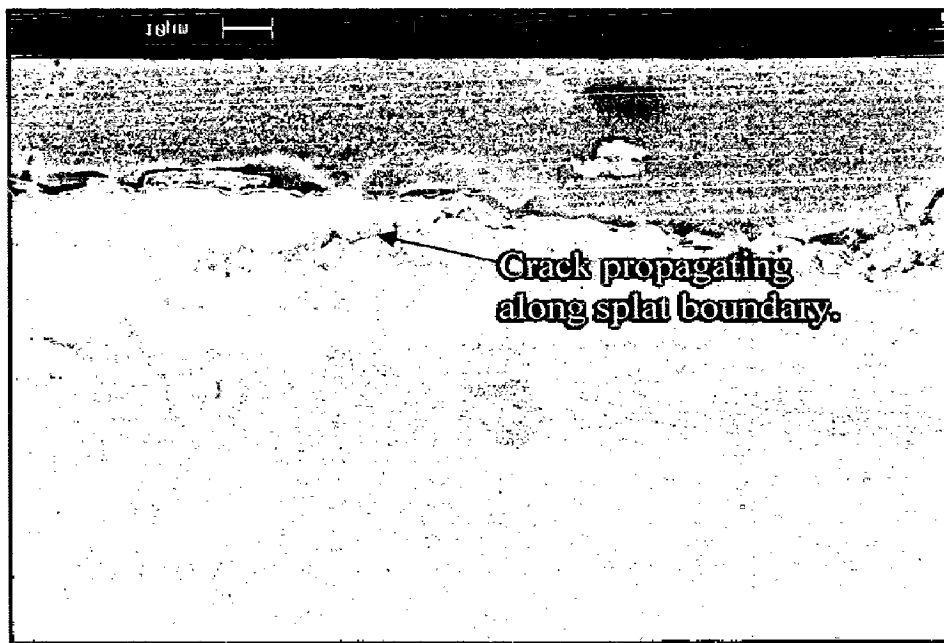
(b)

Fig.8.19   SEM micrographs across the cross-section of the eroded region of
NiAlCrFeMo coatings.
(a) Eroded at 30° impact angle;
(b) Eroded at 90° impact angle
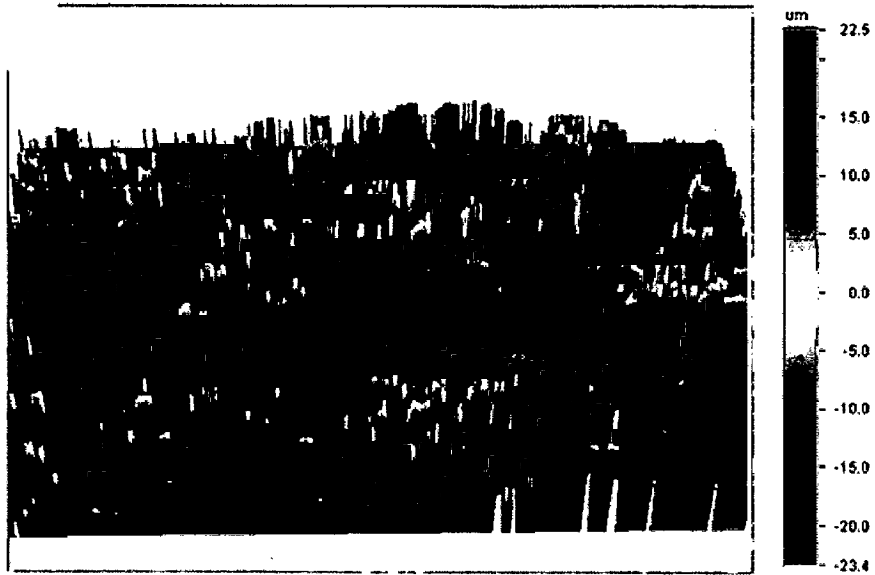
(a)
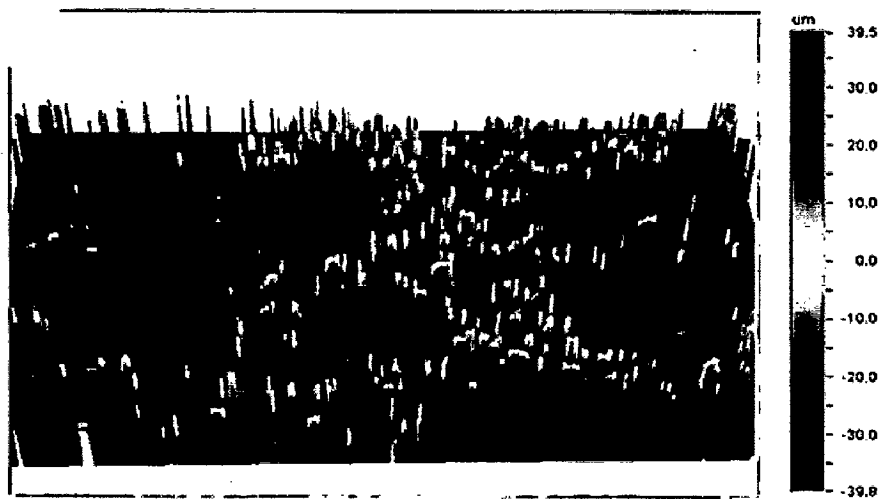
(b)

Fig.8.20   3D optical profile from the centre of an eroded NiAlCrFeMo coating
which shows depth profiles (Scanned area-591 X 449 μm)
(a) Eroded at 30° impact angle; (b) Eroded at 90° impact angle
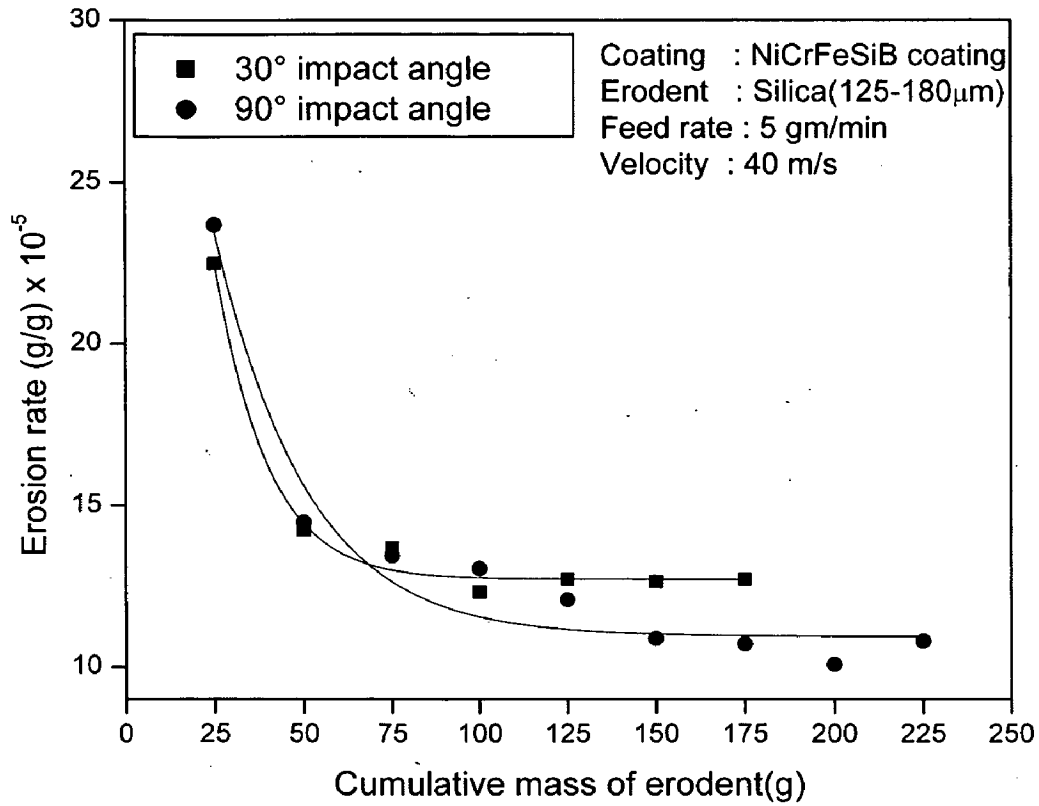
Fig.8.21   Variation of the Incremental erosion rate with the cumulative weight of the erodent for NiCrFeSiB coatings at 30° and 90° impact angle.
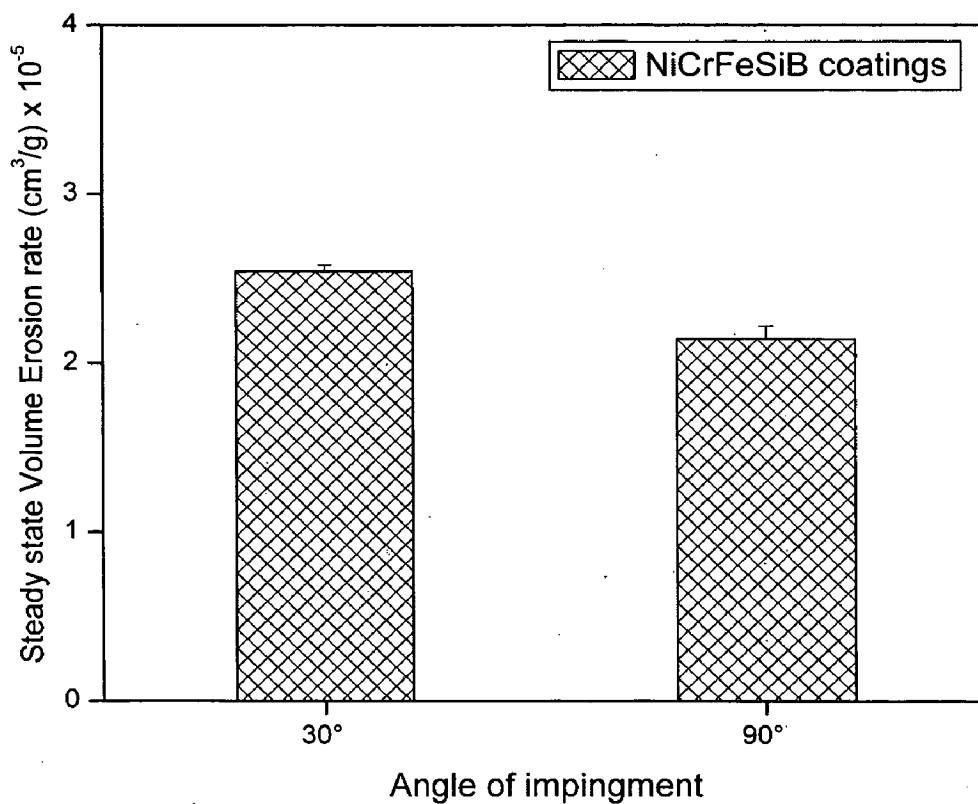

Fig.8.22   Histogram illustrating the steady state volume erosion rate of NiCrFeSiB coatings at different impact angles.

66.47% Ni
23.56% Cr
04.79% Fe
05.18% Si

78.09% Ni
15.93% Cr
03.38% Fe
02.60% Si
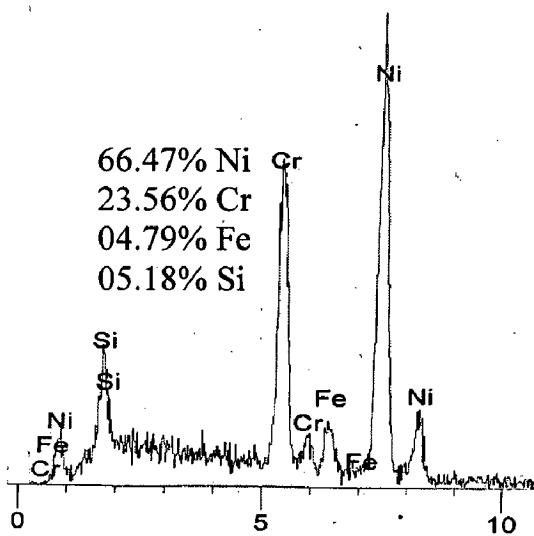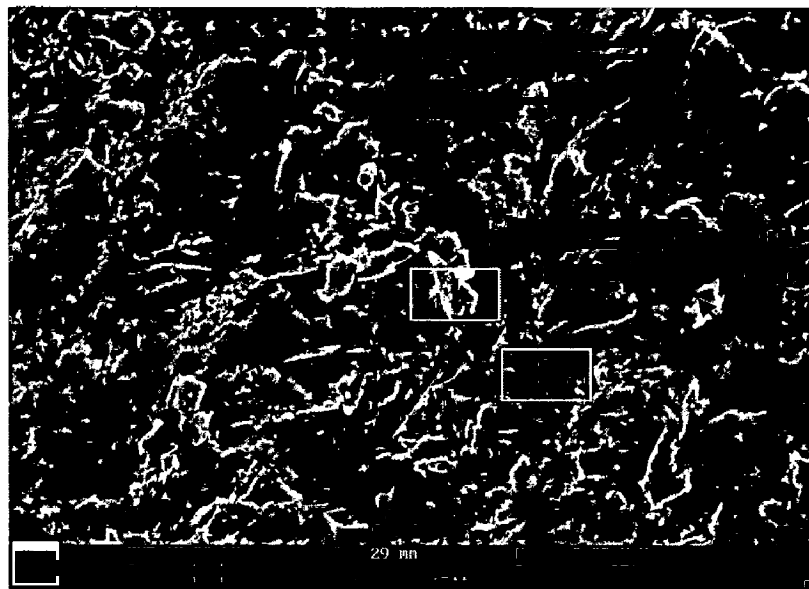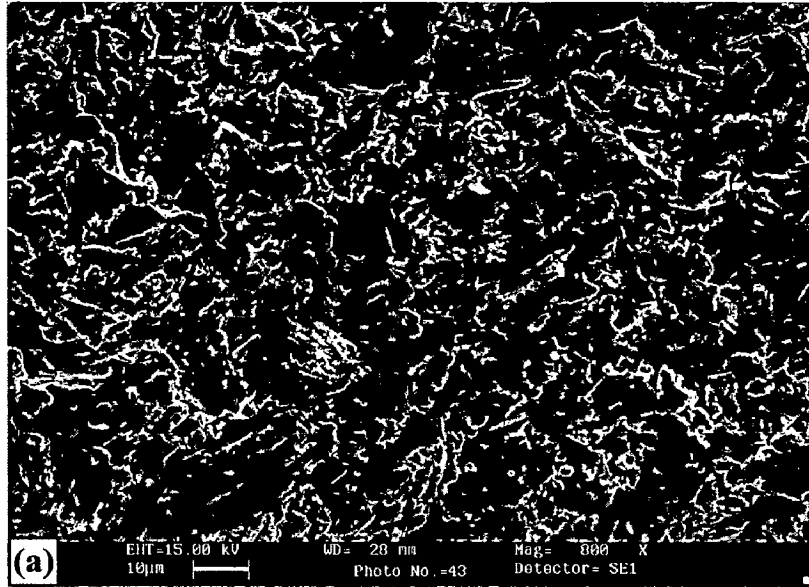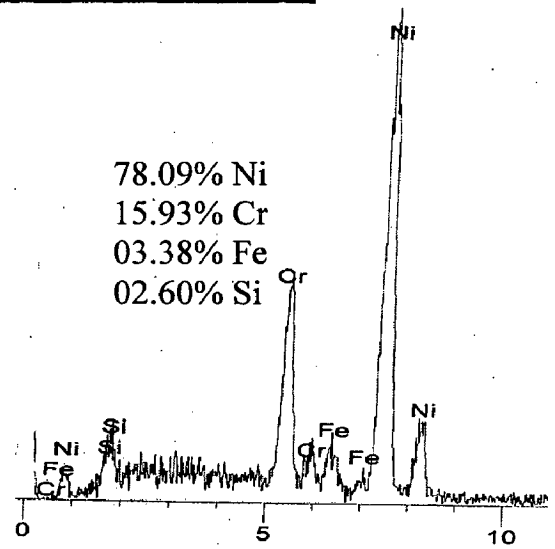
EDAX at point 1

EDAX at point 2

Fig.8.23   SEM micrographs showing the surface morphology and EDAX compositional analysis at some points on NiCrFeSiB coated steels eroded at 30° impact angle.
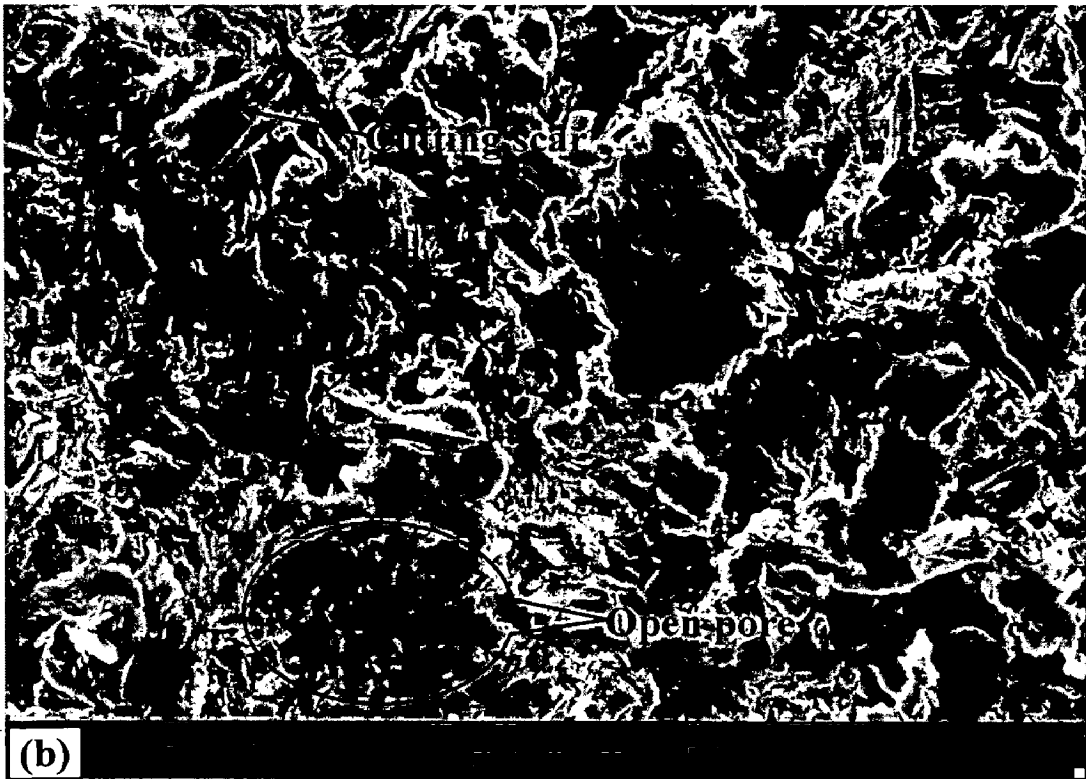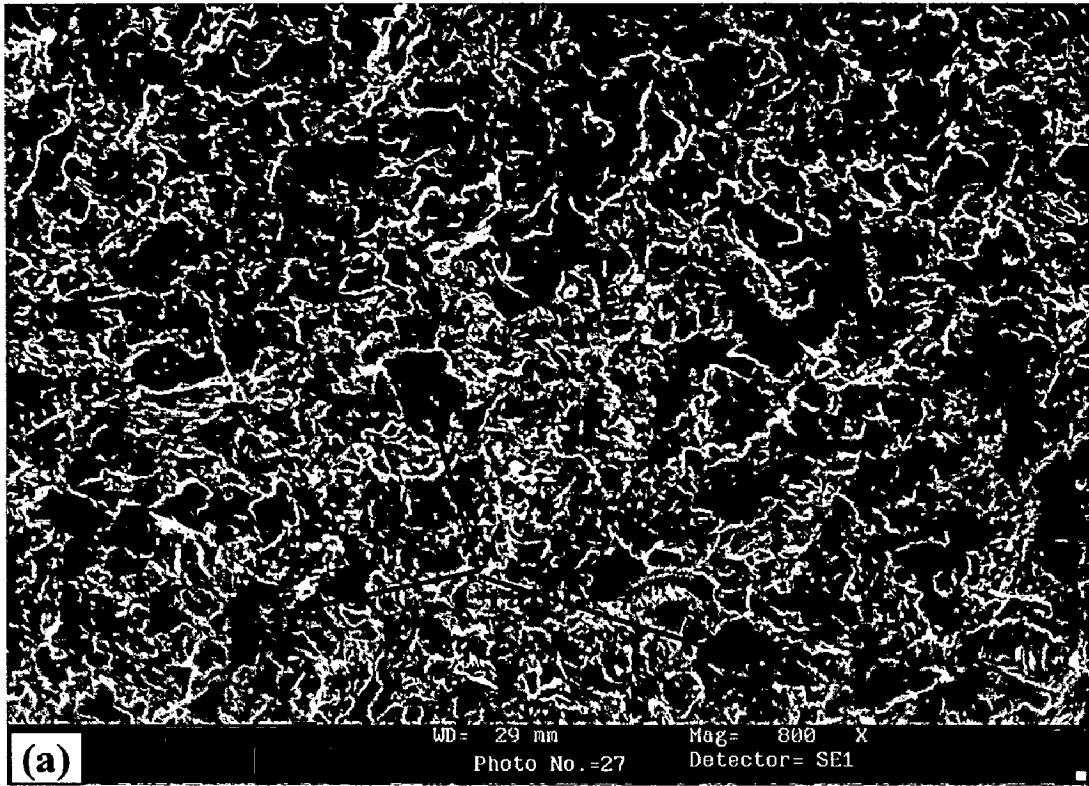
Fig.8.24   SEM micrographs showing the surface morphology of · NiCrFeSiB coated steels eroded at 90° impact angle.
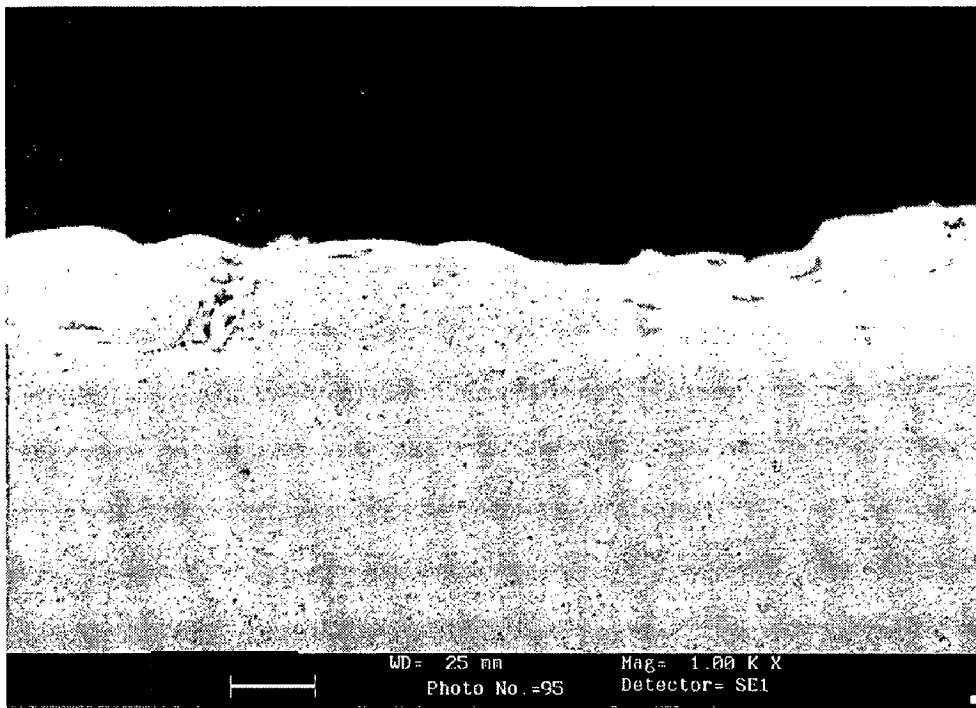
(a)
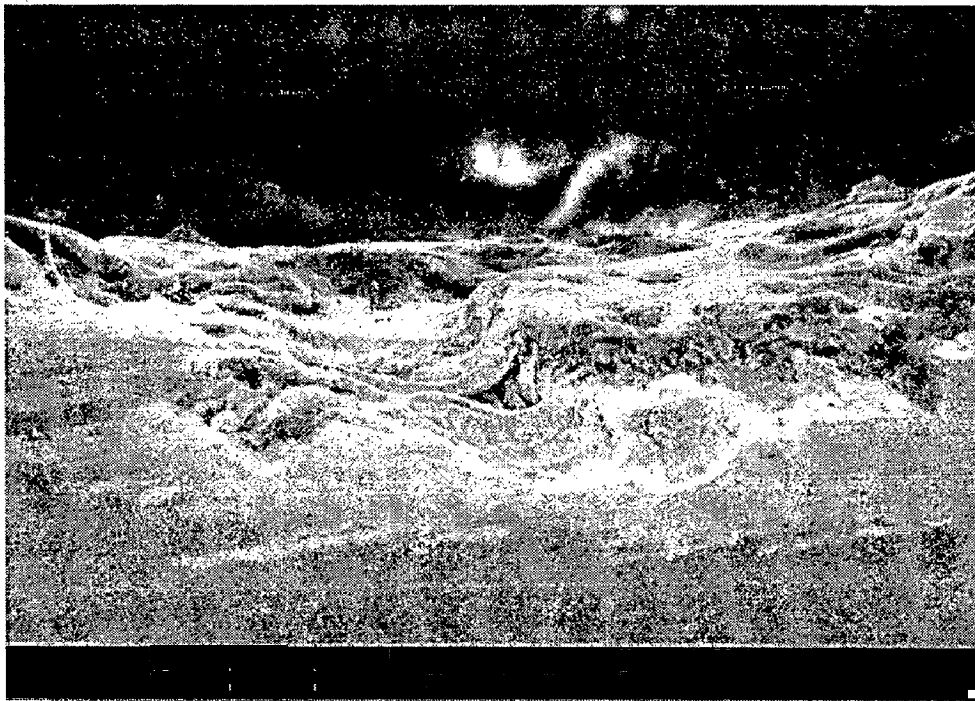
Fig.8.25   SEM micrographs across the cross-section of the eroded region of NiCrFeSiB coatings.
(a) Eroded at 30° impact angle;
(b) Eroded at 90° impact angle

291

shows erosion at impact sites. The surface roughness of the coating eroded at 30° impact angle found to be 3.53 µm where as for normal impact angle it is 3.24 µm.

Thus the surface morphology of the eroded surface indicates that the predominant mechanism of material removal is ploughing and cutting resulting in formation of platelets. Levy et al., (1986B) reported ductile behavior of NiCrFeSiBC coatings eroded with SiC particles impacting at 30 m/s.

8.1.5   WC-Co/NiCrFeSiB Coating

It is known that materials that consist of both brittle and ductile constituents can behave in either a ductile or a brittle manner, as indicated by different parameters (Levy 1986A). In the present study, it is apparent from the erosion rate charts (Figs.8.27 & 8.28), WC-Co/NiCrFeSiB coatings shows brittle behavior as a function of impact angle, where it shows higher wear rate at 90° impact angle. However the difference in magnitude of steady state erosion rates at 30° and 90° impact angles are marginal and lie in a narrow range and hence it may not be conclusive in predicting the ductile or brittle nature of the coating. Hutchings (1992) and Sundararajan et al., (1997) reported that the angular dependence of erosion is not a characteristic of the material alone, but depends also on the conditions of erosion and hence suggest that the terms brittle and ductile in the context of erosion should therefore be used with caution. This leads to the further detailed microscopic analysis.

The coating eroded at 30° impact angle shows a surface morphology (Fig8.29) with number of grooves and lips which indicated the material removal by ploughing and cutting mechanism. Material loss is in the form of platelets by repeated impact of erodent. It is apparent from the micrograph that groove might have formed predominantly in the softer binder region, leads to dislocation of hard WC particles. The grooves in the binder region act as failure initiating concentrators and small carbide grains crumble off uncrushed, where as the main mechanism of large grains failure is chipping (Hussainova et al., 1999). The magnified micrograph (Fig.8.29b) shows a evidence of carbide particle pull out. The EDAX analysis at point 1, confirm the particle as tungsten carbide and analysis at point 2 represent nickel rich binder matrix. Similar observations of carbide pull out from the WC-Co, WC-Co-Cr and Cr3C2-20NiCr coating surface at shallow angle of impact has been reported by Hawthorne et al., 1999, Feng et al., 1999 and Murthy et al., 2001.

The coating eroded at 90° impact angle showed a surface morphology (Fig.8.30) with a numerous crater formed by impacting silica erodent. The groove marked in Fig 8.30c shows the evidence of carbide particle pull out and gross spalling of the coating. Craters formed are surrounded by lips suggesting strain localization which is common feature in ductile erosion mode. Such ductile extrusion of material might have predominantly occurred in the softer nickel based metallic binder matrix.

There are indications of subsurface cracks in the cross-sectional view as shown in Fig.8.31. The crater and hillocks observed on the surface indicated the material removal by eroding silica particles. 3D optical profile (8.32) of eroded coating at shallow impact angle shows material removal from the binder matrix. Channel like regions observed, indicate the regions of exaggerated material removal from the surface. Wider crater of 11.3 μm deep has been observed at normal impact. The surface roughness of the coating eroded at 30° and 90°impact angle found to be 2.85 and 3.84 μm respectively.

Thus the morphology of the eroded surface point out craters, groove formation in binder matrix characterized by lips at their rim, platelet formation and carbide particle pull out as the prevailing erosion mechanism. These mechanisms signify composite ductile and brittle modes of erosion, although the brittle mode is dominant. Erosion rate of WC-Co/NiCrFeSiB coating is lower when compared to other coatings under study, reported in previous sections 8.1.2 through 8.1.4, because of the mixed nature of material removal and hardness ratio between the coating and the silica erodent. Wang et al., 1996 and Kulu et al., 2002 reported that the wear resistance of NiCrFeSiB coatings can be greatly increased by adding refractory carbides such as WC, VC, and CrC to the metallic matrix. The obtained structure is also termed as "double cemented" structure as the carbide particles are binded in a Co and Ni matrix. Kulu et al., 2005, Hussainova et al., 1999 and Feng et al., 1999 also observed combination of ductile and brittle mode of erosion with WC-Co hard metals and coatings and titanium carbide base cermets.

\
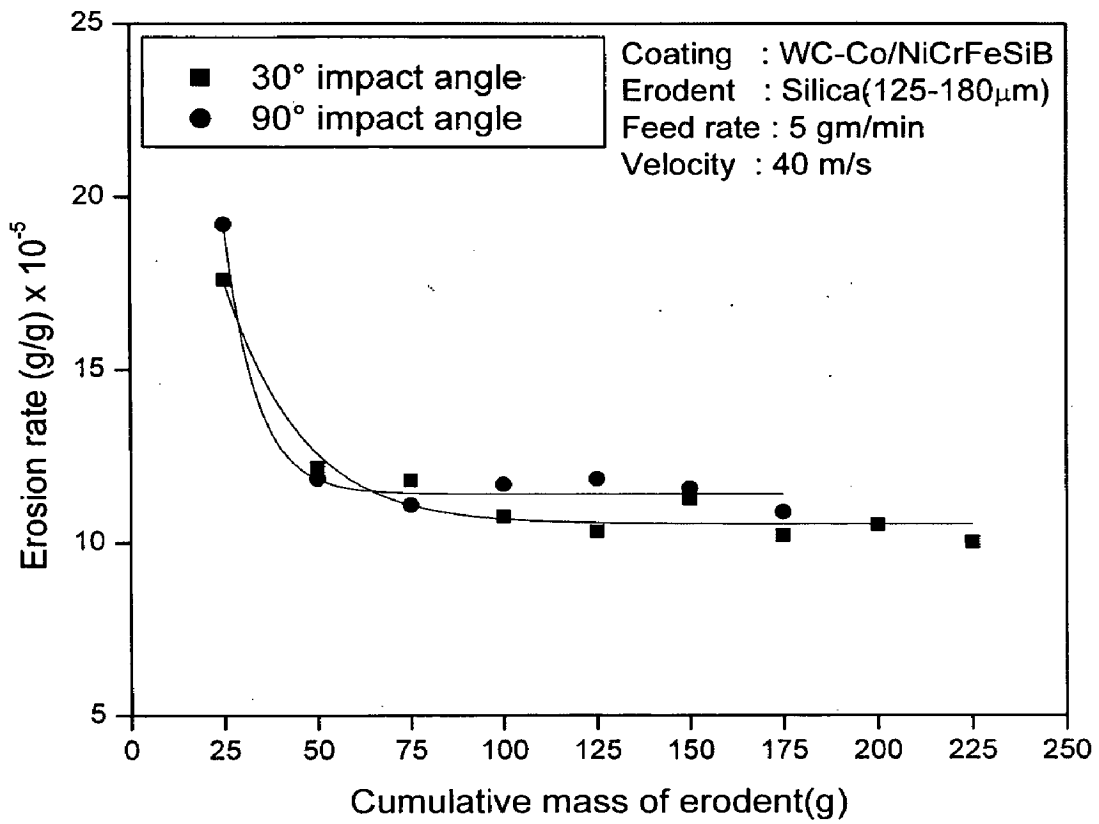
Fig.8.27   Variation of the Incremental erosion rate with the cumulative weight of the erodent for WC-Co/NiCrFeSiB coatings at 30° and 90° impact angle.
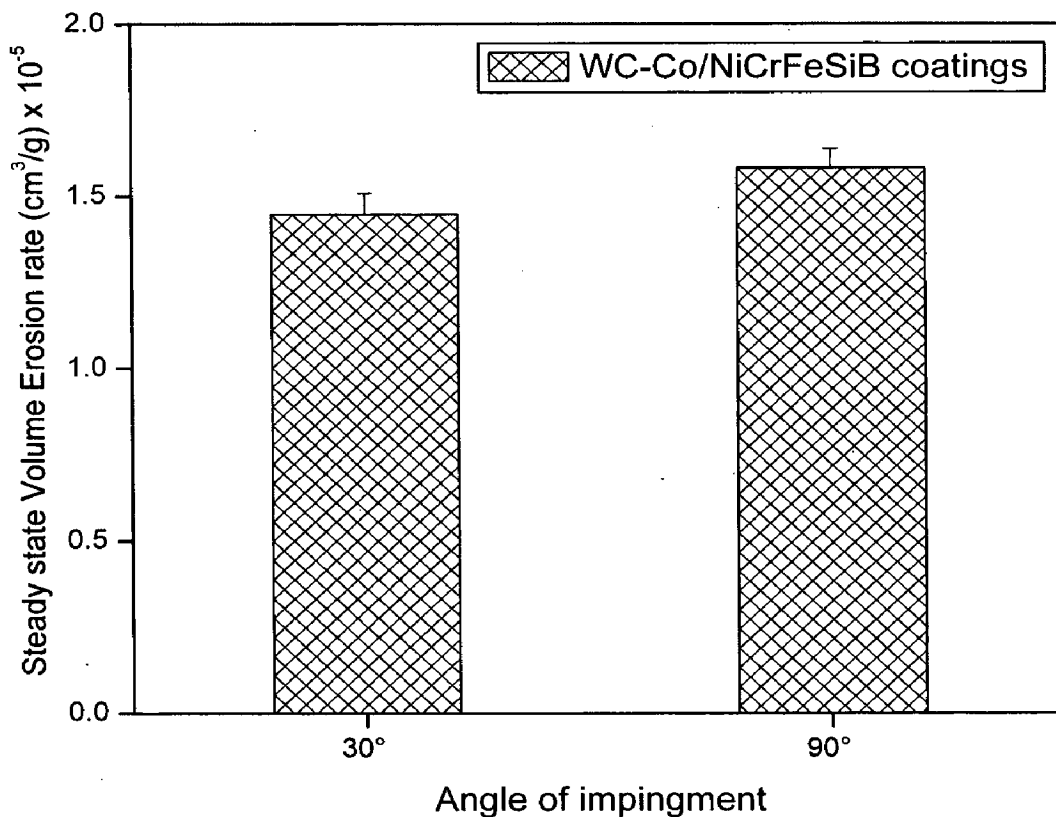
Fig.8.28   Histogram illustrating the steady state volume erosion rate of WC-Co/NiCrFeSiB coatings at different impact angles.

33.34% W	01.31% W
44.89% Ni	79.80% Ni
10.52% Cr	12.16% Cr
03.41% Fe	03.94% Fe
04.49% Si	02.14% Si
03.34% Co	

EDAX at point 1   EDAX at point 2
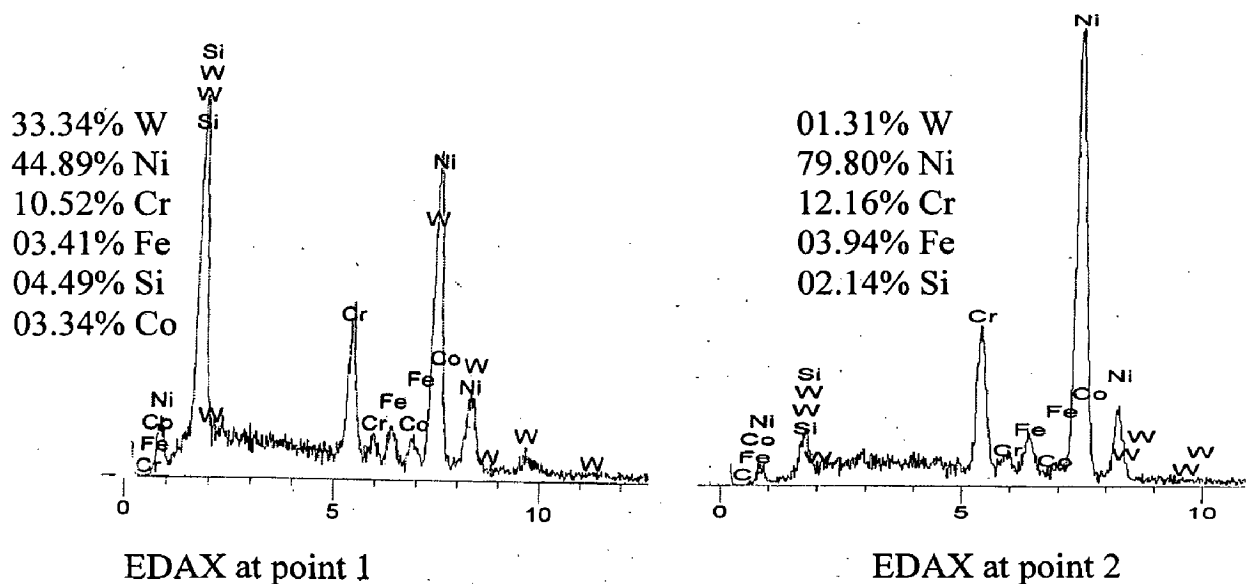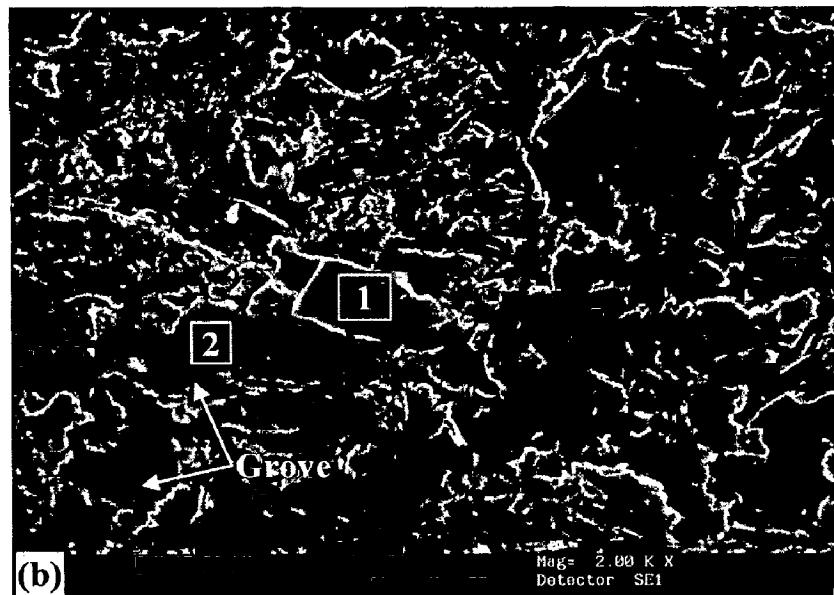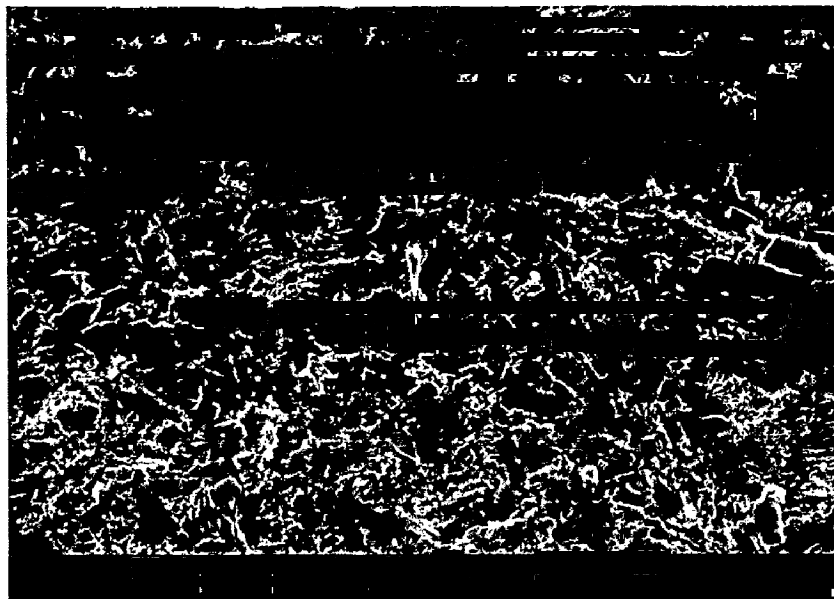
Fig.8.29   SEM micrographs showing the surface morphology and EDAX compositional analysis at some points on WC-Co/NiCrFeSiB coated steels eroded at 30° impact angle.
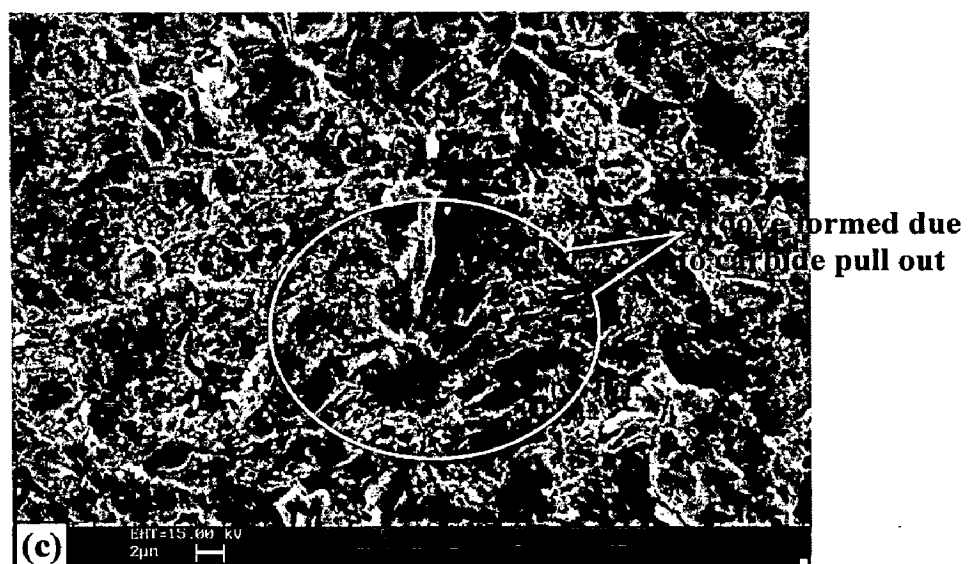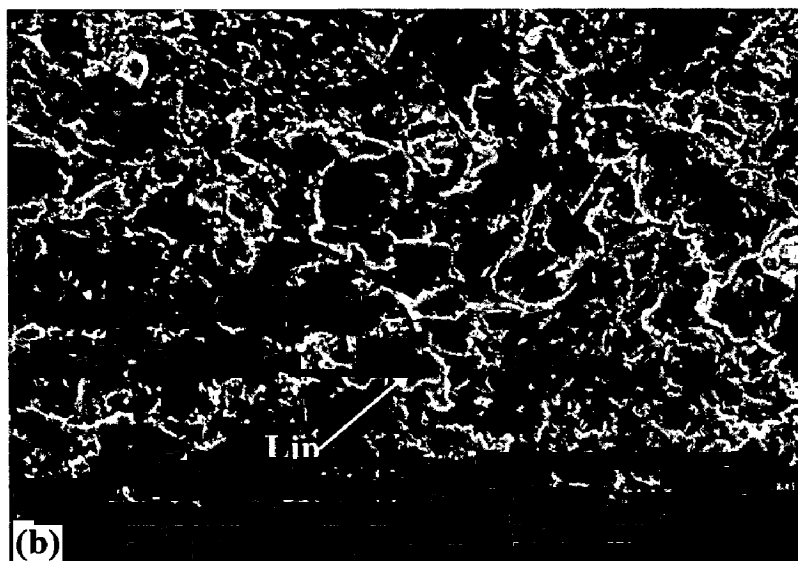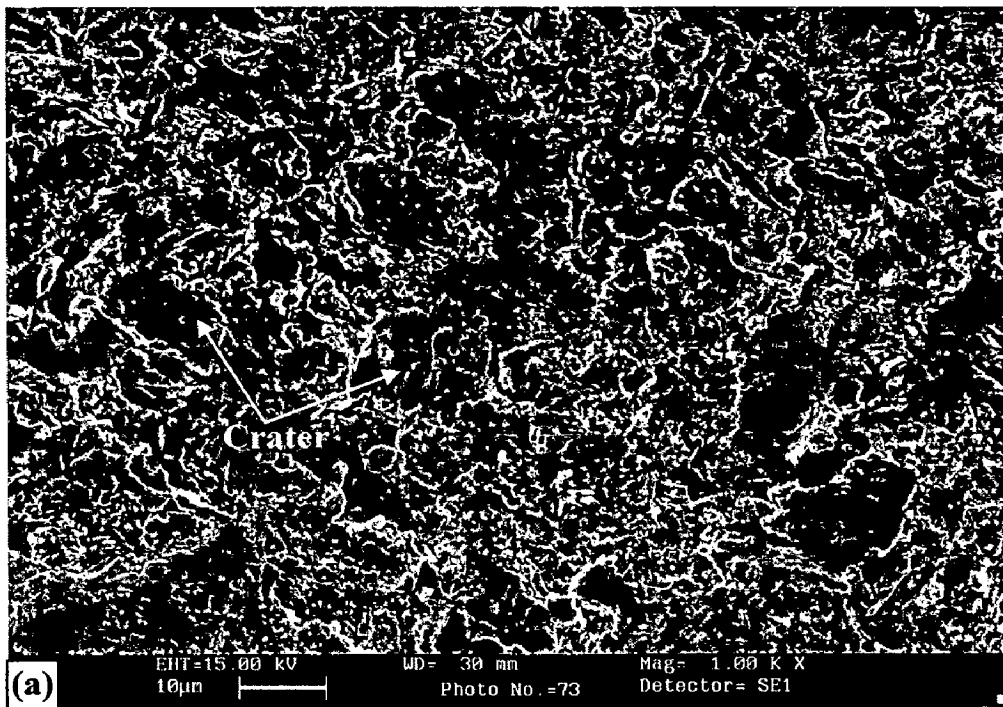
Fig.8.30 SEM micrographs showing the surface morphology of WC-Co/NiCrFeSiB coated steels eroded at 90° impact angle. Note crater and lips in (a) and (b) and groove formed due to carbide pull out in (c).

297

(a)
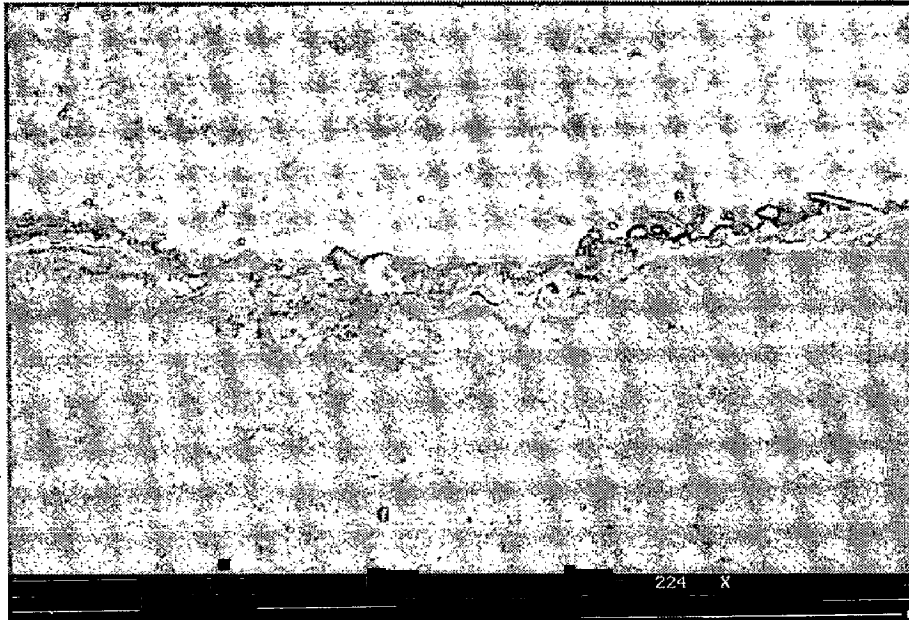
(b)

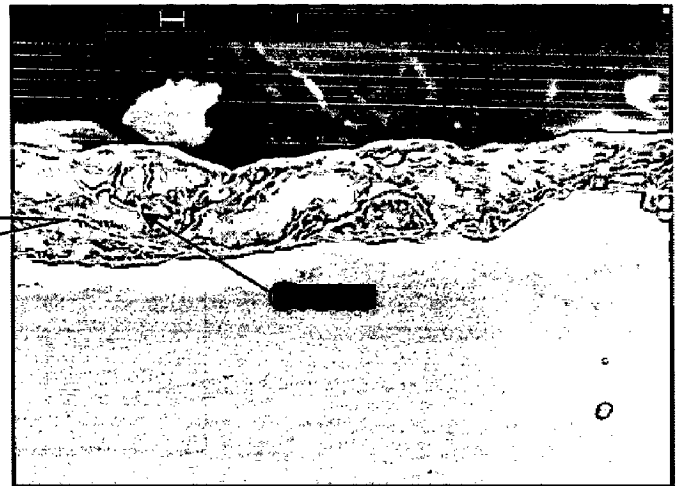**Fig.8.31**   SEM micrographs across the cross-section of the eroded region of WC-Co/NiCrFeSiB coatings.
(a) Eroded at 30° impact angle;
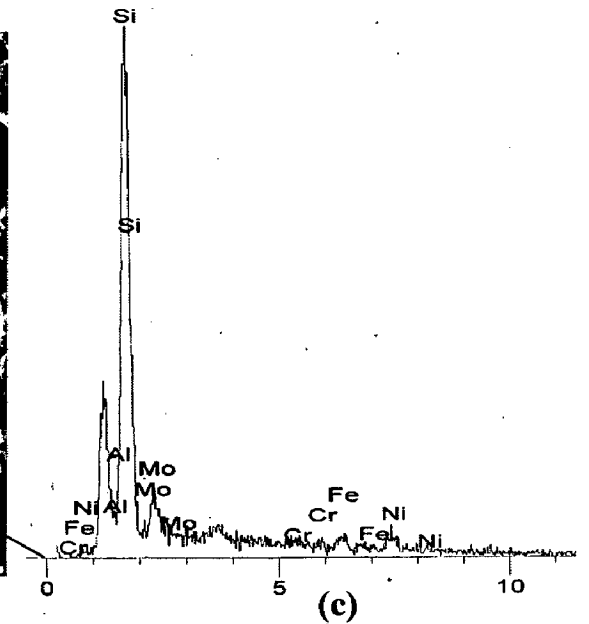(b) Eroded at 90° impact angle

(a)
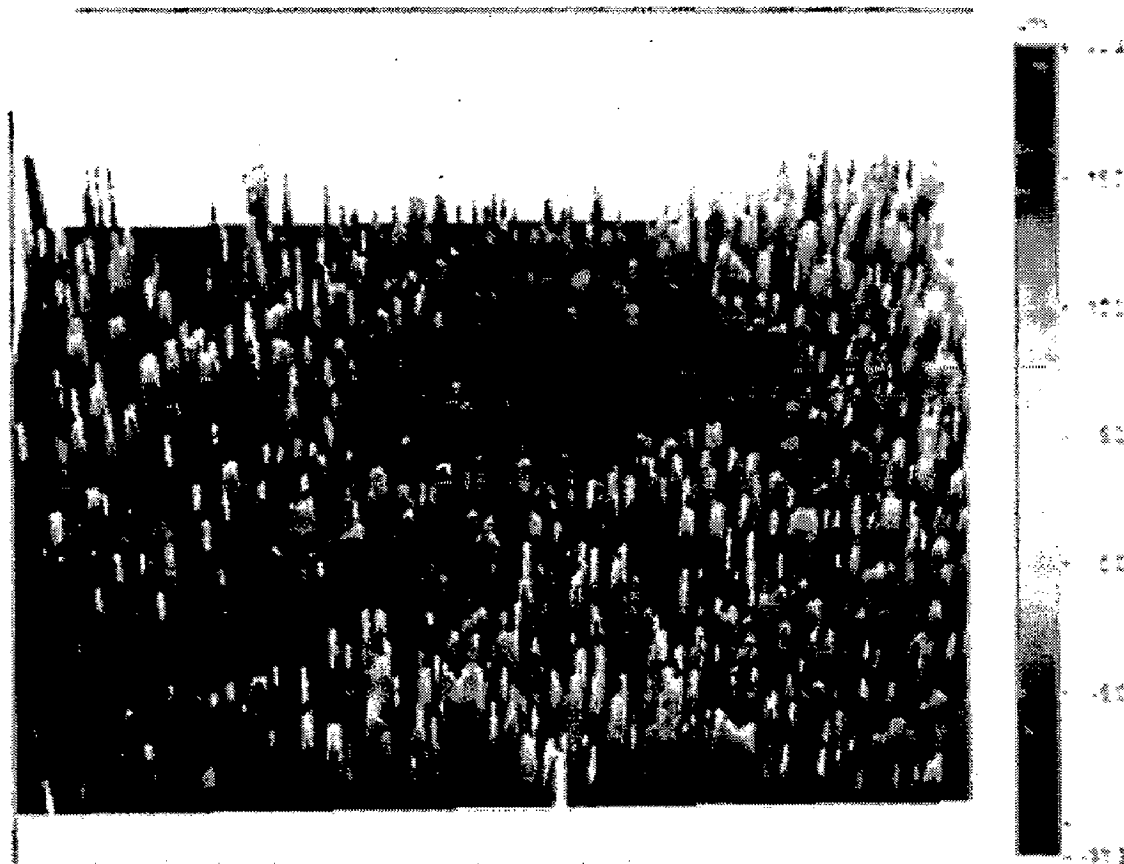
(b)

Fig.8.32   3D optical profile from the centre of an eroded WC-Co/NiCrFeSiB coating which shows depth profiles (Scanned area-591 X 449 μm) (a) Eroded at 30° impact angle; (b) Eroded at 90° impact angle

299

8.2   COMPARATIVE DISCUSSION

Bar chart indicating volumetric steady state erosion rate for uncoated and HVOF coated GrA1 steels at 30° and 90° impact angle is shown in Fig.8.33. From the bar chart it can be inferred that GrA1 steel exhibit lower steady state volume erosion rate in comparison to all the HVOF coatings under similar test conditions. This may be due to the embedment of silica particles in to the surface, which might bestow some shielding effect against impacting particles and leads to lower wear loss. The ratio of hardness of erodent particles (H_p) to the target hardness (H_t) is approximately 4.8, which cause the penetration of silica particles in to the target material. Hutchings, 1992 observed experimentally that abrasive particles of any shape will cause plastic scratching and indent the surface, if Hp/Ht>1.2. SEM micrographs on the surface of eroded GrA1 clearly show the embedment of sand particle and the wear mechanism essentially involves indentation induced severe plastic deformation. Further Mishra, (2006A) reported that relatively higher erosion loss of thermal sprayed coatings in comparison to bulk materials might be partially attributed to the presence of some porosity in the coating.GrA1 steel endure severe plastic deformation in the localized region around the points of impact of each particle in the form of lip and platelets and is detached, result in mass lass.

Relative erosion resistance of the various coating under study can be arranged in the following sequence:

WC-Co/NiCrFeSiB > NiCrFeSiB > NiCrAl > NiAlCrFeMo

Erosion rate of WC-Co/NiCrFeSiB coating is lower when compare to other coatings under study because of the composite ductile and brittle modes of material removal, although the brittle mode is dominant and the hardness ratio between the coating and the silica erodent. The coating shows brittle behavior as a function of impact angle where as the morphology of the eroded surface point out deep craters, groove formation in binder matrix characterized by lips at their rim suggesting strain localization, platelet formation and carbide particle pull out as the prevailing erosion mechanism. The grooves in the binder region act as failure initiating concentrators and small carbide grains crumble off uncrushed, where as the main mechanism of large grains failure is chipping. The wear resistance of NiCrFeSiB coatings found to be increased by adding refractory carbides.

The better erosion resistance of NiCrFeSiB coatings may be attributed to its higher ductility and homogeneous microstructure. The surface morphology of the eroded

surface shows that the plastic rupture of the metal by the silica particles resulted in highly deformed platelets which are displaced by subsequent impacts. Compositional analysis on the platelet shows relatively higher content of chromium. The predominant mechanism of material removal is ploughing and cutting which resulted in formation of platelets.

The eroded surface morphology of NiCrAl coating showed evidence of severe plastic deformation. The wider grooves resulted due to pullout of Ni rich unmelted particles are observed. The presence of indentation induced crack networks is an indicative of brittle fracture of some Ni-rich splats. The material removal occur from the lips formed on the bank of crater or on the particle exit end of the crater, under going repeated deformation and detached in the form of platelets. Although microscopic observation of surface layer suggests composite ductile-brittle behavior of this coating, the predominant erosion process is by plastic deformation and not fracture.

Higher erosion losses observed for NiAlCrFeMo coatings might be attributed to relatively higher porosity of the coatings. The embedment of silica particles into the open porosity are evident from the micrograph which resulted in deeper craters. The cross sectional view along the eroded region shows the crater associated with subsurface cracks which propagates along splat boundary probably due to presence of porosity and oxide interface. Smear craters surrounded by wider lips is an indicative of extensive plastic flow. Similar to NiCrAl coatings, deeper grooved formed as a result of pullout of Ni-rich unmelted particles are observed on the surface. Indentations, craters, and lips observed on the surface demonstrate the ductile erosion behavior of the coatings.

Fig.8.34 shows the effect of hardness on the erosion behavior of coatings. The compositions and hardness of the coatings do not relate directly with the erosion loss rates but their morphologies do (Levy 1988 and Shui et al. 1990). How ever at both 30° and 90° impingement, a general trend shows that the increase in hardness of HVOF coatings under study leads to an increase in their erosive wear resistance. The variation in the porosity contents of the coatings might have contributed to the variation in erosion rates of the different coatings. Relatively higher porosity with the NiAlCrFeMo coatings leads to lower erosion resistance. The porosity content of the coatings shows negative effect on the erosion resistance. Greater the porosity of the coating, the easier it is for the erodent particles to knock off pieces of exposed surface, and the greater is the removal rate (Levy 1988).
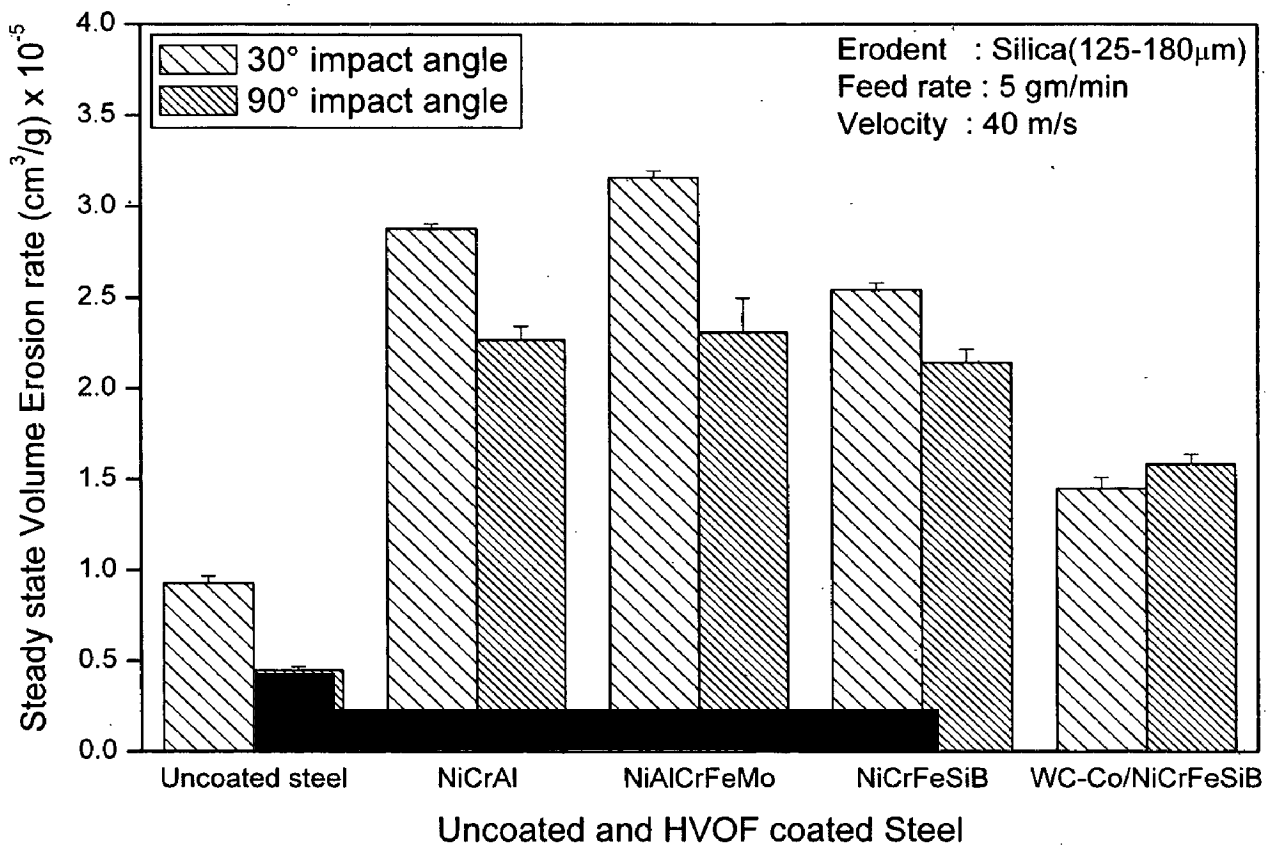
Fig.8.33 Bar chart indicating volumetric steady state erosion rate for uncoated and HVOF coated GrA1 steels at 30° and 90° impact angle
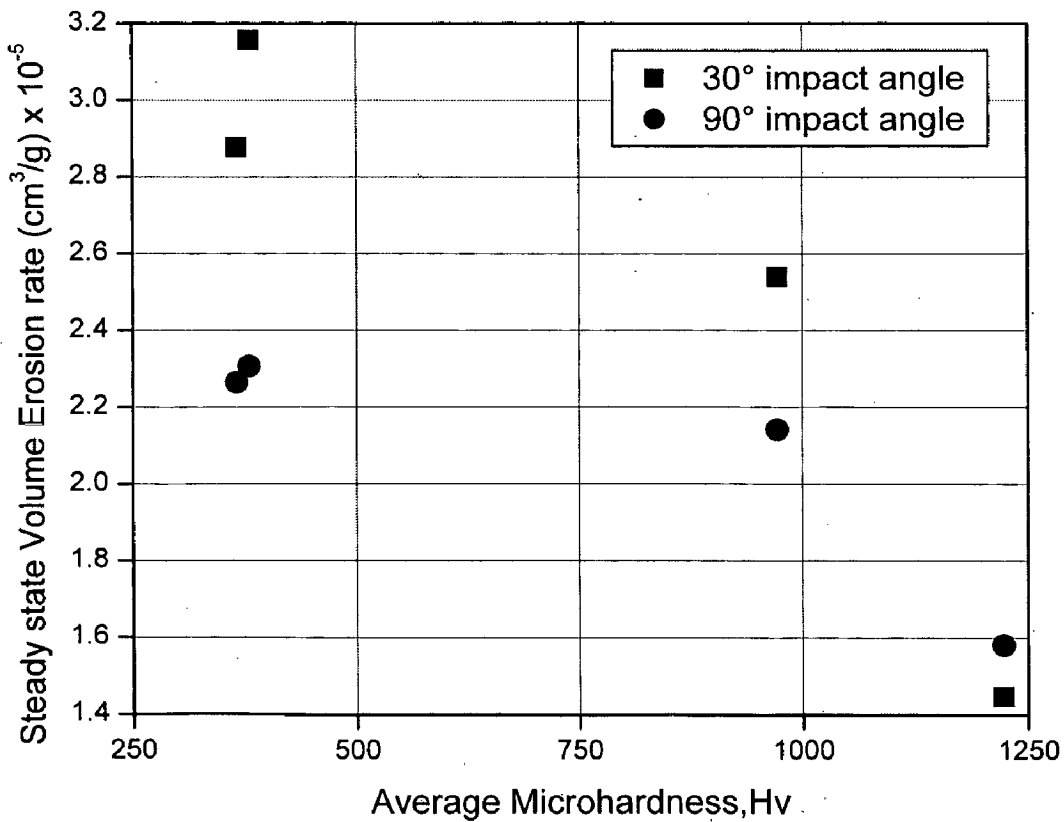
Fig.8.34 Correlation of Volumetric steady state erosion rate with coating hardness at 30° and 90° impact angle

The salient conclusions resulting from the present investigations are summarized as follows:

1) High velocity oxy-fuel thermal spraying with oxygen and liquid petroleum gas as the fuel gas has been used successfully to deposit NiCrAl, NiAlCrFeMo, NiCrFeSiB and WC-Co/NiCrFeSiB alloy coatings on boiler tube steels. LPG fuel gas is cheap and readily available as compared to other fuels used for HVOF spraying. Under the given spray parameters, seemingly dense laminar structured coating with thickness in the desired range of 260-295 μm and porosity less than 2 % has been achieved.

2) All the coatings have retained the phases observed in starting powder, containing nickel rich FCC structure as a principal phase and does not undergone significant phase transformation. NiCrAl and NiAlCrFeMo coatings show the formation of Ni-Al intermetallic compounds like $AlNi_3$ and Ni_2Al_3. In case of NiCrFeSiB coating, presence of CrSi and CrB phases indicates melting of powder during spraying to the extent of dissolution of borides and silicides in the liquid phase and confirms the formation of amorphous matrix. WC-Co/NiCrFeSiB coatings show retention of higher amount of WC in matrix with a minor amount of W_2C brittle phase. Oxidation, decomposition and decarburization of the coating powder are found to be negligible due to higher particle speed and chosen parameters during HVOF spraying.

3) The higher hardness value of 1223Hv obtained for WC-Co/NiCrFeSiB coatings is much higher than the hardness reported for similar coating by Miranda et al. 2001, Hawthorne et al. 1999 and Clark et al. 1999. This may be due to higher cohesive strength accompanied with lower porosity of the coating obtained by the optimum process parameter adopted for HVOF spraying in the present study. Microhardness of NiCrAl, NiAlCrFeMo and NiCrFeSiB coatings are 366Hv, 380Hv and 972Hv respectively with a standard deviation of less than 15.

4) Minor diffusion of nickel from coating in to the substrate and iron from substrate to coating has been observed across the coating-substrate interface. This suggests that

the adhesion between coating and substrate is due to combined mechanical interlocking and some metallurgical bonding effect.

OXIDATION STUDIES IN AIR

5) HVOF coated steels subjected to cyclic oxidation in air for 50 cycles at 900°C showed considerably lower weight gains than that of uncoated steels. All the uncoated steels suffered intense spalling of oxide scale.

6) Based on the thermogravimetric data, the relative oxidation resistance attained by the various coating under study can be arranged in the following sequence:

$$NiCrFeSiB > WC-Co/NiCrFeSiB > NiCrAl > NiAlCrFeMo$$

The oxidized coatings appeared to be compact and adherent. The substrate steels are not affected by the oxidizing environment. The oxidation kinetics of all the coated GrA1, T11 and T22 steels showed nearly parabolic behavior up to 50 cycles except for NiAlCrFeMo coated T22 steel, where it showed linear kinetics.

7) The superior performance of NiCrFeSiB coating can be attributed to continuous and protective thin oxide scale of amorphous glassy SiO_2 and Cr_2O_3 formed on the surface of the oxidized coatings. The coating region beneath this thin oxide scale remain unoxidised, hence it can be concluded that 4.3% Si content in the present coating may be considered as the critical concentration to maintain sufficient oxidation resistance.

8) Relatively higher oxidation resistance of WC-Co/NiCrFeSiB coated steels can be credited to oxides and spinels of Si, Cr and Co formed on surface. This protective oxide scale stabilized the formation of volatile tungsten oxide. The presence of the refractory tungsten as strengthener is quite necessary to maintain mechanical properties of the coating. Oxidation of the coating has been observed only at the outermost surface and rest of the coating remains unoxidised, which reflects the protective behavior of this coating.

9) The protection offered by NiCrAl coatings can be attributed to the oxide layer of α-Al_2O_3 and Cr_2O_3 formed on the outermost surface. α-Al_2O_3 is thermodynamically stable phase and showed slow scale growth kinetics during oxidation. The preferential oxidation of Al and Cr along the nickel rich splat boundary blocks the transport of oxygen into the coating through pores and voids, thereby making the oxidation rate to reach steady state.

10) Comparatively lower oxidation resistance of NiAlCrFeMo coated steels may be attributed, to some extent, to severe internal oxidation along the splat boundary due to higher porosity content. Oxidizing atmosphere penetrates in to the coatings through open porosity during the early stage of oxidation, until a continuous, stable protective scale formed on the surface. The protective oxide scale formed on the outermost surface mainly composed of oxides of nickel, chromium and aluminum and mixed spinel oxide $NiCr_2O_4$.

11) The corroded surface of NiCrAl and WC-Co/NiCrFeSiB coated T22 steels contains iron oxide protrusions. The probable cause of oozing out of iron oxide might be attributed to the presence of molybdenum in the T22 steel substrate. In case of NiAlCrFeMo coatings, these iron oxide protrusions have been observed in both T11 and T22 steels. These oxide protrusions are more pronounce in coated T22 steel (Mo-1.1%) in comparison to T11 steel (Mo-0.52%). The extent of oxide protrusions observed on the surface and the oxidation rate seems to be related to the Mo content in the base steel. In general coated GrA1 steels showed lower weight gain in comparison to coated T11 and T22 steels.

HOT CORROSION STUDIES IN Na₂SO₄-60%V₂O₅ SALT MIXTURE.

12) The cumulative weight gain for all the HVOF coated GrA1, T11 and T22 steels are significantly lower than that of uncoated steels subjected to hot corrosion in Na_2SO_4-60%V_2O_5 molten salt environment for 50 cycles at 900°C. Uncoated steels suffered a higher corrosion rate and intense spalling of oxide scale was observed. The main constituent of oxide scale formed on all the steels is iron oxide. The acidic fluxing of the oxides by the molten salt mixture resulted in massive, porous oxide scale. In case of T22 steel, dissolution of initially formed chromium oxide film on the surface might be responsible for higher corrosion rate.

13) Based on the thermogravimetric data, the relative oxidation resistance of the various coatings under study can be arranged in the following sequence:

NiCrFeSiB > NiCrAl > NiAlCrFeMo > WC-Co/NiCrFeSiB

All the coated steels exhibit characteristic thick protective oxide scale, composed of oxides and spinel oxides of the active elements of the coating and imparted resistance to the hot corrosion in the given molten salt environment. In general

305

weight gains observed for hot corrosion in molten salt environment is higher than that for oxidation in air.

14) Analogous to the oxidation studies in air, NiCrFeSiB coating showed superior hot corrosion resistance amongst all the coatings even in molten salt environment. The continuous film of SiO_2 on the uppermost surface promotes the formation of Cr_2O_3 sub-scale barrier layer. The coating region beneath this oxide scale remains unoxidised. The main reason for this good performance may be due to fact that V_2O_5 renders the Na_2SO_4 melt more acidic and in highly acidic melts SiO_2 scales have minimal solubility. All the three coated steels showed slow oxidation kinetics which indicated that the reaction rate is diffusion limited.

15) The oxide scale on the surface of corroded NiCrAl coatings mainly consists of oxides of Ni and Cr along with patches of blade like structured θ-Al_2O_3. Because of accelerated oxidation induced by the molten salt, which act as catalyst and oxygen carrier, metastable Al_2O_3 has formed in the initial cycles of studies and undergoes polymorphic transformation.

16) The lower hot corrosion resistance of NiAlCrFeMo coatings can be attributed to formation of nickel and chromium molybdates which are liquid at 900°C and induce formation of a highly friable and porous scale. The corrosion rate reduces once the available Mo at the surface has been consumed. Spalling of oxide scale in the form of tiny flakes has been observed. With the progress of oxidation, protective oxides of Ni, Cr and Al are formed at the subscale level.

17) In contrary to the oxidation studies in air, WC-Co/NiCrFeSiB coatings showed relatively lesser hot corrosion than NiCrAl and NiCrFeSiB coatings in molten salt environment. Preferential oxidation of W and Cr during the initial stage impedes the formation of continuous layer of SiO_2. Tungsten oxide decreases the oxide ion activity of the molten salt environment to cause acidic fluxing of the active elements in the coating. Acidic fluxing initiated at the tungsten rich particles in the coating and appeared as open bud shaped protrusion on the surface. Massive, porous and loosely held oxide scale mainly consists of oxides and spinels of Ni, Cr, Co and W and some metal vanadates.

18) Iron oxides protrusions are observed on the corroded surface of all the coated T22 steels except NiCrFeSiB coated steels. These protrusions lead to higher weight gains and rapid growth of inhomogeneous oxides. In general coated GrA1 steels showed lower weight gain in comparison to coated T11 and T22 steels.
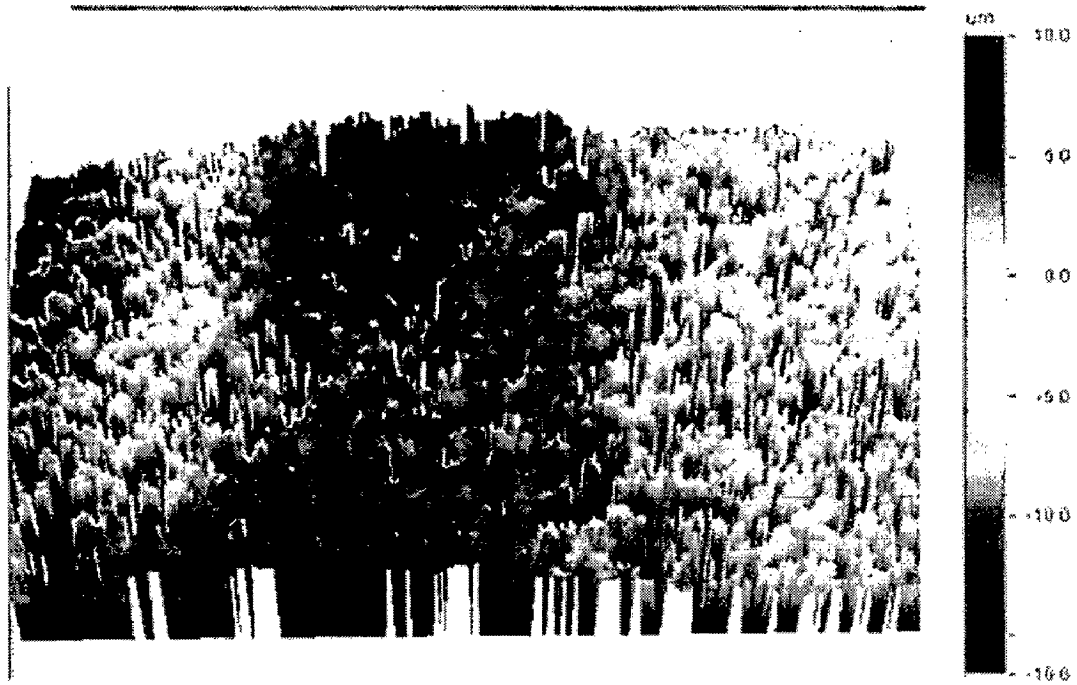
(a)
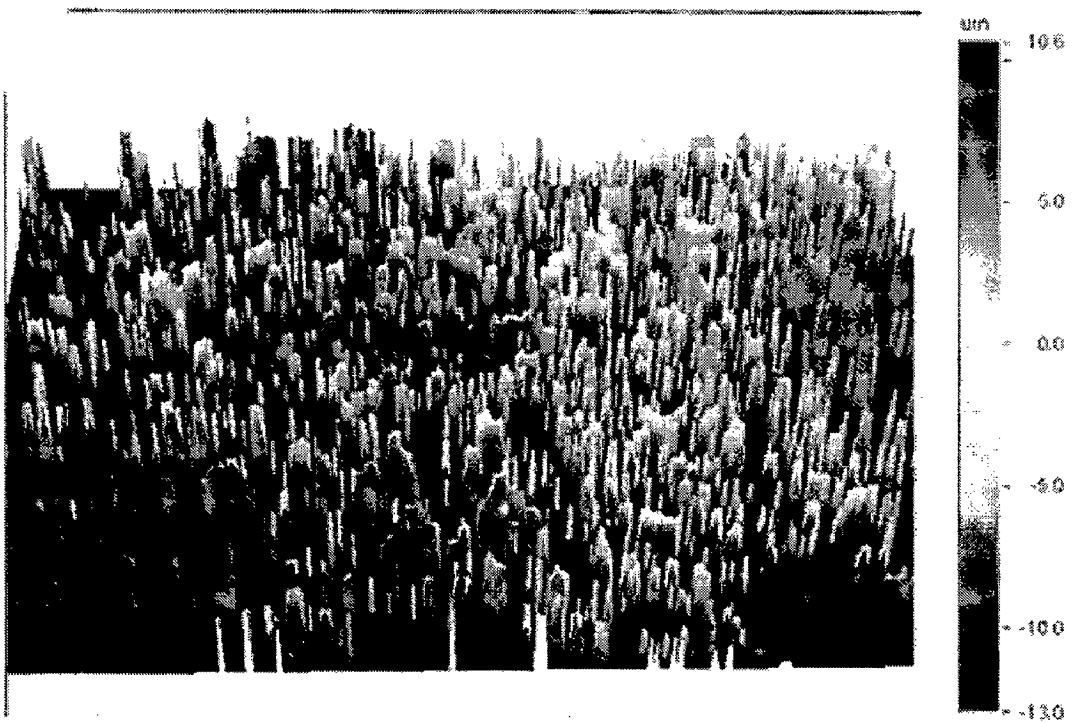
(b)

Fig.8.26 3D optical profile from the centre of an eroded NiCrFeSiB coating which shows depth profiles (Scanned area-591 X 449 μm)
(a) Eroded at 30° impact angle; (b) Eroded at 90° impact angle

EROSION-CORROSION STUDIES IN THE SUPERHEATER ZONE OF COAL FIRED BOILER

19) Condensed phases of ash deposits mainly oxides of Si, Al, Fe, Na, S and Ti are observed on the surface of exposed samples. These constituent have significant effect on erosion-corrosion behavior of uncoated and coated steels and can cause material wastage. Even though fly ash consists of very small particles, high velocity gas streams wear away or fused deposits on the surfaces, create the environment in which complex sulphates can form. XRD analysis confirmed the presence of sulphide deposits (FeS) in the corroded coating. The FeS has been identified as the promoter of sulphidation attack of metallic surfaces.

20) The weight gains observed for coated steels exposed to industrial environment are much lower than the weight gains observed in laboratory conditions (air and salt environment). The oxidation kinetics of all the coated steels showed perceptible deviation from the parabolic rate law, which may be attributed to fly ash erosion and rapid thermal cycling as a result of gas temperature variations in the actual plant. The falling off and the regeneration of the ash deposit and oxide scale are repeated.

21) Scale formed on uncoated GrA1 steel is highly porous and showed intense spalling. The selective oxidation of chromium in T11 and T22 steels produce bulk oxide scale, which resulted in a weight gain during the initial hours of exposure to boiler environment. In general all the uncoated steels suffered a weight loss. The thickness losses for uncoated steels are considerably higher in comparison to coated steels.

22) From a practical point of view, although 1000 hours of exposure to boiler environment is relatively short duration to extrapolate the obtained result to predict the coating performance in long term of service, the erosion corrosion behavior of all the HVOF sprayed coating is promising in comparison to substrate steels used in the present study.

23) Analogous to the observations in laboratory conditions, NiCrFeSiB coating shown superior hot corrosion resistance amongst all the coatings in the real coal fired boiler. Lower thickness loss from the surface has been observed and the degradation

rate is minimum. The protective oxides formed on the surface mainly consist of SiO_2, Cr_2O_3 and NiO.

24) The weight gains for WC-Co/NiCrFeSiB coated steels are almost equivalent to that of NiCrFeSiB coated steels. While minor cracks have been noticed at the subsurface that might have lead to slightly higher thickness loss in WC-Co/NiCrFeSiB coating relative to NiCrFeSiB. Both the coatings got oxidized only at the uppermost surface to form thin protective oxide scale and rest of the coatings remain unoxidised. Low porosity content (<0.5%) and rapid growth of protective oxides during the initial cycles lead to enhanced hot corrosion resistance of these coatings.

25) The better performance of NiCrAl coatings can be credited to thin protective oxide scale of α-Al_2O_3 and Cr_2O_3 formed on the surface. NiAlCrFeMo coatings showed lower resistance to erosion-corrosion when compared to other coatings under study. This might be associated with relatively higher porosity content in the coating. Preferential oxidation along the splat boundary has been observed in both NiCrAl and NiAlCrFeMo coatings. It is observed that the oxides formed at splat boundaries also determine the protection capability of the coating by blocking the open pores and voids, which are the path for the corrosive species to reach substrate.

26) Weight gains observed for HVOF coated GrAl, T11 and T22 steels are not very different and significant differences in erosion-corrosion behavior has not been observed among the different coated steels.

27) The splats observed in NiCrFeSiB and WC-Co/NiCrFeSiB coatings are very flat where as splats in NiCrAl and NiAlCrFeMo coatings are dense and less flattened. The flat splat structure increases the distance for the corrosive species to traverse from the coating surface to coating/substrate interface along splat boundaries and there by enhance hot corrosion resistance of the coatings.

SOLID PARTICLE EROSION STUDIES

28) Relative room temperature erosion resistance of the various coating under study can be arranged in the following sequence

WC-Co/NiCrFeSiB > NiCrFeSiB > NiCrAl > NiAlCrFeMo

29) The superior erosion resistance of WC-Co/NiCrFeSiB coating may be attributed to composite ductile and brittle modes of material removal, although brittle mode is

dominant and the greater hardness ratio between the coating and the silica erodent. The morphology of the eroded surface point out craters, groove formation in binder matrix, lips and platelet formation, and carbide particle pull-out as the prevailing erosion mechanism. The wear resistance of NiCrFeSiB coatings found to be improve by incorporation of refractory WC-Co particles.

30) The better erosion resistance of NiCrFeSiB coatings may be ascribed to its higher ductility and homogeneous microstructure. The predominant mechanism of material removal is ploughing and cutting which resulted in formation of platelets.

31) The main erosion mechanism in NiCrAl coating is by severe plastic deformation even though fracture of some Ni-rich splats is observed. Presence of unmelted particle in the coating microstructure might be leading to composite ductile-brittle behavior.

32) Higher erosion losses observed for NiAlCrFeMo coatings might be attributed to relatively higher porosity of the coatings. The embedment of silica particles into the open porosity are evident from the micrograph which resulted in deeper craters. Indentations, craters, and wider lips observed on the surface demonstrate the ductile erosion behavior of the coatings resulting from extensive plastic flow.

33) The variation in the porosity contents of the coatings might have partly contributed to the variation in erosion rates of the different coatings. The increase in porosity of the coatings shows negative effect on the erosion resistance.

34) Substrate GrA1 steel exhibit lower steady state volume erosion rate in comparison to all the HVOF coatings under similar test conditions. The higher hardness ratio between silica erodent particle and substrate steel might have caused the penetration of silica particles in to the surface which bestow some shielding effect against impacting particles leading to lower wear loss.

35) Based on the findings of the present study, NiCrFeSi coating shows superior performance in laboratory as well as in real coal fired boiler environment. In addition to applications in superheater zone of coal fired boilers, these coatings can be applied to other applications like fluidized bed combustors, industrial waste incinerators, internal combustion engines, gas turbine, steam turbines etc. The detailed study of properties of these coating and their behavior in various environments can be a guide to the end users to select appropriate coatings based on requirements.

SUGGESTIONS FOR FUTURE WORK

In light of the significant results observed in the present study, some of the recommendations for future work are as follows:

1. All the investigated coatings showed promising results in real as well as laboratory simulated boiler environment. The electrochemical corrosion behaviour of these coatings should be studied in reducing sulphur and chlorine containing environment.

2. The potential of these coatings should be explored in various salt mixtures relevant to other industrial applications.

3. Elevated temperature erosion behaviour of the coatings may also be investigated.

4. Attempts can be made to estimate the useful life of these coated steels by extrapolation of the laboratory data by mathematical modeling.

5. Relatively higher porosity content of NiAlCrFeMo coatings should be reduced, so as to further enhance the corrosion and erosion resistance. In this regard effect of post coating treatments such as laser remelting, furnace heat treatment and ion beam treatment should be explored.

6. Hot stage microscopy may be used to understand the development of the scale as well as mechanism of transport of species during the oxidation and hot corrosion runs.

RESEARCH PAPERS PRESENTED

1) Ramesh M.R., Nath S.K., Prakash S. (2006), Deposition and Characterization of HVOF Sprayed NiCrFeSiB Coatings on Boiler Steels, (2006),International symposium for Research Scholars on Metallurgy, Materials Science and Engineering, Dec 18-20,held at Department of Metallurgical and Materials Engineering, Indian Institute of Technology Madras,pp.154-162.

2) Ramesh M.R., Nath S.K., Prakash S., (2006)," Processing and Characterization of HVOF Sprayed NiCrAI Coatings", First International & 22nd All India Manufacturing Technology Design & Research Conference (22nd AIMTDR), 21st - 23rd December, IIT Roorkee, pp-210.

3) Ramesh M.R., S.K.Nath, S.Prakash, (2005)"HVOF Coatings for Boiler Tube Protection Against Coal Ash Corrosion and Erosion" Abstract published in International journal of Minerals, Metals and Materials Engineering,Vol.58,No.5,pp69.(Also presented at NMD-ATM conference, IIT Madras).

4) Ramesh, M.R.., Nath, S. K., and Prakash, S., (2005) "High Temperature Corrosion and Erosion Resistant Coatings", Published in the proceedings of MetaVista-2005 symposium (16"-18'" Feb.), held at Department of ~ Metallurgical Engineering, Institute of Engineering & Technology, Pune,pp.14.

REFERENCES

1. **Aalamialeagha, M.E.**, Harris, S.J., Emamighomi, M., (2003), "Influence of the HVOF spraying process on the microstructure and corrosion behavior of Ni-20%Cr coatings," Journal of Materials Science, Vol. 38, pp. 4587 – 4596.

2. **Agarwal, D.C.**, Herda, W.R. and Brill, U., (1995), "Nickel alloys combat high-temperature corrosion," Adv. Mater. Process, Vol. 148, pp. 42.

3. **Ahila, S.**, Ramakrishna Iyer and Radhakrishnan, V.M., (1994), "Measurement of Hot Corrosion of 2.25 Cr-1 Mo steel-347H steel Welded joint in K2SO4-NaCl mixture," Materials Letters, Vol. 18, pp. 243-245.

4. **Ahila, S.**, Ramakrishna Iyer, Radhakrishnan, V.M. and Prasad P.B.S.N.V., (1993), "A Comparative Study of Hot Corrosion of Welded and Unwelded 2.25 Cr-1Mo Steel," Materials Letters, Vol. 16, pp. 130-133.

5. **Ajdelsztajn, L.**, Picas, J.A., Kim, G.E., Bastian, F.L., Schoenung, J. and Provenzano, V, (2002), "Oxidation behavior of HVOF sprayed nanocrystalline NiCrAlY powder," Materials Science and Engineering A, Vol. 338, pp. 33-43.

6. **Ak, N.F.**, Tekmen, C., Ozdemir, I., Soykan, H.S.and Celik, E. (2003), "NiCr coatings on stainless steel by HVOF technique," Surface and Coatings Technology. Vol. 173 – 174, p. 1070–1073.

7. **ASM Handbook**, (2001), "Properties and Selection: Irons, steels and high performance alloys," Vol. 1, ASM Publication, Materials park, Ohio.

8. **ASM Handbook**, (1992), Volume 13, Corrosion.

9. **Bellman, R.**, and Levy, A., (1981), "Erosion mechanism in ductile metals," Wear, Vol.70, pp. 1-27.

10. **Belzunce, F.J.**, Higuera, V., and Poveda, S., (2001), "High temperature oxidation of HFPD thermal-sprayed MCrAlY coatings," Materials Science and Engineering A, Vol. 297, pp. 162-167.

11. **Berger, L.**, Vuoristo, P., Mantyla, T., and Gruner, W.,(1998), "A study of oxidation behaviour of WC–Co, Cr_3C_2–NiCr and TiC–Ni-based materials in thermal spray processes," Proc. 15th Int. Thermal Spray Conference, Nice ,France, pp. 75–82.

12. **Birks, N.** and Meier, G.H., (1983), "Introduction to High Temperature Oxidation of Metals," 1st Ed., London: Edward Arnold Ltd.

13. **Bitter, J.G.A.,** (1963A), "A Study of Erosion Phenomena," Part I, Wear, Vol. 6, pp. 5-21.

14. **Bitter, J.G.A.,** (1963B), "A Study of Erosion Phenomena," Part I, Wear, Vol. 6, pp. 169-190.

15. **Bluni, S.T.** and Marder, A.R., (1996), "Effect of thermal spray coating composition and microstructure on coating response and substrate protection at high temperatures," Corrosion, Vol. 52, No.3, pp. 213-218.

16. **Bornstein, N.S.,** DeCrescente, M.A. and Roth, H.A., (1973), "The Relationship Between Relative Oxide Ion Content of Na_2SO_4, the Presence of Liquid Metal Oxides and Sulfidation Attack," Metall. Trans., Vol. 4, pp. 1799-1810.

17. **Bornstein, N. S.,** DeCrescente, M. A. and Roth, H. A., (1975), "Effect of Vanadium and Sodium Compounds on the Accelerated Oxidation of Nickel Base Alloys," Proc. of Conf. on Gas Turbine Mater. in the Marine Environment, MMIC-75-27, Columbus, Ohio, USA, pp. 115-60.

18. **Bornstein, N.S.** and DeCrescente, M.A., (1969), "The relationship between compounds of sodium and sulfur and sulfidation," Trans. TMS-AIME, Vol. 242, pp. 1947-1952.

19. **Boudi, A.A.,** Hashmi, M. S.J. and Yilbas, B.S.,(2004), "HVOF coating of Inconel 625 onto stainless and carbon steel surfaces: corrosion and bond testing," Journal of Materials Processing Technology, Vol. 155-156, pp. 2051-2055

20. **Brandl, W.,** Toma, D. and Grabke, H. J., (1998), "The characteristics of alumina scales formed on HVOF-sprayed MCrAlY coatings," Surface and Coatings Technology, Vol. 108-109, pp. 10-15.

21. **Brown, R.,** Jun, E.J. and Edington, J.W.,(1981), "Mechanisms of solid particle erosive wear for 90° impact on copper and iron," Wear, Vol. 74, pp. 143-156.

22. **Buecker Brad,** (2002), "Basics of Boiler and HRSG Design,"Penn Well publications, Oklahoma.

23. **Bunshah, R.F.,** (1994), "Hand Book of Deposition Technologies for Films and Coatings," William Andrew Publishers.

24. **Bunshah, R.F.**, (2001), "Hand Book of Hard Coatings," William Andrew Publishers.

25. **Chatterjee,** U.K., Bose, S.K. and Roy, S.K., (2001), "Environmental Degradation of Metals," Marcel Dekker Publications, New York.

26. **Chou, S.F.,** Daniel, P.L., Blazewicz, A.J., and Dudek, R.F., (1986), "Hydrogen Sulfide Corrosion In Low-NoX Combustion Systems," Journal Mater. Energy Syst., Vol. 7, pp. 361.

27. **Clark H.McI,** Hawthorne H.M. and Xie Y., (1999), "Wear rates and specific energies of some ceramic, cermet and metallic coatings determined in the Coriolis erosiontester," Wear, Vol. 233-235, pp. 319-327.

28. **Cutler, A.J.B.,** (1971), "The Effect of Oxygen and SO3 on Corrosion of Steels in Molten Sulphates," Journal Appl. Electrochem, Vol. 1, pp. 19-26.

29. **Davis, J.R.,** (2001), "Surface engineering for corrosion and wear resistance," ASM International.

30. **Deb, D.,** Ramakrishna Iyer, S., and Radhakrishnan, V.M.,(1996), "Assessment of high temperature performance of a cast nickel base superalloy in corrosive environment," Scripta Materialia, Vol. 35, pp. 947-952.

31. **Deng Xiaohua ,** Ping Wei, M. Reza Bateni, Anthony Petric,(2006), "Cobalt plating of high temperature stainless steel interconnects," Journal of Power Sources, Vol. 160, pp 1225–1229.

32. **Dent,A.H.,** Horlock A.J., McCartney D.G. and Harris S.J.,(2001) "Microstructural characterisation of a Ni-Cr-B-C based alloy coating produced by high velocity oxy-fuel thermal spraying," Surface and Coatings Technology, Vol. 139, pp 244-250.

33. **Douglass, D. L.,** Nanni, P., Asmundis, C. and Bottino, C.,(1987), "The transition from internal oxidation to continuous-film formation during oxidation of dilute Ni-Si alloys," Oxidation of Metals, Vol. 28, pp. 309.

34. **Doychak, J.,** (1995), "Ch. 43: Oxidation Behaviour of High-Temperature Intermetallics," in 'Intermetallic Compounds, Principles and Practice, Vol. 1-Principles,' Eds. Westbrook, J.H. and Fleischer, F.L., Pub. John Wiley & Sons Ltd., England.

35. **Edris,H.**, Mccartney, D. G. and Sturgeon, A. J., (1997), "Microstructural characterization of high velocity oxy-fuel sprayed coatings of Inconel 625," Journal of Materials Science, Vol. 32, Issues 4, pp. 863 – 872.

36. **Eigena, N.**, Gartner, F., Klassen, T., Aust, E., Bormann, R. and Kreye, V., (2005). "Microstructures and properties of nanostructured thermal sprayed Coatings using high-energy milled cermet powders," Surface & Coatings Technology, Vol. 195, pp. 344– 357.

37. **Eliaz, N.**, Shemesh, G. and Latanision, R.M., (2002), "Hot Corrosion in Gas Turbine Components," Eng. Fail. Anal., Vol. 9, pp. 31-43.

38. **Elliott, P.** and Taylor, T.J., (1977), "Some aspects of silicon coatings under vanadic attack." Proc. Conf. on Materials and Coatings to Resist High Temperature Corrosion, Düsseldorf, Applied Science, London, pp. 353.

39. **Espevik, S.**, Rapp, R.A., Daniel, P.L. and Hirth, J.P., (1980), "Oxidation of Ni-Cr-W Ternary Alloys," Oxidation of Metals, Vol. 14, No. 2, pp. 85.

40. **Evans, H. E.** and Taylor, M. P., (2001), "Diffusion Cells and Chemical Failure of MCrAlY Bond Coats in Thermal-Barrier Coating Systems," Oxid. Met., Vol. 55, No. 1-2, pp. 17-34.

41. **Fagoaga, I.**, Viviente, J. L., Gavin, P., Bronte, J. M., Garcia, J. and Tagle, J.A., (1998), "Multilayer coatings by continuous detonation system spray technique," Thin Solid Films, Vol. 317, pp. 259-265.

42. **Feng, Z.** and Ball, A., (1999), "The erosion of four materials using seven erodents — towards an understanding," Wear, Volumes 233-235, pp. 674-684.

43. **Finnie, I.**, (1958), "The mechanism of erosion of ductile metals," Proceedings of the Third U.S. National Congress of Applied Mechanics, pp. 527–532.

44. **Finnie, I.** (1960), "Erosion of surfaces by solid particles, Wear 3, pp. 87–103.

45. **Fitzer, E.**, Nowak, W., and Mäurer, H.J., (1978), "Properties of Silicon-Based Protective Coatings for Nickel Alloys," Arch. Eisenhüttenwes, Vol. 49, pp. 211.

46. **Frankel, H.E.**, and Dapkunas, S.J., (1977), "The Necessity for Coatings in Fossil Energy Conversion Systems," Thin Solid Films, Vol. 45, pp. 211-234.

47. **French, David N.** (1983), "Metallurgical Failures in Fossil Fired Boilers," A Wiley-Interscience Publication, Singapore.

315

48. **Fryburg, G. C.,** Kohl, F. J., Stearns, C. A. and Fielder, W. L., (1982), "Chemical Reactions Involved in the Initiation of Hot Corrosion of B-1900 and NASA-TRW VIA," J. Electrochem. Soc., Vol. 129, No. 3, pp. 571-85.

49. **Fukuda, Y.** and Kumon, M., (1995), "Application of High Velocity Flame Sprayings for the Heat Exchanger Tubes in Coal Fired Boilers," Proceedings of ITSC, Kobe, pp. 107.

50. **Godoy, C.,** Lima, M.M., Castro, M.M.R. and Avelar-Batista, J.C.,(2004), "Structural changes in high-velocity oxy-fuel thermally sprayed WC–Co coatings for improved corrosion resistance," Surface and Coatings Technology, Vol. 188-189, pp. 1-6 .

51. **Goebel, J. A.,** Pettit, F. S. and Goward, G. W., (1973), "Mechanisms for the Hot Corrosion of Nickel-Base Alloys," Metall. Trans., Vol. 4, pp. 261-275.

52. **Goebel, J. A.** and Pettit, F. S., (1970B), "The Influence of Sulphides on the Oxidation Behaviour of Nickel-base Alloys," Metall Trans, Vol. 1, pp. 3421-3429.

53. **Goebel, J. A.** and Pettit, F. S., (1970A), "Na_2SO_4 - Induced Accelerated Oxidation (Hot Corrosion) of Nickel," Metall. Trans., Vol. 1, pp. 1943-1954.

54. **Goward, G.W.,** (1986), "Protective coatings - purpose, role and design," Materials Science and Technology, Vol. 2, pp. 194-200.

55. **Grünling, H. W.** and R. Bauer, R., (1982), "The role of silicon in corrosion-resistant high temperature coatings," Thin Solid Films, Vol. 95, pp. 3-20.

56. **Guofeng** Chen and Hanyi Lou.(1999), "Oxidation behavior of sputtered Ni-3Cr-20Al nanocrystalline coating," Materials Science and Engineering A, Vol. 271, pp. 360-365.

57. **Gurrappa, I.,** (1999), "Hot Corrosion Behaviour of CM 247 LC Alloy on Na_2SO_4 and NaCl Environments," Oxidation of Metals, Vol. 51, pp. 353.

58. **Gurrappa I.,** (2003), "Influence of alloying elements on hot corrosion of superalloys and coatings: necessity of smart coatings for gas turbine engines," Materials Science and Tech., Vol. 19, pp. 178-183.

59. **Harb.J.N.** and Smith, E.E., (1990), "Fireside Corrosion in PC-Fired Boilers," Prog. Energy Combust. Sci., Vol. 16, pp. 169-190.

60. Hawthorne,H.M.,Arsenault,B., Immarigeon,J.P., Legoux J.G. and Parameswaran V.R.,(1999), "Comparison of slurry and dry erosion behaviour of some HVOF thermal sprayed coatings," Wear, Vol. 225-229,Part2, pp. 825-834.

61. Hearley, J. A., Little, J.A., and Sturgeon,A.J.,(1999), "The erosion behaviour of NiAl intermetallic coatings produced by high velocity oxy-fuel thermal spraying," Wear, Vol. 233-235, pp. 328-333.

62. Heath, G. R., Heimgartner, P., Irons, G., Miller, R. and Gustafson, S., (1997), "An Assessment of Thermal Spray Coating Technologies for High Temperature Corrosion Protection," Mater. Sci. Forum, Vol. 251-54, pp. 809-16.

63. Hidalgo, H.V., Belzunce Varela, J., Carriles Menéndez, A. and Poveda Martínez, S., (2001A), "High temperature erosion wear of flame and plasma-sprayed nickel–chromium coatings under simulated coal-fired boiler atmospheres," Wear, Vol. 247, pp. 214-222.

64. Hidalgo, H.V., Varela, F.J.B., Menéndez, A.C., and Martínez, S.P., (2002), "Influence of the thermal-spray procedure on the properties of a nickel-chromium coating," Journal of Materials Science, Vol. 37, pp. 649-654.

65. Hidalgo,H.V., Varela, F.J.B., Menéndez,A.C., and Martínez,S.P., (2001B), "A comparative study of high-temperature erosion wear of plasma-sprayed NiCrBSiFe and WC–NiCrBSiFe coatings under simulated coal-fired boiler conditions," Tribology International, Vol. 34, pp.161-169.

66. Hocking, M. G., (1993), "Coatings Resistant to Erosive/Corrosive and Severe Environments," Surf. Coat. Technol., Vol. 62, pp. 460-66.

67. Hoop, P.J. and Allen, C., (1999), "The High Temperature Erosion of Commercial Thermally Sprayed Metallic and Cermet Coatings by Solid Particles," Wear, Vol. 233-235, pp. 334-341.

68. Huo,X., Zhang,J.S., Wang,B.L., Wu,F.J. and Han,Y.F.,(1999), "Evaluation of NiCrAlYSi overlay coating on Ni_3Al based alloy IC-6 after an engine test," Surface and Coatings Technology, Vol. 114, pp. 174-180.

69. Hurricks, P. L., (1972), "Some aspects of the metallurgy and wear resistance of surface coatings," Wear, Vol. 22, pp. 291-320.

70. **Hussainova, I.**, Kübarsepp, J., and Shcheglov, I., (1999), "Investigation of impact of solid particles against hard metal and cermet targets," Tribology International, Vol. 32, pp. 337-344.

71. **Hutchings, I.M.**, (1992), Tribology: Friction and Wear of Engineering Materials, Edward Arnold Publication.

72. **Hutchings, I.M.**, in Edler, W.F. (Ed.), (1979), Erosion: Prevention and Useful Applications, ASTM Sp. Tech. Pub., Vol. 664, pp. 59-76.

73. **Hutchings, I.M.** and Winter, R.E., (1974), "Particle Erosion of Ductile Metals: A Mechanism of Material Removal," Wear, Vol. 27, pp. 121-128.

74. **Hwang, Y. S.** and Rapp, R. A., (1989), "Thermochemistry and Solubilities of Oxides in Sodium Sulfate-Vanadate Solutions," Corrosion, Vol. 45, pp. 933-937.

75. **Kawahara, V.**, (1997), "Development and application of high-temperature corrosion-resistant materials and coatings for advanced waste-to-energy plants," Materials at High Temperatures, Vol. 14, pp. 261.

76. **Kawahara Y**, Orita N, Nakamura M, Ayukawa S, Hosoda T (1999) "Application of new corrosion resistant superheater tubings for a 5001C, 100 kgf/cm^{2}g high efficiency waste-to-energy plant," In:Corrosion 1999, San Antonio, TX, USA, 25-30 Houston, TX, USA, NACE International, paper 91, pp. 19.

77. **Kbaschewshki, O.**, and Hopkins, B.E., (1967), "Oxidation of Metals and Alloys," 2nd ed., London: Butterworths.

78. **Kerr, T.W.**, (1975), "Hot corrosion and oxidation studies of pure nickel and Ni-Cr, Ni-Si and Ni-Cr-Si alloys at 1000 °C. In: Rep. AD-A024, U.S. Department of Commerce (1975), pp. 708.

79. **Khajavi, M. R.**, and Shariat, M. H., (2004), "Failure of first stage gas turbine blades," Engineering Failure Analysis, Vol. 11, pp. 589-597.

80. **Khanna, A.S.** and Gnanamoorthy, J., B., (1982), "Post breakaway oxidation kinetics of two ferritic steels," Oxidation of Metals, Vol. 18, pp. 315-331.

81. **Khanna, A. S.** and Jha, S. K., (1998), "Degradation of Materials Under Hot Corrosion Conditions," Trans. Indian Inst. Met., Vol. 51, No. 5, pp. 279-90.

82. **Kim Hyung-Jun**, Hwang Soon-Young, Lee Chang-Hee and Juvanon Philippe,(2003), "Assessment of wear performance of flame sprayed and fused Ni-based coatings," Surface and Coatings Technology, Vol.172, pp. 262-269 .

83. **Kofstad**, P. (1966), "Chapter 1": General Introduction in 'High Temperature Oxidation of Metals,' John Wiley & Sons Inc. USA.

84. **Kofstad**, P., (1988), "Chapter 14" in 'High Temperature Corrosion,' Elsevier Applied Science, London & New York, pp. 465.

85. **Koger, J. W.**,(1987), "Fundamentals of High-Temperature Corrosion in Molten Salts," in Metals Handbook: Corrosion, Metals Park, ASM International, pp. 50–55.

86. **Kolta, G. A.**, Hewaidy, L. F. and Felix, N. S., (1972), "Reactions between Sodium Sulphate and Vanadium Pentoxide," Thermochim. Acta, Vol. 4, pp. 151-164.

87. **Kosel, T.H.**, (1992), "Solid particle erosion, in: Friction," in: Lubrication and Wear Technology, ASM Handbook, Vol. 18, pp. 199-213.

88. **Kulu, P.**, Hussainova, I. and Veinthal, R., (2005), "Solid particle erosion of thermal sprayed coatings," Wear, Vol. 258, pp. 488-496.

89. **Kulu, P.** and Pihl, T., (2002), "Selection criteria for wear Resistance Powder Coatings under Extreme Erosive Wear Conditions," Vol. 11, pp. 517.

90. **Kumar, S.**, Subramanya Sarma, V.,and Murty,B.S.,(2008), "A statistical analysis on erosion wear behaviour of A356 alloy reinforced with in situ formed TiB_2 particles," Materials Science and Engineering: A, Vol. 476, pp. 333-340.

91. **Lai, G.Y.**, (1990), "High-Temperature Corrosion of Engineering Alloys," ASM International, Materials Park, OH, pp. 230.

92. **Lambert, P.**, Champagne, B., Arseneault, B., (1991),"Oxidation and hot corrosion in Na2SO4-10%V2O5 of Ni-17Cr-6Al-0.5Y and Ni-16Cr-5.7Al-0.47Y-5Si MCrAlY alloys at 700°C,"Vol. 30, pp. 125-130.

93. **Lathabai, S.**, Ottmüller, M. and Fernandez, I., (1998), "Solid particle erosion behaviour of thermal sprayed ceramic, metallic and polymer coatings," Wear, Vol. 221, pp. 93-108.

94. **Lee,D.B.**, Ko,J.H. and Kwon,S.C.,(2005), "Oxidation of Ni–W coatings at 700 and 800 °C in air," Surface and Coatings Technology, Vol. 193, pp. 292-296.

95. **Levi, T.R.,** Lichti, K.A., and Tack, A.J.,(2001), "Corrosion performance of types 310S and 410 stainless steels in forming gas containing 1% H_2S or 1% $H_2S/1\%$ HCl at 600°C," Mater. High Temp., Vol. 18, pp. 65.

96. **Levy, A.V.,** Aghazadeh, M. and Hickey, G., (1984), "The effect of test variables on the platelet mechanism of erosion," Rep. LBL-17835, Lawrence Berkeley Laboratory, University of California, Berkeley, CA, U.S.A.

97. **Levy, A.,** (1983A), "Erosion Mechanism in Ductile and Brittle Materials," Proc. Of 6th Int. Con. On Erosion by Liquid and Solid Impact, Sept.5-8, Cavendish Laboratory, Cambridge.

98. **Levy, A.,** (1986A), "The platelet Mechanism of Erosion of Ductile Metals," Wear, Vol. 108, pp. 1-21.

99. **Levy, A.V.,** (1988), "The erosion-corrosion behavior of protective coatings," Surface and Coatings Technology, Vol. 36, pp. 387-406.

100. **Levy, A. V.,** (1993), "The Erosion-Corrosion of Tubing Steels in Combustion Boiler Environments," Corros. Sci., Vol. 35, No. 5-8, pp. 1035-43.

101. **Levy, A.** and Hickey, G., (1986B), "Erosion of corrosion-resistant surface treatments on alloy steels," Wear, Vol.108, pp. 61-79.

102. **Levy, A.V.** and Chik, p., (1983), "The Effects of Erodent Composition and Shape on the Erosion of Steel," Wear, Vol. 89, pp. 151-162.

103. **Levy, A.,** (1995), "Solid Particle Erosion and Erosion-Corrosion of Materials," ASM International, Materials Park, OH 44073-0002, U.S.A.

104. **Li, Chang-Jiu,** Wang Yu-Yue and Li, Hua (2004), "Effect of nano-crystallization of high velocity oxy fuel sprayed amorphous NiCrBSi alloy on properties of the coatings," Journal Vac. Sci. Technol. A, Vol. 22, No. 5, pp 2000-2004.

105. **Li Chang-Jiu,** Wang Yu-Yue and Li Hua,(2004), "Effect of nano-crystallization of high velocity oxy fuel sprayed amorphous NiCrBSi alloy on properties of the coatings," Journal Vac. Sci. Technol. A, Vol. 22, No. 5, pp 2000-2004.

106. **Li Ming, (1997),** "Study on Long-Term Oxidation and Hot Corrosion Behaviour of Gas Turbine Superalloys," Ph.D Thesis, University of Central Florida.

107. **Liangquan Shi,** (1993), "Accelerated Oxidation of Iron Induced by Na_2SO_4 Deposits in Oxygen at 750°C-A New Type Low-Temperature Hot Corrosion," Oxidation of Metals, Vol. 40, pp. 197-211.

108. **Lima, M.M.,** Godoy, C., Batista, J.C.A. and Modenesi, P.J.,(2003), "Toughness evaluation of HVOF WC–Co coatings using non-linear regression analysis," Mater. Sci. Eng. A, Vol. 357, pp. 337.

109. **Longa-Nava, Y.,** Zhang, Y. S., Takemoto, M. and Rapp, R. A., (1996), "Hot Corrosion of Nickel-Chromium and Nickel-Chromium-Aluminum Thermal-Spray Coatings by Sodium Sulfate-Sodium Metavanadate Salt," Corros., Vol. 52, pp. 680-689.

110. **Longa-Nava** and Takemoto, M., (1992), "High-Temperature Corrosion of Laser–Glazed Alloys in Na_2SO_4-V_2O_5," Corros., Vol. 48, pp. 599-607.

111. **Lowell1, Carl E.,**(1973), "Cyclic and isothermal oxidation behavior on some Ni-Cr alloys," Oxidation of metals, Vol. 7, pp. 95.

112. **Luer, K.R.,** DuPont, J.N., and Marder, A.R., (2000), "High Temperature Sulfidation of Fe_3Al Thermal Spray Coatings at 600 o C,"Corrosion, Vol. 56, pp. 189-198.

113. **Luthra,** K. L., (1985), "Kinetics of the Low Temperature Hot Corrosion of Co-Cr-Al Alloys," J. Electrochem. Soc., Vol. 132, No. 6, pp. 1293-98.

114. **Malik, A. U.,** Ahmad, R., Ahmad, S. and Ahmad S., (1992), "High Temperature Oxidation Behaviour of Nickel Aluminide Coated Mild Steel," Practical Metallography, Vol. 29, pp. 255-68.

115. **Matthews, A.,** Areley, R.J. and Holiday, P., (1998), "Futures Bright for Surface Engineering," Mater. World, Vol. 6, pp. 346-347.

116. **Mayoral, M.C.,** Andrés,J.M., Belzunce, J. and Higuera, V.,(2006), "Study of sulphidation and chlorination on oxidized SS310 and plasma-sprayed Ni–Cr coatings as simulation of hot corrosion in fouling and slagging in combustion," Corrosion Science, Vol .48, pp. 1319-1336.

117. **Meadowcroft, D.B.,** (1987), "High temperature corrosion alloys and coatings in oil- and coal-fired boilers," Mater. Sci. Eng., Vol. 88, pp. 313–320.

118. **Metals Handbook,** (1975), 'Failure analysis and Prevention,' Vol. 10, ASM Publication, Metals Park OH, USA.

119. **Miguel J.M.,**Guilemany J.M.,Vizcaino S., (2003), "Tribological study of NiCrBSi coating obtained by different processes," Tribology International, Vol. 36, pp. 181-187.

120. **Mingheng Li,** Dan Shi and Panagiotis D. Christofides,(2004), "Model-based estimation and control of particle velocity and melting in HVOF thermal spray," Chemical Engineering Science, Vol. 59, pp. 5647-5656.

121. **Miranda,J.C.,**Ramalho,A.,(2001), "Abrasion resistance of thermal sprayed composite coatings with a nickel alloy matrix and a WC hard phase. Effect of deposition technique and re-melting," Tribology Letters, Vol. 11, pp 37-48.

122. **Mishra, S.B.,** Prakash,S. and Chandra,K., (2006), "Studies on erosion behavior of plasma sprayed coatings on a Ni-based superalloy," Vol. 260, pp. 422 - 432

123. **Mishra S.B.,** (2006), "Development of Erosion-Corrosion Wear Resistant Coatings on Superalloys," Ph.D.Thesis, Met. & Mat. Engg. Dept., Indian Institute of Technology Roorkee, Roorkee.

124. **Misra,** A. K., (1986), "Mechanism of Na_2SO_4-Induced Corrosion of Molybdenum Containing Nickel-Base Superalloys at High Temperatures," J. Electrochem. Soc., Vol. 133, pp. 1029-37.

125. **Mohanty, M.,** Smith, R. W., Bonte, M. De, Celis, J. P. and Lugscheider, E., (1996), "Sliding wear behavior of thermally sprayed 75/25 Cr_3C_2/NiCr wear resistant coatings," Wear, Vol. 198, pp. 251-266.

126. **Moskowitz, L.N.,** (1993), "Application of HVOF thermal spraying to solve corrosion problems in the petroleum industry—an industrial note," J. Therm. Spray Technology., Vol. 2, pp. 21.

127. **Mukhopadhyay, R.,** Mandal, P.K., (1999), "Clinkering problem in 500MW unit of a pulverised coal based power station," R&D Journal (NTPC),Vol. 5, pp. 9-12.

128. **Murthy, J. K. N.,** Rao, D. S. and Venkataraman, B., (2001), "Effect of grinding on the erosion behavior of a WC–Co–Cr coating deposited by HVOF and detonation gun spray processes," Wear, Vol. 249, pp. 592-600.

129. **Natesan, K.,** (1993), "Applications of coatings in coal-fired energy systems," Surface and Coatings Technology, Vol. 56, pp. 185-197.

130. **Neilson, J.H.** and Gilchrist, A., (1968), "Erosion by a Stream of Solid Particles," Wear, Vol. 11, pp. 111.

131. **Nicholls J.R.**, (2000), "Designing Oxidation-resistant Coatings", JOM, Vol. 52, pp 28-35.

132. **Nicoll,A.R.**,(1982), "Self-fluxing coatings for stationary gas turbines," Thin Solid Films, Vol. 95, pp. 285-295

133. **Niranatlumpong,P.**, Ponton,C.B. and Evans,H.E.,(2000), "The Failure of Protective oxides on Plasma-Sprayed NiCrAlY Overlay Coatings," Oxidation of Metals, Vol. 53, pp. 241.

134. **Norton, J F**, Maier, M, and Bakker, W,(1999),"Corrosion of Heat Exchanger Alloys Exposed to Non equilibrate CO-based Sulfidizing Environment at 550°C," Paper No. 99069, NACE 99, San Antonio.

135. **Otero, E.**, Merino, M. C., Pardo, A., Biezma, M. V. and Buitrago, G., (1987), "Study on Corrosion Products of IN657 Alloy in Molten Salts," Proc. of 10th ICMC, Madras, India, Vol. IV, pp. 3583-91.

136. **Otero,E.**, Pardo,A., Pérez,F.J., Perosanz,F.J., Parra,A. and Maffiotte,C.A.,(1996), "Coating protection of several steels after their exposure at high temperature to oxygen and sulfur mixtures," Surface and Coatings Technology, Vol. 86-87,Part1, pp. 61-69.

137. **Palit,A.** and Mandal,P.K.,(1994), "Slagging and clinkering problem at vindhyachal super thermal power station," R&D Journal (NTPC),Vol.1, pp. 1-11.

138. **Paul, L.D.** and Seeley, R.R., (1991), "Oil Ash Corrosion-A Review of Utility Boiler Experience," Corrosion, Vol. 47, pp. 152-159.

139. **Pawlowski, L.**, (1995), "The Science and Engineering of Thermal Spray Coatings," Wiley, New York, 1995.

140. **Peters, K. R.**, Whittle, D. P. and Stringer, J., (1976), "Oxidation and Hot Corrosion of Nickel-Based Alloys Containing Molybdenum," Corros. Sci., Vol. 16, pp. 791-804.

141. **Pettit, F. S.** and Meier, G. H., (1984), "Oxidation and Hot corrosion of Superalloys," Superalloys 85 Eds. (1985), M. Gell, C. S. Kartovich, R. H. Bricknel, W. B. Kent, J. F. Radovich (Eds.), The Met. Soc. of AIME, Warrendale, Pensylvania, pp. 651-687.

142. **Pettit, F.S.,** (1977), "Design of structural alloys with high temperature corrosion resistance," Fundamental Aspects of Structural Alloy Design," New York: Plenum Press.

143. **Pettit, F. S.** and Giggins, C. S., (1987), "Hot Corrosion, Ch. 12," Superalloys II, Sims, C. T., Stollof, N. S. and Hagel, W. C. (Eds.), Wiley Pub., N. Y.

144. **Picas J.A.,** Forn A. and Matthäus G.,(2006), "HVOF coatings as an alternative to hard chrome for pistons and valves," Wear, Vol. 261, pp. 477-484.

145. **Pinder L.W.,**(1981), "Oxide Characterization for Service Failure Investigations," Corrosion Science, Vol. 21, pp. 749-763.

146. **Planche M.P.,** Liao H., Normand B. and Coddet C.,(2005), "Relationships between NiCrBSi particle characteristics and corresponding coating properties using different thermal spraying processes," Surface and Coatings Technology, Volume 200, pp. 2465-2473.

147. **Prakash, S.,** Singh, S., Sidhu, B. S. and Madeshia, A., (2001), "Tube Failures in Coal Fired Boilers," Proc. National Seminar on Advances in Material and Processing, IITR, Roorkee, India, pp. 245-253.

148. **Raask, E.** (1985), Mineral Impurities in Coal Combustion, Hemisphere publishing, Washington.

149. **Rajiv Asthana,** Ashok Kumar and Narendra B. Dahotre, (2006), "Coatings and Surface Engineering," Materials Processing and Manufacturing Science, 2006, pp. 313-395.

150. **Ramesh,C.S.,** Seshadri,S.K. and Iyer,K.J.L.,(1991), "A survey of aspects of wear of metals," Indian Journal of Technology, Vol. 29, pp. 179-185.

151. **Ramesh,C.S.,** Seshadri,S.K. and Iyer, K.J.L.,(1991), "Wear resistance of nickel-fly ash composite coatings," Wear, Vol. 145, pp. 189-195.

152. **Rapp, R. A.** and Goto, K. S., (1981), "The Hot Corrosion of Metals by Molten Salts," Sympos. Fused Salts, Eds. Braunstein, J. and Selman, J. R., The Electrochem. Soc., Pennington, N. J., pp. 159.

153. **Rapp, R. A.** and Zhang, Y. S., (1994), "Hot Corrosion of Materials: Fundamental Studies," JOM, Vol. 46, No. 12, pp. 47-55.

154. **Rapp.R.A.,**(1965), "Kinetics, microstructures and mechanism of internal oxidation, its effect and prevention in high-temperature alloy oxidation," Corrosion, Vol.21, pp. 382.

155. **Reid, W.T.,** (1971), External Corrosion and Deposits--Boilers and Gas Turbines, Elsevier.

156. **Roberge, Pierre R.,**(2000), Handbook of Corrosion Engineering, McGraw-Hill publication

157. **Rodríguez, J.,** Martín, A., Fernández, R. and Fernández, J. E., (2003), "An experimental study of the wear performance of NiCrBSi thermal spray coatings," Wear, Vol. 255, pp. 950-955.

158. **Rogers, P.M.,** Hutchings, I.M. and Little, J.A., (1995), "Coatings and surface treatments for protection against low-velocity erosion–corrosion in fluidized beds," Wear, Vol. 186/187, pp. 238–246.

159. **Ruff A.W.** and L.K. Ives,(1975), "Measurement of solid particle velocity in erosive wear, " Wear, Vol. 35, pp. 195-199.

160. **Sahraoui,** Nour-Eddine Fenineche, Ghislain Montavon and Christian Coddet,(2003), "Structure and wear behaviour of HVOF sprayed Cr_3C_2–NiCr and WC–Co coatings," Materials & Design, Vol. 24, pp. 309-313.

161. **Santorell, R.,** Sivieri, E., and Reggiani, R.C., (1989), "High-Temperature Corrosion of Several Commercial Fe-Cr-Ni Alloys under a Molten Sodium Sulphate Deposit in Oxidizing Gaseous Environments," Materials Science and Engineering A, Vol. 120, pp. 283.

162. **Saxena, D.,** (1986), "Effect of Zr and Y Addition on High Temperature Sulphidation Behaviour of Fe-15Cr-4Al," Ph.D. Thesis, Met. Mat. Engg. Dept., University of Roorkee, Roorkee, India.

163. **Schneider, K.,** Bauer, R., and Grunling,H.W.,(1978), "Corrosion and Failure Mechanisms of Coatings for Gas Turbine Applications," Thin Solid Films, Vol. 54, pp. 359-367.

164. **Schütze, M.,** Malessa, M., Rohr, V. and Weber, T.,(2006), "Development of coatings for protection in specific high temperature environments," Surface and Coatings Technology, Vol. 201, pp. 3872-3879 .

165. **Seiersten, M.** and Kofstad, P., (1987), "The Effect of SO$_3$ on Vanadate-Induced Hot Corrosion," High Temp. Technol., Vol. 5, pp. 115-122.

166. **Seong Byeong Geun,** Young Hwang Soon and Young Kyoo Kim, (2000), "High-temperature corrosion of recuperators used in steel mills," Surface and Coatings Technology, Vol. 126, pp. 256-265.

167. **Seybolt, A.U.,** (1968), "Contribution to the study of Hot Corrosion," Transaction of the Metallurgical Society of AIME, Vol. 242, pp. 1955-1961.

168. **Seybolt, A.U.,** (1970), High Temperature Metallic Corrosion by Sulfur and its Compound, Electrochemical Society, New York, pp. 160.

169. **Sharma, R. N.,** (1996), "Hot Corrosion Behaviour of Iron- and Nickel-Base Superalloys in Salt Environments at Elevated Temperatures," Ph. D. Thesis, Met. Mat. Engg. Deptt., University of Roorkee, Roorkee, India.

170. **Sheldon, G.L.** and Kanhere, A., (1972), "An Investigation of Impingement Erosion Using Single Particles," Wear, Vol. 21, pp. 195-209.

171. **Sheldon, G.L.** and Finnie, I., (1966), "The Mechanism of Material Removal in the Erosive Cutting of Brittle Materials," Trans. ASME, 88B, pp. 393-400.

172. **Shipway, P.H.,** and Wirojanupatump, S., (2002), "The role of lubrication and corrosion in abrasion of materials in aqueous environments," Tribol. Int., Vol. 35, pp. 661.

173. **Shipway, P.H.,** and Hutchings, L.M., (1996), "The role of particle properties in the erosion of brittle materials," Wear, Vo. 193, pp. 105-113.

174. **Shores, D. A.,** (1983), "New Perspectives on Hot Corrosion Mechanisms," High Temperature Corrosion, R.A. Rapp (Ed.), NACE, Houston, Texas.

175. **Shui, Z.R.,** and Wang, B. Q., (1990), "Erosion of protective coatings," surface and Coating Technology, Vol. 43/44, pp. 875 – 887

176. **Sidhu,T.S.,** Prakash,S. and Agrawal, R.D., (2006E), "Characterisations of HVOF sprayed NiCrBSi coatings on Ni- and Fe-based superalloys and evaluation of cyclic oxidation behavior of some Ni-based superalloys in molten salt environment," Thin Solid Films, Vol. 515, pp. 95-105.

177. **Sidhu,T.S.**, Prakash,S. and Agrawal,R.D.,(2006F), "Characterisation of NiCr wire coating on Ni- and Fe-based superalloys by the HVOF process," Surface and coating technology, Vol. 200, pp. 5542-5549.

178. **Sidhu, T.S.**, (2006), "Studies on the hot corrosion behaviour of HVOF coatings on some Ni- and Fe-based superalloys", Ph.D. Thesis, Met. & Mat. Engg. Dept., Indian Institute of Technology Roorkee, Roorkee.

179. **Sidhu, T.S.**, Prakash S. and Agrawal R.D., (2006), "Performance of High Velocity Oxyfuel-sprayed coatings on an Fe-based superalloy in Na_2SO_4-60%V_2O_5 environment at 900°C, Part I Characterization of the coatings," Journal of materials Engineering and Performance,Vol. 15, pp. 122-129.

180. **Sidhu, T.S.**, Prakash, S., and Agrawal, R.D., (2006D), "Hot corrosion studies of HVOF NiCrBSi and Stellite-6 coatings on a Ni-based superalloy in an actual industrial environment of a coal fired boiler," Surface and Coatings Technology, Vol. 201, pp. 1602-1612.

181. **Sidhu Buta Singh**, (2003A), "Studies on the Role of Coatings in Improving Resistance to hot corrosion and degradation," Ph.D. Thesis, Met. & Mat. Engg. Dept., Indian Institute of Technology Roorkee, Roorkee.

182. **Sidhu Buta Singh** and Prakash, S.,(2003B), "Evaluation of the corrosion behaviour of plasma-sprayed Ni_3Al coatings on steel in oxidation and molten salt environments at 900°C," Surface and Coatings Technology, Vol. 166, pp. 89-100.

183. **Sidhu Buta Singh** and Prakash, S., (2006B), "Erosion-corrosion of plasma as sprayed and laser remelted Stellite-6 coatings in a coal fired boiler," Wear, Vol. 260, pp. 1035-1044.

184. **Sidhu Buta Singh** and Prakash, S., (2006C), "Evaluation of the Behavior of Shrouded Plasma Spray Coatings in the Platen Superheater of Coal-Fired Boilers," Metallurgical and Materials Transactions, Vol. 37A, pp. 1927-1936.

185. **Sidhu Buta Singh** and Prakash, S., (2005B), "High Temperature Oxidation Behaviour of NiCrAlY Bond Coats and Stellite-6 Plasma Sprayed Coatings," Oxidation of Metals, Vol. 63, pp. 241.

186. **Sidhu Buta Singh** and Prakash S., (2005A), "Degradation Behaviour of Ni₃Al Plasma Sprayed Boiler Tube Steels in Actual Conditions of Energy Generation System," Journal of Materials Engineering and Performance, Vol. 14, pp. 356-362.

187. **Sidhu Buta Singh** and Prakash S.,(2006A), "Performance of NiCrAlY, Ni–Cr, Stellite-6 and Ni₃Al coatings in Na₂SO₄–60% V₂O₅ environment at 900°C under cyclic conditions," Surface and Coatings Technology, Vol. 201, pp. 1643-1654.

188. **Sidhu Hazoor Singh**, Buta Singh Sidhu and S. Prakash,(2006G), "The role of HVOF coatings in improving hot corrosion resistance of ASTM-SA210 GrA1 steel in the presence of Na₂SO₄–V₂O₅ salt deposits, Surface and Coatings Technology, Vol. 200, pp. 5386-5394.

189. **Sidhu Hazoor Singh**, Buta Singh Sidhu and S. Prakash, (2007), "Solid particle erosion of HVOF sprayed NiCr and Stellite-6 coatings," Surface and Coatings Technology, Vol 202, pp. 232-238.

190. **Sidky, P.S.**, Hocking, M.G., (1999), "Review of Inorganic Coatings and Coating Processes For Reducing Wear and Corrosion," Brit. Corros. J., Vol. 34, pp. 171-183.

191. **Sidky, P.S.** and Hocking, M.G., (1987), "The Hot Corrosion of Ni-Based Ternary Alloys and Superalloys for Application in Gas Turbines Employing Residual Fuels," Corros. Sci., Vol. 27, pp. 499-530.

192. **Simons, E.L.**, Browning, G.V. and Liebhafsky, H.A., (1955), "Sodium Sulfate in Gas Turbines," Corrosion, Vol. 11, pp. 505-514.

193. **Singh, H.**, Puri, D. and Prakash, S., (2005A), "Corrosion Behaviour of Plasma Sprayed Coatings on a Ni-base Superalloy in Na₂SO₄-60%V₂O₅ Environment at 900°C," Metall. Mater. Trans. A, Vol. 36, pp. 1007-1015.

194. **Singh, I.B.**, (2003), "Corrosion and Sulphate Ion Reduction Studies on Ni and Pt Surfaces in with and with out V₂O₅ in (Li,Na,K)₂SO₄ Melt," Corros. Sci., Vol. 45, pp. 2285-2292.

195. **Singh H.**, D. Puri and S. Prakash, (2006), "High Temperature Oxidation Behaviour of Plasma Sprayed NiCrAlY coatings on Ni-Based Superalloys in Air," Trans. Indian Inst. Met., Vol. 59, pp. 215-227.

196. **Singh H.**, D. Puri and S. Prakash,(2005B), "Some studies on hot corrosion performance of plasma sprayed coatings on a Fe-based superalloy," Surface and Coatings Technology, Vol. 192, pp. 27-38.

197. **Smeltzer, C.E.**, Gulden, M.E., and Compton, W.A., (1970), "Mechanism of Metal Removal by Impacting Dust Particles," Journal of Basic Engineering, pp. 639-646.

198. **Sobolev, V.V.**, Guilemany, J.M., and Nutting, J., (2004), "High Velocity Oxy-Fuel Spraying, Theory, Structure-Property Relationships and Application," Maney Publishing.

199. **Soderberg, S.**, Hogmark, S., Engman, U., Swahn, H.,(1981), "Erosion classification of materials using a centrifugal erosion tester," Tribology International, pp. 333-343.

200. **Solomon, N.G.**, (1998), "Erosion-resistant coatings for fluidised bed boilers," Mater. Performance, Vol. 37, pp. 38–43.

201. **Srikanth, S.**, Ravikumar, B., Das, S. K., Gopalakrishna, K., Nandakumar, K. and Vijayan, P., (2003), "Analysis of Failures in Boiler Tubes due to Fireside Corrosion in a Waste Heat Recovery Boiler," Engg. Failure Analysis, Vol. 10, pp. 59-66.

202. **Srivastava, S.C.**, and Godiwalla, K.M., (1997), "Fuel ash corrosion of boiler and superheater tubes," Journal of Materials Science, Vol. 32, pp. 835-849.

203. **Stott, F. H.**, Wet, D. J. De and Taylor, R., (1994), "The Degradation Resistance of Thermal Barrier Coatings to Molten Deposits at very High Temperatures," Trans. Mater. Res. Soc. Japan., Vol. 14A, pp. 135-140.

204. **Stott, F. H.**, (1998), "The Role of Oxidation in the Wear of Alloys," Trib. Int., Vol. 31, pp. 61-71.

205. **Strafford, K.N.**, and Datta, P.K.,(1989), "Design of sulphidation resistant alloys," Mater. Sci. Technology, Vol. 5, pp. 765.

206. **Stringer John**, (1998), "Coatings in the electricity supply industry: past, present, and opportunities for the future," Surface and Coatings Technology, Vol.108-109, pp.1-9.

207. **Stringer John** (1987A), "Role of Coatings in Energy-producing Systems: An Overview," Vol .87, pp. 1-10

208. **Stringer John** (1995), "Practical experience with wastage at elevated temperatures in coal combustion systems," Wear, Vol. 186-187, Part 1, pp 11-27.

209. **Stringer John.**, (1987B), "High Temperature Corrosion of Superalloys," Mater. Sci. Technol., Vol. 3, pp. 482-493.

210. **Stroosnijder, M. F.**, Mevrel, R. and Bennet, M. J., (1994), "The Interaction of Surface Engineering and High Temperature Corrosion Protection," Mater. High Temp., Vol. 12, pp. 53-66.

211. **Stultz, S.C.** and Kitto, J.B., Editors, (1992), "Steam: Its Generation and Use," Babcock and Wilcox, Barberton, OH.

212. **Suckling M.** and Allen C.,(1995), "The design of an apparatus to test wear of boiler tubes," Wear, Vol. 186-187, pp. 266-272.

213. **Sundararajan,T.**, Kuroda,S. and Abe,F.,(2004). "Steam oxidation studies on 50Ni-50Cr HVOF coatings on 9Cr-1Mo steel: Change in structure and Morphology across the Coating/Substrate interface," Mater. Trans., Vol. 45, pp. 1299-1305.

214. **Sundararajan, T.**, Kuroda,S., Itagaki,T. and Abe,F.,(2003), "Steam oxidation Resistance of Ni-Cr Thermal Spray Coatings on 9Cr-1Mo steel," ISIJ International, 43 (1) pp. 95-103.

215. **Sundararajan, G.**, (1995), "The solid particle erosion of metallic materials: The rationalization of the influence of material variables," Wear, Vol. 186-187, pp.129-144.

216. **Sundararajan, T.** and Roy, M. (1997), "Solid particle erosion behavior of metallic materials at room and elevated temperatures," Tribology International, Vol. 30, pp. 339-359.

217. **Sundararajan, G.**, (1984), "The effect of temperature on solid particle erosion," Wear, Vol. 98, pp. 141-149.

218. **Sundararajan G.**, (1991), "An Analysis of the Erosion-Oxidation Interaction Mechanisms," Wear, Vol. 145, pp. 251-282.

219. **Tani, K.**, Harada, Y., Kobayashi, Y., (1998), "Unusual application of plasma-sprayed coatings for boiler tubes in oil-fired boilers," Proceedings of the 15th International Thermal Spray Conference, Niza, ASM International, pp. 951–956.

220. **Tilly, G.P.**, (1969), "Erosion caused by Airborne Particles," Wear, Vol. 14, pp. 63-79.

221. **Tilly, G.P.,** (1973), "A Two Stage Mechanism of Ductile Erosion," Wear, Vol. 23, pp. 87-96.

222. **Tiwari, S. N.,** (1997), "Investigations on Hot Corrosion of Some Fe-, Ni- and Co-Base Superalloy in Na_2SO_4-V_2O_5 Environment under Cyclic Conditions," Ph. D. Thesis, Met. Mat. Engg. Deptt., University of Roorkee, Roorkee, India.

223. **Tiwari, S. N.** and Prakash, S., (1997), "Studies on the Hot Corrosion Behaviour of Some Superalloys in Na_2SO_4-V_2O_5," Proc. of SOLCEC, Kalpakkam, India, pp. C33.

224. **Tiwari, S. N.** and Prakash, S., (1996), "Hot Corrosion Behaviour of an Iron-Base Superalloy in Salt Environment at Elevated Temperatures," Proc. of Sympos. Metals and Materials Research, Indian Institute of Technology Madras, Madras, pp. 107-117.

225. **Uusitalo, M.A.,** Vuoristo, P.M.J. and Mantyla, T.A., (2003), "High Temperature Corrosion of Coatings and Boiler Steels in Oxidizing Chlorine-containing Atmosphere," Mater. Sci. Eng. A-Struct., Vol. 346, pp. 168-177.

226. **Uusitalo, M.A.,** Vuoristo, P.M.J., and Mantyla, T.A., (2002A), "High temperature corrosion of coatings and boiler steels in reducing chlorine-containing atmosphere," Surface and coating technology, Vol. 161, pp. 275-285.

227. **Uusitalo, M.A.,** Vuoristo, P.M.J., and Mäntylä, T.A., (2002B), "Elevated temperature erosion–corrosion of thermal sprayed coatings in chlorine containing environments," Wear, Vol. 252, pp. 586-594.

228. **Vicenzi, J.,** Villanova, D.L., Lima, M.D., Takimi, A.S., Marques, C.M. and Bergmann, C.P., (2006), "HVOF-coatings against high temperature erosion (∼300 °C) by coal fly ash in thermoelectric power plant," Materials & Design, Vol. 27, pp 236-242.

229. **Wang,H.,** Xia,W. and Jin,Y.,(1996), "A study on abrasive resistance of Ni-based coatings with a WC hard phase," Wear, Vol. 195, pp. 47–52.

230. **Wang, B.Q.,** and Geng, G.Q., (1990), "Erosion-Corrosion of Thermal Spray Coatings," Surface and Coatings Technology, Vol. 43/44, pp. 859.

231. **Wang, B.,** Gong, J., Wang, A.Y., Sun, C., Huang, R.F., Wen, L.S.,(2002A), "Oxidation behaviour of NiCrAlY coatings on Ni-based superalloy," Surface and Coatings Technology 149, pp. 70–75.

232. **Wang, B.,**(1997), "The erosion–corrosion behaviour of thermal-sprayed coatings in fluidized bed combustor systems," Surface Modification Technologies X, The Institute of Metals, London, England, pp. 265–279.

233. **Wang, D.,** (1988), "Corrosion Behavior of Chromized and/or Aluminized 21/4Cr-1Mo Steel in Medium-BTU Coal Gasifier Environments," Surf. Coat. Technol., Vol. 36, pp. 49-60.

234. **Wang, B.Q.,** (1999), "Chromium–titanium carbide cermet coating for elevated temperature erosion protection in fluidized bed combustion boilers," Wear, Vol .225-229, pp. 502-509.

235. **Wang, B.Q.,** and Luer, K.,(1994), "The relative erosion-corrosion resistance of commercial thermal sprayed coatings in a simulated circulating fluidized bed combustor environment," Proceedings of the 7th National Spray Conference 20–24 June, Boston, Massachusetts, pp. 115–120.

236. **Wang, C.J.** and Lin, J.S., (2002B), "The oxidation of MAR M247 superalloy with Na_2SO_4 coating," Materials Chemistry and Physics, Vol. 76, pp. 123-129.

237. **Wang Jun,** Ke Li, Da Shu, Xin He, Baode Sun, Qixin Guo, Mitsuhiro Nishio and Hiroshi Ogawa,(2004), "Effects of structure and processing technique on the properties of thermal spray WC–Co and NiCrAl/WC–Co coatings," Materials Science and Engineering A, Vol. 371, pp. 87-192

238. **Warren, E.J.M.,** (1992), "Thermal Spraying for Boiler Tube Protection," Welding and Metal Fabrication, Vol. 60, pp. 25-35.

239. **Wensink, H.,** and Elwenspoek, M.C.(2002) "A closer look at the ductile-brittle transition in solid particle erosion," Wear, Vol. 253, pp. 1035-1043.

240. **Weulersse-Mouturat,K.,**Moulin,G.,Billard,P. and Pierotti,G.,(2004), "High Temperature Corrosion of Superheater Tubes in Waste Incinerators and Coal-Fired Plants," Mater.Sci.Forum, Vol. 461-464, pp. 973-980.

241. **Wright, I.G.,** (1987), "High-Temperature Corrosion," in 'Metals Handbook,' Vol. 13, 9th Ed., Metals Park, ASM, pp. 97-103.

242. **Wu,Y.N.,** Wang, Q.M., Ke, P.L., Sun, C., Gong, J., Wang, F.H., and Wen, L.S., (2006), "Evaluation of arc ion plated NiCoCrAlYSiB coatings after oxidation at 900–1100°C," Surface and Coatings Technology, Vol. 200, pp. 2857-2863.

243. **Wu, X.**, Weng, D., Chen, Z. and Xu, L., (2001), "Effects of Plasma-Sprayed NiCrAl/ZrO$_2$ Intermediate on the Combination Ability of Coatings," Surf. Coat. Technol., Vol. 140, pp. 231-37.

244. **Wu, Y.** and Niu, Y.,(2005),"Effect of silicon additions on the oxidation of a Ni–6 at.%Al alloy at 1273 K," Scripta Materialia, Vol. 53, pp. 1247-1252.

245. **Yamada,K.**, Tomono,Y., Morimoto,J., Sasaki,Y., and Ohmori,A.,(2002), "Hot corrosion behavior of boiler tube materials in refuse incineration environment," Vacuum, Vol.65, No. 3-4, pp. 533-540.

246. **Yu, S.**, Zhu,S., Wei,D., and Wang,F.,(2007), "Oxidation and H2O/NaCl-induced corrosion behavior of sputtered Ni–Si coatings on Ti6Al4V at 600–650 °C," Surface and Coatings Technology, Vol. 201, pp. 7530-7537.

247. **Yuuzou Kawahara** (2006), "Application of high temperature corrosion-resistant materials and coatings under severe corrosive environment in waste-to-energy boilers," Journal of Thermal Spray Technology, Vol. 16 (2), pp. 202-213.

248. **Zahs, A.**, Spiegel, M., and Grabke, H.J.,(2000), "Chloridation and oxidation of iron, chromium, nickel and their alloys in chloridizing and oxidizing atmospheres at 400-700°C," Corros. Sci., Vol. 42, pp. 1093.

249. **Zambelli, G.** and Levy, A.V., (1981), "Particulate Erosion of NiO Scales," Wear, Vol. 68, No.3, pp. 305-331.

250. **Zhang, Y.S.** and Rapp, R.A., (1987), "Solubilities of CeO$_2$, HfO$_2$ and Y$_2$O$_3$ in Fused Na$_2$SO$_4$-30 mol% NaVO$_3$ and CeO$_2$ in Pure Na$_2$SO$_4$ at 900^{0}C," Corros Vol. 43, No.6, pp. 348-352.

251. **Zhenyu Liu** and Wei Gao, (1998), "Oxidation Behaviour of Microcrystalline Ni-Cr-Al Alloy Coatings at 900°C," Scripta Materialia, Vol. 38, pp. 877-885.